STATIC AND DYNAMIC PERFORMANCE OF RC BRIDGE BENTS WITH ARCHITECTURAL-FLARED COLUMNS

REPORT No. CCEER-03-08

Suhas S. Chandane
David. H. Sanders
M. Saiid Saiidi

Center for Earthquake Engineering Research
Department of Civil Engineering
University of Nevada
Reno, Nevada 89557

ABSTRACT

A study was performed on architectural-flared column bents. The objective was to evaluate the static and dynamic performance of the bents. The unique aspect of the bents is a gap at the top of the flares to separate the flares from contributing structurally. The project concentrated on the effect of the gap width at the top of the column section. The study included both experimental and analytical investigations. Two specimens were tested statically that had been partially tested on a shake table in a previous study. The objective of the static tests was to evaluate the performances of the bents till failure. One specimen had columns that were flexure dominated while the other had shear dominated columns. Each column had same reinforcement except for the flare transverse reinforcement. A newly constructed specimen was tested to evaluate the performance of the bents with twice the gap that had been used in the previous study. The flare had the minimum longitudinal and transverse reinforcement. A non-linear finite element analysis program DIANA was used to perform the analytical study. The results were also compared with the results of programs like RCMC, RC-Shake and wFRAME. The performances of the specimens were compared. The behavior of the specimens during testing was discussed. Design recommendations were developed.

ACKNOWLEDGEMENTS

TABLE OF CONTENTS

iv

LIST OF TABLES

LIST OF FIGURES

1. INTRODUCTION

1.1 General

The state of California has a large number of highways bridges; many of them have flared columns because they are aesthetically pleasing. During the 1994 Northridge Earthquake, it was observed that these columns can perform poorly (Fig. 1.1).

The bridge shown in Figs. 1.1 and 1.2 was designed in 1972, after the San Fernando Earthquake. It had seismic detailing including closely spaced spiral hoops. The columns were approximately 7200 mm (24 ft) tall and 1800 m (6 ft) wide with an aspect ratio of 4:1. Columns had approximately 3600 mm (12 ft) tall flares at the top. The flares were designed as a non-structural member and were intended to spall off during an earthquake. The plastic hinge was intended to form at the top of the column after spalling of the flare. During the 1994 earthquake, instead of the plastic hinges forming at the top they shifted to the base of the flares. Due to lowering of plastic hinge, the column behaved like a much shorter column, resulting in an increased shear demand. This behavior was not included in the design and led to brittle shear column failures. The flares had minimum longitudinal reinforcement and minimum transverse reinforcement but did not fail during the earthquake. Studies after the earthquake showed that these flares essentially behave as structural flares under both static and dynamic loading[2, 16].

Since the flare behaved as a structural member, it increased the column flexural capacity. Caltrans has developed new details to keep flares from contributing to the columns capacity. Flares are separated from the bent cap by providing a gap between the top of flare and the beam bottom surface (Fig. 1.3). The following points summarize the Caltrans[4] design provisions:

- Existence of flare is ignored in analysis and design of all major bent elements. Only the column core should be considered.
- Typically the thickness of the flare gap shall be 50 mm (2 inches). However, if significant relative rotation between the cap and the column is expected, then the required gap thickness to accommodate this rotation without gap closure should be calculated and provided.
- The longitudinal flare reinforcement is nominal. The maximum spacing between longitudinal flare reinforcement shall not exceed 450 mm (18 inches) and the spacing shall not be less than 150 mm (6 inches).
- The transverse flare reinforcement ratio in the upper 1/3 of the flare height is ρ_h=0.45%±0.05 while that ratio for the lower 2/3 of the flare height is ρ_h=0.075%±0.025.

Where;

$$\rho_h \quad = 2\,A_b\,/\,s\,D,$$

s   = Tie spacing,

D   = Diameter of the non-flared part of the column, and

A_b = Area of ties.

1.2 Previous Work Done

1.2.1 Previous Work Done on Single Columns

The initial research done on flared columns with a gap at the top of the flares was done at the University of California, San Diego, by Sanchez et al[2]. All models were forty-percent scale. Ten models were tested. In the first phase of testing, four specimens were models of the Mission Gothic undercrossing of SR-118 in Los Angeles County. In the second phase of testing, four models with light flare reinforcement and gaps at the top of the flare were tested. In the third phase of testing, two models were tested with increased transverse reinforcement in the flares and gaps to keep the damage level to the acceptable limits even at large seismic drifts. Models in first phase of testing showed significant stiffness and strength because of the column flares. The plastic hinges were shifted away from the top of the column to the base of the flare. This increased the shear and caused failure at a lower ductility and drift than was originally designed. In some specimens the gap was not wide enough to prevent closer. The gap closed and the flares were pushed away from the column core. The flare concrete was crushed but it did not affect the overall performance of the specimens. The specimens showed good ductility with a lower level of shear force development than the specimens without a gap.

In specimens with wide gaps, the gap did not close and had lower level of damage. The only damage was due to the large tension force developed in the flare as the flare pulled away from the core. The damage kept on reducing with increased amount of transverse reinforcement in the flares. The ductility and the capacities of the specimens with gaps were close to each other. All the specimens with a gap failed due to the flexural failure in column core at the gap, which was the plastic hinge location.

1.2.2 Previous Work Done on Two-Column Bents

Research was done at the University of Nevada, Reno, by Nada et al. to evaluate the dynamic performance of the two-column bents with flared columns and a gap at the top of the flare[16]. Three 0.18-scale models with the same gap thickness were tested. Two models were taller with high flexural demand. The first model had the transverse flare reinforcement specified in the current Caltrans recommendations and was designated as LFCD1. The second model had minimum transverse flare reinforcement throughout the flare height and was designated as LFCD2. The third model was shorter in height with high shear demand. This model had minimum transverse reinforcement in the flare and was designated as SFCD2.

2

The gap thickness was 9.53 mm (0.375 in) in all specimens. This is equivalent to 50 mm (2.0 in) in the prototype. The specimens were designed as strong beam weak column with a two-way hinge at the base of the columns. LFCD1 and LFCD2 had clear column height of 1626 mm (64.0 in) and SFCD2 had 991 mm (39.0 in). The behaviors of LFCD1 and LFCD2 were basically the same. Figs. 1.4 and 1.5 show the load-displacement relationship for LFCD1 and LFCD2, respectively. The difference in transverse flare reinforcement showed only a slight effect through a slight decrease in post-peak strength in the specimen with less flare reinforcement. Fig. 1.6 shows the load-displacement relationship for SFCD2. All the specimens showed gap closure at low levels of ductilities. The gap closure caused increase in the lateral force of the structure, resulting in damaging the cap beam. The ultimate displacements shown in the figures are the displacement at which testing was stopped and not the failure displacement. All specimens reached high ductility levels but were not able to be fully tested because of reaching capacity limits of the shake table.

1.3 Objectives

The objectives of this research can be summarized as follows.

1. Since it was not possible to fully test the LFCD1 and SFCD2 bents during the Nada et al. study, there was desire to observe the post-peak performance of flared column bents with gaps using static tests.

2. The impact of the gap is very significant; therefore there is a need to see the impact of an increased gap size on the bent performance.

1.4 Scope of Work

The first objective was achieved by performing cyclic static tests on LFCD1 and SFCD2 until failure. The static testing of LFCD1 and SFCD2 were designated as LFCD1S and SFCD2S, respectively.

The second objective was achieved by constructing a new model that was the same as SFCD2 with twice the flare gap thickness, 19.05 mm (0.75 in). In addition the cap beam skin reinforcement was changed to be more representative of current design. The beam skin reinforcement was distributed instead of being concentrated. This specimen was designated as SFCD3. It was tested on the shake table using the Sylmar record of the 1994 Northridge Earthquake. All the tests were conducted at Large-Scale Structures Laboratory at the University of Nevada, Reno.

1.5 Document Layout

This document contains five more chapters. The following is a list with brief description of each chapter.

- Chapter 2 "Experimental Method and Tests Setup" contains construction process, specimen details, description of the test setup and testing program.

- Chapter 3 "Testing Results for SFCD3" describes testing procedure, processed data and basic results for SFCD3.

- Chapter 4 "Testing and Results for LFCD1S and SFCD2S" describes testing procedure, processed data and results with comparisons to the shake table test results for LFCD1S and SFCD2S.

- Chapter 5 "Discussion of Results" compares and discusses the results of all the specimens.

- Chapter 6 "Summary, Conclusions and Recommendation" summarizes the work done in this research, describes the important findings and provides recommendations for design.

2. EXPERIMENTAL METHOD AND TEST SETUP

2.1 Introductory Remarks

This chapter describes the development of three 0.18-scale models of two-column bents. Two of these were constructed and tested dynamically by Nada et al.[16] and were statically tested in this project (LFCD1S and SFCD2S). The third specimen was designed, constructed and tested using a shake table (SFCD3).

2.2 Development of Specimens

The three models tested were SFCD3, SFCD2S, and LFCD1S (Figs. 2.1 through 2.3). LFCD1S had column clear height of 1626 mm (64.0 in), with the flare confinement detail as described in the Caltrans Seismic Design Criteria (Dept. of California Transportation)[4]. SFCD2S and SFCD3 had a clear column height of 991 mm (39.0 in) with lower confinement reinforcement ratio extended along the entire flare height. LFCD1S and SFCD2S were tested statically (Refer to section 1.2.2). There are two differences between SFCD2S and SFCD3 (Figs. 2.1 and 2.2). SFCD3 had a 19.0 mm (0.75 in) gap at the beam-column joint with distributed skin reinforcement in the beam, compared to 9.5 mm (0.38 in) gap at the beam-column joint with only one reinforcement bar as skin reinforcement in SFCD2S (Figs. 2.1 and 2.2). The gap was doubled with the anticipation that the gap would not close during testing. The skin reinforcement was distributed to be more representative of actual design.

2.2.1 Columns

All the columns had a 305 mm (12.0 in) diameter (Figs. 2.1 through 2.3). The columns were spaced 2718 mm (107.0 in) apart from each other. There were 14 main reinforcement bars, 12.7-mm diameter (# 4) bars, with a reinforcement ratio of approximately 2.5 %. The main reinforcement had hooks at the column base and extended 387.0 mm (15.2 in) inside the cap-beam at the top. The spiral reinforcement was 5.0 mm (0.19 in) in diameter with 31.0 mm (1.25 in) spacing.

Flare reinforcement was also provided. The longitudinal reinforcement consisted of 12 wires (4.0 mm (0.15 in) in diameter), with a maximum 102 mm (4.0 in) transverse spacing at the top of the column and 36.0 mm (1.4 in) spacing at the bottom of the flare. The total flare length was 915 mm (36.0 in). The top width of the flare was 635 mm (25.0 in) and 305 mm (12.0 in) at the base in the strong direction of the bent, which was equal to the diameter of this column. In the transverse direction the width of the section was 305 mm (12.0 in) throughout the column. The lateral reinforcement was 4.0 mm (0.15 in) diameter throughout the flare. In LFCD1S the top one-third of the flare had hoop spacing 28 mm (1.1 in),

while bottom two-third had 97 mm (3.8 in) (Fig. 2.3). For SFCD2S and SFCD3 the spacing was 97 mm (3.8 in) throughout the flare height (Figs. 2.1 and 2.2).

2.2.2 Beam

The beam section was rectangular. The width was 406 mm (16.0 in), and the depth was 457 mm (18.0 in) (Figs. 2.1 through 2.3). The beam was 4394 mm (173.0 in) long with an 838 mm (33.0 in) overhang on both sides. The top reinforcement of the beam was six, 15.9-mm diameter (# 5) bars. The bottom reinforcement was six, 12.7-mm diameter (# 4) bars. Both sets had 90 degrees hooks that were 305 mm (12.0 in) long at the end of the beam. The skin reinforcement was one 12.7-mm diameter (# 4) bar on each face of the beam for LFCD1S and SFCD2S. In SFCD3 it was six bars of 5.0 mm (0.2 in) diameter on each face.

The shear reinforcement varied along the length of the beam. In the south overhang (left side in the figure) and in the joint, 9.5 mm diameter (# 3) ties at 102 mm (4.0 in) were provided. The total beam length covered by these ties was 1143 mm (45.0 in). Between south and north beam-column joints over a length 2108 mm (83.0 in), 5.0-mm (0.2 in) diameter ties were provided at 102 mm (4.0 in). In the north beam-column joint, 9.5-mm diameter (# 3) ties at 102 mm (4.0 inch) were provided. In the north overhang, 9.5-mm diameter (# 3) ties at 76 mm (3.0 in) were provided. North end of the beam was connected to the mass rig for the shake table testing and was connected to an actuator in the static testing. To make north end stronger, shorter spacing of ties was provided. U clips were provided as horizontal shear reinforcement in the beam-column joint in the weak direction, which consisted of 18 sets of two U clips inserted from each side face of the beam with 9 sets at each beam-column joint. The set of clip was provided as 3 rows each in the vertical and horizontal directions.

On each end face of the beam four 25 mm (1.0 in) diameter threaded rods were provided for connecting the mass-rig to the bent (Fig. 2.1) or to the end plate of the actuator.

2.2.3 Hinge

The bottom hinge of the column consisted of four, 12.7-mm diameter (# 4) bars dowels (Figs. 2.1 through 2.3). The dowels extended 254 mm (10.0 in) above the footing surface into the column. The dowels had 90 degrees hooks at the bottom. These dowels were surrounded by spiral wire of 4.9 mm (0.192 inch) diameter with spacing of 57 mm (2.3 inch). This spiral was provided throughout the length of dowel bars.

6

2.2.4 Footing

The behavior of the bent along with bottom hinge was the focus of the study. Therefore, the footing was over-designed to avoid damage and to remain rigid. The footing dimensions were 4267 mm (168.0 in) long by 1829 mm (72.0 in) wide by 711 mm (28.0 in) high (Fig. 2.1). Mats of reinforcement on the top and bottom consisted of 22.2 mm diameter (# 7) bars at 152 mm (6.0 in) on center. Vertical 9.5-mm diameter (#3) bars were placed at every alternate joint of longitudinal reinforcement as shear reinforcement. For fixing the specimen to the table, 15 prestressing bars were used. The bars were passed through 76-mm (3.0 in) diameter vertical holes in the footing aligned with the threaded anchor holes of the table (Fig. 2.4).

2.3 Material Properties and Construction

The prototype concrete was 27 MPa (4.0 Ksi), and the reinforcement was 414 MPa (60 Ksi). Materials used in the model were chosen to match those of prototype. Tension tests were performed on the reinforcement prior to use in the models to verify their material properties. Fig. 2.5 shows the stress-strain relationship for reinforcement bars used. The results for the reinforcement in the specimens are summarized in Table 2.1. A 28-day strength specified for concrete in the specimens was between 27 MPa (4.0 Ksi) to 35 MPa (5.0 Ksi) with specified aggregate size of 9 mm (3/8 in). Table 2.2 summarizes the mix design.

First the footing was cast, and then the columns followed by the beam. The compression tests were done on standard 152 x 305 mm (6 x 12 in) cylinders at 7 and 28 days as well as testing day. The results for footing, column and beam are shown in Table 2.3. Table 2.4 shows the concrete and reinforcement properties for LFCD1S and SFCD2S.

2.4 Test Setup

There were two test-setups: one for the shake table testing and the other for the static testing (Figs. 2.6 and 2.7). A pair of steel frames consisting of two columns and beam was used to support the structures after failure and is shown in the Figs. 2.6 and 2.7. For the static tests, wheels were extended from the frame to the bent beam to hold it transversely. In the shake table test steel box-sections were attached to the bottom of the cap-beam. They extended from just above one supporting frame beam to the other supporting frame to hold the specimen in case of collapse. Following sections describes each setup separately.

2.4.1 Shake Table Test Setup for SFCD3

The specimens were tested using a 4.3 x 4.4 m (14.0 x 14.5 ft) shake table. The specimen was tied to the table with prestressing bars that went through the 15

holes provided in the footing. Lead was used to provide the majority of the axial and inertia load. The lead was placed inside the steel buckets (Fig. 2.8). A total 12 buckets were used. The total mass of these buckets was 222 KN (50 Kips). The total axial load was 400 KN (90 Kips) and caused an axial force in the columns equal to 0.1 f'c Ag. Part of the axial load was applied through the vertical rams. Rams were connected to a spreader beam mounted on the top of beam over the beam-column-joint. The total axial load applied through these rams was 178 KN (40 kips). An accumulator was used in the hydraulic line to minimize fluctuation of axial load.

The inertia load had two parts: lead attached to the specimen and the mass rig. The mass rig was necessary for the portion of the axial load applied by the rams. The mass rig was a mechanism consisting of four steel pins (Fig. 2.8). The mass rig had one 89 KN (20 Kip) block sitting on it and was connected to bent by a rigid link. The effective mass of the frame is 89 KN (20 Kips), so the total inertia mass produced was 178 KN (40 Kips).

In the tests conducted by Nada et al.[16] a series of earthquakes of increasing acceleration were applied to the specimen until failure. It was decided to use the same sequence of earthquakes for the SFCD3. In this study the 1994 Sylmar record for the Northridge California Earthquake was selected because it caused the greatest damage to the tall specimens. The time of the motions was factored proportional to the square root of the scale of the specimen ($\sqrt{0.185}$ = 0.43). The length of the record does not change but the acceleration amplitude does change as the test progresses (Table 2.5).

Initially the specimen was subjected to fifteen percent of the scaled Sylmar record. This was pre-yield as indicated in dynamic modeling. Then 25 % of Sylmar was run with subsequent runs increasing by one forth (of the original full-scaled motion) until failure. In addition to the earthquake records some snap-back (quick release tests) tests were performed to estimate low level stiffness and damping of the specimens. These test consisted of a sequence of sudden small initial displacement and free vibration.

Preliminary analysis of the specimen was done to determine the force and displacement of the specimen at yield and ultimate. RCMC 2.0 was used to determine the moment-curvature behavior of the column core section and base hinge. Nadim Wehbe, while at the University of Nevada, Reno[17], developed this program. The program assumes that the plane sections remains plane after bending and ignores concrete tension strength. The program uses Park & Kent model for unconfined concrete and Mander's model for confined concrete. Figs. 2.9 and 2.10 show the moment-curvature relationship for the column and base-hinge, respectively. From these data, force and displacement at yield and ultimate were calculated using the moment area method. The yield force was 244 KN (55 Kips) with a displacement of 8.4 mm (0.33 in), whereas the ultimate force was same as yield and the displacement was 45.2 mm (1.78 in).

RC-Shake is a program that determines the behavior of the specimen and shake table in the shake table testing. Laplace et al. developed this program at the University of Nevada, Reno[20]. The program is useful in determining forces generated in the shake table actuator, displacement time history of the specimen and inertia forces generated in system. The program assumes that the system is single degree of freedom system and does not consider the failure displacement of the specimen. This program was used to determine the response of the SFCD3. Fig. 2.11 shows the response of SFCD3 for various magnitudes of the Sylmar records. The applied Sylmar records are summarized in Table 2.5.

2.4.2 Static Testing Setup for LFCD1S and SFCD2S

The total axial load was provided through rams that were placed on top of the beam (Fig. 2.12). Rams were connected to a spreader beam mounted on the top of the beam over the beam-column-joint. The total axial load applied through these rams was 400 KN (90 Kips). This is same axial load that was applied in the original shake table test through lead on the bent and rams. An accumulator was used in the hydraulic line to minimize fluctuation of axial load. While the concentrated loads do not represent the gravity distribution well, the moment from the gravity loads is small in comparison to the moments caused by the lateral loads.

Lateral load was applied to the north end of the beam (which is the east end of the beam when it was shake table tested) using 1779 KN (400 Kips) actuator. To connect the actuator to the north end of the beam an end plate was used. The other end of the actuator was connected to the reaction tower built of concrete blocks and post-tensioned to the floor (Fig. 2.9). The specimens were tied to the test floor with prestressing bars that went through the 15 holes provided in footing.

2.5 Instrumentation and Data Collection

Strain gages, displacement transducers, accelerometer and load cells were used to collect data. Data was recorded on a system that combined both Pacific & National Instruments data collection systems. The rate of recording was set to 160 Hz and 2 Hz for shake table and static tests, respectively.

Hundred and fifty-five strain gages were used in SFCD3 (Fig. 2.13). The strain gages were placed in the structural hinge at the column bottom, column and beam. The gages were manufactured by Tokyo Sokki Kenkyujo Co., Ltd. of Japan. The gages used were 5.0 mm (0.2 in) (YFLA-2-5L) on all reinforcement. Strain gages were not used in the static specimens.

Twenty *Novotechnik* displacement transducers were used to measure the curvature at five locations along the height of column for all specimens (Figs. 2.14 and 2.15). Twenty transducers were used to measure shear deformation in the beam-

column-joint and flared section of column in SFCD3. Statically tested specimens had no transducer to measure shear in flared section of column but did measured shear deformation in the beam-column connection. The transducers had a displacement range of $\pm$ 25 mm (1.0 in) and $\pm$ 50 mm (2.0 in) with accuracy of 0.0127 mm (0.0005 in). Transducers were mounted on 9.5 mm (0.4 in) threaded rods that ran horizontally into the core of column and inside the beam-column joint (Figs. 2.14 and 2.15).

The lateral loads on SFCD3 were measured by three accelerometers. Two were mounted on the top of the beam over the beam-column-joint, one was fixed to the link that connects the beam to the mass rig and one was placed inside one of the lead buckets (Fig. 2.6). One accelerometer on the top of the beam measured the transverse acceleration of the specimen. These accelerations were multiplied by contributing masses of the structure, loading buckets and inertia mass rig to calculate force. This total mass was 427 KN (96 Kips), which included self-weight of beam and half the weight of the columns.

Four load cells were used to measure actuator applied vertical force. Load cells were placed beneath the center hole rams at the ends of each spreader beam, which were mounted over the beam-column-joint. In the shake table test (SFCD3), one load cell was attached to the link that connected the specimen beam to the inertia mass rig to determine the inertial load for the mass rig. The actuator in LFCD1S and SFCD2S had pressure gages to determine the force.

Displacement transducers were attached to the beam to measure absolute displacement of the top of the frame. One was set in the direction of loading and other one in the transverse direction, for both the static and shake table testing. In the case of shake table testing, table displacement was measured using the displacement transducer built inside the table. The top displacement was subtracted from the table displacement to measure relative displacement of the structure to the table. In the case of the static test the transducer was attached to the footing to measure the slippage of the footing over the floor. The top of bent displacement was subtracted from footing displacement to measure relative displacement of the structure to the footing.

Five additional vertical displacement transducers were attached to SFCD3. Four of them were from the beam bottom just next to the flare edge to surface of footing. One was connected in the same way in the middle of the beam. These transducers were used to measure beam deflection at five locations along the beam (Fig. 2.14). Static specimens had only one additional transducer at the center of the beam.

3. TESTING AND RESULTS FOR SFCD3

3.1 Introduction

SFCD3 was tested dynamically by shake table excitation. A series of time-scaled Sylmar records were applied till specimen failure. This chapter discusses the testing procedure and the behavior of the specimen at each run. The behavior of specimen is explained with the help of observations and collected data.

3.2 Test Procedures and Observations

The specimen was loaded with increasing magnitudes of the 1994 Sylmar record from the Northridge Earthquake. The peak acceleration was 0.6g. Time was scaled based on the scale of the specimen. Accelerations were scaled based on the intensity of the earthquake desired. Table 3.1 shows the records that were applied. SFCD3 was equipped with 154 strain gages. Some strain gages were damaged during construction and handling and some were damaged during testing. Strain gages working properly through the tests are shown in Fig. 3.1. Locations of levels in the figure are described in Fig. 2.10.

No cracks were observed for run 0.25 times Sylmar (Fig. 3.2). Some vertical cracks were observed in the beam-column joint for the 0.50 and 0.75 times Sylmar runs, Figs. 3.3 and 3.4. These cracks propagated for the 1.00 times Sylmar run. There were flexural cracks in both columns with some shear cracks, Figs. 3.5 and 3.6. For the same run, flexural cracks propagated along with shear cracks in the beam-column joint, Fig 3.7. For 1.25 and 1.50 times Sylmar, cracks in beam-column joint and column-flares increased (Fig. 3.8). First crack at both the column-bases was observed at 1.75 times Sylmar (Fig. 3.9). This indicated gap closure at the column-base hinge in both columns. All preexisting cracks continued to propagate and widened throughout the test. New cracks (both shear and flexure) at column-base, column-flares and beam-column joint developed until 2.50 times Sylmar. Cracks in the beam-column joint and column flares were a combination of shear and flexure (Figs. 3.10 and 3.11). The first vertical crack in the flare developed at 2.50 times Sylmar (Fig. 3.12). This crack indicated the gap closure on the north flare edge side of south column. Through runs of 2.75 and 3.00 times Sylmar, all cracks continued to widen with spalling at the column-base and north flare edge of the south column (Figs. 3.13 and 3.14). At 3.25 times Sylmar, significant spalling occurred at the top flare edge of the south column. Hoop reinforcement in flare and hoop reinforcement at the column base were exposed in this column (Figs. 3.15 and 3.16). Intensive cracking in the column below the cap-beam was observed (Figs. 3.17 and 3.18). At 3.50 times Sylmar, the specimen failed at the south column base (i.e. hinge failure) with the extensive damage to the column core at the top of the columns (Figs. 3.19 and 3.20). The residual transverse displacement after failure was 9.0 mm (0.36 in) in the west direction. System showed almost no transverse displacement for all runs

except the last run of 3.50 times Sylmar. The maximum transverse displacement in this run was 14.9 mm (0.59 in), which was due to failure of the specimen. After bucket removal, small amount of flexural cracks were observed along with a shear crack in the cap-beam above the south column flare-edge (Fig. 3.21). Table 3.2 summarizes the cracking pattern in each structural element for each run of Sylmar.

Fig. 3.22 shows the actual earthquake record for 0.25 times Sylmar. Figs. 3.23 through 3.25 compare the target acceleration and achieved accelerations for 0.25, 1.00 and 3.00 times Sylmar. The light line is for the target acceleration and the dark is for achieved. This difference was due to the inelastic interaction between the specimen and the table. Fig. 3.26 shows the time history for all runs. Table 3.1 shows both the target and achieved table accelerations. Figs. 3.27 through 3.29 compare the target and achieved response spectra with the calculated period of the structure for 0.25, 1.00 and 3.00 times Sylmar runs, respectively. The period of the structure was calculated using the stiffness obtained by joining the points of maximum and minimum displacement for each particular run. This will be discussed in more details in section 3.3. For the period of the structure at those run, figures indicates that the achieved excitations were close to the desired level of excitations.

3.3 Load-Displacement Relationship

The load-displacement relationship is used to calculate properties like cracking, first yielding, effective yielding, maximum displacement and displacement ductility. Displacement ductility is defined as the ratio of ultimate displacement (Δ_u) to effective yield displacement (Δ_y). The Caltrans Seismic Specification requires that the structures have a minimum displacement ductility ratio of 5 for bridge structures[4].

Figs. 3.30 through 3.43 show load-displacement relationship for each Sylmar run. The load is calculated by taking the acceleration measured on top of the cap-beam times the effective mass of 430 KN (96.5 Kips). Fig. 3.44 shows the cumulative plot with the dotted line being the envelope. The envelope was developed using peak values from the individual records. At approximately 92 mm (3.6 in) the envelope was extended until intersecting the next record. This corresponded to the point of gap closure and was verified by examining displacement data at the top of the flare. This will be discussed more in section 3.10. Table 3.3 shows maximum and minimum force with corresponding maximum and minimum displacement of the bent. The data was filtered to remove the noise level vibrations of the measuring instruments. The natural period of the structure was 0.19 sec (5.23 Hz) and the data was filtered for frequencies above 15 Hz. Table 3.3 also give the values for maximum and minimum displacement of the bent. Maximum and minimum displacements are measured as north and south displacements, respectively. Permanent displacement of the bent is the residual horizontal displacement after each run. Maximum and minimum net displacement is calculated by subtracting

permanent displacement of the previous run from maximum and minimum displacements.

Chord-stiffness is the slope of the line connecting points of maximum and minimum total displacement for each individual run. It is used to calculate period and frequency of the structure. Values are summarized in Table 3.3 and the equations used are as follows.

$$T_n = 2\pi\sqrt{\frac{m}{k}}$$

$f_n = 1/T_n$

Where;

T_n = Structure period,

f_n = Structure natural frequency,

m = Total mass of the structure, and

k = Chord stiffness.

The table shows the initial period of structure was 0.19 sec. The initial stiffness was 47.5 KN/mm (271.5 Kips/inch), which dropped to 38.9 % of initial value by the 1 times Sylmar run. This was because of cracking and yielding of the specimen. Between 1.25 to 2.5 times Sylmar, the rate of stiffness degradation was constant. The rate of stiffness degradation decreased after 2.75 times Sylmar. This is because of gap closure, which caused an increase in the slope of the load-displacement curve.

Base hinge slippage was included in the recorded displacement data. Base hinge slippage contributes to absorption of energy. The column base-hinge displacements are not the same for each column (Table 3.4).

The observations of load-displacement curve are as follows:

At 0.25 times Sylmar the system is almost linear (Fig. 3.30).

At 0.5 and 0.75 times Sylmar load-displacement curve started to show some non-linearity (Figs. 3.31 and 3.32). The first yielding occurred at 0.75 times Sylmar run.

At 1.0 times Sylmar, the system started to have wider loops (Fig. 3.33).

At 1.25 times Sylmar, the displacement loops widened. The maximum and minimum forces were 242.8 KN (54.1 Kips) and -333.8 KN (-74.3 Kips), respectively. The displacements ranged between 11.4 mm (0.45 in) to -31.3 mm (-1.23 in) (Fig. 3.34).

At 1.5 times Sylmar, the loops widened with higher peak loads. The load varied from a maximum of 266.1 KN (59.3 Kips) to a minimum of -349.5 KN (77.8 Kips). The maximum and minimum displacements recorded were 14.4 mm (0.56 in) and -42.4 mm (-1.67 in), respectively (Fig. 3.35).

From 1.75 to 2.5 times Sylmar the load was almost constant, with increase in displacement for each run (Figs. 3.36 through 3.39).

At 2.75 times Sylmar a sudden increase in absolute minimum force occurred with respect to previous runs (Fig. 3.40).

At 3.0 and 3.25 times Sylmar the absolute minimum load values were -398.4 KN (-88.7 Kips) and -403.9 KN (-89.9 Kips), which is close to each other and lower than the -434.6 KN (-96.8 Kips) of 2.75 times Sylmar. The displacements continued to increase for these runs of Sylmar (Figs. 3.41 and 3.42).

At 3.5 times Sylmar the system had a larger minimum displacement for almost same loads. This was the last run due to failure of the structure (Fig. 3.43). Fig. 3.44 shows the cumulative load-displacement for all Sylmar runs. This data was filtered at 15 Hz. At 2.75 times Sylmar run and displacement of -78.7 mm (-3.1 in) system started to gain stiffness. From observations it shows that stiffness was gained due to gap closure. Visual observation shows concrete spalling at the top of flare. This indicated gap closure at the top of the flares. Stiffness decreased beyond this point. Overall observations show that this was because of extensive damage and spalling at column bases. The base-hinge dowels started to yield as early as 0.5 times Sylmar run. This will be discussed in section 3.5.

3.4 Data Filtration

When data was measured, the readings had the effect of both the structure's natural vibration and instruments noise level vibrations. Data was filtered at various levels of frequencies to remove noise level vibrations of the measuring instruments. Figs. 3.45a, 3.45b, 3.45c and 3.45d show, the unfiltered data, filtered at 10Hz, 20 Hz and 25 Hz, respectively. Data shows that the change is not significant between filtering at 15 Hz, 20 Hz and 25 Hz. This indicated that noise level was removed at 15 Hz filtering. As discussed earlier in section 3.3, the natural frequency of the structure was 5.26 Hz. So filtering at 15 Hz will represent the true response of the structure.

3.5 Base-Hinge

Displacement transducers were installed at the base of each column to measure slippage. Figs. 3.46 and 3.47 show the history of measured displacement at north and south column base respectively. In Table 3.4, maximum, minimum and permanent displacements at the column base are summarized. These maximum slippages occurred almost at the same time instant when the bent displacement reached the maximum displacement. A maximum absolute displacement of 24.64 mm (0.97 in) was measured at south column base prior to failure. This is equal to 12.1 % of total displacement at the top of the beam. North column base had a maximum displacement of 22.1 mm (0.87 in). This is equal to 10.8 % of total displacement at the top of the beam. The maximum absolute permanent sliding at the base of the south column prior to failure was 24.6 mm (0.97 in) and in the north column was 20.8 mm (0.82 in), which are 27.17 % of recorded permanent displacement at the top of the beam for the south column and 22.96 % for the north column. As the system failed at the south column base, the maximum and permanent

displacements mentioned in the Table 3.4 are just prior to failure. Maximum and permanent slippages at the column bases are not the same because of unequal load sharing by the columns due to framing action. Permanent sliding lowers the overall stiffness of the system compared to undamaged hinge.

Figs. 3.48 and 3.49, show the strain history for the strain gages located on the hinge dowel bars at the base of both columns (gages SG2 and SG79, respectively). The profiles show that dowels yielded at 0.5 times Sylmar. The yield strain for all the reinforcement was approximately 2100 micro strains, as all reinforcement had properties very close to each other. Strain gages SG1 and SG78 were damaged at 2.5 and 2.0 times Sylmar runs, respectively (Figs. 3.50 and 3.51). There was a sudden decrease in the strain level of the dowel bar (SG2) in south column base at 2.0 times Sylmar and no significant change in the strain for further runs, (Figs. 3.48). This indicated the slippage of this dowel bar at the 2.0 times Sylmar. The other instrumented dowel bar in the same hinge (SG1) performed well till 2.5 times Sylmar, (Fig. 3.50). Strain profile of the north column dowel bar (SG79) indicates less damage to north column base. Table 3.5 shows maximum and minimum strains for each run in the base-hinge strain gages. The maximum and minimum recorded strains in base hinge dowels were 38431 and -48550 micro strains.

3.6 Beam-Column Connections

The beam-column connections were damaged. There was extensive cracking along with yielding of reinforcement within the connection. Tables 3.6 through 3.9 show maximum and minimum strains in the beam reinforcement. Beam top reinforcement yielded in tension within the joint. Fig. 3.52 shows strain history of SG61, which is located in the south beam-column connection. It shows that this reinforcement yielded in tension at 1.25 times Sylmar. Maximum and minimum strains recorded for this reinforcement were 3102 and -111 micro strains, respectively. The measured yield strain was 2100 micro strains. Fig. 3.53 shows the strain history of beam bottom reinforcement (SG65) within the south beam-column connection. The reinforcement yielded at 1.5 times Sylmar and had a maximum strain of 2675 micro strain. The column longitudinal reinforcement yielding extended into the beam-column joint. The horizontal shear reinforcement used in the joint never yielded. The maximum and minimum values of strains in this reinforcement were 199 and -233 micro strains, respectively, which is way below yielding (Table 3.9).

To measure strain in the concrete, five displacement transducers were used. These transducers were attached to four fixed points in the joint. Displacements at each point were measured and used to calculate strains. These strains were then used to estimate stress. In calculating stresses, the following assumptions were made.
    1. Connection has a plane stress condition.
    2. Joint is an infinitesimal element.

3. Hooks law is applicable to the joint as the objective is to calculate when cracking is occurring and not to calculate post-cracking stresses.
4. Deformations are small.
Displacements were converted to strains using equations 3.1 and 3.2. Fig. 3.54 shows a deformed joint with respect to original beam-column connection.

$$\varepsilon_x = \frac{\Delta_x}{b_x} \qquad \varepsilon_y = \frac{\Delta_y}{b_y} \qquad \varepsilon_{xy} = \frac{1}{2}\left(\frac{\Delta_x}{b_y} + \frac{\Delta_y}{b_x}\right) \qquad (3.1)$$

$$\begin{Bmatrix} \sigma_x \\ \sigma_y \\ \sigma_{xy} \end{Bmatrix} = \frac{E}{1-v^2}\begin{bmatrix} 1 & v & 0 \\ v & 1 & 0 \\ 0 & 0 & (1-v)/2 \end{bmatrix}\begin{Bmatrix} \varepsilon_x \\ \varepsilon_y \\ \varepsilon_{xy} \end{Bmatrix} \qquad (3.2)$$

Where;
σ_x = Horizontal stress,
σ_y = Vertical stress,
σ_{xy} = Shear stress,
Δ_x = Average horizontal deformation,
Δ_y = Average vertical deformation,
ε_x = Horizontal strain,
ε_y = Vertical strain,
ε_{xy} = Shear strain,
b_x = Joint horizontal dimension,
b_y = Joint vertical dimension,
E = Concrete modulus of elasticity, and
v = Concrete Poisson's ratio.

Principal stresses were calculated using equations 3.3 and 3.4.

$$\sigma_1 = \frac{\sigma_x + \sigma_y}{2} + \sqrt{\left(\frac{\sigma_x - \sigma_y}{2}\right)^2 + \sigma_{xy}^2} \qquad (3.3)$$

$$\sigma_2 = \frac{\sigma_x + \sigma_y}{2} - \sqrt{\left(\frac{\sigma_x - \sigma_y}{2}\right)^2 + \sigma_{xy}^2} \qquad (3.4)$$

Figs. 3.55 through 3.58 show the principal stresses in both south and north column connections. Limits for principal stresses in joints are defined by Caltrans for tension as $\sqrt{f'_c}$ MPa ($12\times\sqrt{f'_c}$ psi) and $0.25\times f'_c$ MPa(psi) for compression. Thick horizontal lines show these limits. The figures show that tension stresses in the south connection started to exceed the limit at 0.75 times Sylmar. At the same run the stresses exceeded limits in the north columns. Table 3.2 shows that the visible shear cracks started at 0.50 times Sylmar.

3.7 Column

The gap had a significant role in the load capacity of bent for particular Sylmar runs. Figs. 3.59 and 3.60 show strain history for the longitudinal reinforcement in the column-core at the gap, SG38 and SG113 respectively. Longitudinal reinforcement in both columns started to yield at 0.75 times Sylmar with a corresponding maximum load of 46.24 Kips (207.6 KN). Table 3.10 also summarizes the maximum and minimum strains for each run in the column longitudinal reinforcement strain gages located at the gap. The maximum and minimum strains for column longitudinal reinforcements were 79993 and -95880 micro strains, respectively.

Figs. 3.61 and 3.62 show the strain history of spiral reinforcement in the column-core just below gap, SG29 and SG111 respectively. These spirals yielded at 3.25 times Sylmar. The maximum and minimum strains for spiral reinforcement were 12180 and -2511 micro strains, respectively (Table 3.11). This reinforcement yielded very late in the entire loading history. The flare and beam performance changed once the gap closed. Nada et al. proposed a strut-and-tie model for the behavior of the flared column bent (Fig. 3.63). After gap closure a strut is formed inside the flare causing compression in the flare and in column spiral hoops at the location where this strut merges into the column core section. One of the hoops in south column flare (SG20) yielded in compression (Table 3.12 and Fig. 3.64). The maximum and minimum strains recorded for flare hoops were 3812 and -2710 micro strains, respectively (Table 3.12). This reinforcement started to yield during the 3.25 times Sylmar run.

Flare longitudinal reinforcement started to yield at 1.00 times Sylmar run. The maximum and minimum values of strains recorded were 39611 and -92212, respectively (Table 3.13). One of the longitudinal flare bars (SG 107) yielded in both tension and compression (Table 3.13 and Fig. 3.65). These results confirm the strut-and-tie model proposed by Nada et al.[16].

Figs. 3.66 and 3.67 show the principal stresses in the north column. These stresses were calculated by same procedure discussed in section 3.6. Stresses are compared with Caltrans criteria for beam-column connection. Both principal stresses in column started to exceed limits at 0.75 times Sylmar run. Table 3.2 shows at 1.00 times Sylmar the first visible cracking in column was observed. The problem with instruments in the south column prevented measurements.

3.8 Curvature

Curvature is important in defining flexural stiffness of the element. Curvature for this specimen was calculated using the measurements (d1, d2, h and b), Fig. 3.68. Displacements d1 and d2 were converted into strains by dividing them by the gage

length (b) and curvature was determined by dividing the strains by the distance between the transducers (h) (Equation 3.5).

$$\phi = \frac{(d1 - d2)}{hb}$$ (3.5)

Figs. 3.69 through 3.78 show the measured curvature history. At top of the south column and for Sylmar runs of 2.5 and 2.75, there is sudden decrease in rate of increase of peak curvature, which indicates gap closure that adds to stiffness (Fig 3.69). Some instruments reached their limits due to high curvature at some sections. In cases when this occurred, the range of earthquake for which data is provided is shown on the graph. Figs. 3.79 through 3.82 show maximum and minimum curvature for both columns. Maximum and positive notations are arbitrary. Study of the graphs indicates that some sections at the top of the columns have curvatures opposite in sign to the sections above and below it, which is in contrast to the expected shape of the deformed column. This was due to shear deformation of the sections. Measured curvatures are a combined effect of shear and flexure. It is not possible to separate them from each other with the provided information. This is discussed in more detail by Nada et al.[16] and is due to the irregular shape of the column.

Instruments used at the top of column were far from the column core, due to existence of flare. As a result, reference points in the beam were far from beam-column connection vertical edges, which are the extreme fibers of the section under consideration. The deflection of beam and cantilever contributed to measured curvature at the top section of the columns. This indicates curvatures are not pure curvatures but they include effect of beam deflection.

3.9 Beam Performance

Much of the skin reinforcement in the beam equipped with strain gages yielded in tension (SG73) (Fig. 3.83). Beam shear ties in the beam-column-connection yielded in tension (Table 3.6).

Reinforcement in the beam started to yield at 1.00 times Sylmar run. Tables 3.6, 3.7, 3.8 and 3.9 show maximum and minimum strains recorded for all beam reinforcement. The reinforcement to yield first was the beam bottom reinforcement at 1.0 times Sylmar. The skin reinforcement yielded at 2.5 times Sylmar. The maximum strains recorded for this reinforcement were 16978 at failure of the specimen. The maximum and minimum strains recorded for shear reinforcement in beam were 11149 and -133. This reinforcement started to yield at 1.25 times Sylmar. The overall maximum and minimum strains recorded in beam reinforcement were 23524 and -1019 micro strains, respectively.

3.10 Gap Closure

Load-displacement diagram showed the increase in load carrying capacity at 2.75 times Sylmar. This was due to the flare gap closure at the top of the south column. The data from transducer no. 10 and load-displacement diagram was used to determine the gap closure. Fig. 3.84 compares the displacement in transducer no. 10 for 2.75 times Sylmar with global displacement. After a global displacement of 92 mm (3.6 in) the global displacement continued to increase while the transducer no. 10 displacement stayed approximately the same. The load-displacement curve (Fig. 3.8) shows gap closure at 374 KN (84.1 Kips) and a displacement of 92 mm (3.6 in).

Fig. 3.85 compares displacement in displacement transducer no. 1 at base of the south column with the global displacement. The graph does not show gap exact point of gap closure. The gap at the base-hinge was 12.7 mm (0.5 in) and the displacement in transducer exceeded 12.7 mm (0.5 in). This indicates gap closure but it is not shown in the graph.

3.11 Displacement Ductility

A yield displacement is required to calculate the ductility index. An equivalent bilinear load-displacement curve is obtained using measured accumulative load-displacement envelope curve. First slope of the curve is obtained by connecting the origin of the curve and the first yield point occurring in the longitudinal reinforcement, which is determined from the measured strain. Second slope is chosen such that the areas above and below the curve are the same. The end point is ultimate measured displacement and its corresponding force. Intersection point of these two lines is the effective yield point (Fig. 3.86). Fig. 3.87 shows the measured envelope with solid lines and idealized curve with dashed lines. Table 3.14 summarizes the values of these curves along with the calculated displacement ductilities. The maximum ductility achieved by the specimen was 14.15. The ductility ratio exceeded the ductility ratio of 5, which was minimum ductility capacity specified by Caltarns Seismic Specifications[4]. The ductility ratio at gap closure was 6.8 and was above the Caltrans target capacity. This ductility ratio includes slippage at the column-base. The ductility of this structure is also calculated with no base slippage. The value of ductility without base-hinge slippage is 12.44. An average value of maximum base slippage is deducted from the maximum total displacement of the structure, to achieve the ductility of the structure without base-hinge. The maximum displacement of the structure was the displacement at the base-hinge failure.

4. TESTING AND RESULTS FOR LFCD1S AND SFCD2S

4.1 Introduction

This chapter describes the testing procedure and results of the static testing of LFCD1S and SFCD2S. These specimens were initially tested on the shake table by Nada et al. (LFCD1 and SFCD2), respectively. Specimens were aligned in the north-south direction with the actuator at the north end. The north end in static test is the east end in the shake table tests. In shake table test they were aligned east west with mass-rig at the east end. Following is the discussion of the individual specimens.

4.2 LFCD1S Testing and Results

4.2.1 Test Procedure and Observations

LFCD1S was severely damaged in the shake table testing but did not fail. There were shear cracks in the beam-column connections, plastic hinge region of the columns, base-hinge, and in the beam. There were flexural cracks in the beam-column connections and the plastic hinge region of the column. Spalling was seen at the top of the flare and in the middle of flare height (Fig. 4.1). The applied shake table displacement can be seen in Fig. 4.2 as the dotted line.

LFCD1S was tested with a limited number of cyclic static loads and then pushed to failure. The actuator was mounted on the north end of the specimen. Push will be used to describe the movement of the specimen to the south while pull will be to the north. In the testing direction, the specimen was off plumb by approximately 25.0 mm (1.00 in). Specimen was plumbed using the columns as the references. The total force required to plumb was 46.1 KN (10.4 Kips) pull, causing tension in the cap beam. Fig. 4.2 shows load-displacement diagram for LFCD1S. Table 4.1 shows the chord stiffness of the specimen for each load step.

The first step in loading was 18.0 mm (0.70 in) push, which corresponds to the first yield in the specimen. The actual displacement reached was 18.6 mm (0.73 in). The difference between the target and achieved displacement was because of the slippage between the footing and the flooring. Displacements given are bent displacements that were determined after subtracting bent displacement from footing displacement. No new cracking was observed at this stage. Load Step-2 was pulling specimen to 17.8 mm (0.70 in). The actual displacement reached was 18.3 mm (0.72 inch). There was no new significant cracking or damage at this stage. Load Step-3 was a push of 23.4 mm (0.92 in), which corresponds to the idealized yield displacement. The actual displacement reached was 23.9 mm (0.94 in). No new damage and cracking were observed at this load step. Load Step-4 was to pull the specimen to 23.4 mm (0.92 in). The actual displacement reached was 23.9 mm (0.94 in). New diagonal cracking in both beam-column connections was observed. There

were also new shear and some flexural cracks observed in the flare at this load step (Fig. 4.3). Load Step-5 was to push the system to 67.3 mm (2.65 in), which was equal to the gap closure at the top of column flare. The actual displacement achieved at this load step was 67.6 mm (2.66 in). Additional cracking was observed at this stage. The cracks observed were the same as Load Step-4 but opposite in direction (Fig. 4.4). Load Step-6 was to pull the specimen to 67.3 mm (2.65 in). The actual displacement achieved was 67.8 mm (2.67 in). New shear and flexure cracks were observed in the column throughout the height. More cracks in the joint were observed. Load Step-7 was to push the specimen to 165 mm (6.50 in), which was the maximum displacement when tested on the shake table. Specimen went through all the displacements of Load-Steps 1 through 7, when it was tested on the shake table. The actual displacement achieved for Load-Step 7 was 164 mm (6.46 in). New shear and flexural cracks observed over both columns. Preexisting flexural cracks widened (Fig. 4.5). New cracks were observed at the base-hinge (Fig. 4.6). Load Step-8 was to pull the specimen to 165 mm (6.5 inch). Specimen never went through this displacement when tested on the shake table. The actual displacement achieved was 164 mm (6.46 in). Intense cracking was observed at this stage. Extensive shear cracking was observed in the columns and the beam. These cracks were long and wide (Figs. 4.7 through 4.9). Load Step-9 was to push the specimen till failure. After 209 mm (8.22 in) of displacement, the load carried by system started to drop. The specimen was pushed to a displacement of 388 mm (15.3 in), where the load had dropped to 91 % of the maximum load. Very wide shear and flexural cracks in the beam were observed. Extensive spalling in the flare was also observed. The flare longitudinal reinforcement buckled (Fig. 4.10). A wide gap opening was observed at the base-hinges (Fig. 4.11). Flexural cracks were large in the column (Fig. 4.12).

4.2.2 Shake Table vs. Static Tests Displacement and Stiffness

For the pull zone, the static load graph is very close to the end points of the shake table tests (Fig. 4.2). Where in the push zone, the static test looks like a continuation of dynamic test. During Load Step-8, when the specimen was pulled to 165.1 mm (6.5 in), it suffered new damage lowering the stiffness and capacity of the structure. The maximum force was 305.4 KN (68.66 Kips) at the displacement of 205 mm (8.09 in). Maximum displacement (Δu) was determined as the displacement corresponding to the maximum absolute load (Pu) carried by structure during the shake table test. The maximum load (Pu) was taken from the shake table testing. The maximum displacement corresponding to this load was 389 mm (15.3 in).

Table 4.1 shows, the chord stiffness of the structure for each particular push and pull. It was calculated by joining the maximum load points for load steps with the corresponding displacements in the opposite directions. For the last push, it was calculated using maximum load point and origin, instead of the opposite load step. As the specimen was already tested dynamically it showed lower chord stiffness inside the dynamic tests displacement zone. The maximum chord stiffness of

specimen during the shake table testing was 13.93 KN/mm (79.57 kips/in) and the minimum chord stiffness was 1.69 KN/mm (9.68 kips/in), which is 12.2 % of this maximum stiffness. The maximum stiffness in the static test was 2.57 KN/mm (14.7 kips/in) and minimum was 1.37 KN/mm (7.84 kips/in). At ultimate displacement in static testing, the chord stiffness was 0.72 KN/mm (4.09 kips/in). This is 5.1 % of the maximum stiffness shown by specimen.

4.2.3 Performance of Base Hinge and Beam-Column Connection

Figs. 4.13 and 4.14 show the base hinge slippage at the south and north columns, respectively. South column base slipped more than the north column base, for all steps except for the last load step. The north column had lower axial load, due to the overturning. The maximum slippages corresponding to the maximum bent displacement of 389 mm (15.3 in) were 34.8 mm (1.37 in) and 34.5 mm (1.36 in) for south and north column bases, respectively. Initially the structure had permanent displacement from shake table testing. At the start of the testing the columns were plumbed, which removed permanent offset of the total structure but not necessarily the base hinges. As there were no reference points for the base hinge it was hard to pull them back to the zero position. All the measurements were taken treating the post-plumbed base-hinge position as the reference position. Table 4.2 shows slippage at base hinge for every load step. The final slippages at the end of the test were 34.8 mm (1.37 in) and 34.5 mm (1.36 in) for the south and north columns, respectively.

The beam-column connection was cracked during the shake table testing (Fig. 4.15). The displacement transducers were used to determine the relative post-cracking principal stresses. These transducers helped in studying the level of cracking and variation in the principal stresses in the beam-column connection. The principal stresses were calculated by using the same procedure described in section 3.5. Figs. 4.16 and 4.17 show the maximum and minimum relative principal stresses, respectively, in the south beam-column connection. The sudden change in the stress values at the end of the loading curve indicates development of a large crack inside the instrumented area of the beam-column connection. Figs. 4.18 and 4.19 show the maximum and minimum principal stresses, respectively, in the north beam-column connection. The comparison of principal stresses in both beam-column connections shows approximately the same stress range. Principle stress values were very close to each other in both the beam-column connections except for the last load step.

4.2.4 Curvature

Curvature is measured by using same procedure described in section 3.7. Fig. 4.20 shows the locations of curvature measurement. Figs. 4.21 through 4.30 show the relationship between force and curvatures. Figs. 4.31 and 4.32 show the maximum values of curvature for each load step along the height of the column for south and north columns, respectively. Table 4.3 shows, values for maximum curvature for

22

each load step. All the curvature measured here also had the effect of shear deformation as described in SFCD3.

4.2.5 Gap Closure

The first gap closure in the flare took place in the north column. This was determined by comparing the reading of transducer no. 9, which is located at the top of north side of the column, with the global displacement (Fig. 4.33a). The figure shows that the gap closed at the global displacement of 117 mm (4.61 in). This corresponds to a load of 180 KN (40.5 Kips). The gap closure is not shown in the load-displacement curve since the curve is heavily influenced by previous damage.

Fig. 4.33b compares displacement in displacement transducer no. 2, which is located at base of the north column, with the global displacement. The graph does not show the exact point of gap closure. The gap at the base-hinge was 12.7 mm (0.5 in) and the displacement in transducer exceeded 12.7 mm (0.5 in). This indicates gap closure, but it is not seen in the graph.

4.3 SFCD2S Testing and Results

4.3.1 Test Procedure and Observations

SFCD2S was initially tested on the shake table by Nada et al[16]. There were shear cracks in the beam-column connections, plastic hinge region of columns, base-hinge, and in the beam. There were flexural cracks in the beam-column connection and the plastic hinge region of the column (Fig. 4.34). Fig. 4.35 show the load-displacement envelop for the shake table test.

SFCD2S was tested with limited number of a static cyclic load and then pushed to its ultimate limit. Actuator was mounted on the north end of the specimen. Push will be used to describe the movement of the specimen to the south while pull will be to the north. The specimen was initially off the plumb by approximately 11.4 mm (0.45 in). The specimen was plumbed using the columns as a reference. The total force required to plumb the specimen was 6.5 KN (1.46 Kips), causing tension in the cap beam. Fig. 4.35 show load-displacement diagram for SFCD2S.

Table 4.4 shows the stiffness of the specimen for each load step. Load Step-1 was to push and pull back the specimen to 8.2 mm (0.33 in). This displacement was equal to the specimens first yield (experimental) displacement from the shake table testing. The idealized yield displacement of the structure was 10.2 mm (0.40 in). As both the first yield and idealized displacements were very close to each other, it was decided to displace the specimen through 8.4 mm (0.33 in), which is the first yield displacement. The actual achieved displacements were 8.6 mm (0.34 in) push and 8.6 mm (0.34 in) pull. The final displacement was equal to the bent displacement minus footing slippage, as described in section 4.2.1. No new cracking was observed.

Load Step-2 was to push the specimen to 41.9 mm (1.65 in). This displacement caused gap closure at the top of the column. The actual displacement achieved was 35.6 mm (1.40 in). No new cracking was observed. Load Step-3 was to pull the specimen to 41.9 mm (1.65 in). Actual displacement achieved was 31.0 mm (1.22 in). The difference between the target and achieved displacement was because of the slippage between the footing and the flooring. There were some new cracks observed in both beam and columns. The cracks were very small and comprised of both shear and flexure. Minor cracks were observed at the base hinge. Load Step-4 was to push the specimen to 94.0 mm (3.70 in). This displacement was equal to the maximum displacement the specimen went through when tested on the shake table. The actual displacement achieved was 88.6 mm (3.49 in). New flexural and shear cracks were observed. Some of the preexisting flexural cracks widened. The shear cracks that developed were very long (Figs. 4.36 and 4.37). The shear cracks developed were perpendicular to the cracks developed in the Load Step-3. Load Step-5 was to pull the specimen to 94.0 mm (3.70 inch). Specimen never went through this displacement when tested on the shake table. The maximum shake table test displacement in this direction was 60.0 mm (2.36 in). The actual displacement achieved was 93.7 mm (3.69 in). New shear and flexure cracks developed in the column and beam column connection (Fig. 4.38). Widening and lengthening of shear cracks were observed in the beam (Figs. 4.39 and 4.40). Load Step-6 was to push the system to failure. The maximum displacement achieved was 134.1 mm (5.28 in). The structure failed at this displacement due to beam shear (Figs. 4.41 and 4.42). Shear and flexural reinforcement in the beam were exposed at failure.

4.3.2 Shake Table vs. Static Tests Displacement and Stiffness

In both the push and pull directions the static load-displacement envelope is close to the shake table load-displacement envelope at the end points of the shake table envelope (Fig. 4.35). The maximum push force taken by the system was 482.2 KN (108.4 Kips) at the displacement of 120.8 mm (4.75 in) and the maximum pull force taken by the structure at 93.7 mm (3.69 in) was 497.3 KN (111.8 Kips). The maximum force measured in the shake table test was 433.2 KN (97.4 Kips). The ratio of the maximum absolute push and maximum push dynamic load is 1.11. The maximum displacement (Δu) of the structure was 134.1 mm (5.28 in). This was the displacement of the specimen at beam shear failure.

Table 4.4 shows the chord stiffness of the structure for particular push and pull. The chord stiffness was calculated by same method used for LFCD1S. For the last push, it was calculated using maximum load point and origin. As the specimen was already tested on the shake table, it showed lower chord stiffness inside the dynamic test displacement zone. The maximum chord stiffness shown by specimen in shake table testing was 50.71 KN/mm (289.60 kips/in) and the minimum chord stiffness shown in static testing was 2.17 KN/mm (12.4 kips/in). The minimum stiffness shown by the specimen in the shake table testing was 5.24 KN/mm (29.95 kips/in), which was 10 % of the maximum stiffness shown by the structure. The

minimum stiffness of the specimen in the static testing was 4.3 % of the maximum stiffness shown by specimen.

4.3.3 Performance of Base Hinge, Beam-Column Connection

Figs. 4.43 and 4.44 show base hinge slippage at the south and north columns, respectively. Slippages were same at the base of north and south columns except for the last load step. The maximum slippages at the base hinge were 16.1 mm (0.64 in) and 13.6 mm (0.54 in) for south and north column bases, respectively. Initially the structure had permanent displacement from shake table testing. At the start of the static testing the columns were plumbed, which removed permanent offset of the total structure except base hinges. As there were no reference points for base hinge it was not possible to pull them back to the zero position. All the measurements were taken treating the post-plumbed base hinge position as the reference position. Table 4.5 shows slippage at base hinge for every load step.

The beam-column connection was cracked during the shake table test. The displacement transducers in the joint were used to determine the relative post-cracking principal stresses. These transducers helped in studying the amount of cracking and variation in the principal stresses in the beam-column connection. Figs. 4.45 and 4.46 show the maximum and minimum principal stresses, respectively, in the south beam column connection. Figs. 4.47 and 4.48 show the maximum and minimum principal stresses, respectively, in the north beam column connection. The diagrams show that there was a large amount of cracking and damage in the beam-column connection for load steps with displacements that the specimen never went through in shake table testing (Load Step-5 and Load Step-6).

4.3.4 Curvature

Curvature is measured by using the same procedure described in section 3.7. Figs. 4.49 through 4.58 show the relationship between force and curvatures. Figs. 4.59 and 4.60 show the maximum values of curvature for each load step along the height of the column for the south and north columns, respectively. Table 4.6 shows values for maximum curvature for each load step. Transducer NV17 maxed out at Load Step-5. Fig 4.54 shows the data till Load Step-5 for curvature at section NV17 and NV18. All the curvature measured also include the effect of shear deformation. Curvatures at the top of the flare include beam rotations.

4.3.5 Gap Closure

The first flare gap closure took place in the south column. This was determined by comparing the reading of transducer no. 9, which is located at the top of south side of the column, with the global displacement (Fig. 4.61a). The figure shows that the gap closed at the global displacement of 76.4 mm (3.01 in). This

corresponds to a load of 332 KN (74.6 Kips). The load-displacement curve does not show gap closure.

Fig. 4.61b compares displacement in displacement transducer no. 2, which is located at the base of the north column, with the global displacement. Figure shows that the gap closed at global displacement of 72.6 mm (2.86 in). This corresponds to a load of 319 KN (71.7 kips).

5. DISCUSSION OF RESULTS

5.1 Introduction

In this chapter, the responses of specimens are compared to evaluate the effects of detailing. A comparison between tall and short column specimens is made along with a discussion of the finite element analysis results. Design recommendations are also developed.

5.2 Finite Element Analysis

In this section the finite element analysis for SFCD3 is discussed including the modeling of the materials, mesh and loading. Comparisons of the measured and calculated load-displacement curves are made for SFCD2 and SFCD3. The non-linear finite element program DIANA 7.0[8].

5.2.1 Finite Element Modeling

5.2.1.1 Mesh Formation

Two-dimensional mesh was formed for the specimen based on previous work done by Nada et al.[16]. Plane stress elements were used for the concrete. To model gaps at the top of the flare and the bottom of the column, spring elements were used (Fig. 5.1). Fig. 5.2 shows the load-displacement relationship for the spring element used in the gap at top of the flare and column base-hinge. The force generated in the spring was zero till gap closure and had constant stiffness after that. The value used was based on judgment and was selected so as to not change the stiffness of the structure and not cause instability. These elements do not prevent the relative displacements between the concrete faces of the gap because they do not have infinite stiffness.

Interface elements were used to model bond slip between concrete and base-hinge dowels. The concrete elements had thickness equal to the out-of-plane dimensions of the structure. The reinforcement was modeled as truss elements with perfect bond between the surrounding concrete and reinforcement except for the base-hinge dowel reinforcement. Fig. 5.3 shows the finite element mesh for the structure.

5.2.1.2 Material Modeling

In DIANA any stress-strain curve can be modeled using multi-linear idealization. As the mesh is two dimensional, the biaxial failure mode was achieved by forming a failure envelope with the stress-strain relationship of material and the cracking pattern.

Kupfer's model was used to define uniaxial stress-strain relationship for concrete. When the specimen was cast, the curing conditions were different for the test cylinders and specimen. The cylinders were encased and covered in such a way that moisture was maintained till testing, whereas the specimen was exposed to air and formwork was removed after hardening of concrete. A strength reduction factor of 0.85 was used to account for cracking in the specimen due to handling and difference in curing conditions between specimen concrete and test cylinders. Average value of 1.2 was used to account for strain rate effect based on the calculation by Nada et al.[16] The net magnification factor for the uniaxial curve was 1.02 (Fig. 5.4). Biaxial stress state in tension and compression, defined with Drucker-Prager failure criteria, was combined with a cracking model. This was done to achieve the failure envelope of concrete when one of the principal stresses is tension in the biaxial stress-state (Fig. 5.5). This helped in modeling brittle behavior of concrete. Angle of internal friction assumed was 30^0 for Drucker-Prager model as recommended in the DIANA manual.

Cracking is modeled as the combination of tension cut-off, tension softening and shear retention. Tension cut-off is the failure envelope for tension-tension and tension-compression stress state. It indicates linear stress cut-off where a crack arises if the major principal tension stress exceeds the minimum of f_t and f_t $(1+\sigma_{lateral} / f_c)$, with $\sigma_{lateral}$ being the lateral principal stress, f_c is compressive and f_t is the tension strength of concrete. The tension softening relates to the concrete post-cracking stress-strain relationship. A linear stress-strain relationship was assumed to model tension softening. Shear retention is the capability of the element to transfer the shear through aggregate interlock after cracking. In previous studies a shear retention value of 0.2 was used for plain and reinforced concrete based on experience. Reinforcement is modeled as a truss element with no dowel action after cracking. To account for reinforcement dowel action, a value of 0.6 was used for shear retention. This provided good comparison with experimental results. The value is close to that recommended by the ACI code of practice, which reduces the concrete shear strength to 0.5 of its value before cracking[1]. The change from 0.2 to 0.6 did not cause significant change in the behavior of the specimen and insured the stability of the specimen till failure.

A bond-slip mechanism was used to model the relative slip between concrete and reinforcement. An interface element with zero thickness was used to model bond-slip and was placed between the concrete and reinforcement. The relationship between normal traction and the normal displacement was elastic, whereas the relationship between the shear traction and slip was assumed to be a non-linear function. The cubic function according to Dorr was used to model the slippage between reinforcement and concrete to account for yield penetration in the base-hinge (Fig. 5.6).

Stress-strain relationships were slightly different for each size of bars. Yield values were close to each other and for simplicity one curve was used for stress-strain relationship, which was a standard Grade 60 stress-strain curve. To account for strain rate effect, the yield value was increased by 20% (Fig. 5.7). A Von-Mises failure criterion was used to model the biaxial stress-state for the material.

5.2.1.3 Loading and Boundary Conditions

Support was provided only for the footing (Fig. 5.3). The side and bottom faces of the elastic footing are simply supported. The lateral load was a single concentrated load applied at the end of the beam. The lateral load was incrementally increased till the failure of the system.

The actual specimen was subjected to a dynamic load, with a change in its loading direction as the shake table moved. Analytically, two runs were made to see this change in loading. In the first run the specimen was pushed in the south direction till failure. Second run consisted of pulling the specimen in the north direction. Results obtained from these two loadings are plotted on the same graph. The results are discussed in section 5.2.2

5.2.1.4 Solver Technique

The ordinary iteration processes with the loading increment can result in very large displacement increments. This is especially important when the load-displacement curve is horizontal. In this situation, arc-length method is very useful. The snap-through behavior can be analyzed. Snap-through is any curve with only positive and negative slopes (Fig. 5.8). Arc-length method is also capable of passing through the snap-back behavior where displacement control fails. Snap-back applies to curves, which have any type of slope including positive and less than one (Fig. 5.8).

In the incremental method, the incremental displacement norm is controlled by a prescribed value and simultaneously adapting the value of the increment. The value of the increment is decided at the start of the increment and is not fixed. This method was most suitable for the current case as the specimen had gap closure.

5.2.2 Load-Displacement Curve

Fig. 5.9 shows the load-displacement diagram for the finite element analysis of SFCD3 and compares it with the measured one. In the measured load-displacement relationship, the curve continues with the negative slope after the peak load at the approximate displacement of 127 mm (5 in), whereas the finite element model shows failure in the vicinity of this displacement. Both the finite element and specimen show failure at the base hinge. In the finite element analysis the strains in the base-hinge dowels reached very high values causing failure.

5.2.3 Curvature

Mander's model[15] of the confined section showed that the ultimate strain of column core concrete was 0.0115. A confinement effect was assumed in determining the concrete stress-strain curve. The finite element analysis showed that the reinforcement at the gap and the concrete reached a maximum strain of 0.2242 just prior to the gap closure (Fig. 5.10). This indicated that the concrete had almost 19.5 times the strain predicted by Mander's model. The finite element is not well defined in this area and so the strain is over estimated but it does show a trend of very high strains. Bond-slip was not modeled in the gap region but was observed in the testing. The study of the stress and cracking patterns at the instant of gap closure and the strut-and-tie model proposed by Nada et al.[16] indicates that the concrete in compression at the gap is highly concentrated. Fig. 5.11 shows the strut-and-tie model at the gap and the 3-way (C-C-C) node.

Fig. 5.10 indicates that the plane sections are not remaining plane at the gap. In the same figure it shows the strains in the reinforcement just above and below the gap. They indicate sections above and below the gap are almost plane. The measured total rotation of the gap section was 0.01855 radians if extreme reinforcement strains are used and was 0.06003 radians if the reinforcement in compression only was used. The rotation was calculated by determining the curvature in the gap. Curvature was calculated by dividing the difference in strain by the distance between the values. Since the curvature value was an average, the rotation was determined by multiplying the curvature by the gap width. Reinforcement in compression gave the location of the neutral axis at 183 mm (7.2 in) from the extreme tension face of the throat section at the gap. With help of the depth of neutral axis and rotation of the concrete in compression, displacement of the top of the flare edge was calculated. This displacement was equal to 17.22 mm (0.68 in). The remaining displacement to close the gap was provided by the beam rotation, which was 0.00634 radians. This indicates that the gap section provides most of the rotation, while little rotation is provided from the beam.

Mander's model for confined concrete is underestimating the ultimate strain in the confined concrete, when applied to the gap in this study. This is why the prediction of gap closure based on Mander's model is not accurate.

5.3 Comparison between LFCD1 and LFCD1S

The west and east sides in the shake table tests correspond to the south and north sides, respectively, in the static tests. LFCD1S is the static test conducted on LFCD1 after the shake table test. In the discussion, pull is in the north direction for shake table test and west in the static test. Push is in the south direction for the shake table test and east for the static test.

5.3.1 Load-Displacement Relationship

Fig. 5.12 compares the shake table and static test load-displacement relationships for the specimen. Ultimate displacement for LFCD1 is not the failure displacement but the displacement at the last run in the shake table test. Ultimate displacement for LFCD1S is the displacement when lateral load dropped to the ultimate load measured in the shake table test. Both pull and push parts of the static curve are close to the shake table test envelope. The differences are caused by the dynamic effect in the shake table test and the additional damage caused by the static test. The ultimate displacement of the specimen in the static test was 389 mm (15.3 in). The idealized yield displacement for the specimen in the shake table test was 23.4 mm (0.92 in). The displacement ductility of the specimen exceeded 15. The test was stopped due to the decrease in load carrying capacity compared to its peak load capacity and the large displacement. The test could have been continued.

5.3.2 Curvatures

Table 5.1 compares the maximum absolute values of curvature for the last run in the shake table test (LFCD1) and last load step in static test (LFCD1S). The curvature values are high at the south column top in LFCD1S compared to its corresponding column in LFCD1, showing more plastic rotation at the gap in the south column. The curvature values are close to each other in the bottom and top of the north column and bottom of the south column of LFCD1S and the corresponding column in LFCD1. Figs. 5.13 through 5.16 compare the curvature at the top and bottom of column for LFCD1 and LFCD1S. The graphs show the increased in curvature at the top caused by the increase in overall displacement.

5.3.3 Base Hinge Slippage

Figs. 5.17 and 5.18 compare the base hinge slippage for the LFCD1 and LFCD1S, for corresponding columns. They show an almost linear relationship between overall bent displacement and base-slippage. The contribution of the base-hinge slippage compared to the total displacement of the bent for the shake table test varies from 9.2 % to 14.8 % and varies from 6.1 % to 14.6 % for the static test.

Table 5.2 compares the maximum absolute values of slippage for the last run in the shake table test (LFCD1) and the last load step in the static test (LFCD1S). The contribution of each base hinge in the shake table test is different. The ultimate slippages at the base hinges are almost same in the static test. The average slippage of the two columns in the base hinge for the static test is 34.7 mm (1.36 in), which is equal to the 8.93 % of the ultimate displacement of the specimen.

5.4 Comparison between SFCD2, SFCD2S and SFCD3

The west and east sides in the shake table test correspond to south and north sides, respectively, in the static test. SFCD2S is the static test conducted on SFCD2 after the shake table test. SFCD3 is a new specimen with slightly different details compared to SFCD2 and was only shake table tested. In the discussion, pull for SFCD2S and SFCD3 are in the north direction, while push is in the south direction. For SFCD2 pull is in the west direction and push is in the east.

5.4.1 Load-Displacement Relationship

Fig. 5.19 compares the measured load-displacement envelopes for SFCD2, SFCD2S and SFCD3. The curves for SFCD2S and SFCD2 show very good correlation to each other. Both push and pull parts of the curves are close to each other indicating that the static test envelope is almost a continuation of the shake table test. The differences are very small and caused by the dynamic effect and the preexisting damage from the shake table test. The ultimate displacement for SFCD2S was 134.1 mm (5.28 in) at which the specimen failed in beam shear. The idealized yield displacement of SFCD2 was 10.2 mm (0.40 in). The resulting displacement ductility of this specimen is 13.2. Idealized yield displacement was calculated only from the shake table test envelope.

Comparison of the load-displacement envelopes for SFCD2 and SFCD3 show that the curves are close to each other before yield in both push and pull zones. For SFCD2 the first yield occurred at 0.5 times Sylmar in the column longitudinal reinforcement while in SFCD3 the first yield occurred at 0.75 times Sylmar in the column longitudinal reinforcement. The idealized yield displacement (section 3.11) for SFCD3 was 13.7 mm (0.54 in). The gap closure in SFCD2 occurred at 1.25 times Sylmar, displacement of 41.9 mm (1.65 in) and displacement ductility of 4.0. In SFCD3 gap closure occurred at 2.75 times Sylmar, displacement of 91.7 mm (3.61 in) and displacement ductility of 6.68. This shows that the displacement ductility at gap closure was high in SFCD3. The scale of the Sylmar run for SFCD3 was more than twice that of SFCD2 to close the gap. SFCD2 and SFCD2S show that this specimen had displacement ductility capacity of 13.2. SFCD3 had a displacement ductility capacity of 14.1. Ductility for both the specimens was close but the difference was in failure mode. Failure in SFCD2S was beam shear, while SFCD3 failed in the base hinge. The specimens had different skin reinforcement in the beam, which can impact the beam shear resistance. The larger shear demand in the beam of SFCD3 did not occur until very late in the test when compared to SFCD2. If the base hinge slippage is removed, the maximum bent displacement is 171 mm (6.72 in) and 119 mm (4.69 in), the ductility is 12.44 and 8.69, and the drift is 14 and 9.8 for SFCD3 and SFCD2S, respectively.

5.4.2 Curvatures

Table 5.3 compares the maximum absolute curvature values at the top and bottom of the SFCD2, SFCD2S and SFCD3. For SFCD2S, curvatures at the column base hinges are larger than in SFCD2. This indicates that the south column base-hinge sustained more plastic rotation before failure. Curvatures at the top of the south column in SFCD2S and in the west column in SFCD2 were close.

In the static test the maximum curvature at the base of south column was 0.0010 rad/mm (0.0251 rad/in). In the shake table test of SFCD3 the maximum curvature recorded at 2.75 times Sylmar was 0.0008 rad/mm (0.0219 rad/in) for the south column base-hinge. Due to the technical difficulties the data for further runs was not recorded. As the system showed more ductility for further runs, it is likely that this base hinge of SFCD3 suffered from more curvature. The recorded base hinge curvature in the south column at 2.75 times Sylmar for SFCD3 was close to the curvature measured at the south column base-hinge in SFCD2S. This indicates that the south column base of SFCD3 likely suffered from more plastic rotation than that of the SFCD2S.

The maximum load sustained by SFCD3 was 430.54 KN (96.79 kips). The maximum load sustained by SFCD2S was 482.2 KN (108.4 kips) in push and 497.3 KN (111.8 kips) in pull. There was shear failure at the south base hinge in SFCD3 and beam shear failure in SFCD2. The load sustained by both the systems was close. It is believed that the shear capacity of the south column base hinge in SFCD3 was reduced due to the increased plastic rotations. The increased plastic rotations were due to the larger gap at the top of the column.

Fig. 5.20 shows the strain history for the strain-gages located on the south column longitudinal reinforcement inside the flare gap. Curvature was calculated by dividing the difference in bar strains by the distance between them. The curvature value was assumed constant over the gap. The gap rotation was determined by multiplying the curvature by the gap width. The rotation of the gap was 0.00038 radians at the instant of maximum curvature measured from the reinforcement. From section 5.2.3, finite element analysis showed a curvature of 0.06003 radians. There is a huge difference in the calculated gap rotations from reinforcement strain and the curvature from finite element results. The curvature difference was due to the bond slip of the reinforcement and cracking in the gap. Figs. 5.21 through 5.24 show the maximum strains measured over the height of the column longitudinal reinforcement for each run. These figures show that the top of the reinforcement inside the beam-column connection was below yielding. They also show a reduction in strain at the gap location indicating bond slip. Other strain gauges inside the column height indicate that the yielding penetrated to the 558.8 mm (22.0 in) below the gap. The total height of the column is 990.6 mm (39.0 in). Therefore a large portion of the column yielded. The pictures of the gap at 2.75 times Sylmar show a large crack inside the gap (Fig. 5.25). This shows a large contribution of bond slip and cracking

in the gap closure. Figs. 5.26 through 5.29 compare the curvature at top and bottom of SFCD2, SFCD2S and SFCD3 with the overall displacement of the beam. Almost all the graphs show a linear relationship with the overall displacement of the bent.

5.4.3 Base Hinge Slippage

Figs. 5.30 and 5.31 compare the base hinge slippage for the SFCD2, SFCD2S and SFCD3 for corresponding columns. The diagrams show similar behavior among all three tests for both column base hinges except for a large increase in slippage in the north column of SFCD3. This column is on the lower axial load side of the bent due to frame action. Therefore, it has a lower shear capacity. It also indicates an almost linear relationship between overall bent displacement and base slippage. The contribution of the base-hinge slippage compared to the total displacement of the bent for SFCD2 varies from 3.3 % to 7.9 %, varies from 6.6 % to 12.1 % for SFCD2S and varies from 5.0 % to 16.6 % for SFCD3. Table 5.4 shows the maximum base hinge slippage for SFCD2 and SFCD3 and SFCD2S, respectively. Comparison of the values for each particular column shows that base-hinge displacements are higher in SFCD3 indicating more damage and slippage.

5.4.4 Beam-Column Connections

Figs. 5.32 and 5.33 show principal stresses for SFCD2.   Figs. 3.55 through 3.58 show the relative principal stresses for SFCD3. In the shake table tests of SFCD2 and SFCD3, initially, there were no cracks in the joint. The readings are positive indicating tensile stresses. The stresses in SFCD3 are higher than in SFCD2 indicating more cracking and damage to the beam-column joint. As gap closer in the SFCD3 was very late and the gap width was high, the stresses concentrated in the joint in the vicinity of the column core. In SFCD2, the gap closed earlier and the effective column area in contact with the beam increased earlier than that of SFCD3, which relieved the stresses in the beam-column joint.

In SFCD3, the beam bottom reinforcement in beam-column connection yielded very early at 0.75 times Sylmar. The horizontal U-clips used in the beam-column connection showed small strains well below yielding. The horizontal U-clips do not carry any significant load under the action of this loading system.

The strains in the column shear reinforcement yielded very late. This indicates the high shear capacity of the column shear reinforcement. The flare hoops also contribute to the shear capacity after gap closer.

5.5 Comparison of SFCD3 with the wFRAME Predictions

The prediction of the system was made using the program wFRAME[28]. This program was developed by Caltrans to predict the behavior of the bents under lateral loading. The program is capable of modeling soil-structure interaction and calculates

the load and displacement at the instance of hinge formation at every location. The program needs geometry and moment curvature relationship as its input, and calculates the collapse state but not the failure state. To calculate the failure displacement, the designer has to add the plastic deformation to the collapse state. The plastic deformation is calculated by using plastic rotation capacity and plastic hinge length of the section. The plastic rotation capacity was multiplied by the distance between the top of the column and the center of plastic hinge to get the plastic deformation. Fig. 5.34 shows the load-displacement curve for SFCD3 predicted by wFRAME with and without the effect of strain rate. The input moment-curvature relationship was calculated by RCMC[17] as discussed in detail in chapter 2. The base-hinge was restrained against slippage. As seen from previous tests, the base hinges undergo high rotation; the failure point of the system was calculated using ultimate curvatures only at the top of the columns. The comparison show that all of the curves are very close to each other in the pre-yielding range. Both the wFRAME curves show lower load carrying capacity than the measured. The wFRAME curve with strain rate effect shows more strength than the curve without strain rate effect. The failure displacements were 54.6 mm (2.15 in) for wFRAME and 194 mm (7.64 in) for measured. This shows the large difference between the failure points for the wFRAME and measured. wFRAME does not include the effect of gap closure.

5.6 Gap Width Calculations

5.6.1 Caltrans Method

Current Caltrans procedure[4] was used to estimate the gap closure status. The procedure is based on curvature analysis of the section. Using the effective yield curvature value and the ultimate curvature value, the yield rotation and plastic rotation at the top section of the flare can be determined. The yield rotation, θ_y, can be calculated using the moment-area method by integrating the M/EI along the column height. For the plastic rotation, θ_p, equation 5.1 was used.

$$\theta_p = L_p (\phi_u - \phi_y)$$ (5.1)

Where,
L_p = Plastic hinge length,
ϕ_y = Effective yield curvature, and
ϕ_u = Ultimate yield curvature.
The value of the plastic hinge length (L_p) is calculated using equation 5.2 provided by Caltrans.

$$L_p = G + 0.3 f_{ye} d_{bl}$$ (5.2)

Where,
G = Gap width,
f_{ye} = Expected yield stress for longitudinal reinforcement, and
d_{bl} = Bar diameter for longitudinal reinforcement

The total deformation of the flare edge can be calculated by multiplying the total rotation, which is the summation of θ_p and θ_y, by the distance from the neutral axis of the section at the ultimate curvature to the edge of the flare. The gap will not close as long as the calculated deformation was less than the gap width.

The needed gap width for the current specimens was calculated to be 9.4 mm (0.372 in). The gap width was set at 9.5 mm (0.375 in) for the initial specimens. In the case of SFCD3, the gap was increased to 19 mm (0.75 in) but it still closed in the tests. Finite element analysis done by Nada et al. showed that a specimen with gap width of 25 mm (1.0 in) would have gap closer. The gap closed at a displacement ductility of 10, which is much higher than required. The procedure was also applied to the specimens RDS-3 (gap width 25 mm (1.0 in)) and RDS-4 (gap width 50 mm (2.0 in)) tested at University of California, San Diego by Sanchez et al[2]. The Caltrans method gives minimum gap width of 18 mm (0.72 in) for the San Diego specimens. In RDS-3 the gap width was greater than the minimum but still had gap closure. The closure did occur at a high displacement ductility of 8.2 and drift of 4.7 %, while it failed at a displacement ductility of 13.6 and drift of 7.8 %. In RDS-4 the gap width was doubled and failed without gap closure. Therefore the gap size in which failure in the column will occur at the same time as gap closure, is somewhere in between 25 mm (1.0 in) and 50 mm (2.0 in). It will be closer to 25 mm (1.0 in) because the gap closure in RDS-3 was very late and was close to the failure ductility.

To determine a sufficient gap width to prevent gap closure with the Caltrans method, a factor of safety is required. The minimum factor of safety of 3 is recommended for gap width calculation if Caltrans method is used. The method is based on plane sections remaining plane and does not include bond slip, which is not the case in the gap region.

5.6.2 NCHRP 12-49 Method

NCHRP 12-49[24] recommends a minimum gap width of 0.05 times the distance from the center of the column to the extreme edge of the flare or 1.5 times the calculated plastic hinge rotation from the pushover analysis times the distance from the center of the column to the extreme edge of the flare. NCHRP 12-49 provides an equation for plastic hinge rotation capacity of the section, which can be used to predict the minimum gap width. This minimum gap width is multiplied by a factor of 1.5 to determine the required gap width. The equations are 5.3 through 5.6.

$\theta_p = 0.11 \, (L_p / D') \, (N_f)^{-0.5}$ (5.3)
$N_f = 3.5 \, (T_n)^{-1/3}$ (5.4)
$L_p = L_g + 8800 \, \varepsilon_y \, d_b$ (5.5)
$L_{G \, required} = \theta_P \, L_{FLARE} \times 1.5$ (5.6)
Where,
θ_p = Plastic rotation capacity of the section (rad),
L_p = Plastic hinge length,

D' = The distance between the outer layers of the longitudinal reinforcement on opposite faces of the member,

N_f = number of cycles of loading expected at the maximum displacement amplitude,

T_n = natural period of vibration of the structure,

L_g = Gap width provided,

ε_y = Yield strain of the longitudinal reinforcement,

d_b = Diameter of member longitudinal bar,

L_{FLARE} = Distance from the center of the column to the extreme edge of the flare, and

$L_{G\ required}$ = Minimum gap width required for no gap closure.

The 0.05 times the distance from the center of the column to the extreme edge requires a gap size of 16 mm (0.63 in) for the current specimens. The plastic rotation procedure gives the minimum gap width of 13 mm (0.52 in) and a required value of 20 mm (0.78 in). As shown from the specimens, this gap would not be sufficient to prevent gap closure. The procedure was also applied to the specimens RDS-3 (gap width 25 mm (1.0 in)) and RDS-4 (gap width 50 mm (2.0 in)) tested at University of California, San Diego by Sanchez et al[2]. The plastic hinge method gives minimum gap width of 22 mm (0.86 in) and a required size of 33 mm (1.29 in). The distance from the center of the column to the extreme edge is 760 mm (30 in). Therefore, the 0.05 estimates required gap size of 38 mm (1.5 in). The 0.05 limit is sufficient but the plastic hinge method predicts too small of a gap to prevent closure.

Based on a comparison between experimented specimens and the analysis for both the tests at San Diego and Reno, a factor of safety of 2 is needed instead of only 1.5 recommended by the NCHRP method to ensure no gap closure, when calculating plastic hinge rotation. The set value of 0.05 was too low for the Nevada specimen and should be increased to 0.08. Table 5.5 shows the calculations for both San Diego and Reno specimens.

5.6.3 Drift Method

Another way to estimate minimum gap width is with demand drift. Calculating a demand drift and then multiply it with a factor of safety, say 1.5. A required plastic rotation can be calculated from the required demand drift using the equations 5.7 to 5.9. This is done assuming that all displacement of the system is handled by the rotations at the top of the columns.

$$\Delta_{FDD} = \text{Drift}_{FDD}\ L_D \qquad\qquad\qquad (5.7)$$
$$\theta_P = \Delta_{FDD}\ /\ H_C \qquad\qquad\qquad (5.8)$$
$$L_G = \theta_P\ L_{FLARE} \qquad\qquad\qquad (5.9)$$

Where,

Δ_{FDD} = Displacement at factored demand drift,

Drift_{FDD} = Demand drift multiplied by the safety factor,

L_D = Height of structure considered for drift,

H_C = Height of column,

θ_P = Minimum required plastic hinge rotation for the required demand drift,
L_G = Minimum gap width required, and
L_{FLARE} = Distance from the center of the column to the extreme edge of the flare.

The gap is then sized so that under this very conservative estimate of demand, the gap does not close.

5.7 Conclusions

The experiments show that tall specimens can have displacement ductility as much as 15. The short specimen with a gap width of 9.5 mm (3/8 in) can achieve a displacement ductility of 13. These specimens carry high loads due to gap closure. The gap closure caused a large increase in the shear demand in the beam. Increased shear reinforcement in the beam can prevent beam shear failure resulting in increased ductility of the specimens. The shear demand in the beam can be calculated by analysis the column flare section without a gap. The column spiral yielded very late and hoops in flare also contribute to the shear capacity. This indicates that the current specification for column shear reinforcement is sufficient.

SFCD3 had a gap of 19 mm (0.75 in) and displacement ductility capacity of 14. SFCD3 failed in the base hinge. Base hinge data for SFCD3 shows that, there was large plastic deformation in the base hinge. As gap closure at the top of the columns was very late in this specimen, the section at the top of the column sustained large plastic rotations. The base hinge suffered from high plastic rotations. The study of SFCD3 data shows that the shear capacity of the two-way hinge sections reduced with increases in plastic curvature and high rotation. This caused the brittle shear failure in the base hinge. None of the specimens failed in the column or at the gap at top of the flare, which was the primary objective of this study.

The longitudinal reinforcement in the column showed bond slip in the top gap region. There was no bar slip, as the strains in the beam-column-connection end of the reinforcement did not drop. Finite element analysis showed that the concrete at the gap reached the strain of 0.22 at the time of gap closure. This was caused due to the stress concentration in the gap zone. The reinforcement strains showed that the plane sections do not remain plane. Therefore the estimation of the moment-curvature relationship could not be made. The concrete in the gap was under high level of stress concentration. Mander's stress-strain model showed very low strains in comparison to the finite element and the experiment. As Mander's model is under-estimating the strain in the concrete it was not applicable to the gap region. The rotation at the gap is the main mode of providing ductility. The beam rotation is very small compared to the gap rotation.

As seen from the testing of SFCD2S and SFCD3, SFCD2S failed in beam shear, while SFCD3 failed in the base-hinge. If the beam-shear strength of the SFCD2S was increased it would have provided more ductility. As the load-carried by both SFCD2S and SFCD3 are close and SFCD2S failed in beam shear, it indicates

that the beam shear reinforcement in SFCD2S behaved poorly in comparison to the SFCD3. Both the specimens had same area of skin reinforcement. SFCD2S had only 1 12.7-mm diameter (# 4) bar, where SFCD3 had 6 bars of 4.9-mm (0.19 in) diameter. This concludes that the distributed skin reinforcement provides better performance. The beam bottom reinforcement in the beam-column connection yielded very earlier in both the specimens. This indicates that more attention is required for the design of such beam bottom reinforcement. The strut-and-tie model by Nada et al. shows that extending the longitudinal bars to the top of the section helps to delay the yielding of the beam bottom bars. The strains in the horizontal clips provided in the beam-column connection were always below yield indicating no significant load carried by this reinforcement under unidirectional action of loading.

For calculating minimum gap width, Caltrans method can be used but with a factor of safety of at least 3.0. The NCHRP 12-49 method can also be used but with a minimum factor of safety of 2.0. The set multiplying value of 0.05 should be increased to 0.08. Another method is to back calculate the gap width from a conservative demand drift, including a factor of safety. A factor of safety of 1.5 was assumed for this method.

6. SUMMARY, CONCLUSIONS AND RECOMMENDATIONS

6.1 Summary

The work that has been done in this research can be summarized as follows.

- Two specimens shake table tested by Nada et al. (LFCD1 and SFCD2) were chosen to test statically. These specimens were 1/5 scaled with 9.5 mm (3/8 in) gap at the top of the column flare, which is 50.8 mm (2.0 in) according to the prototypes, the minimum gap thickness according to the Caltrans specifications. These specimens were designated as LFCD1S and SFCD2S in this research.

- One more specimen was constructed with the properties close to the SFCD2. The differences were the beam skin reinforcement and gap at the top of the column flare. The skin reinforcement was distributed in SFCD3 whereas SFCD2 had only one reinforcing bar. The gap used in the SFCD3 was 19.0 mm (3/4 in), which is double the gap used for SFCD2.

- LFCD1S and SFCD2S were statically tested till failure. These specimens were tested with a number of cycles under displacement control. SFCD3 was tested dynamically using the shake table. The testing was done at the Large Scale Structures Laboratory of the University of Nevada Reno.

6.2 Conclusions

- All the specimens showed very high displacement ductility. LFCD1S, SFCD2S and SFCD3 reached a maximum displacement ductility of 15, 13 and 14 respectively.

- The gap closure in the SFCD3 was at a displacement of 91.7 mm (3.61 in) and at 41.9 mm (1.65 in) in the SFCD2. This indicates that the gap closure in SFCD3 was at a higher displacement compared to the SFCD2 (which was the specimen with the smaller gap width). The ductility at the gap closure in SFCD3 was 6.7, whereas it was 4.0 in the SFCD2. The ductility ratio at which the gap closed in SFCD3 was over the minimum ductility specified by the Caltrans specifications. SFCD3 flare had very low damage till high values of ductility.

- The base-hinge in the specimen with a large gap at the top of column (SFCD3) behaved poorly compared to the specimens with the lower gap width. SFCD3 failed in the base hinge. In SFCD3 the base-hinge dowel reinforcement yielded earlier than the column core longitudinal reinforcement. Slippage was observed in some of the base-hinge dowels indicating insufficient development length. Very high rotations were

observed at the base-hinge indicating that base hinges loose their shear capacity at the high level of rotations. The hooks provided to the column core longitudinal reinforcement at the base-hinge increased cracking and spalling at the base-hinge. This was due to the large amount of concrete that was outside the reinforcement. Hooks also make it difficult to place confining reinforcement near the base.

- Finite element analysis was done to check the behavior of the SFCD3. The analysis showed good relationship with the measured, except at large displacements. The finite element predicted failure displacement of 126.7 mm (4.99 in), where the system failed at 194.1 mm (7.64 in). The maximum displacement achieved in the analysis was in the displacement range of peak load but the actual specimen continued while loosing strength.

- The concrete in the gap zone is under a high level of stress concentration. According to the finite element analysis, the strain in the concrete reached 0.22 at the time of gap closure. The maximum strain predicted by Mander's model was 0.01556. The finite element analysis showed that the plane sections in the gap do not remain plane. In addition, bond slip was large increasing rotations. Therefore, the prediction of gap closure is not accurate.

- The behavior of flares in SFCD3 was satisfactory eventhough the percentage of transverse reinforcement provided was 0.0075 %, minimum as per the current Caltrans recommendations. This concludes that the flares of the specimens with large gap and minimum transverse reinforcement can perform well.

- wFRAME provided a good estimation of yield strength of the specimens. The program was not able to predict the increase in capacity from the closing of the gap at top of the flare and the large displacement capacity.

6.3 Recommendations

On the basis of the results and the analysis performed, some recommendations can be made in the design of the architecturally flared column bents with gap at the top of the column flare and two-way hinge at the column base.

6.3.1 Recommendations for Flare and Gap Details

- The increased gap width at the top of the flares provides good performance, so a minimum gap width of 19.5 mm (0.75 in) is recommended for specimens and 101 mm (4.0 in) for the prototypes. The gap did close at this width but at a large drift and ductility. A minimum gap size of 25 mm (1.0 in) in the specimen was shown to work well in the finite element analysis and further delayed gap closure. Even if the minimum gap size 101 mm (4.0 in the

prototype) is used, the cap beam should be design for the increase shear force that comes from gap closure.

- If the Caltrans method is used in calculation of minimum gap width, a factor of safety of at least 3 should be used. A factor of safety of at least 2 is recommended for determining plastic hinge rotation, when using the NCHRP 12-49 method. The fixed value for rotation for the NCHRP method should be increased from 0.05 to 0.08. The gap could also be calculated by back-calculating the minimum gap width from the factored demand drift.

- Minimum transverse flare reinforcement of 0.075 % throughout the flare and minimum flare longitudinal reinforcement is recommended.

6.3.2 Recommendations for Beam and Beam-Column Connection Details

- The current design needs to consider the increased tension force demand on the beam bottom reinforcement. This can be done using strut-and-tie models.

- The horizontal u-clips used in the beam-column connections do not contribute to the behavior of the structure when loaded in the bent in-plane direction.

- While designing the beam shear reinforcement, the force should be calculated from the analysis of the flared-column section assuming the gap will close.

6.3.3 Recommendations for Base-Hinge design

- The base-hinge dowels need additional development length. As no tool is currently available, development length should be increase by 50%.

- More sophisticated method is required to analyze the base-hinge.

6.3.3 Recommendations for analysis

- wFRAME can be used to calculate the yield strength of specimens but is not effective in predicting ultimate behavior of a column with a gap.

- Finite element can be used to predict gap closure.

- Simple methods can be used to predict the before gap closure behavior.

REFERENCES

1. American Concrete Institute Committee 318,"Building Code Requirements for Structural Concrete (ACI 318-99)", American Concrete Institute, Farmington Hills, Michigan, 1999.

2. Sanchez, Anthony V., Frieder Seible, and M.J. Nigel Priestley, "Seismic Performance of Flared Bridge Columns", Report No. SSRP-97/06, University of California, San Diego, 1997.

3. Kunnath, Sashi K., Ashraf El-Bahy, Andrew Taylor, and William Stone, "Cumulative Seismic Damage of Reinforced Concrete Bridge Piers", Report NCEER-97-0006, University of Central Florida, Orlando, 1997.

4. California Department of Transportation,"Seismic Design Criteria Version 1.1", Engineering Service Center, Earthquake Engineering Branch, California, July 1999.

5. Chopra, A.,"Dynamics of Structures", Prentice Hall, USA 1995.

6. Cook, William D. and Mitchel Denis, "Studies of Disturbed Regions near Discontinuities in Reinforced Concrete Members", ACI Journal, V 85, No. 2 Mar.-Apr. 1988, pp 206-216.

7. Todd, Diana , Nicholas Carino, Riley M. Chung, H.S. Lew, Andrew W. Taylor, William D. Walton, James D. Cooper, and Roland Nimis, "1994 Northridge Earthquake Performance of Structures, Lifelines, and Fire Protection Systems", NIST Special Publication 862, May 1994.

8. DIANA User's Manuals, TNO Building and Construction Research, Inc, Netherlands, 1999.

9. El-Din, El-Metwally Salah, "On The Behavior And Design of Reinforced Concrete Beam-Column Connection", Journal of Helwan University, V 1, January, 1992 pp.104-121.

10. Fu, H.C., M.A. Erki, M. Seckin, "Review of Effect of Loading Rate on R/C", ASCE Structural Journal, Vol. 117, pp. 3660-3679, October - December 1991.

11. Fung, Y. C., "A First Course in Continuum Mechanics", 2nd Edition, Prentice-Hall Inc., Englewood cliff, NJ, 1977

12. Gere, James M., "Mechanics of Materials", Thomson Learning, USA, 2001.

13. Bathe, Klaus-Jürgen,"Finite Element Procedures", Prentice Hall, USA, 1996.

14. Kulkarni, Sha, "Response of R/C Beams at High Stain Rates", ACI Structural Journal, Vol. 95, No. 5, pp 705-715, November - December 1998.

15. Mander, J., M.J.N. Priestley and R. Park, "Theoretical Stress-Strain Model for Confined Concrete Columns", ASCE Journal of Structural Engineering, Vol.114, No.8, August 1988, pp 1804-1826.

16. Nada, Hisham M., David Sanders, M. Saiid Saiidi, "Seismic Performance of RC Bridge Frames with Architectural Flared Columns", Report No. CCEER-03-01, University of Nevada, Reno, 2003.

17. Wehbe, Nadim I., M. Saiid Saiidi, "User's Manual for RCMC v 1.2", Report No. CCEER-97-4, University of Nevada, Reno, 1997.

18. Park, R. and T. Paulay,"Reinforced Concrete Structures", John Wiley & Sons, USA, 1975.

19. Laplace, Patrick, David Sanders, M. Saiid Saiidi, "Experimental Study and Analysis of Retrofitted Flexure and Shear Dominated Circular Reinforced Concrete Bridge Columns Subjected to Shake Table Excitation", Report No. CCEER-01-6, University of Nevada, Reno, 2001.

20. Laplace, Patrick, "User's Manual for RC-Shake", Version 2.0, University of Nevada, Reno, May 2003.

21. Paulay, T. and M.J.N Priestley, "Seismic Desiqn of Reinforced Concrete and Masonry Buildings", John Wiley & Sons, USA, 1992.

22. Paulay, T., "Equilibrium Criteria for Reinforced Concrete Beam-Column Joints", ACI Journal V. 86, No 6, Nov.-Dec 1989, pp 635-643.

23. Pulido-Collantes, Claudia, M. Saiid Saiidi, David Sanders, Ahmad Itani, "Seismic Performance and Retrofitting of Reinforced Concrete Bridge Bents", Report Number CCEER 02-01, University of Nevada, Reno, January 2002, pp 517.

24. "NCHRP Project 12-49, FY-98" Prepared under the MCEER Highway project, Project 094, Task F3-1, November 2001

25. Saiidi, M, "Hysteresis Model for Reinforced Concrete", Journal of Structural Engineering, ASCE, Vol. 108, No. ST5, pp. 1077-1087, May 1982.

26. Saiidi, M., N. Wehbe, D. Sanders, and C. Caywood, "Shear Retrofit of Flared RC Bridge Columns Subjected to Earthquakes", Journal of Bridge Engineering, ASCE, Vol. 6, No. 2, March/April 2001, pp. 189-197.

27. Saiidi, M., D. Sanders, F. Gordaninejad, F. Martinovic, and B. McElhaney, "Seismic Retrofit of Non Prismatic Bridge Columns with Fibrous Composites", Proceedings, 12th World Conference on Earthquake Engineering, Auckland, New Zealand, Topic 6, Paper No. 0143, February 2000.

28. Seyed, Mark, M.,"User's Manual for xSECTION", Version 2.40, California Department of Transportation, USA March 1999.

29. Seyed, Mark, M.,"User's Manual for wFPREP and wFRAME", Version 1.13, California Department of Transportation, USA May 1995.

30. Sritharan, Sri, M.J. Nigel Priestley, Frieder Seible, " Seismic Design and Performance of Concrete Multi-Column Bents for Bridges", Report No. SSRP-97/03, University of California, San Diego, 1997.

31. Sritharan, Sri, M.J. Nigel Priestley, Frieder Seible, "Nonlinear Finite Element Analyses of Concrete Bridge Joint Systems Subjected to Seismic Actions", Finite Elements in Analysis and Design, 36 (2000), pp 215-233.

32. Van Mier, J.G.M., "Examples of Non-Linear Analysis of Reinforced Concrete Structures with DIANA," Heron, V.32, No.3, August 1987, pp 5-57.

33. Chen, W.F., "Plasticity in Reinforced Concrete", McGraw-Hill, USA, 1982.

Table 2.1 Yield Stresses of Reinforcement Used in SFCD3

Bar size	Average yield stress (Ksi)	Average stress (MPa)
9.5 mm diameter (# 3)	63.35	437.1
12.7 mm diameter (# 4)	65.45	451.6
15.9 mm diameter (# 5)	61.05	421.2
3.76 mm (0.148 in) diameter	59.06	407.5
4.87 mm (0.192 in) diameter	67.77	467.6

Table 2.2 Concrete Mix Design

DESIGN CRITERIA	
28 DAY COMPRESSIVE STRENGTH	31.05 MPa (4.5 ksi)
DESIGN SLUMP	101.6 mm (4 in)
DESIGN AIR CONTENT %	6
THEORETICAL UNIT WEIGHT	21.79 KN/m^3 (138.74 pcf)
WATER CEMENT RATIO BY WEIGHT	0.41

ONE CUBIC YARD	
CEMENT - NEVADA TYPE II	3.34 KN (752 lbs)
WATER	1.36 KN (305 lbs)
No. 8 STONE - PAIUTE PIT	4.54 KN (1120 lbs)
SAND - PAIUTE PIT	6.98 KN (1569 lbs)
MASTER BUILDERS 344 N	1275 g (45 oz)
MASTER BUILDERS MICRO AIR	226 g (8 oz)
TOTAL	16.66 KN (3746 lbs)

MASTER BUILDERS 344 N - ml/Kg (oz per 100 lbs of cement)	4.75 (6)
MASTER BUILDERS MICRO AIR - ml/Kg (oz per 100 lbs of cement)	0.8 (1)

Table 2.3 Concrete Strengths

CONCRETE LOCATION	COMPRESSIVE STRENGTH, MPa (KSI)		
	7 DAY	28 DAY	TEST DAY
FOOTING	25.7 (3.73)	36.2 (5.24)	41.3 (5.98)
COLUMN	25.7 (3.73)	34.8 (5.05)	45.9 (6.65)
BEAM	26.5 (3.84)	36.0 (5.22)	42.6 (6.18)

Table 2.4 Material Properties for LFCD1s and SFCD2S

	FOOTING MPa (psi)	COLUMN MPa (psi)	BEAM MPa (psi)
LFCD1S	39(5647)	41(5992)	45(6523)
SFCD2S	42(6089)	45(6549)	43(6278)

	15.9 mm Dia. (# 5) MPa (ksi)	12.7 mm Dia. (# 4) MPa (ksi)	5.mm (0.192 in) Dia. MPa (ksi)	4 mm (0.148 in) Dia. MPa (ksi)
STEEL YIELD STRENGTH	483(70)	428(62)	418(60)	492(71)

Table 2.5 Proposed Shake Table Runs for SFCD3

RUN	SCALE	% GRAVITY (g)
1	0.25 SCALE	15.15
2	0.50 SCALE	30.30
3	0.75 SCALE	45.46
4	1.00 SCALE	60.61
5	1.50 SCALE	90.91
6	2.00 SCALE	121.22
7	2.50 SCALE	151.52
8	3.00 SCALE	181.83
9	3.50 SCALE	212.13
10	4.00 SCALE	242.44

Table 3.1 Sylmar Runs for Testing SFCD3

RUN	SYLMAR STRENGTH (TIMES)	TARGET ACC. (g) (MAX.)	ACHIEVED ACC. (g) (MAX.)	TARGET ACC.(g) (MIN.)	ACHIEVED ACC.(g) (MIN.)
1	0.15 SCALE				
2	0.25 SCALE	0.07	0.10	-0.15	-0.16
3	0.50 SCALE	0.15	0.24	-0.30	-0.31
4	0.75 SCALE	0.22	0.36	-0.45	-0.32
5	1.00 SCALE	0.30	0.55	-0.60	-0.63
6	VERY SMALL RANDON VIBRATIONS TO VERIFY DRIVE FUNCTION				
7	SNAP				
8	1.25 SCALE	0.37	0.48	-0.75	-0.85
9	1.50 SCALE	0.45	0.57	-0.90	-1.09
10	1.75 SCALE	0.52	0.54	-1.06	-1.22
11	2.00 SCALE	0.60	0.60	-1.21	-1.51
12	2.25 SCALE	0.67	0.60	-1.36	-1.55
13	2.50 SCALE	0.74	0.61	-1.51	-1.50
14	2.75 SCALE	0.82	0.76	-1.66	-1.99
15	SNAP				
16	3.00 SCALE	0.89	0.94	-1.81	-1.58
17	3.25 SCALE	0.97	0.94	-1.96	-1.58
18	3.50 SCALE	1.04	1.08	-2.11	-2.20

Table 3.2 Observations for SFCD3

TIMES SYLMAR	COLUMNS	BEAM-COLUMN CONNECTION	BASE HINGE
0.25	No damage	No damage	No damage
0.50	No damage	Starting of vertical cracks	No damage
0.75	No damage	Some new vertical cracks	No damage
1.00	Starting of flexural and shear cracks	Starting of shear cracks	No damage
1.25	Increase in number of shear cracks below beam-column connection	Increase in shear cracks	No damage
1.50	Propagation of existing cracking	Propagation of shear cracking	No damage
1.75	Some new flexural and shear cracks	Shear cracks increasing in width	First cracking in south column-base
2.00	New shear cracks lower in the column than previous cracks	Very few new shear cracks	More vertical cracks
2.25	More shear cracks below the beam column connection	Lengthening of existing shear cracks and new shear cracks	Initiation of shear cracks
2.50	First vertical crack in flare	Extension of previous cracks	More cracking
2.75	Major widening of flexural crack in flares	Limited new shear cracks	Very wide cracks
3.00	Spalling at south column flare edge along with some new shear cracks	Some new long shear cracks	Spalling at south column base
3.25	Shear cracking throughout the column height along with spalling at south column flare edge	Almost no new cracks	Spalling at north column base. Reinforcement exposure in south column base
3.50	Extensive damage along with spalling below beam-column connection	Very wide shear cracks	South column base failure in slippage

Table 3.3 Structural and Dynamic Properties of SFCD3

RUNS	0.25	0.50	0.75	1.00	1.25	1.50	1.75	2.00	2.25	2.50	2.75	3.00	3.25	3.50
Max. Disp. (in)	0.04	0.11	0.20	0.38	0.45	0.56	0.82	0.69	0.70	0.72	1.00	0.28	0.19	1.89
Max. Disp. (mm)	1.00	2.81	5.01	9.69	11.4	14.4	20.8	17.5	17.9	18.2	25.3	7.0	4.9	48.0
Max. Force (Kips)	20.47	34.95	43.29	56.28	54.09	59.26	61.03	49.77	48.47	48.37	55.19	37.14	38.04	59.05
Max. Force (KN)	91.93	156.9	194.4	252.7	242.8	266.1	274.0	223.4	217.6	217.2	247.8	166.8	170.8	265.1
Min. Disp. (in)	-0.10	-0.20	-0.33	-0.94	-1.23	-1.67	-2.00	-2.18	-2.48	-2.89	-4.04	-4.33	-5.21	-8.04
Min. Disp. (mm)	-2.58	-5.08	-8.50	-23.8	-31.3	-42.4	-50.8	-55.5	-63.0	-73.3	-103	-110	-132	-204
Min. Force (Kips)	-19.20	-35.66	-46.24	-67.95	-74.33	-77.83	-79.40	-80.13	-81.71	-84.10	-96.79	-88.72	-89.95	-93.72
Min. Force (KN)	-86.23	-160.1	-207.6	-305.1	-333.8	-349.5	-356.5	-359.8	-366.9	-377.6	-434.6	-398.3	-403.9	-420.8
Permanent Disp. (in)	-0.02	-0.03	-0.03	-0.10	-0.14	-0.24	-0.26	-0.36	-0.45	-0.62	-1.33	-1.69	-2.77	-3.56
Permanent Disp. (mm)	-0.51	-0.72	-0.73	-2.43	-3.54	-6.08	-6.59	-9.18	-11.4	-15.8	-33.8	-42.8	-70.5	-90.5
Max. Net Disp. (in)	0.04	0.13	0.23	0.41	0.54	0.70	1.06	0.95	1.07	1.17	1.62	1.60	1.88	4.66
Max. Net Disp. (mm)	1.00	3.32	5.73	10.4	13.8	17.9	26.9	24.1	27.1	29.6	41.2	40.8	47.7	118.5
Min. Net Disp. (in)	-0.11	-0.18	-0.31	-0.91	-1.14	-1.53	-1.76	-1.93	-2.12	-2.44	-3.42	-3.00	-3.53	-5.27
Min. Net Disp. (mm)	-2.79	-4.57	-7.79	-23.1	-28.9	-38.9	-44.7	-48.9	-53.8	-61.9	-86.8	-76.1	-89.6	-134
Chord Stiffness (Kips/in)	271.5	227.3	167.4	93.39	76.46	60.10	46.96	44.08	40.34	35.70	27.37	26.16	23.18	13.94
Chord Stiffness (KN/mm)	47.51	39.77	29.30	16.34	13.38	10.52	8.22	7.71	7.06	6.25	4.79	4.58	4.06	2.44
% of Initial Stiffness	100.00	94.69	69.77	38.91	31.86	25.04	19.57	18.37	16.81	14.87	11.41	10.90	9.66	5.81
Tn (sec.)	0.19	0.21	0.24	0.32	0.36	0.40	0.46	0.47	0.49	0.52	0.60	0.61	0.65	0.84
fn (Hz)	5.25	4.81	4.13	3.08	2.79	2.47	2.18	2.12	2.03	1.90	1.67	1.63	1.54	1.19
% of Initial Frequency	100.0	97.28	83.50	62.36	56.43	50.03	44.22	42.84	40.99	38.56	33.76	33.01	31.07	24.10

Table 3.4 Base-Hinge Displacement for SFCD3

SYLMAR RUNS		0.25	0.50	0.75	1.00	1.25	1.50	1.75	2.00	2.25	2.50	2.75	3.00	3.25	3.50
SOUTH COLUMN	Max. Disp. (in.)	0.01	0.01	0.02	0.04	0.04	0.07	0.10	0.09	0.09	0.10	0.15	0.11	0.10	0.78
	Max. Disp. (mm)	0.14	0.38	0.59	1.04	1.14	1.81	2.57	2.24	2.35	2.53	3.90	2.91	2.44	19.7
	Min. Disp. (in)	-0.01	0.02	-0.03	-0.09	-0.12	-0.16	-0.20	-0.22	-0.24	-0.29	-0.41	-0.38	-0.53	-0.97
	Min. Disp. (mm)	-0.13	0.42	-0.77	-2.34	-3.11	-4.12	-5.01	-5.46	-6.21	-7.32	-10.5	-9.66	-13.4	-24.6
	Permanent Disp. (in)	0.00	0.00	0.00	-0.01	-0.01	-0.02	-0.03	-0.03	-0.04	-0.06	-0.10	-0.14	-0.28	0.37
	Permanent Disp. (mm)	-0.02	-0.03	-0.04	-0.22	-0.26	-0.51	-0.67	-0.87	-1.05	-1.43	-2.41	-3.46	-7.20	9.30
NORTH COLUMN	Max. Disp. (in.)	0.01	0.02	0.02	0.05	0.05	0.08	0.11	0.09	0.09	0.08	0.10	0.01	-0.05	-0.03
	Max. Disp. (mm)	0.14	0.38	0.63	1.18	1.36	1.98	2.68	2.17	2.18	2.15	2.62	0.19	-1.30	-0.84
	Min. Disp. (in)	0.00	-0.01	-0.03	-0.09	-0.12	-0.16	-0.20	-0.22	-0.25	-0.29	-0.44	-0.49	-0.87	-0.87
	Min. Disp. (mm)	-0.12	-0.36	-0.73	-2.28	-2.99	-4.08	-5.07	-5.52	-6.28	-7.37	-11.0	-12.5	-22.2	-22.2
	Permanent Disp. (in)	0.00	0.00	0.00	0.00	-0.01	-0.02	-0.02	-0.03	-0.04	-0.06	-0.16	-0.23	-0.54	-0.82
	Permanent Disp. (mm)	0.01	0.02	0.01	-0.12	-0.17	-0.45	-0.56	-0.80	-1.07	-1.62	-4.14	-5.85	-13.8	-20.8

Table 3.5 Maximum and Minimum Measured Strain for Base-Hinge Dowels

Strain gage	Sylmar	0.25	0.50	0.75	1.00	1.25	1.50	1.75	2.00	2.25	2.50	2.75	3.00	3.25	3.50
SG1	Max.	400	1304	2091	3790	10333	17843	18846	14681	14577	14416	18903	-110	-19969	-43947
	Min.	-194	-225	-322	-265	-280	4477	6697	6730	6161	-47307	-48168	-46694	-48550	-43950
SG2	Max.	125	850	1885	13245	13918	14760	15860	12400	3117	2539	2247	1853	1944	32796
	Min.	-74	-105	-141	-171	4123	3895	4274	3115	1417	1414	1129	1418	1439	889
SG78	Max.	276	1095	2369	16317	18845	24395	28940	38431	38401	38230	37780	36989	36667	38268
	Min.	-213	-264	-341	-93	4463	4439	4624	4392	2667	4467	6968	10582	10899	3885
SG79	Max.	118	621	1281	4385	7202	9165	12383	13852	16322	18872	27062	23177	11012	12040
	Min.	-114	-140	-181	-183	474	1284	1276	1819	2327	3011	4008	5645	-6052	-13388
Max.		400	1304	2369	16317	18845	24395	28940	38431	38401	38230	37780	36989	36667	38268
Min.		-213	-264	-341	-265	-280	1284	1276	1819	1417	-47307	-48168	-46694	-48550	-43950

			Max.	38431	Min.	-48550

Table 3.6 Maximum and Minimum Strains in Beam Ties

Strain gage	Sylmar	0.25	0.50	0.75	1.00	1.25	1.50	1.75	2.00	2.25	2.50	2.75	3.00	3.25	3.50
SG48	Max.	15	35	48	152	236	346	475	549	666	808	955	975	1101	1061
	Min.	-30	-58	-53	-75	-79	-78	-42	-12	-15	-18	-32	31	82	74
SG52	Max.	-28	-3	19	439	717	900	1025	1091	1189	1340	1930	2016	2306	2272
	Min.	-60	-77	-82	-87	-51	-6	40	59	80	89	141	526	588	669
SG60	Max.	-14	-7	8	217	310	442	825	834	880	927	1054	950	1145	1059
	Min.	-44	-77	-86	-133	-94	12	89	108	98	105	51	65	77	-52
SG71	Max.	27	35	54	256	436	492	581	588	598	610	680	602	619	683
	Min.	6	-20	-12	24	190	230	300	311	327	344	316	301	271	288
SG125	Max.	-64	-52	-38	-35	-40	-87	69	78	119	153	299	316	344	595
	Min.	-102	-130	-136	-177	-191	-215	-126	-119	-118	-119	-120	-87	-86	-46
SG130	Max.	-40	-19	-4	512	786	981	1105	1145	1205	1273	1514	1475	1528	2901
	Min.	-82	-105	-122	-130	4	24	76	140	145	167	192	241	242	253
SG137	Max.	-27	-9	-16	1559	2569	3129	3660	3909	4306	4988	7545	7500	7773	11149
	Min.	-52	-83	-110	-108	230	992	1354	1714	1907	2229	2760	4858	5048	5258
SG148	Max.	26	45	142	336	539	750	941	1065	1179	1329	1636	1600	1705	1933
	Min.	11	10	26	122	252	277	234	278	316	329	339	419	446	467
Max.		27	45	142	1559	2569	3129	3660	3909	4306	4988	7545	7500	7773	11149
Min.		-102	-130	-136	-177	-191	-215	-126	-119	-118	-119	-120	-87	-86	-52

			Max.	11149	Min.	-215

Table 3.7 Maximum and Minimum Strains in Beam Longitudinal Reinforcement

Strain gage	Sylmar	0.25	0.50	0.75	1.00	1.25	1.50	1.75	2.00	2.25	2.50	2.75	3.00	3.25	3.50
SG54	Max.	118	659	931	1514	1645	1743	1708	1676	1715	1741	1855	1915	2160	1972
	Min.	-41	-120	-122	-167	-76	-99	-123	-66	-48	-37	-62	29	33	-81
SG58	Max.	100	260	965	1733	2018	2314	2563	2321	2328	2333	2667	2246	2306	3239
	Min.	-118	-236	-314	-561	-571	-582	-549	-520	-532	-543	-653	-592	-536	-387
SG61	Max.	172	756	1246	2000	2146	2260	2214	2177	2231	2271	2445	2529	3102	2924
	Min.	-16	-94	-75	-112	1	-33	-82	-29	-22	-19	-50	18	13	58
SG65	Max.	123	220	1239	1948	1991	2253	2429	2165	2165	2165	2390	2021	2068	2690
	Min.	-81	-206	-281	-509	-524	-560	-531	-506	-520	-528	-664	-759	-1019	-705
SG131	Max.	298	868	1324	1707	1712	1844	1926	1693	1698	1702	1846	1470	1519	2135
	Min.	-63	-152	-192	-375	-415	-421	-466	-466	-455	-486	-560	-490	-490	-736
SG135	Max.	112	584	1266	2447	2775	3230	7013	9056	11464	13476	15746	15086	15872	23524
	Min.	-127	-269	-339	-452	-311	-363	-429	1790	3131	4634	5415	6376	6710	5244
SG138	Max.	228	685	1325	1781	1850	1984	2085	1872	1889	1898	2024	1625	1652	2223
	Min.	-10	-68	-94	-284	-330	-345	-377	-369	-367	-377	-420	-385	-391	-556
SG142	Max.	124	218	856	1993	2248	2446	2557	2611	2686	2741	2838	2749	2765	17931
	Min.	-108	-203	-255	-297	-176	-186	-235	-144	-134	-104	-155	-29	-56	-233
Max.		298	868	1325	2447	2775	3230	7013	9056	11464	13476	15746	15086	15872	23524
Min.		-127	-269	-339	-561	-571	-582	-549	-520	-532	-543	-664	-759	-1019	-736

| | | | | | | | | | | | | | Max. | 23524 | Min. | -1019 |

53

Table 3.8 Maximum and Minimum Strains in Beam Skin Reinforcement

Strain gage	Sylmar	0.25	0.50	0.75	1.00	1.25	1.50	1.75	2.00	2.25	2.50	2.75	3.00	3.25	3.50
SG49	Max.	39	377	601	1022	1024	1074	1082	1068	1089	1124	1201	1154	1263	1200
	Min.	-2	-14	189	191	179	169	167	185	159	158	169	163	161	189
SG50	Max.	79	79	368	871	986	1143	1171	1221	1301	1352	1391	1389	1468	1377
	Min.	17	1	20	308	373	417	447	435	439	432	432	469	488	483
SG53	Max.	32	55	106	738	1049	1255	1337	1370	1459	1556	1639	1491	1461	1604
	Min.	14	13	16	50	236	240	229	242	240	244	251	339	334	358
SG55	Max.	44	180	204	616	664	741	707	686	724	751	765	754	975	779
	Min.	9	-23	-76	-130	-158	-187	-207	-208	-214	-220	-247	-232	-244	-244
SG56	Max.	58	705	1087	1287	1312	1422	1456	1453	1502	1572	1608	1611	1783	1595
	Min.	39	37	538	444	488	555	594	585	575	575	562	551	580	623
SG59	Max.	39	723	1195	1572	1552	1633	1688	1693	1758	1817	2015	2009	2377	2154
	Min.	26	32	587	638	556	606	621	661	648	640	634	649	675	768
SG62	Max.	113	497	739	1362	1518	1651	1651	1623	1666	1717	1732	1746	2059	1875
	Min.	24	14	275	412	388	398	383	411	386	385	373	411	412	406
SG63	Max.	20	406	578	1052	1136	1182	1219	1179	1233	1262	1327	1415	1694	1551
	Min.	4	4	234	258	312	351	378	399	423	431	430	489	483	530
SG64	Max.	87	268	728	1098	1269	1405	1535	1376	1386	1389	1525	1398	1400	1778
	Min.	-27	-41	45	59	147	147	127	128	153	169	176	280	295	339
SG67	Max.	28	53	467	1503	1582	1652	1634	1623	1667	1704	1899	2031	2551	2482
	Min.	15	8	15	333	481	496	463	509	495	508	517	668	690	934
SG73	Max.	29	36	38	423	914	1172	1224	1207	1257	1323	1628	2027	3099	3212
	Min.	21	18	-1	-9	206	292	335	363	393	406	419	538	851	1841
SG125	Max.	-64	-52	-38	-35	-40	-87	69	78	119	153	299	316	344	595
	Min.	-102	-130	-136	-177	-191	-215	-126	-119	-118	-119	-120	-87	-86	-46
SG126	Max.	60	520	755	960	989	1126	1245	1056	1063	1072	1174	1099	1126	1861
	Min.	-4	-12	132	171	257	280	287	308	322	337	372	472	478	469
Max.		113	723	1195	1572	1582	1652	1688	1693	1758	1817	2015	2031	3099	3212
Min.		-102	-130	-136	-177	-191	-215	-207	-208	-214	-220	-247	-232	-244	-244
												Max.	3212	Min.	-247

Table 3.8 Maximum and Minimum Strains in Beam Skin Reinforcement (Continued)

Strain gage	Sylmar	0.25	0.50	0.75	1.00	1.25	1.50	1.75	2.00	2.25	2.50	2.75	3.00	3.25	3.50
SG127	Max.	78	89	434	1322	1465	1585	1656	1716	1803	1945	2336	2344	2470	4384
	Min.	51	40	82	412	483	532	545	568	577	599	638	837	879	931
SG129	Max.	54	358	702	1281	1416	1551	1683	1683	1762	1904	5786	5944	6198	16978
	Min.	17	18	320	456	457	496	503	492	487	506	549	4188	4345	4567
SG132	Max.	199	768	1109	1321	1416	1655	1801	1616	1628	1643	1790	1603	1626	7684
	Min.	14	-58	-17	61	139	179	168	212	227	254	311	509	544	638
SG133	Max.	104	561	923	1143	1098	1224	1322	1191	1232	1328	1635	1541	1626	3620
	Min.	44	43	387	359	387	416	436	455	468	501	552	677	705	696
SG136	Max.	61	447	817	1396	1591	1735	1941	1978	2086	2283	2788	2683	2804	11639
	Min.	3	2	339	304	340	339	340	351	366	390	473	818	880	934
SG139	Max.	92	463	800	1084	1117	1216	1280	1133	1123	1119	1195	1065	1077	1800
	Min.	-27	-43	117	145	179	197	198	220	231	254	284	414	447	481
SG140	Max.	76	499	944	1184	1056	1182	1309	1224	1246	1345	1768	1729	1841	6655
	Min.	38	42	209	265	302	352	375	386	398	445	521	858	915	943
SG143	Max.	31	86	152	758	919	1077	1192	1260	1372	1548	1952	1873	1984	1992
	Min.	-29	-43	-73	-33	186	320	397	444	497	553	575	815	890	844
SG144	Max.	53	119	1027	1557	1753	1889	2010	1894	1888	1901	1986	1807	1797	2152
	Min.	9	6	51	310	559	684	753	795	821	889	973	1094	1121	616
SG149	Max.	-5	-3	-5	54	29	-31	-47	-56	-58	-60	-55	-66	-68	-59
	Min.	-15	-22	-44	-38	-54	-79	-92	-98	-99	-102	-106	-98	-96	-114
SG150	Max.	34	47	27	195	615	758	842	843	877	936	1085	1088	1106	1635
	Min.	6	-7	-22	-15	158	364	376	397	417	454	521	661	672	652
SG151	Max.	1	8	28	33	35	56	58	63	70	75	85	72	80	147
	Min.	-13	-17	-23	-36	-20	-4	-12	-14	-15	-18	-22	-21	-18	-21
Max.		199	768	1109	1557	1753	1889	2010	1978	2086	2283	5786	5944	6198	16978
Min.		-29	-58	-73	-38	-54	-79	-92	-98	-99	-102	-106	-98	-96	-114

		Max.	16978	Min.	-114

Table 3.9 Maximum and Minimum Strains in Beam Horizontal U-Clips

Strain gage	Sylmar	0.25	0.50	0.75	1.00	1.25	1.50	1.75	2.00	2.25	2.50	2.75	3.00	3.25	3.50
SG68	Max.	22	62	123	137	141	144	151	149	153	152	159	167	184	162
	Min.	14	14	34	58	65	66	74	78	82	84	86	94	96	101
SG69	Max.	15	16	168	199	125	119	129	116	114	107	90	38	25	20
	Min.	4	1	1	71	65	66	72	71	70	62	-100	-137	-146	-233
SG145	Max.	-6	41	58	80	88	92	96	88	89	88	87	74	73	85
	Min.	-11	-12	7	10	20	23	33	36	40	42	40	43	43	43
SG146	Max.	-25	-24	-6	18	27	32	62	50	44	36	31	9	12	11
	Min.	-31	-31	-29	-12	-4	-10	6	-4	-12	-26	-38	-46	-65	-82
Max.		22	62	168	199	141	144	151	149	153	152	159	167	184	162
Min.		-31	-31	-29	-12	-4	-10	6	-4	-12	-26	-100	-137	-146	-233

		Max.	199	Min.	-233

Table 3.10 Maximum and Minimum Strains in Column Longitudinal Reinforcement

Strain gage	Sylmar run	0.25	0.50	0.75	1.00	1.25	1.50	1.75	2.00	2.25	2.50	2.75	3.00	3.25	3.50
SG5	Max.	48	145	224	866	1284	1563	1567	1664	1760	1869	2310	2401	2691	2686
	Min.	-87	-143	-166	-242	-138	-176	-211	-181	-183	-177	-150	-56	-77	-81
SG6	Max.	-28	25	77	582	1119	1505	1594	1611	1625	1621	2013	2265	2525	2027
	Min.	-105	-144	-156	-174	-60	-78	-83	-78	-106	-151	-224	-307	-373	-470
SG10	Max.	88	164	214	564	823	1038	1258	1169	1217	1278	1494	1239	1258	1432
	Min.	-98	-202	-274	-414	-436	-445	-455	-502	-531	-539	-581	-629	-743	-783
SG11	Max.	69	124	165	465	757	963	1198	1134	1187	1230	1415	1107	1104	1492
	Min.	-56	-124	-167	-232	-236	-336	-542	-636	-676	-766	-811	-869	-973	-1065
SG16	Max.	57	121	266	2455	2784	3006	3144	3214	3262	3427	4605	5122	14080	12949
	Min.	-54	-97	-114	-173	-61	-130	-195	-170	-188	-213	-210	304	400	5267
SG17	Max.	22	58	196	1305	1337	1445	1535	1538	1483	1263	1068	1144	3873	2682
	Min.	-35	-56	-63	-157	-315	-402	-495	-543	-594	-638	-868	-962	-968	-794
SG21	Max.	78	144	196	724	1538	1874	2144	2123	2221	2317	2629	2399	2424	2765
	Min.	-97	-196	-274	-510	-651	-746	-886	-964	-1065	-1173	-1240	-1324	-1452	-1620
SG22	Max.	64	134	201	845	1741	2044	2395	2295	2366	2414	2603	2002	1964	2520
	Min.	-103	-188	-263	-439	-541	-886	-964	-966	-1046	-1158	-1252	-1297	-1412	-1557
SG27	Max.	112	470	1603	3039	7998	16494	23041	26919	32150	50876	27761	24426	35246	23310
	Min.	-128	-234	-356	-810	-989	15	1722	2789	-82080	-91011	-93322	-93626	-95357	-95880
SG28	Max.	52	441	1287	2180	2543	8359	4119	2471	806	-21	-197	-324	-259	473
	Min.	-167	-242	-252	-709	-885	-773	-62	-302	-568	-951	-1353	-1095	-1086	-4261
SG33	Max.	114	440	977	2104	2843	3073	6621	6030	6333	6906	15733	5309	3418	19543
	Min.	-225	-374	-536	-616	-671	-1100	-1626	-2008	-2736	-4142	-5071	-6205	-8825	-11764
SG36	Max.	527	1495	2398	10865	7370	7292	7471	6873	6692	6487	5807	2378	1962	38450
	Min.	-368	-752	-982	-2013	-4260	-1295	-1565	-1122	-971	-344	-1023	-2371	-770	-52704
SG37	Max.	488	1047	1357	1936	3098	13050	18224	14560	14651	14844	14075	9493	8447	9518
	Min.	-236	-287	-313	-323	-378	131	7815	8612	8068	7340	1787	1135	305	-3936
SG38	Max.	845	1665	2148	3008	10036	14992	19949	8535	7953	7406	8212	6003	5483	6851
	Min.	-443	-822	-1258	-3545	-6935	-6378	-3520	-889	-246	-145	451	-301	-838	-856
SG40	Max.	62	152	478	1772	1962	2046	2150	2113	2116	1901	1512	1574	1645	1682
	Min.	-70	-134	-141	-187	-288	-350	-406	-406	-477	-561	-595	-305	-273	-215
SG42	Max.	83	677	1163	1826	2129	2434	2730	2682	2754	2826	3082	2905	2940	3475
	Min.	-74	-141	-278	-582	-742	-848	-958	-1030	-1070	-1170	-1071	-1062	-1035	-1437
SG44	Max.	20	30	59	315	353	394	439	480	551	580	633	641	697	713
	Min.	12	8	13	15	62	60	71	80	86	89	83	80	66	39
SG82	Max.	0	63	104	207	388	564	728	727	790	835	932	903	946	1040
	Min.	-127	-204	-242	-315	-320	-322	-302	-297	-318	-344	-358	-345	-377	-400
SG83	Max.	-26	12	37	100	219	344	539	575	656	699	715	811	832	1074
	Min.	-82	-117	-135	-144	-151	-125	-107	-88	-86	-94	-103	-60	-47	-55
SG87	Max.	90	257	369	1604	1623	1540	1616	1587	1607	1618	1617	1433	1547	2476
	Min.	-243	-348	-405	-515	-618	-661	-658	-584	-576	-580	-599	-572	-502	-489
Max.		845	1665	2398	10865	10036	16494	23041	26919	32150	50876	27761	24426	35246	38450
Min.		-443	-822	-1258	-3545	-6935	-6378	-3520	-2008	-82080	-91011	-93322	-93626	-95357	-95880

	Max.	50876	Min.	-95880

Table 3.10 Maximum and Minimum Strains in Column Longitudinal Reinforcement (Continued)

Strain gage	Sylmar run	0.25	0.50	0.75	1.00	1.25	1.50	1.75	2.00	2.25	2.50	2.75	3.00	3.25	3.50
SG88	Max.	42	134	223	1547	1736	1890	2036	2074	2133	2191	2362	2298	2434	2607
	Min.	-106	-167	-208	-284	-212	-225	-255	-239	-259	-246	-310	-223	-232	-318
SG93	Max.	36	100	152	1490	2052	2370	2551	2381	2441	2480	2697	2265	2333	2788
	Min.	-99	-162	-205	-390	-550	-755	-840	-872	-908	-955	-1050	-939	-1030	-1230
SG94	Max.	-12	39	91	1317	1907	2326	2713	2571	2759	2744	2916	2641	2625	2636
	Min.	-91	-124	-150	-120	-42	-68	-106	-182	-235	-267	-371	-454	-579	-974
SG98	Max.	33	117	720	372	386	308	396	399	353	292	278	216	53	1140
	Min.	-147	-227	-557	-881	-1095	-1162	-1156	-1121	-1150	-1192	-1435	-1615	-1722	-1967
SG99	Max.	7	76	661	1665	1891	1998	2291	2273	2305	2353	2580	2596	2943	9164
	Min.	-122	-175	-221	-333	-520	-575	-559	-578	-613	-625	-794	-890	-868	-1076
SG104	Max.	127	423	1215	2928	3222	3656	5886	5918	6454	7674	19549	12628	13295	26647
	Min.	-135	-247	-453	-1144	-1384	-1606	-2294	-2370	-2494	-2769	-2396	-4338	-6187	-8099
SG105	Max.	110	354	1152	2381	2671	3080	9887	9395	11876	14251	20219	16548	16915	26960
	Min.	-119	-162	-155	-22	-38	-344	-245	3379	3948	5834	8599	10660	10762	5749
SG109	Max.	140	305	315	5237	5332	4963	3621	36598	38979	36723	38473	35909	34720	34585
	Min.	-230	-349	-402	-356	259	-169	569	-4529	-51503	-49713	-6769	-6550	-5211	-9111
SG113	Max.	497	1433	2047	3194	9556	9045	6487	4559	5043	5476	6422	5713	5153	21446
	Min.	-296	-411	-456	-469	-369	2576	1591	1816	1899	1852	1525	2224	2145	20
SG114	Max.	540	1333	1959	10033	11308	15160	14722	8949	8340	6319	32655	7916	32160	64640
	Min.	-370	-811	-1255	-7683	-9489	-7707	-6953	-9615	-13718	-14145	-86408	-89000	-88824	-88112
SG115	Max.	568	1285	1754	19663	20566	19192	10468	9521	9478	9563	9050	5037	3985	79993
	Min.	-323	-489	-567	-701	6348	5043	3420	3514	3451	-4268	-1196	-20353	-30553	-77306
SG116	Max.	911	1800	2514	21482	9910	10412	10282	9026	9172	7687	7580	10039	6133	79765
	Min.	-566	-1038	-1401	-2229	-5528	-11843	-15187	-13178	-14802	-12753	-91452	-75135	-84938	-94785
SG117	Max.	73	139	210	697	1278	1587	1975	1927	1992	2047	2298	2190	2208	2817
	Min.	-55	-85	-133	-225	-290	-352	-386	-425	-438	-496	-573	-542	-564	-839
SG121	Max.	29	32	51	92	174	366	499	472	480	497	555	565	587	740
	Min.	20	20	25	20	38	65	125	144	145	143	129	123	116	99
SG123	Max.	27	78	182	706	782	791	851	846	861	911	996	933	988	1285
	Min.	-18	-50	-23	5	-16	-51	-72	-77	-74	-76	-73	1	7	-42
Max.		911	1800	2514	21482	20566	19192	23041	36598	38979	50876	38473	50876	35246	79993
Min.		-566	-1038	-1401	-7683	-9489	-11843	-15187	-13178	-82080	-91011	-93322	-93626	-95357	-95880

				Max.	79993	Min.	-95880

Table 3.11 Maximum and Minimum Strain for Column Spiral Reinforcement

Strain gage	Sylmar	0.25	0.50	0.75	1.00	1.25	1.50	1.75	2.00	2.25	2.50	2.75	3.00	3.25	3.50
SG7	Max.	46	51	64	87	103	110	127	141	161	206	441	456	513	507
	Min.	32	29	30	25	49	61	62	70	77	92	138	210	206	209
SG12	Max.	19	19	23	24	36	34	-25	-205	-361	-494	-615	-659	-657	-705
	Min.	10	11	11	10	14	-255	-500	-652	-808	-954	-1014	-994	-993	-980
SG18	Max.	38	48	57	81	102	423	615	585	594	571	528	328	249	185
	Min.	19	13	11	6	33	44	190	157	128	70	-134	-185	-248	-306
SG23	Max.	24	24	27	50	-738	-970	-1139	-1198	-1242	-1282	-1091	-1295	-1284	-1302
	Min.	14	11	6	-998	-1293	-1506	-1615	-1696	-1783	-1895	-1940	-1970	-1981	-2019
SG29	Max.	26	37	49	212	218	136	-126	-187	-200	-247	-480	-787	-1010	-1094
	Min.	17	16	24	32	-74	-568	-784	-892	-1053	-1408	-1779	-1910	-2032	-2511
SG34	Max.	30	37	147	138	132	148	156	104	116	153	226	180	423	285
	Min.	11	8	17	-49	-89	-221	-571	-616	-638	-667	-672	-693	-708	-1409
SG41	Max.	59	62	65	98	114	116	155	255	268	266	299	344	381	299
	Min.	45	42	43	41	61	44	-78	-233	-473	-205	-161	-192	-162	-150
SG43	Max.	21	43	43	214	78	55	35	16	19	155	386	297	292	182
	Min.	11	13	14	-5	-78	-183	-235	-248	-245	-249	-275	-294	-329	-321
SG45	Max.	40	41	45	158	214	238	232	225	236	242	284	238	257	230
	Min.	32	31	33	31	21	7	-15	-11	-14	-14	-21	-16	-11	3
SG47	Max.	18	23	32	151	141	191	198	204	224	231	266	240	280	147
	Min.	-6	-13	-14	-142	-193	-220	-240	-250	-263	-270	-331	-340	-429	-482
SG84	Max.	4	11	15	20	31	35	38	39	44	48	73	119	126	113
	Min.	-11	-19	-19	-16	7	11	12	17	17	23	26	48	94	61
SG89	Max.	-10	-8	-6	80	-42	-50	-71	-77	-82	-86	-92	-104	-105	-117
	Min.	-16	-18	-18	-166	-265	-325	-361	-372	-383	-407	-436	-435	-452	-468
SG95	Max.	74	76	74	81	21	66	81	93	102	158	231	240	248	281
	Min.	16	14	10	-36	-83	-117	-141	-160	-158	-179	-216	-234	-232	-260
SG100	Max.	49	50	56	61	-10	-94	-188	-320	-325	-402	-418	-636	-636	-715
	Min.	6	-11	-6	-192	-460	-615	-799	-845	-918	-974	-1134	-1194	-1211	-1939
SG106	Max.	13	26	38	67	-8	-97	-65	-37	-4	66	91	189	167	536
	Min.	-15	-22	-22	-42	-226	-395	-360	-366	-396	-449	-416	-447	-463	-1088
SG111	Max.	55	58	71	11	-227	-368	-518	-608	-824	-1111	-1119	-1204	-1272	12180
	Min.	-7	-23	-25	-533	-741	-946	-1053	-1185	-1418	-1665	-1811	-1961	-2082	-2016
SG118	Max.	22	29	22	78	-32	-80	-86	-83	-75	-69	-63	-124	-119	-150
	Min.	12	6	1	-178	-253	-308	-335	-328	-314	-324	-411	-412	-442	-611
SG120	Max.	6	9	18	36	151	196	258	273	358	372	390	129	201	536
	Min.	-8	-12	-11	-11	3	56	72	-29	-128	-18	-403	-358	-355	-298
SG122	Max.	-3	-2	-46	-46	-71	-69	-94	-104	-111	-119	-132	-172	-181	-187
	Min.	-14	-197	-270	-186	-127	-151	-166	-178	-187	-196	-228	-256	-288	-437
SG124	Max.	6	7	8	11	188	246	292	270	275	281	314	263	273	425
	Min.	1	0	0	0	1	30	28	30	33	35	39	38	34	-44
Max.		74	76	147	214	218	423	615	585	594	571	528	456	513	12180
Min.		-16	-197	-270	-998	-1293	-1506	-1615	-1696	-1783	-1895	-1940	-1970	-2082	-2511

| | | | | | | | | | | | | | | Max. | 12180 | Min. | -2511 |

Table 3.12 Maximum and Minimum Strain for Flare Hoop Reinforcement

Strain gage	Sylmar	0.25	0.5	0.75	1	1.25	1.5	1.75	2	2.25	2.5	2.75	3	3.25	3.5
SG4	Max.	-47	-43	-50	53	2	-28	-82	-150	-185	-211	-238	-281	-306	-349
	Min.	-64	-74	-81	-97	-91	-111	-167	-237	-276	-315	-353	-368	-406	-426
SG9	Max.	41	51	97	343	327	266	224	154	131	101	51	-52	-103	-141
	Min.	31	30	30	10	4	-5	11	24	36	9	-61	-113	-169	-233
SG15	Max.	45	51	53	98	-59	-377	-510	-547	-561	-574	-563	-735	-728	-754
	Min.	30	26	29	-65	-446	-688	-778	-809	-852	-893	-975	-984	-978	-993
SG20	Max.	45	61	72	87	92	94	185	166	-131	-400	-779	-767	-377	-510
	Min.	20	12	13	-3	24	30	34	-273	-675	-1092	-1354	-1619	-2317	-2710
SG26	Max.	43	47	52	68	73	106	95	-884	-1005	-910	-866	-1123	-1396	-1128
	Min.	29	25	14	7	30	24	-895	-1184	-1335	-1454	-1769	-1886	-2020	-2009
SG31	Max.	47	52	66	69	244	69	149	627	1081	1522	1151	802	3812	2626
	Min.	34	30	23	14	31	-581	-774	-848	-856	-689	-690	-954	-1071	278
SG81	Max.	16	17	20	24	42	66	26	28	29	29	42	26	27	26
	Min.	-4	-4	-3	-4	-5	-6	-5	-5	-5	-6	-6	-5	-3	-5
SG86	Max.	20	53	64	57	43	45	44	42	42	40	42	34	40	44
	Min.	-5	-10	-13	-29	-22	-20	-12	-8	-6	-7	-12	-10	-16	-4
SG92	Max.	81	81	82	81	85	115	83	99	82	84	151	-294	-440	-478
	Min.	21	17	9	21	25	38	46	50	51	29	-318	-607	-829	-1111
SG97	Max.	64	67	66	139	-13	-305	-170	-112	-39	39	290	200	136	65
	Min.	6	6	-21	-300	-623	-676	-571	-568	-570	-581	-649	-753	-777	-750
SG103	Max.	10	13	25	32	38	34	54	143	194	-186	-21	-5	-342	-126
	Min.	1	-3	-17	-14	-4	2	2	1	-318	-536	-801	-1146	-1641	-1991
Max.		81	81	97	343	327	266	224	627	1081	1522	1151	802	3812	2626
Min.		-64	-74	-81	-300	-623	-688	-895	-1184	-1335	-1454	-1769	-1886	-2317	-2710

	Max.	3812	Min.	-2710

60

Table 3.13 Maximum and Minimum Strain for Flare Longitudinal Reinforcement

Strain Gage	Sylmar	0.25	0.50	0.75	1.00	1.25	1.50	1.75	2.00	2.25	2.50	2.75	3.00	3.25	3.50
SG3	Max.	8	131	207	795	1156	1375	1410	1494	1558	1606	1761	1779	1926	1704
	Min.	-163	-235	-265	-383	-157	-178	-172	-81	-95	-120	-182	-149	-193	-350
SG8	Max.	151	263	333	704	742	771	893	683	635	561	580	161	34	-322
	Min.	-119	-240	-318	-477	-547	-552	-591	-610	-658	-748	-1173	-1381	-1998	-1870
SG14	Max.	84	143	158	1462	1558	1606	1602	1638	1605	1594	1709	1768	2190	1648
	Min.	-47	-100	-130	-246	-5	-33	-79	36	58	5	29	85	88	-287
SG19	Max.	102	148	155	138	1047	1195	1215	876	756	648	658	485	1011	1234
	Min.	-57	-170	-271	-392	-434	-487	-524	-545	-595	-655	-1133	-1077	-1161	-414
SG25	Max.	14	17	837	1855	967	926	1077	1432	1429	1439	1507	1546	8419	8945
	Min.	-45	-72	-82	-56	276	375	63	237	116	24	-76	92	-92212	-88669
SG30	Max.	38	38	45	1286	1289	1006	847	870	901	923	1034	1192	1114	1207
	Min.	-16	-72	-83	-78	48	141	348	441	456	464	336	401	-447	-13
SG80	Max.	22	82	105	141	281	540	867	975	1047	1062	1063	560	306	502
	Min.	-106	-192	-243	-359	-372	-378	-326	-347	-393	-468	-586	-639	-720	-701
SG85	Max.	150	317	412	1615	1706	1706	1682	1585	1582	1547	1546	1332	1469	1666
	Min.	-196	-290	-340	-460	-587	-656	-685	-621	-606	-600	-621	-631	-615	-650
SG91	Max.	19	31	48	68	83	86	107	129	208	78	-11	49	148	274
	Min.	-14	-27	-33	-26	-16	-10	2	4	16	-104	-354	-458	-538	-642
SG96	Max.	68	123	1652	2838	2259	1769	1714	2078	2069	2005	2269	2252	2225	1851
	Min.	-122	-217	-277	-470	-277	-28	175	318	417	381	230	369	291	-339
SG102	Max.	-1	-1	109	2227	2003	1712	1619	1424	1405	1389	1605	1374	1392	1800
	Min.	-94	-153	-124	-65	207	338	492	579	638	680	697	756	527	-984
SG107	Max.	11	16	195	942	925	806	869	1279	1141	1072	1000	36464	39611	37341
	Min.	-22	-54	-71	-90	35	111	226	142	231	237	9	-5392	-6395	-6815
Max.		151	317	1652	2838	2259	1769	1714	2078	2069	2005	2269	36464	39611	37341
Min.		-196	-290	-340	-477	-587	-656	-685	-621	-658	-748	-1173	-5392	-92212	-88669

	Max.	39611	Min.	-92212

Table 3.14 Ductility Ratios

Specimen	SFCD3
Effective Yield Displacement (in)	0.54
Effective Yield Displacement (mm)	13.7
Effective Yield force (Kips)	82.31
Effective Yield Force (KN)	369.6
Min. Disp. (in)	7.64
Min. Disp. (mm)	194
Max. Drift %	15.92
Max. Measured Force (Kips)	96.8
Max. Measured Force (KN)	435
Ductility Ratio	14.15
Max drift	15.92
Disp. At Gap Closure (in)	3.61
Disp. At Gap Closure (mm)	91.6
Ductility Ratio at Gap Closure	6.68
Drift at Gap Closure %	7.52
Ductility Ratio without Base Hinge Disp.	12.44
Min. Disp. without base hinge disp.	6.72
Max drift without base hinge disp. %	14.00
Max ductility without base hinge disp.	12.44

Table 4.1 Chord Stiffness for Each Loading Cycle in LFCD1S

Load Step	Displacement mm (in)	Chord Stiffness kN/mm (kips/in)
1	-18.6 (-0.73)	2.57 (14.7)
2	18.3 (0.72)	
3	-23.9 (-0.94)	2.45 (14.0)
4	23.9 (0.94)	
5	-67.6 (-2.66)	2.17 (12.4)
6	67.8 (2.67)	
7	-164 (-6.46)	1.77 (10.1)
8	164 (6.46)	
Peak Load	-209 (-8.22)	1.37 (7.85)
Maximum Displ.	-388 (-15.3)	0.72 (4.09)

Table 4.2 Slippage at Column Base for LFCD1S

Load Step	South Column base (inch)	South Column base (mm)	North Column Base (inch)	North Column Base (mm)
1	-0.05	-1.18	-0.11	-2.71
2	0.05	1.16	0.05	1.31
3	-0.06	-1.47	-0.13	-3.35
4	0.06	1.48	0.07	1.76
5	-0.18	-4.51	-0.32	-8.09
6	0.17	4.33	0.25	6.41
7	-0.49	-12.5	-0.79	-20.0
8	0.39	9.92	0.63	16.0
9	-1.37	-34.9	-1.36	-34.5

Table 4.3 Curvature Values vs. Load Step (LFCD1S)

Load Step	Section height from base, mm (inch)	South column				
		952.5 mm (37.5 inch)	850.9 mm (33.5 inch)	673.1 mm (26.5 inch)	457.2 mm (18.0 inch)	50.8 mm (2.0 inch)
1	1/mm	-0.00014	0.00000	0.00000	0.00000	0.00006
	1/inch	-0.00345	-0.00002	-0.00002	-0.00002	0.00162
2	1/mm	0.00011	0.00000	0.00000	0.00000	-0.00008
	1/inch	0.00283	0.00001	0.00008	0.00009	-0.00206
3	1/mm	-0.00017	0.00000	0.00000	0.00000	0.00008
	1/inch	-0.00442	-0.00004	-0.00003	-0.00003	0.00213
4	1/mm	0.00015	0.00000	0.00000	0.00001	-0.00010
	1/inch	0.00371	0.00001	0.00012	0.00013	-0.00256
5	1/mm	-0.00043	-0.00002	0.00000	-0.00001	0.00026
	1/inch	-0.01095	-0.00043	-0.00004	-0.00026	0.00659
6	1/mm	0.00015	0.00001	0.00001	0.00001	-0.00028
	1/inch	0.00371	0.00013	0.00032	0.00038	-0.00709
7	1/mm	-0.00132	-0.00008	-0.00001	-0.00004	0.00066
	1/inch	-0.03351	-0.00195	-0.00021	-0.00099	0.01668
8	1/mm	0.00042	0.00002	0.00003	0.00005	-0.00033
	1/inch	0.01056	0.00041	0.00076	0.00117	-0.00829
9	1/mm	-0.00164	-0.00038	-0.00009	-0.00025	
	1/inch	-0.04155	-0.00970	-0.00224	-0.00631	

Load Step	Section height from base, mm (inch)	North column				
		952.5 mm (37.5 inch)	850.9 mm (33.5 inch)	673.1 mm (26.5 inch)	457.2 mm (18.0 inch)	50.8 mm (2.0 inch)
1	1/mm	-0.00012	0.00000	0.00000	0.00000	0.00008
	1/inch	-0.00307	-0.00002	-0.00005	-0.00007	0.00197
2	1/mm	0.00009	0.00000	0.00000	0.00001	-0.00008
	1/inch	0.00237	0.00005	0.00007	0.00014	-0.00214
3	1/mm	-0.00016	0.00000	0.00000	0.00000	0.00010
	1/inch	-0.00413	-0.00006	-0.00005	-0.00011	0.00250
4	1/mm	0.00012	0.00000	0.00000	0.00001	-0.00011
	1/inch	0.00315	0.00012	0.00007	0.00017	-0.00277
5	1/mm	-0.00037	0.00000	0.00000	-0.00002	0.00030
	1/inch	-0.00949	-0.00007	-0.00005	-0.00054	0.00755
6	1/mm	0.00036	0.00002	0.00002	0.00002	-0.00031
	1/inch	0.00922	0.00040	0.00048	0.00040	-0.00783
7	1/mm	-0.00075	-0.00005	-0.00001	-0.00010	0.00077
	1/inch	-0.01911	-0.00119	-0.00026	-0.00266	0.01946
8	1/mm	0.00068	0.00008	0.00005	0.00005	-0.00069
	1/inch	0.01724	0.00192	0.00138	0.00121	-0.01762
9	1/mm	-0.00092	-0.00012	-0.00001	-0.00041	
	1/inch	-0.02343	-0.00313	-0.00026	-0.01039	

Table 4.4 Chord Stiffness for Each Loading Cycle in SFCD2S

Load Step	Displacement mm (in)	Chord Stiffness kN/mm (kips/in)
1	-8.6 (-0.34)	7.02 (40.1)
	8.6 (0.34)	
2	-41.9 (1.65)	6.67 (38.1)
3	31.0 (1.22)	
4	-88.6 (-3.49)	5.13 (29.3)
5	93.7 (3.69)	
Peak Load	-120.8 (4.75)	3.99 (22.8)
Maximum Displ.	-134.1(-5.28)	2.17 (12.4)

Table 4.5 Slippage at Column Base for SFCD2S

Load Step	South Column base (inch)	South Column base (mm)	North Column Base (inch)	North Column Base (mm)
1 push	-0.02	-0.62	-0.02	-0.55
1 pull	0.02	0.60	0.03	0.71
2	-0.14	-3.58	-0.14	-3.58
3	0.09	2.23	0.10	2.56
4	-0.30	-7.57	-0.32	-8.00
5	0.30	7.70	0.34	8.61
6	-0.64	-16.2	-0.54	-13.7

Table 4.6 Curvature Values vs. Load Step (SFCD2S)

Load Step	Section height from base, mm (inch)	South column				
		952.5 mm (37.5 inch)	850.9 mm (33.5 inch)	673.1 mm (26.5 inch)	457.2 mm (18.0 inch)	50.8 mm (2.0 inch)
1 push	1/mm	-0.000075	0.000000	0.000000	0.000000	0.000061
	1/inch	-0.001915	-0.000004	-0.000003	-0.000004	0.001560
2 pull	1/mm	0.000060	0.000005	0.000002	0.000000	-0.000068
	1/inch	0.001535	0.000115	0.000059	0.000001	-0.001740
2	1/mm	-0.000289	-0.000001	-0.000001	-0.000002	0.000278
	1/inch	-0.007343	-0.000028	-0.000013	-0.000063	0.007056
3	1/mm	0.000204	0.000017	0.000004	0.000003	-0.000262
	1/inch	0.005171	0.000436	0.000092	0.000066	-0.006658
4	1/mm	-0.000634	-0.000010	-0.000006	-0.000008	0.000607
	1/inch	-0.016109	-0.000256	-0.000147	-0.000202	0.015428
5	1/mm	0.000557	0.000048	0.000010	0.000009	-0.000701
	1/inch	0.014142	0.001211	0.000266	0.000234	-0.017813
6	1/mm	-0.000750	-0.000040	-0.000008	-0.000010	0.000989
	1/inch	-0.019057	-0.001022	-0.000211	-0.000263	0.025115

Load Step	Section height from base, mm (inch)	North column				
		952.5 mm (37.5 inch)	850.9 mm (33.5 inch)	673.1 mm (26.5 inch)	457.2 mm (18.0 inch)	50.8 mm (2.0 inch)
1 push	1/mm	-0.000080	0.000000	0.000000	0.000000	0.000034
	1/inch	-0.002028	-0.000007	-0.000009	-0.000009	0.000876
2 pull	1/mm	0.000068	0.000014	0.000002	0.000000	-0.000045
	1/inch	0.001730	0.000363	0.000056	0.000002	-0.001131
2	1/mm	-0.000282	-0.000004	-0.000002	-0.000002	0.000186
	1/inch	-0.007173	-0.000101	-0.000048	-0.000053	0.004736
3	1/mm	0.000208	0.000024	0.000004	0.000005	-0.000181
	1/inch	0.005290	0.000620	0.000100	0.000120	-0.004591
4	1/mm	-0.000575	-0.000056	-0.000002	-0.000006	0.000446
	1/inch	-0.014616	-0.001414	-0.000059	-0.000151	0.011333
5	1/mm	0.000525	0.000082	0.000006	0.000010	-0.000483
	1/inch	0.013331	0.002076	0.000153	0.000259	-0.012263
6	1/mm	-0.000711	-0.000124	-0.000004	-0.000011	0.000784
	1/inch	-0.018052	-0.003152	-0.000100	-0.000271	0.019919

Table 5.1 Comparison of Maximum Absolute Curvature at Top and Bottom in LFCD1 and LFCD1S

LFCD1	Curvature (1/inch)	Curvature (1/mm)	Curvature (1/inch)	Curvature (1/mm)
Location	East	East	West	West
Bottom	0.0233	0.0009	0.0221	0.0009
Top	0.0258	0.0010	0.0155	0.0006

LFCD1S	Curvature (1/inch)	Curvature (1/mm)	Curvature (1/inch)	Curvature (1/mm)
Location	North	North	South	South
Bottom	0.0195	0.0008	0.0167	0.0007
Top	0.0234 *	0.0009 *	0.0415 *	0.0016 *

* Data is incomplete due to reaching the limit of the instrument

Table 5.2 Comparison of the Maximum Slippage at the Base-Hinge for LFCD1 and LFCD1S

LFCD1						
Location	East Column	Total Disp.	Slipaage in East Column % of total	West Column	Total Disp.	Slipaage in West Column % of total
Slippage (in)	0.81	7.29	11.1	1.08	7.29	14.8
Slippage (mm)	20.5	185	11.1	27.4	185	14.8

LFCD1S						
Location	South Column	Total Disp.	Slipaage in North Column % of total	North Column	Total Disp.	Slipaage in South Column % of total
Slippage (in)	1.37	15.3	8.99	1.36	15.3	8.88
Slippage (mm)	34.9	389	8.99	34.5	389	8.88

Table 5.3 Comparison of Maximum Curvature in Push Direction at Top and Bottom of Columns in SFCD2, SFCD2S and SFCD3

SFCD2	Curvature (1/inch)	Curvature (1/mm)	Curvature (1/inch)	Curvature (1/mm)
Location	East Column	East Column	West Column	West Column
Bottom	0.0115	0.0005	0.0195	0.0008
Top	0.0116	0.0005	0.0176	0.0007

SFCD2S	Curvature (1/inch)	Curvature (1/mm)	Curvature (1/inch)	Curvature (1/mm)
Location	North Column	North Column	South Column	South Column
Bottom	0.0199	0.0008	0.0251	0.0010
Top	0.0181	0.0007	0.0191	0.0008

SFCD3	Curvature (1/inch)	Curvature (1/mm)	Curvature (1/inch)	Curvature (1/mm)
Location	North Column	North Column	South Column	South Column
Bottom	0.0340	0.0013	0.0218 *	0.0009 *
Top	0.0157 *	0.0006 *	0.0191 *	0.0007 *

* Data is incomplete due to reaching the limit of the instrument

Table 5.4 Comparison of the Maximum Slippage at the Base-Hinge for SFCD2, SFCD2S and SFCD3

			SFCD2			
Location	East Column	Total Displacement	Slippage in East Column % of Total Disp.	West Column	Total Displacement	Slippage in West Column % of Total Disp.
Slippage (in)	0.31	3.85	7.92	0.29	3.85	7.40
Slippage (mm)	7.7	97.8	7.92	7.24	97.8	7.40

			SFCD2S			
Location	North Column	Total Displacement	Slippage in North Column % of Total Disp.	South Column	Total Displacement	Slippage in South Column % of Total Disp.
Slippage (in)	0.54	3.85	14.0	0.64	3.85	16.5
Slippage (mm)	13.7	97.8	14.0	16.2	97.8	16.5

			SFCD3			
Location	North Column	Total Displacement	Slippage in North Column % of Total Disp.	South Column	Total Displacement	Slippage in South Column % of Total Disp.
Slippage (in)	0.87	7.64	11.4	0.97	7.64	12.7
Slippage (mm)	22.2	194	11.4	24.6	194	12.7

Table 5.5 NCHRP 12-49 Method for Gap Width Calculation

Specimens	Reno	San Diego
Diameter of Longitudinal Bar mm (in)	12.7 (0.5)	19.05 (0.75)
Yield Strain	0.0021	0.0021
Provided gap width mm (in)	9.5 (0.375)	25 (1)
Plastic Hinge Length mm (in)	244.2 (9.615)	377.4 (14.86)
Natural Period (sec)	0.19	0.62
N_f	6.05	4.1
D' mm (in)	263.9 (10.39)	825 (32.5)
θ_p rad	0.042	0.026
$L_{G\ required}$ mm (in)	13.2 (0.52)	19.8 (0.78)

Figure 1.1   Damage to columns of the SR 118 Mission-Gothic Undercrossing Los Angeles County (1994 Northridge Earthquake- Caltrans Report)

Figure 1.2   Aerial View of the SR 118 Mission-Gothic Undercrossing Los Angeles County Showing Collapsed Eastbound Bridge (1994 Northridge Earthquake Caltrans Report)
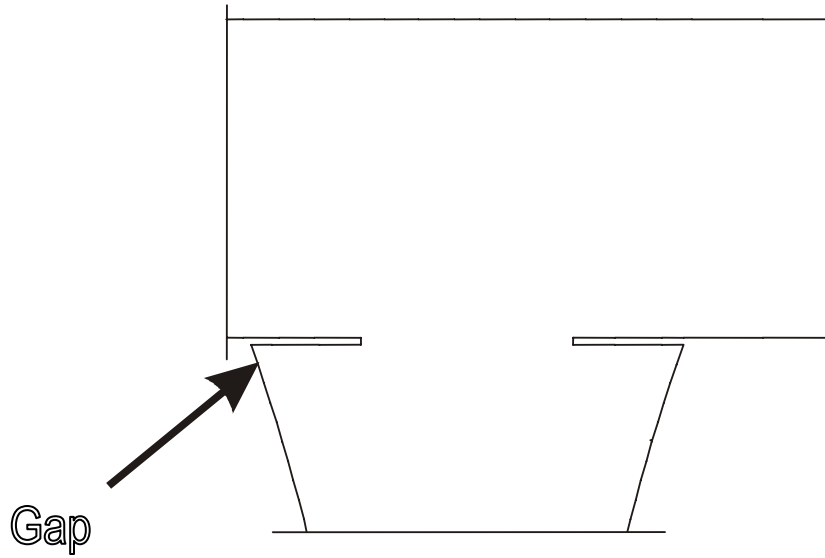
Figure 1.3 Gap Between the Beam and Column to Separate Flares from the Beam Soffit
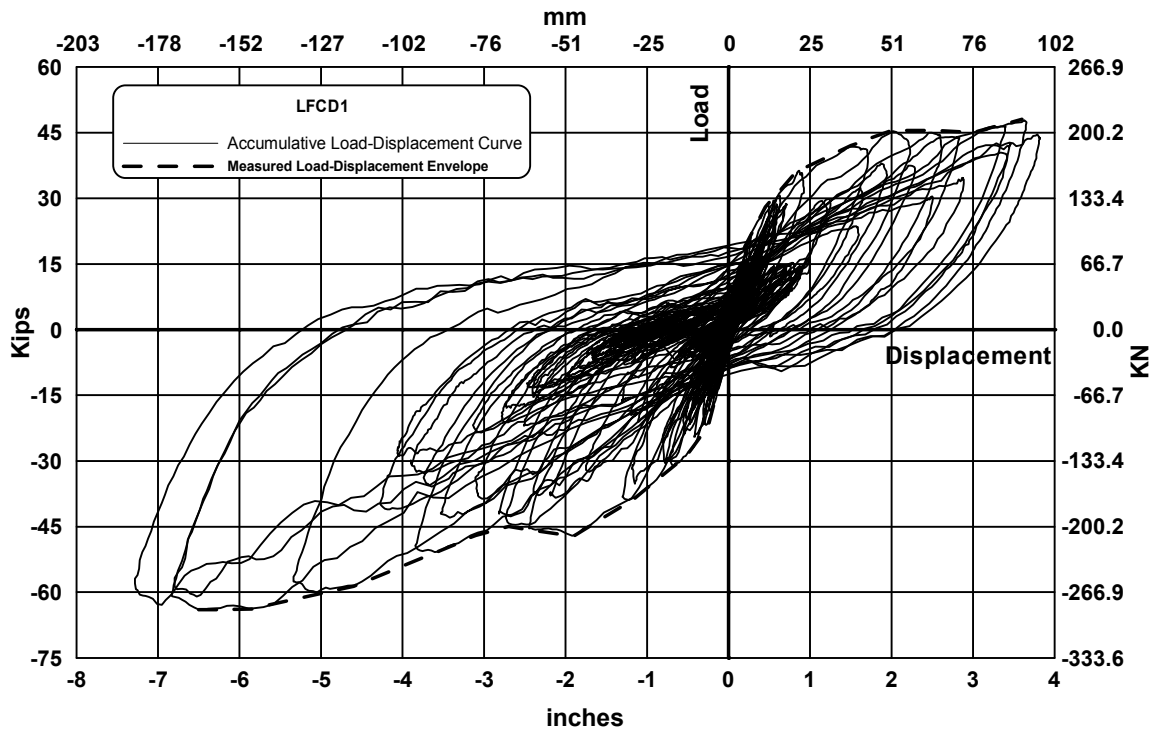
Figure 1.4 Load-Displacement Relationship for LFCD1
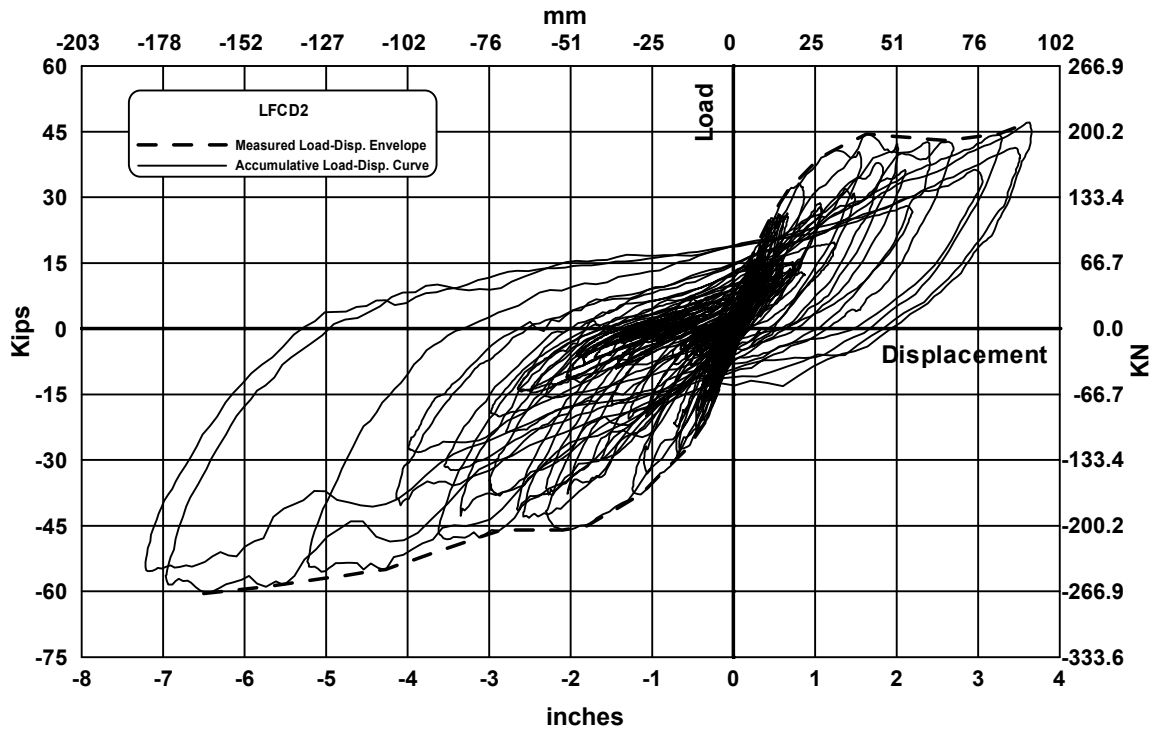
Figure 1.5 Load-Displacement Relationship for LFCD2
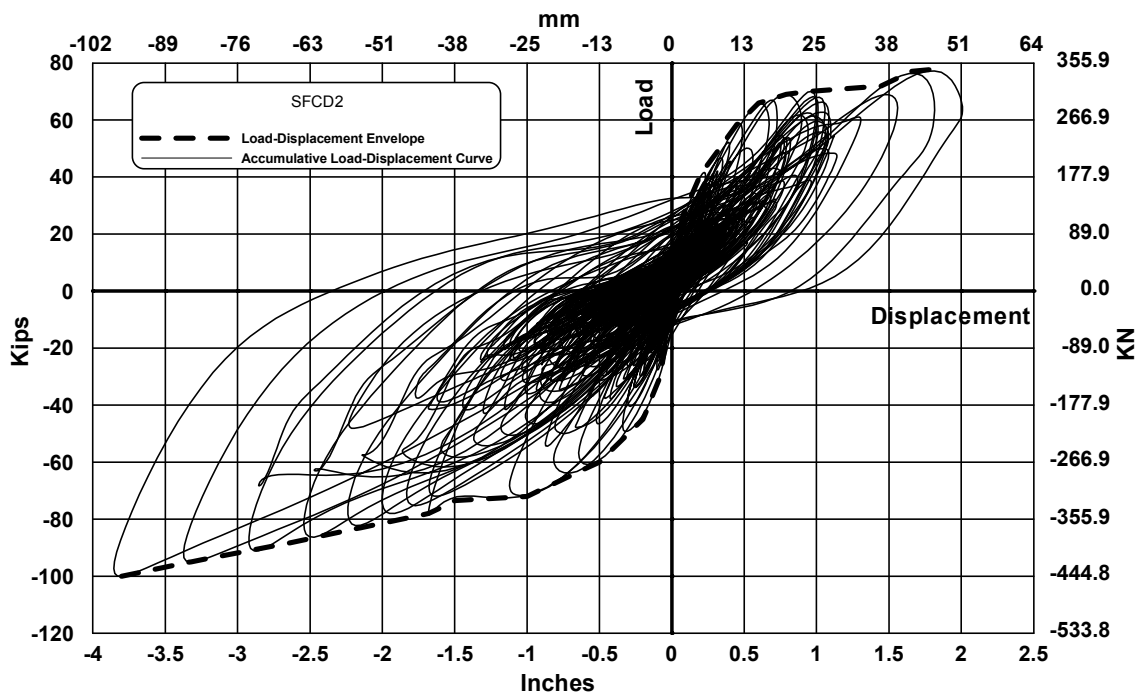
Figure 1.6 Load-Displacement Relationship for SFCD2

Figure 2.1a Reinforcement Details of SFCD3 (English Units)

73

Figure 2.1b Reinforcement Details of SFCD3 (Metric Units)

74
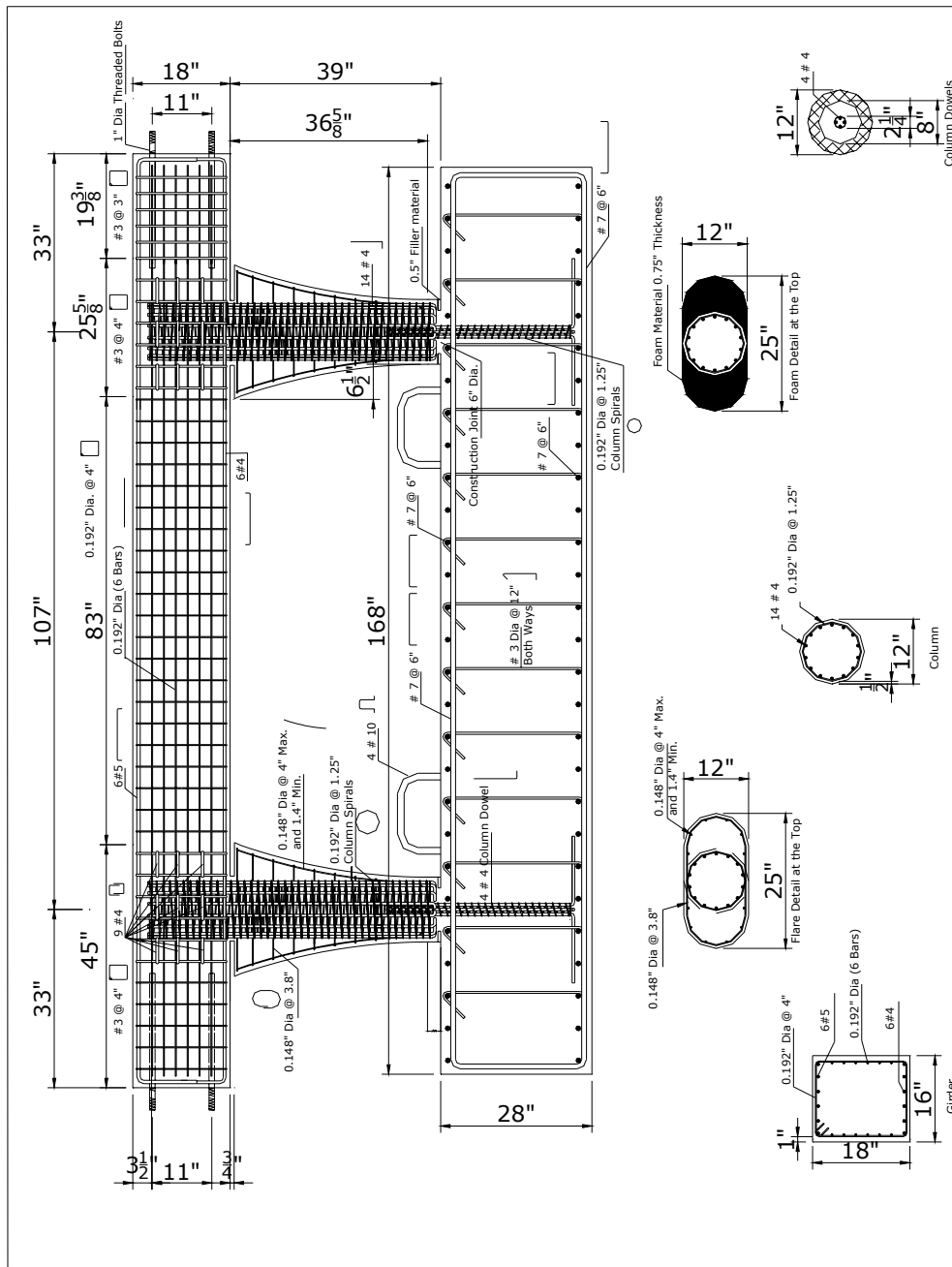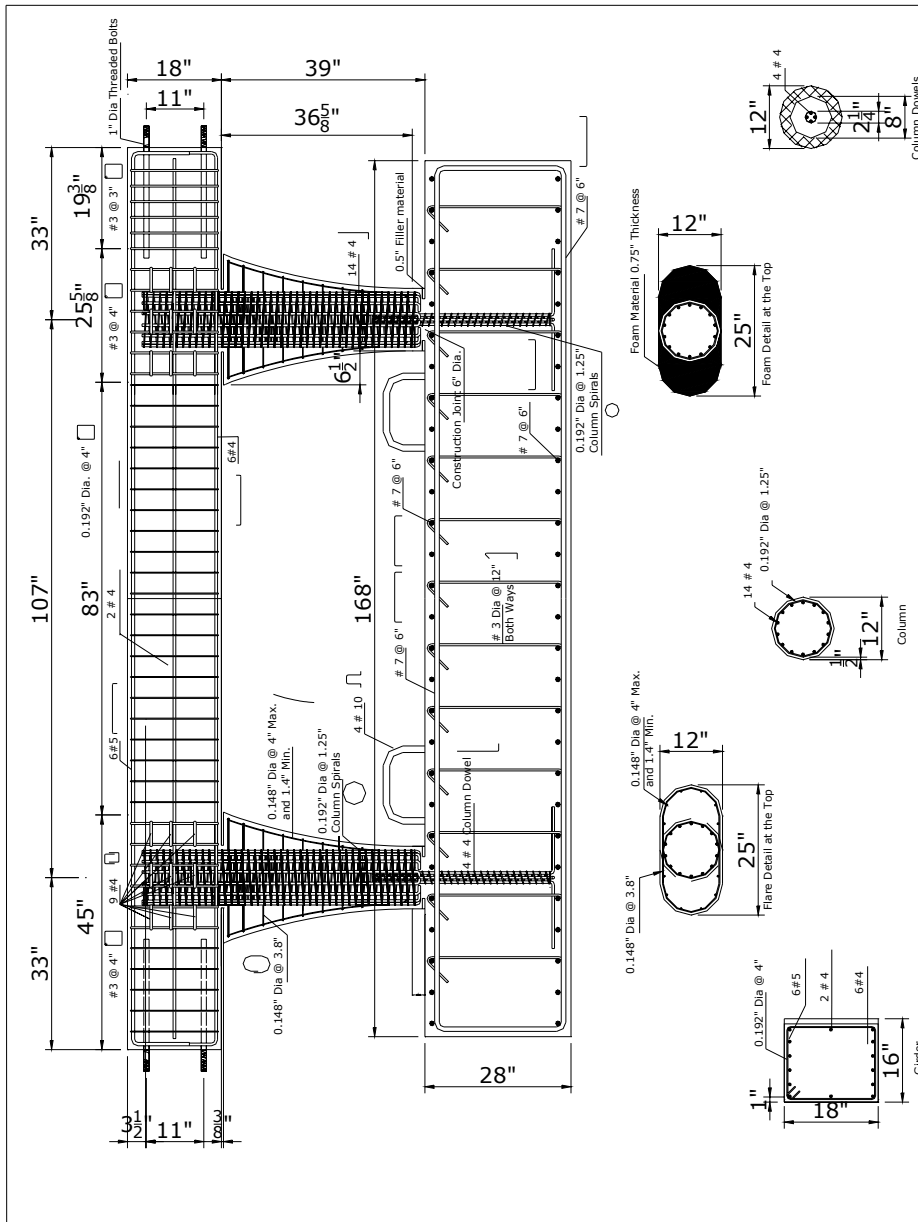
Figure 2.2a Reinforcement Details of SFCD2S (English Units)

75
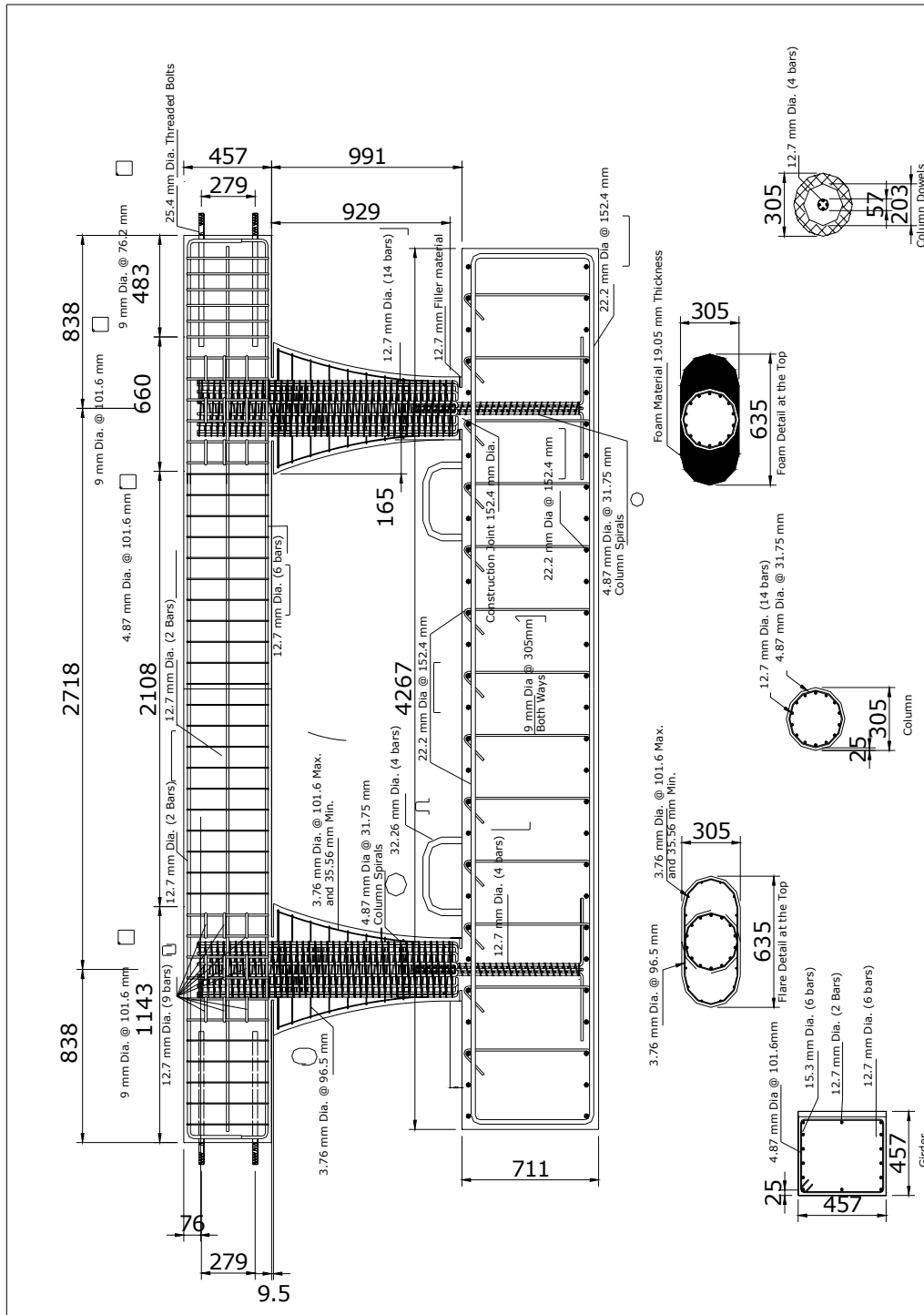
Figure 2.2b Reinforcement Details of SFCD2S (Metric Units)
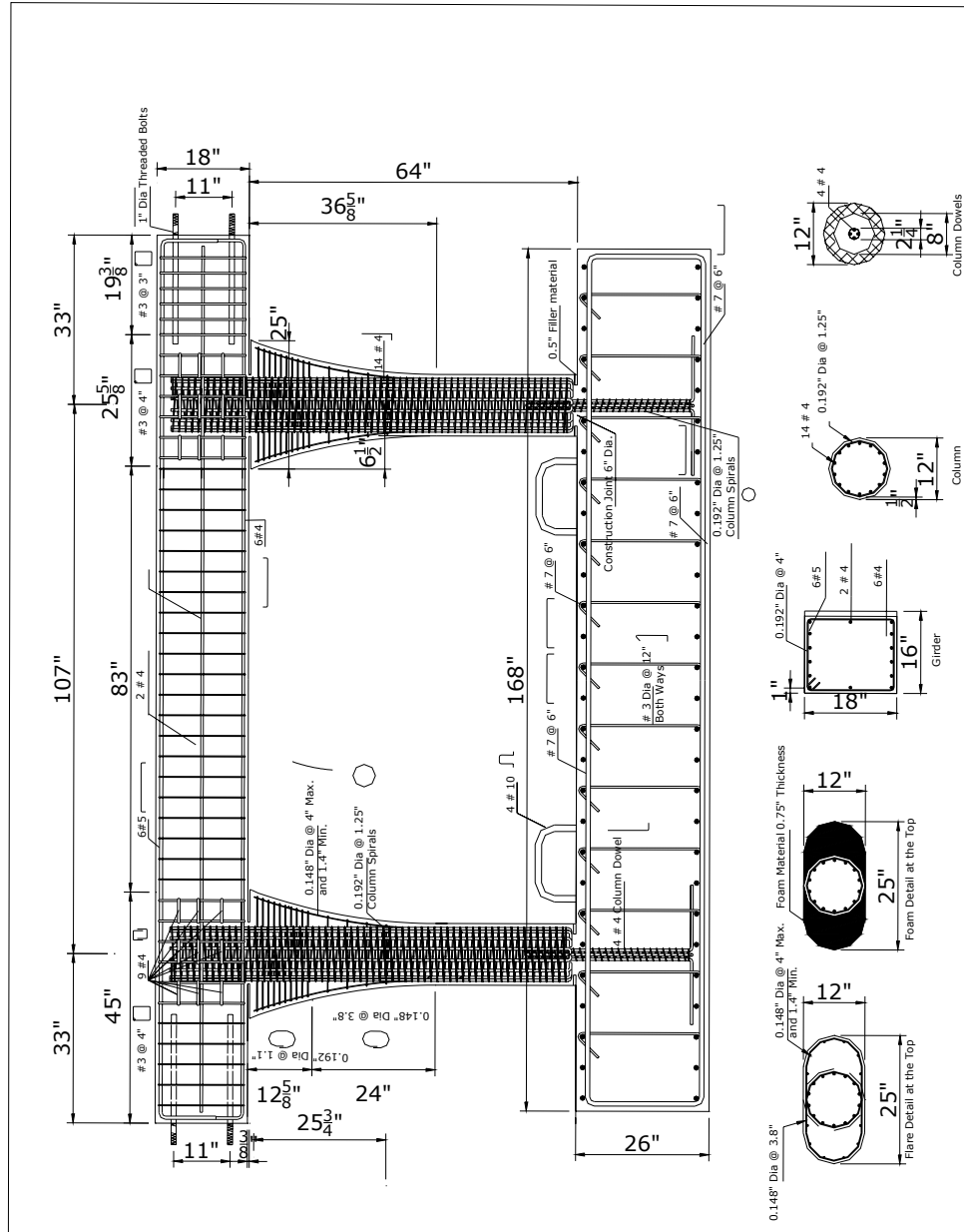
Figure 2.3a Reinforcement Details of LFCD1S (English Units)

77

Figure 2.3b Reinforcement Details of LFCD1S (Metric Units)

78
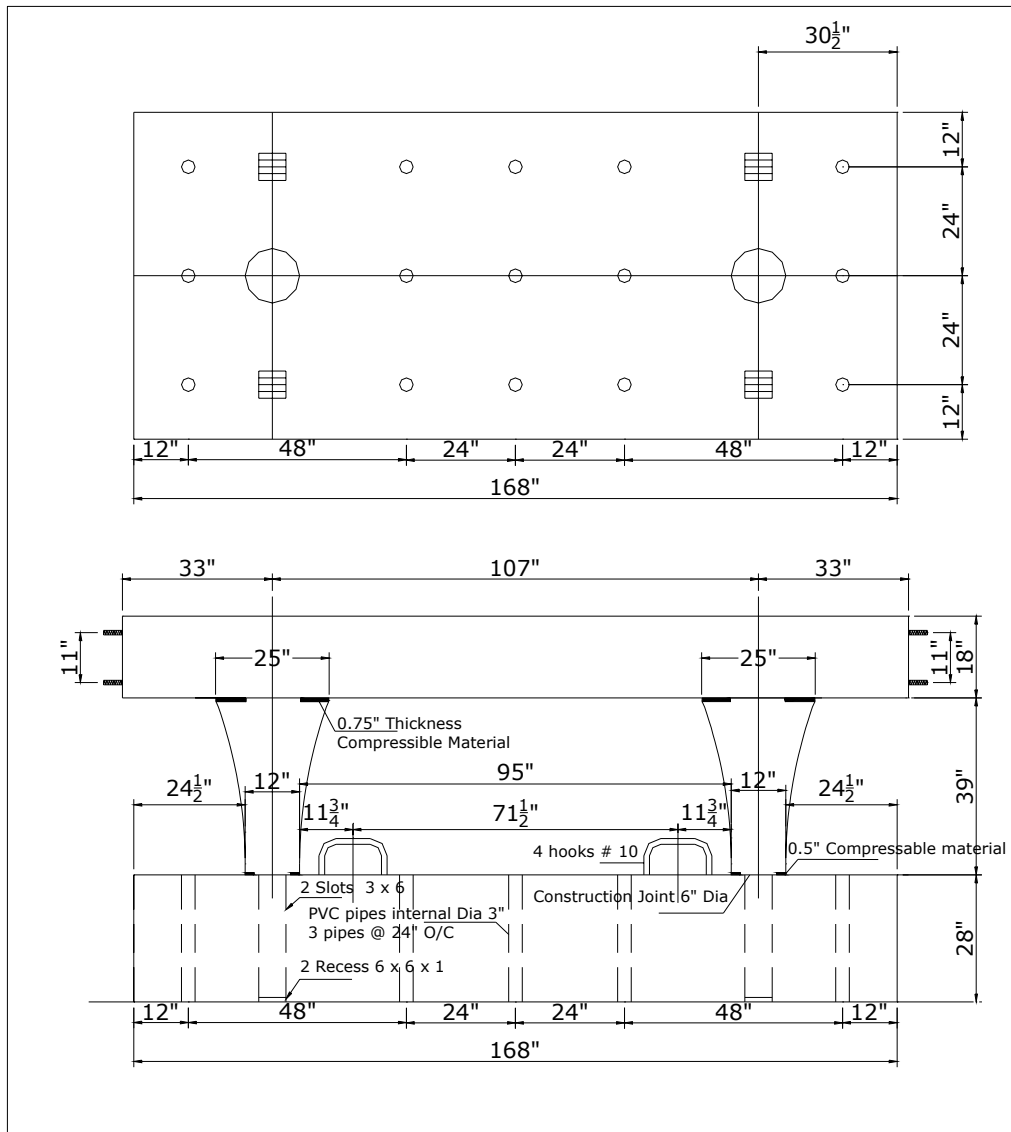
Figure 2.4a Footing Details (English Units)
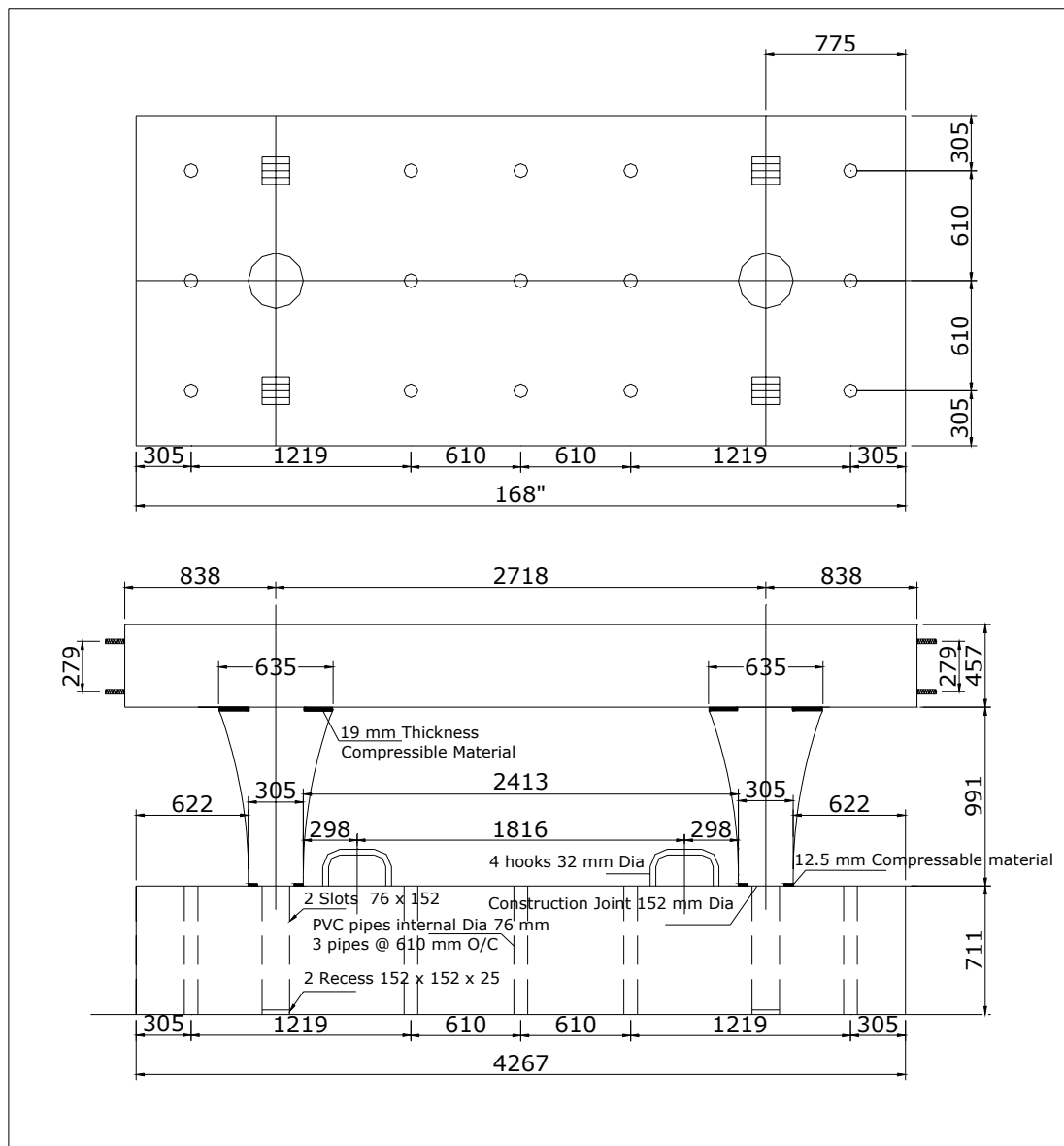
Figure 2.4b Footing Details (Metric Units)
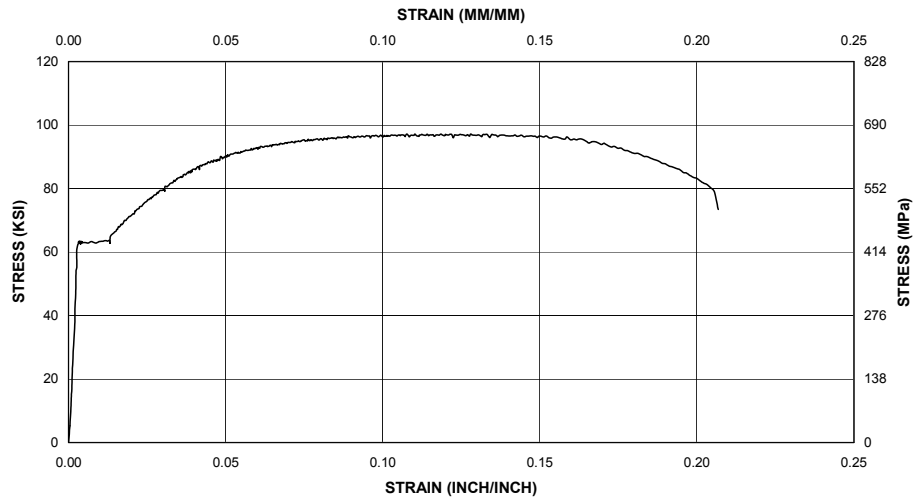
Figure 2.5a Stress-Strain Relationship for 9.5 mm Dia. (# 3) Reinforcement Bar
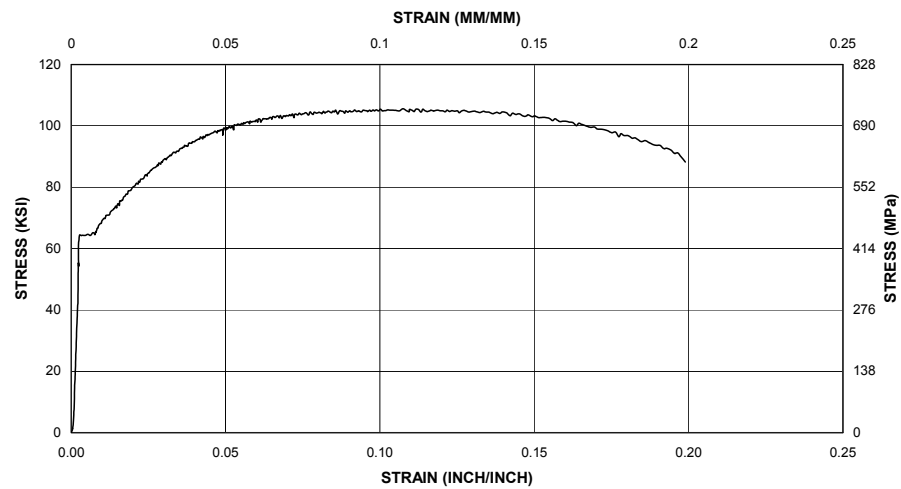
Figure 2.5b Stress-Strain Relationship for 12.5 mm Dia. (# 4) Reinforcement Bar
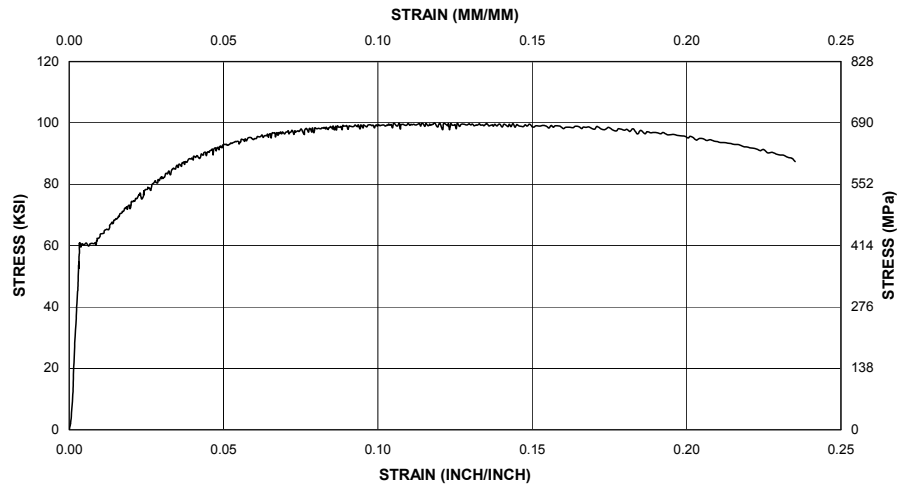
Figure 2.5c Stress-Strain Relationship for 15.9 mm Dia. (# 5) Reinforcement Bar
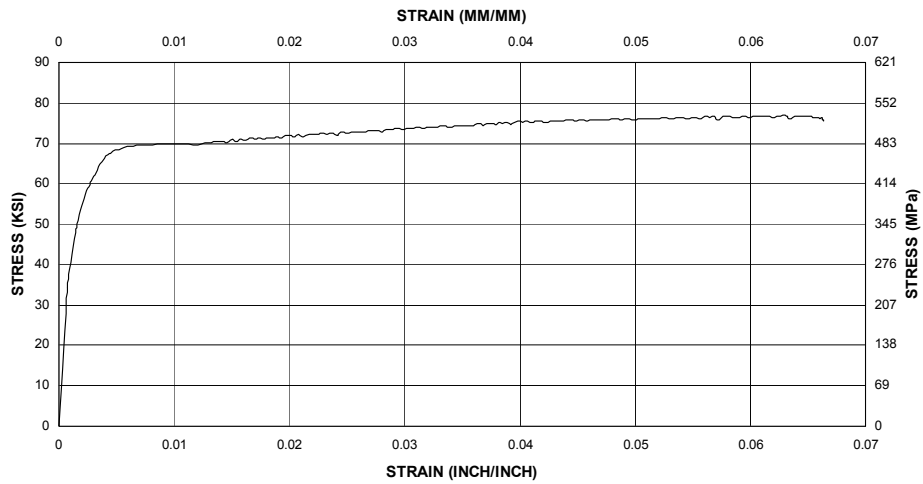
Figure 2.5d Stress-Strain Relationship for 5 mm (0.192 in) Diameter Bars
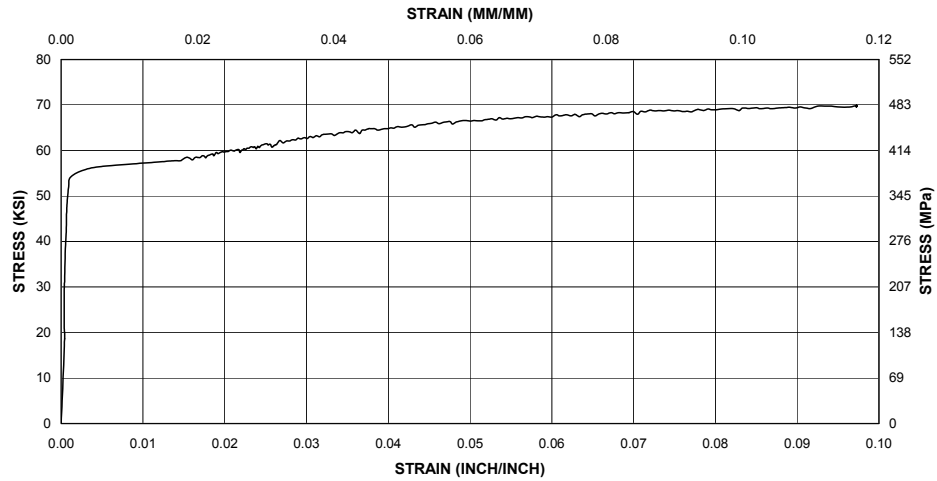
Figure 2.5e Stress-Strain Relationship for 3.8 mm (0.148 in) Diameter Bars
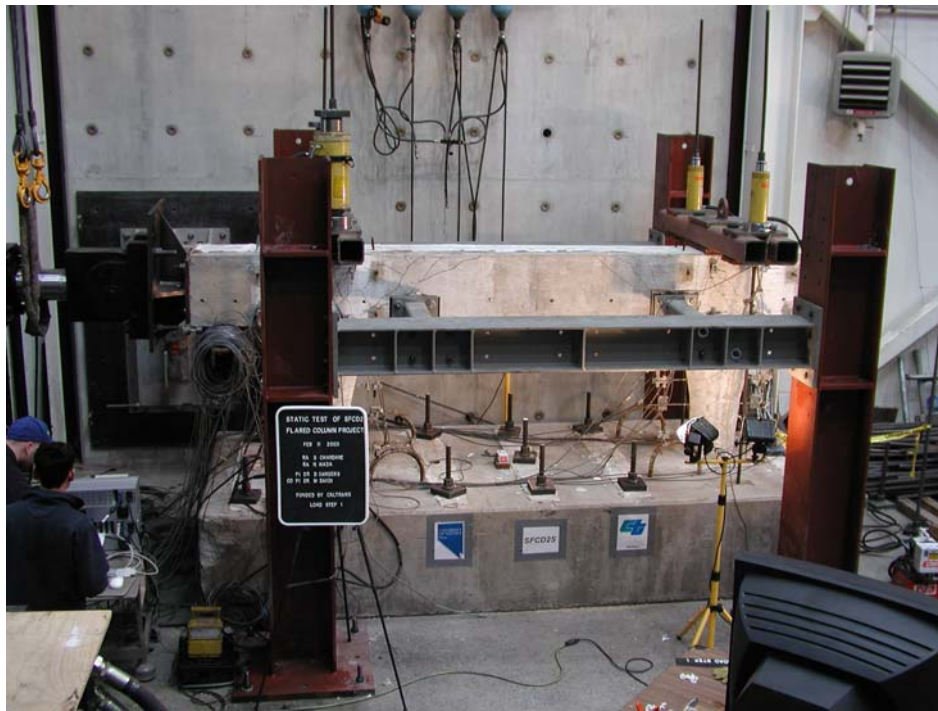
Figure 2.6 Static Test Setup
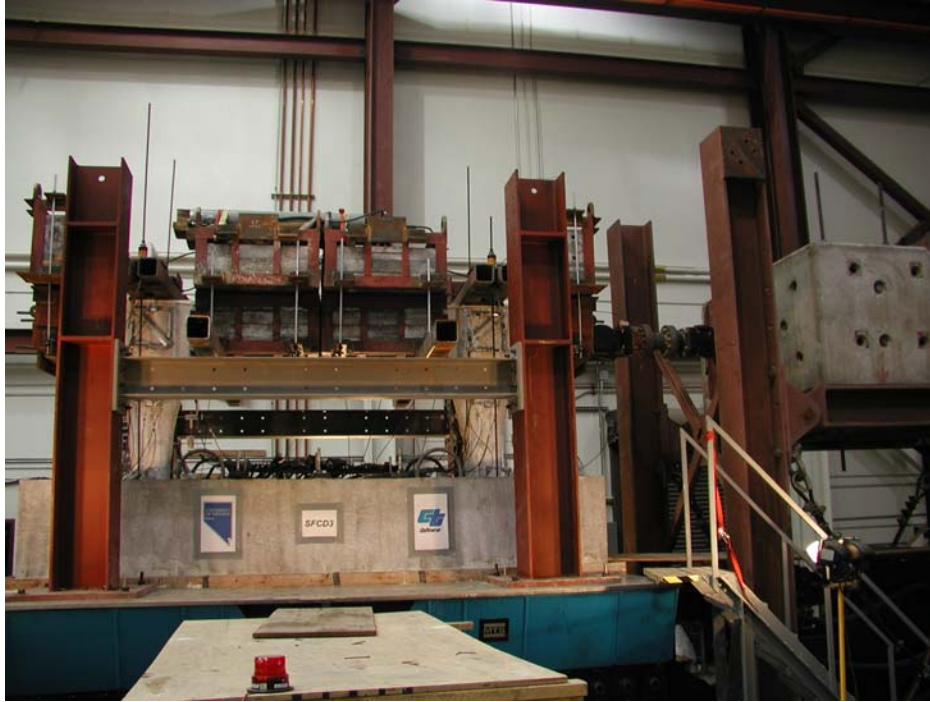
Figure 2.7 Shake Table Test Setup
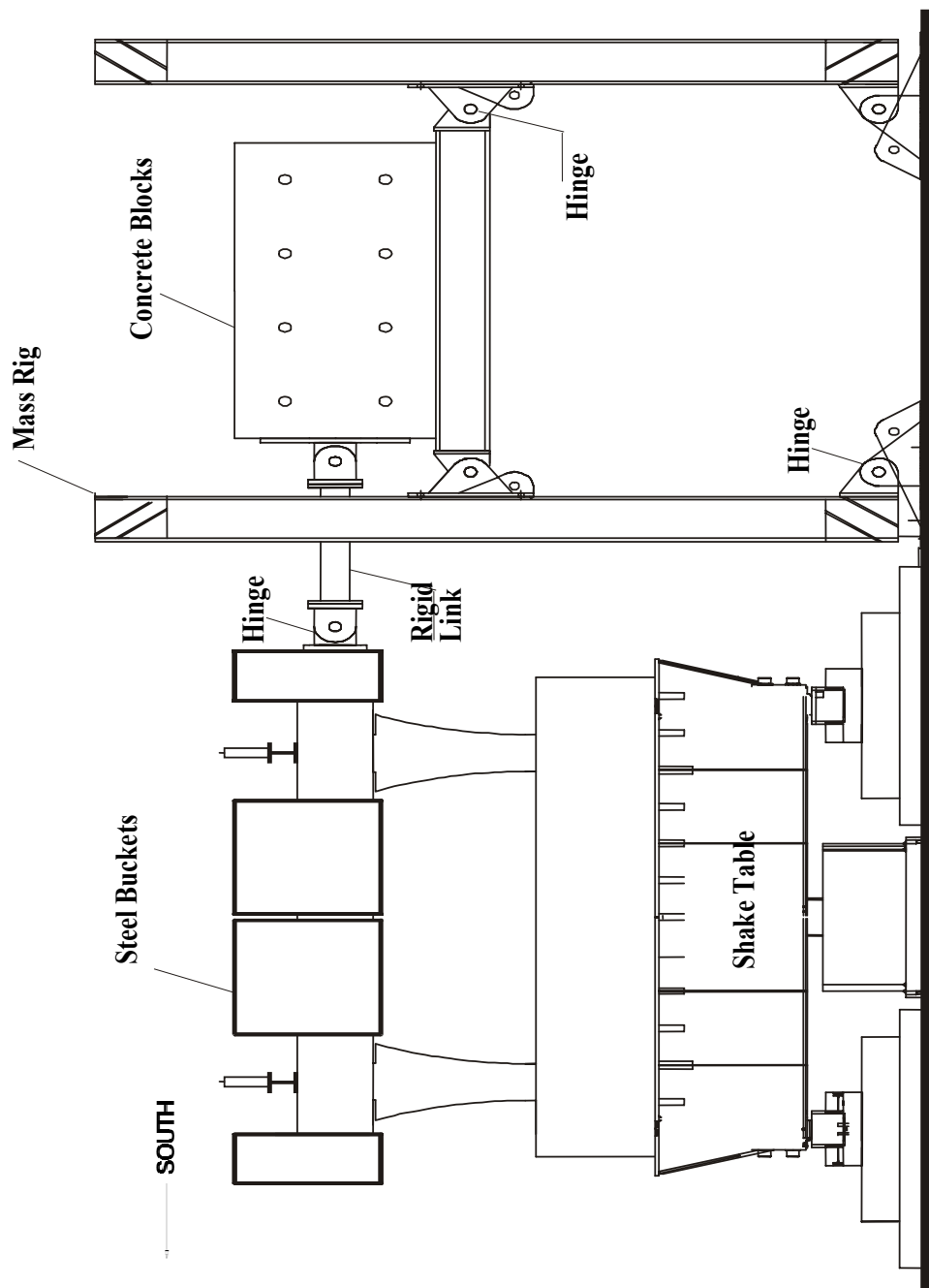
Figure 2.8 Test Setup for SFCD3

Concrete Blocks

Mass Rig

Hinge

Hinge

Hinge

Rigid Link

Steel Buckets

Shake Table

SOUTH
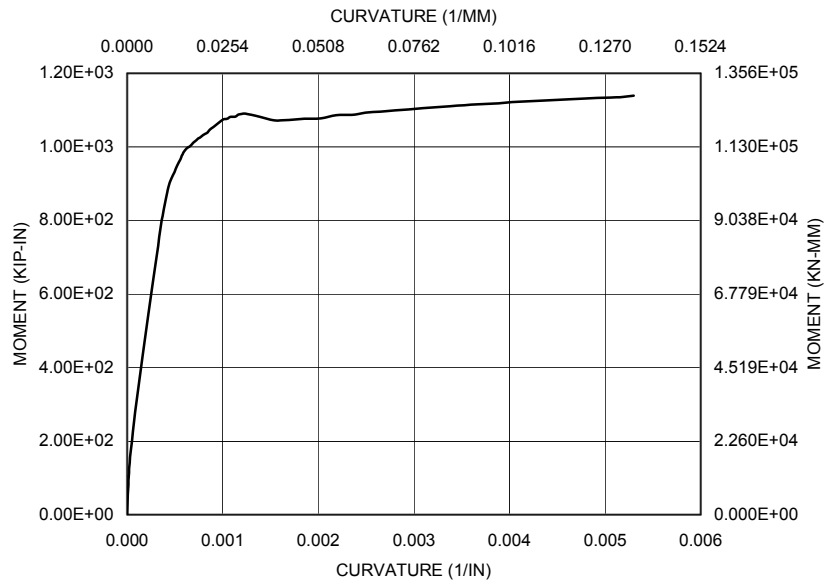
Figure 2.9 Moment-Curvature Relationship for Column Core in SFCD3
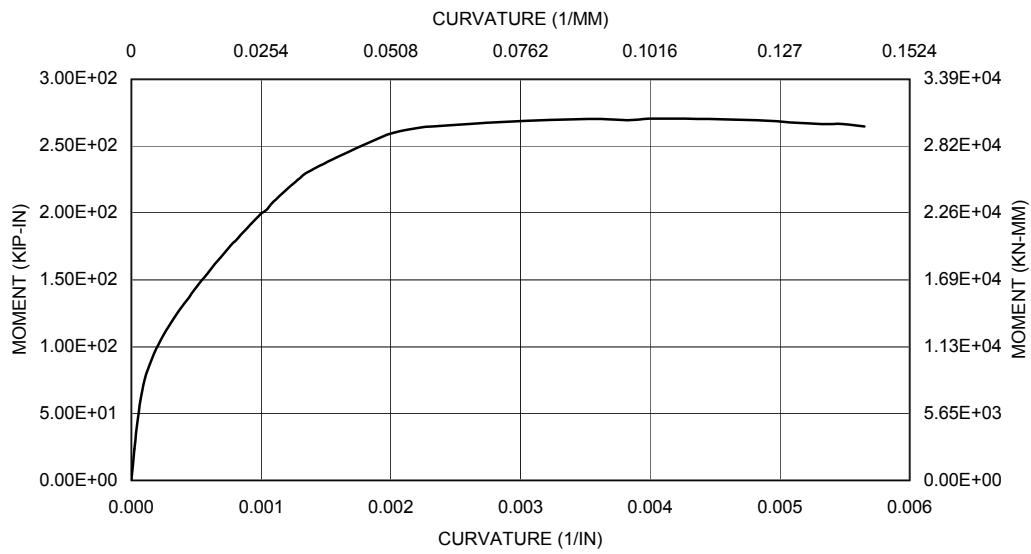
Figure 2.10 Moment-Curvature Relationship for Base-Hinge in SFCD3
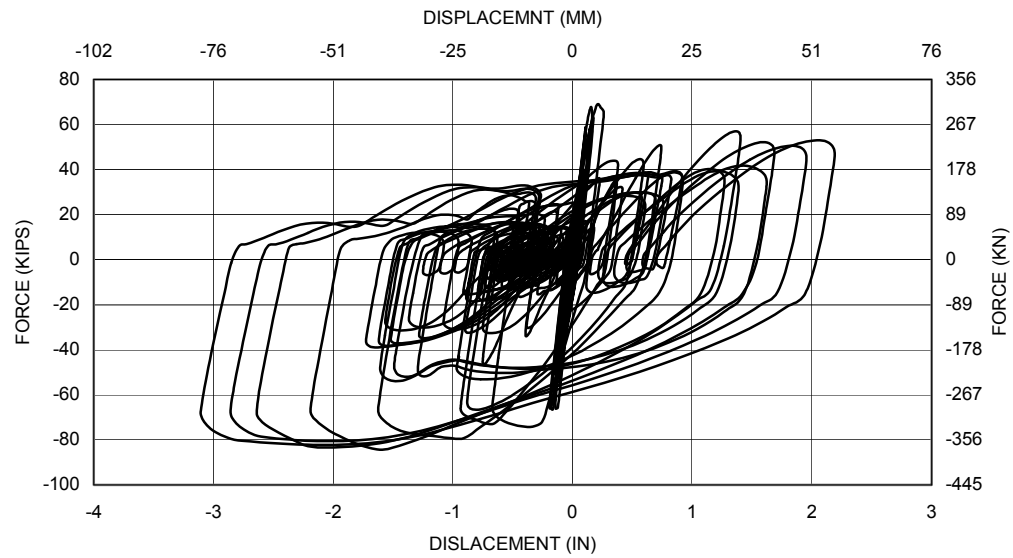
Figure 2.11 Load Deflection Diagram from RC-shake for Sylmar Runs of 0.25, 0.5, 0.75, 1.0, 1.5, 2.0, 2.5, 3.0, 3.25 and 3.5
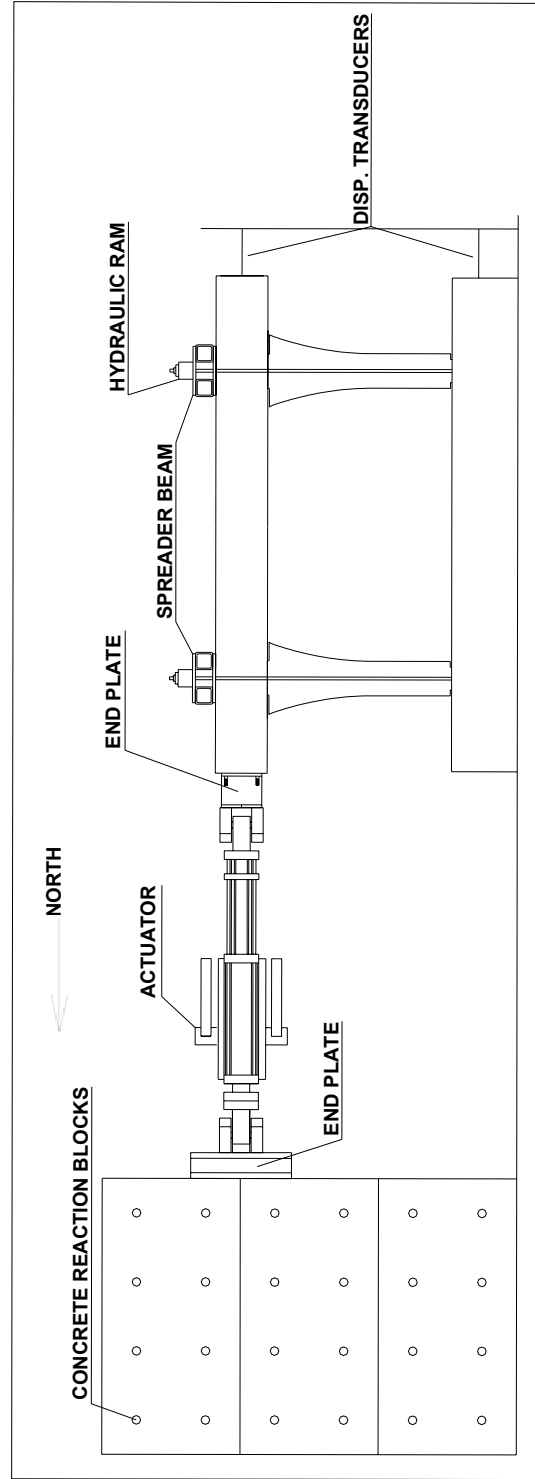
Figure 2.12 Test Setup for LFCD1S and SFCD2S

88
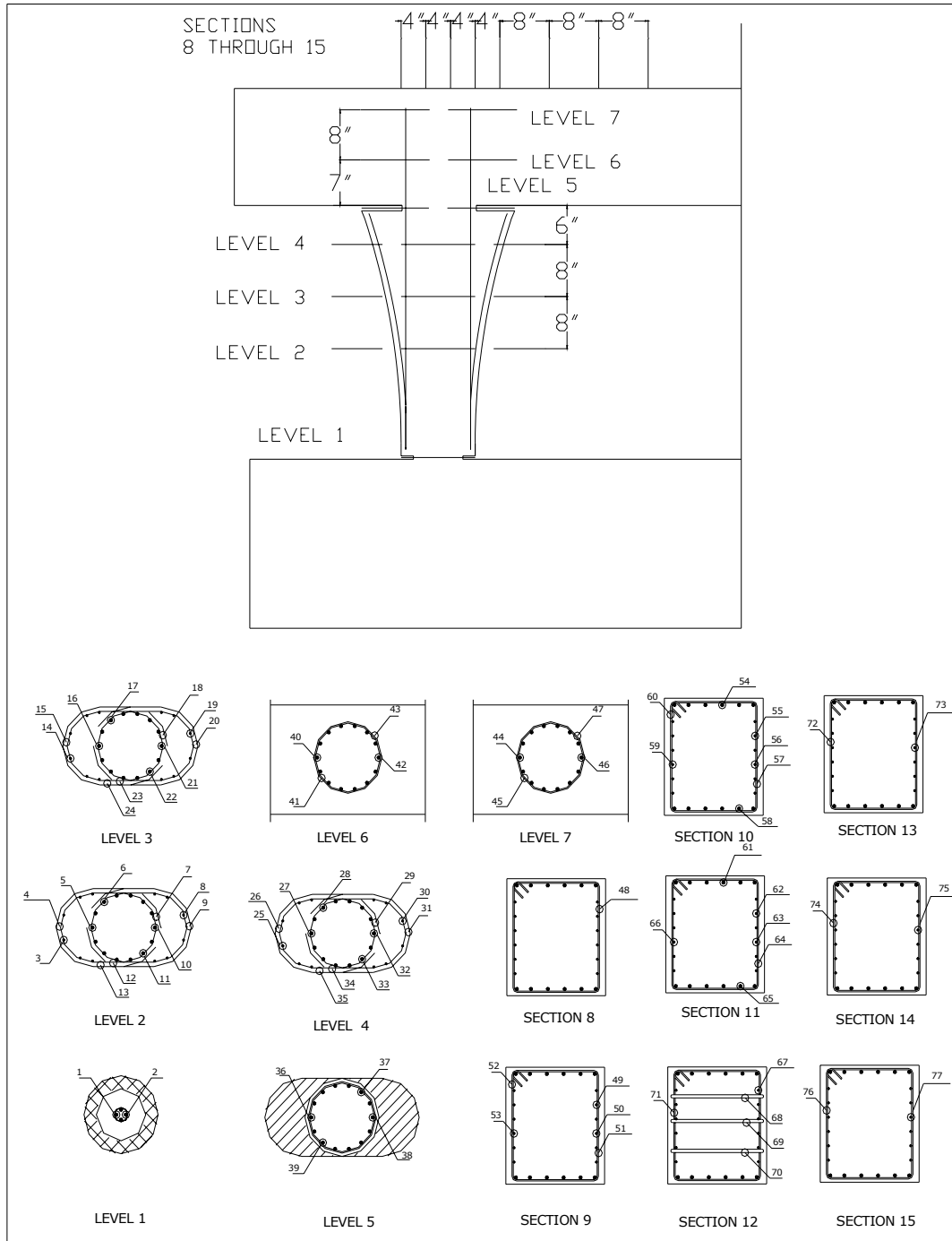
Figure 2.13a Strain Gages for SFCD3 (English)
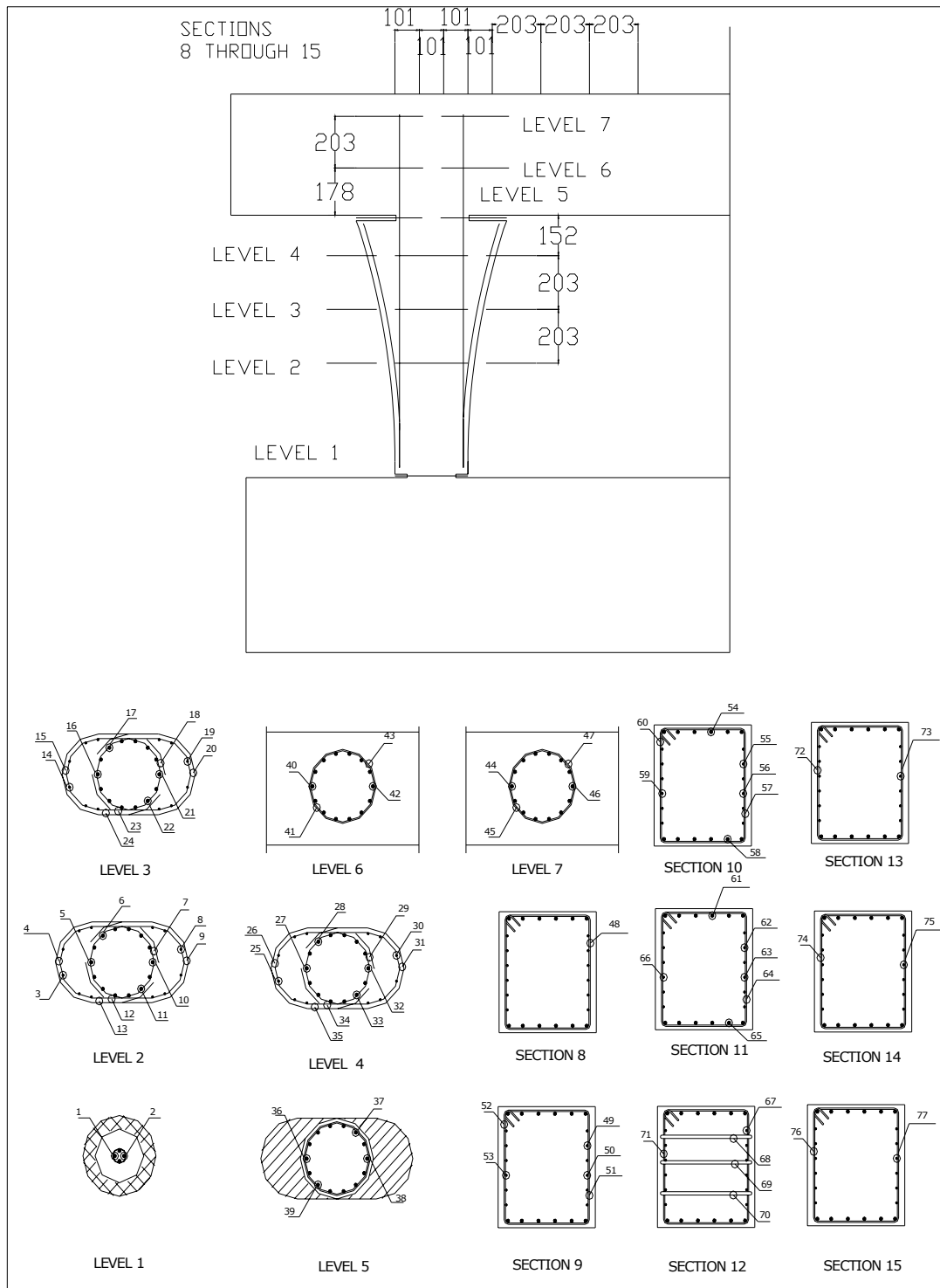
Figure 2.13b Strain Gages for SFCD3 (Metric)
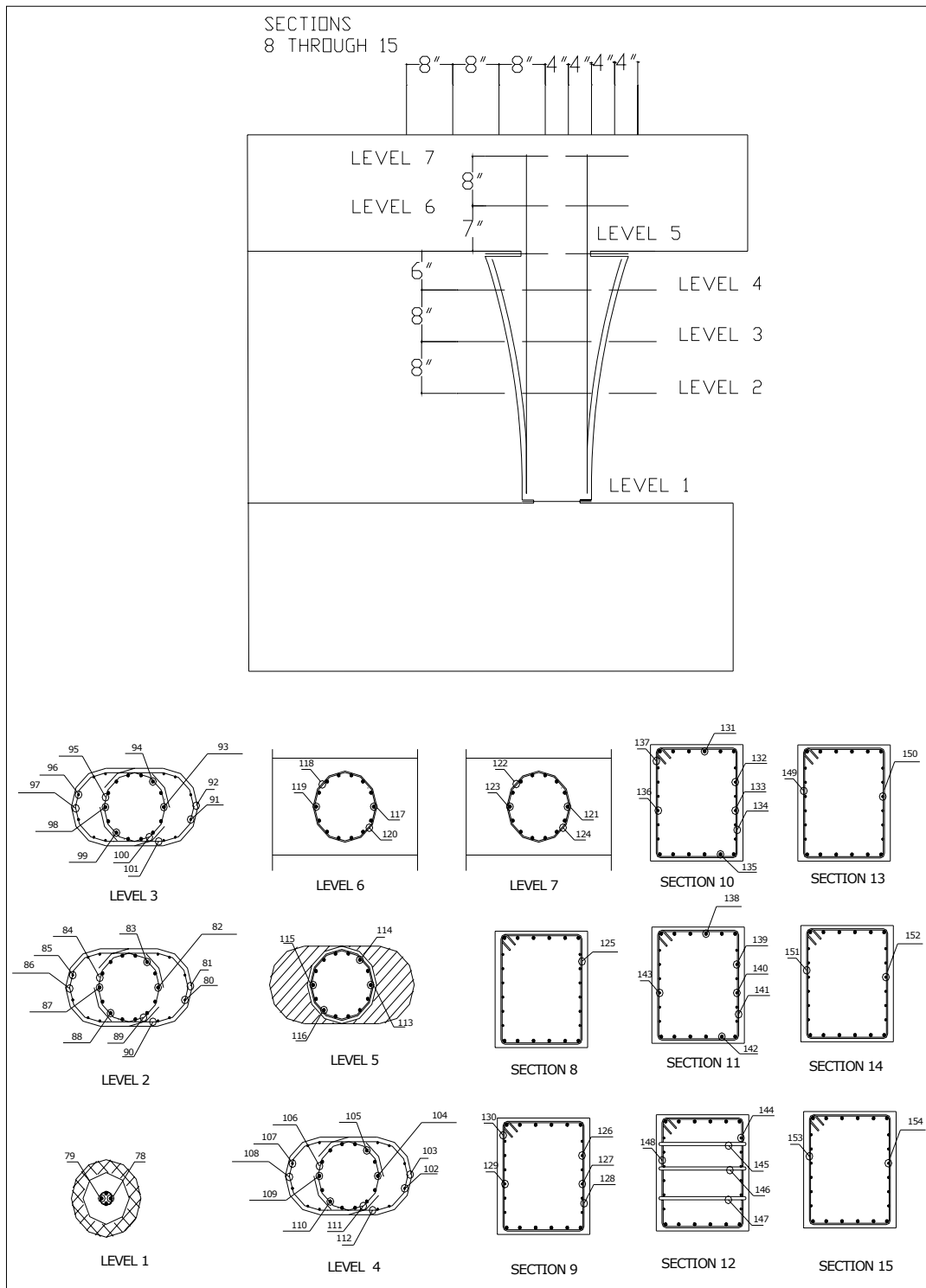
Figure 2.13c Strain Gages for SFCD3 (English)
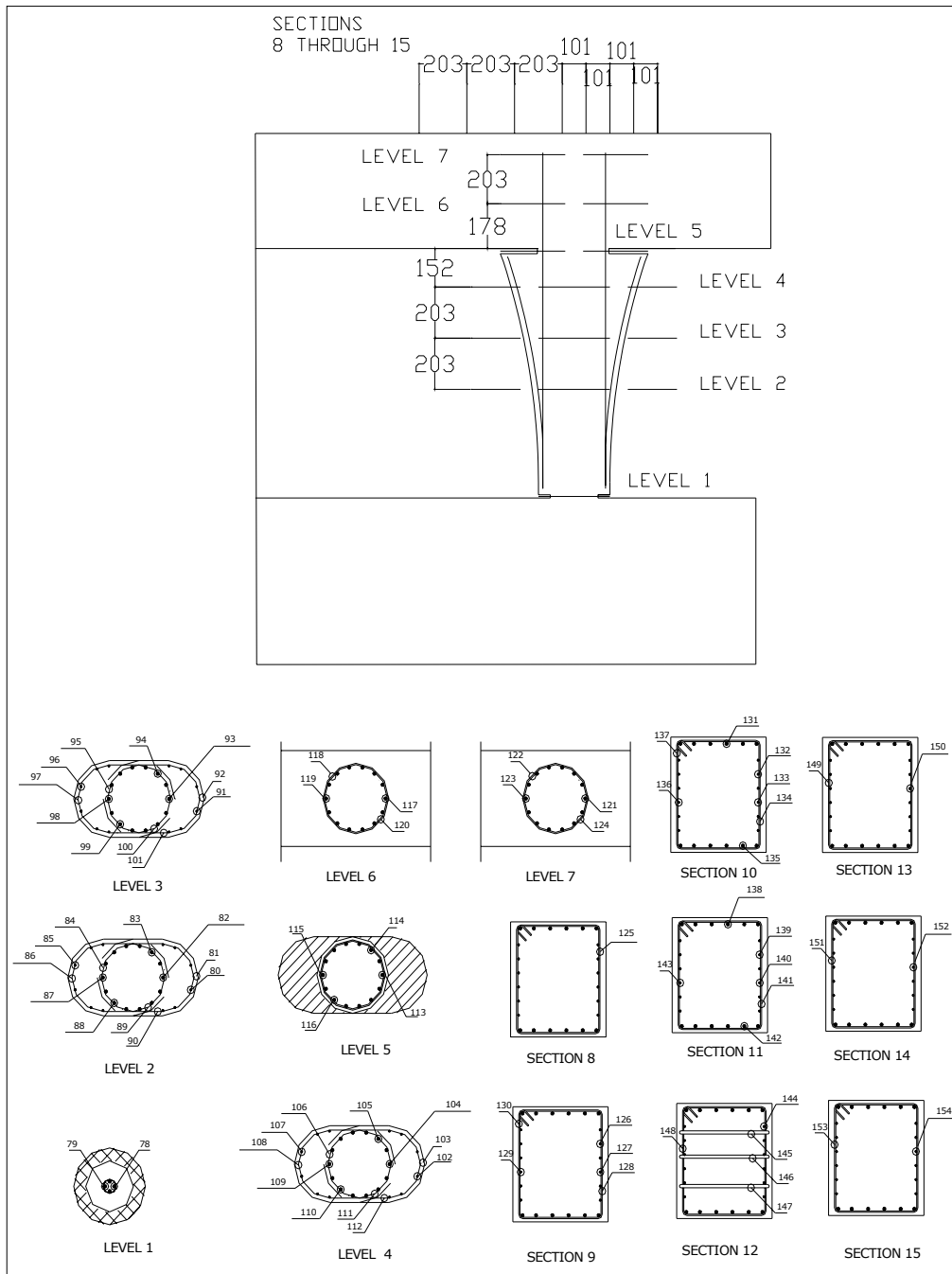
Figure 2.13d Strain Gages for SFCD3 (Metric)

Figure 2.14 Displacement Transducers for SFCD3

93
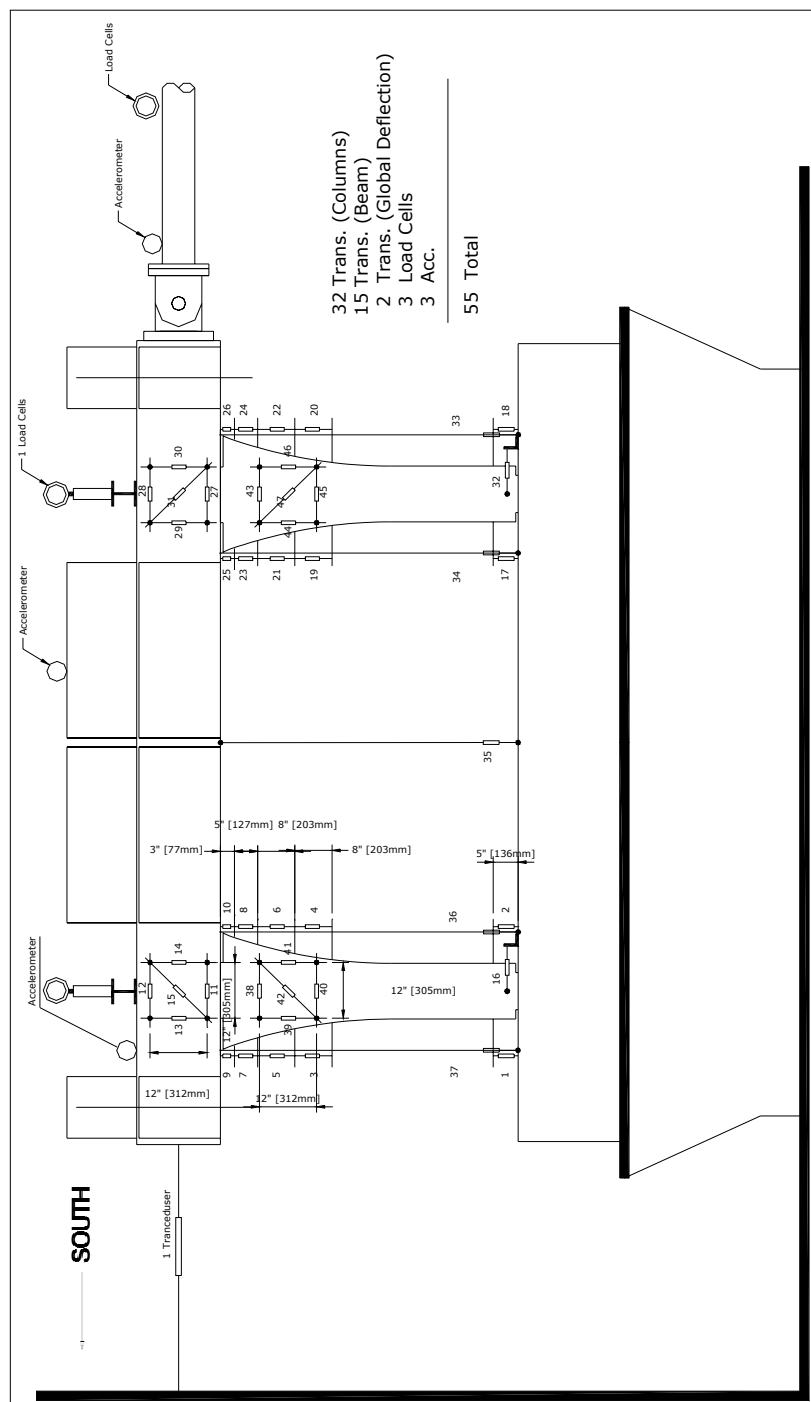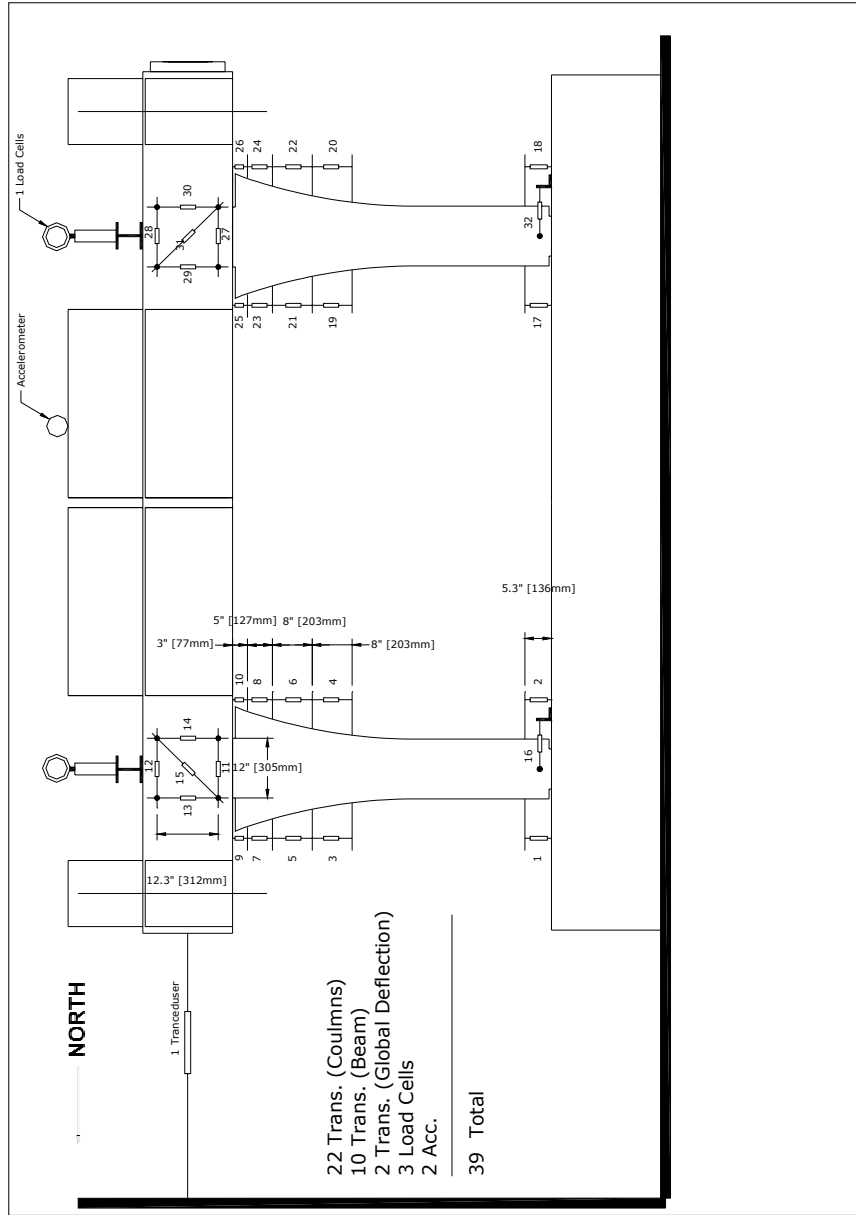
Figure 2.15 Displacement Transducer for LFCD1S and SFCD2S

94
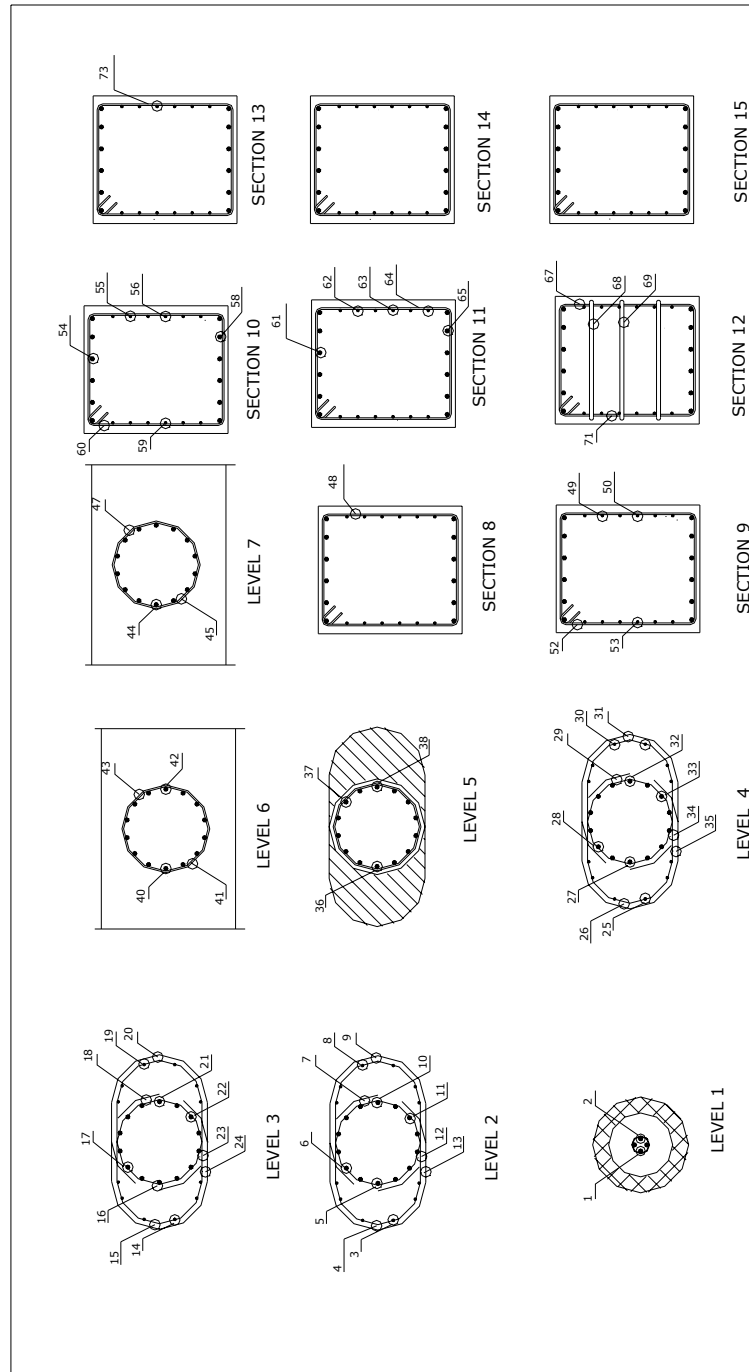
Figure 3.1a Available Strain Gages Through Testing

95
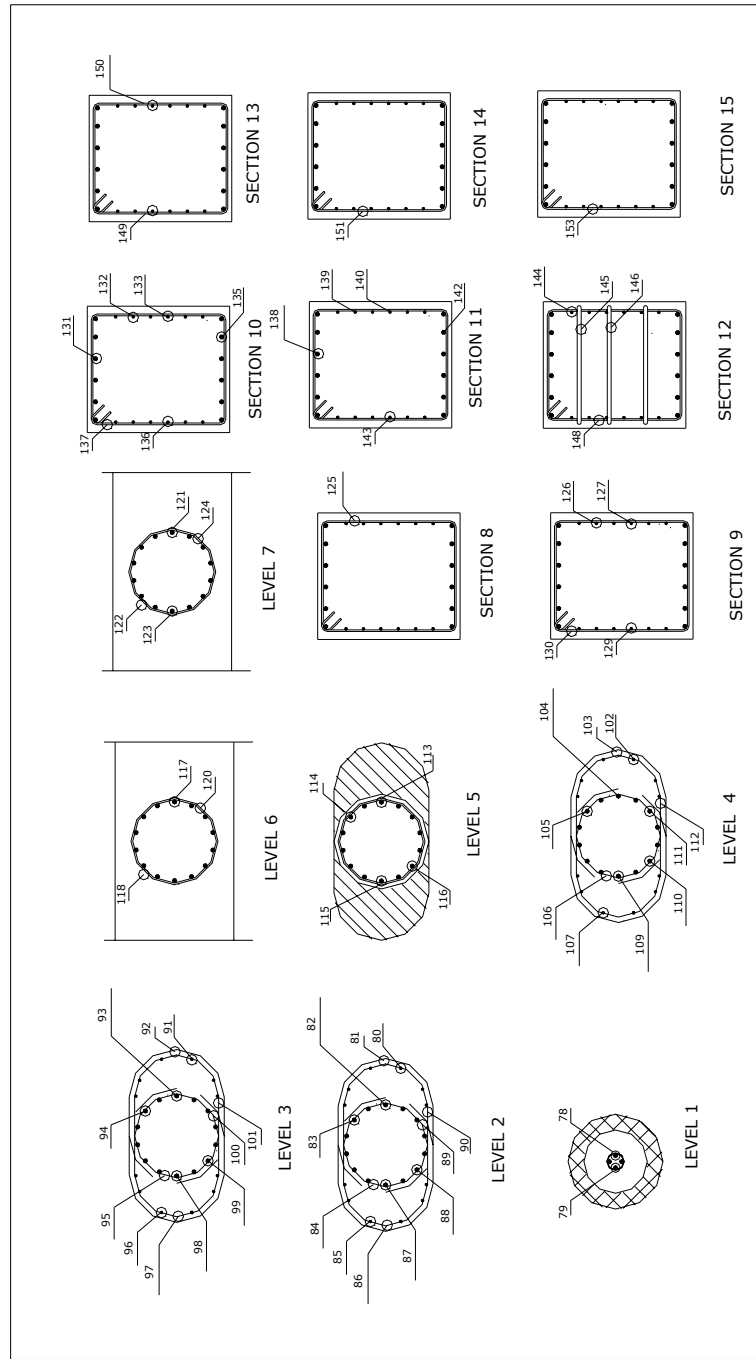
Figure 3.1b Available Strain Gages Through Testing

96

Figure 3.2 No Cracks at 0.25 Times Sylmar

Figure 3.3 Vertical Crack at 0.50 Times Sylmar

Figure 3.4 Vertical Cracks at 0.75 Times Sylmar

Figure 3.5 Flexural and Shear Crack at 1.00 Times Sylmar

Figure 3.6 Flexural and Shear Cracks at 1.00 Times Sylmar
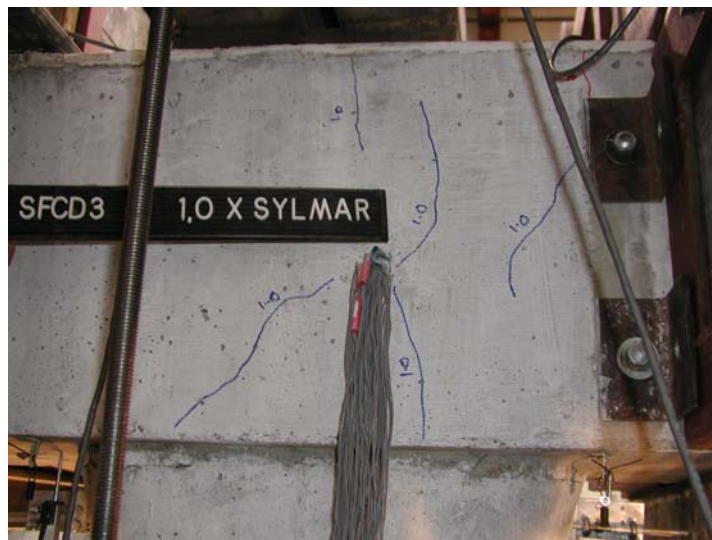
Figure 3.7 Flexural and Shear Cracks in Joint at 1.00 Times Sylmar

99
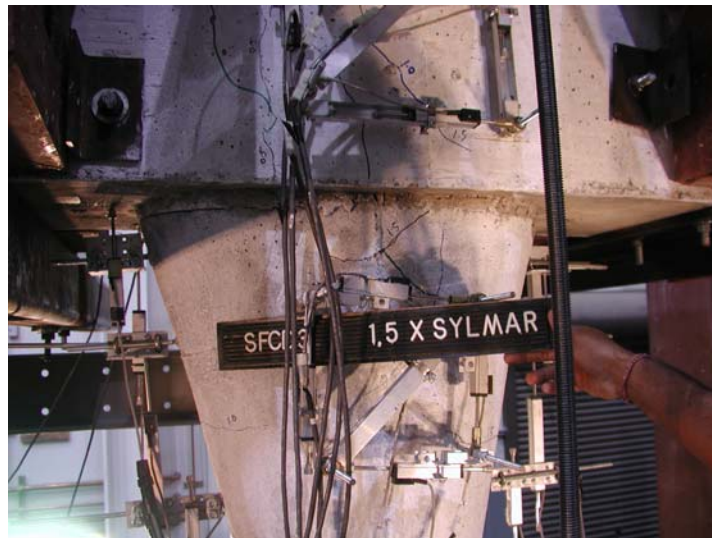
Figure 3.8 Cracks at 1.50 Times Sylmar

Figure 3.9 First Cracking in Base at 1.75 Times Sylmar
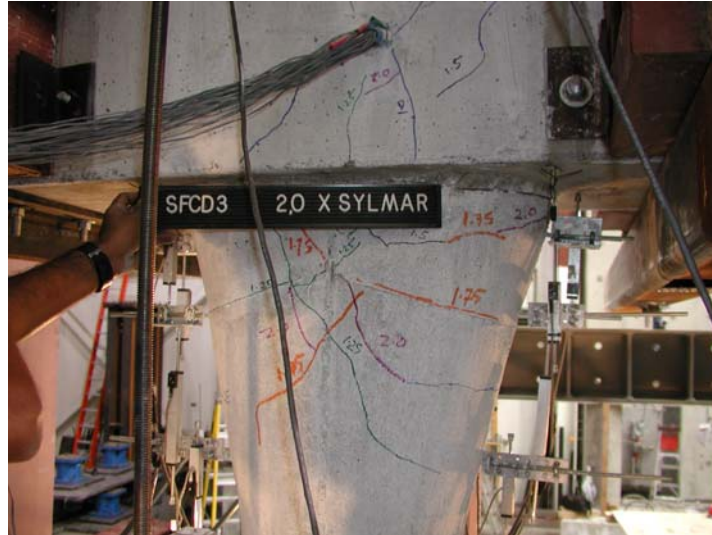
Figure 3.10 Shear Flexure Interaction Cracks at 2.00 Times Sylmar

Figure 3.11 Shear Flexure Interaction Cracks at 2.00 Times Sylmar

Figure 3.12 Vertical Crack in Flare at 2.50 Times Sylmar

Figure 3.13 Spalling at the Column Base at 3.00 Times Sylmar
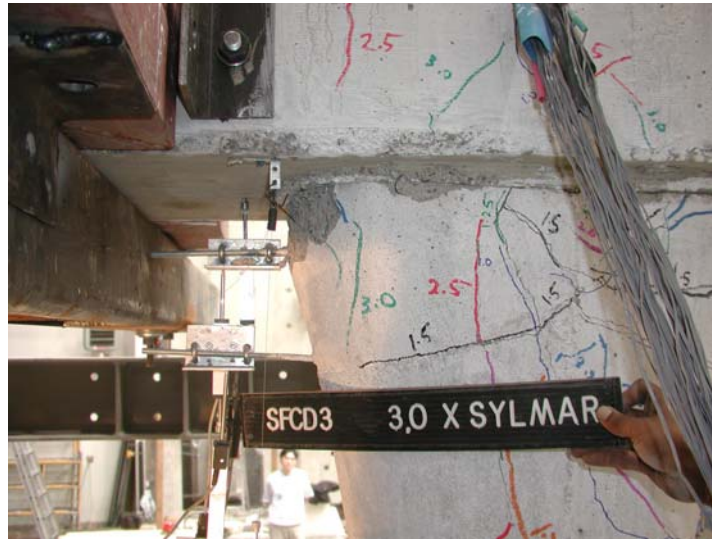
Figure 3.14 Spalling at Flare Edge at 3.00 Times Sylmar
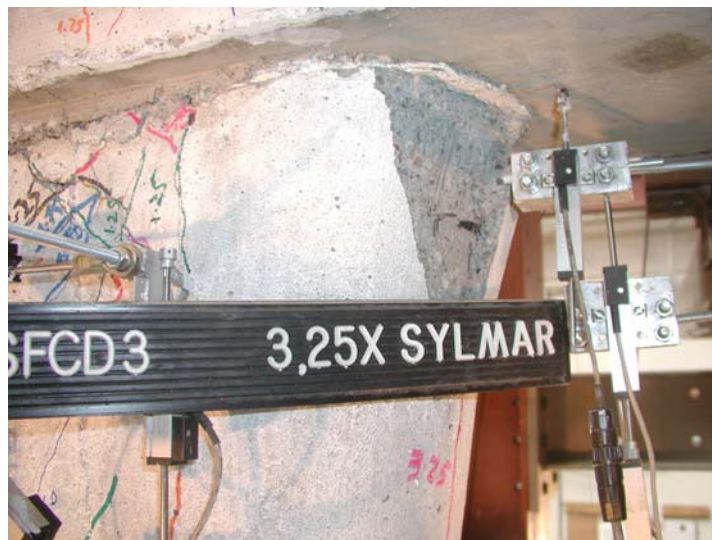
Figure 3.15 Exposed Flare Hoops at 3.25 Times Sylmar

Figure 3.16 Exposed Reinforcement at Base at 3.25 Times Sylmar
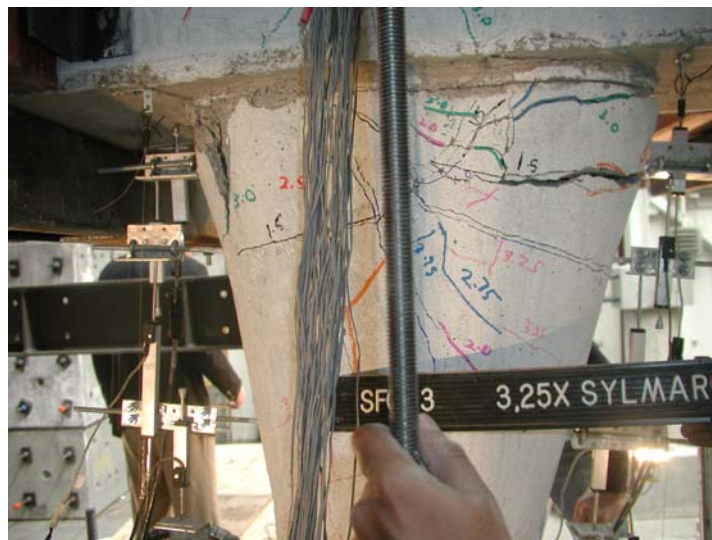
Figure 3.17 Cracking in Column at 3.25 Times Sylmar

Figure 3.18 Cracking in Joint at 3.25 Times Sylmar

Figure 3.19 Intense Spalling at Gap After Failure

Figure 3.20 Failed Column-Base

Figure 3.21 Shear Crack After Bucket Removal
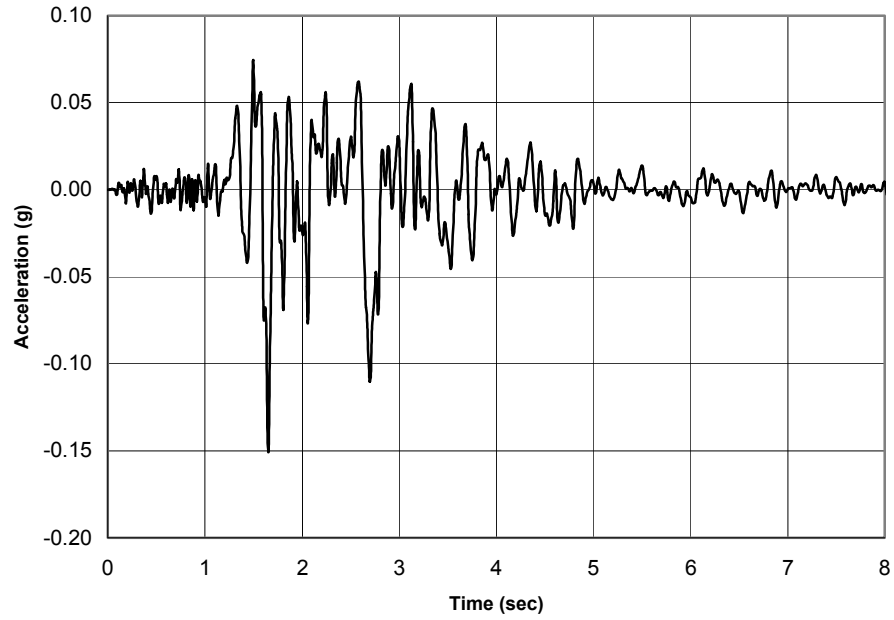
Figure 3.22 Scaled Sylmar Acceleration for 0.25 Times Sylmar
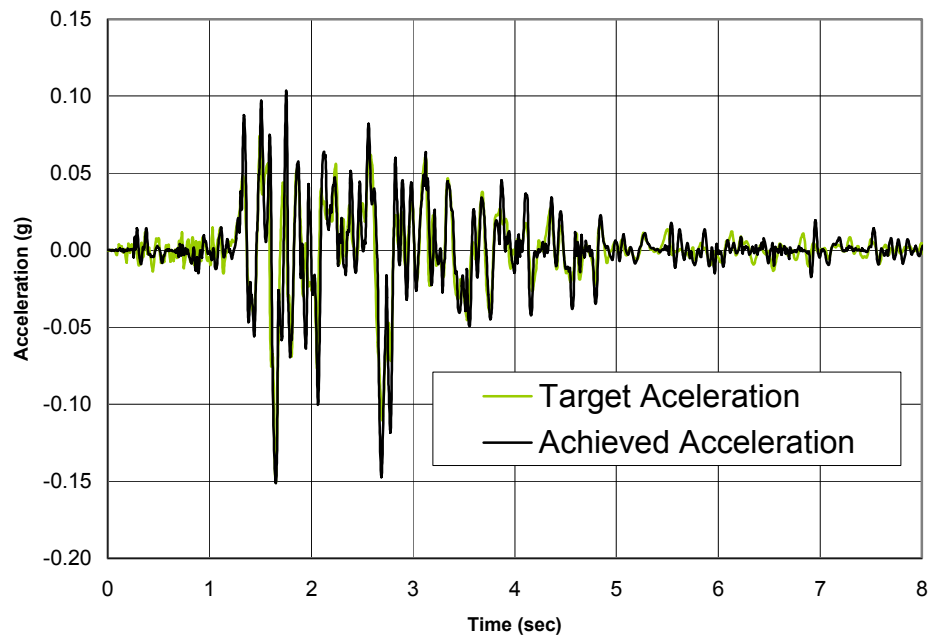
Figure 3.23 Acceleration Target and Achieved at 0.25 Times Sylmar

107
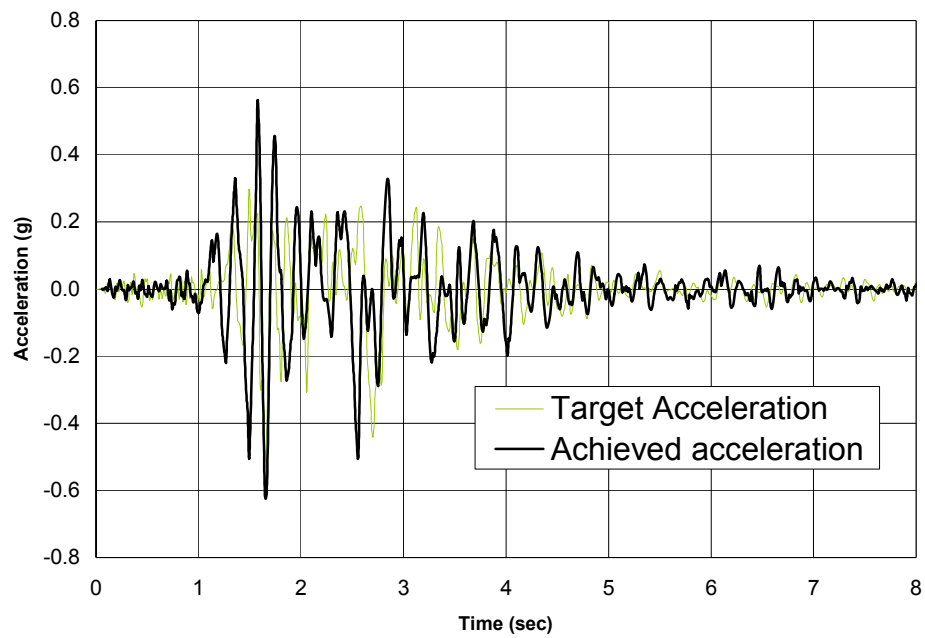
Figure 3.24 Acceleration Target and Achieved at 1.00 Times Sylmar
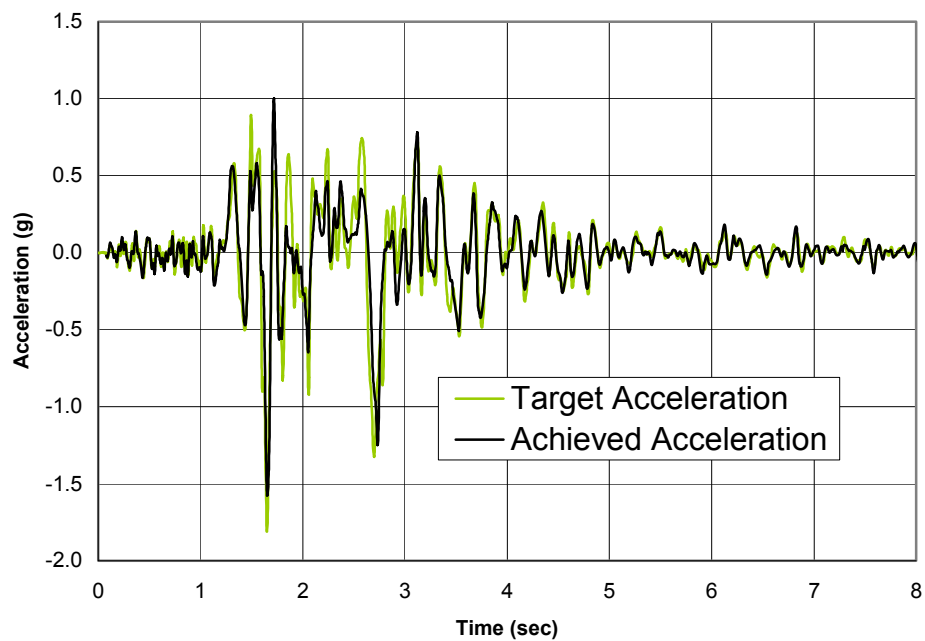
Figure 3.25 Acceleration Target and Achieved at 3.00 Times Sylmar
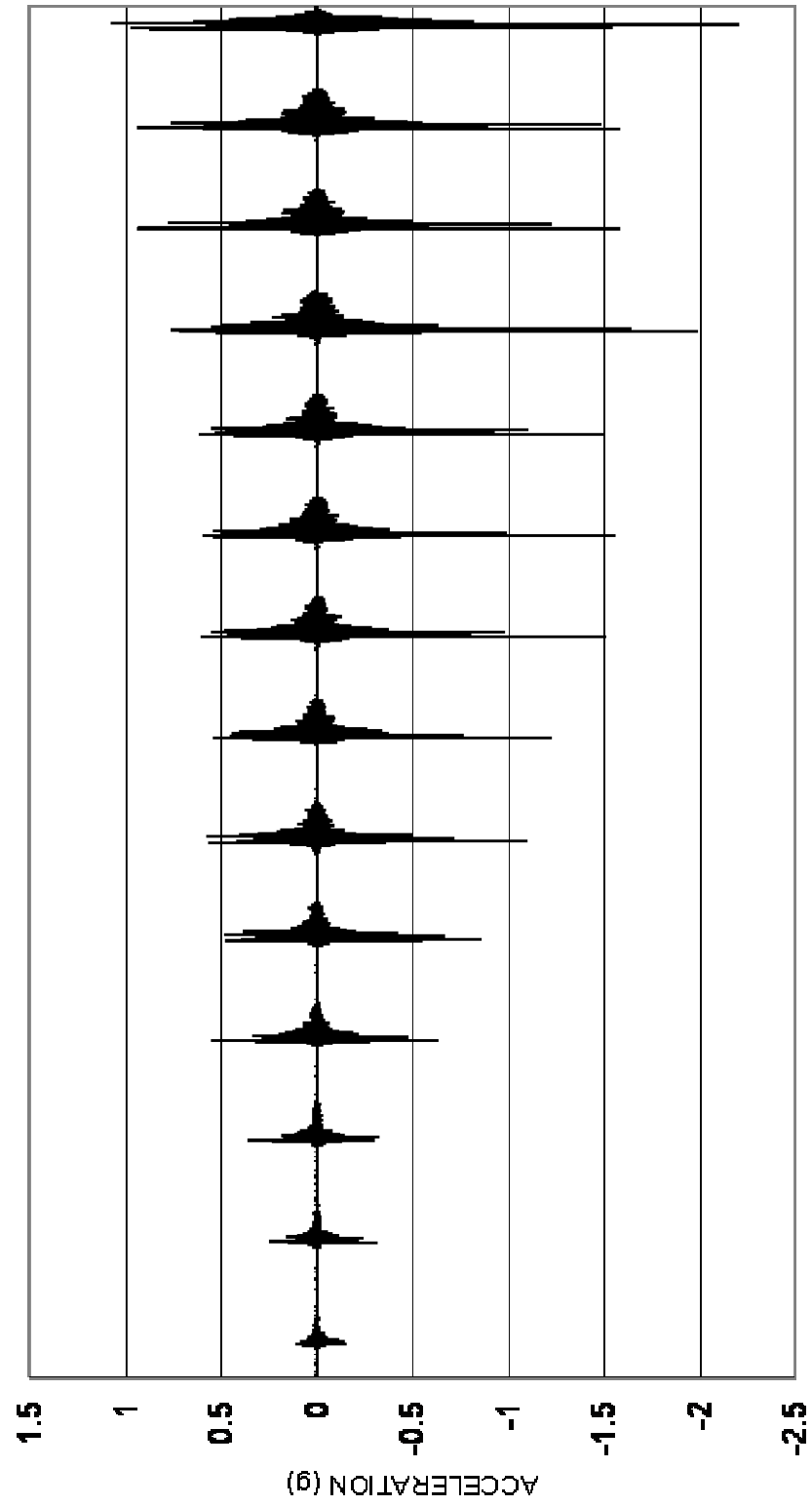
Figure 3.26 Time History of Achieved table Accelerations for All Runs
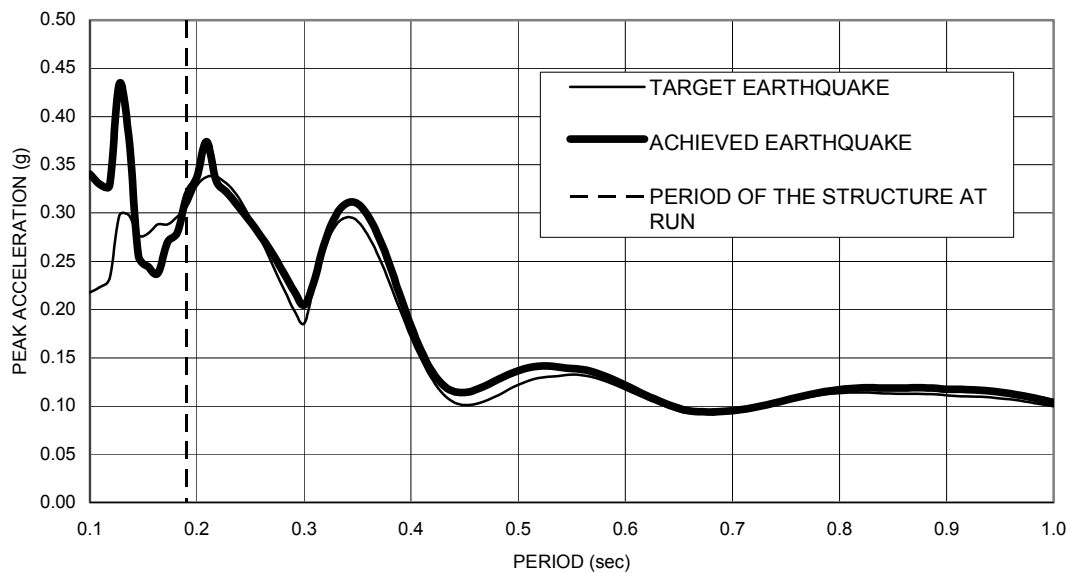
Figure 3.27 Comparison of Period of Structure Against Target and Achieved Response Spectra for 0.25 Times Sylmar Run
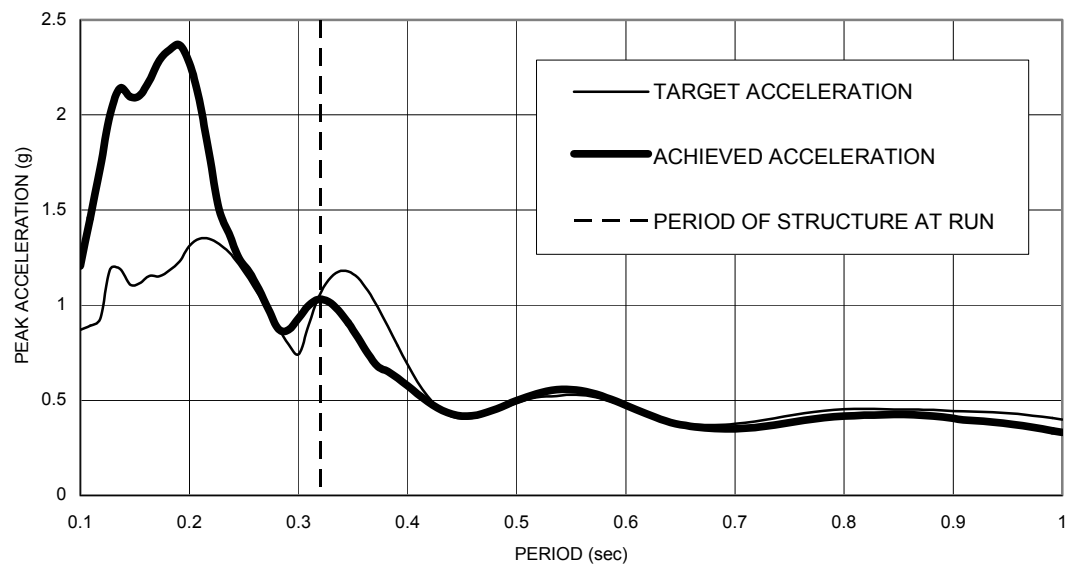
Figure 3.28 Comparison of Period of Structure Against Target and Achieved Response Spectra for 1.00 Times Sylmar Run
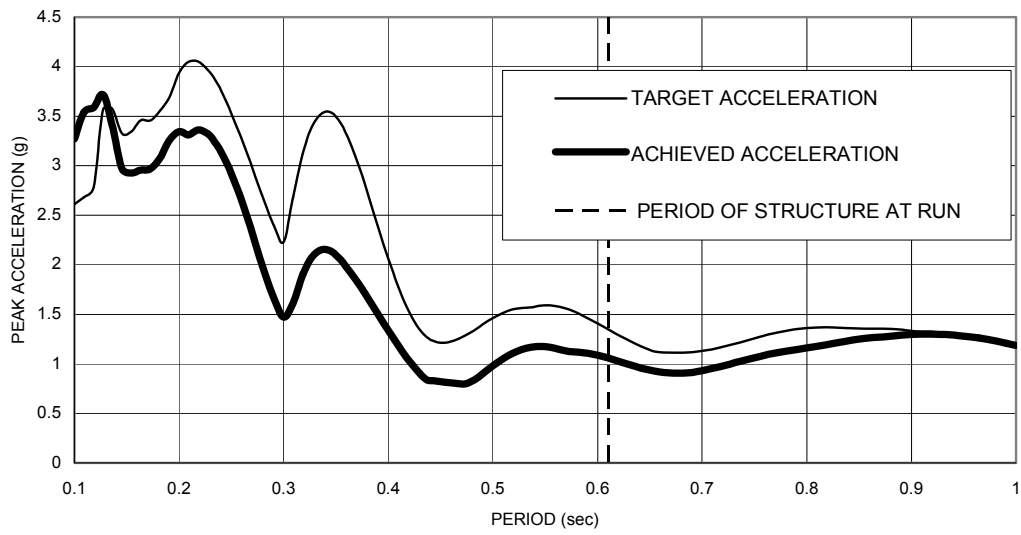
Figure 3.29 Comparison of Period of Structure Against Target and Achieved Response Spectra for 3.00 Times Sylmar Run
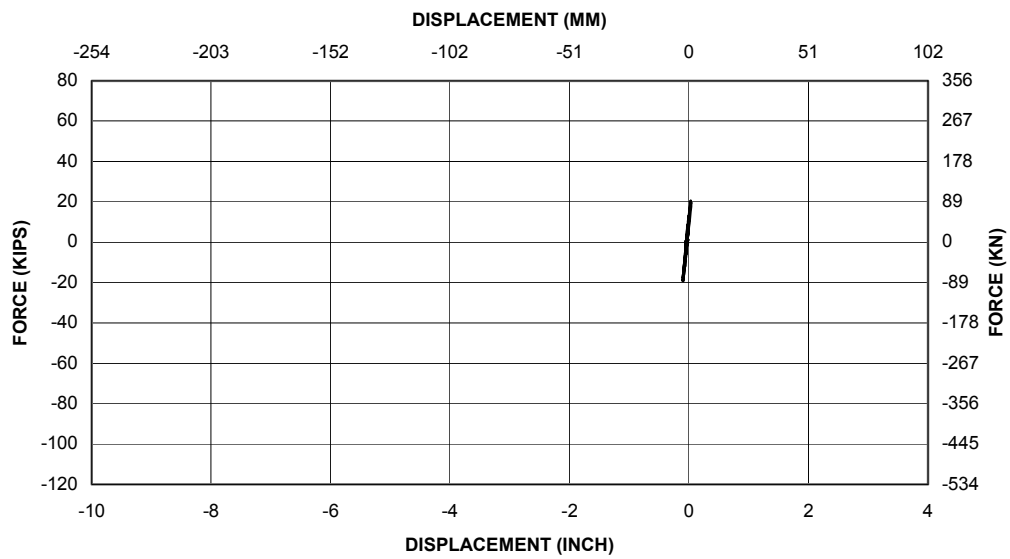
Figure 3.30 Load-Displacement Relationship Curve for SFCD3 at 0.25 Times Sylmar

111
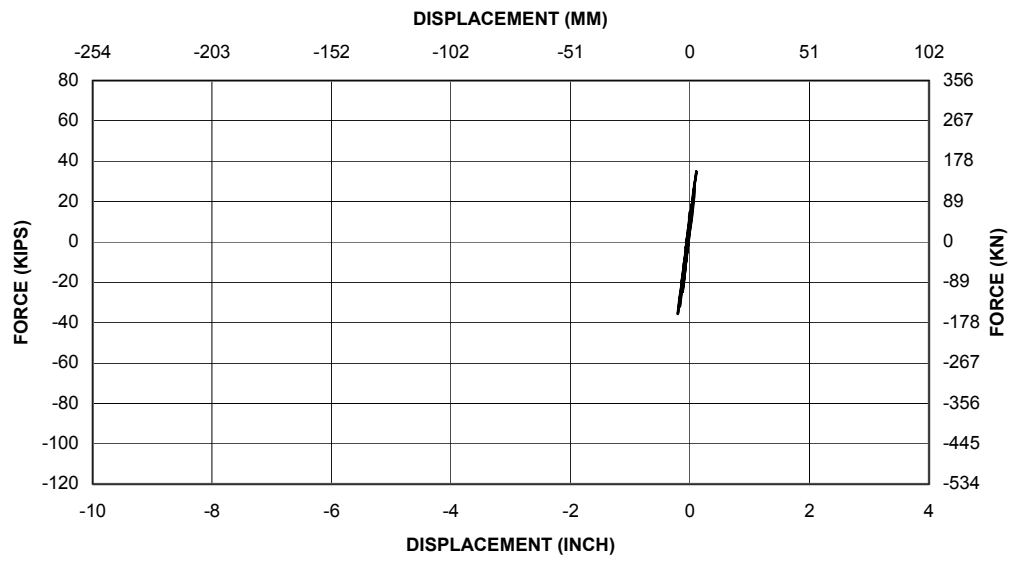
Figure 3.31 Load-Displacement Relationship Curve for SFCD3 at 0.50 Times Sylmar
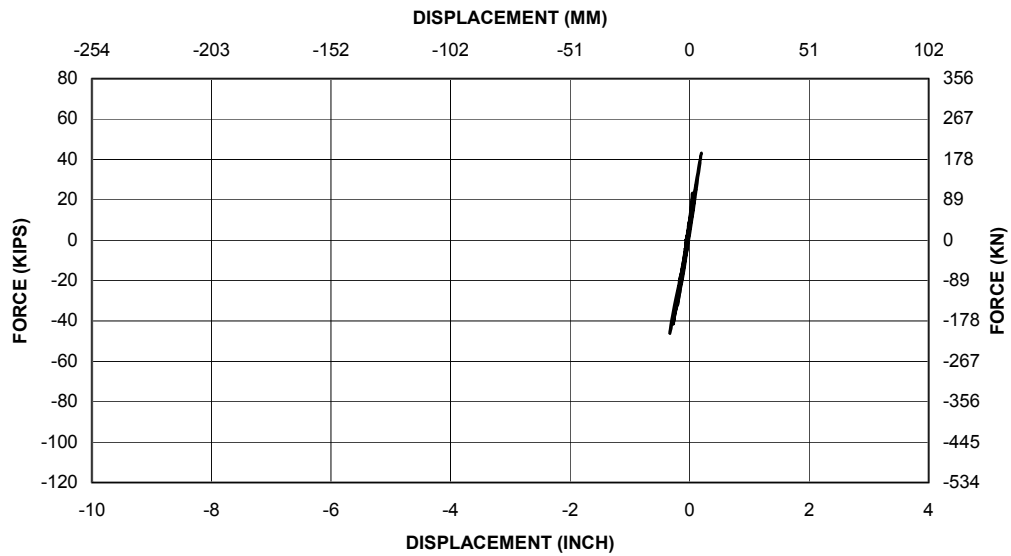
Figure 3.32 Load-Displacement Relationship Curve for SFCD3 at 0.75 Times Sylmar

112

DISPLACEMENT (MM)

-254   -203   -152   -102   -51   0   51   102

FORCE (KIPS)

80
60
40
20
0
-20
-40
-60
-80
-100
-120

356
267
178
89
0
-89
-178
-267
-356
-445
-534

FORCE (KN)

-10   -8   -6   -4   -2   0   2   4

DISPALCEMENT (INCH)
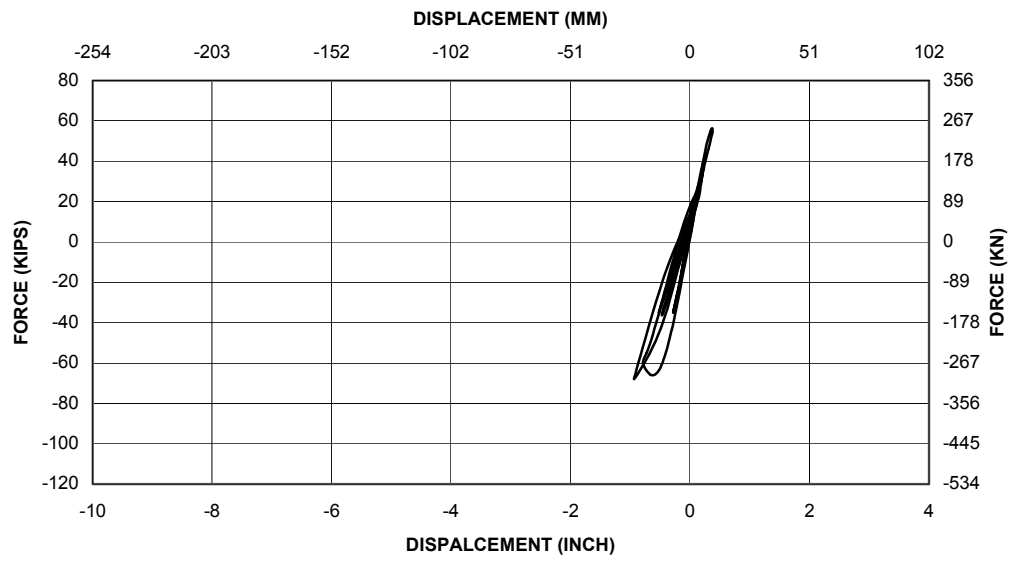
Figure 3.33 Load-Displacement Relationship Curve for SFCD3 at 1.00 Times Sylmar

DISPLACEMENT (MM)

-254   -203   -152   -102   -51   0   51   102

FORCE (KIPS)

80
60
40
20
0
-20
-40
-60
-80
-100
-120

356
267
178
89
0
-89
-178
-267
-356
-445
-534

FORCE (KN)

-10   -8   -6   -4   -2   0   2   4
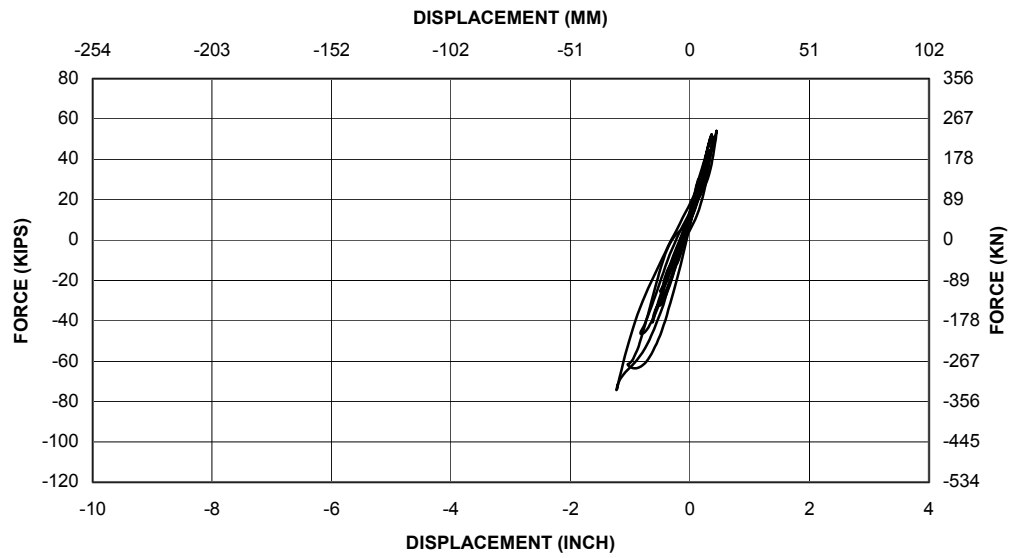
DISPLACEMENT (INCH)

Figure 3.34 Load-Displacement Relationship Curve for SFCD3 at 1.25 Times Sylmar

113
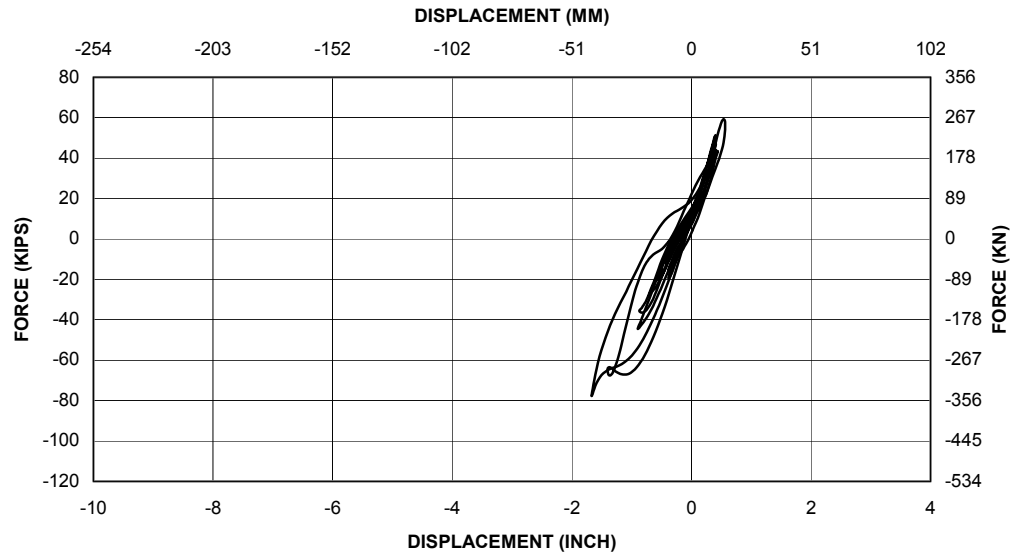
Figure 3.35 Load-Displacement Relationship Curve for SFCD3 at 1.50 Times Sylmar
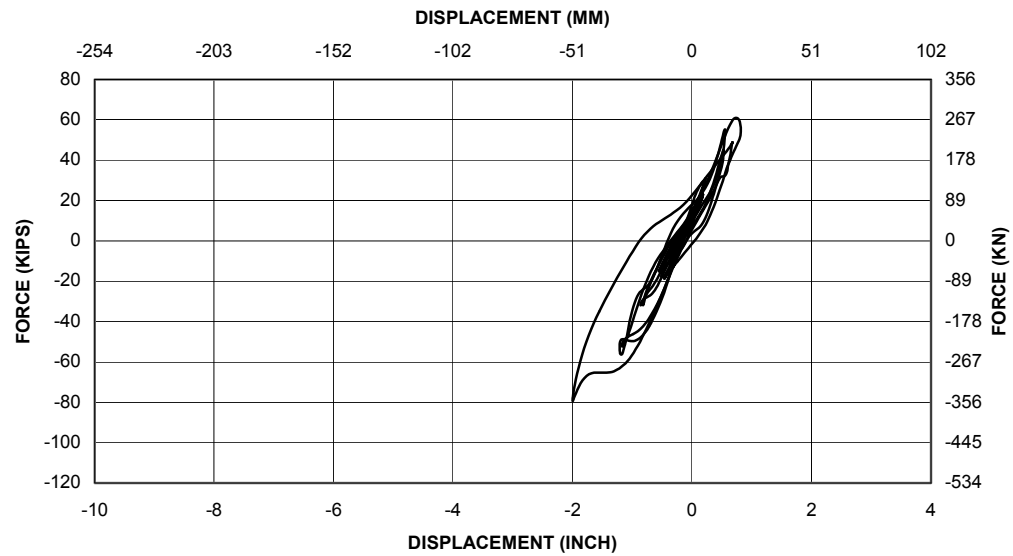
Figure 3.36 Load-Displacement Relationship Curve for SFCD3 at 1.75 Times Sylmar

114
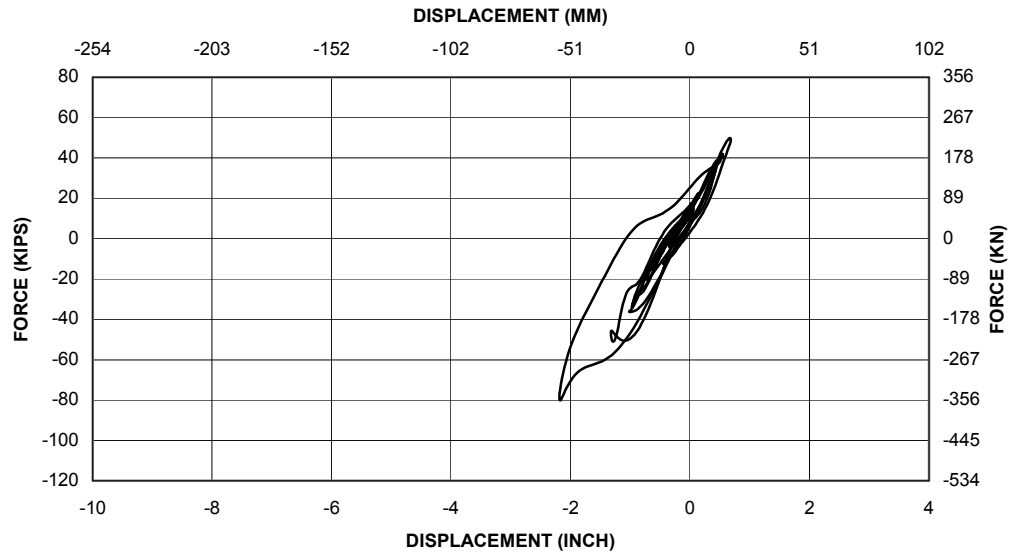
Figure 3.37 Load-Displacement Relationship Curve for SFCD3 at 2.00 Times Sylmar
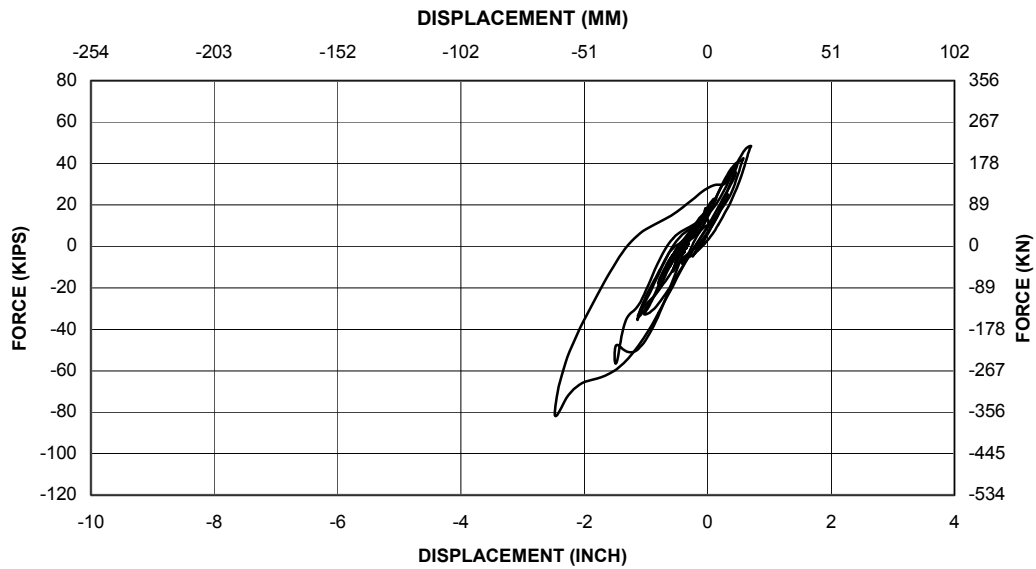
Figure 3.38 Load-Displacement Relationship Curve for SFCD3 at 2.25 Times Sylmar

115
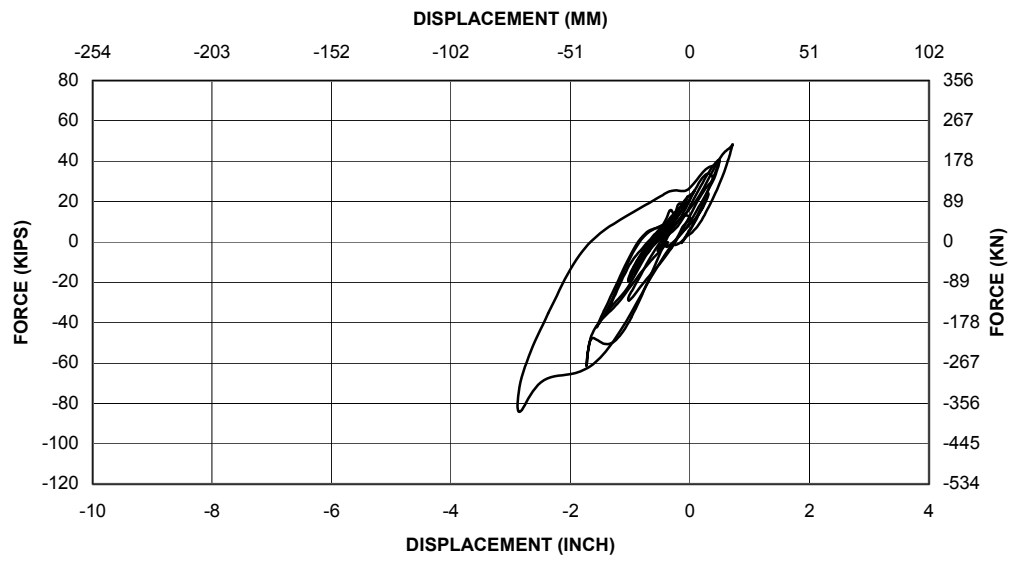
Figure 3.39 Load-Displacement Relationship Curve for SFCD3 at 2.50 Times Sylmar
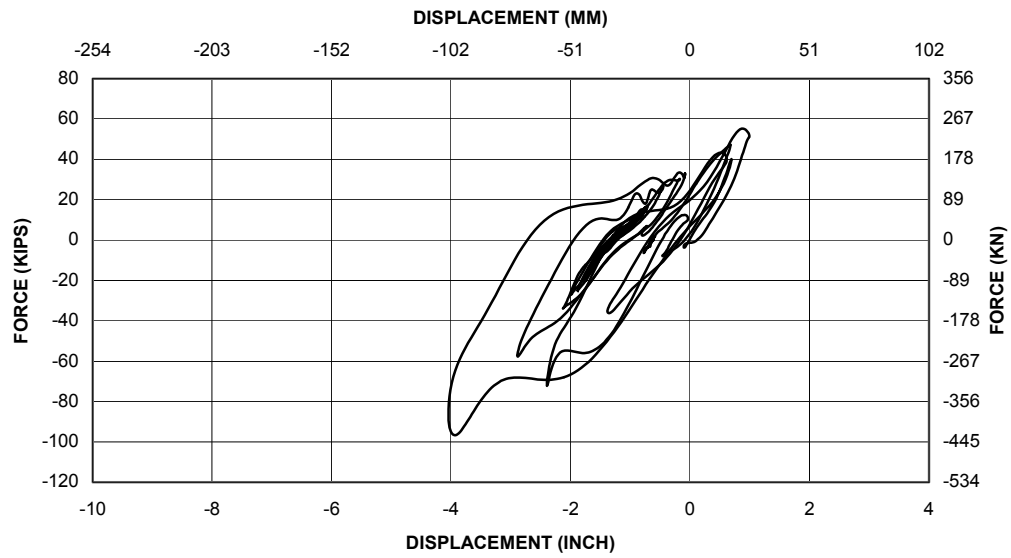
Figure 3.40 Load-Displacement Relationship Curve for SFCD3 at 2.75 Times Sylmar

116
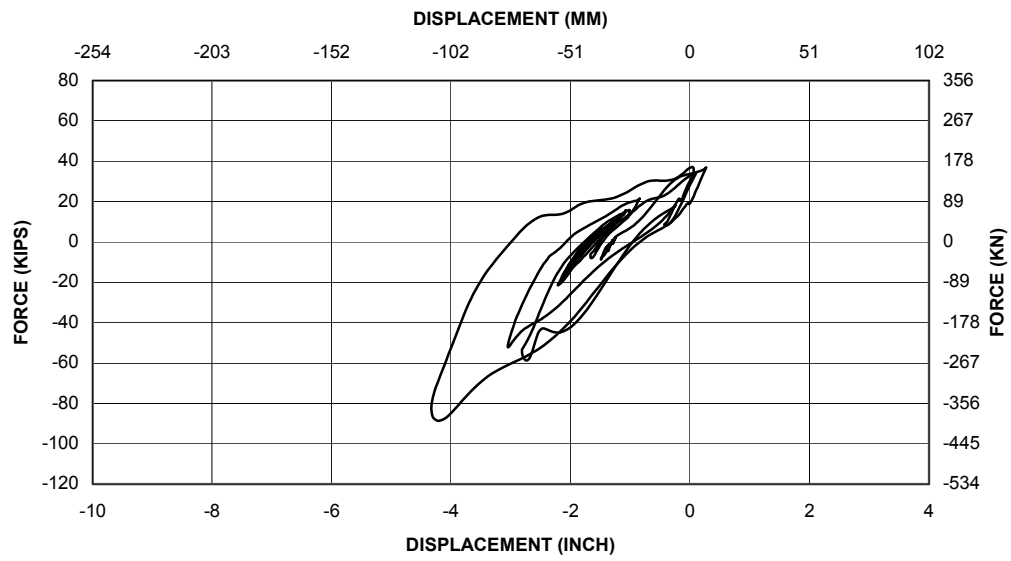
Figure 3.41 Load-Displacement Relationship Curve for SFCD3 at 3.00 Times Sylmar
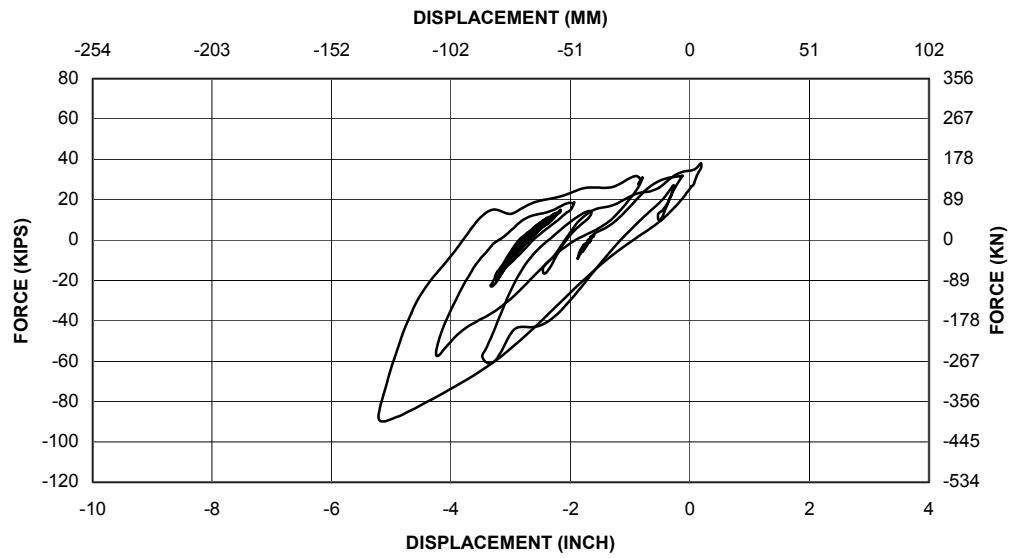
Figure 3.42 Load-Displacement Relationship Curve for SFCD3 at 3.25 Times Sylmar

117
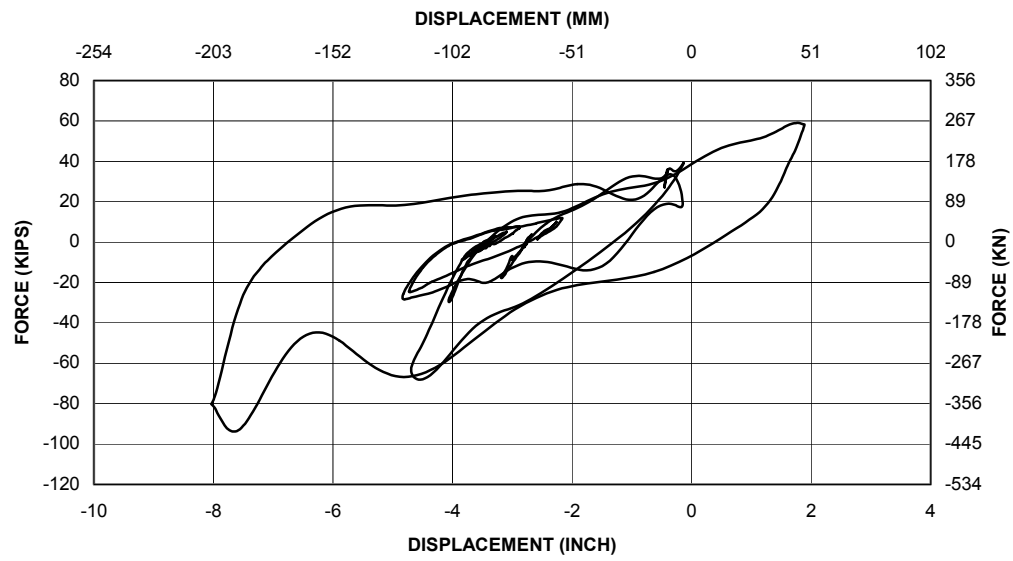
Figure 3.43 Load-Displacement Relationship Curve for SFCD3 at 3.50 Times Sylmar
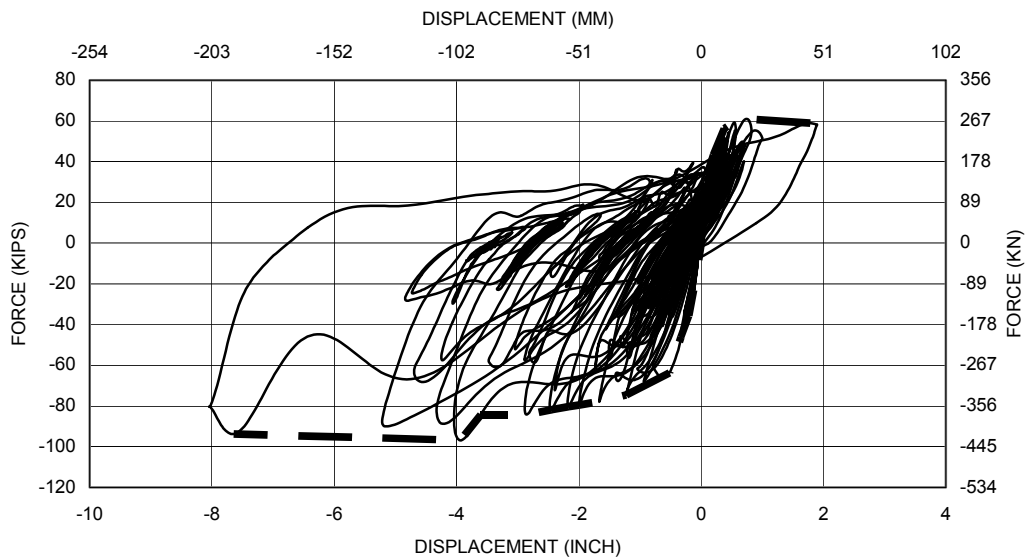
Figure 3.44 Cumulative Load-Displacement Relationship Curve for SFCD3 (Filtered at 15 Hz)

118
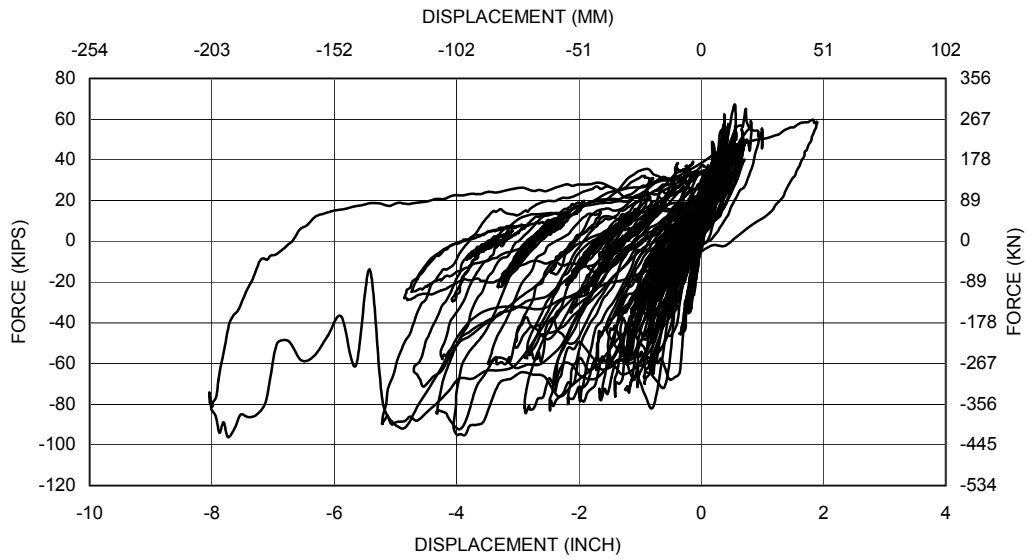
Figure 3.45a Cumulative Load-Displacement Relationship Curve for SFCD3 (Unfiltered)
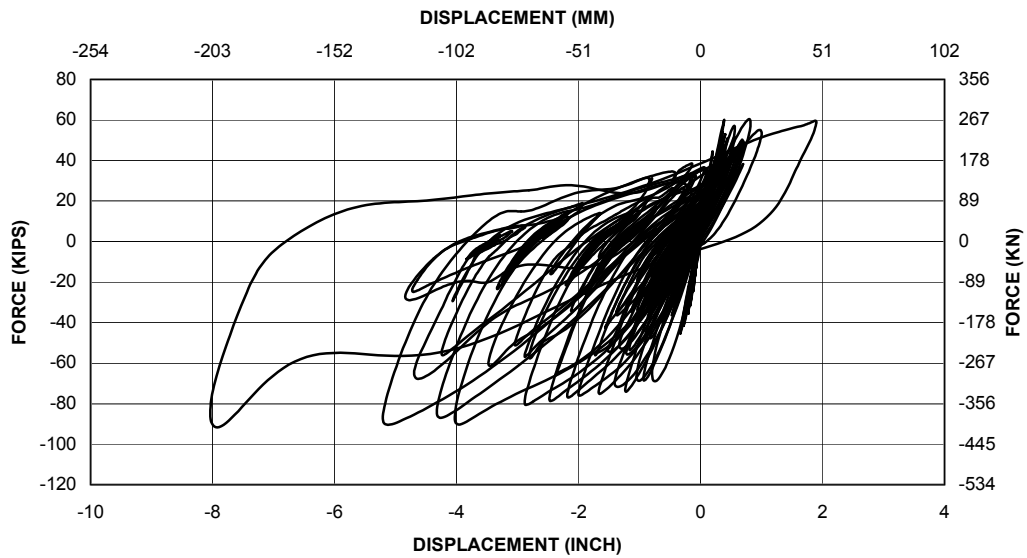
Figure 3.45b Cumulative Load-Displacement Relationship Curve for SFCD3

(Filtered at 10 Hz)
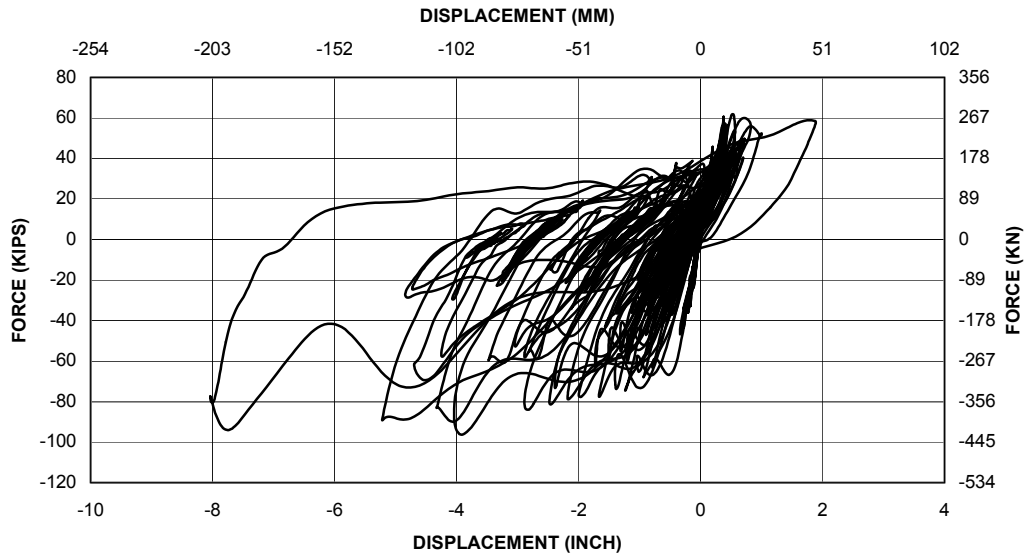
Figure 3.45c Cumulative Load-Displacement Relationship Curve for SFCD3

(Filtered at 20 Hz)
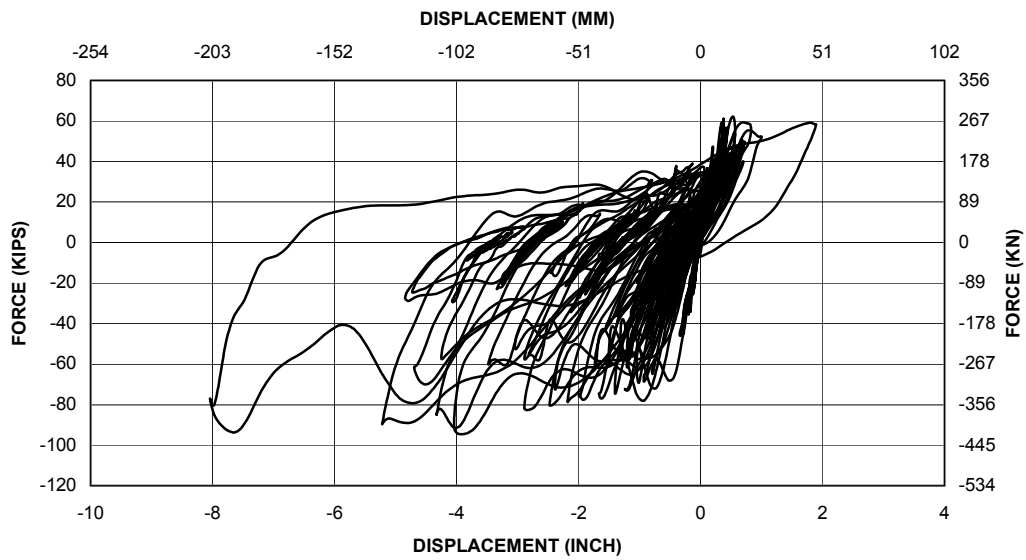
Figure 3.45d Cumulative Load-Displacement Relationship Curve for SFCD3

(Filtered at 25 Hz)

120
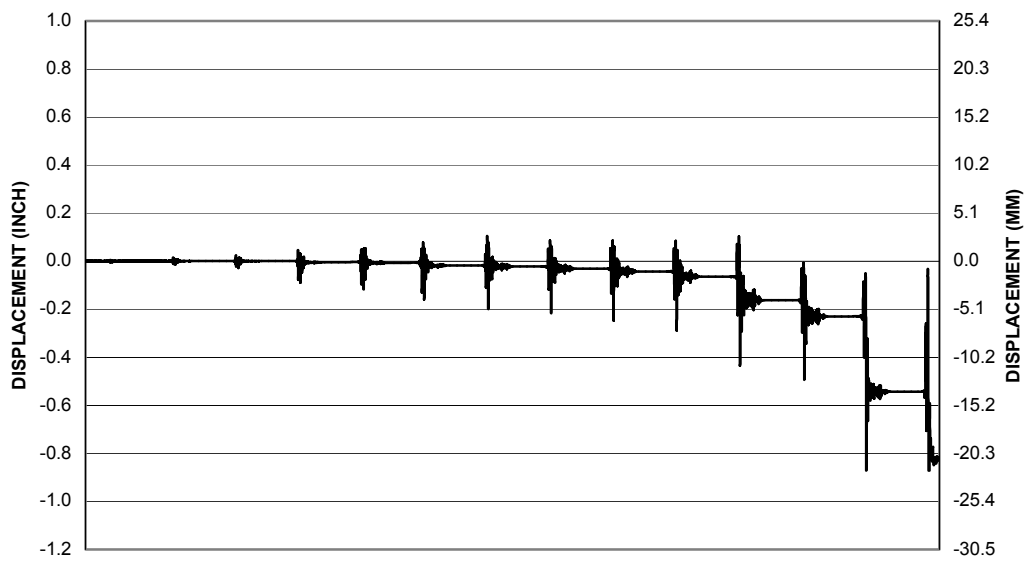
Figure 3.46 North Column Base Slippage Time History
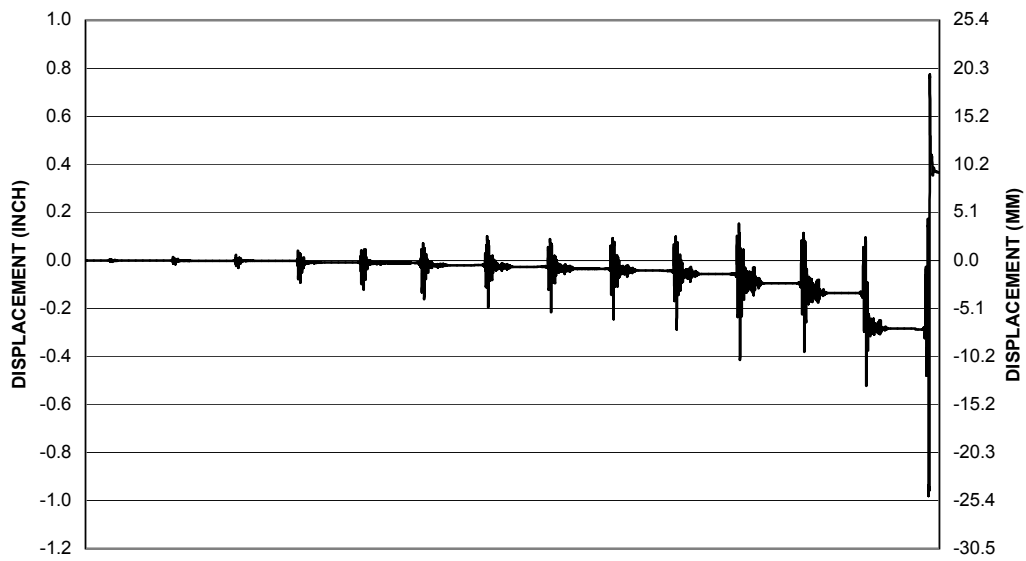
Figure 3.47 South Column Base Slippage Time History

121
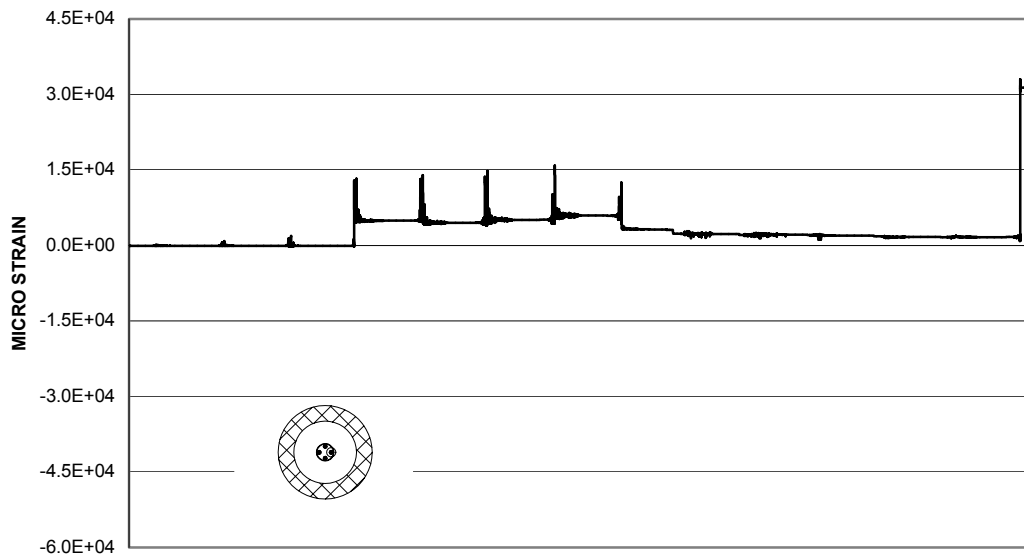
Figure 3.48 South Column Base-Hinge Strain Gage (SG2) Time History
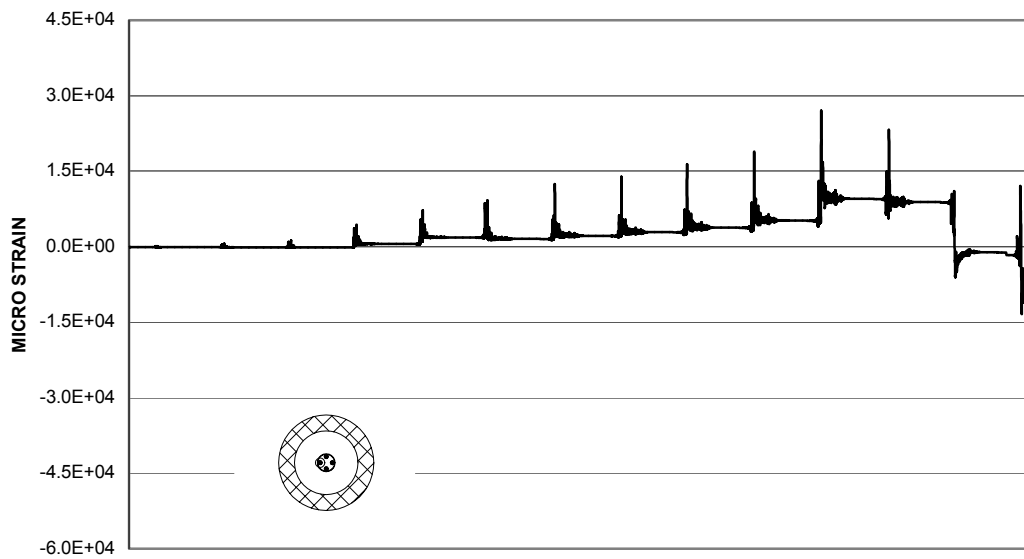
Figure 3.49 North Column Base-Hinge Strain Gage (SG79) Time History
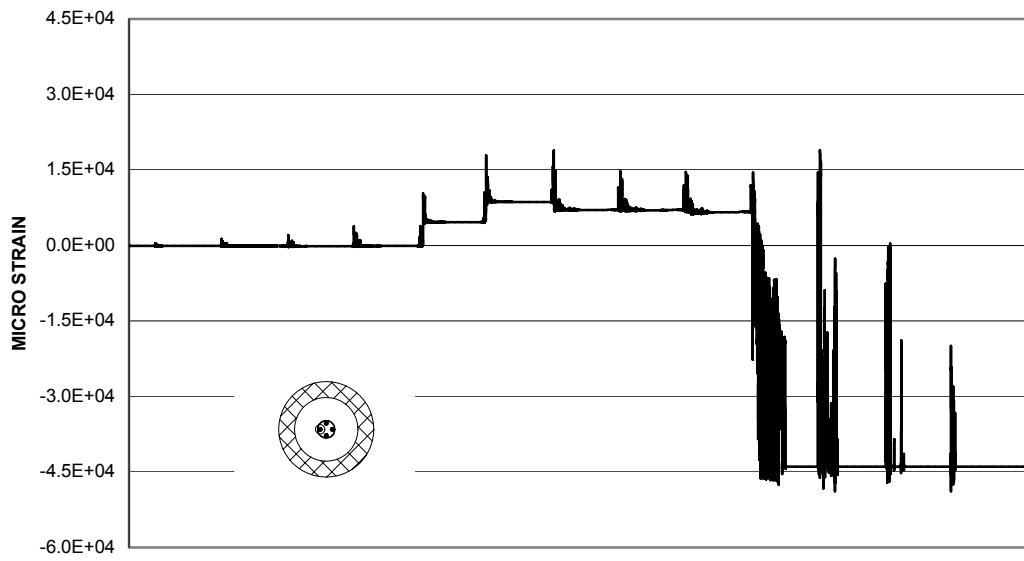
Figure 3.50 South Column Base-Hinge Strain Gage (SG1) Time History
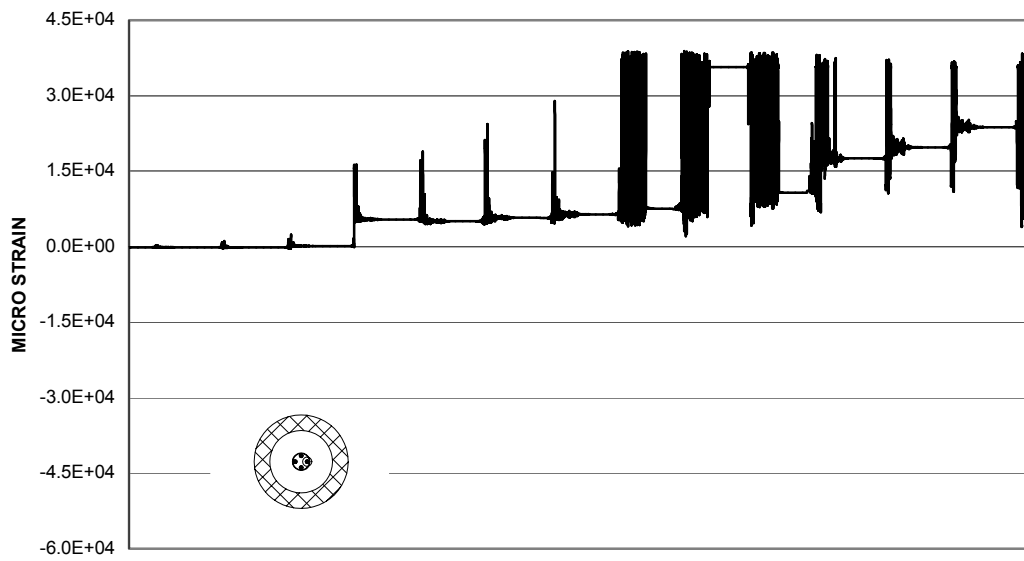
Figure 3.51 North Column Base-Hinge Strain Gage (SG78) Time History
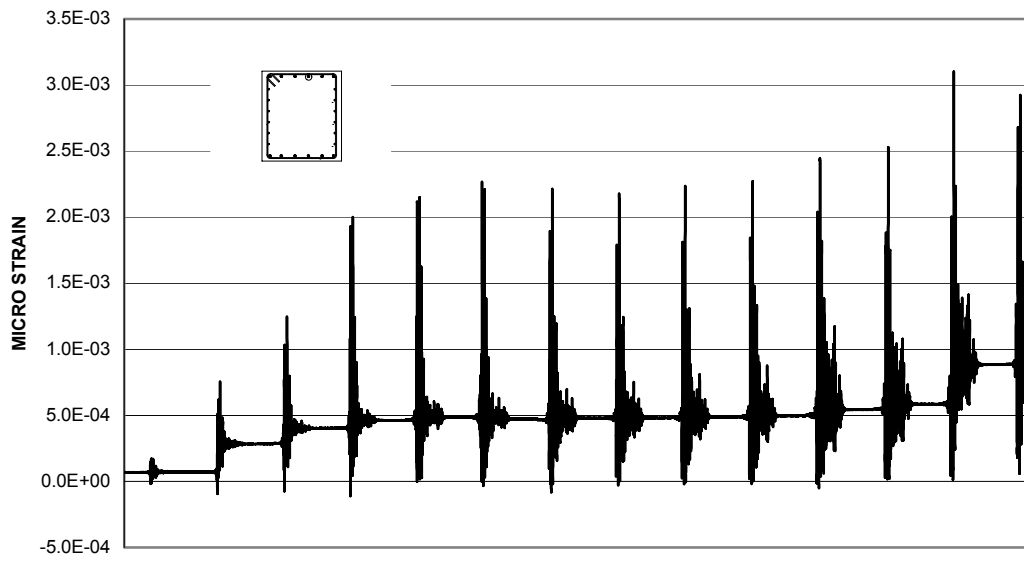
Figure 3.52 Beam Top Reinforcement Strain Gage (SG61) Time History
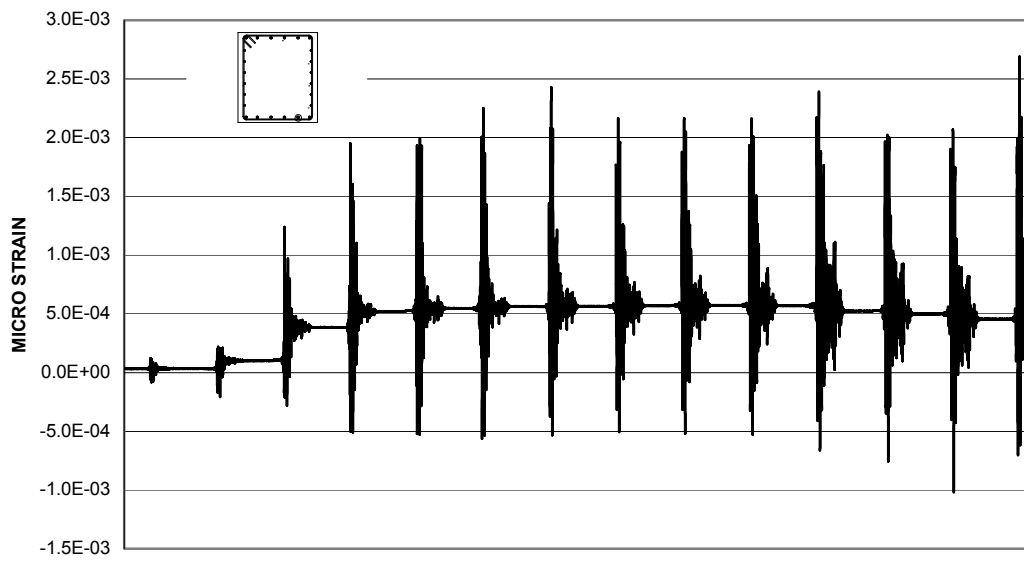
Figure 3.53 Beam Bottom Reinforcement Strain Gage (SG65) Time History
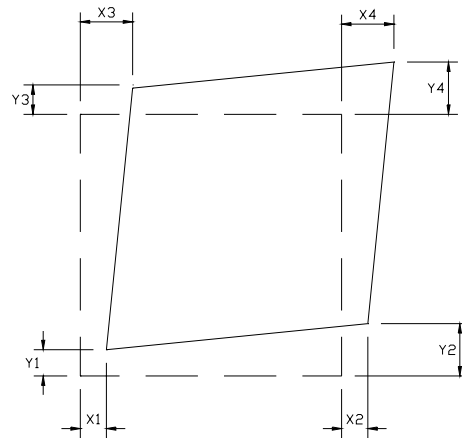
$$\Delta x = [(X2 - X1) + (X4 - X3)]/2$$
$$\Delta y = [(Y3 - Y1) + (Y4 - Y2)]/2$$

Figure 3.54 Beam Column Connection Deformation
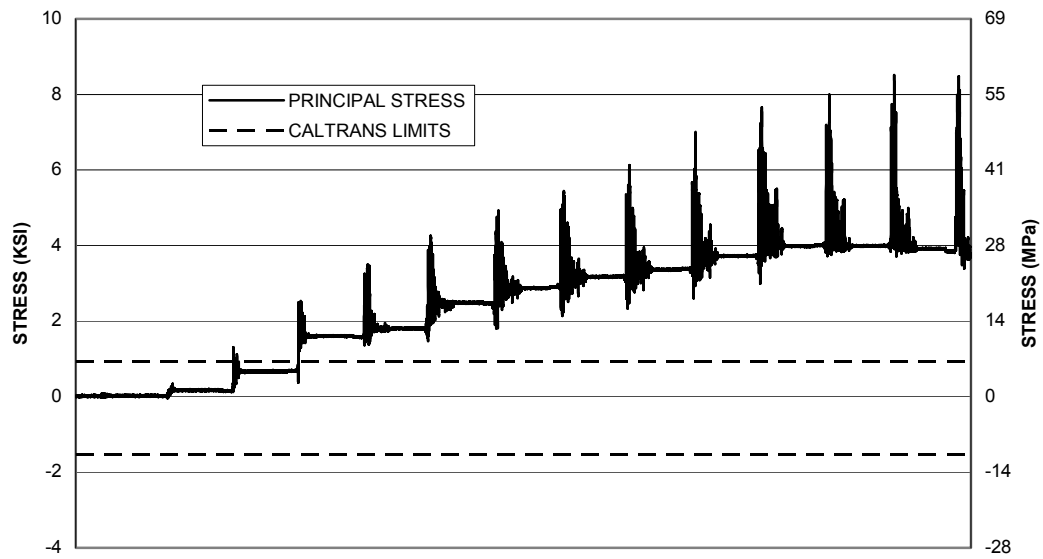
Figure 3.55 Principal Stress (σ_1) in South Beam Column Connection
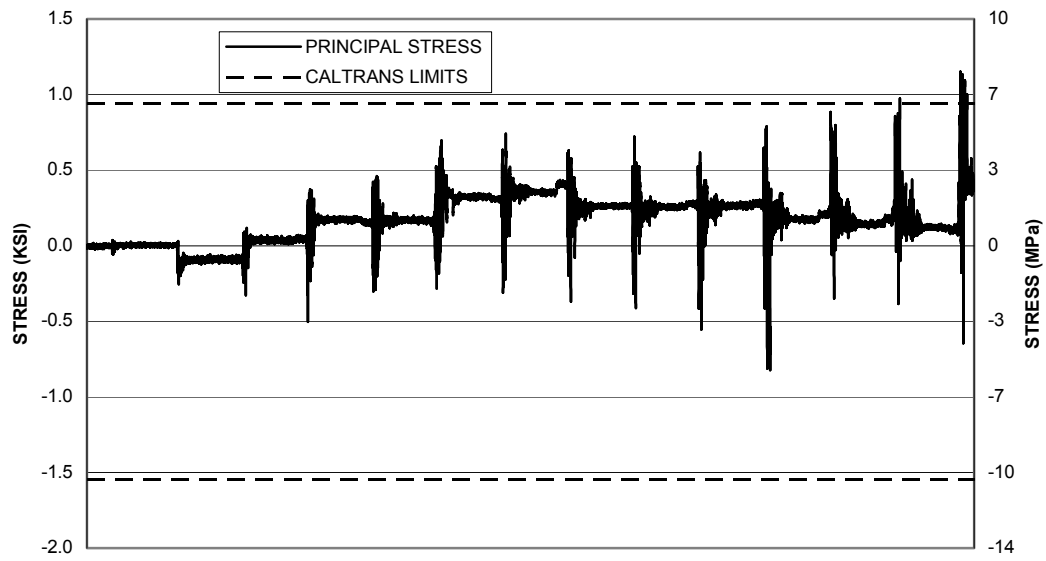
Figure 3.56 Principal Stress (σ_2) **in South Beam Column Connection**
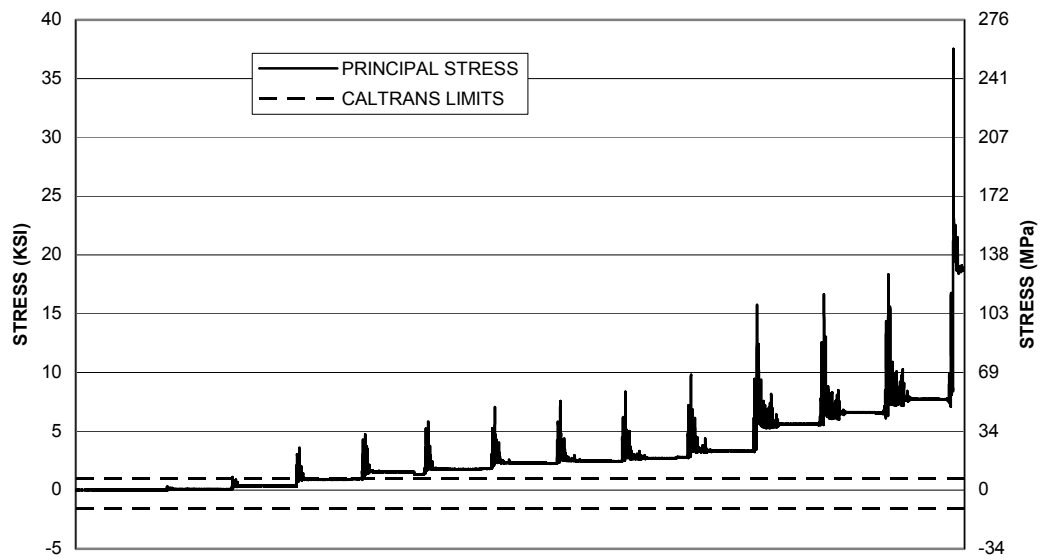
Figure 3.57 Principal Stress (σ_1) **in North Beam Column Connection**
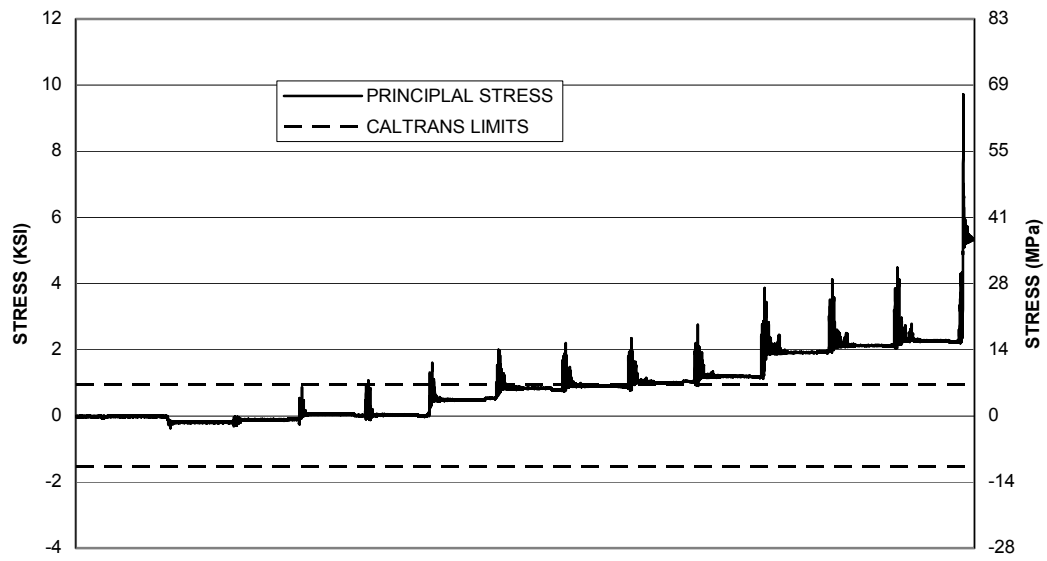
Figure 3.58 Principal Stress (σ_2) in North Beam Column Connection
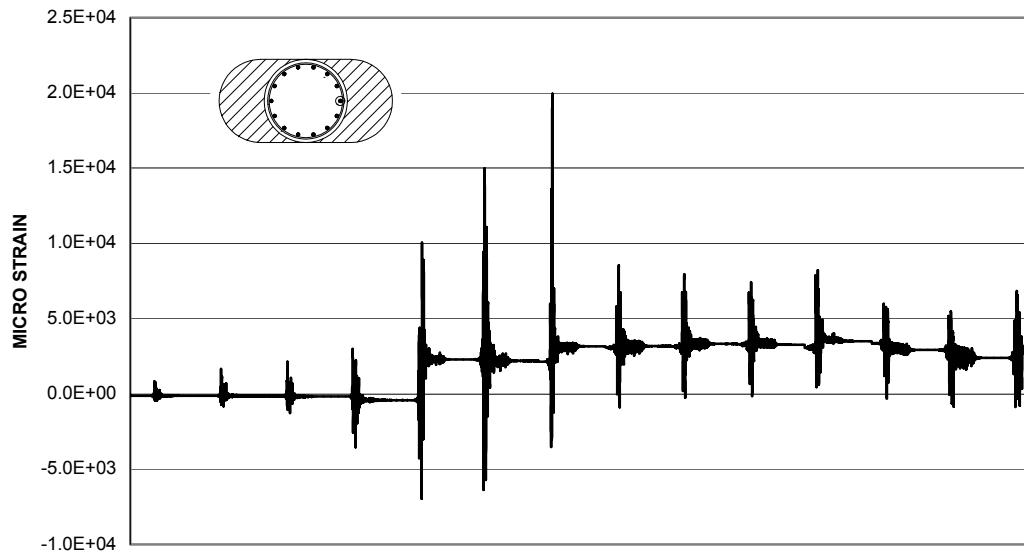
Figure 3.59 Time History for SG38
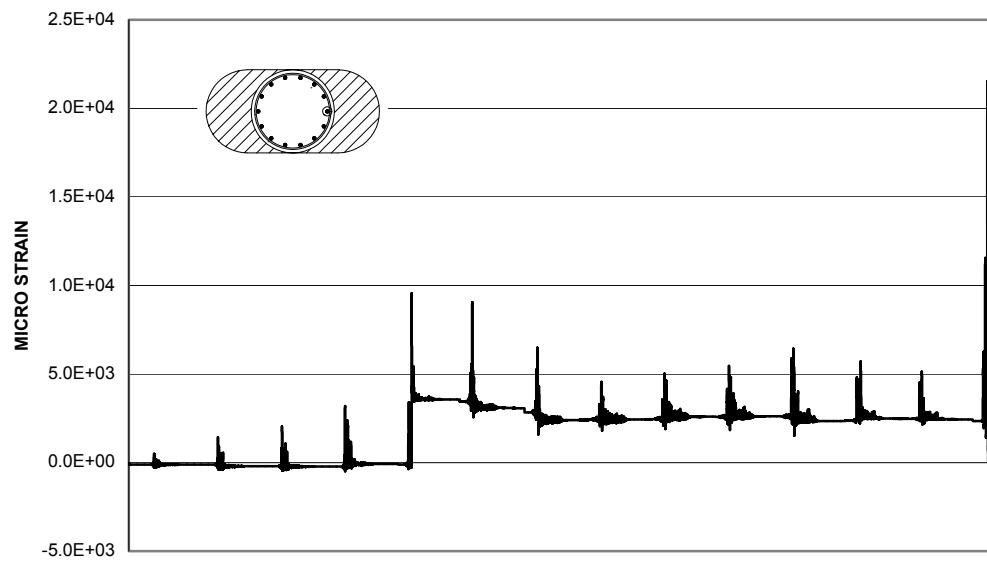
Figure 3.60 Time History SG113
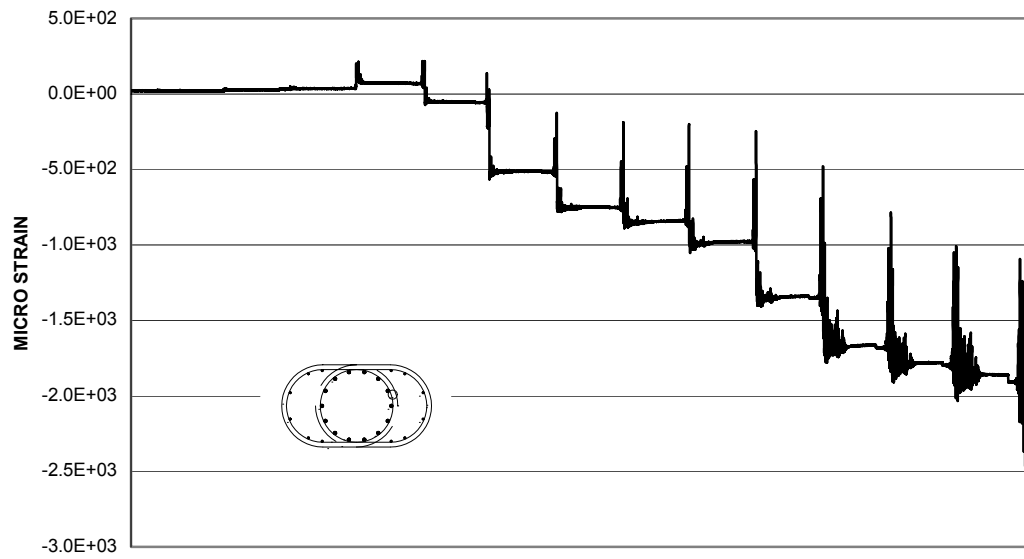
Figure 3.61 Time History for SG29

128
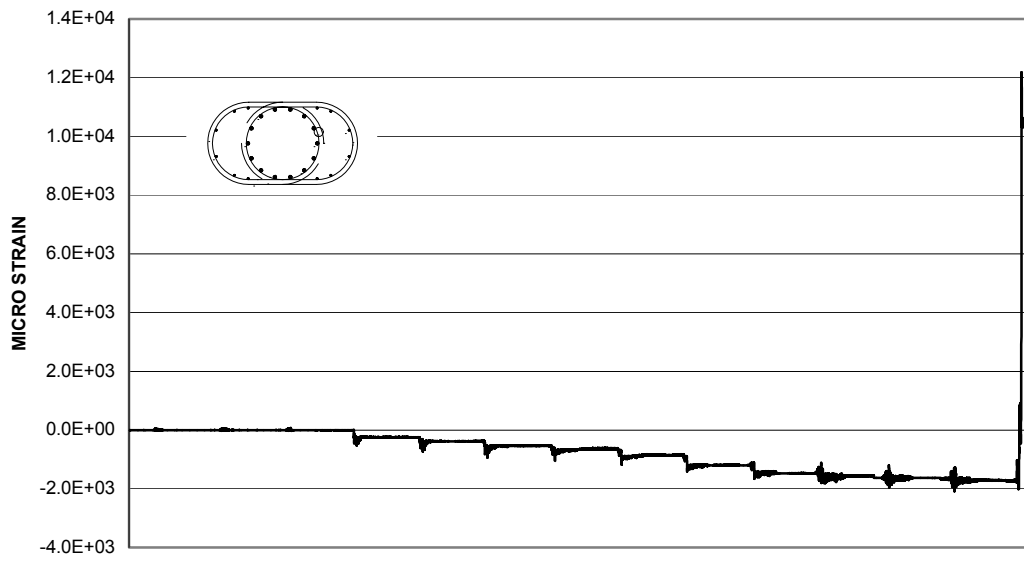
Figure 3.62 Time History SG111
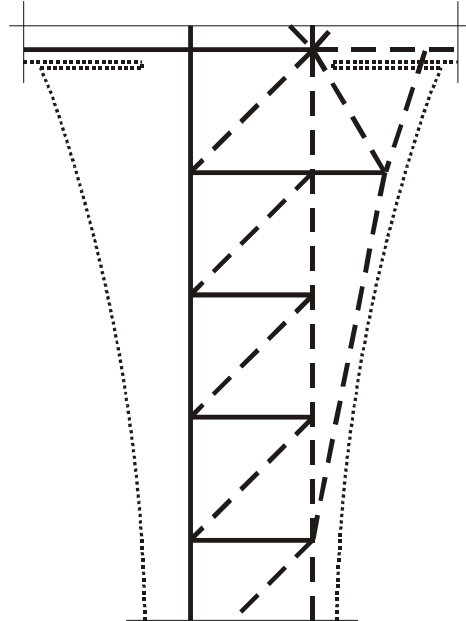
Figure 3.63 Strut-and-Tie Model for the Flare D-Region After Gap Closure

129
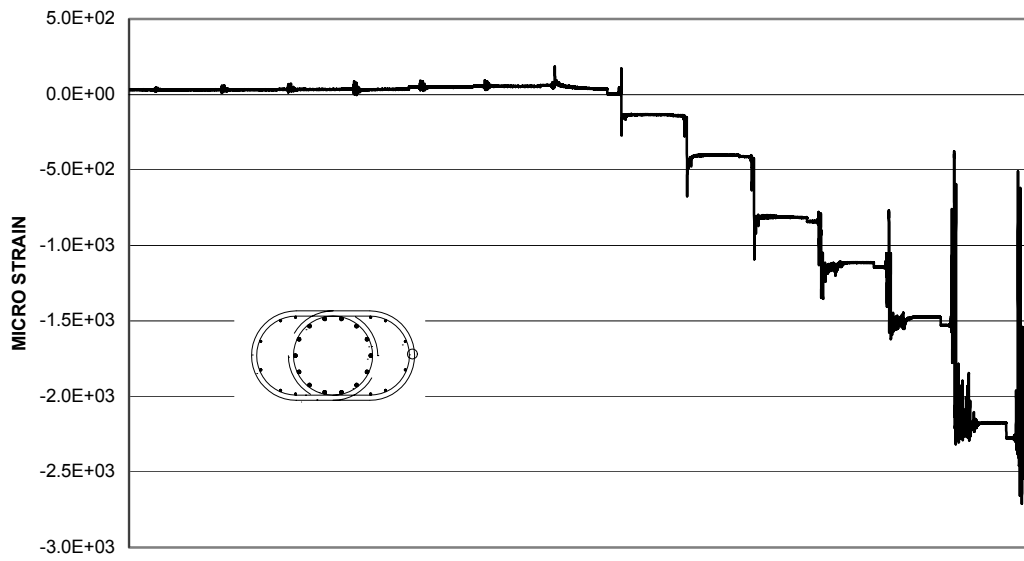
Figure 3.64 Time History for Flare Hoop Reinforcement (SG20)
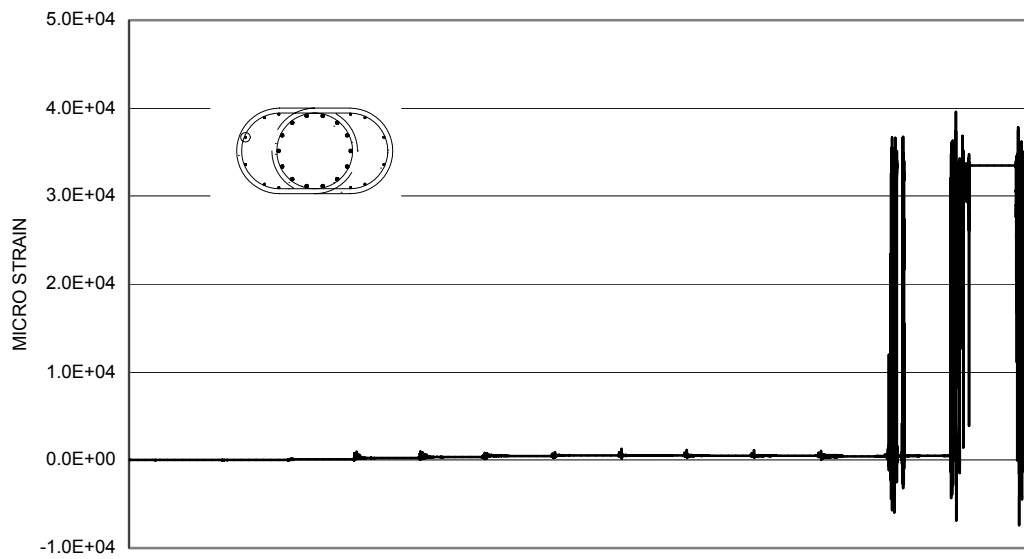
Figure 3.65 Time History for Flare Longitudinal Reinforcement (SG107)
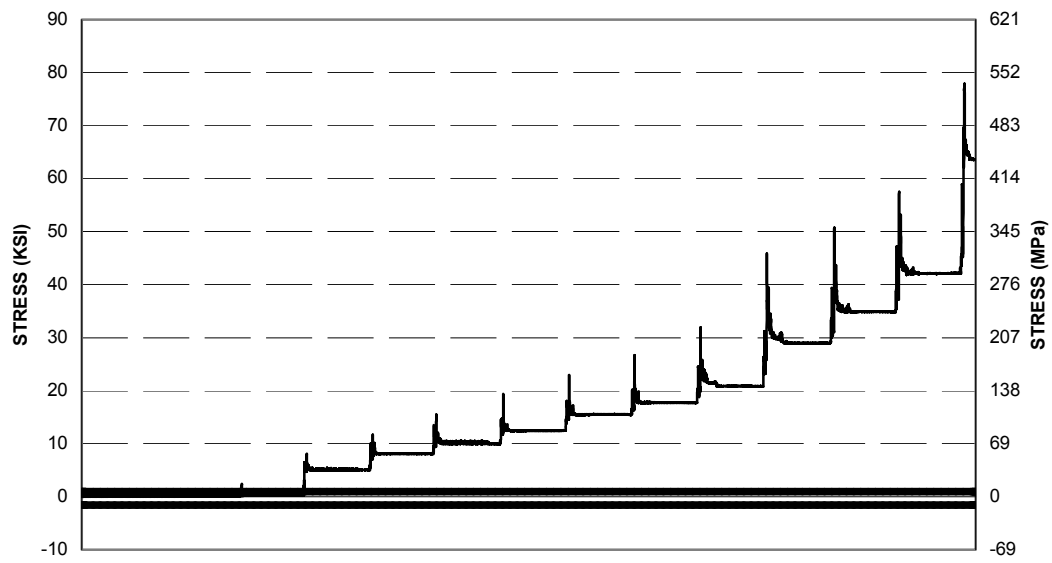
Figure 3.66 Principal Stress (σ_1) in North Column Flare
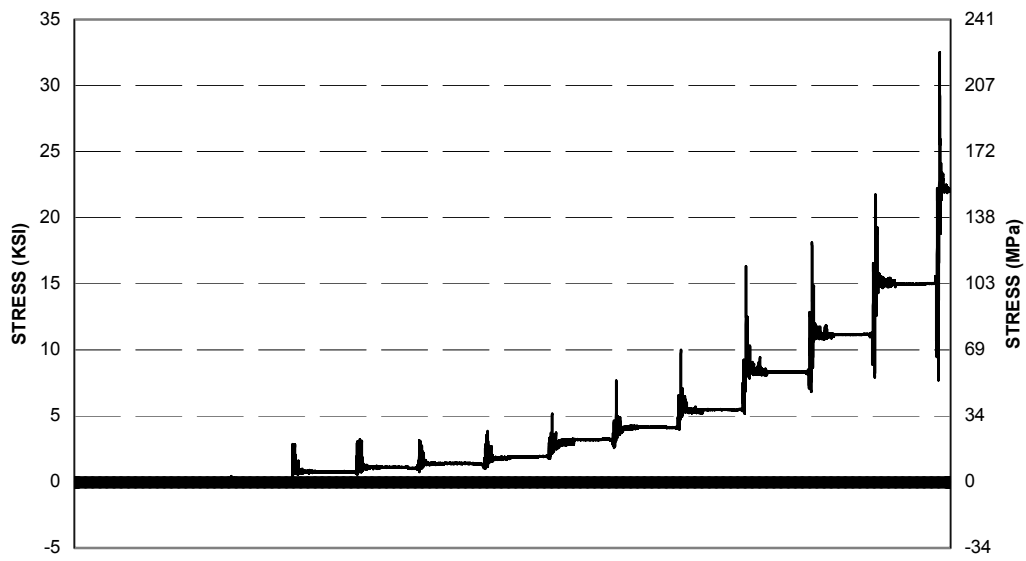
Figure 3.67 Principal Stress (σ_2) in North Column Flare

131
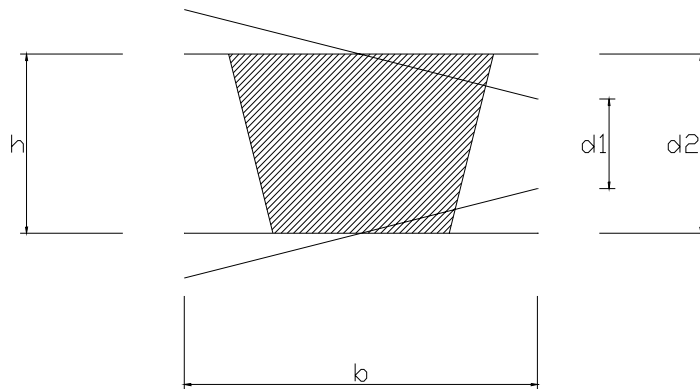
Figure 3.68 Curvature Calculation of Section
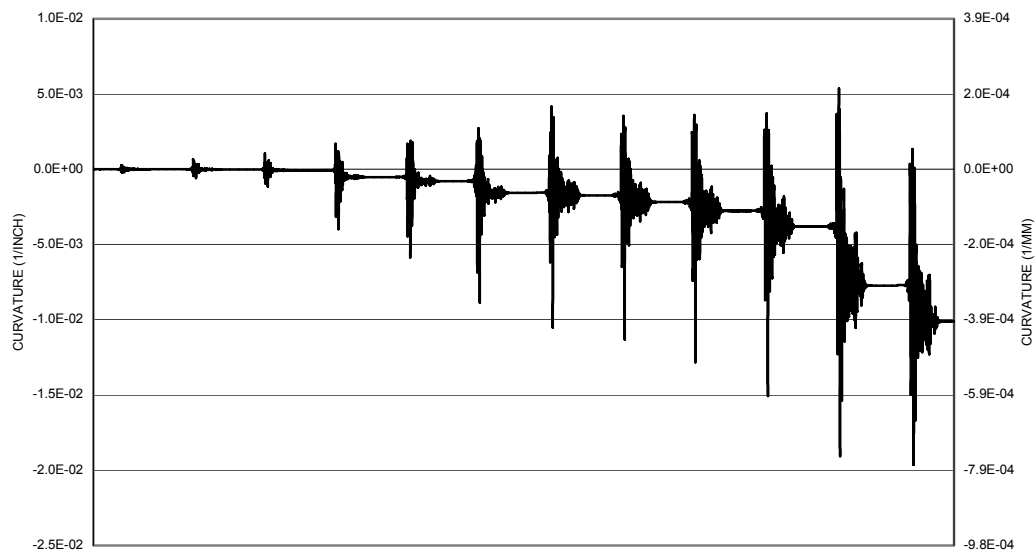
Figure 3.69 Curvature Time-History for NV9-NV10 (Sylmar Runs 0.25 Through 3.00)
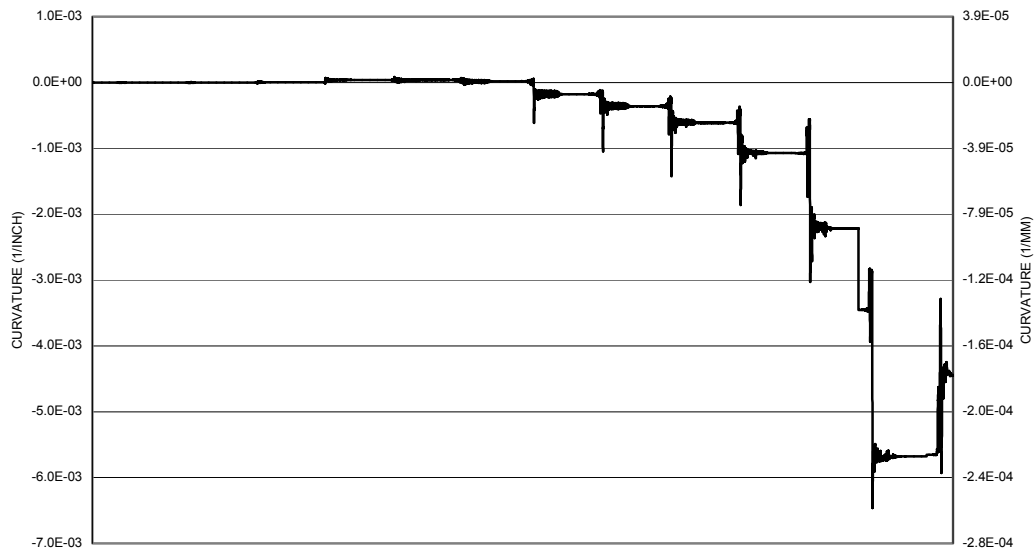
Figure 3.70 Curvature Time-History for NV7-NV8 (Sylmar Runs 0.25 Through 2.75, 3.00, 3.25)
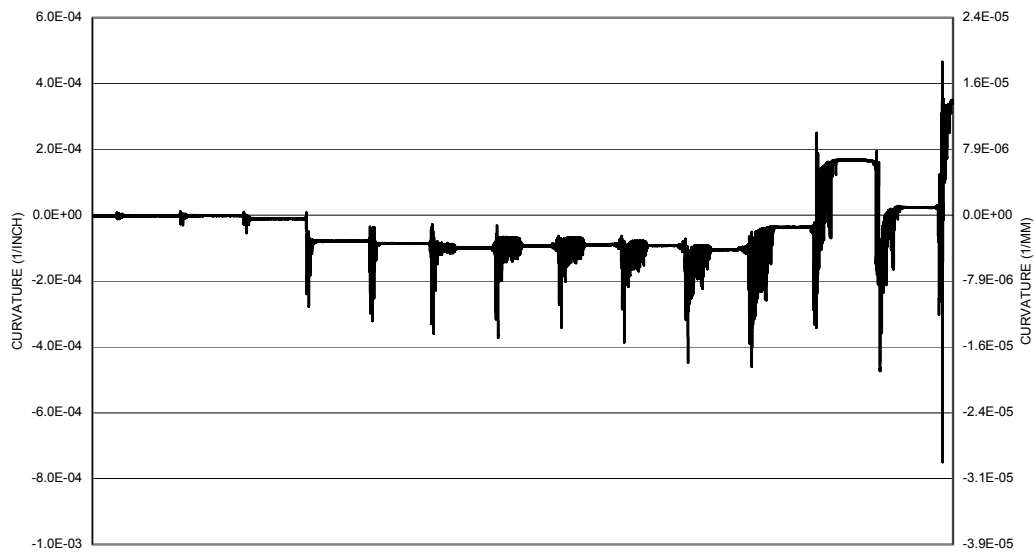
Figure 3.71 Curvature Time-History for NV5-NV6
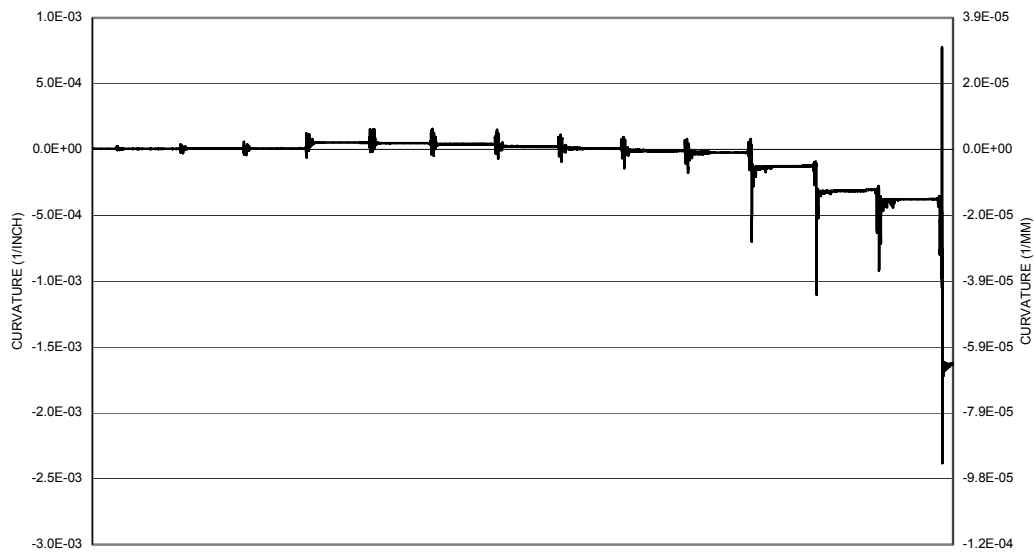
Figure 3.72 Curvature Time-History for NV3-NV4
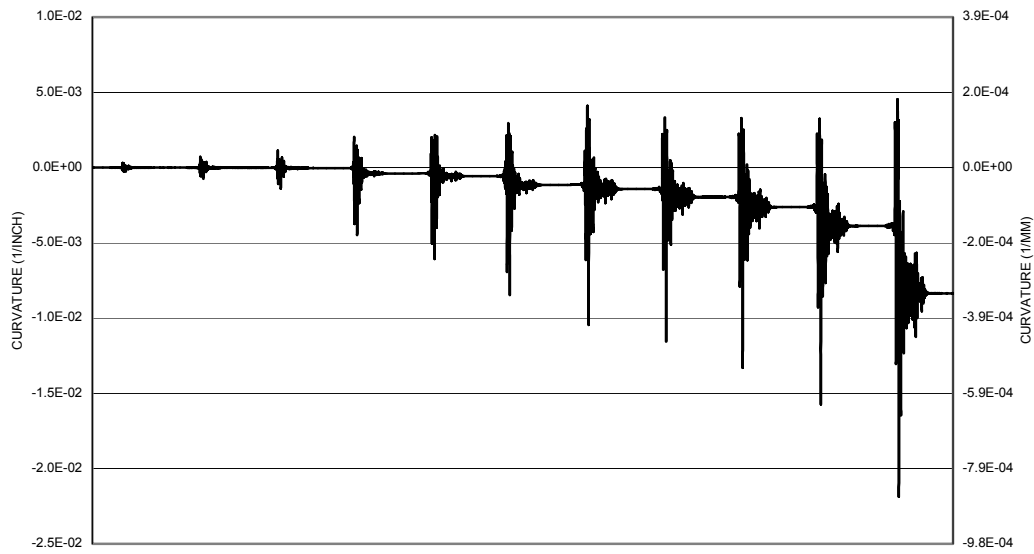
Figure 3.73 Curvature Time-History for NV1-NV2 (Sylmar Runs 0.25 Through 2.75)
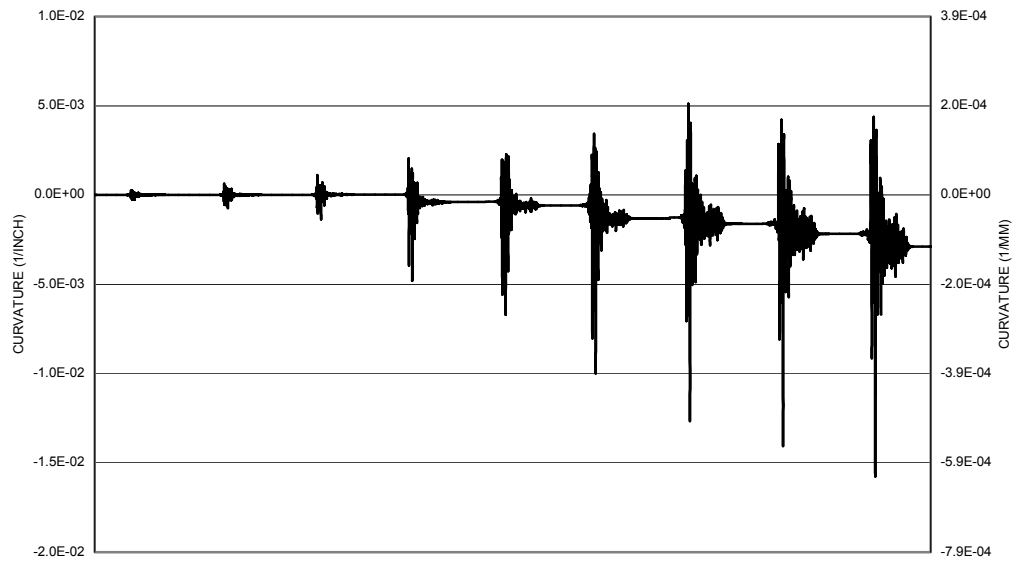
Figure 3.74 Curvature Time-History for NV25-NV26 (Sylmar Runs 0.25 Through 2.25)
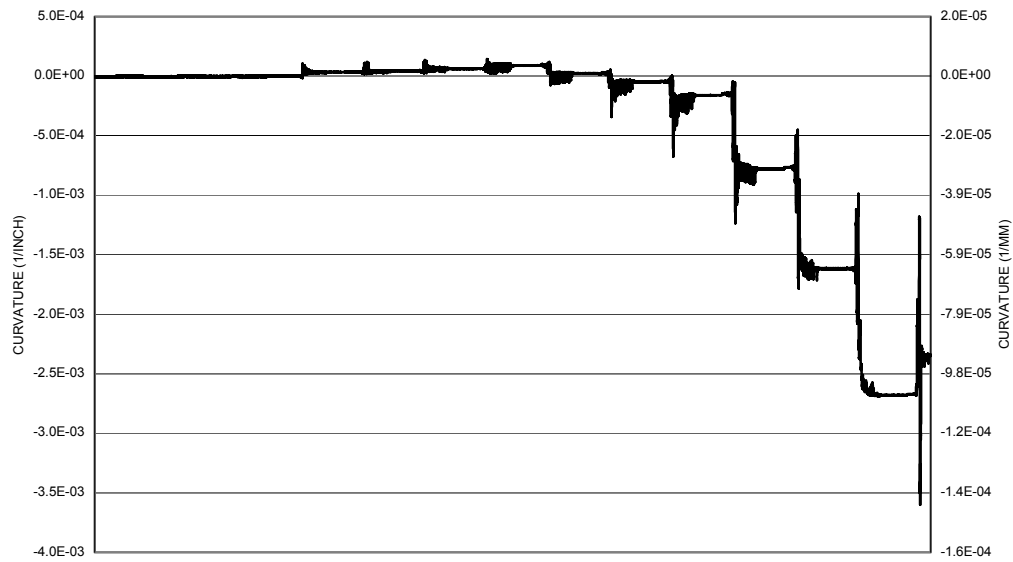
Figure 3.75 Curvature Time-History for NV23-NV24

135
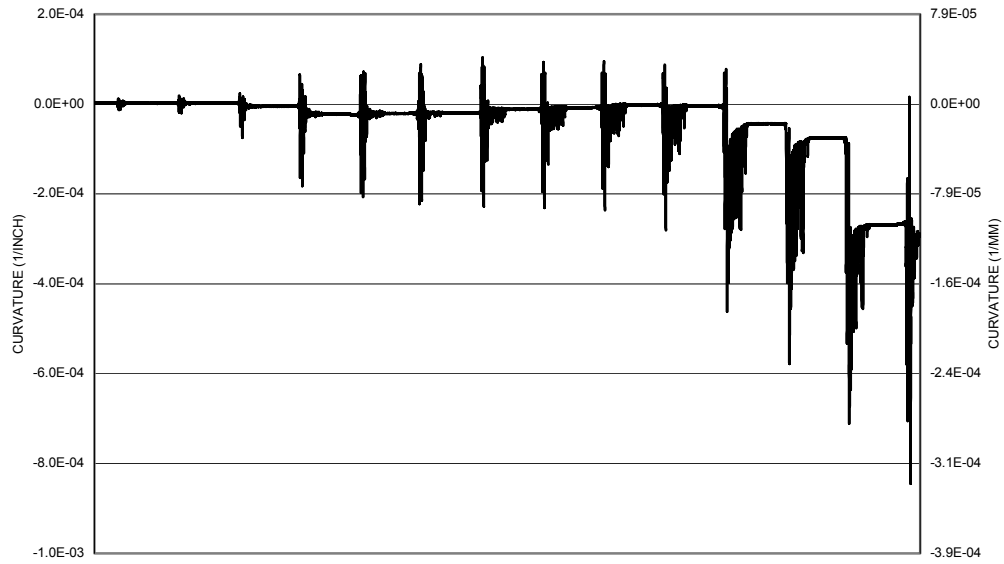
Figure 3.76 Curvature Time-History for NV21-NV22
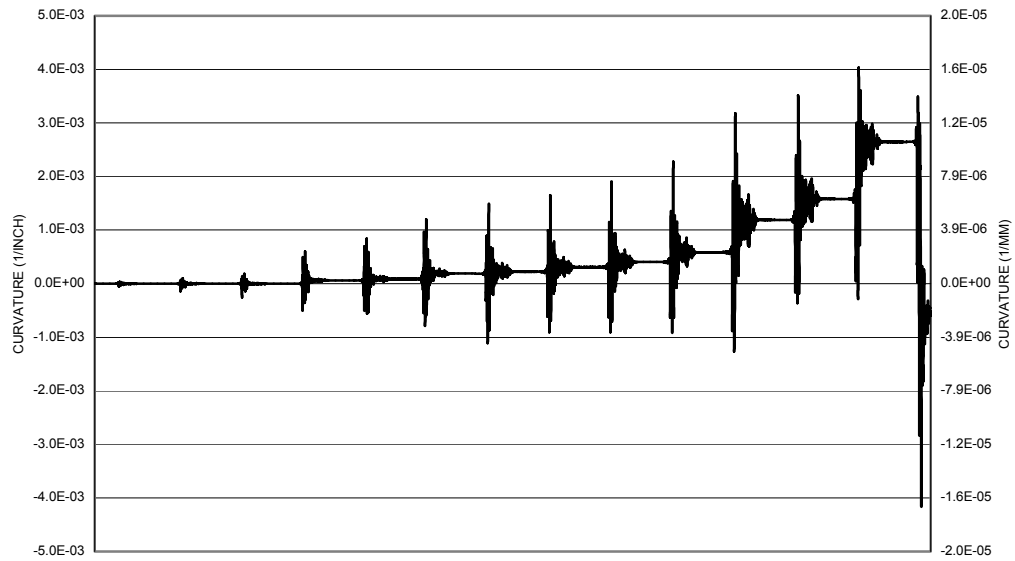
Figure 3.77 Curvature Time-History for NV19-NV20
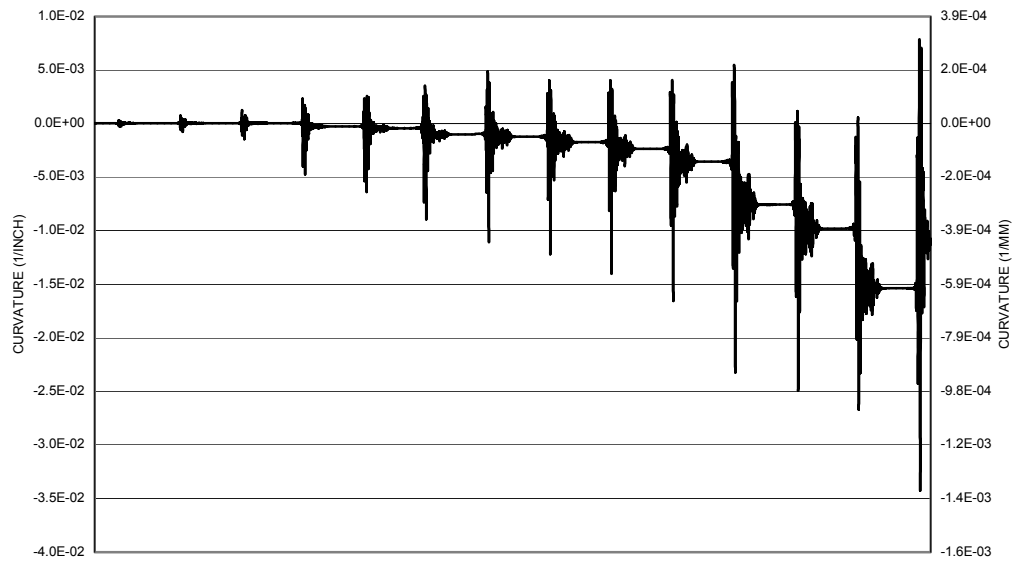
Figure 3.78 Curvature Time-History for NV17-NV18
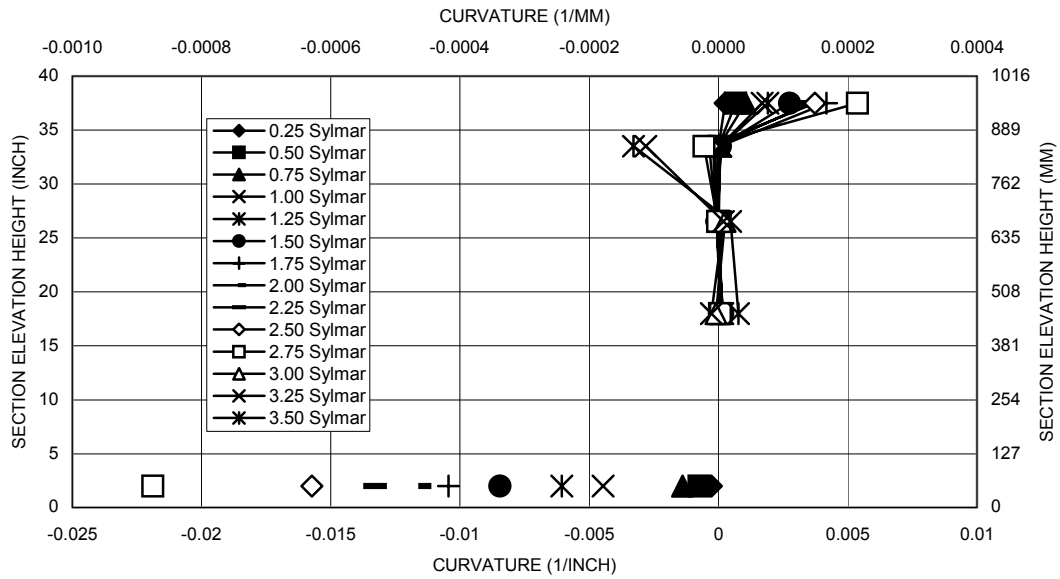
Figure 3.79 Maximum Curvature in South Column
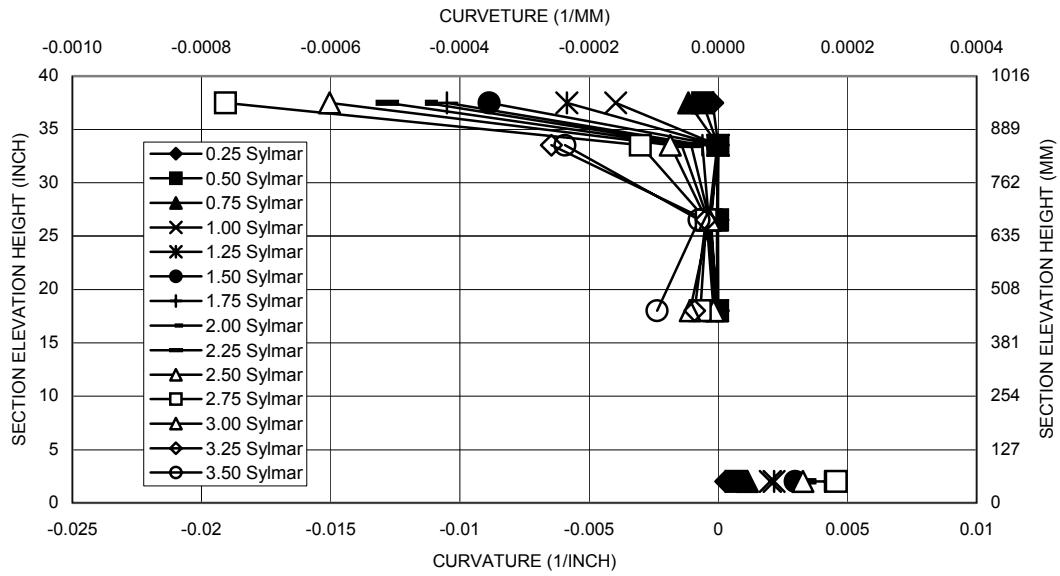
Figure 3.80 Minimum Curvature in South Column
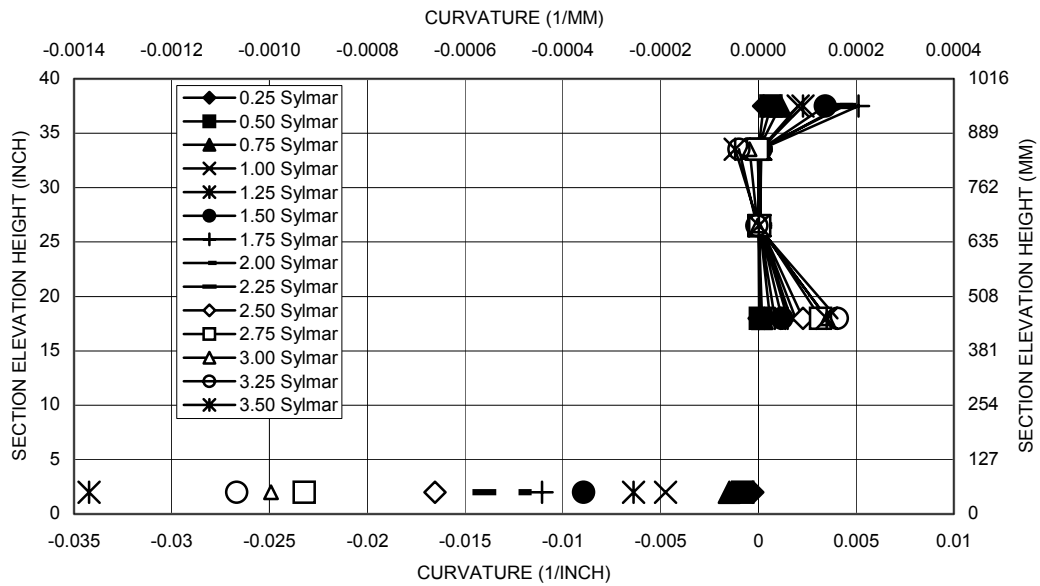
Figure 3.81 Maximum Curvature in North Column

138
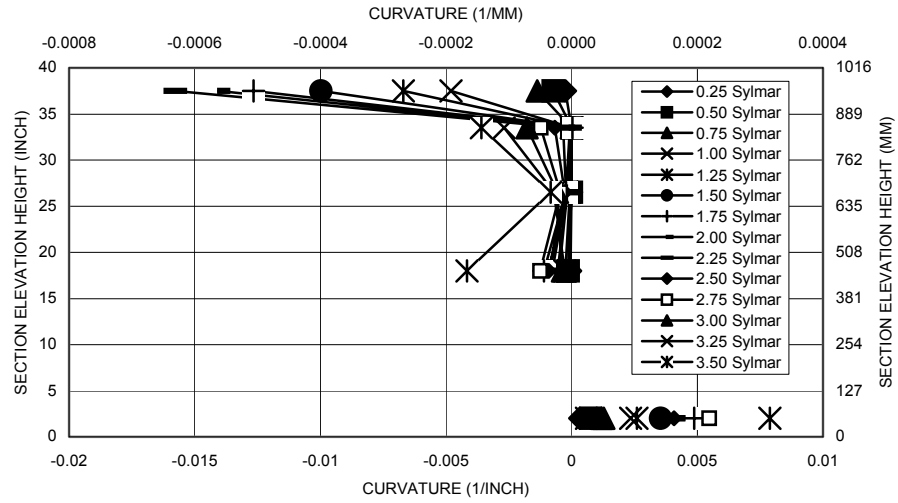
Figure 3.82 Minimum Curvature in North Column
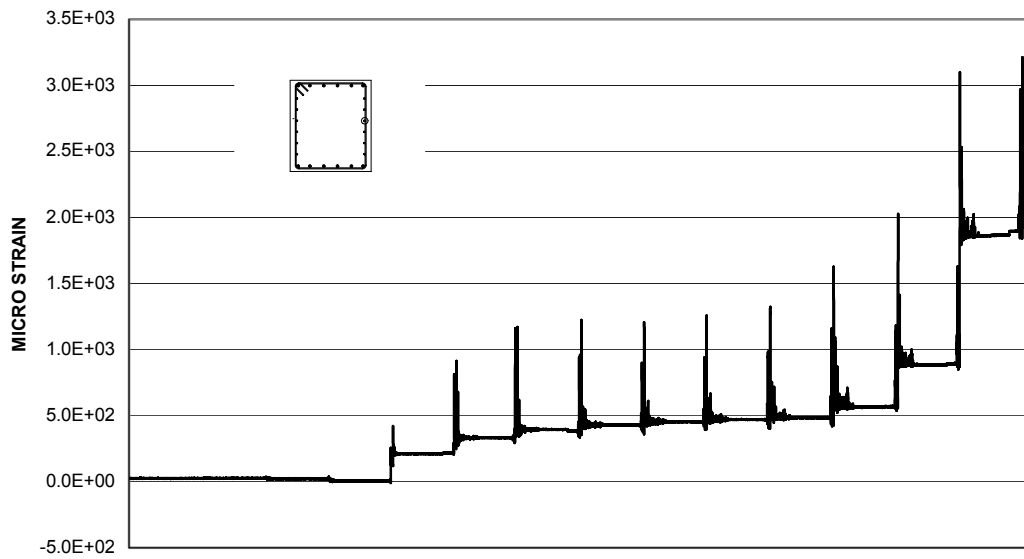
Figure 3.83 Time History for Beam Skin Reinforcement (SG73)

139
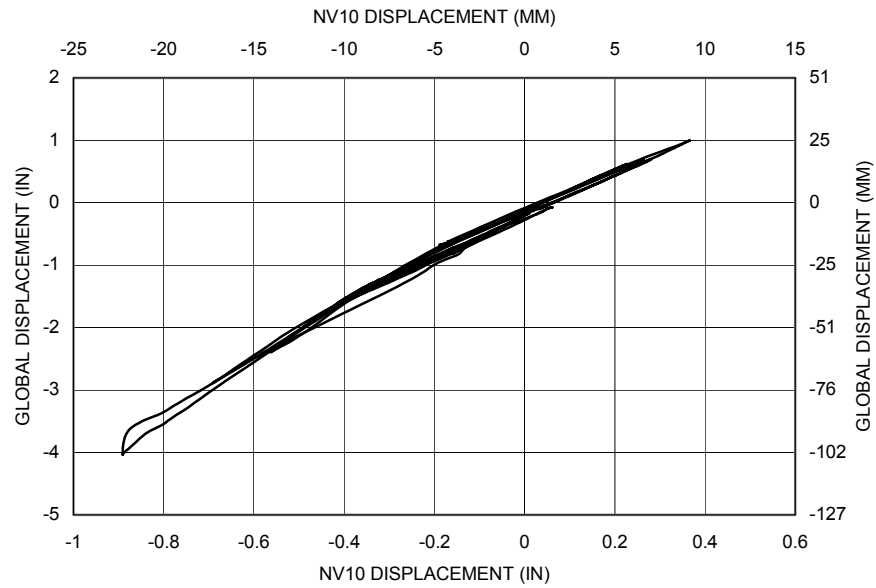
Figure 3.84 Comparison of Displacements of Global and NV10 Displacement
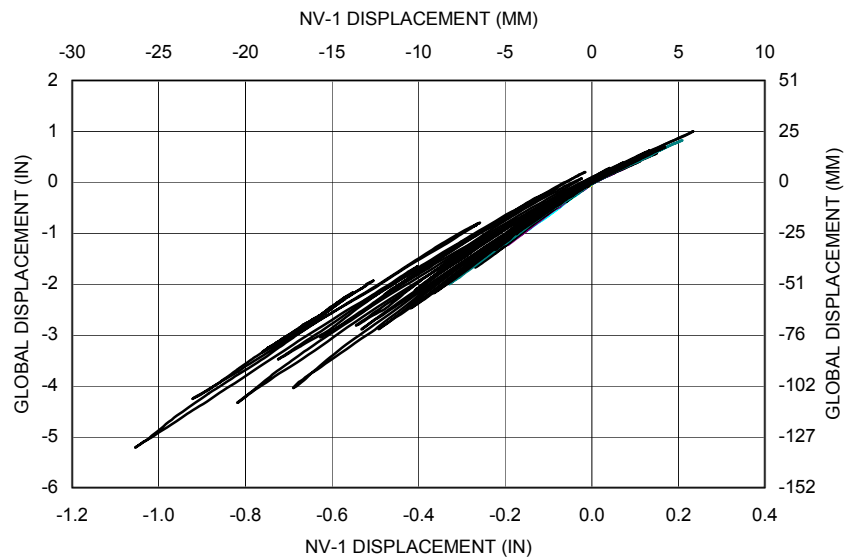
Figure 3.85 Comparison of Displacements of Global and NV1 Displacement
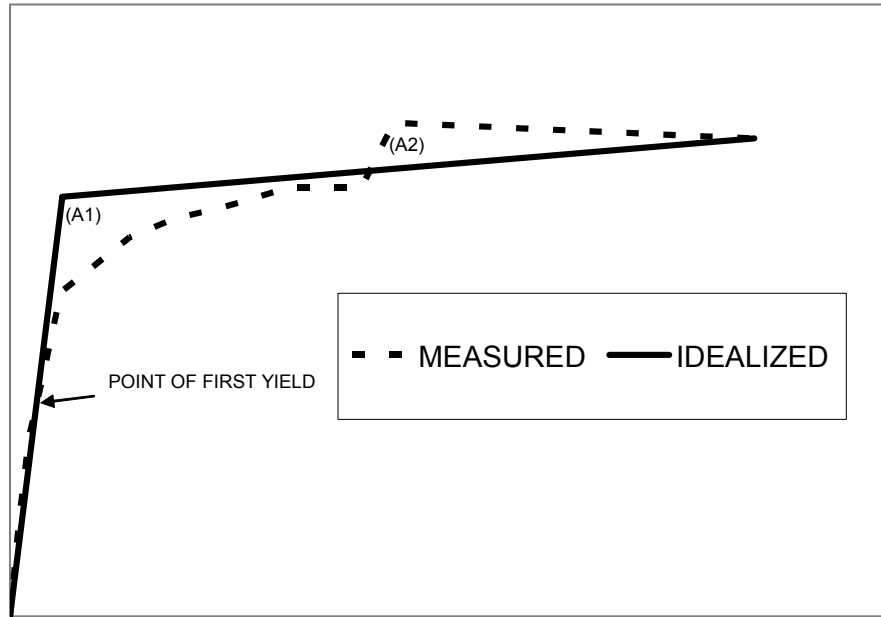
Figure 3.86 Calculating Idealized Curve
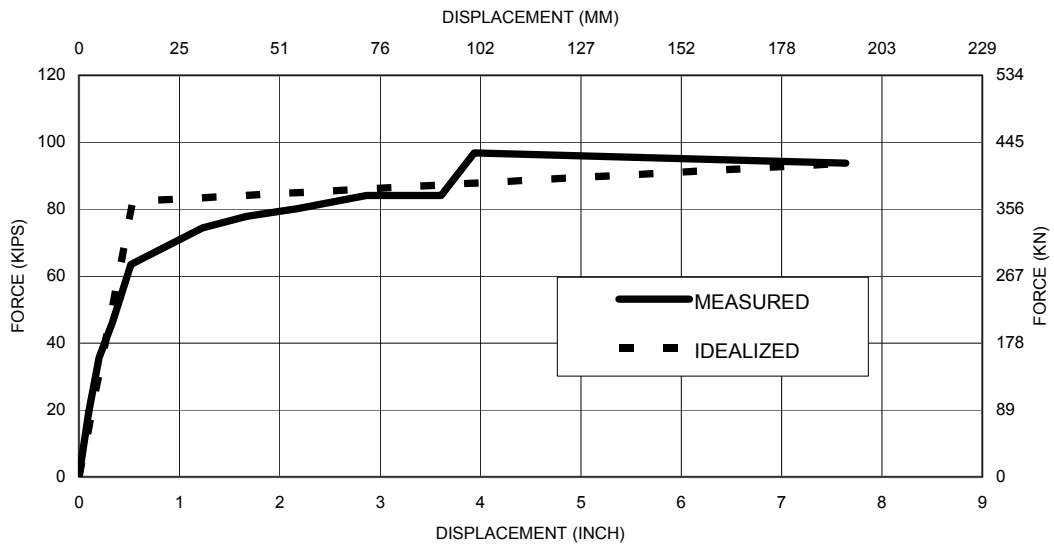
Figure 3.87 Idealized and Actual Load-Displacement Curve

141
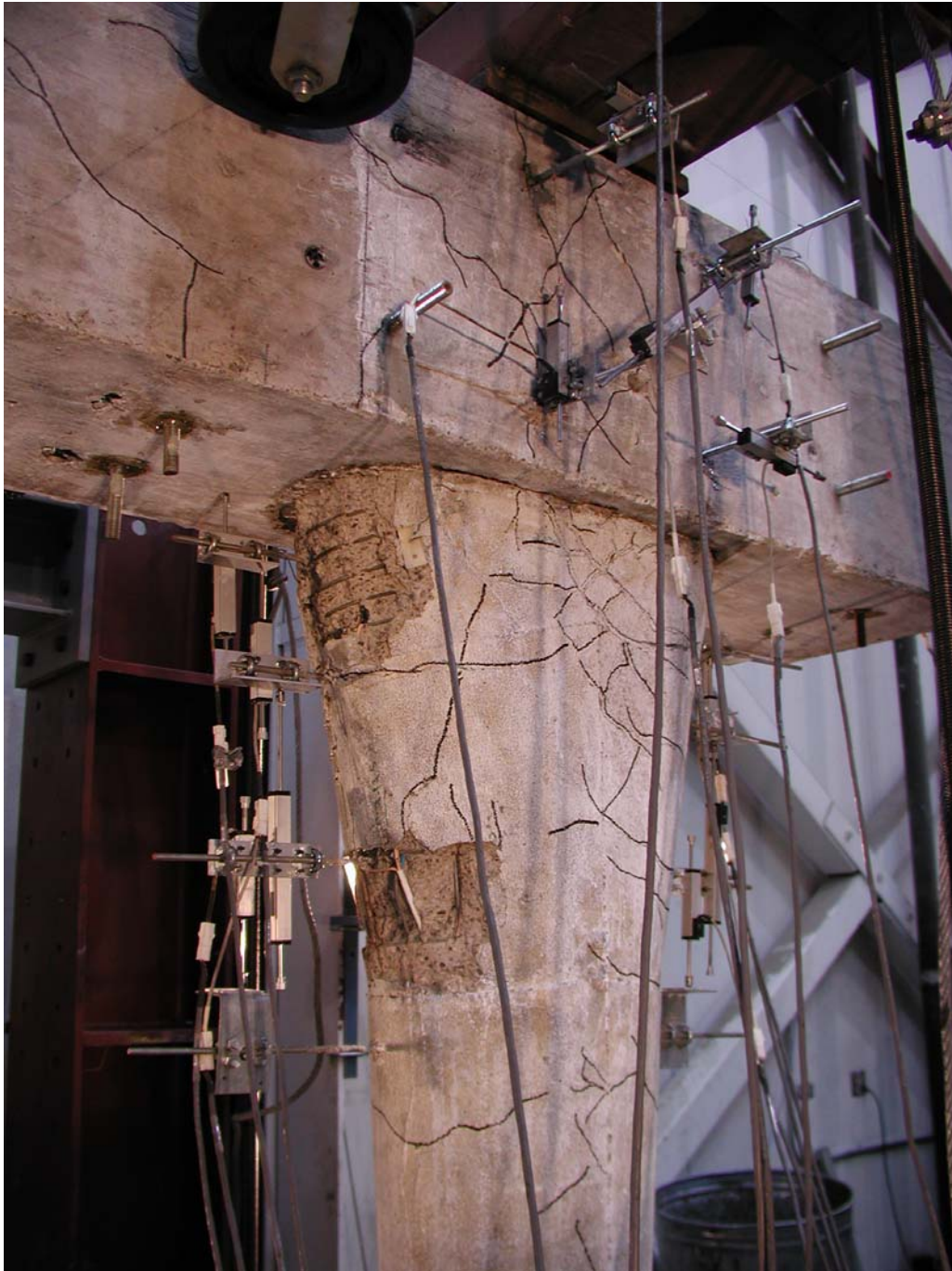
Figure 4.1 Initial Condition of the Structure
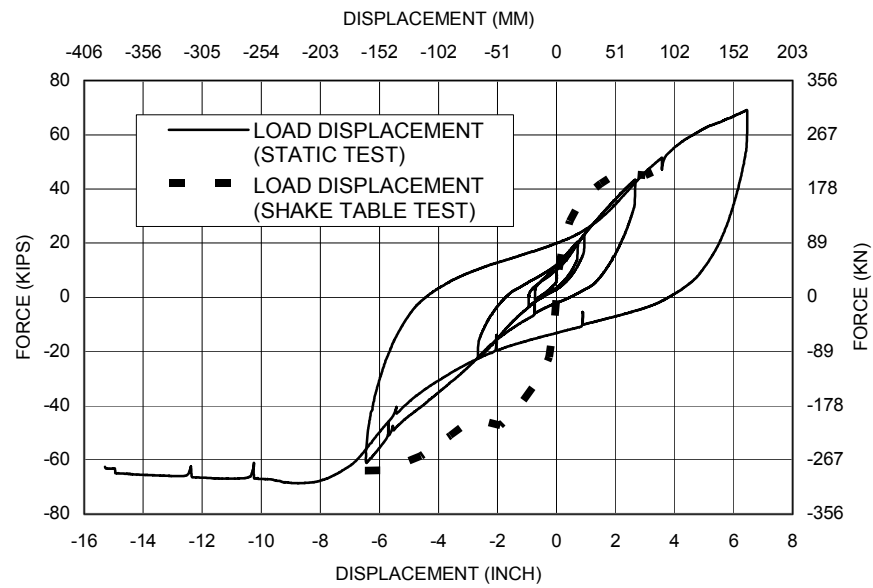
Figure 4.2 Load-Displacement Relation for LFCD1S

Figure 4.3 Cracks in LFCD1S at Load Step-4

143

Figure 4.4 Cracks in LFCD1S at Load Step-5

Figure 4.5 Cracks in LFCD1S at Load Step-7

Figure 4.6 Cracks in LFCD1S at Load Step-7

Figure 4.7 Cracks in LFCD1S at Load Step-8
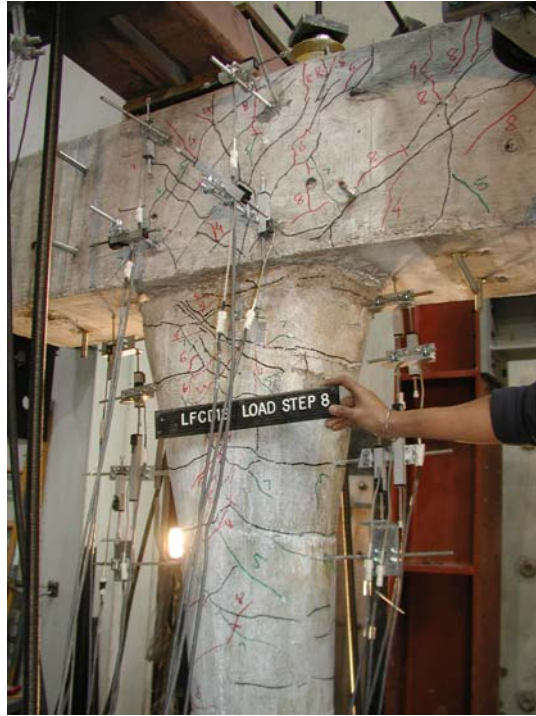
Figure 4.8 Cracks in LFCD1S at Load Step-8

Figure 4.9 Cracks in LFCD1S at Load Step-8

Figure 4.10 Cracks in LFCD1S at Load Step-9

Figure 4.11 Cracks in LFCD1S at Load Step-9

Figure 4.12 Cracks in LFCD1S at Load Step-9
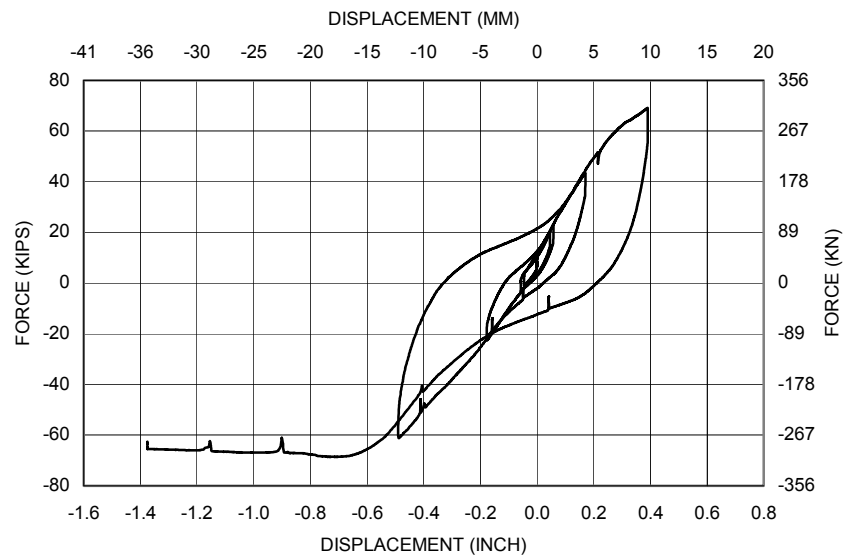
Figure 4.13 Slippage at South Column Base for LFCD1S
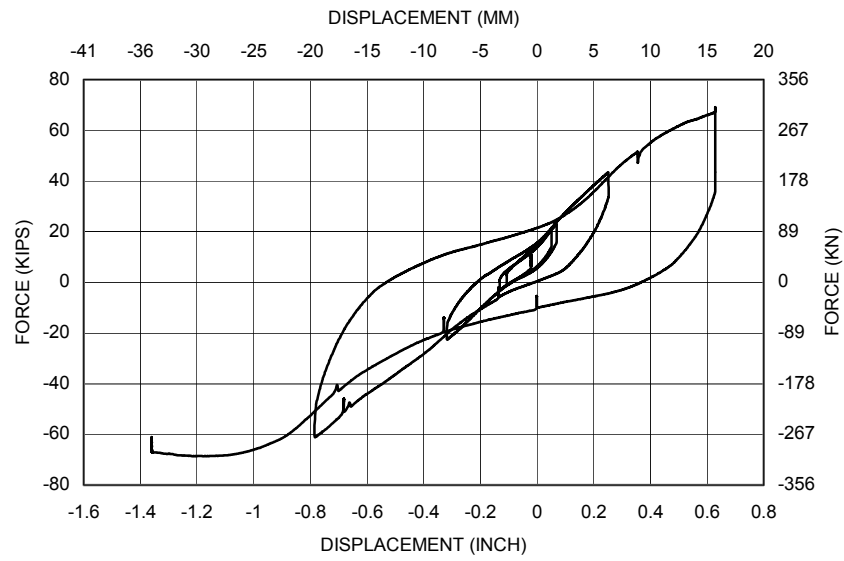
Figure 4.14 Slippage at North Column Base for LFCD1S

Figure 4.15 Initial Cracks in Beam-Column Connection for LFCD1S

149
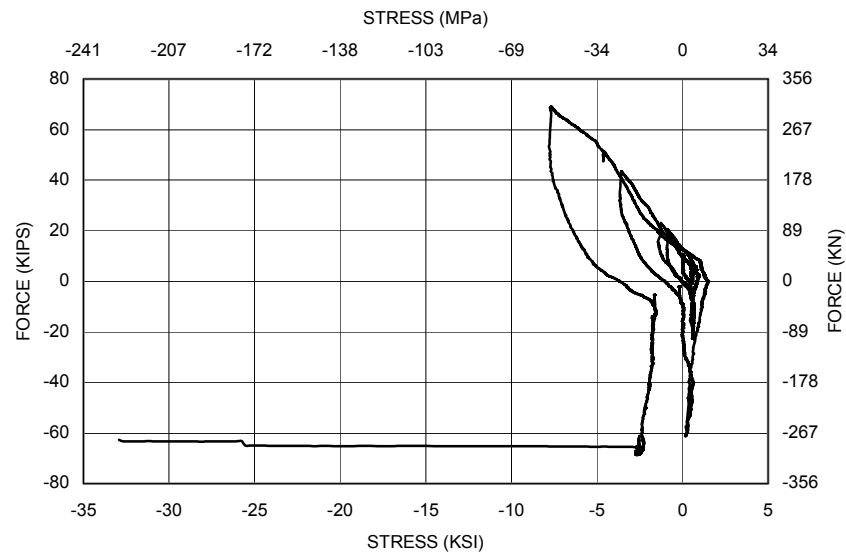
Figure 4.16 Principal Stress (σ_1) in South Beam-Column Connection for LFCD1S
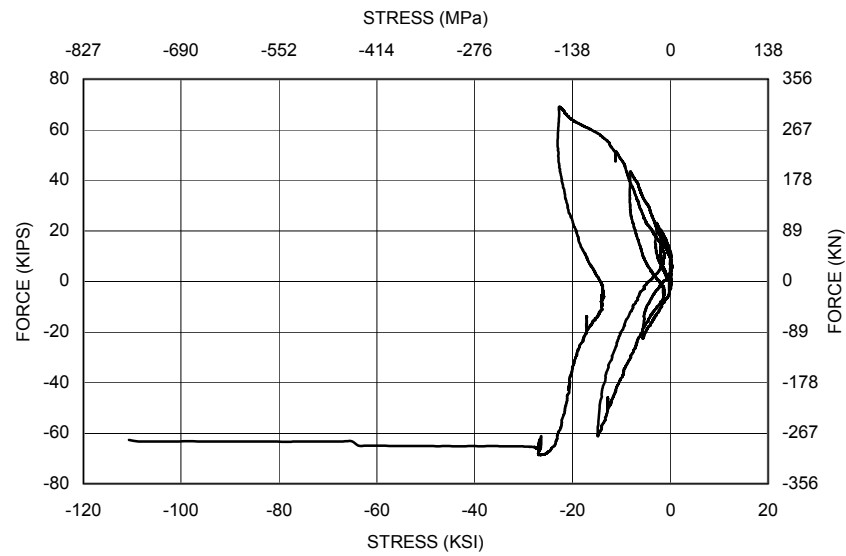
Figure 4.17 Principal Stress (σ_2) in South Beam-Column Connection for LFCD1S

Figure 4.18 Principal Stress (σ_1) in North Beam-Column Connection for LFCD1S
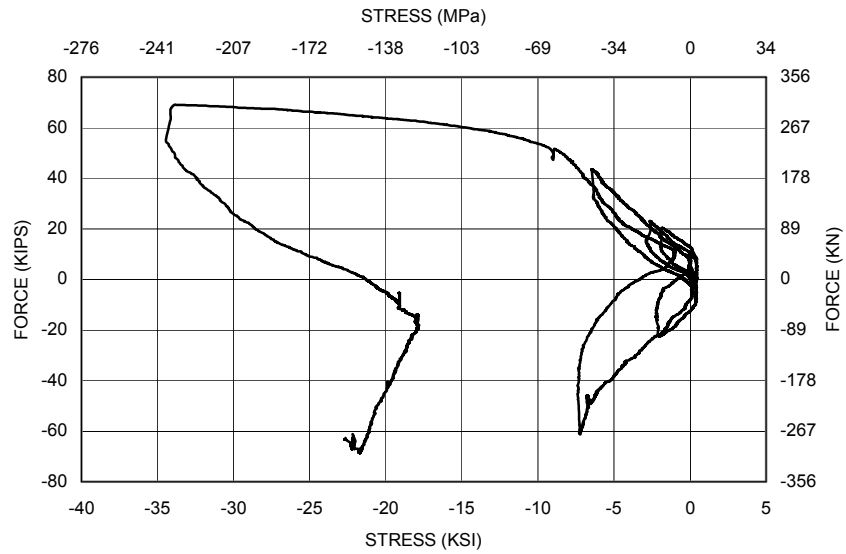
Figure 4.19 Principal Stress (σ_2) in North Beam-Column Connection for LFCD1S

151
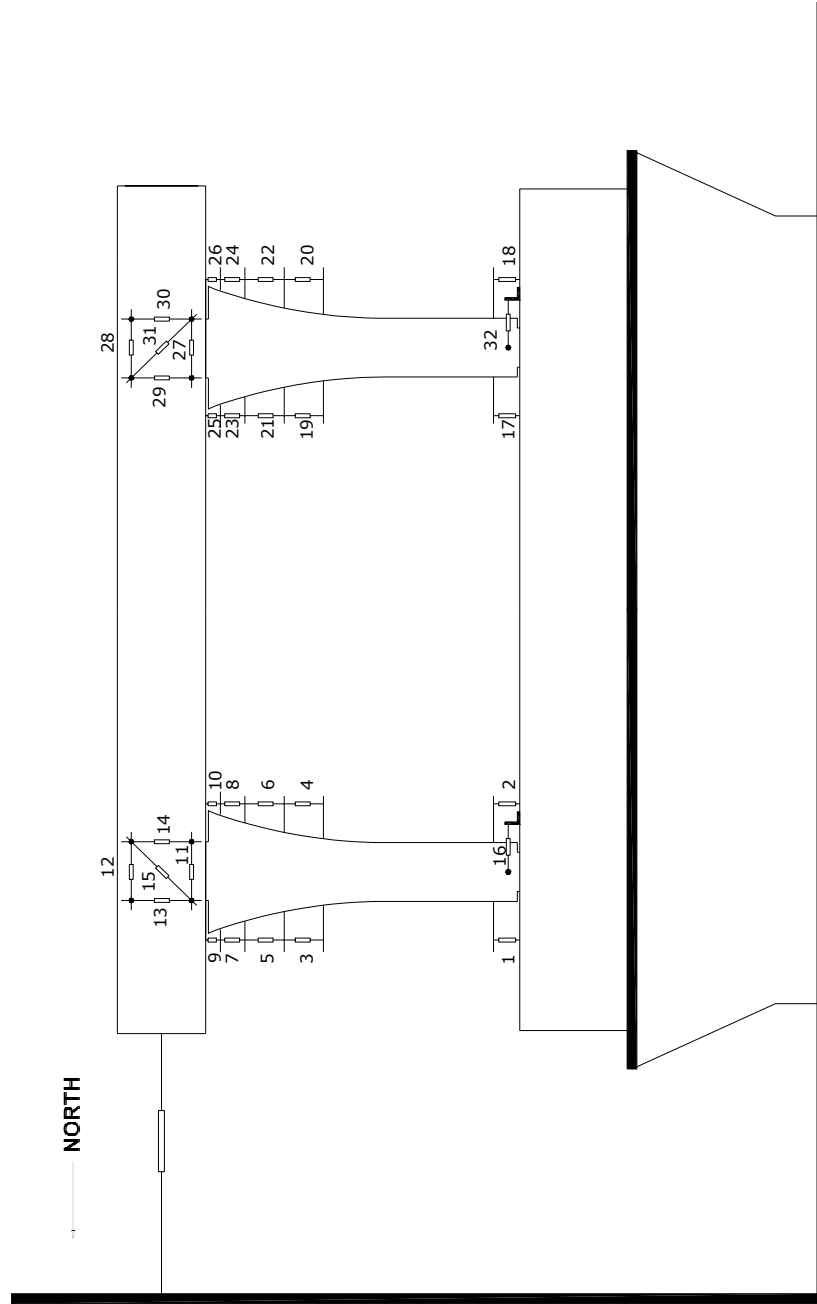
Figure 4.20 Location of Measured Curvature
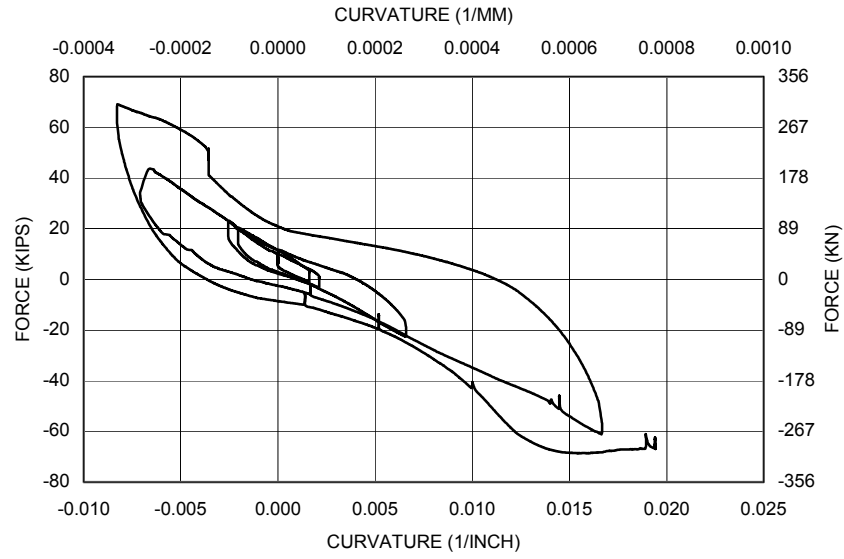
Figure 4.21 Curvature at NV1 and NV2 for LFCD1S
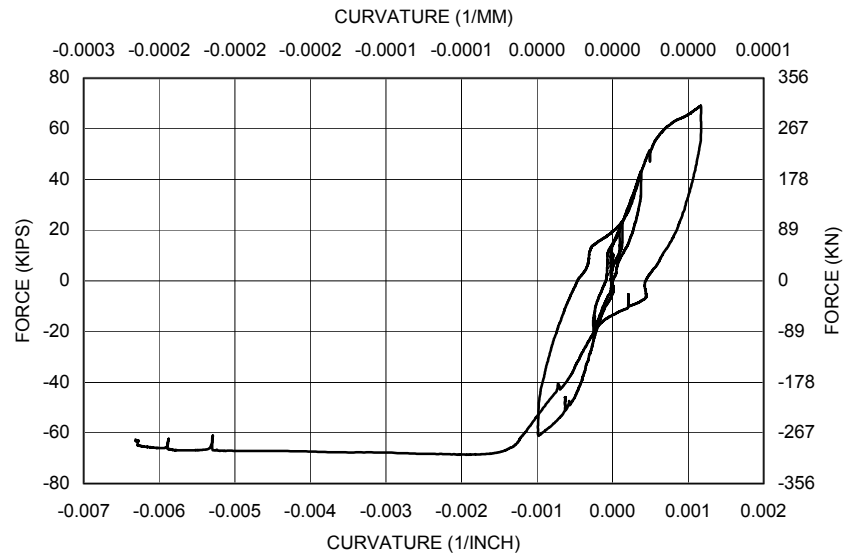
Figure 4.22 Curvature at NV3 and NV4 for LFCD1S

153
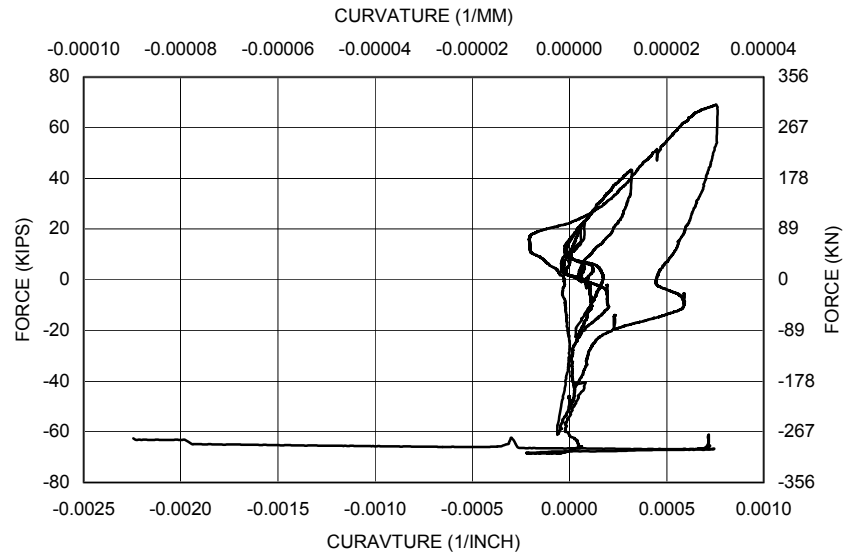
Figure 4.23 Curvature at NV5 and NV6 for LFCD1S
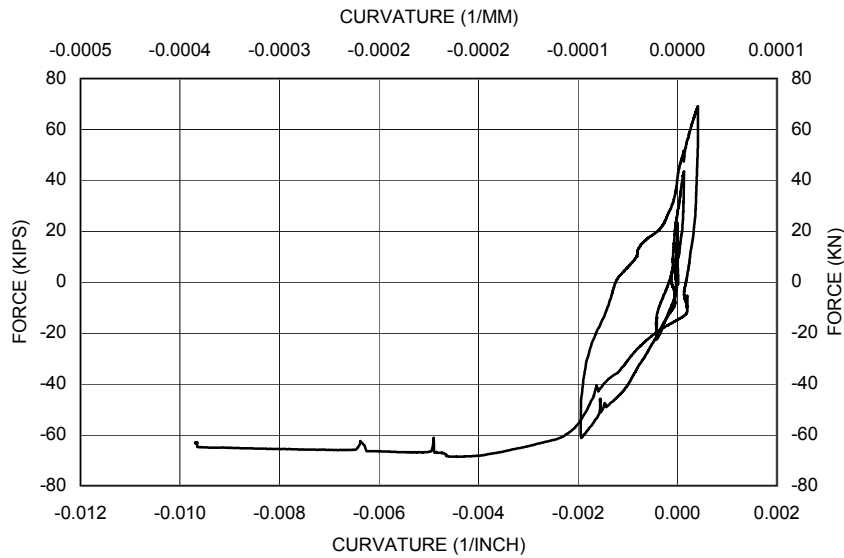
Figure 4.24 Curvature at NV7 and NV8 for LFCD1S

154
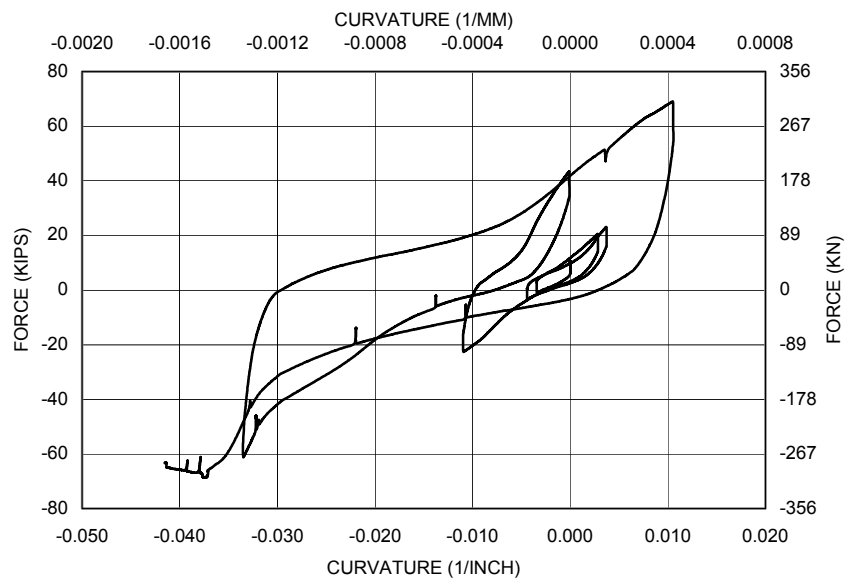
Figure 4.25 Curvature at NV9 and NV10 for LFCD1S
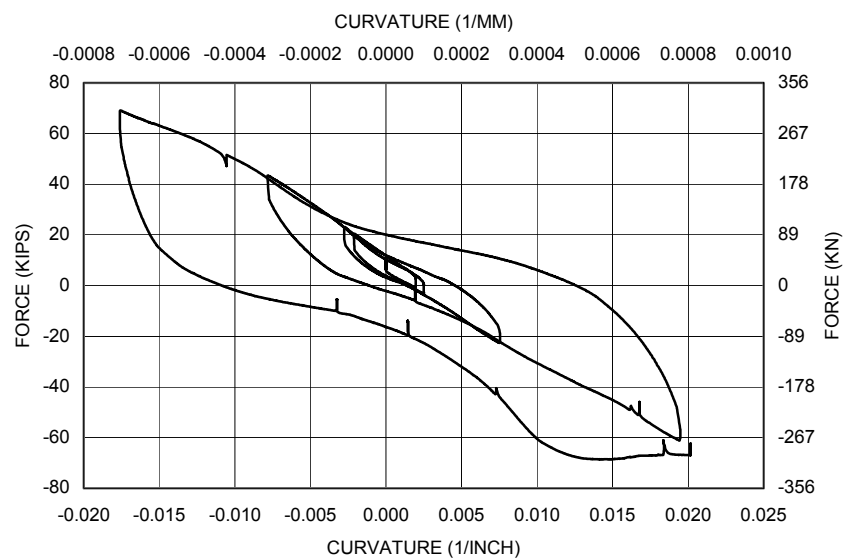
Figure 4.26 Curvature at NV17 and NV18 for LFCD1S

155
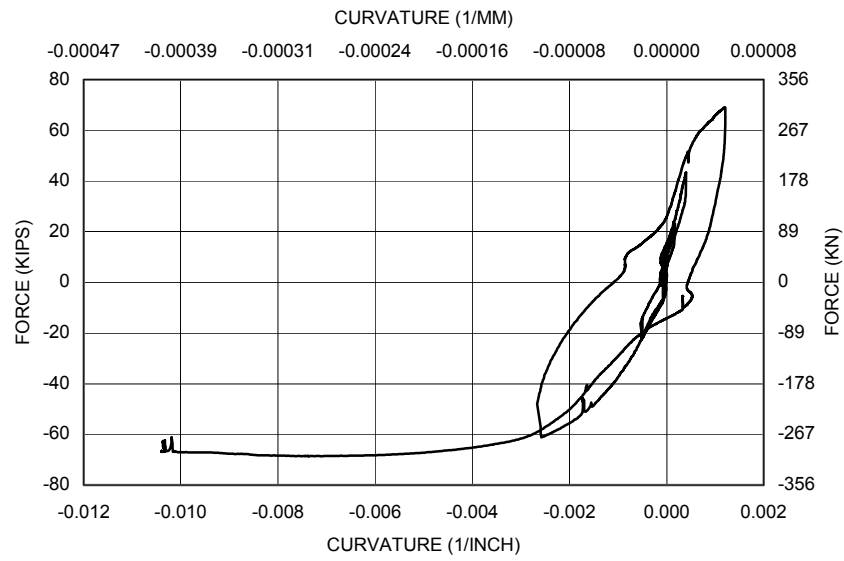
Figure 4.27 Curvature at NV19 and NV20 for LFCD1S
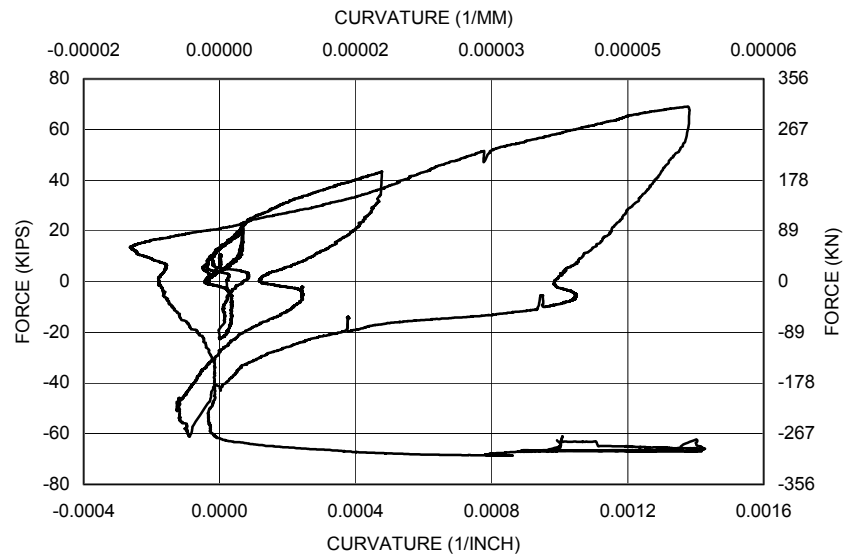
Figure 4.28 Curvature at NV21 and NV22 for LFCD1S
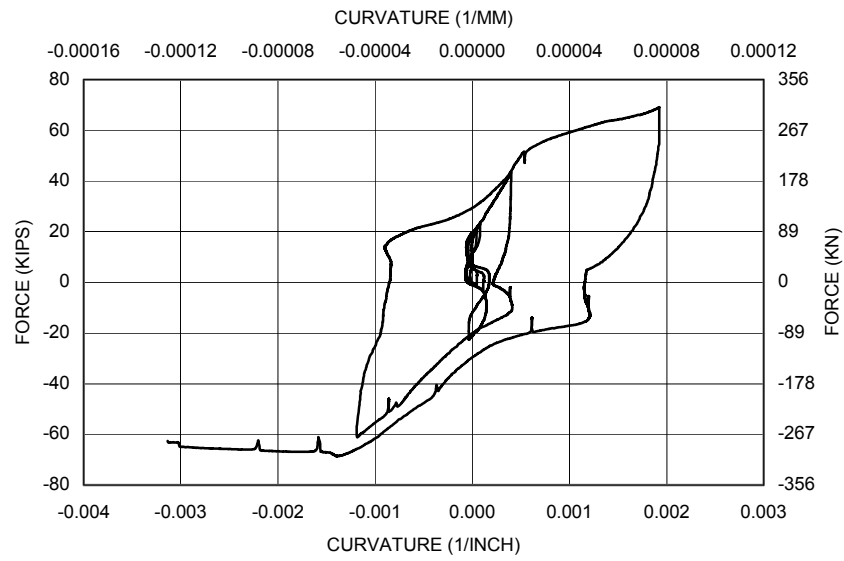
Figure 4.29 Curvature at NV23 and NV24 for LFCD1S
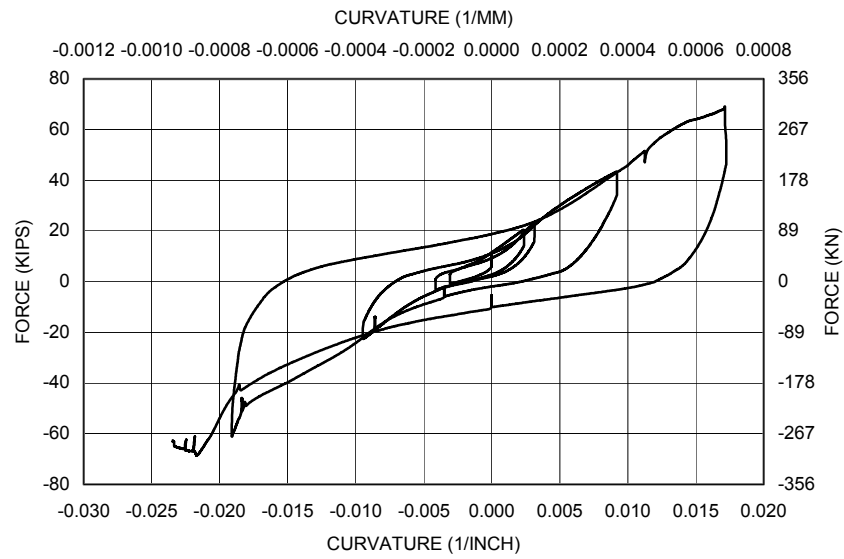
Figure 4.30 Curvature at NV25 and NV26 for LFCD1S

157
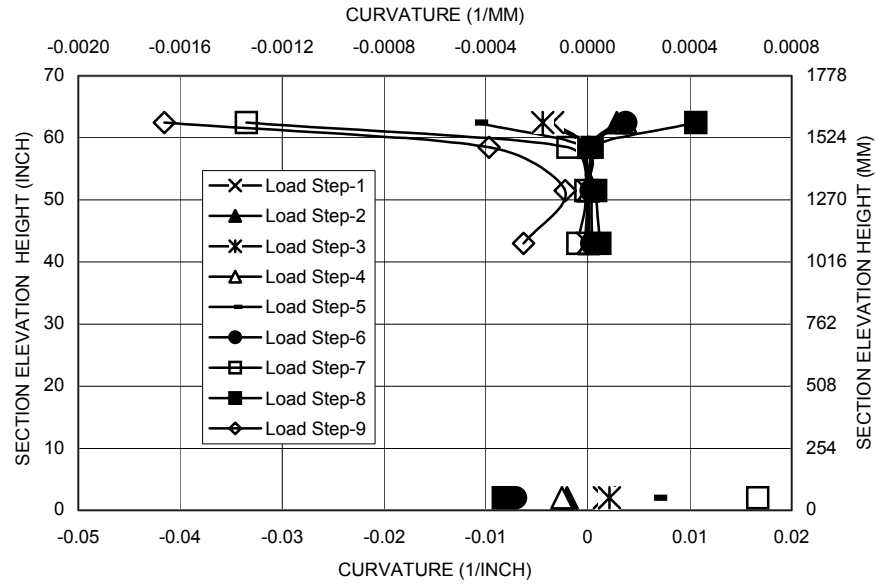
Figure 4.31 Maximum Curvatures for Each Load Step in South Column (LFCD1S)
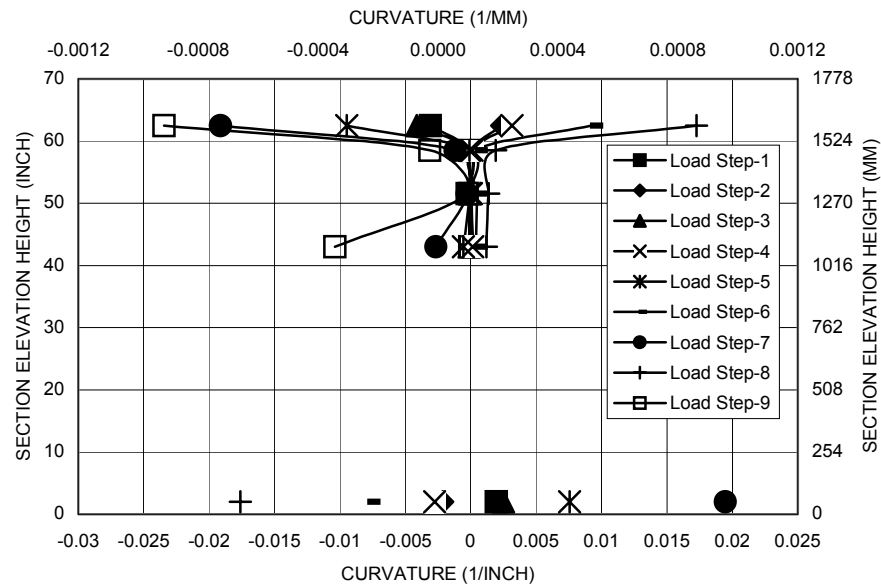
Figure 4.32 Maximum Curvatures for Each Load Step in North Column (LFCD1S)

158
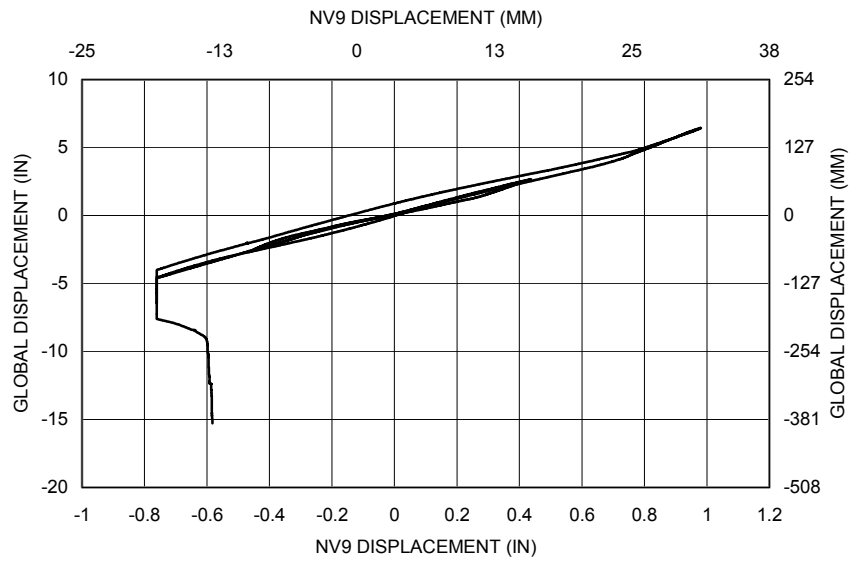
Figure 4.33a Displacement Comparison for Transducer Global and NV9 Displacement
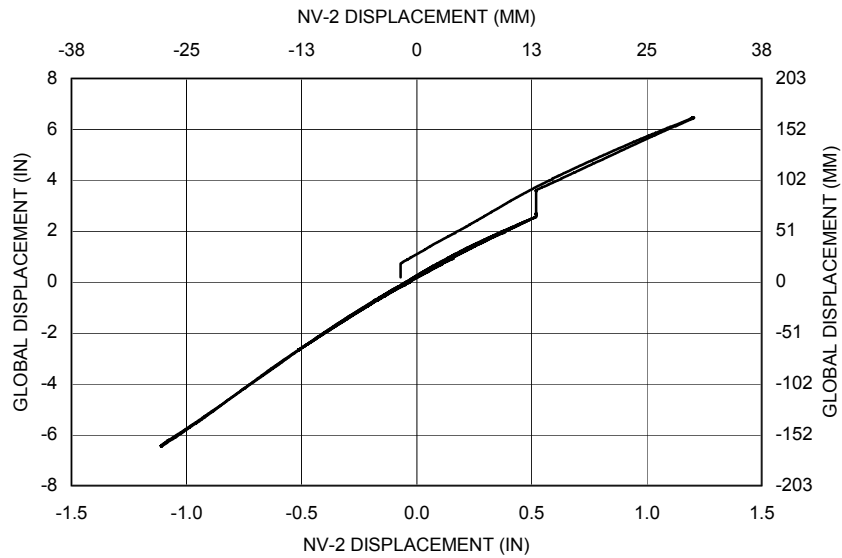
Figure 4.33b Displacement Comparison for Transducer Global and NV2 Displacement
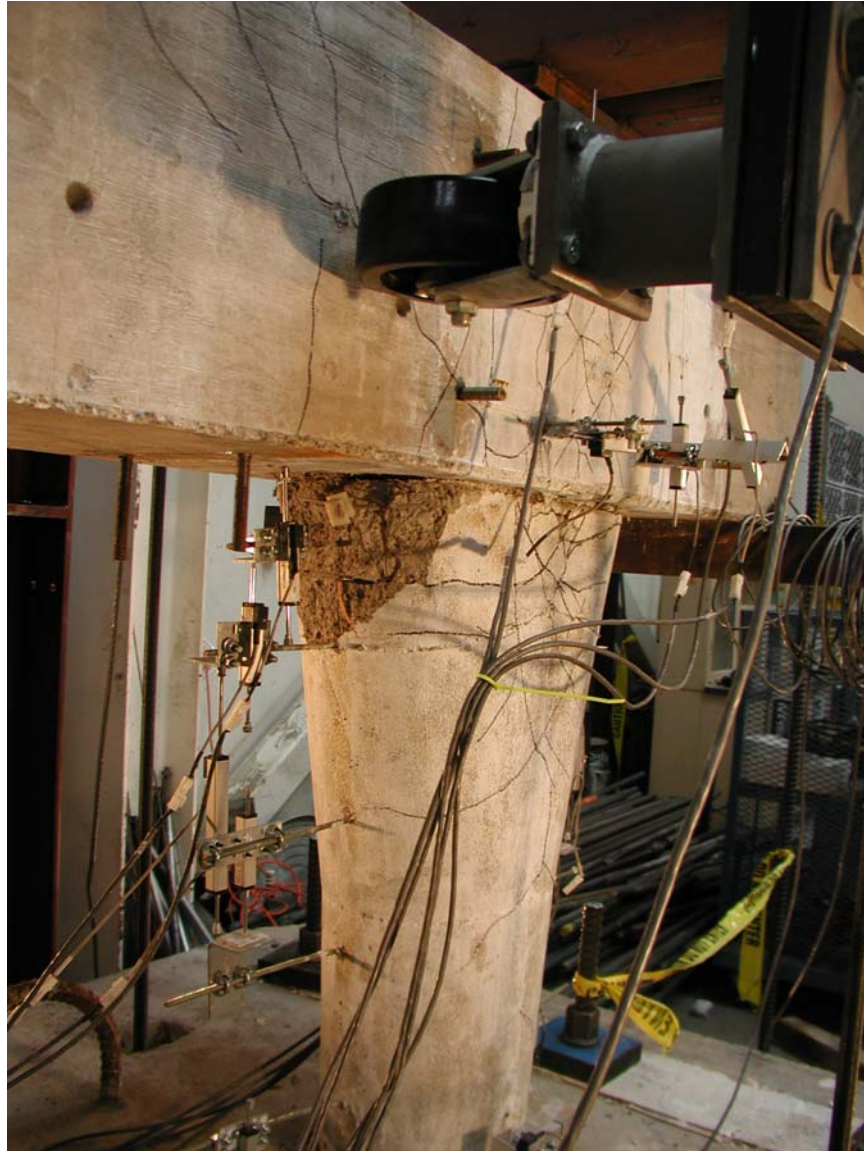
Figure 4.34 Initial Condition of SFCD2S
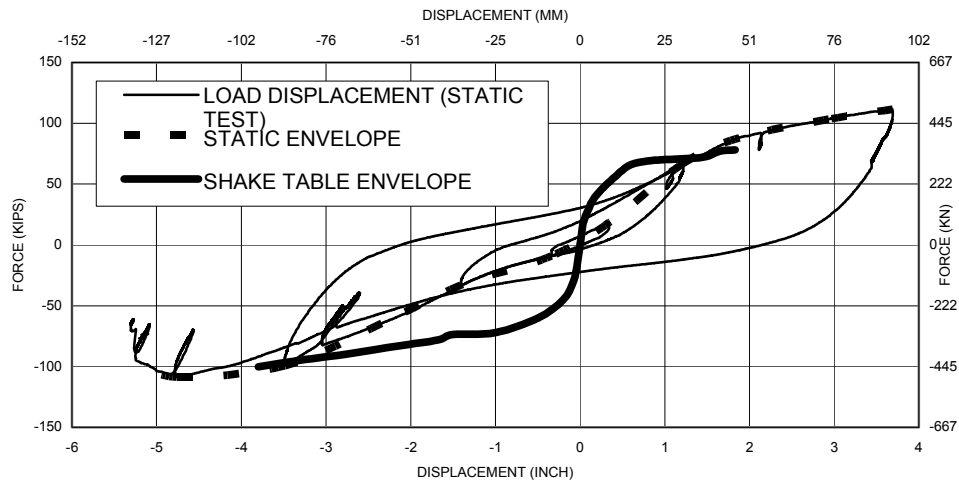
Figure 4.35 Load-Displacement Curve for SFCD2S

Figure 4.36 Shear Cracks in SFCD2S at Load Step-4

161

Figure 4.37 Shear Cracks in SFCD2S at Load Step-4

Figure 4.38 Cracks in SFCD2S at Load Step-5

Figure 4.39 Cracks in SFCD2S at Load Step-5

Figure 4.40 Cracks in SFCD2S at Load Step-5

Figure 4.41 Beams Shear Failure in SFCD2S
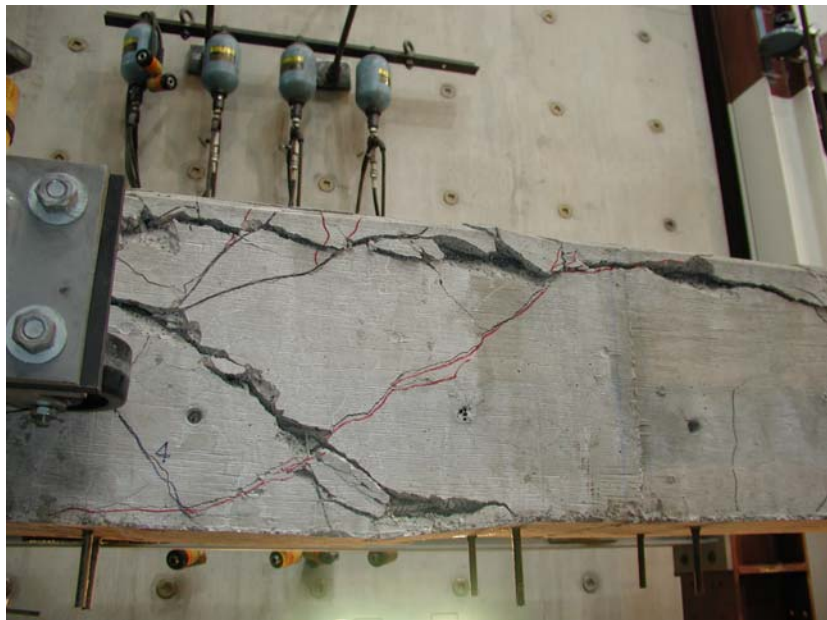
Figure 4.42 Beams Shear Failure in SFCD2S
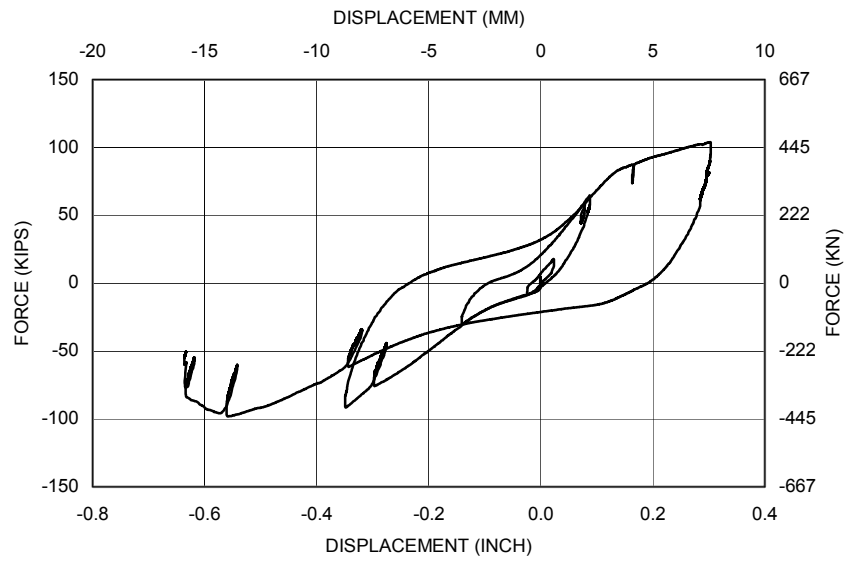
Figure 4.43 Slippage at South Column Base in SFCD2S
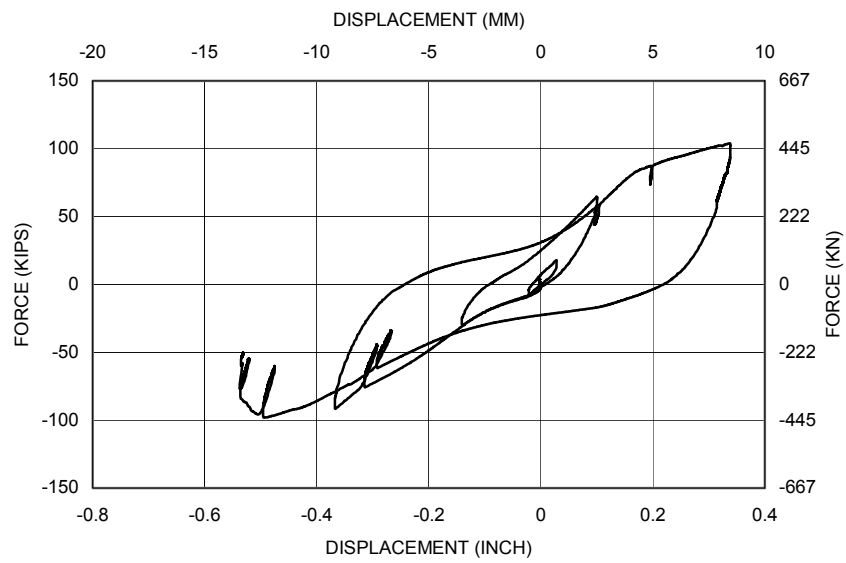
Figure 4.44 Slippage at North Column Base in SFCD2S

165
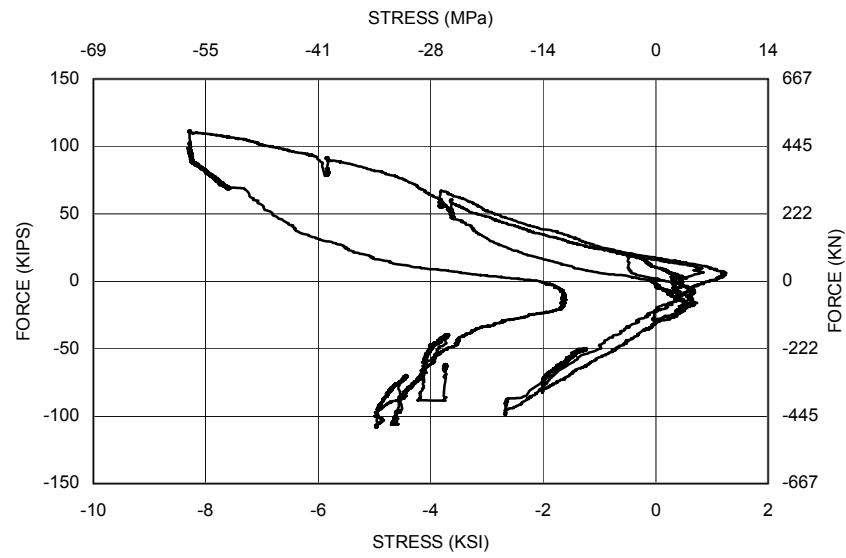
Figure 4.45 Principal Stress (σ_1) in South Beam-Column Connection for SFCD2S
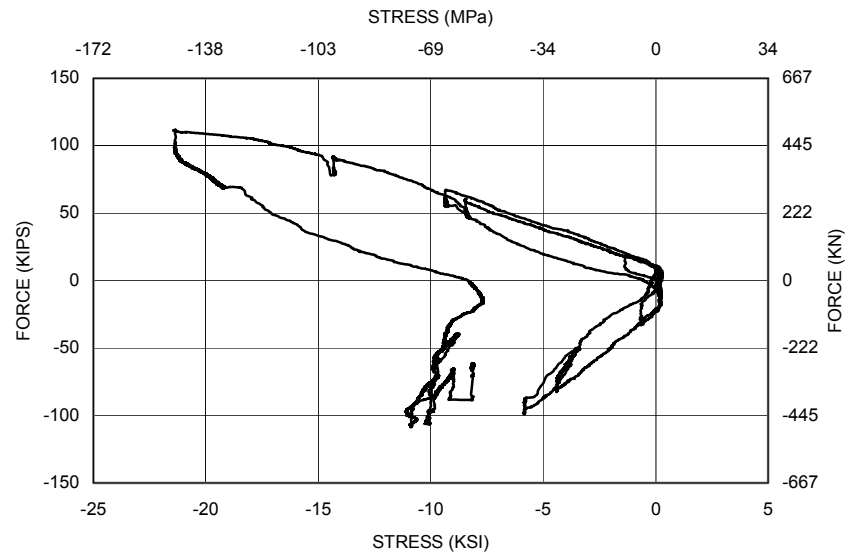
Figure 4.46 Principal Stress (σ_2) in South Beam-Column Connection for SFCD2S

166
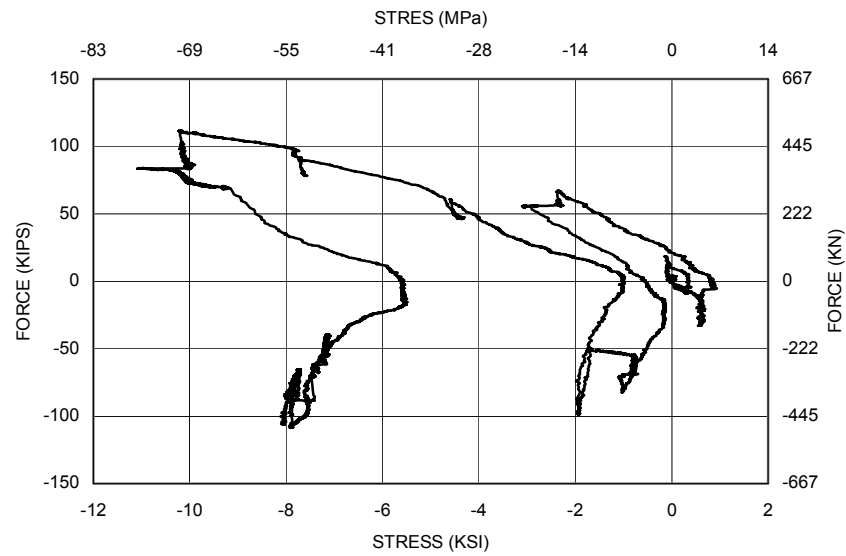
Figure 4.47 Principal Stress (σ_1) in North Beam-Column Connection for SFCD2S
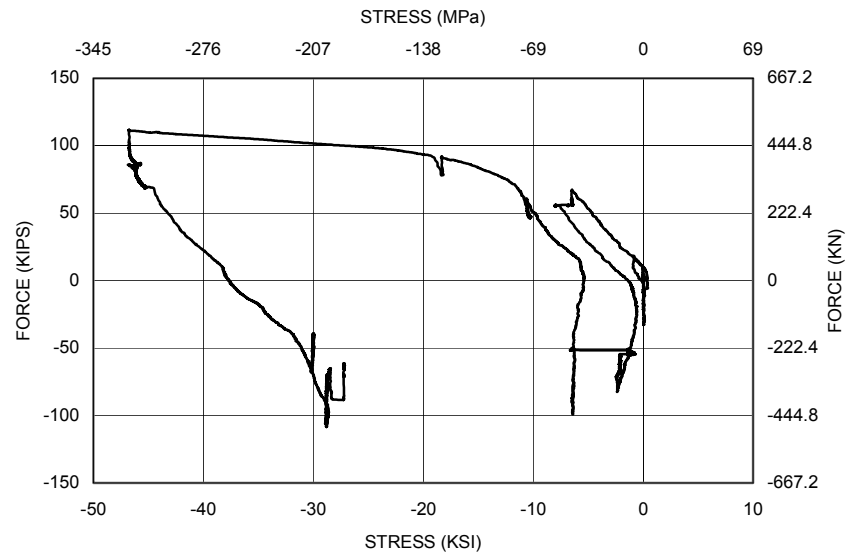
Figure 4.48 Principal Stress (σ_2) in North Beam-Column Connection for SFCD2S
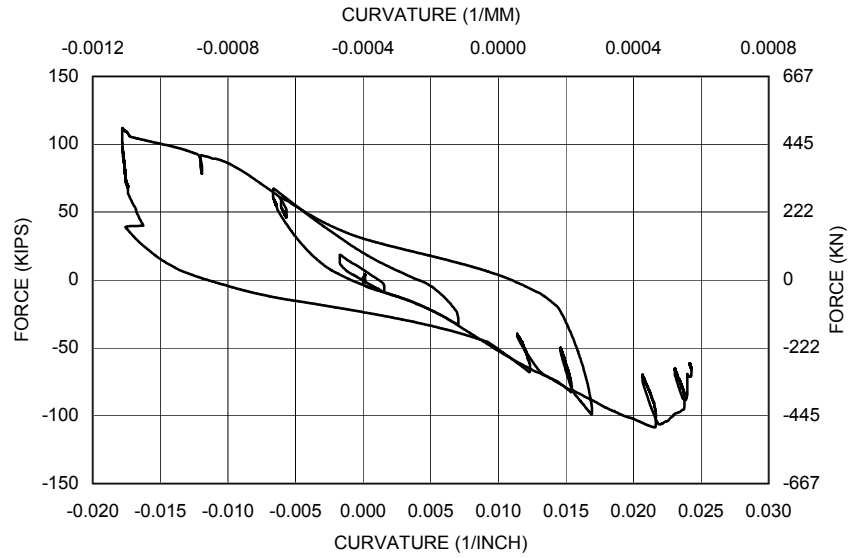
Figure 4.49 Curvature at Section NV1 and NV2 in SFCD2S
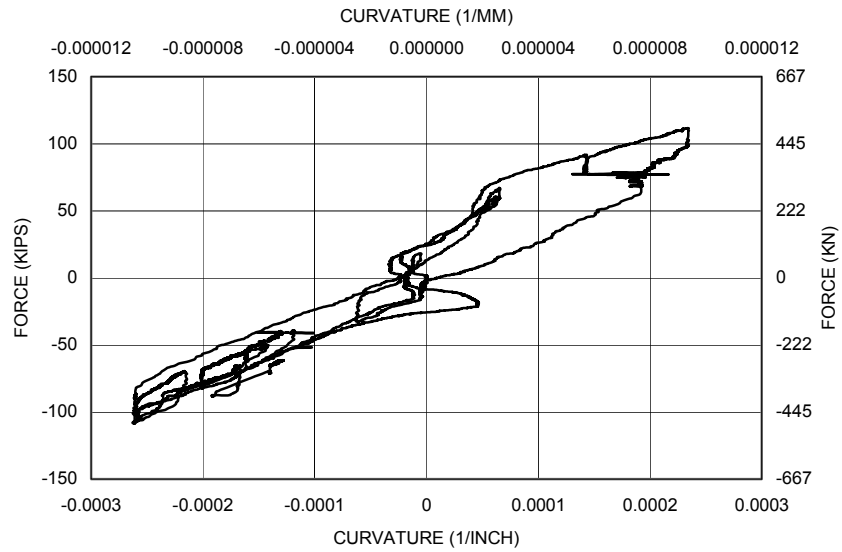
Figure 4.50 Curvature at Section NV3 and NV4 in SFCD2S
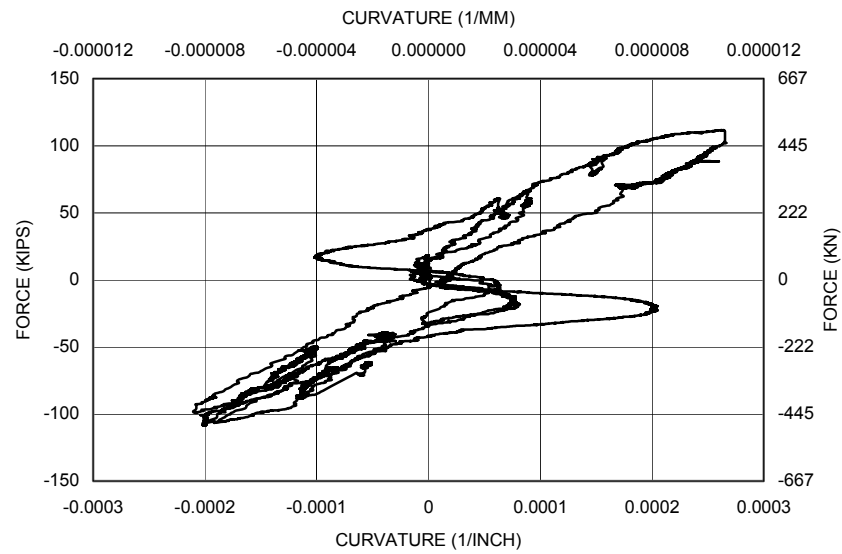
Figure 4.51 Curvature at Section NV5 and NV6 in SFCD2S
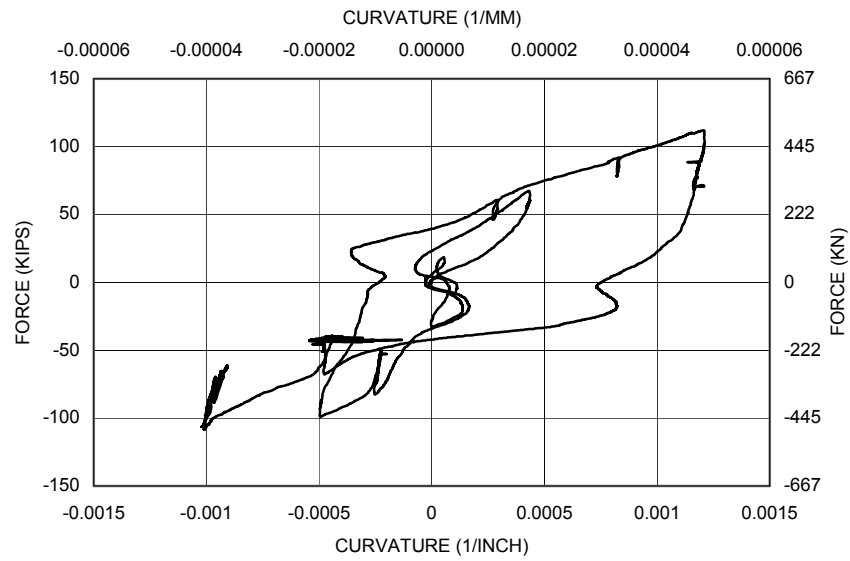
Figure 4.52 Curvature at Section NV7 and NV8 in SFCD2S

169
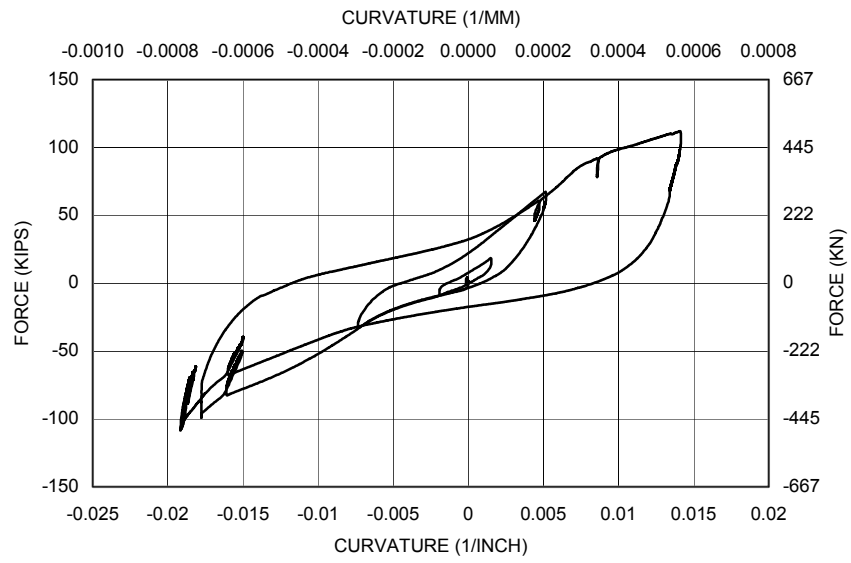
Figure 4.53 Curvature at Section NV9 and NV10 in SFCD2S
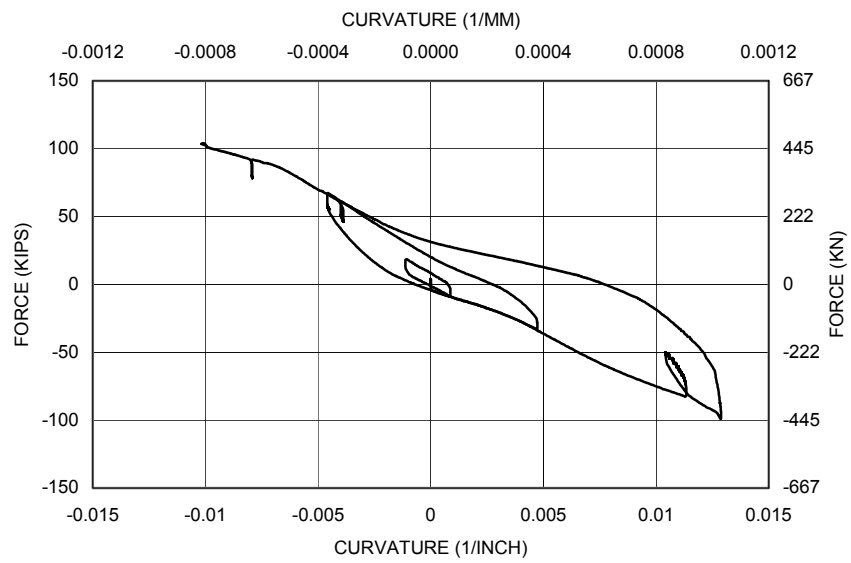
Figure 4.54 Curvature at Section NV17 and NV18 in SFCD2S
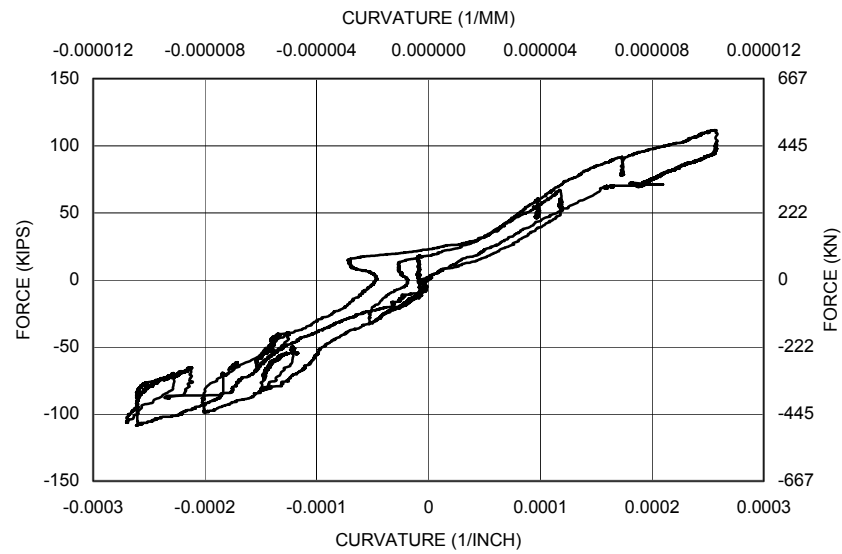
Figure 4.55 Curvature at Section NV19 and NV20 in SFCD2S
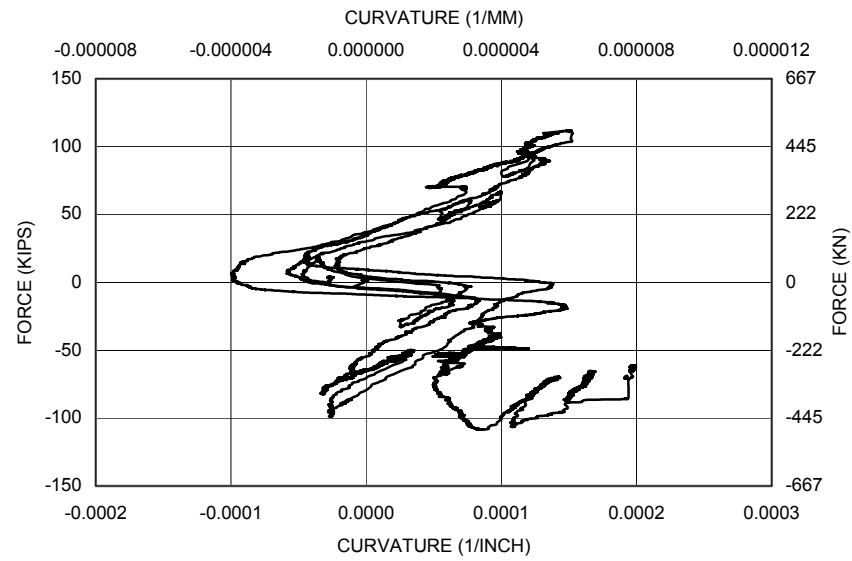
Figure 4.56 Curvature at Section NV21 and NV22 in SFCD2S

171
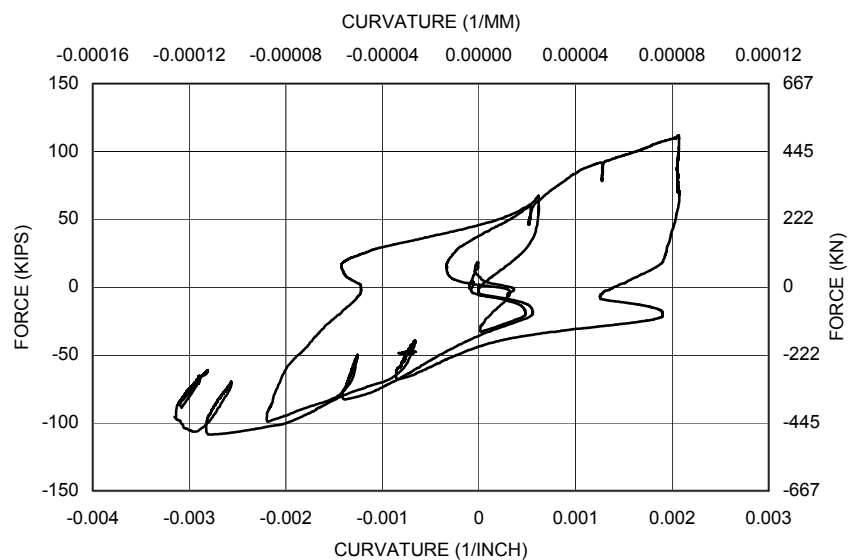
Figure 4.57 Curvature at Section NV23 and NV24 in SFCD2S
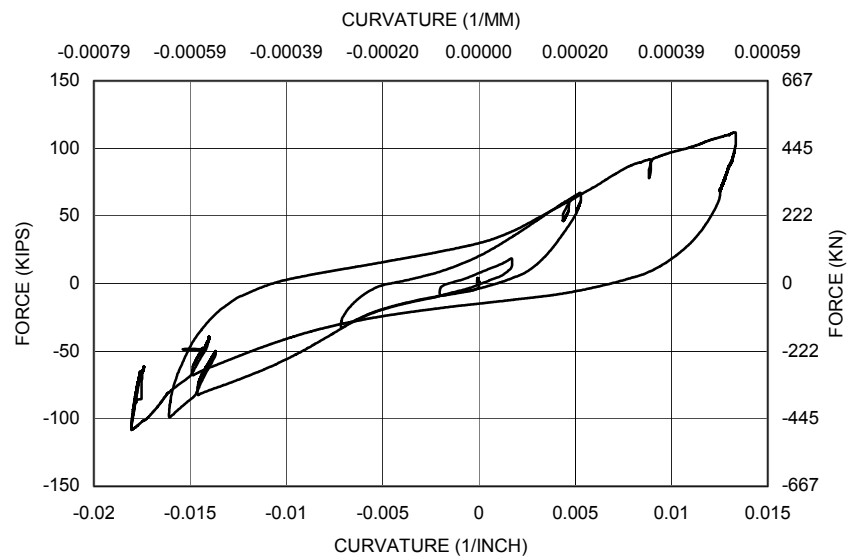
Figure 4.58 Curvature at Section NV25and NV26 in SFCD2S

172
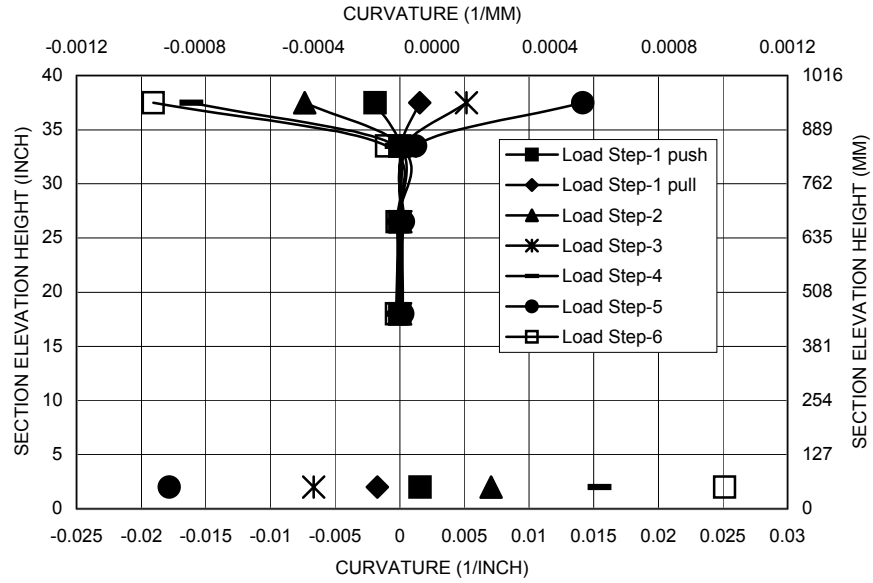
Figure 4.59 Maximum Curvatures for Each Load Step in South Column (SFCD2S)
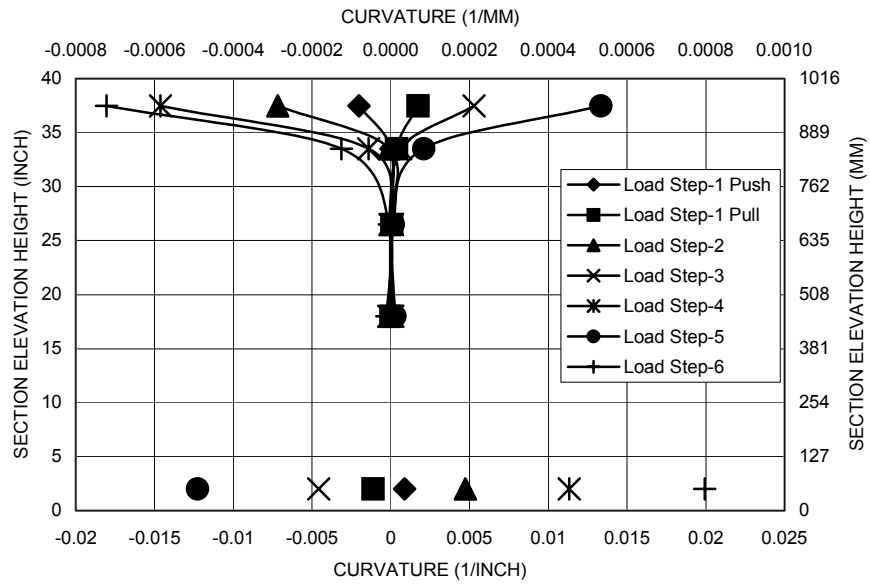
Figure 4.60 Maximum Curvatures for Each Load Step in North Column (SFCD2S)

173
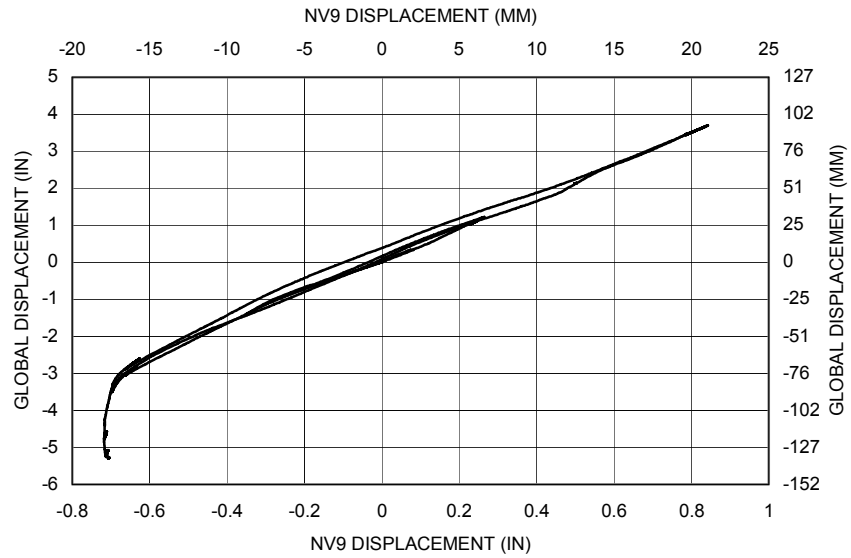
Figure 4.61a Displacement Comparison for Transducer Global and NV9 Displacement
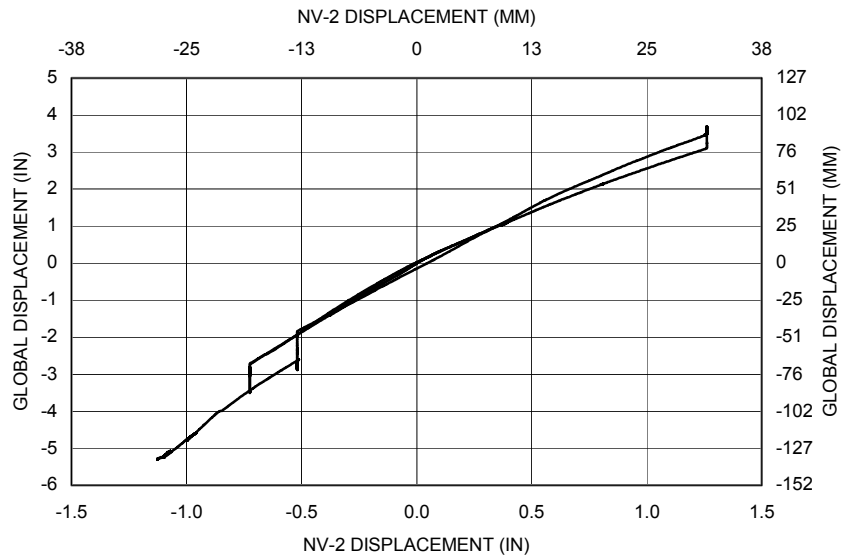
Figure 4.61b Displacement Comparison for Transducer Global and NV2 Displacement
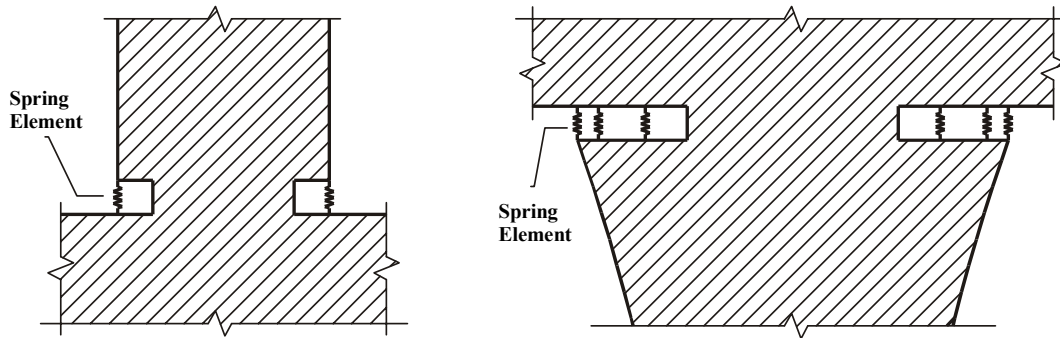
Figure 5.1 Spring Elements (a) At Base Hinge Gap   (a) At Flare Gap
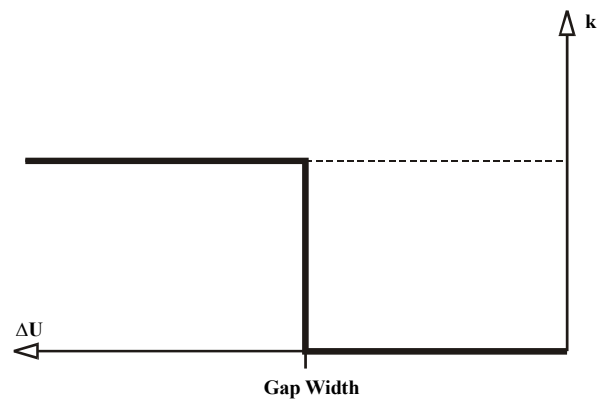
Figure 5.2 Spring Elements Material Model
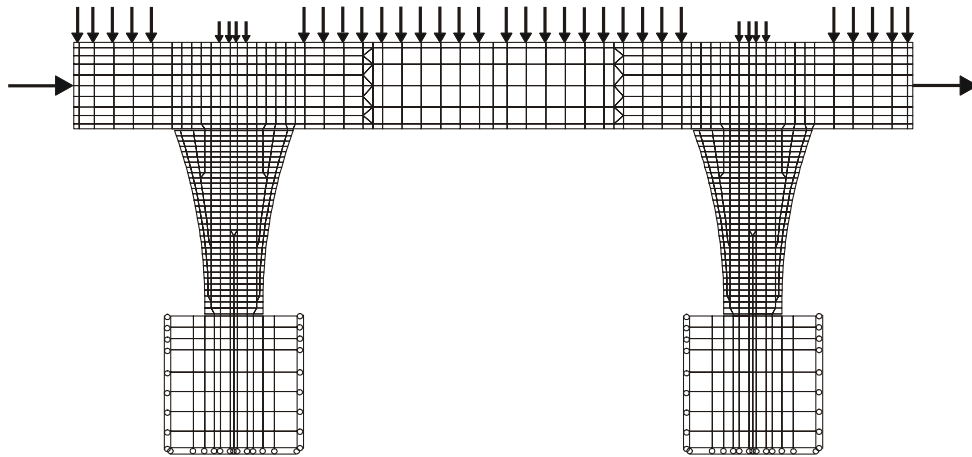
Figure 5.3 Finite Element Mesh for the Structure Along With Loading and Boundary Conditions
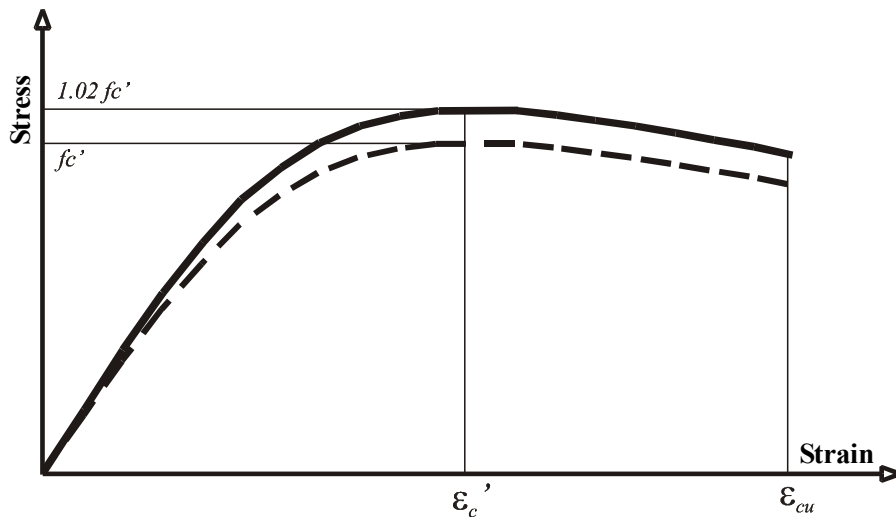
Figure 5.4 Uniaxial Stress-Strain Relationship for Concrete
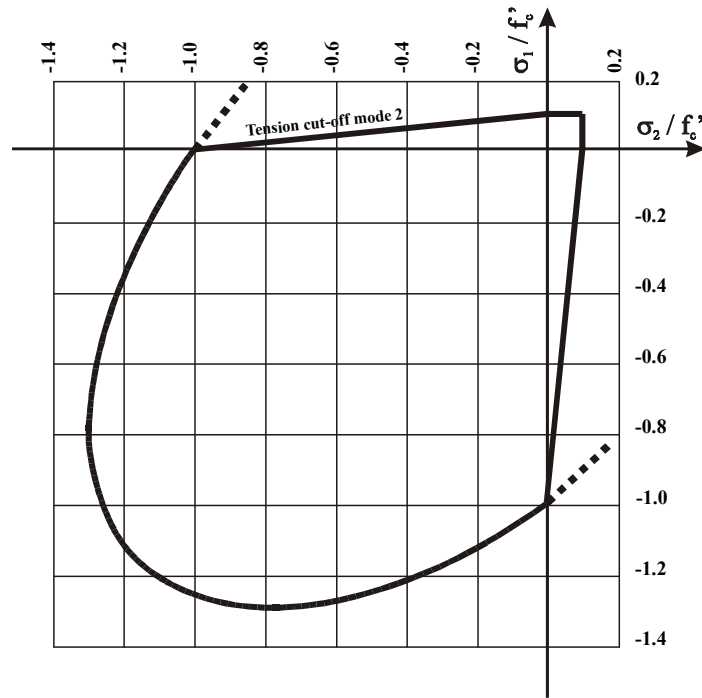
Figure 5.5 Drucker-Prager Biaxial Failure Envelope With Tension Cut-Off

(a)

(b)
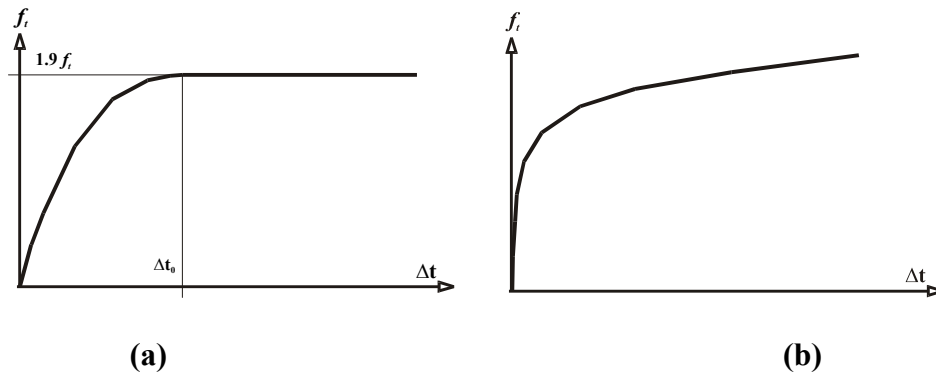
Figure 5.6 Shear-Traction Relationship Models (a) Dörr's Model (b) Noakowski Model
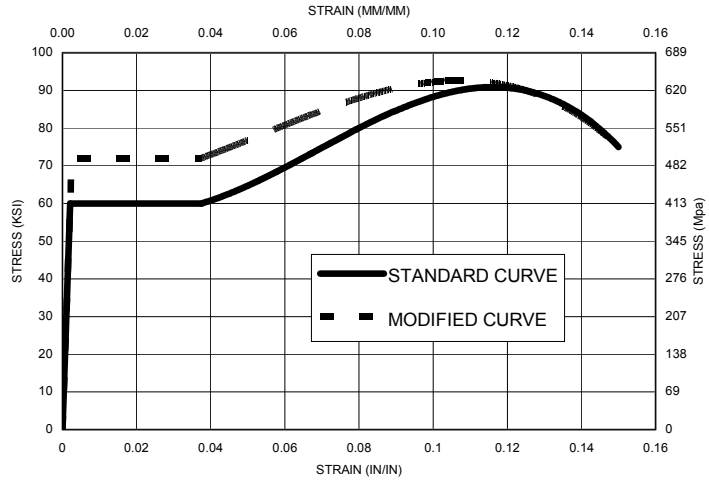
Figure 5.7 Stress-Strain Curve for Steel Including Strain Rate Effect

(a)

(b) Snap Through   **(c) Snap Back**
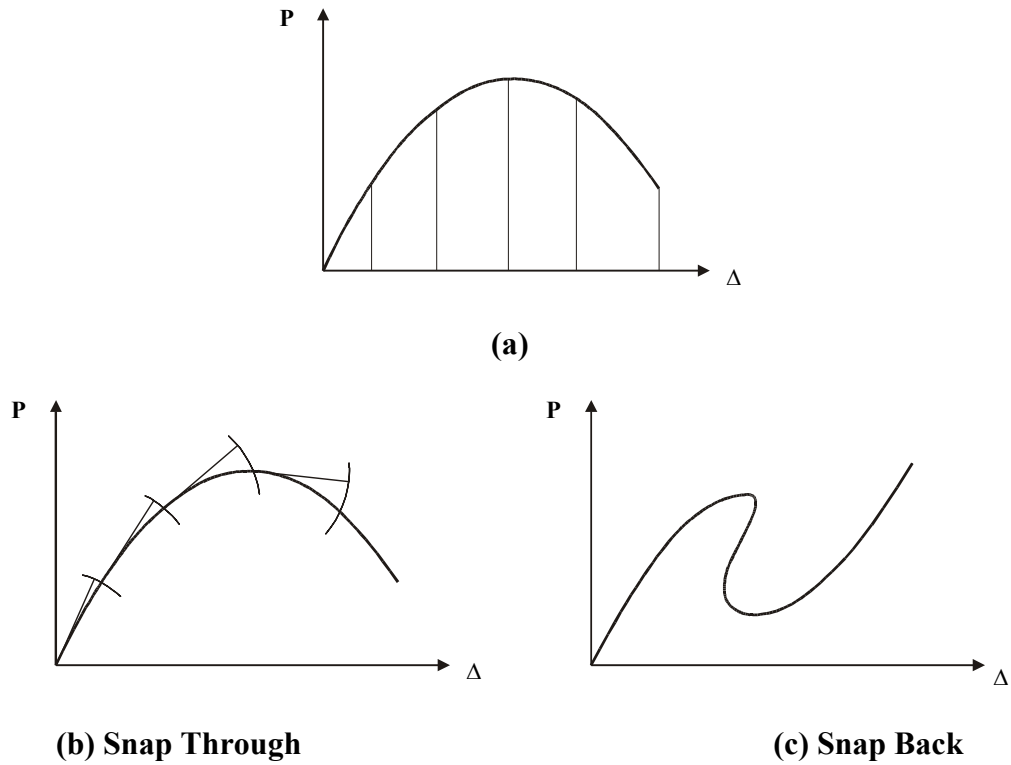
**Figure 5.8 Solver Technique (a) Displacement Controlled (b) Snap Through
Arc-Length Method (c) Snap Back Arc-Length Method**
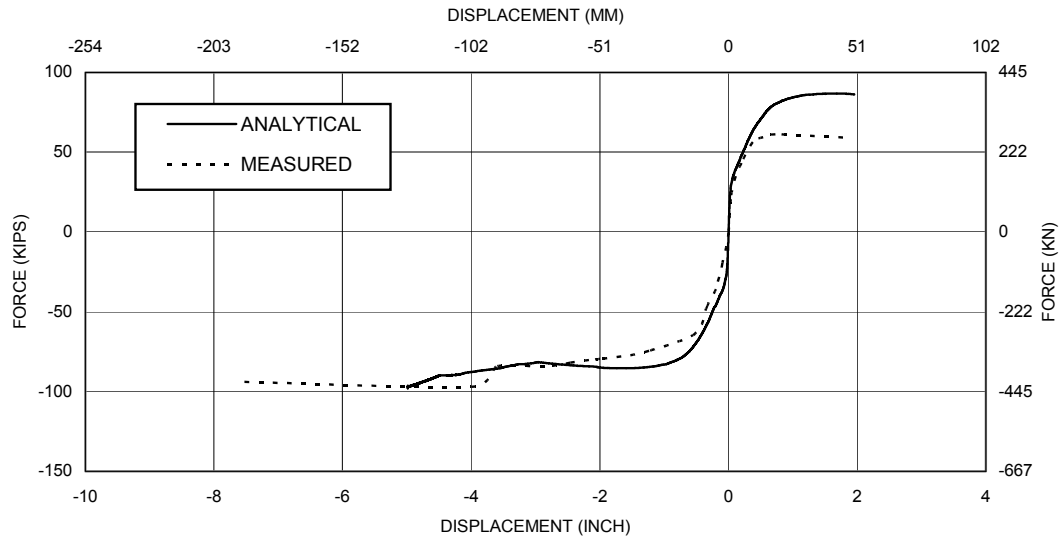
Figure 5.9 Comparison of Load-Displacement Curves from Analysis and Measured
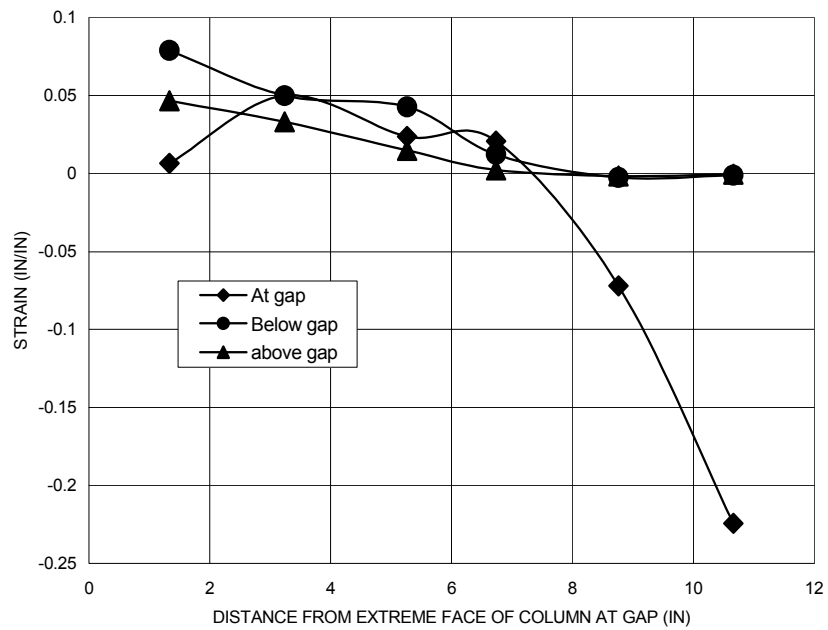
Figure 5.10 Strains in the Column Longitudinal Reinforcement at the Gap Just Prior to Gap Closure from Finite Element Analysis
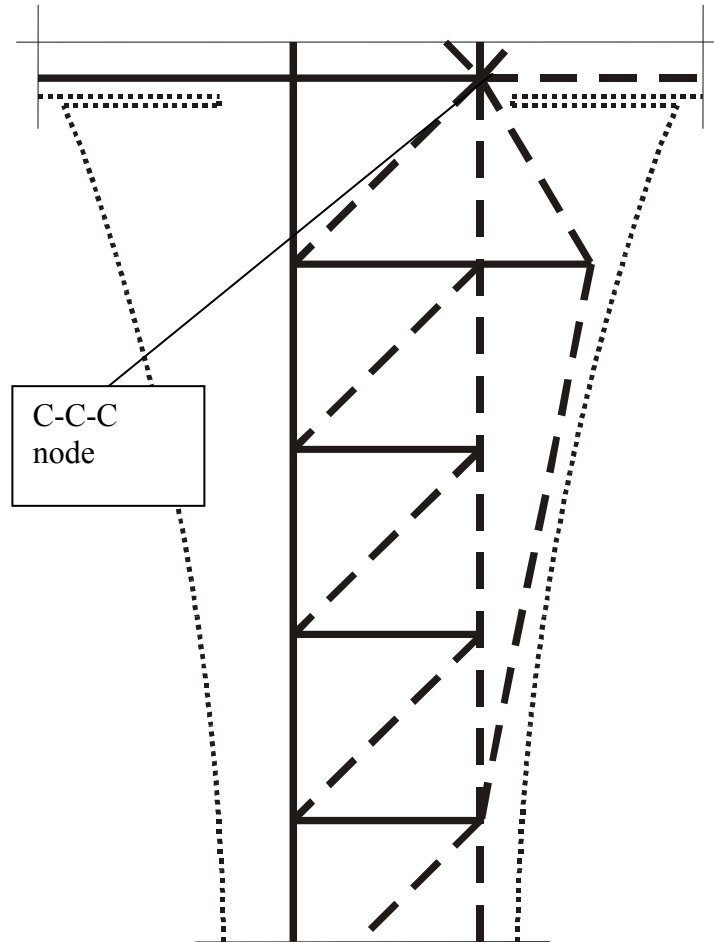
Figure 5.11 Stress Concentration in the Gap Region in Strut and Tie Model
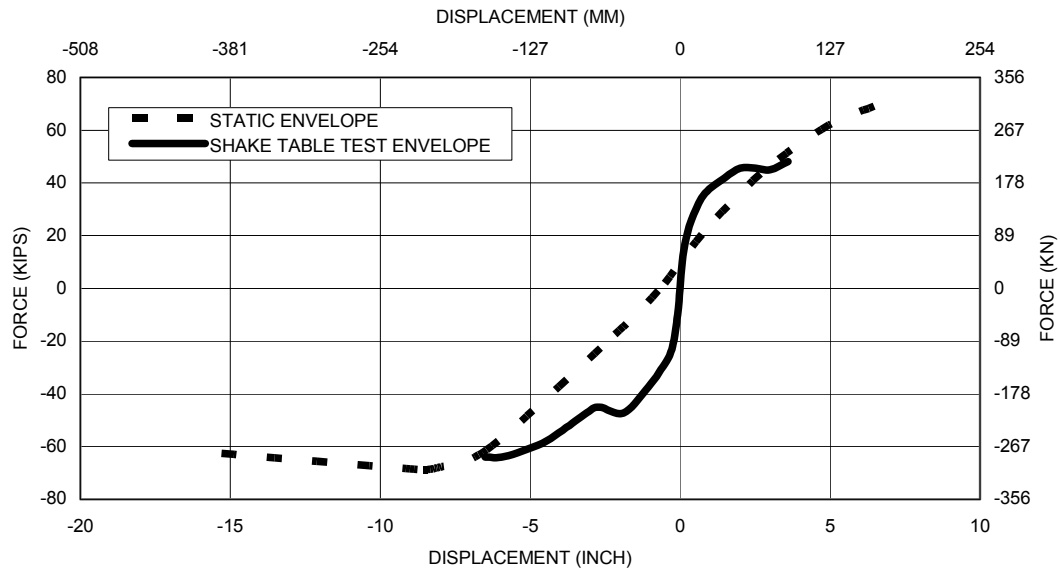
Figure 5.12 Load-Displacement Relationship for LFCD1 and LFCD1S
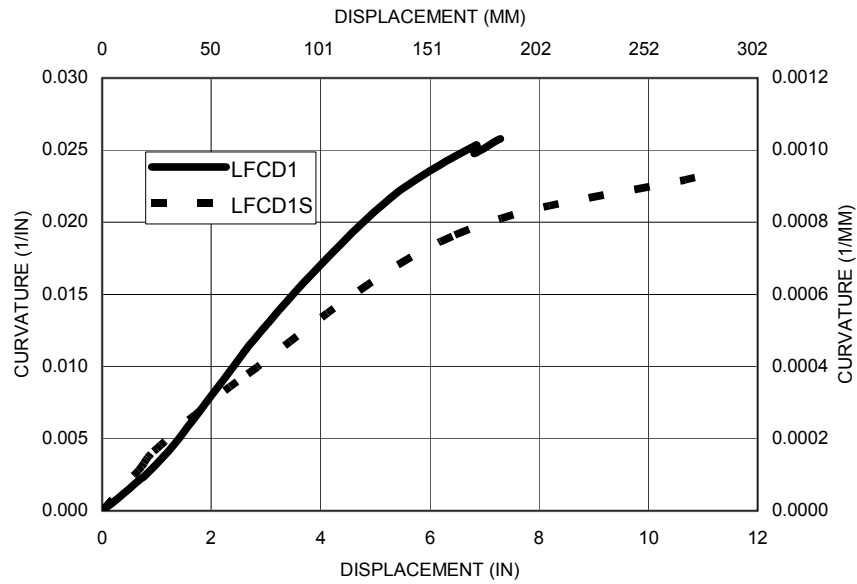
Figure 5.13 Comparison of Curvature at the Top of East Column in LFCD1 and North Column in LFCD1S

181
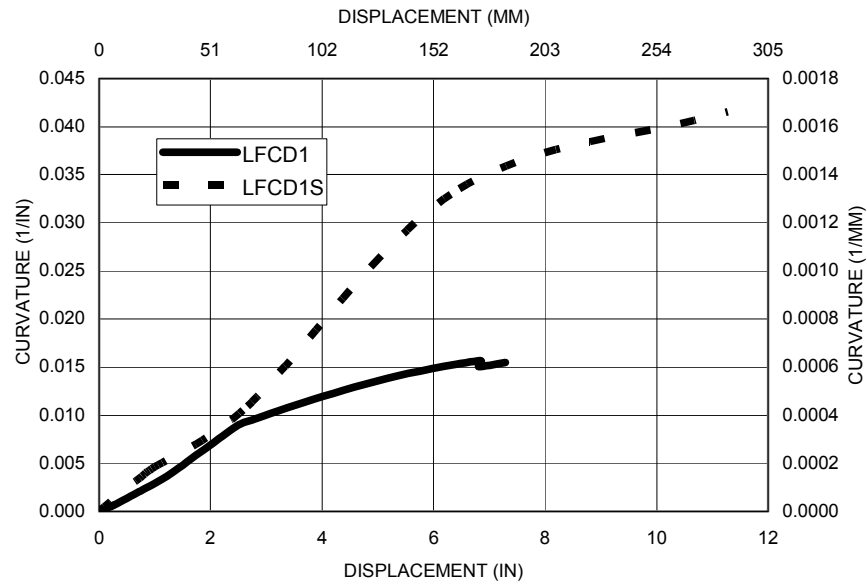
Figure 5.14 Comparison of Curvature at the Top of West Column in LFCD1 and South Column in LFCD1S
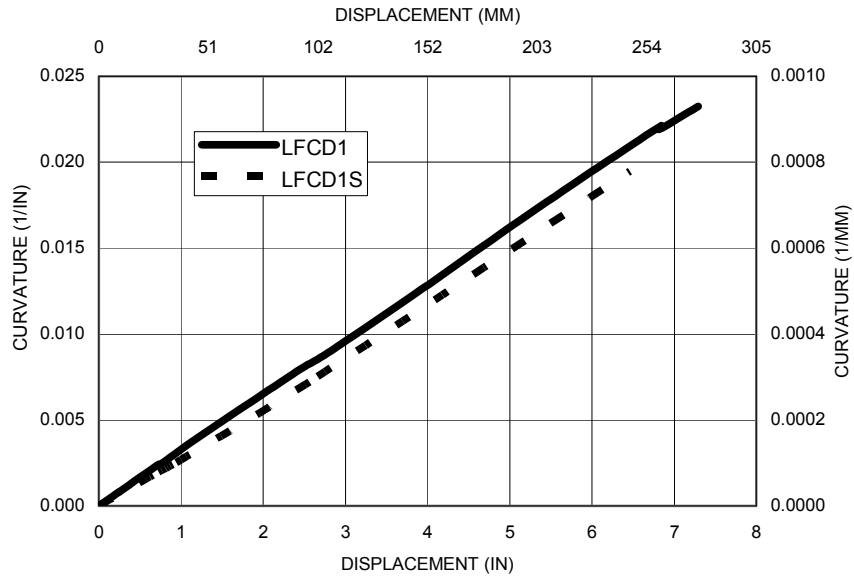
Figure 5.15 Comparison of Curvature at the Base-Hinge of East Column in LFCD1 and North Column in LFCD1S
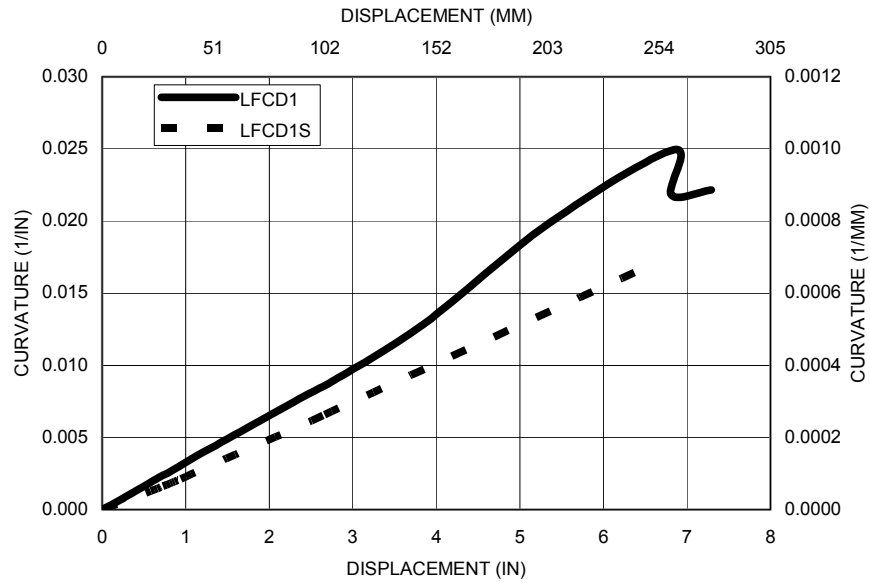
Figure 5.16 Comparison of Curvature at the Base-Hinge of West Column in LFCD1 and South Column in LFCD1S
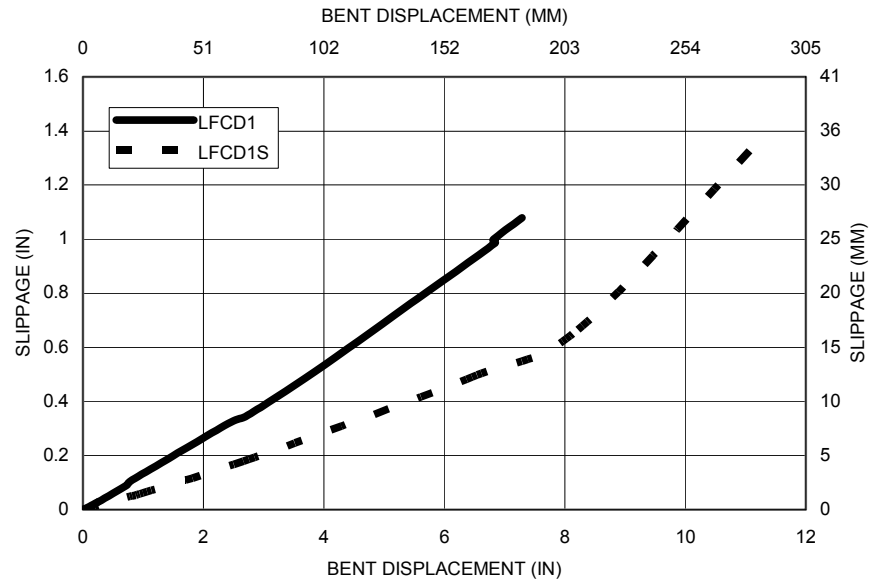
Figure 5.17 Comparison of Base-Hinge Slippage in LFCD1 South Column and LFCD1S West Column
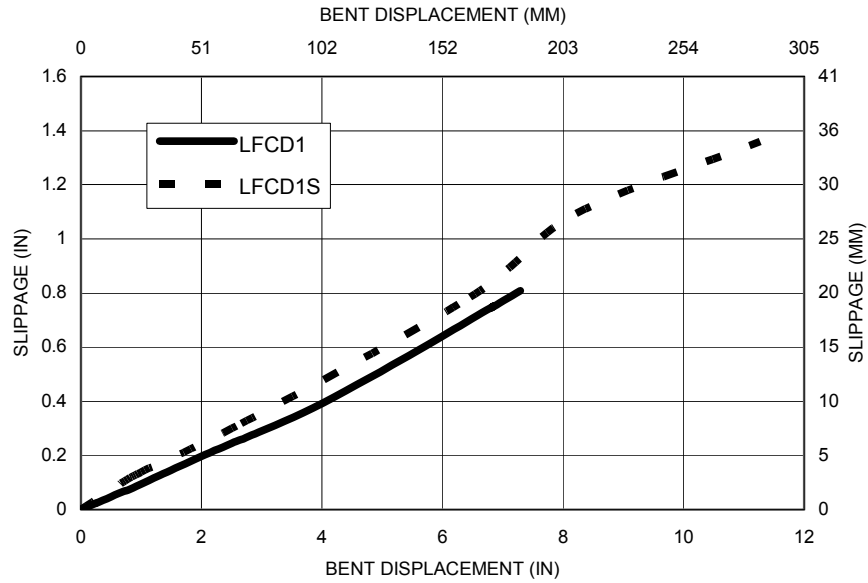
Figure 5.18 Comparison of Base-Hinge Slippage in LFCD1 North Column and LFCD1S East Column
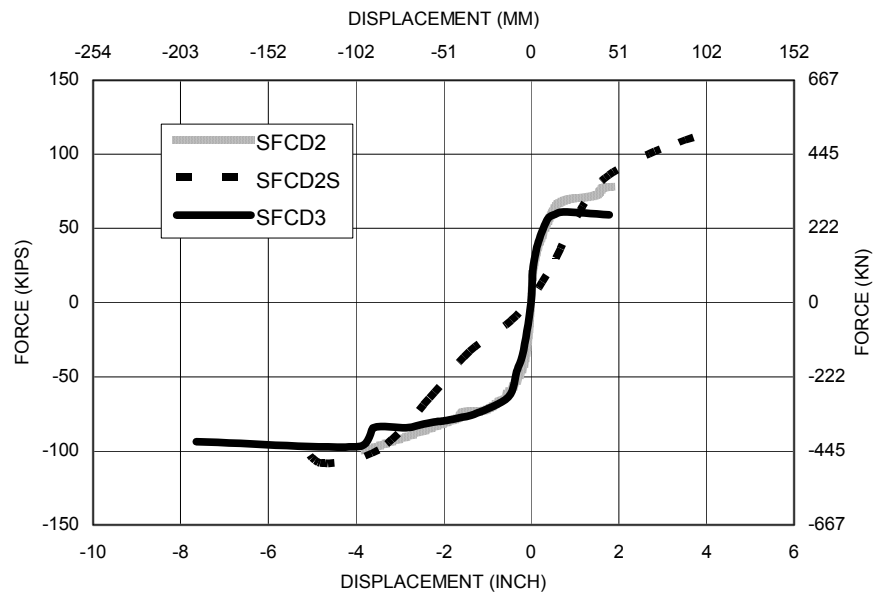
Figure 5.19 Load-Displacement Envelopes for SFCD2, SFCD2S and SFCD3

184
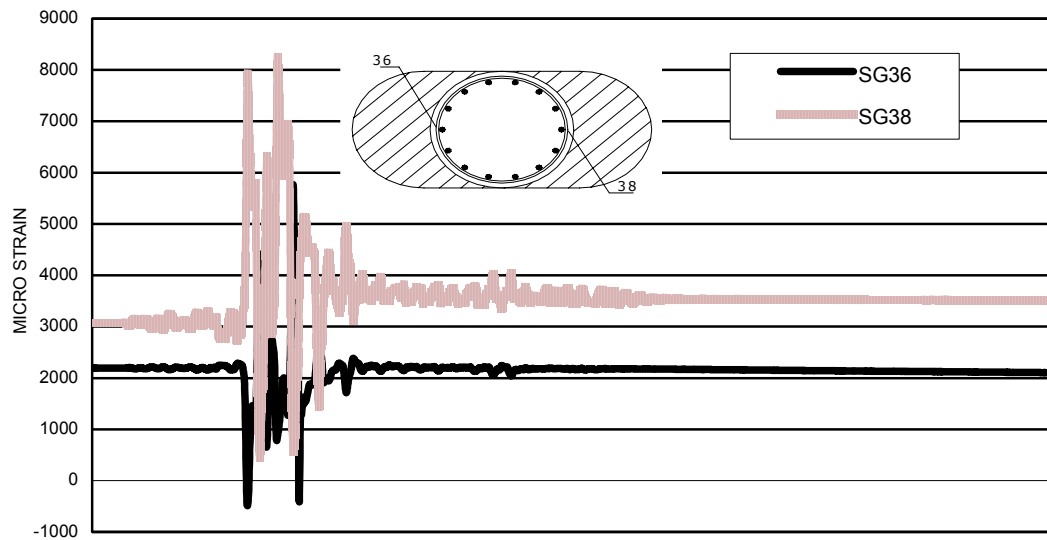
Figure 5.20 Strain History of SG36 and SG38 for SFCD3 and 2.75 Sylmar
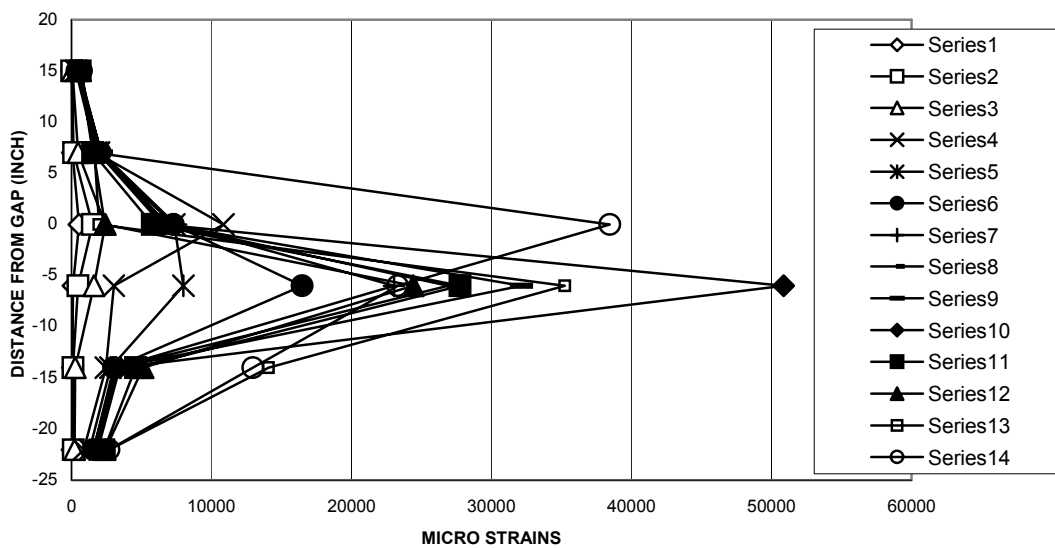
Figure 5.21 Maximum Strains in Column Longitudinal Reinforcement

(South Column Extreme Left Reinforcement)
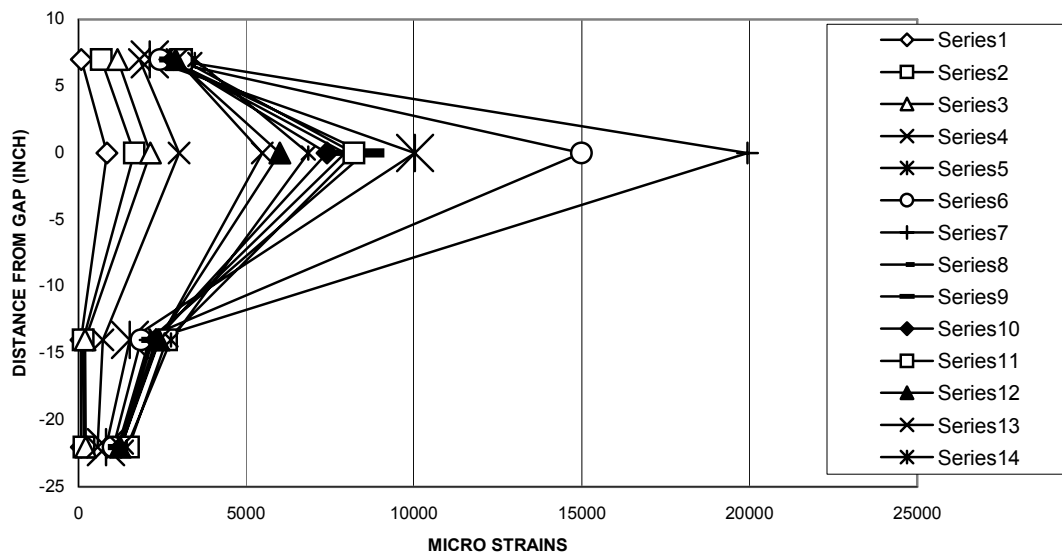
Figure 5.22 Maximum Strains in Column Longitudinal Reinforcement

(South Column Extreme Right Reinforcement)
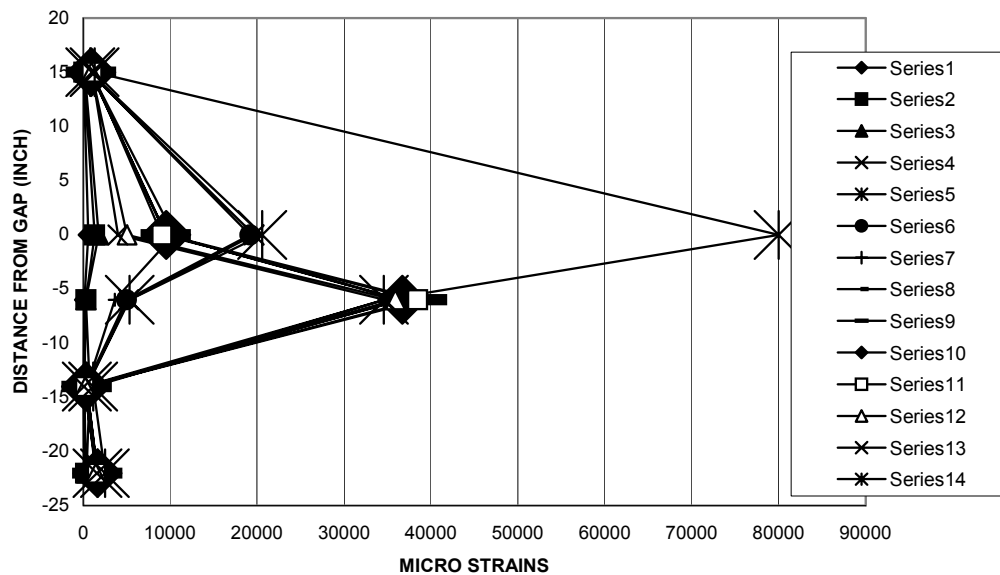
Figure 5.23 Maximum Strains in Column Longitudinal Reinforcement

(North Column Extreme Left Reinforcement)
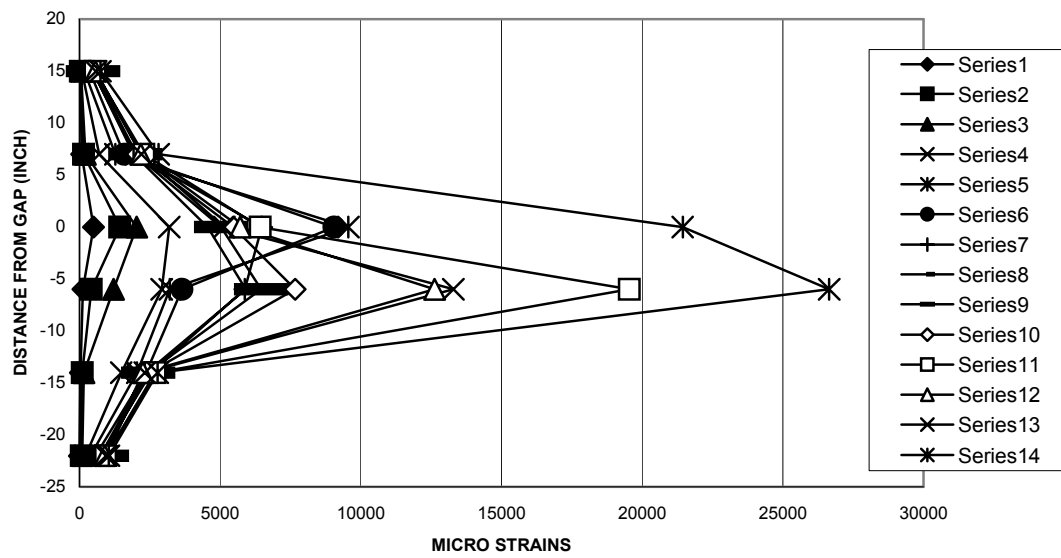
Figure 5.24 Maximum Strains in Column Longitudinal Reinforcement

(North Column Extreme Right Reinforcement)
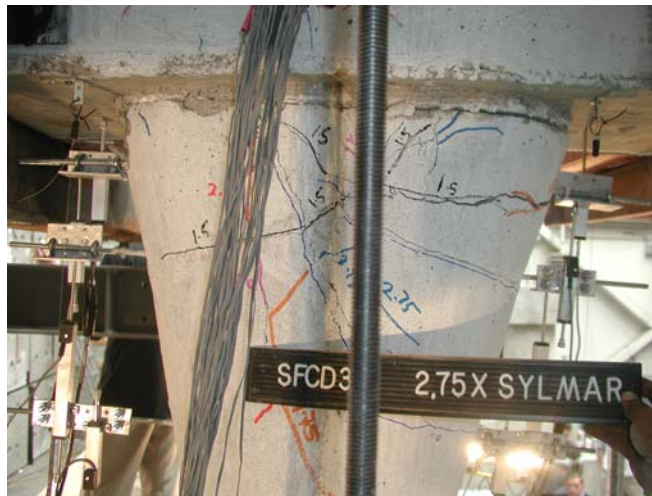
Figure 5.25 Cracking Inside the Gap After 2.75 Times Sylmar
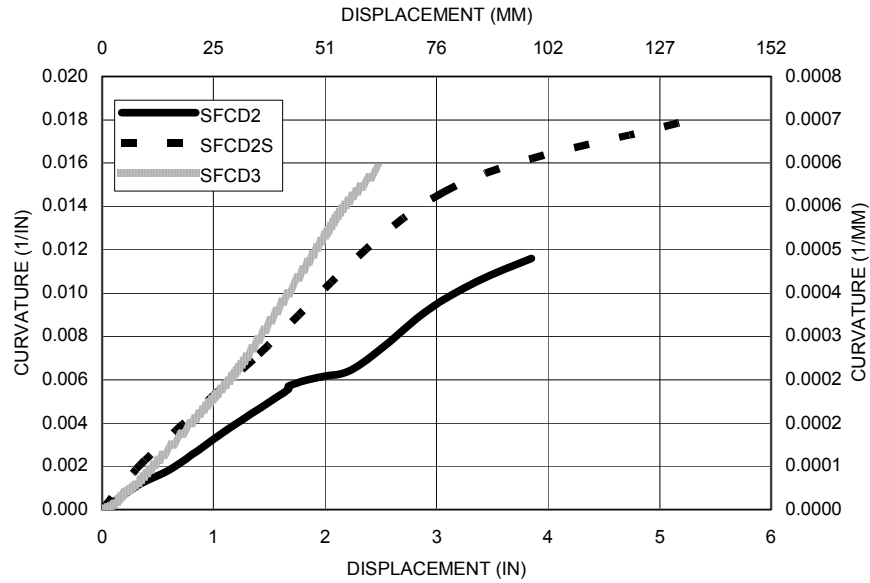
Figure 5.26 Comparison of Curvature at the Top of East Column in SFCD2 and North Column in SFCD2S, SFCD3
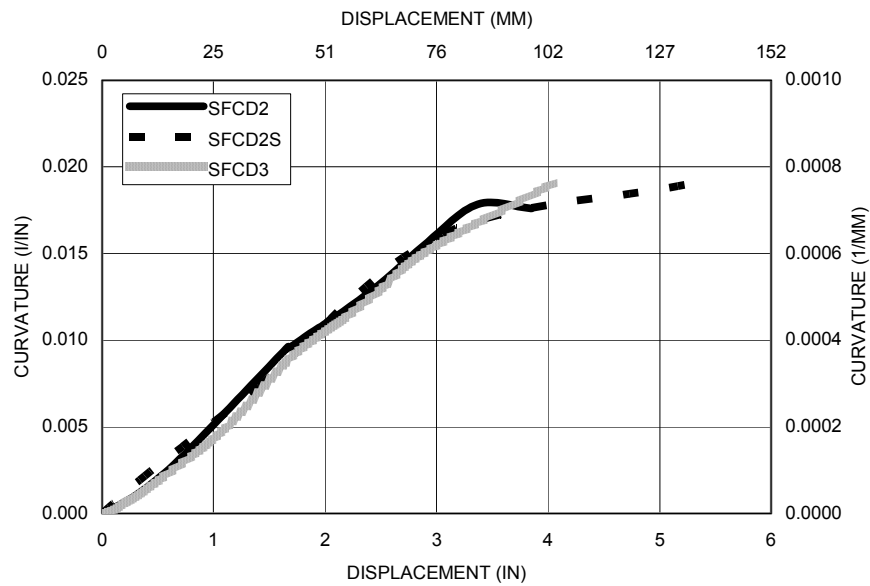
Figure 5.27 Comparison of Curvature at the Top of West Column in SFCD2 and South Column in SFCD2S, SFCD3
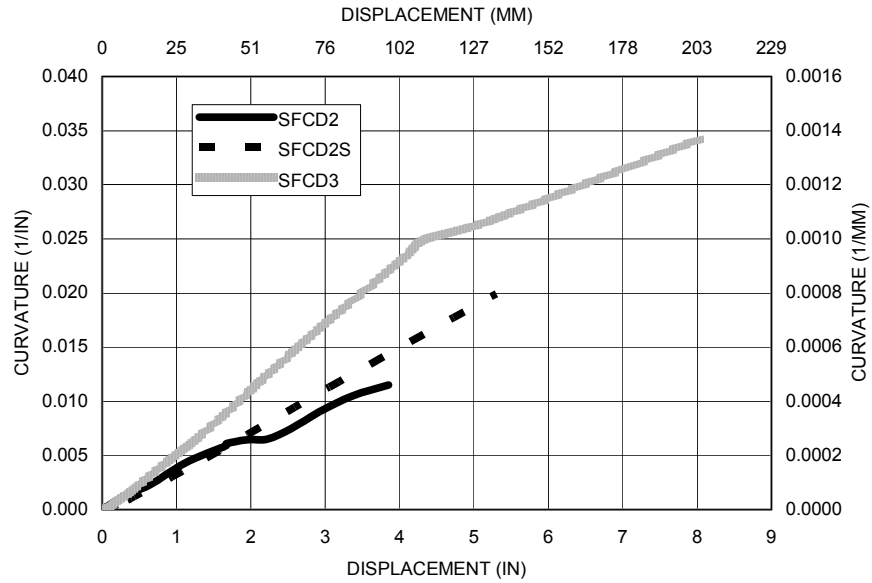
Figure 5.28 Comparison of Curvature at the Base-Hinge of East Column in SFCD2 and North Column in SFCD2S, SFCD3
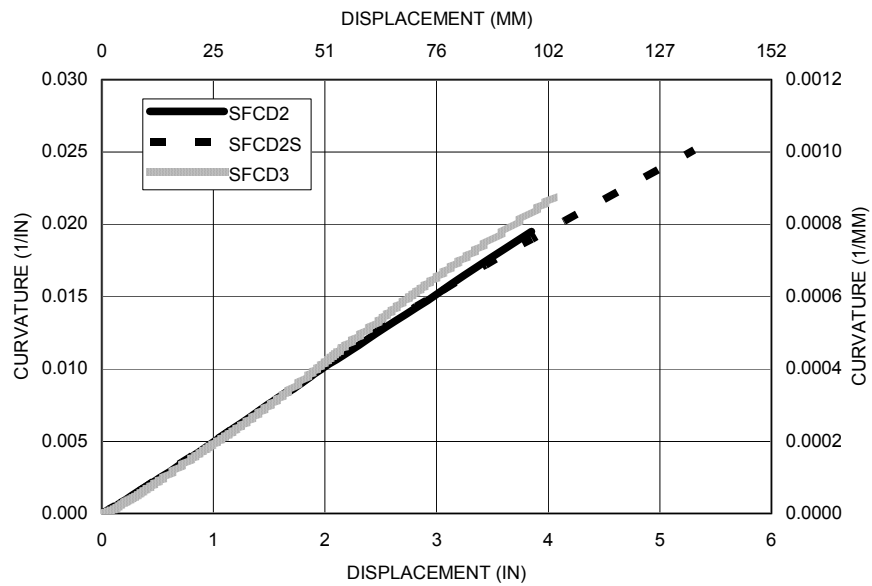
Figure 5.29 Comparison of Curvature at the Base-Hinge of West Column in SFCD2 and South Column in SFCD2S, SFCD3
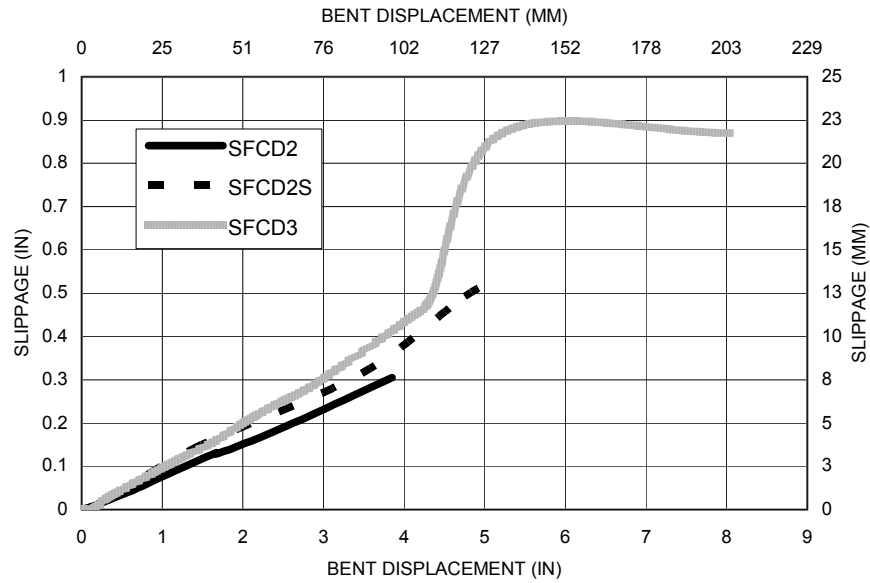
Figure 5.30 Comparison of Base-Hinge Slippage for East Column SFCD2, North Columns for SFCD2S and SFCD3
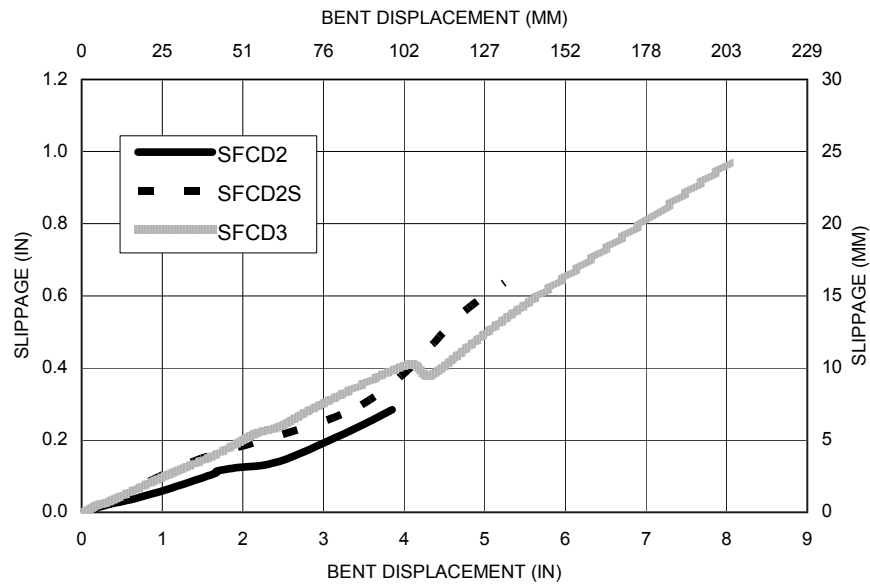
Figure 5.31 Comparison of Base-Hinge Slippage for West Column SFCD2, South Columns for SFCD2S and SFCD3
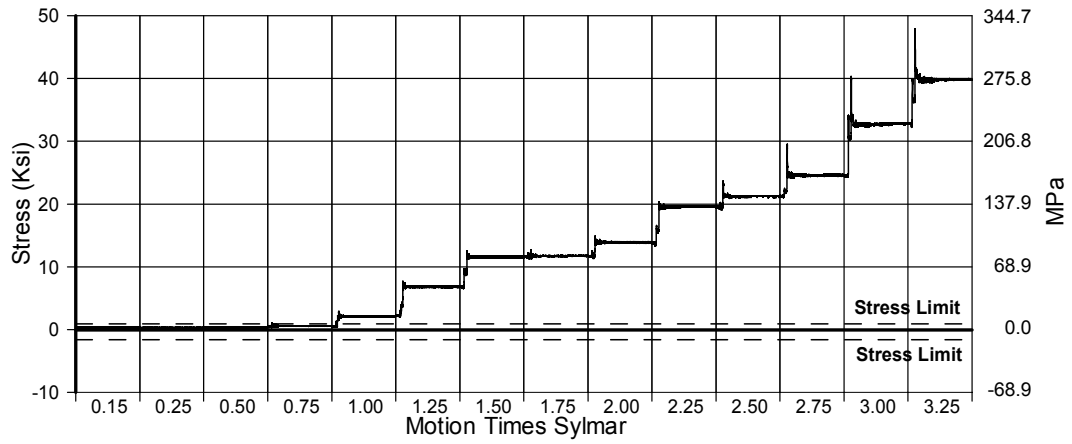
Figure 5.32 Principal Stress (σ_1) in East Beam-Column Connection for SFCD2 (Nada et al)
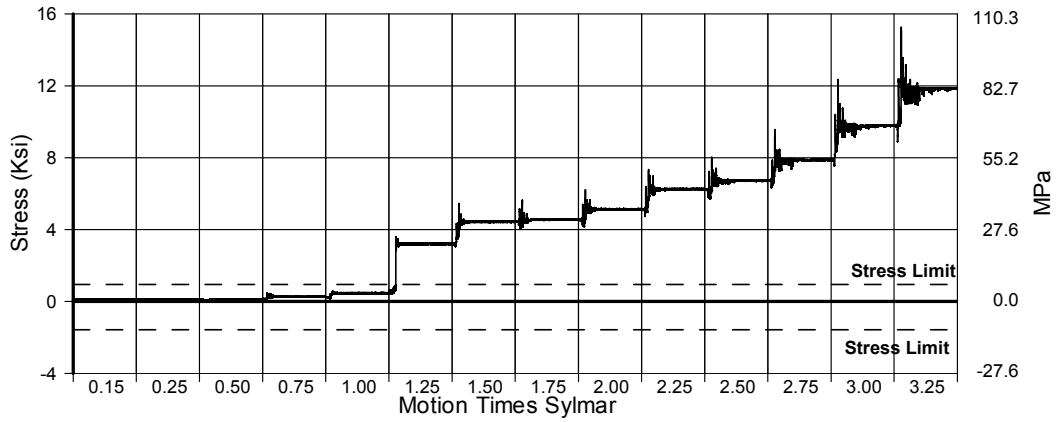
Figure 5.33 Principal Stress (σ_2) in East Beam-Column Connection for SFCD2 (Nada et al)
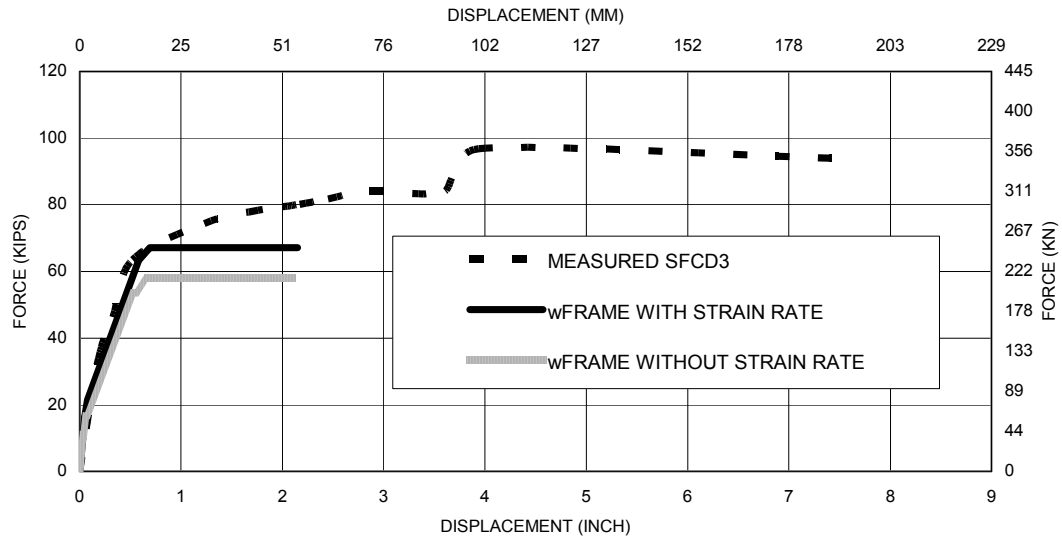
Figure 5.34 Comparison of Load-Displacement Curve Between Measured and Predicted by wFRAME for SFCD3

APPENDIX

Note: All graphs have time as the horizontal axis. The loading levels are given in sections 3.2, 4.2.1 and 4.3.1 for SFCD3, LFCD1S and SFCD2S, respectively.
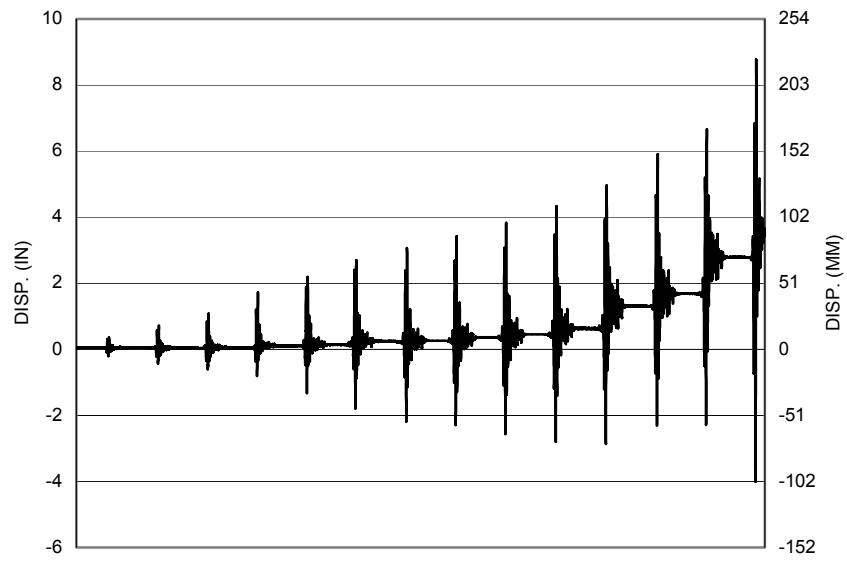
Figure A-1 Absolute Bent Displacement in SFCD3
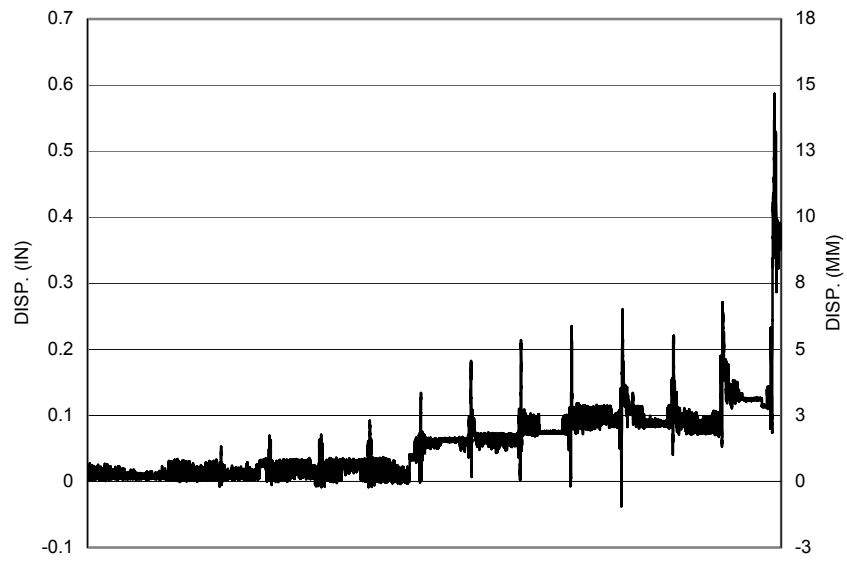
Figure A-2 Absolute Transverse Bent Displacement in SFCD3

194
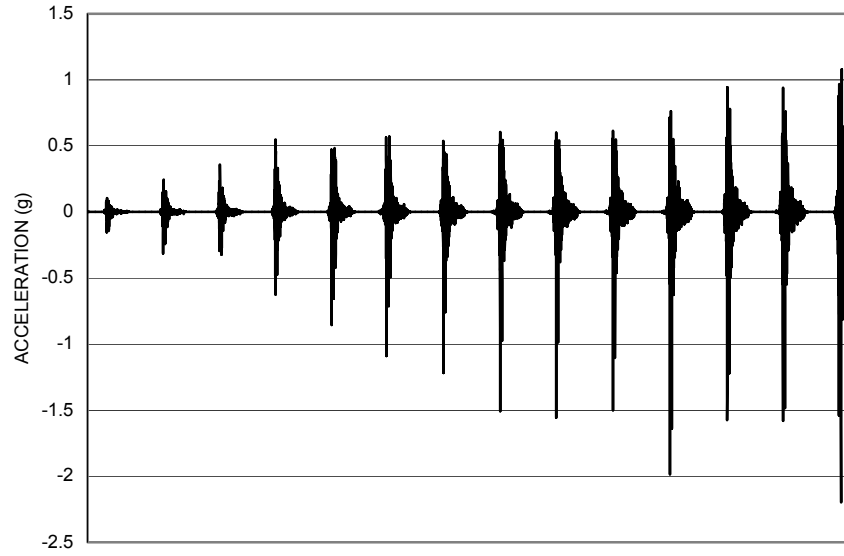
Figure A-3 Measured Table Acceleration for SFCD3
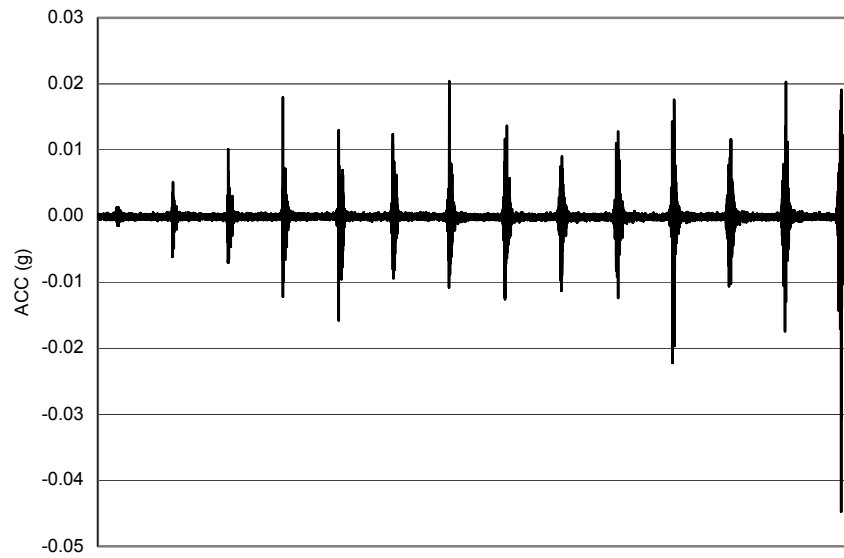
Figure A-4 Measured Transverse Table Acceleration for SFCD3
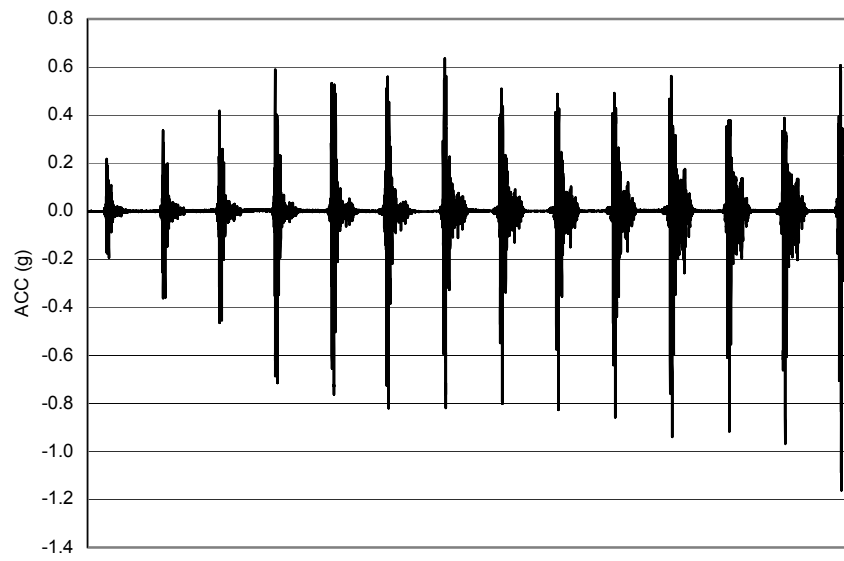
Figure A-5 Measured Lead Bucket Acceleration for SFCD3
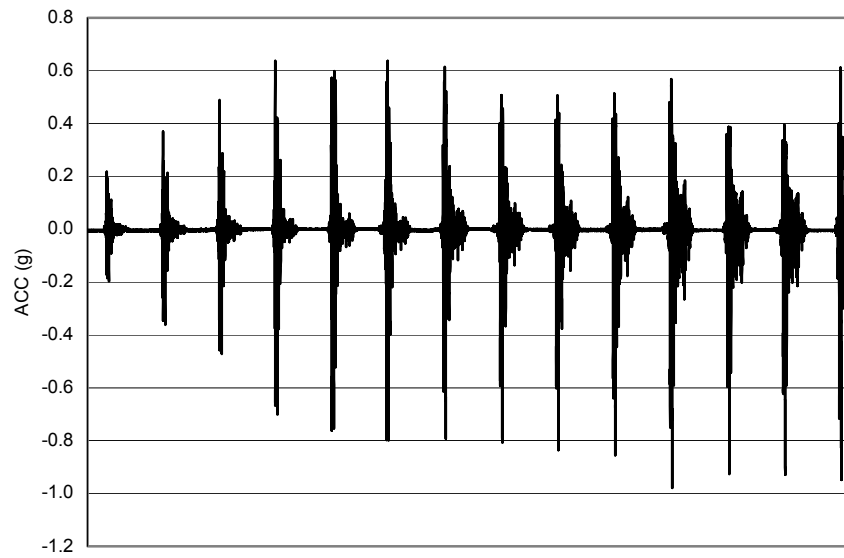
Figure A-6 Measured Bent Acceleration for SFCD3
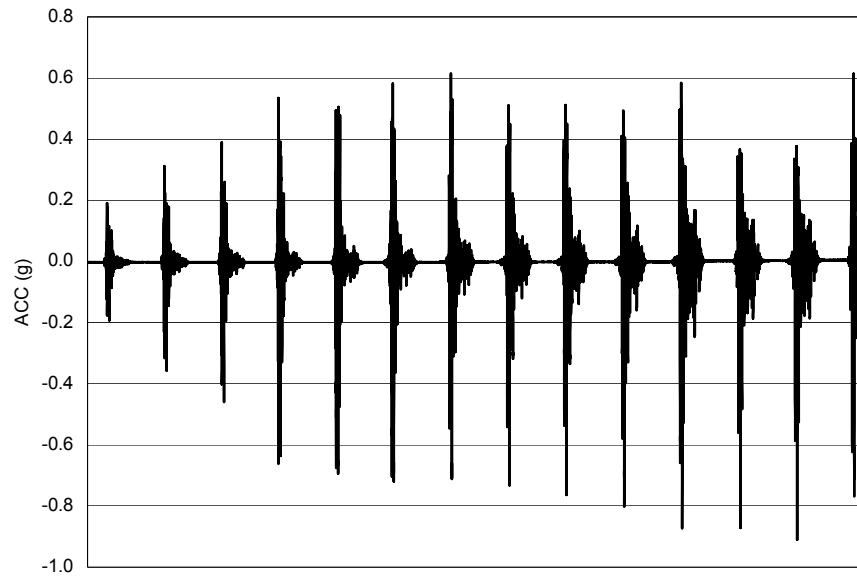
Figure A-7 Measured Link Acceleration for SFCD3
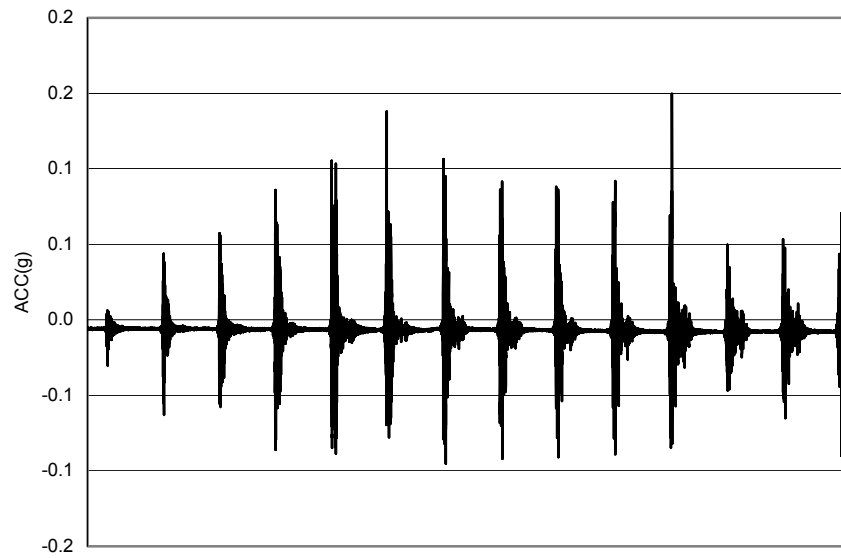
Figure A-8 Measured Transverse Bent Acceleration for SFCD3
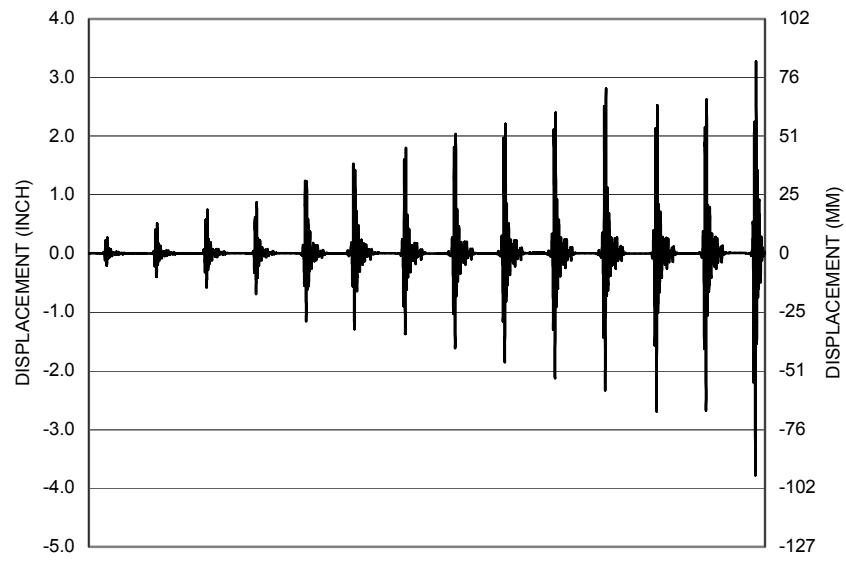
Figure A-9 Measured Table Displacement for SFCD3
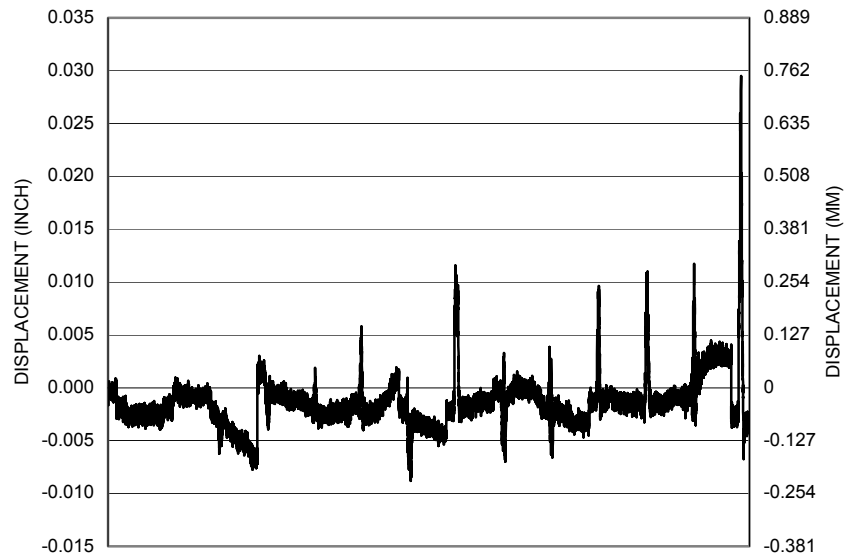
Figure A-10 Measured Table Transverse Displacement for SFCD3
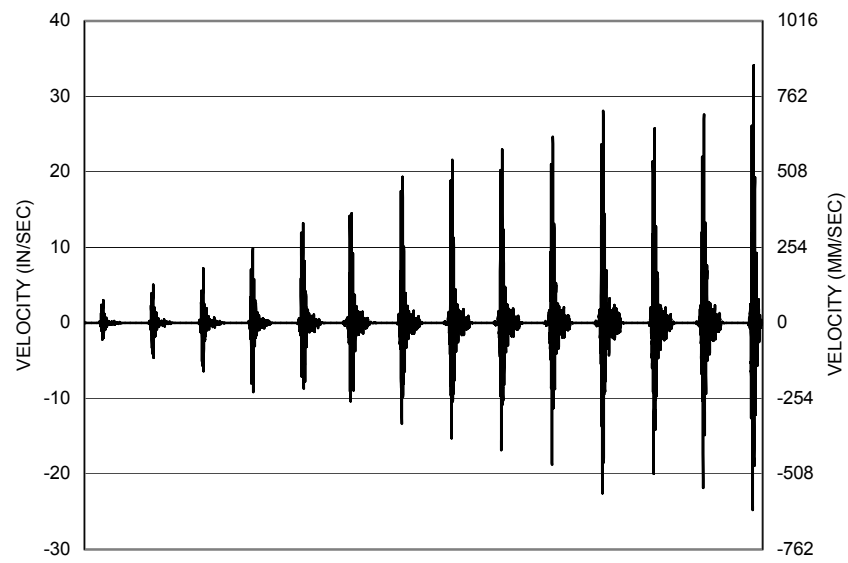
Figure A-11 Measured Table Velocity for SFCD3
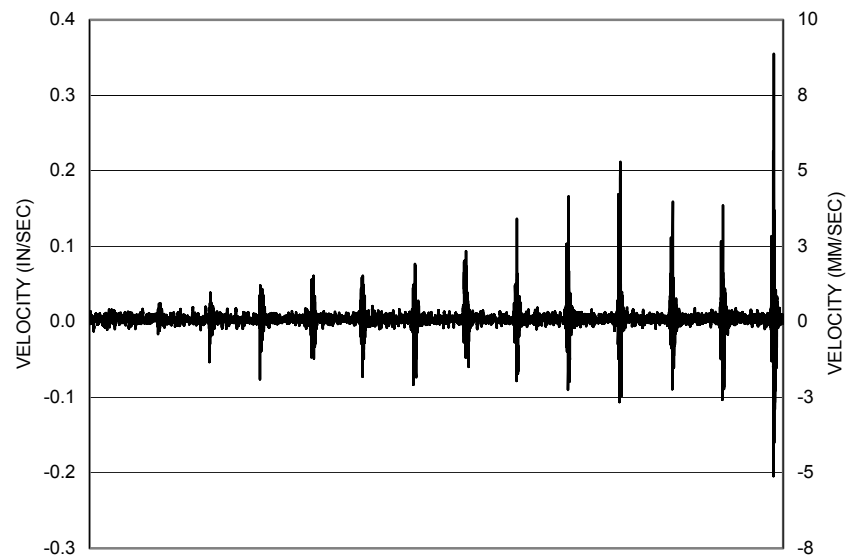
Figure A-12 Measured Table Transverse Velocity for SFCD3
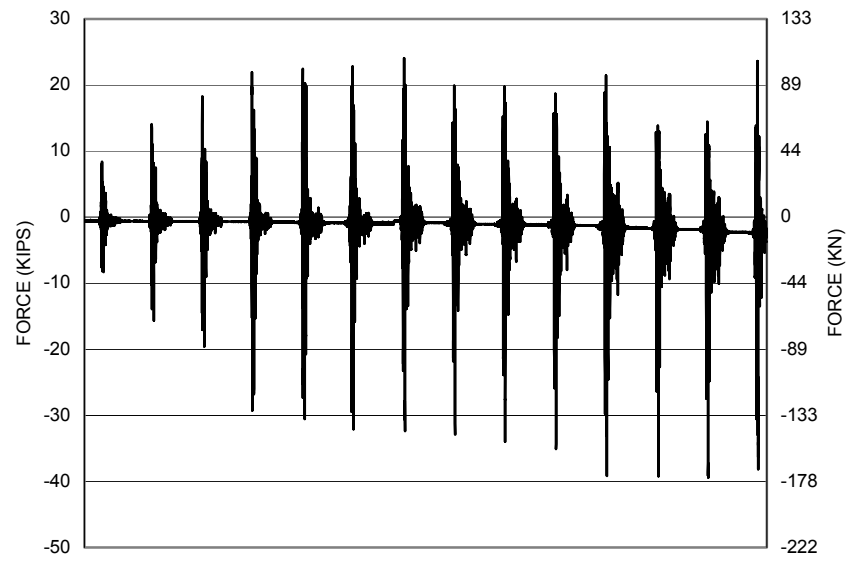
Figure A-13 Measured Load in Rigid Link for SFCD3
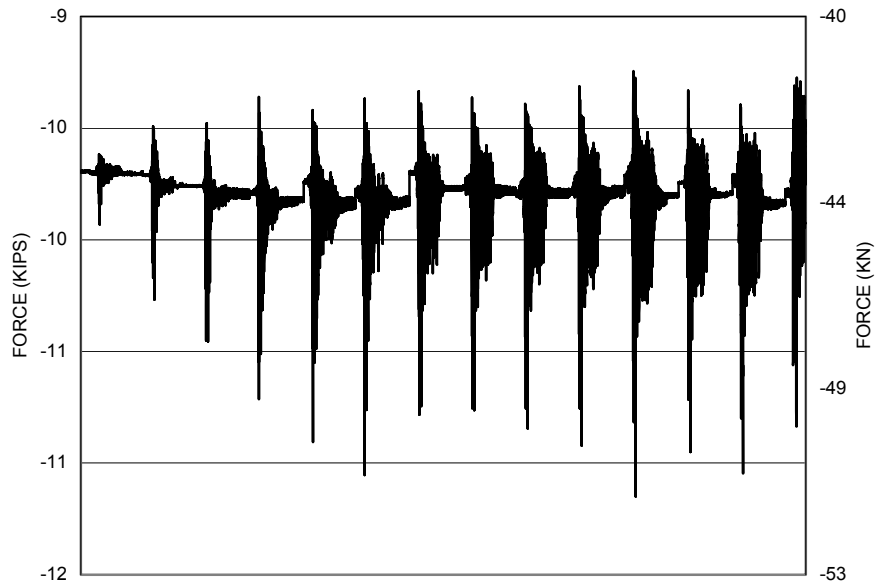
Figure A-14 Measured Load in North Axial Ram for SFCD3
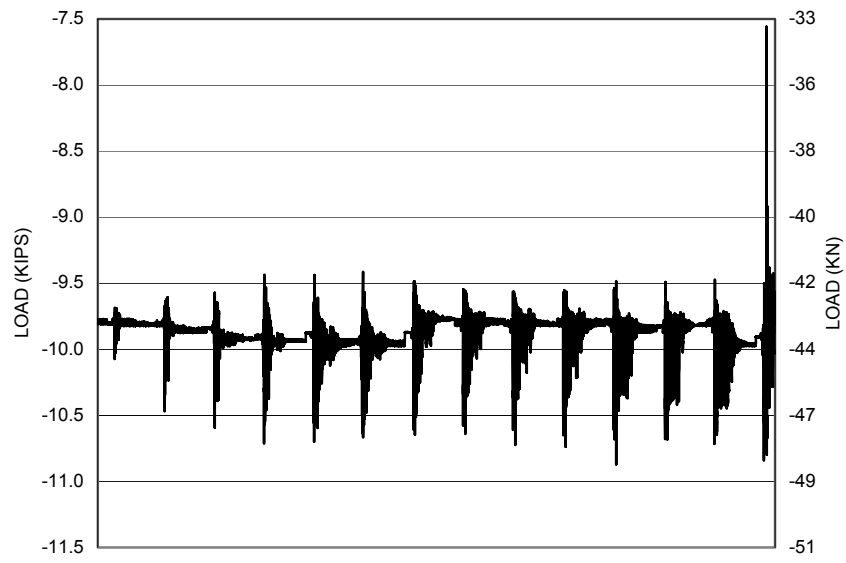
Figure A-15 Measured Load in South Axial Ram for SFCD3
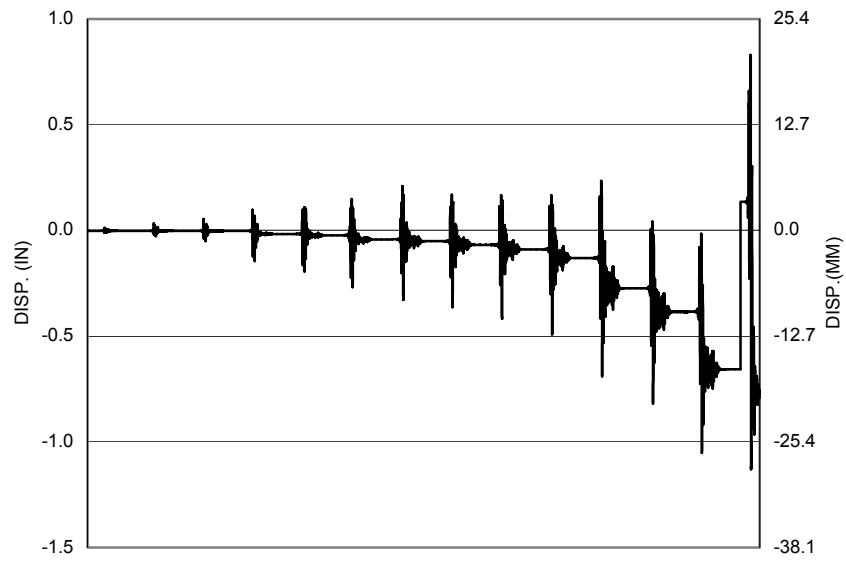
Figure A-16 Measured Displacement in NV1 for SFCD3
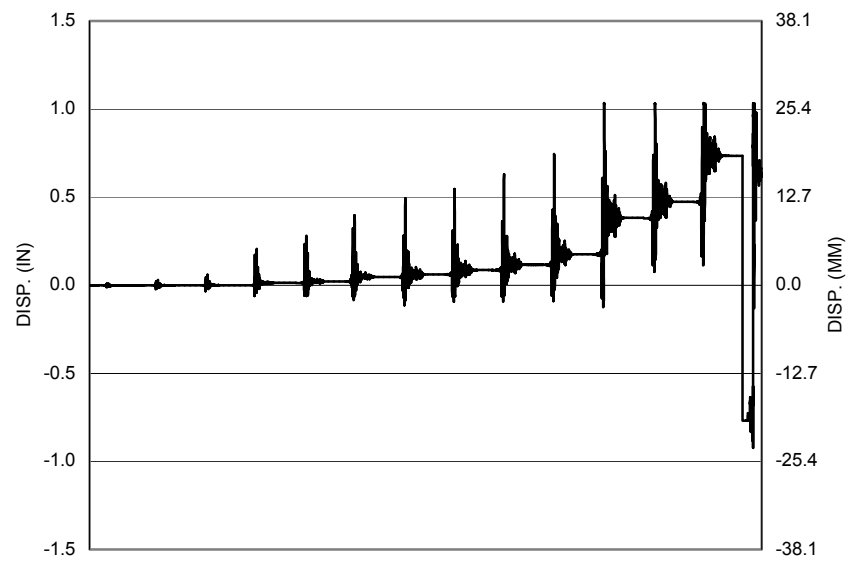
Figure A-17 Measured Displacement in NV2 for SFCD3
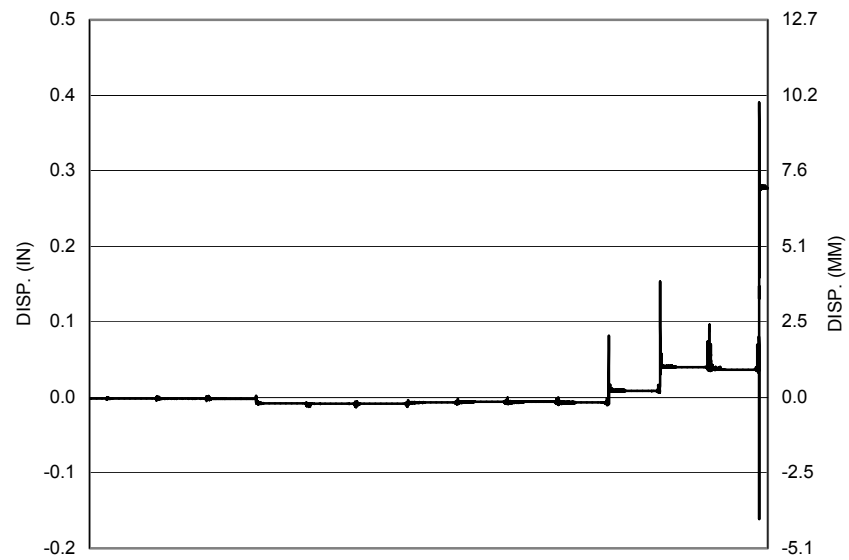
Figure A-18 Measured Displacement in NV3 for SFCD3
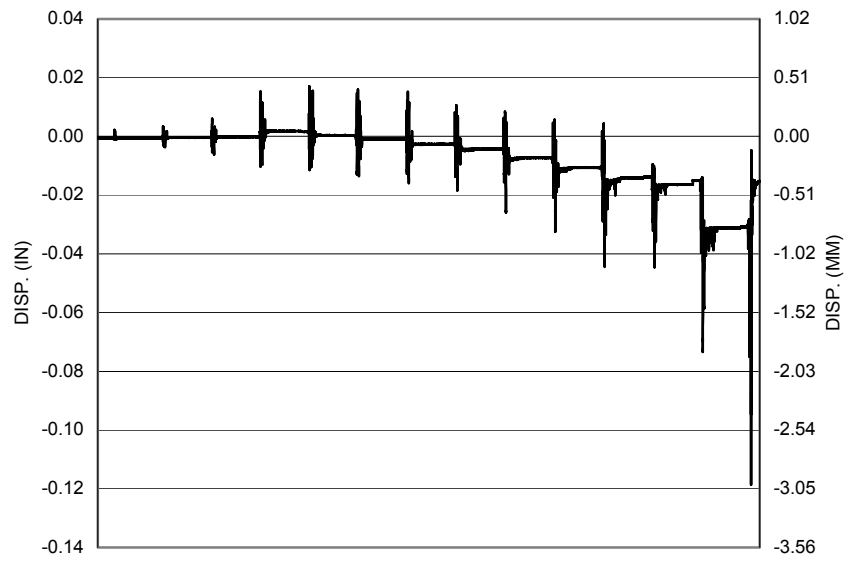
Figure A-19 Measured Displacement in NV4 for SFCD3
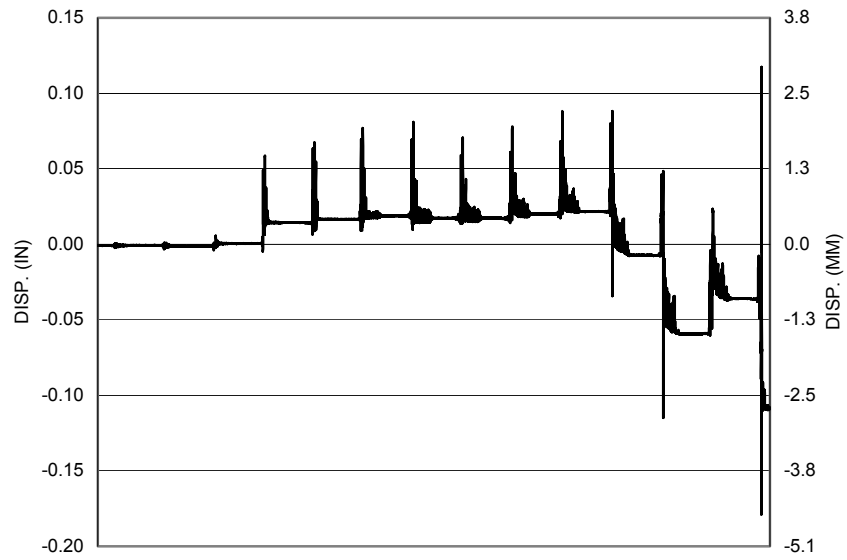
Figure A-20 Measured Displacement in NV5 for SFCD3
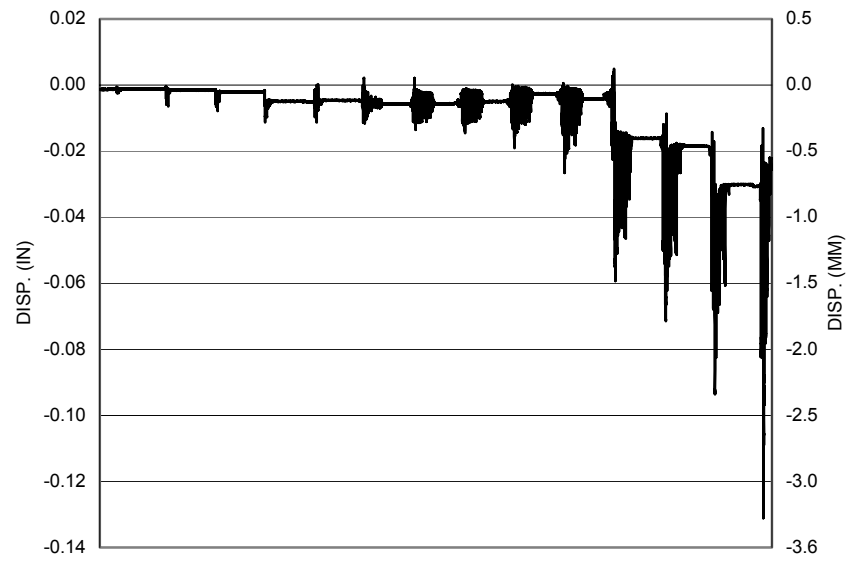
Figure A-21 Measured Displacement in NV6 for SFCD3
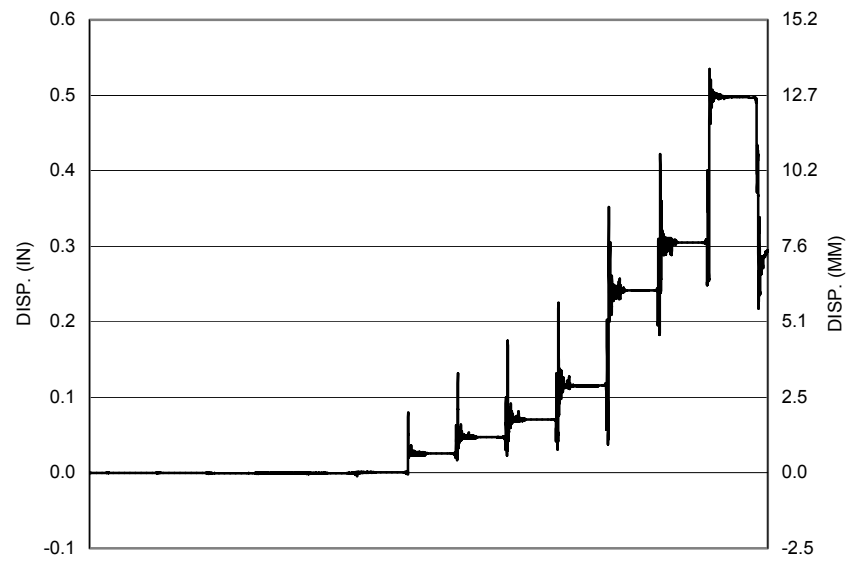
Figure A-22 Measured Displacement in NV7 for SFCD3
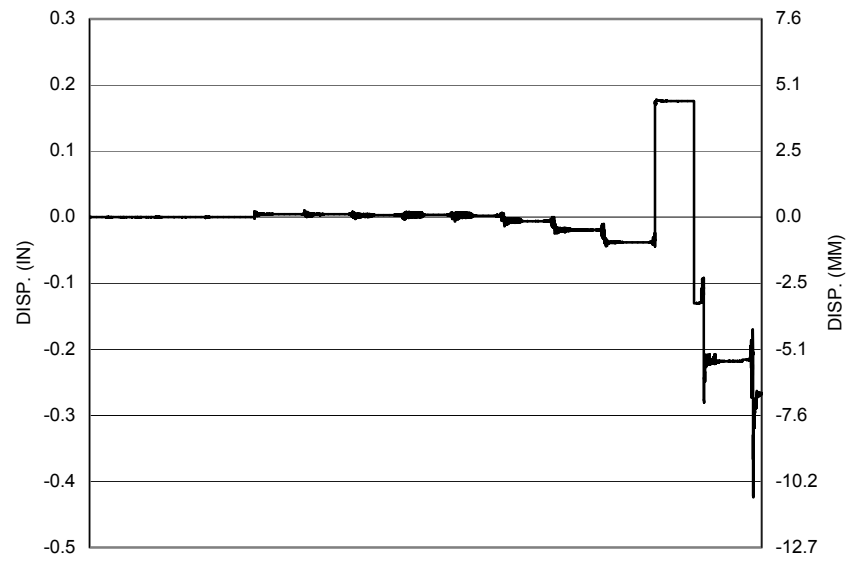
Figure A-23 Measured Displacement in NV8 for SFCD3
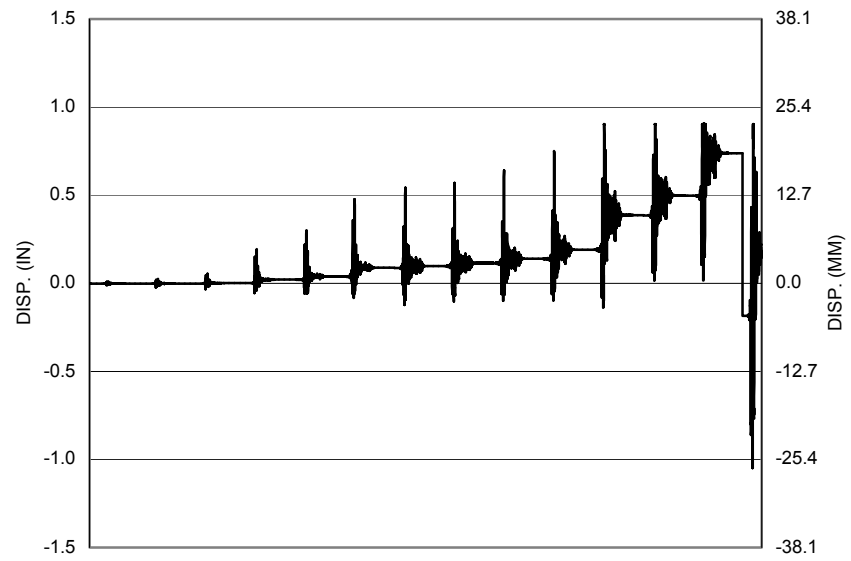
Figure A-24 Measured Displacement in NV9 for SFCD3
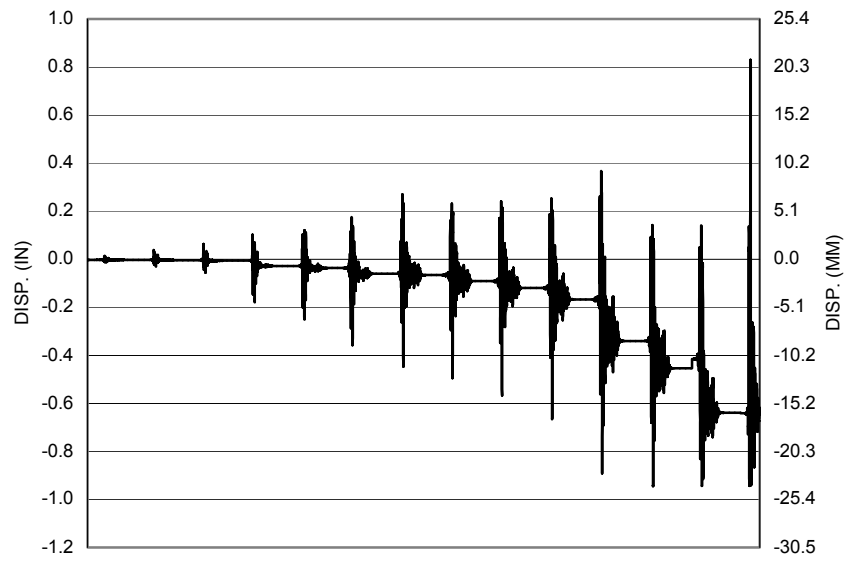
Figure A-25 Measured Displacement in NV10 for SFCD3
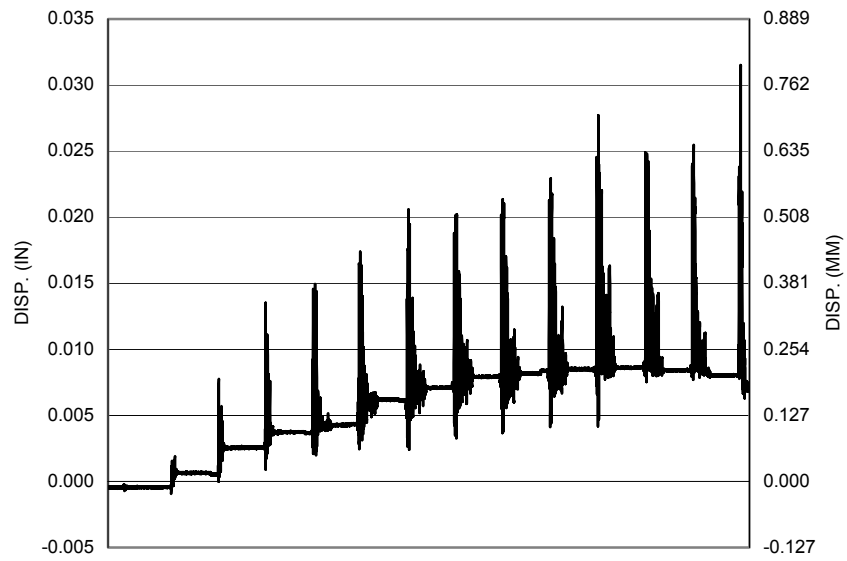
Figure A-26 Measured Displacement in NV11 for SFCD3
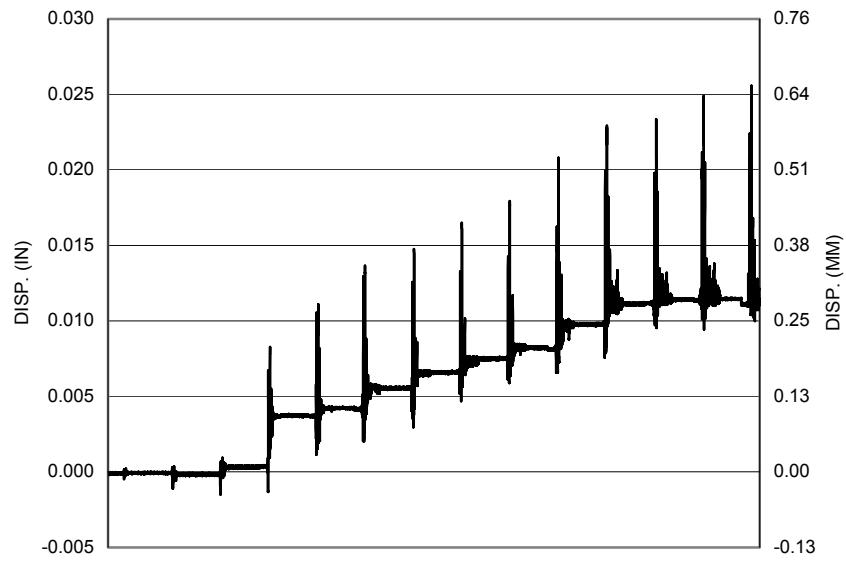
Figure A-27 Measured Displacement in NV12 for SFCD3
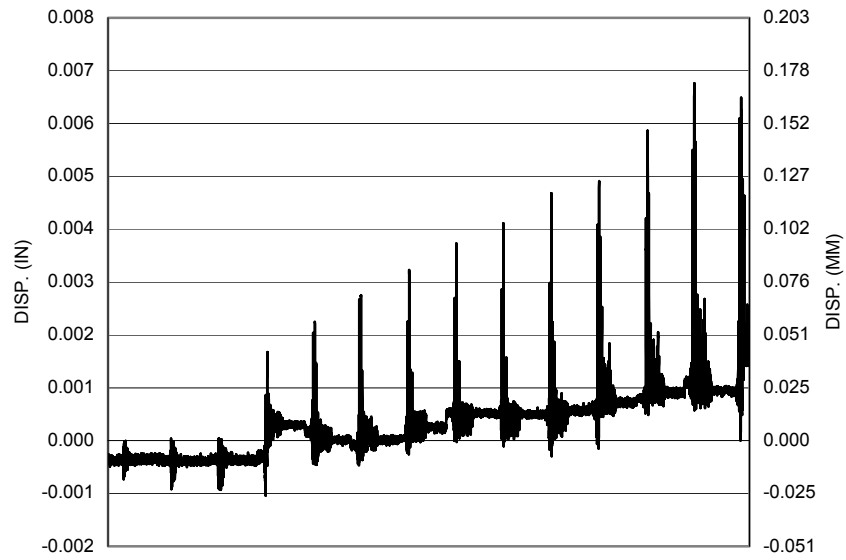
Figure A-28 Measured Displacement in NV13 for SFCD3

207
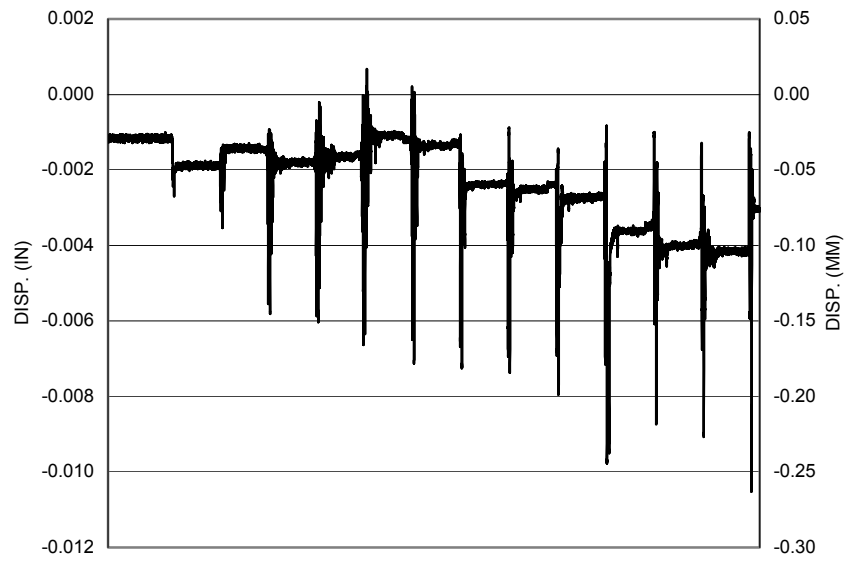
Figure A-29 Measured Displacement in NV14 for SFCD3
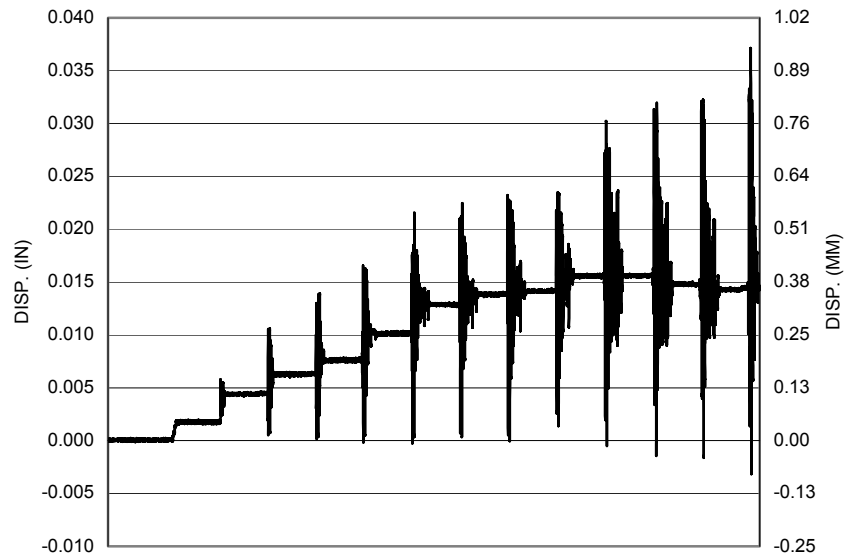
Figure A-30 Measured Displacement in NV15 for SFCD3
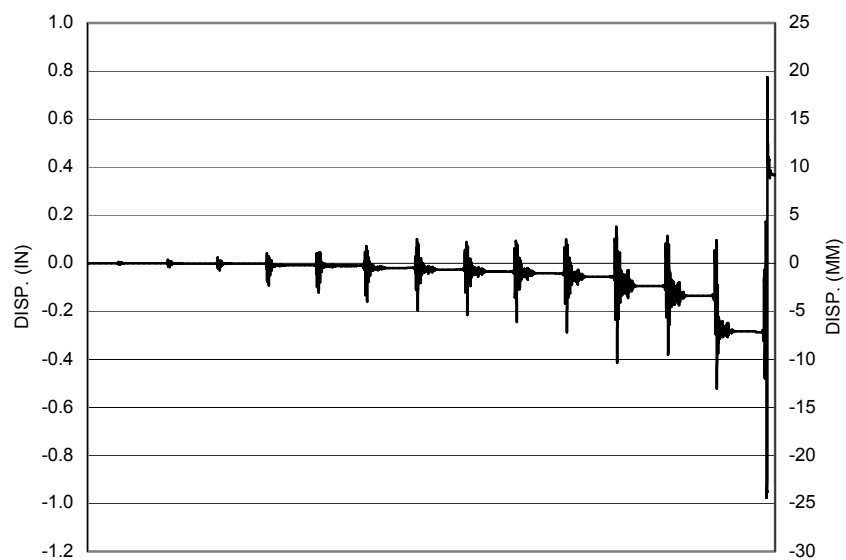
Figure A-31 Measured Displacement in NV16 for SFCD3
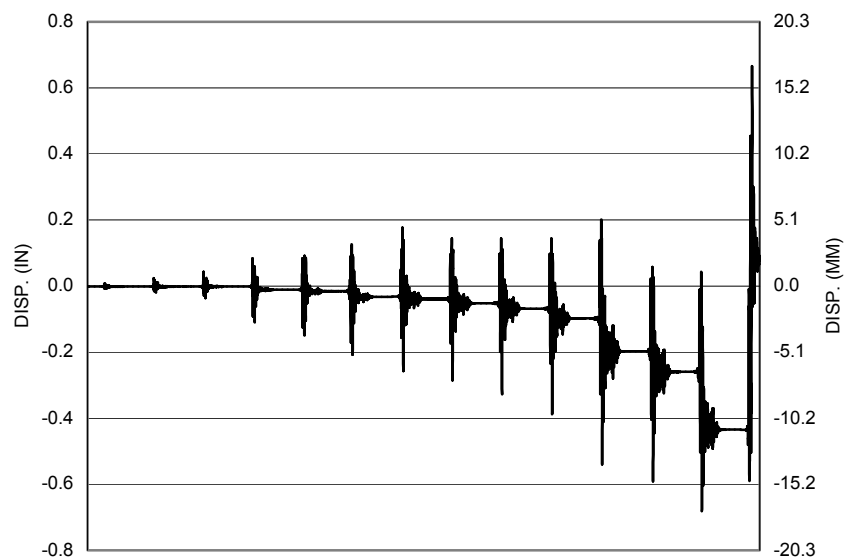
Figure A-32 Measured Displacement in NV17 for SFCD3
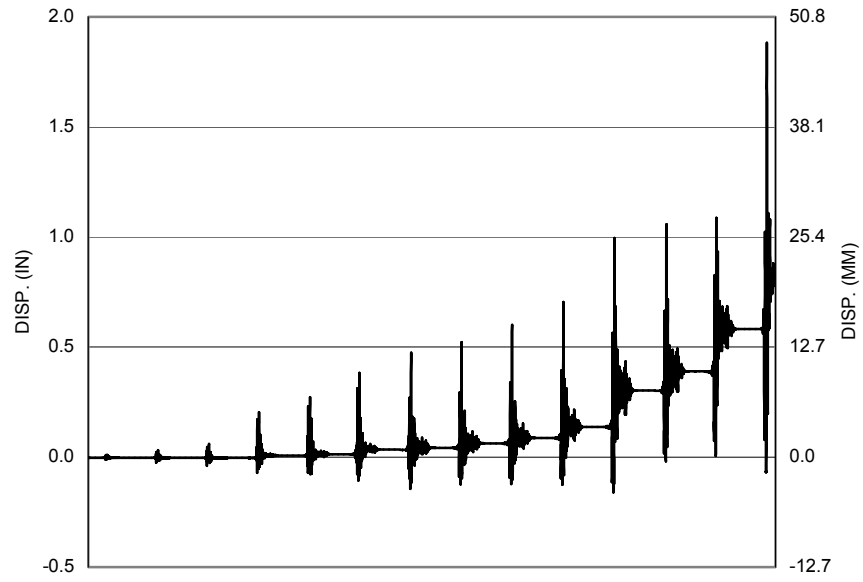
Figure A-33 Measured Displacement in NV18 for SFCD3
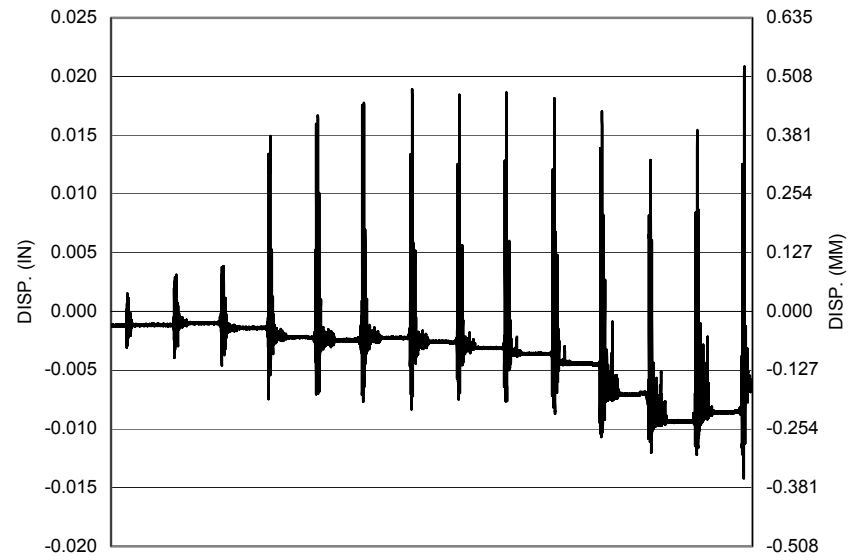
Figure A-34 Measured Displacement in NV19 for SFCD3
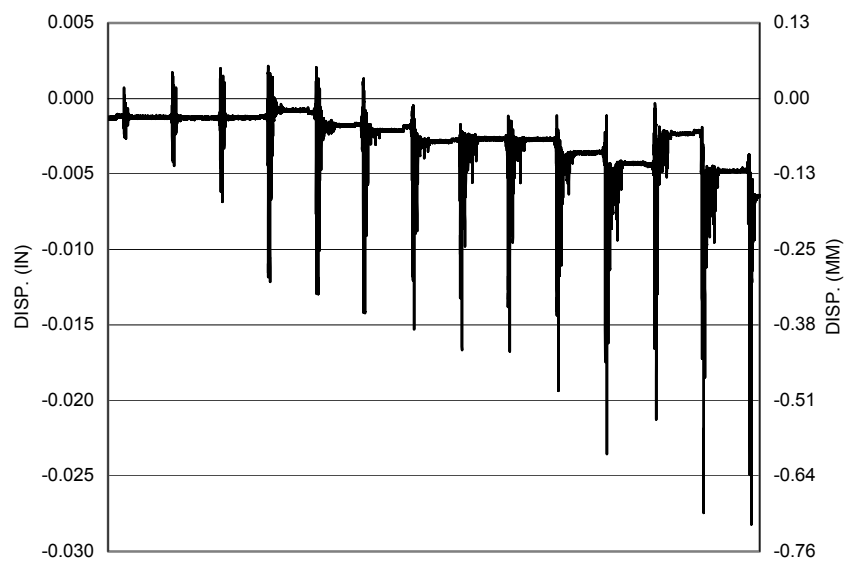
Figure A-35 Measured Displacement in NV20 for SFCD3
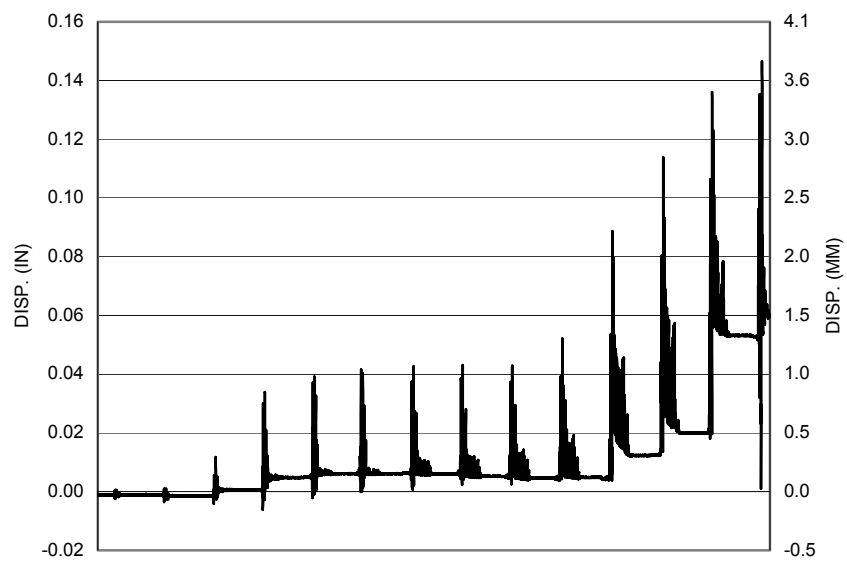
Figure A-36 Measured Displacement in NV21 for SFCD3
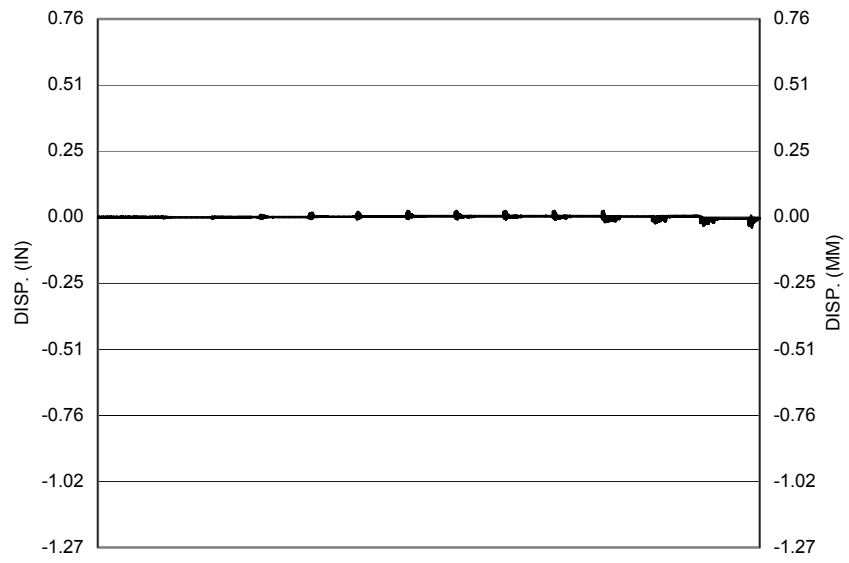
Figure A-37 Measured Displacement in NV22 for SFCD3
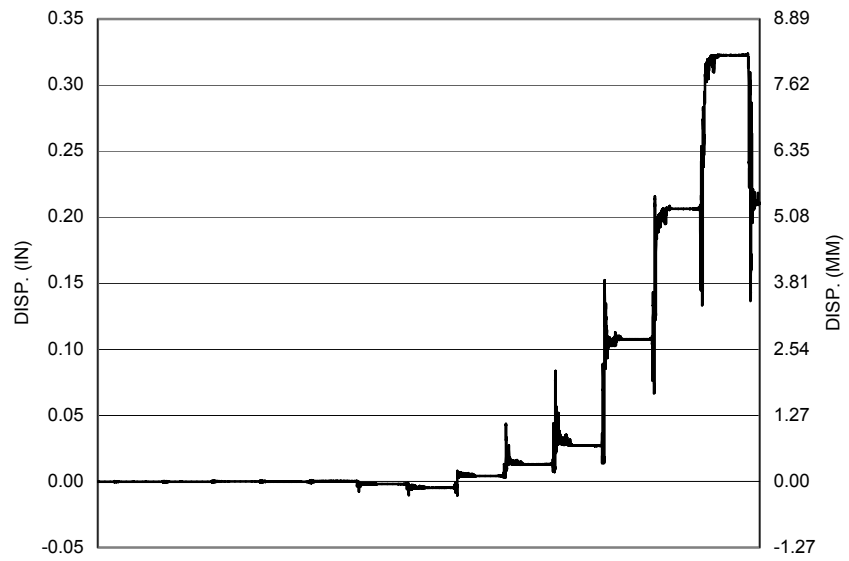
Figure A-38 Measured Displacement in NV23 for SFCD3
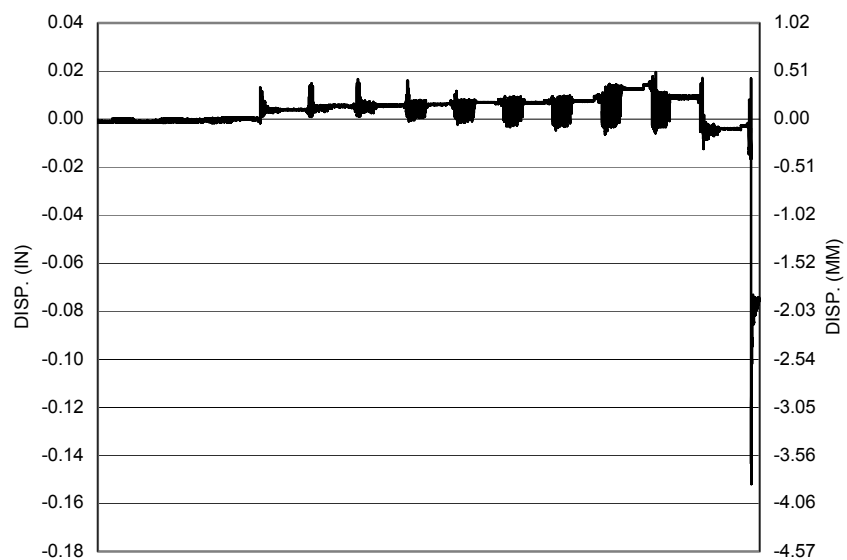
Figure A-39 Measured Displacement in NV24 for SFCD3
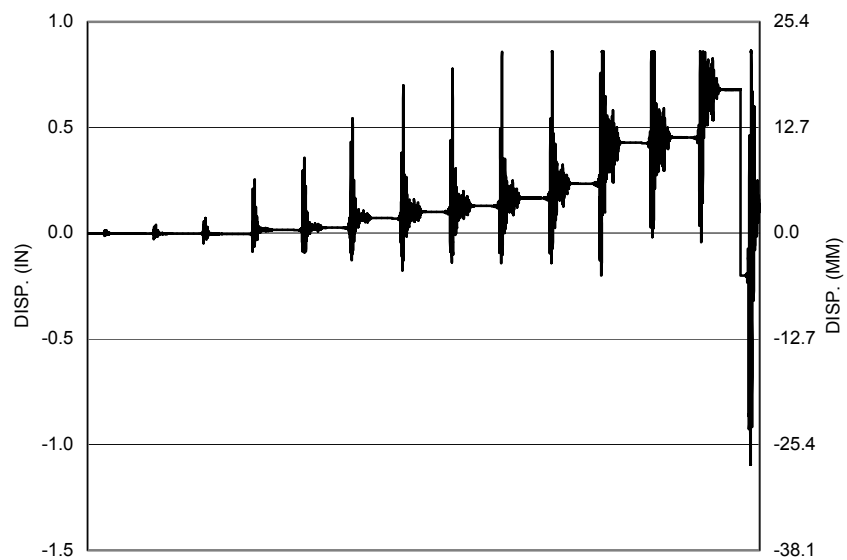
Figure A-40 Measured Displacement in NV25 for SFCD3

213
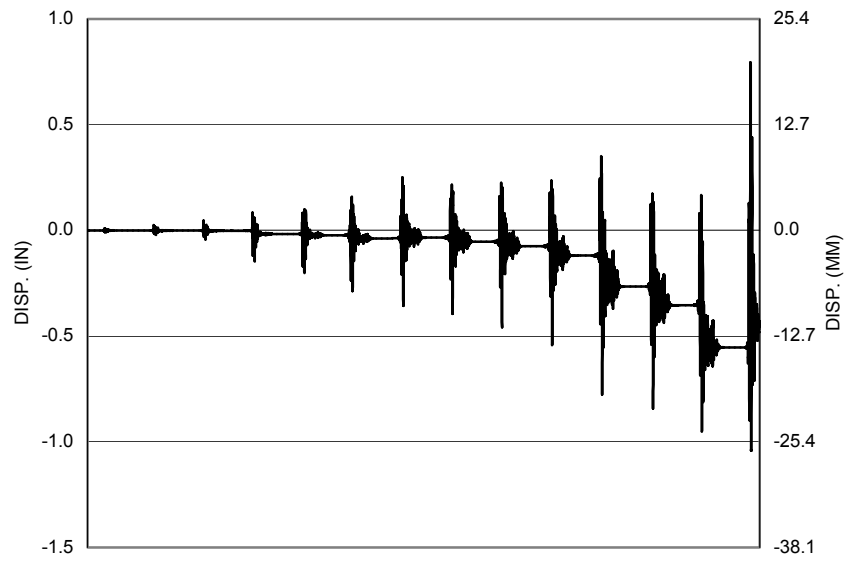
Figure A-41 Measured Displacement in NV26 for SFCD3
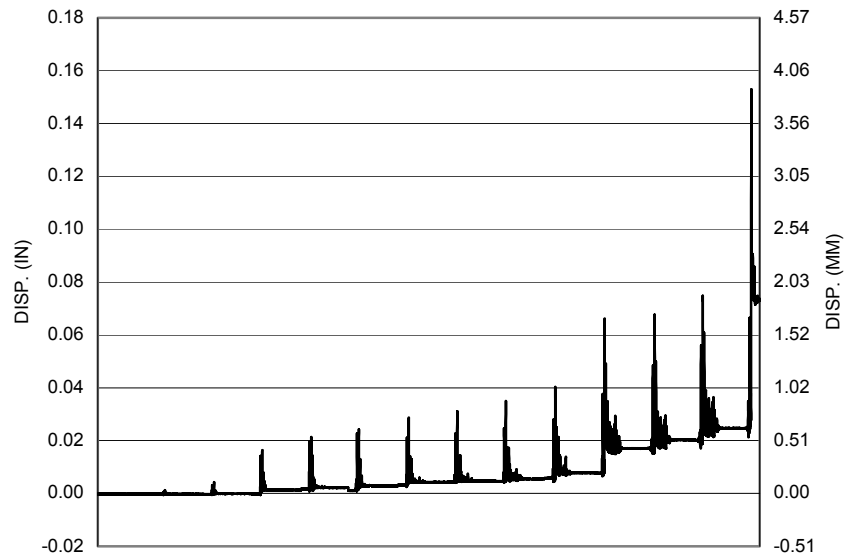
Figure A-42 Measured Displacement in NV27 for SFCD3
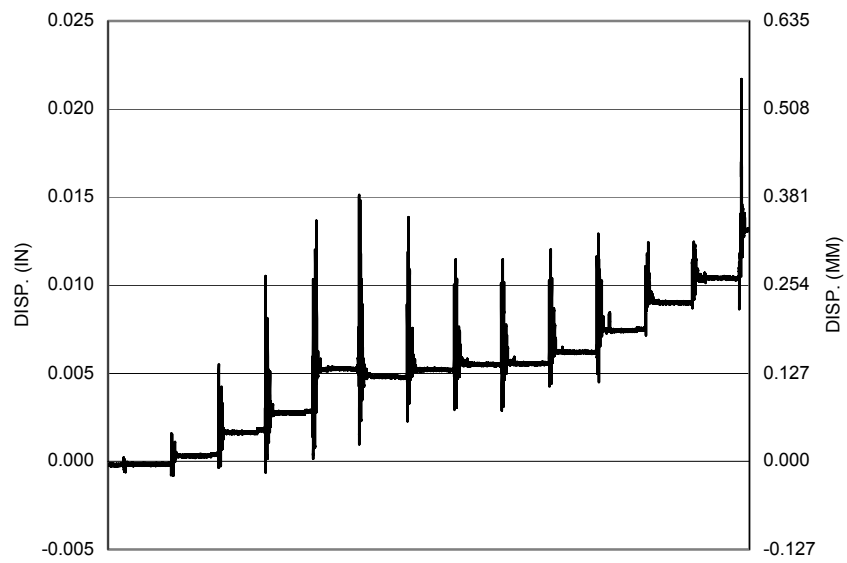
Figure A-43 Measured Displacement in NV28 for SFCD3
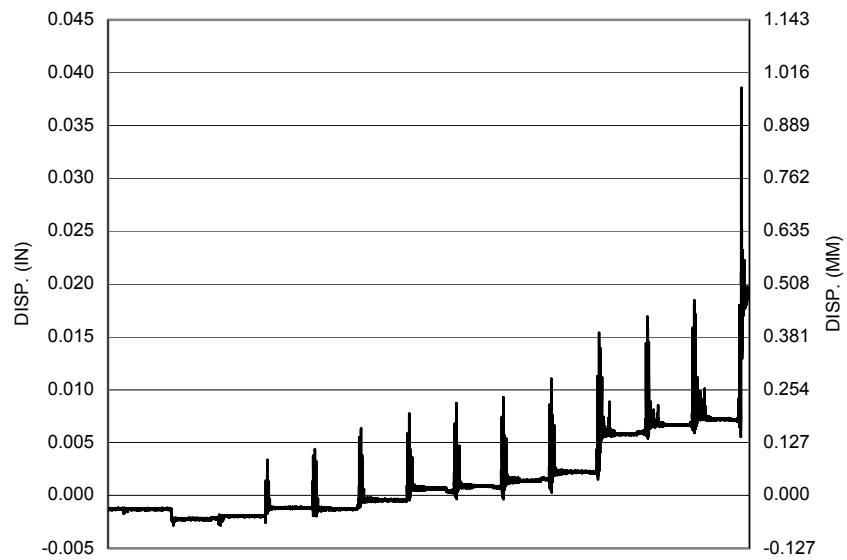
Figure A-44 Measured Displacement in NV29 for SFCD3
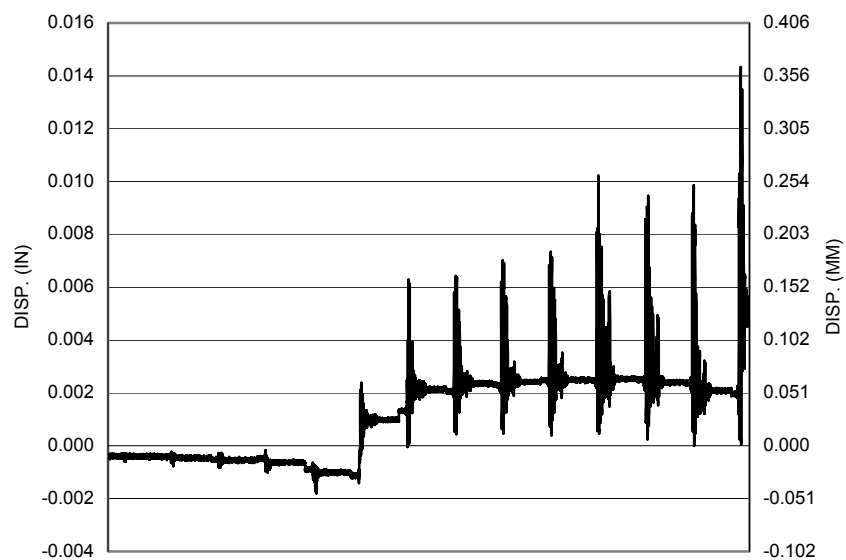
Figure A-45 Measured Displacement in NV30 for SFCD3
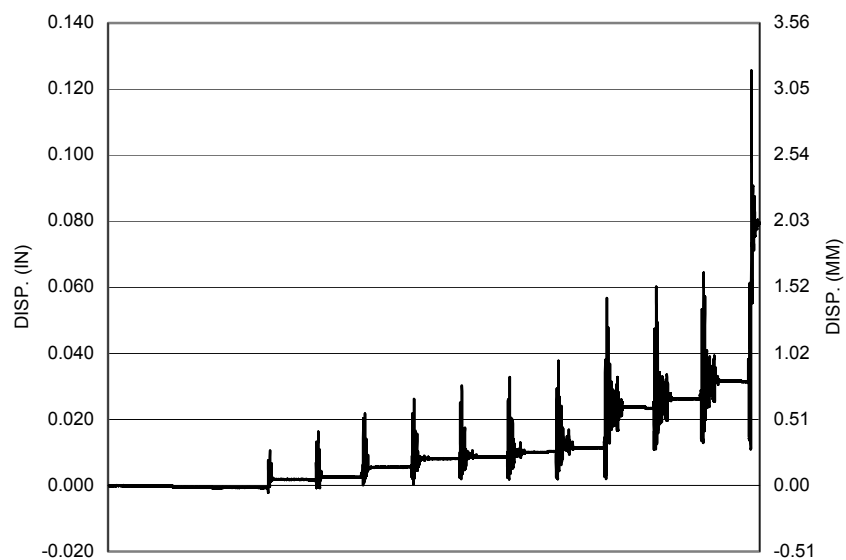
Figure A-46 Measured Displacement in NV31 for SFCD3
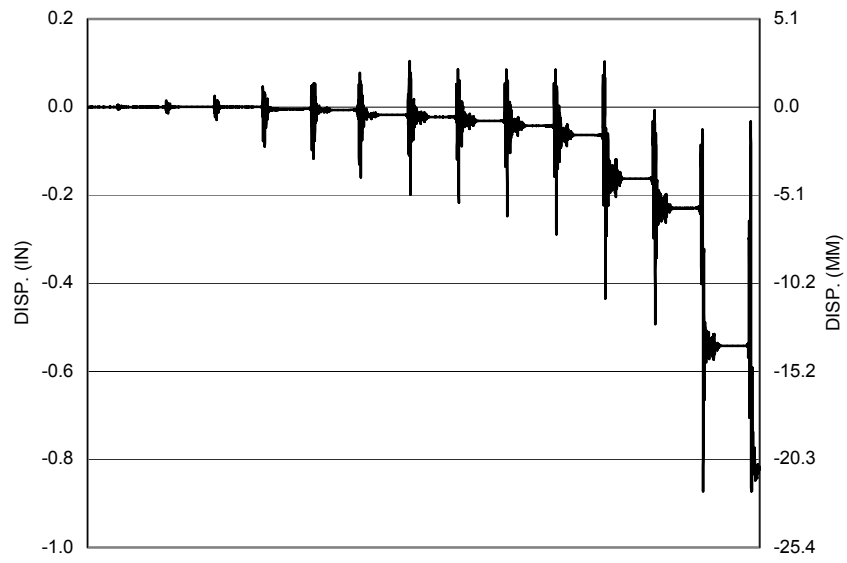
Figure A-47 Measured Displacement in NV32 for SFCD3
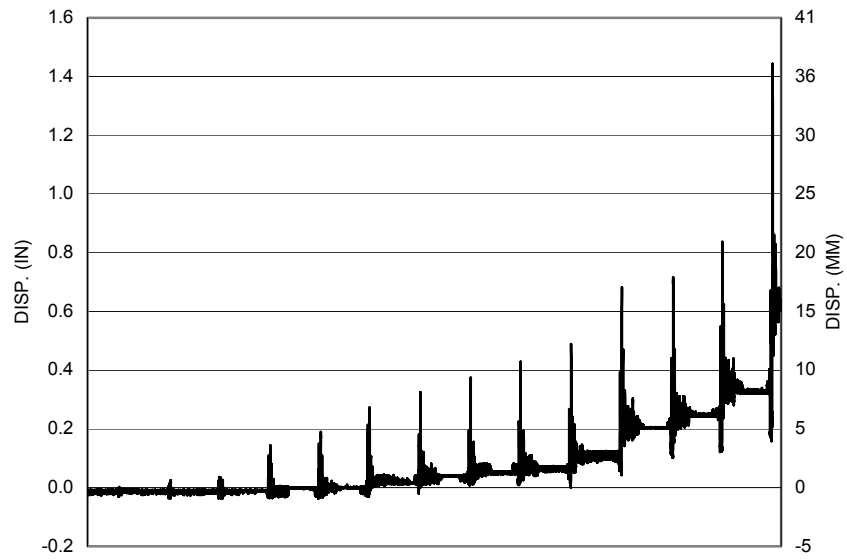
Figure A-48 Measured Displacement in NV33 for SFCD3
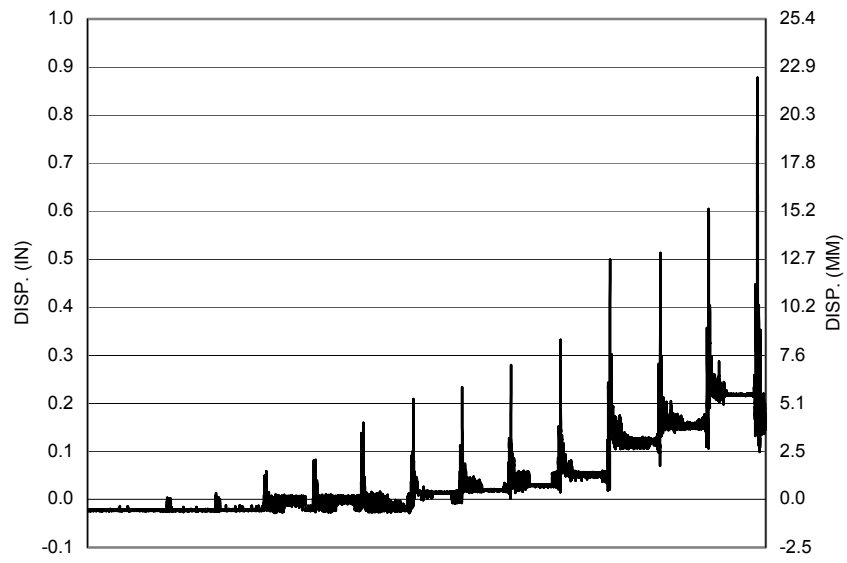
Figure A-49 Measured Displacement in NV34 for SFCD3
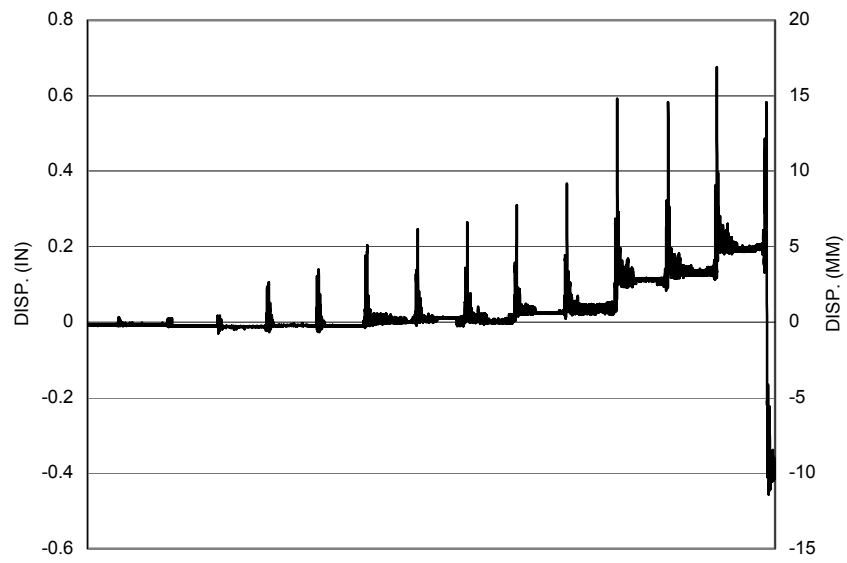
Figure A-50 Measured Displacement in NV35 for SFCD3
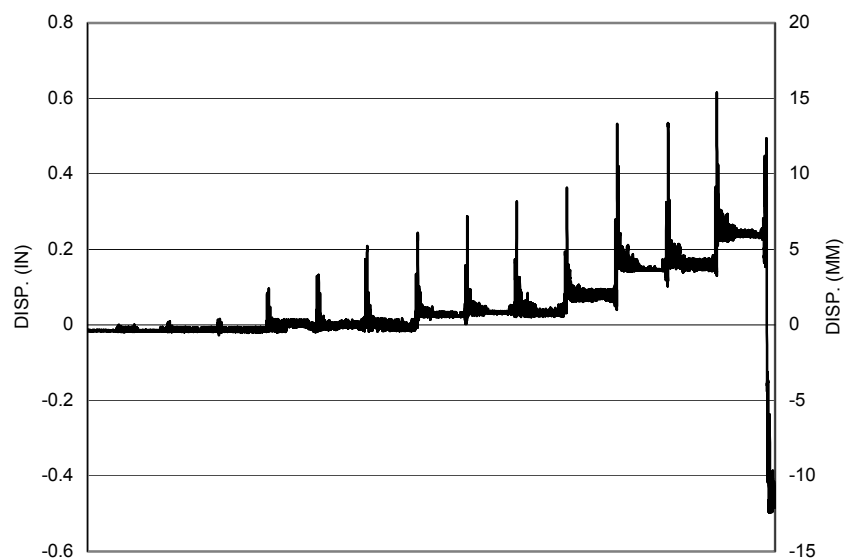
Figure A-51 Measured Displacement in NV36 for SFCD3
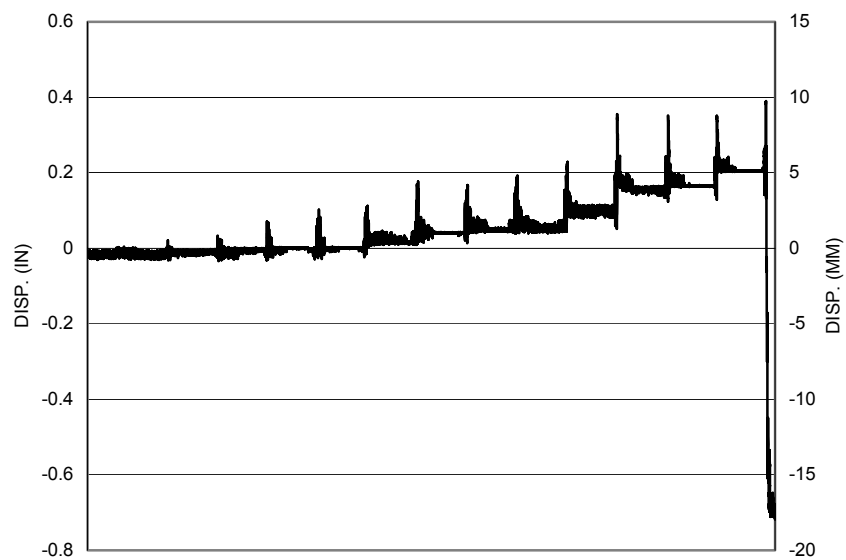
Figure A-52 Measured Displacement in NV37 for SFCD3

219
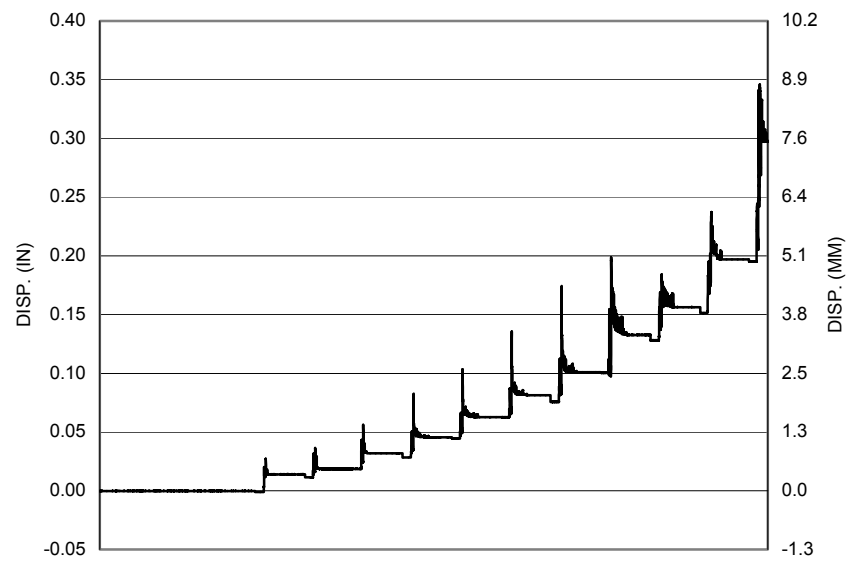
Figure A-53 Measured Displacement in NV38 for SFCD3
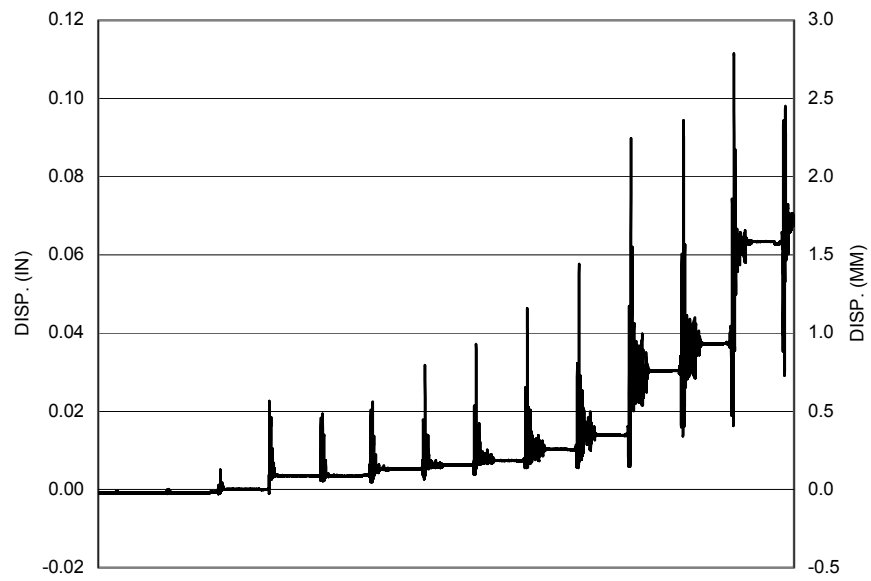
Figure A-54 Measured Displacement in NV39 for SFCD3
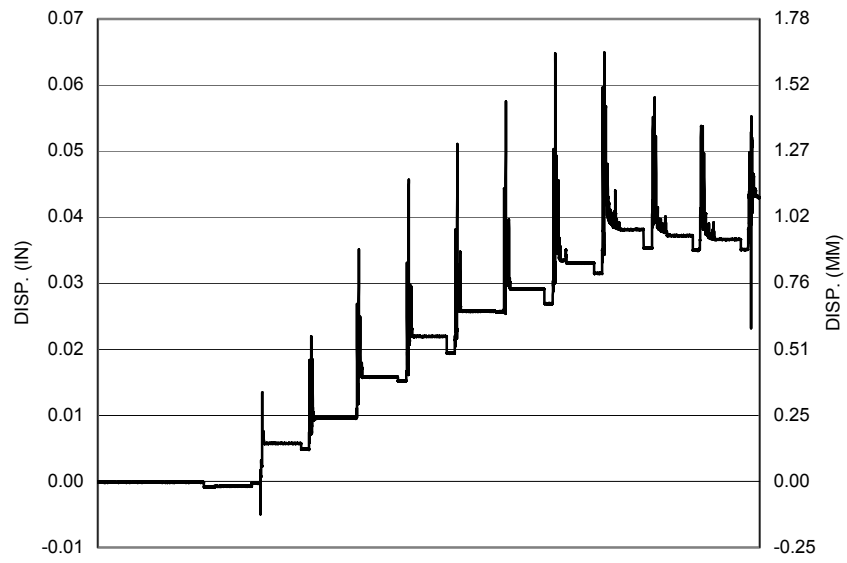
Figure A-55 Measured Displacement in NV40 for SFCD3
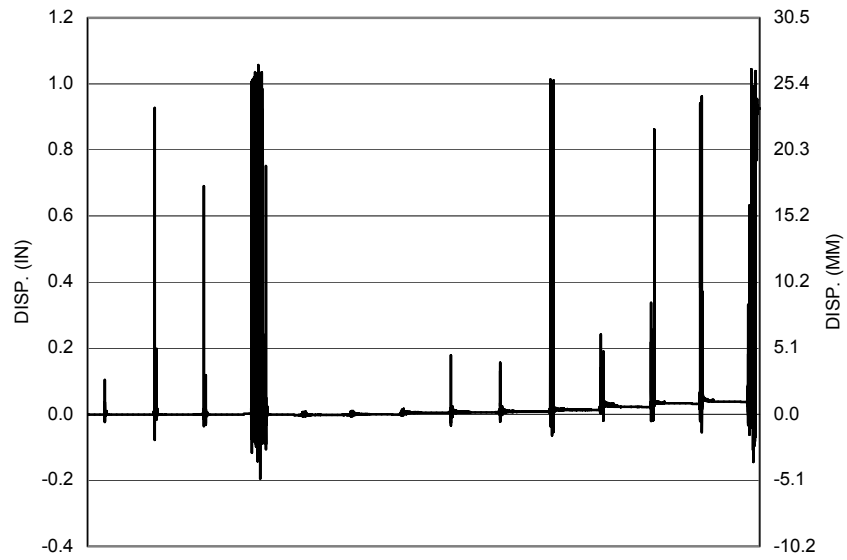
Figure A-56 Measured Displacement in NV41 for SFCD3
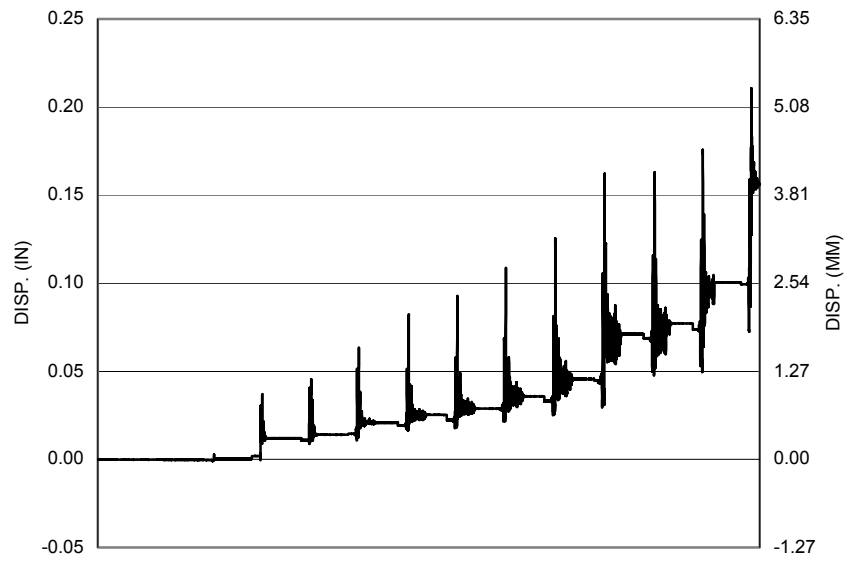
Figure A-57 Measured Displacement in NV42 for SFCD3
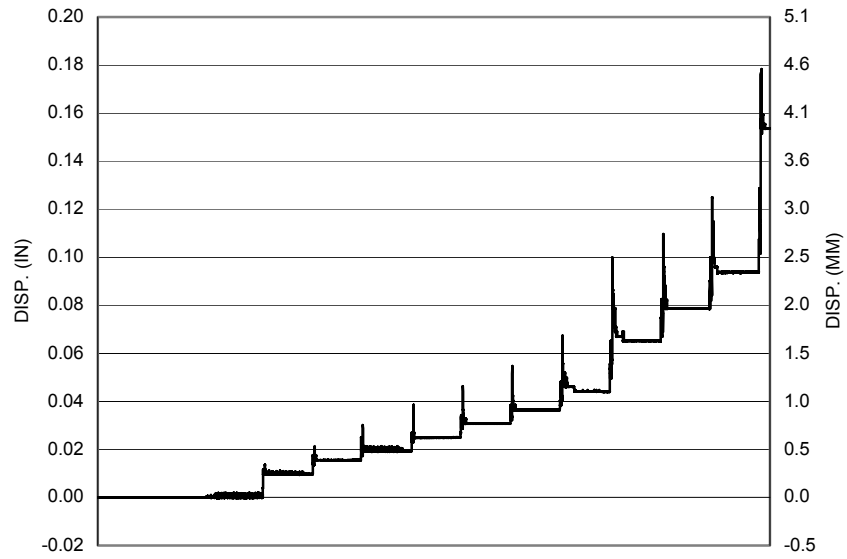
Figure A-58 Measured Displacement in NV43 for SFCD3
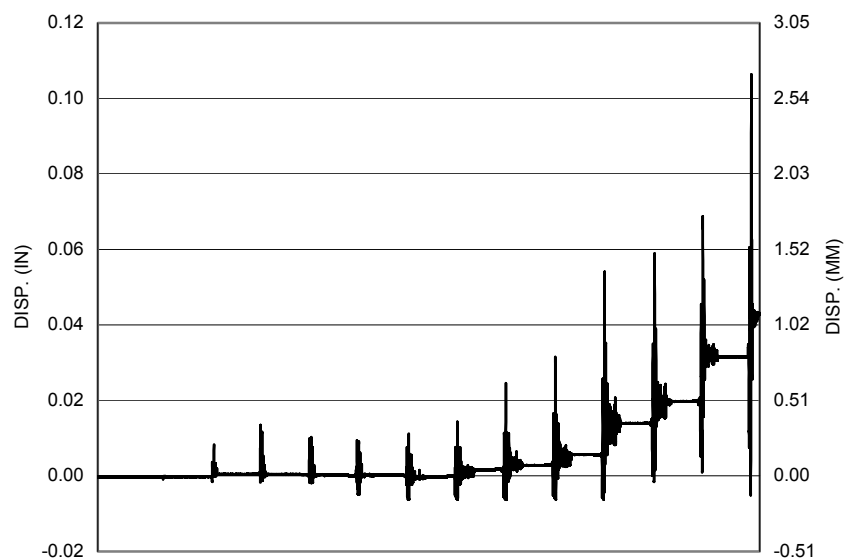
Figure A-59 Measured Displacement in NV44 for SFCD3
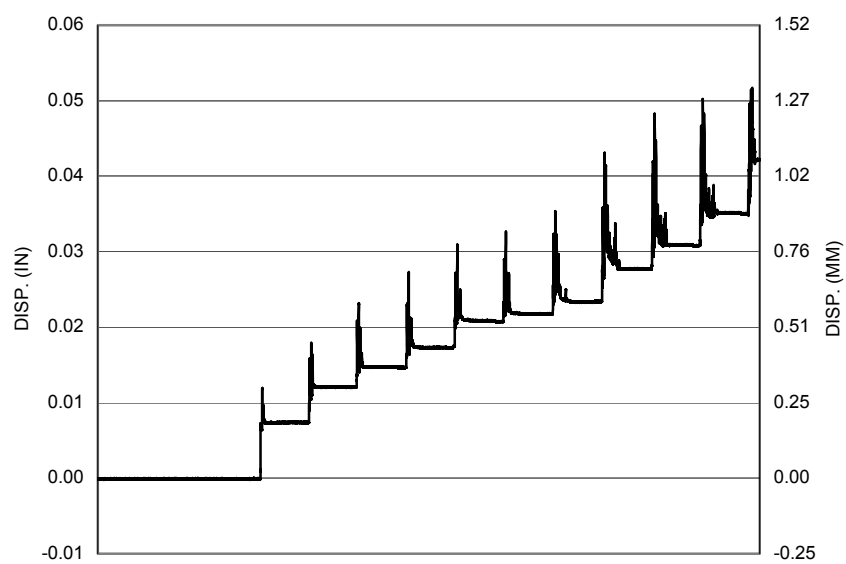
Figure A-60 Measured Displacement in NV45 for SFCD3
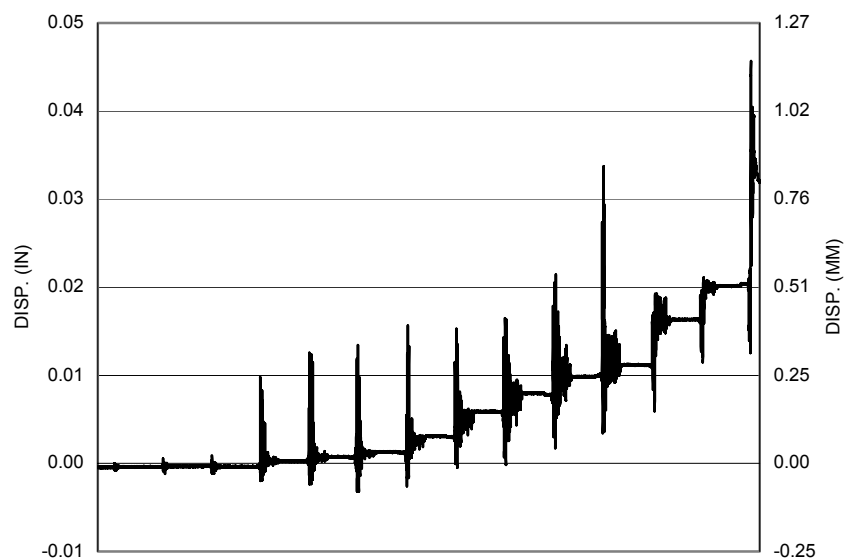
Figure A-61 Measured Displacement in NV46 for SFCD3
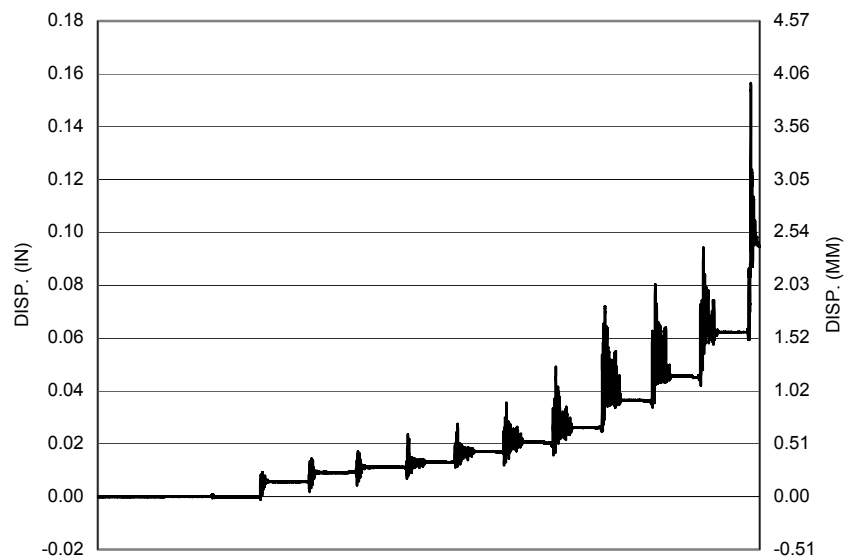
Figure A-62 Measured Displacement in NV47 for SFCD3
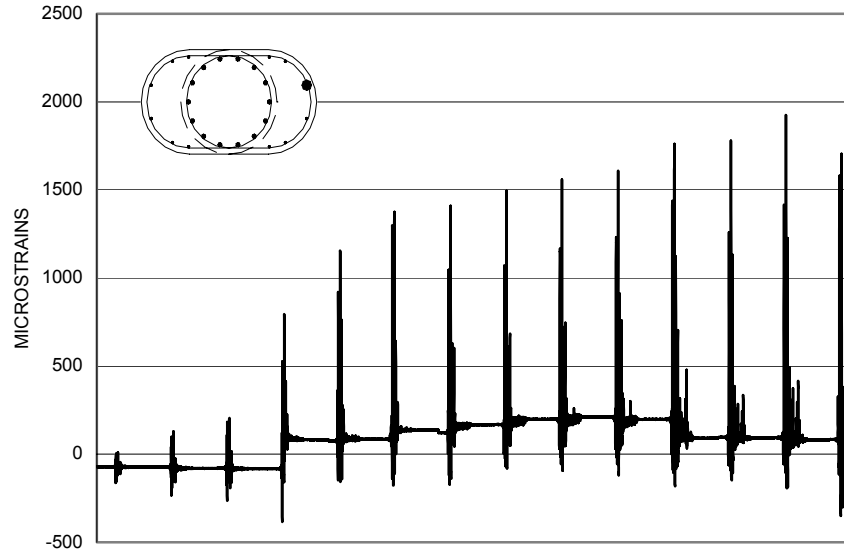
Figure A-63 Measured Strain in SG3 for SFCD3
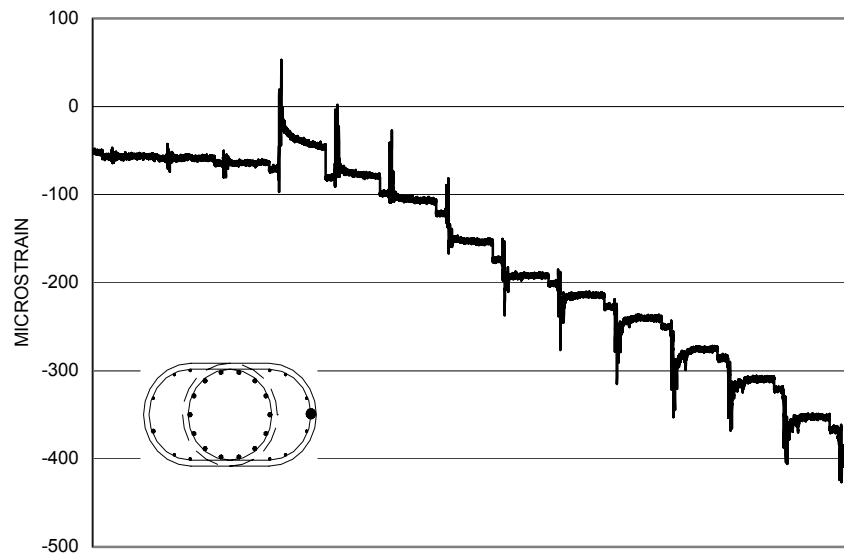
Figure A-64 Measured Strain in SG4 for SFCD3
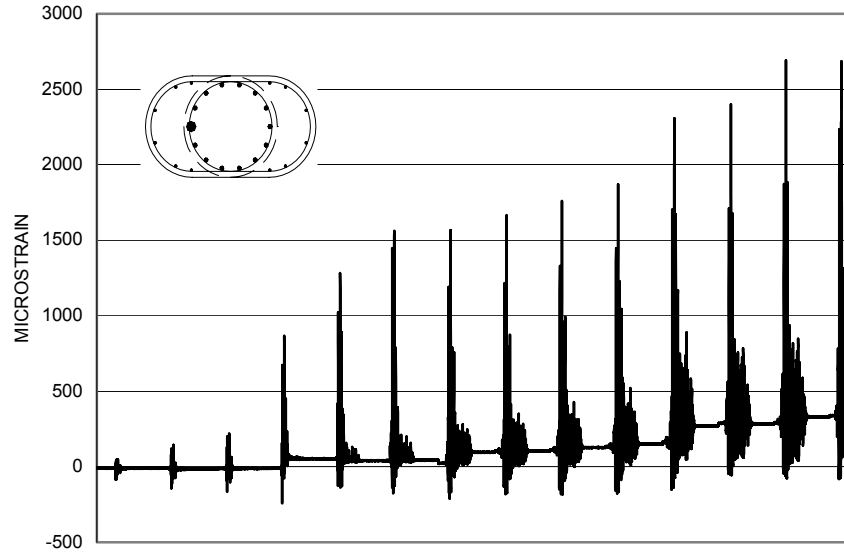
Figure A-65 Measured Strain in SG5 for SFCD3
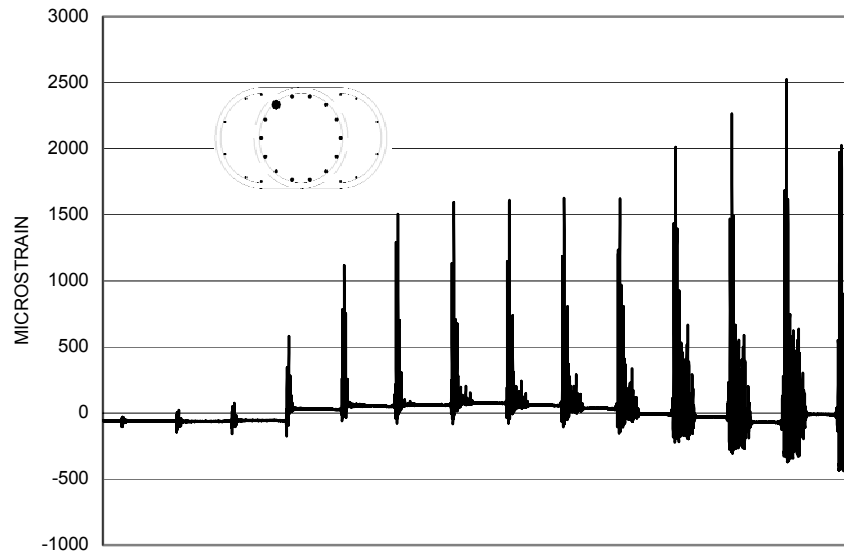
Figure A-66 Measured Strain in SG6 for SFCD3
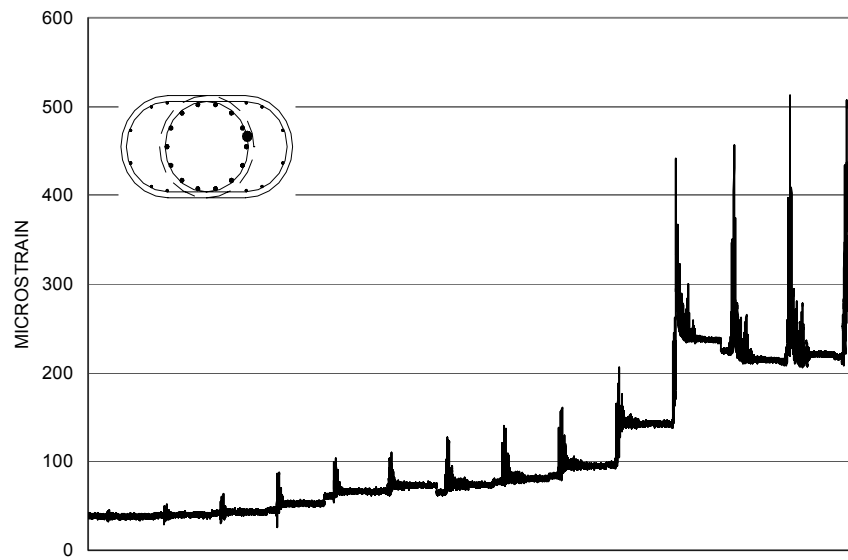
Figure A-67 Measured Strain in SG7 for SFCD3
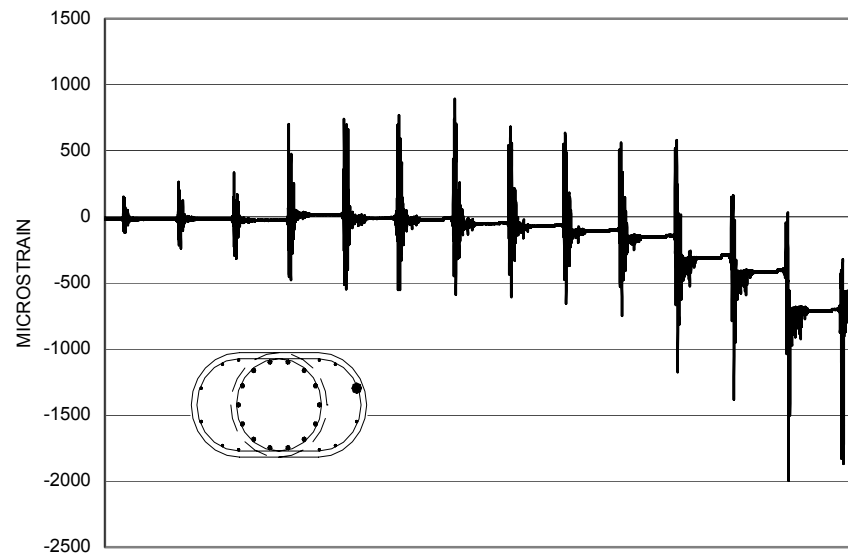
Figure A-68 Measured Strain in SG8 for SFCD3
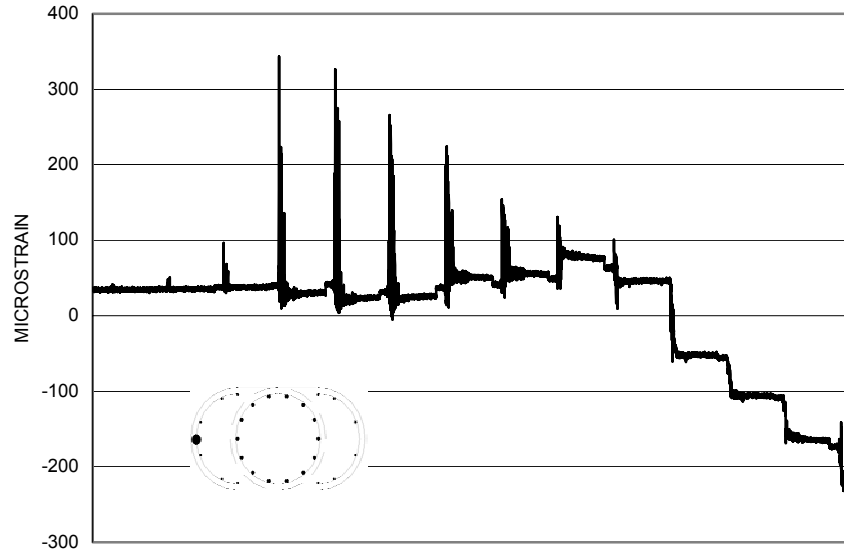
Figure A-69 Measured Strain in SG9 for SFCD3
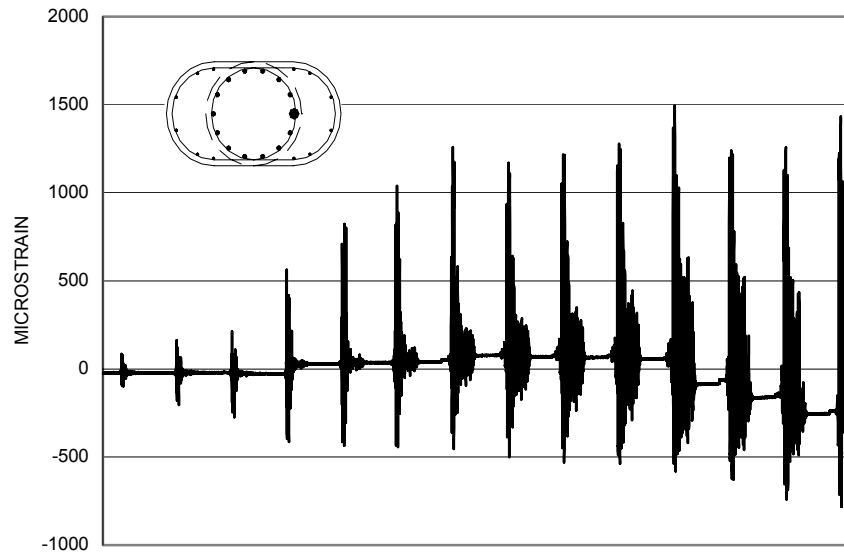
Figure A-70 Measured Strain in SG10 for SFCD3
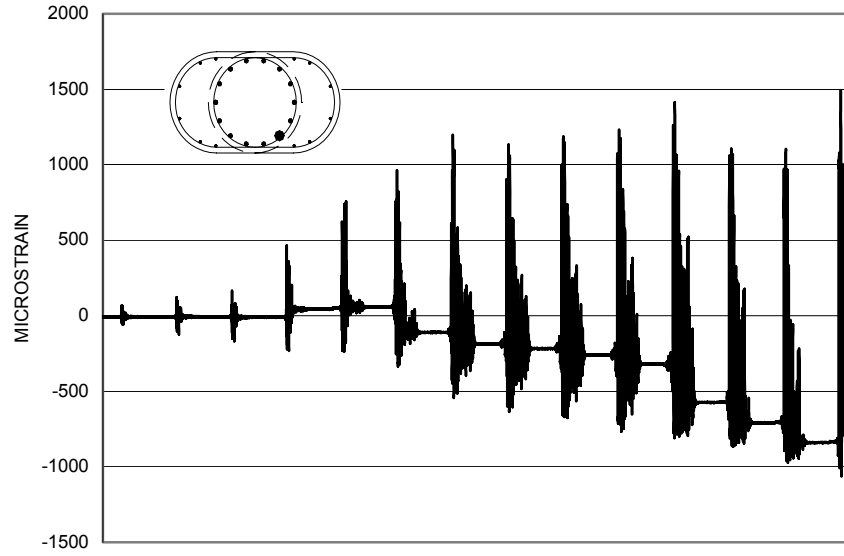
Figure A-71 Measured Strain in SG11 for SFCD3
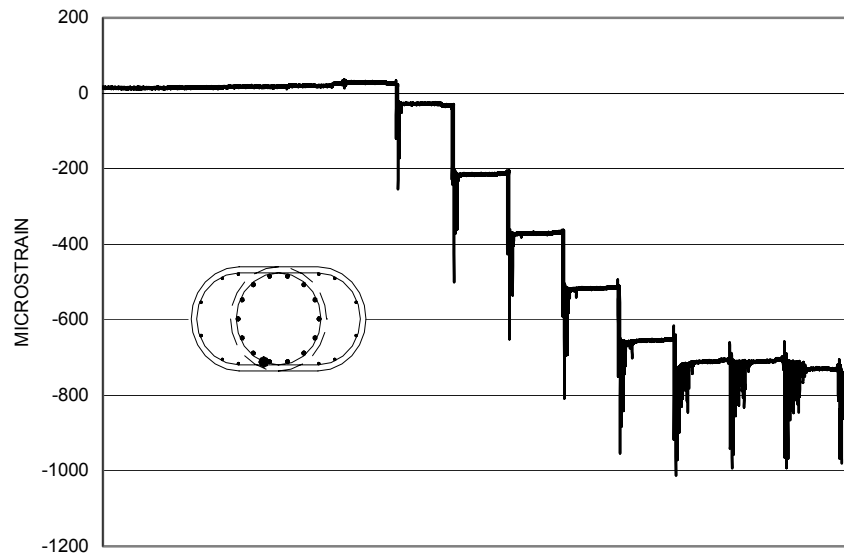
Figure A-72 Measured Strain in SG12 for SFCD3
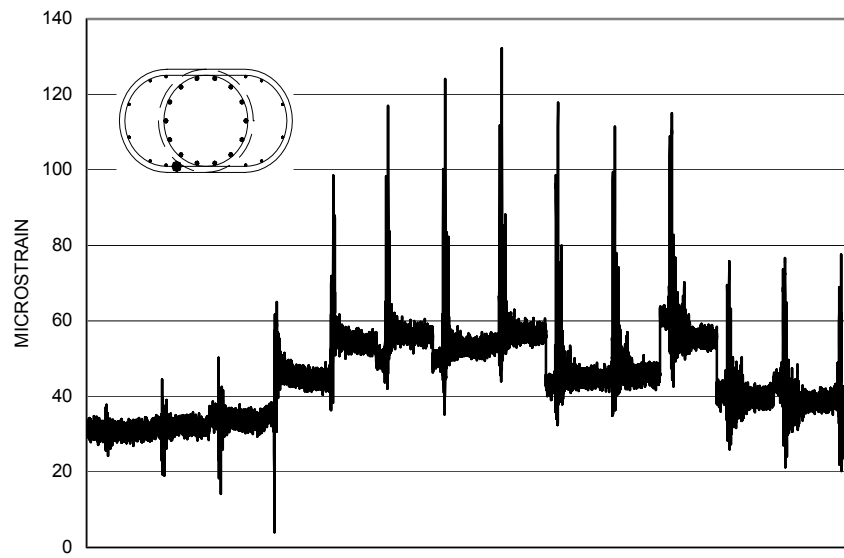
Figure A-73 Measured Strain in SG13 for SFCD3
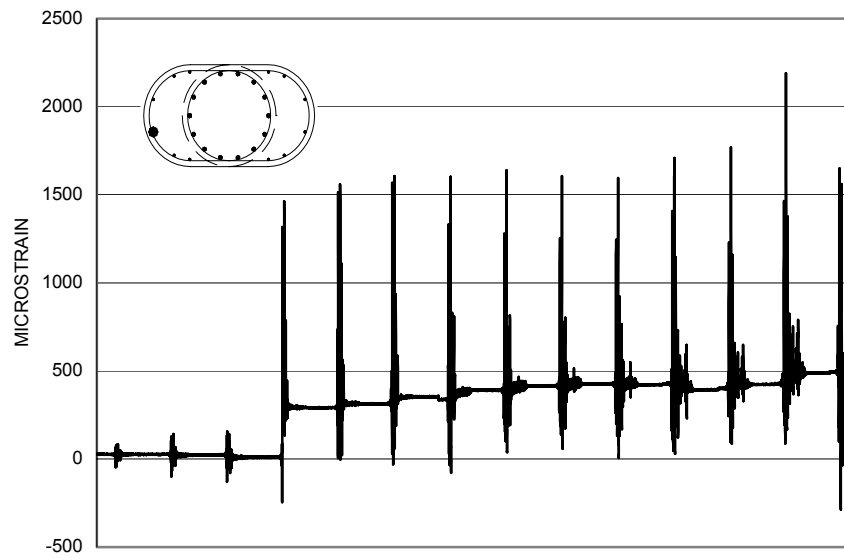
Figure A-74 Measured Strain in SG14 for SFCD3
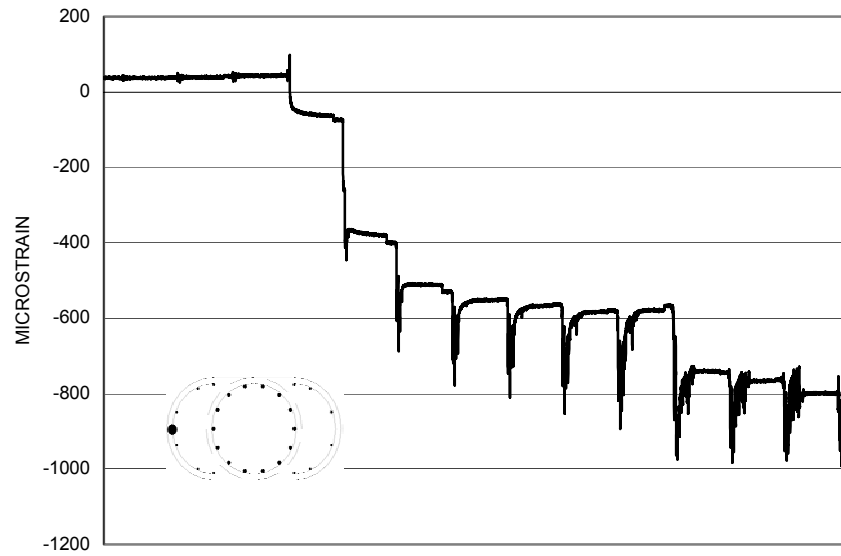
Figure A-75 Measured Strain in SG15 for SFCD3
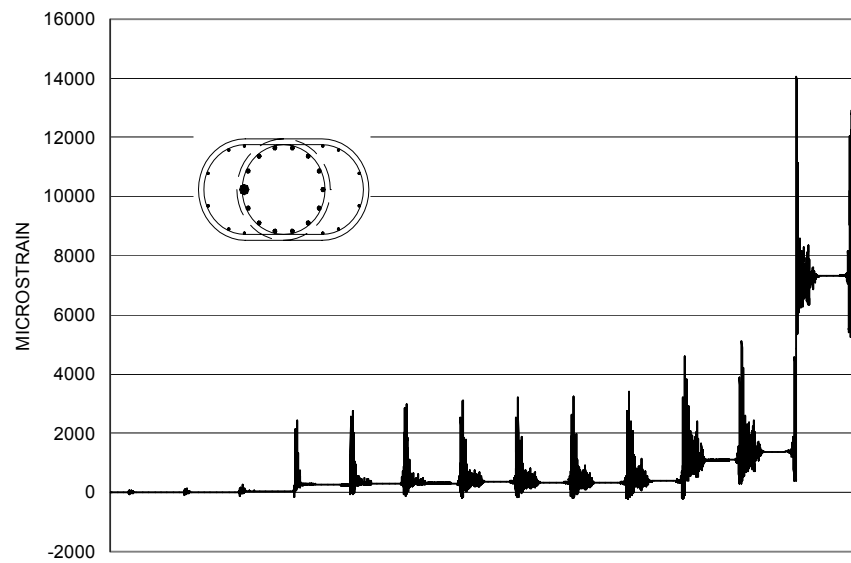
Figure A-76 Measured Strain in SG16 for SFCD3
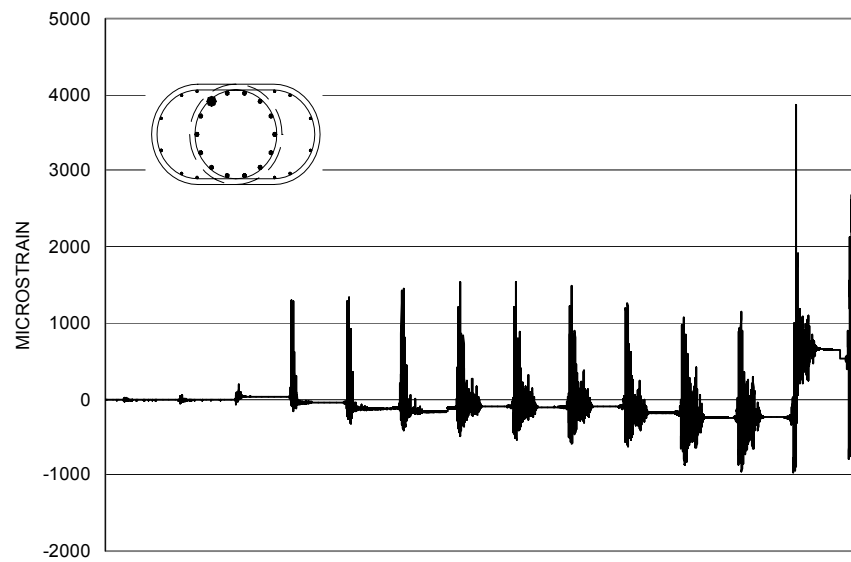
Figure A-77 Measured Strain in SG17 for SFCD3
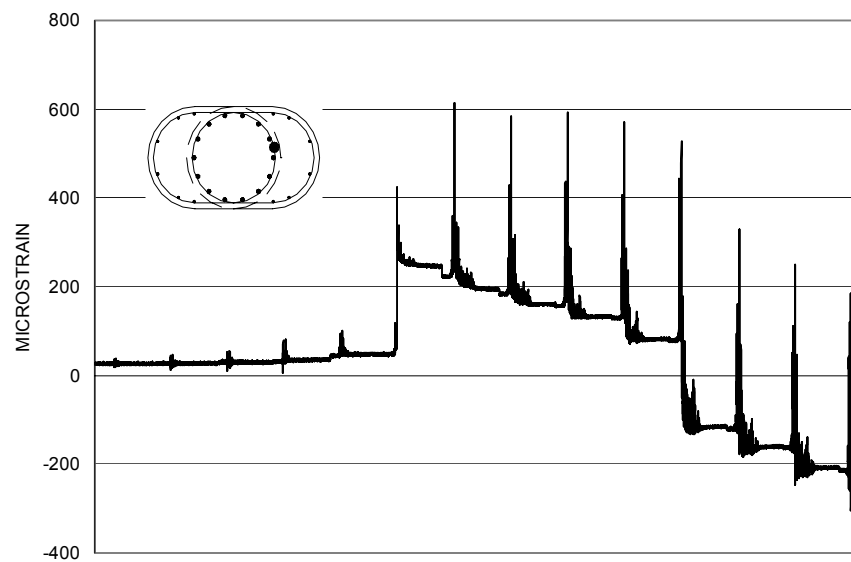
Figure A-78 Measured Strain in SG18 for SFCD3
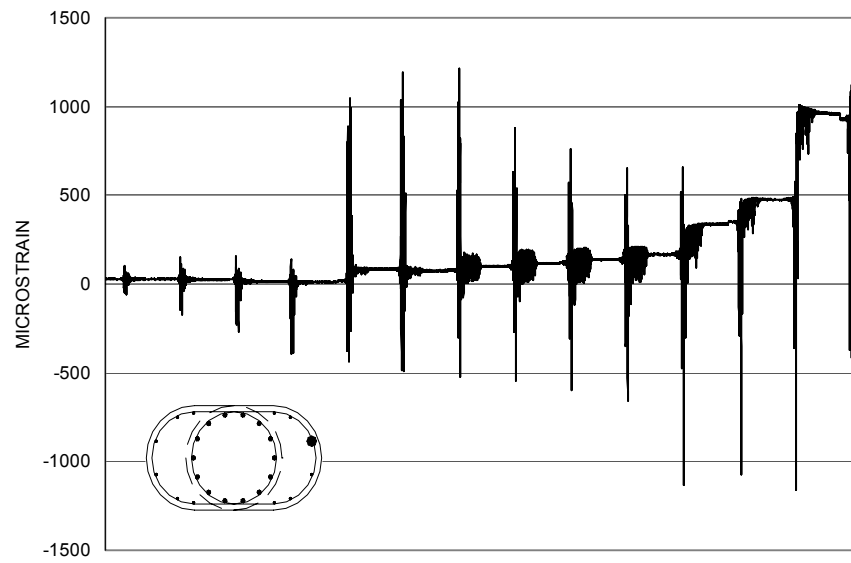
Figure A-79 Measured Strain in SG19 for SFCD3
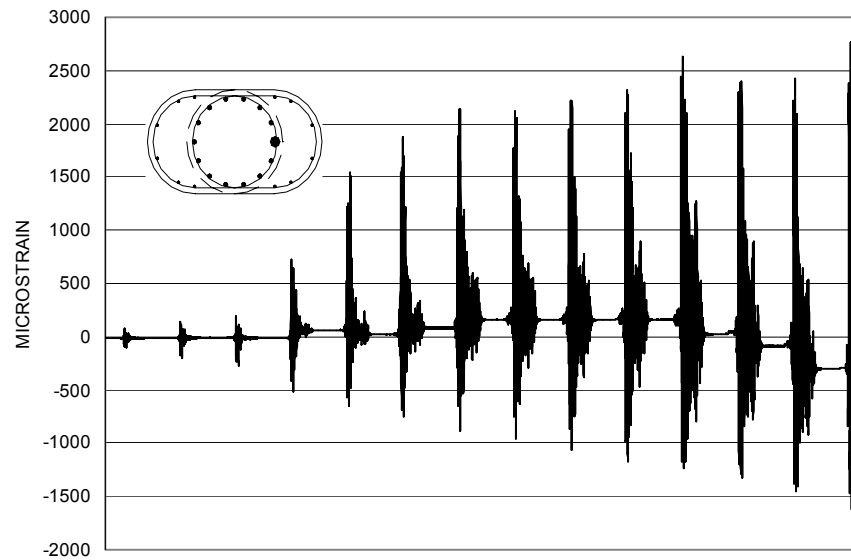
Figure A-80 Measured Strain in SG21 for SFCD3
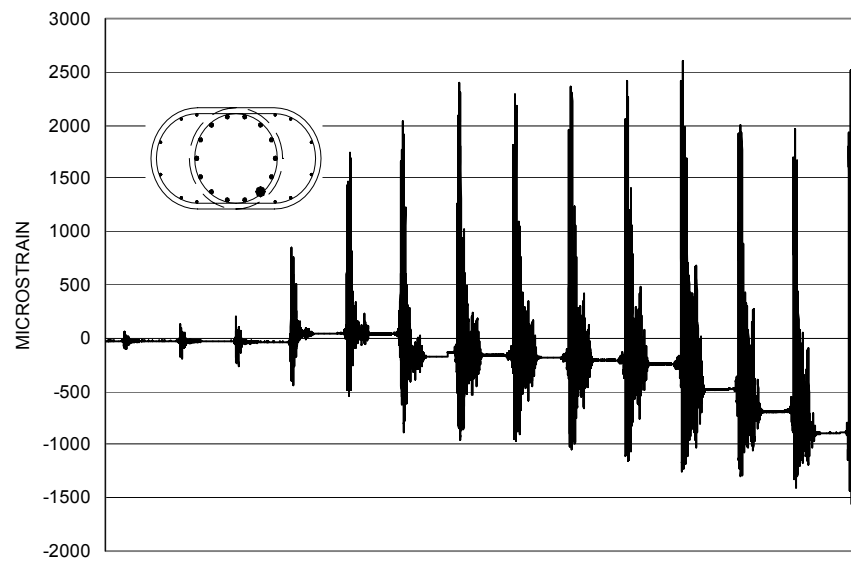
Figure A-81 Measured Strain in SG22 for SFCD3
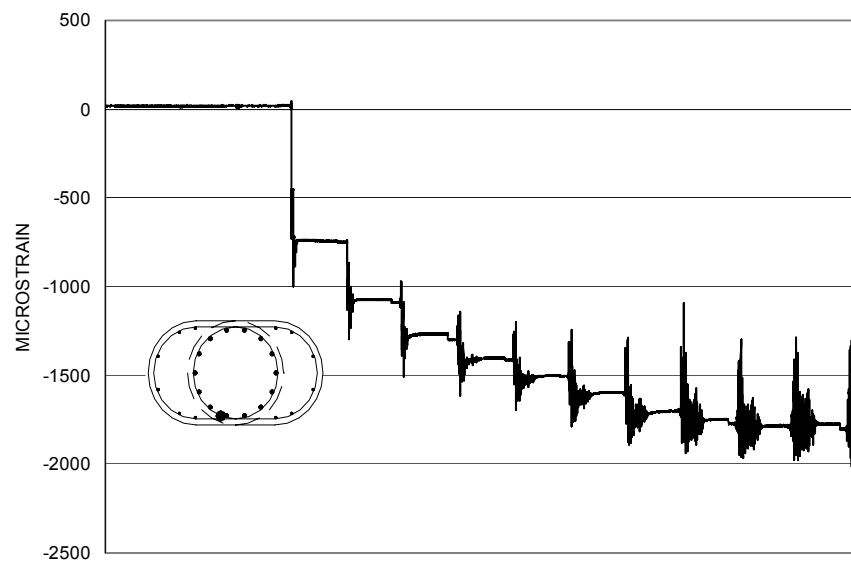
Figure A-82 Measured Strain in SG23 for SFCD3
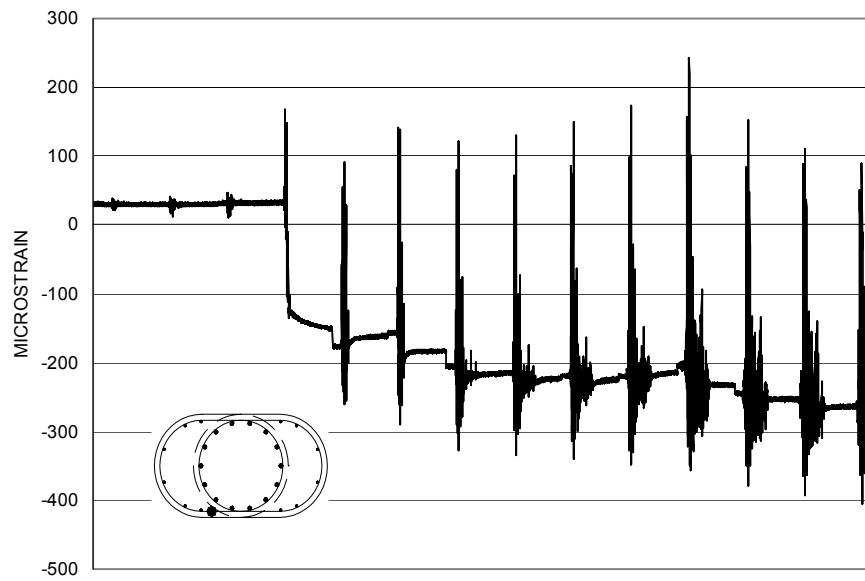
Figure A-83 Measured Strain in SG24 for SFCD3
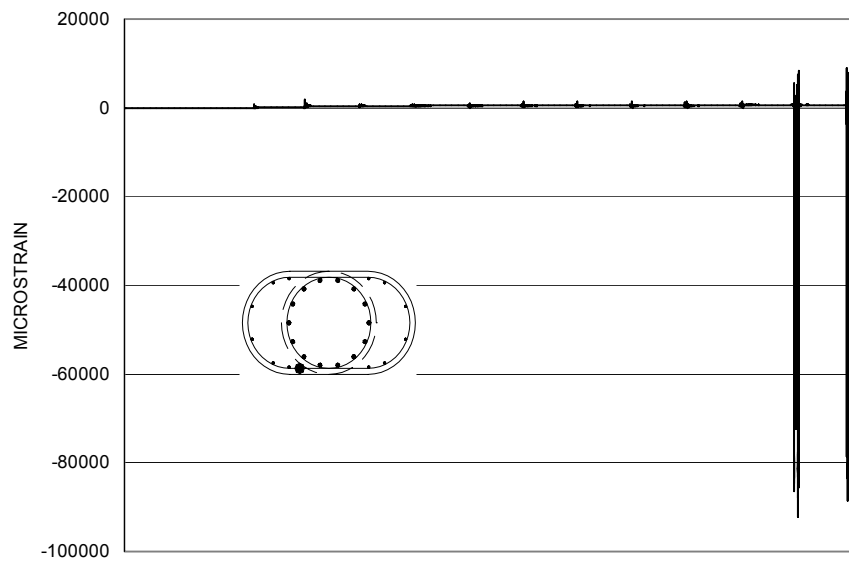
Figure A-84 Measured Strain in SG25 for SFCD3
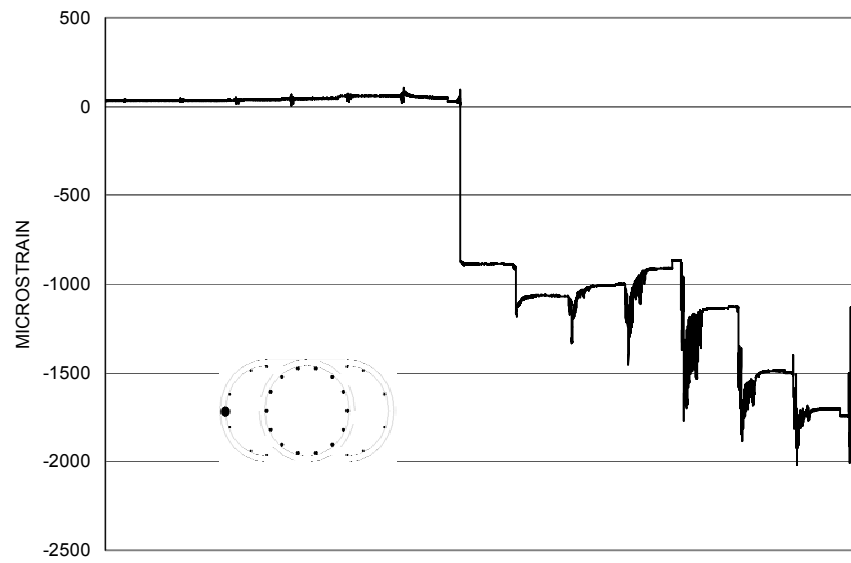
Figure A-85 Measured Strain in SG26 for SFCD3
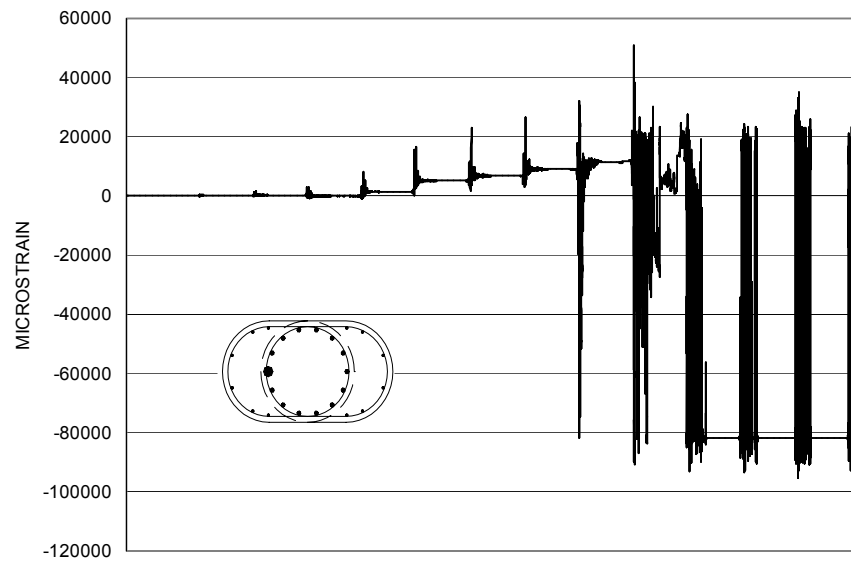
Figure A-86 Measured Strain in SG27 for SFCD3
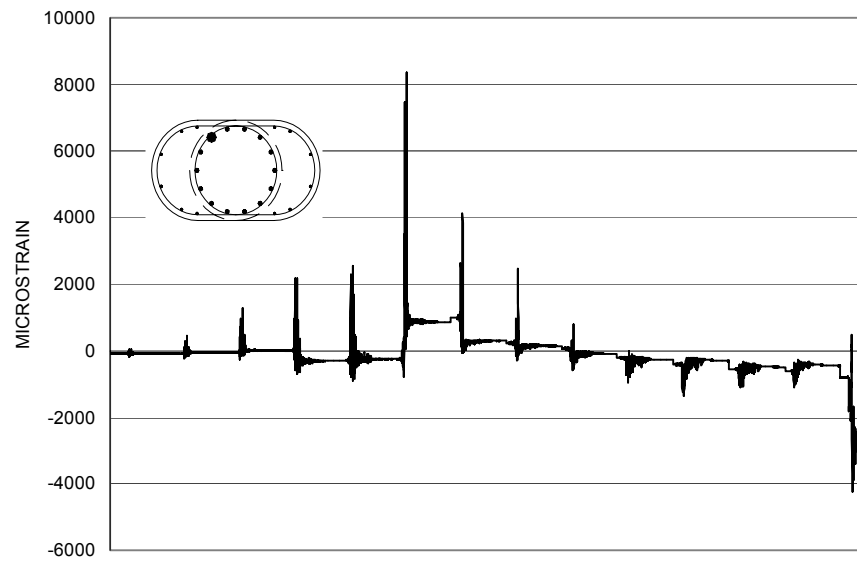
Figure A-87 Measured Strain in SG28 for SFCD3
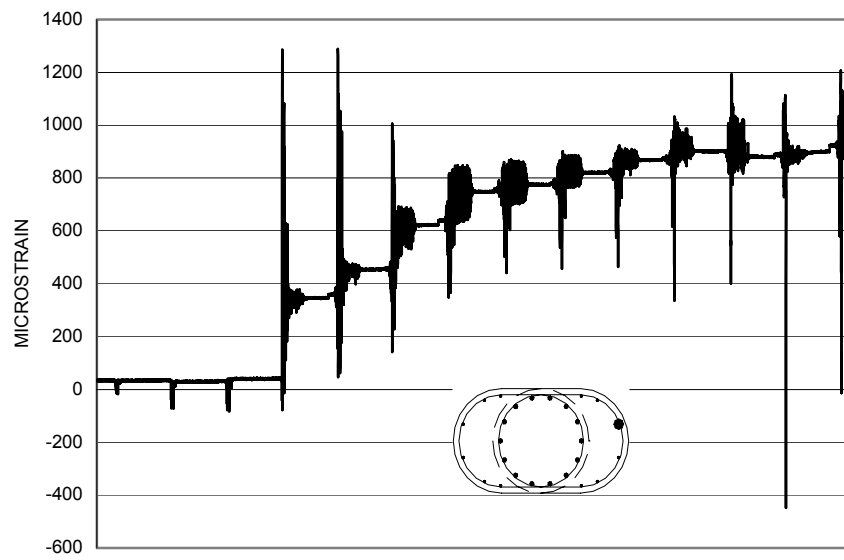
Figure A-88 Measured Strain in SG30 for SFCD3
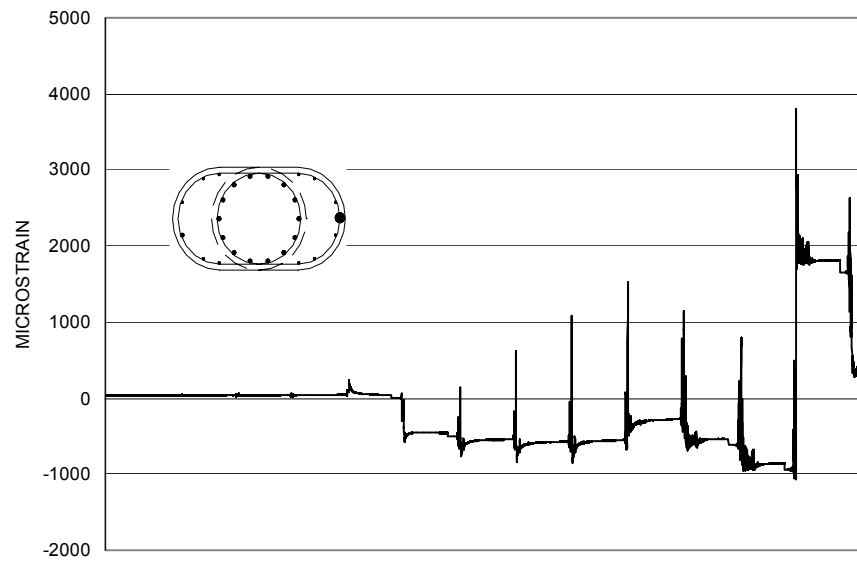
Figure A-89 Measured Strain in SG31 for SFCD3
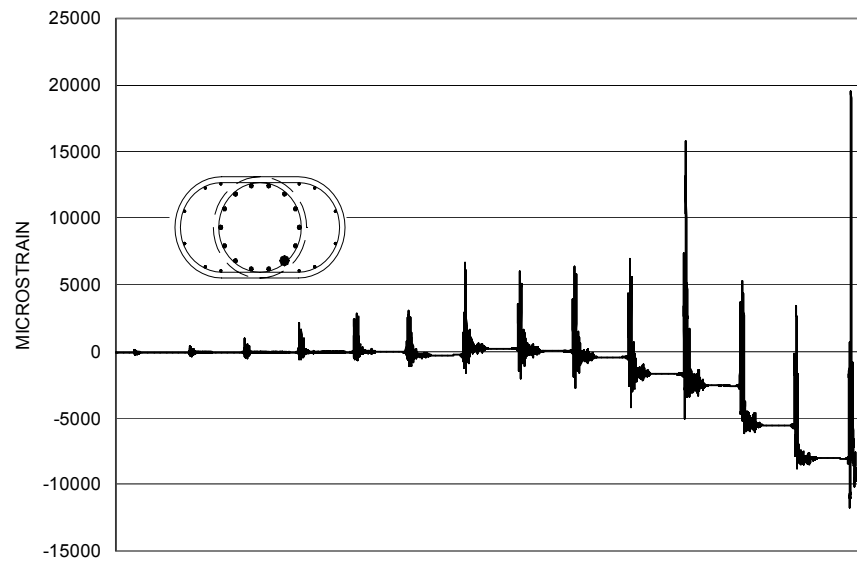
Figure A-90 Measured Strain in SG33 for SFCD3
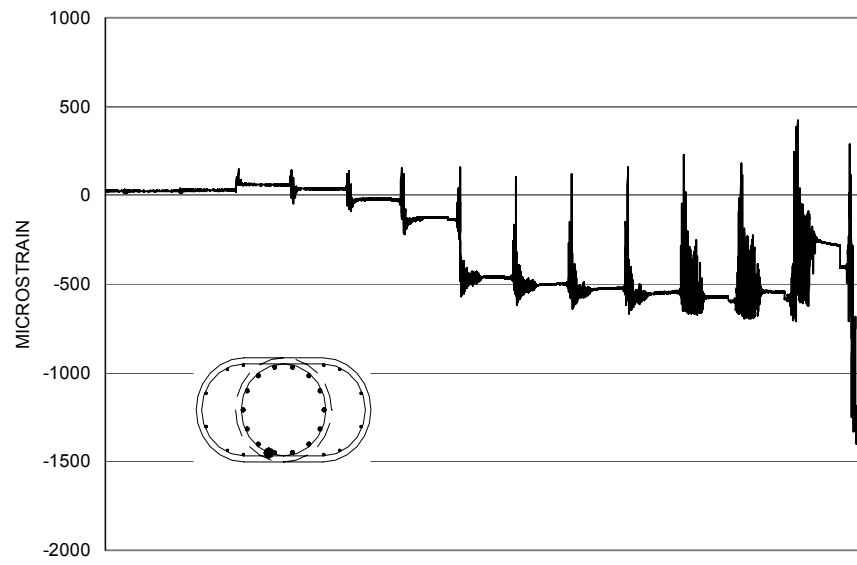
Figure A-91 Measured Strain in SG34 for SFCD3
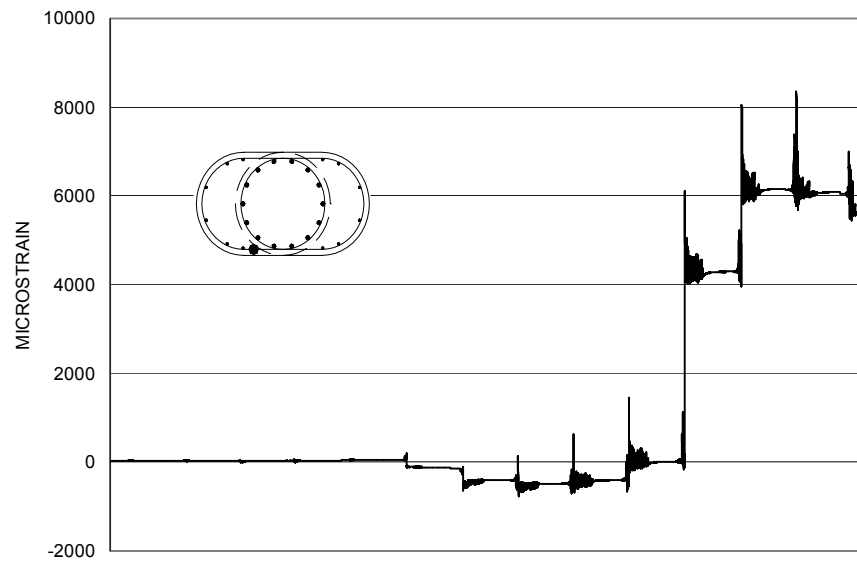
Figure A-92 Measured Strain in SG35 for SFCD3
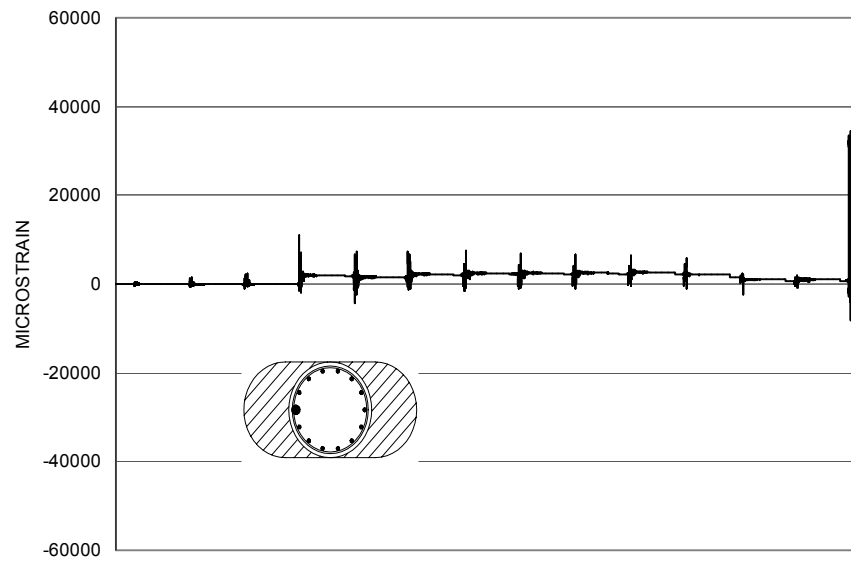
Figure A-93 Measured Strain in SG36 for SFCD3
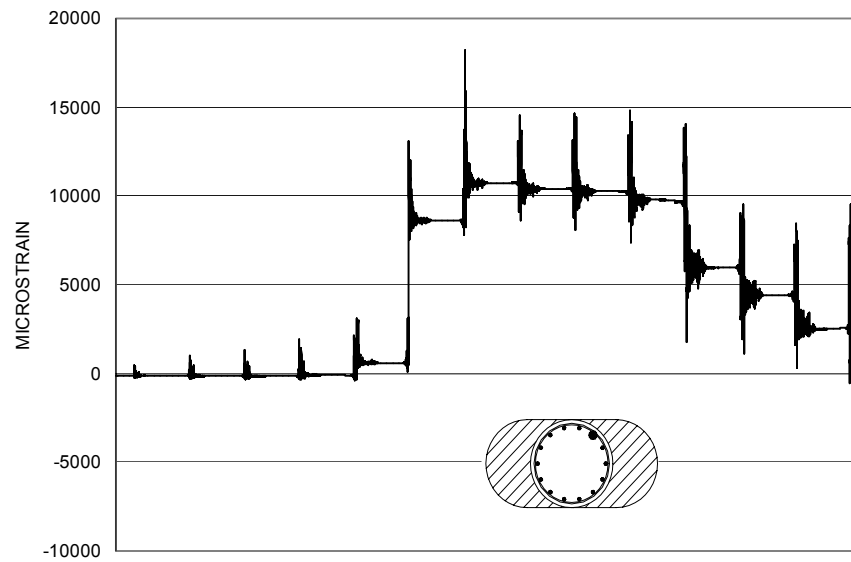
Figure A-94 Measured Strain in SG37 for SFCD3
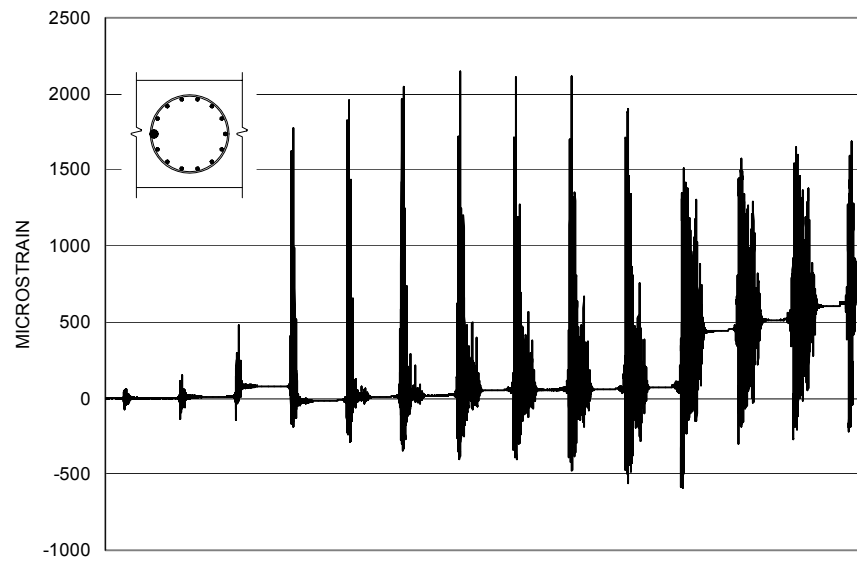
Figure A-95 Measured Strain in SG40 for SFCD3
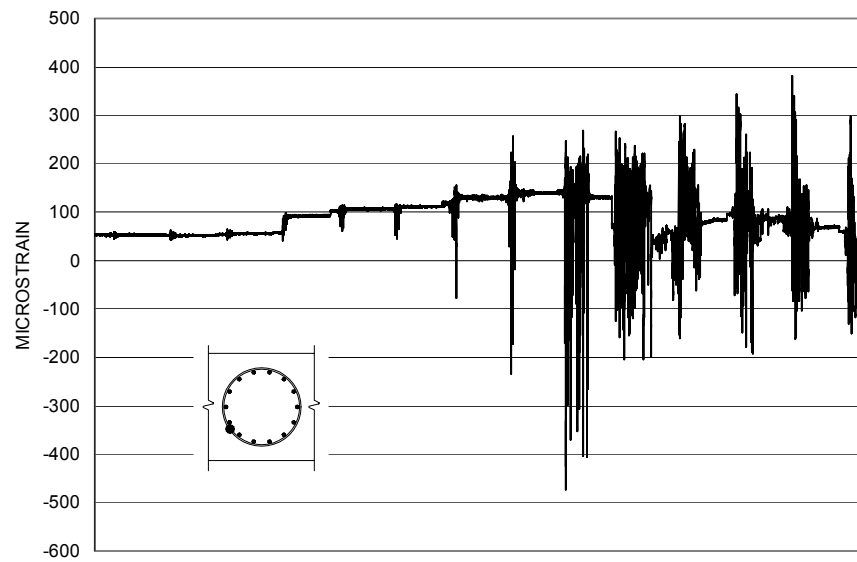
Figure A-96 Measured Strain in SG41 for SFCD3
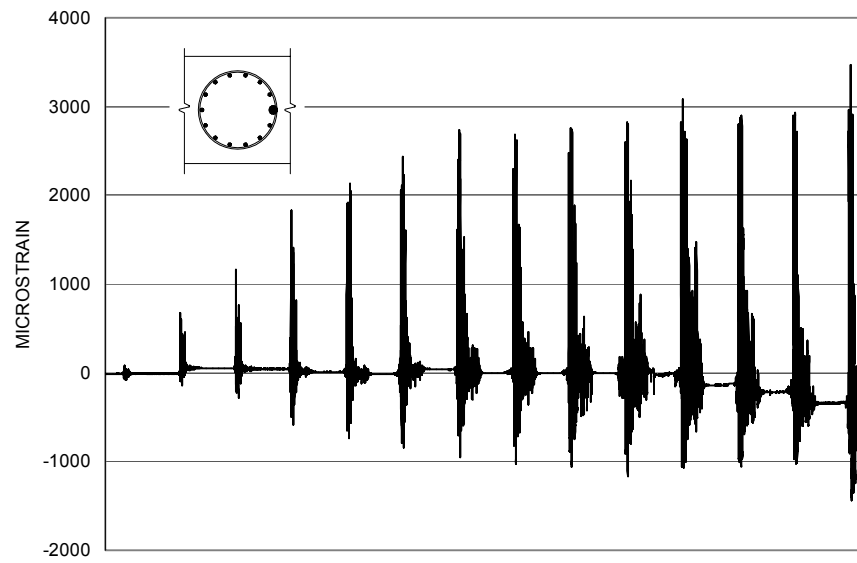
Figure A-97 Measured Strain in SG42 for SFCD3
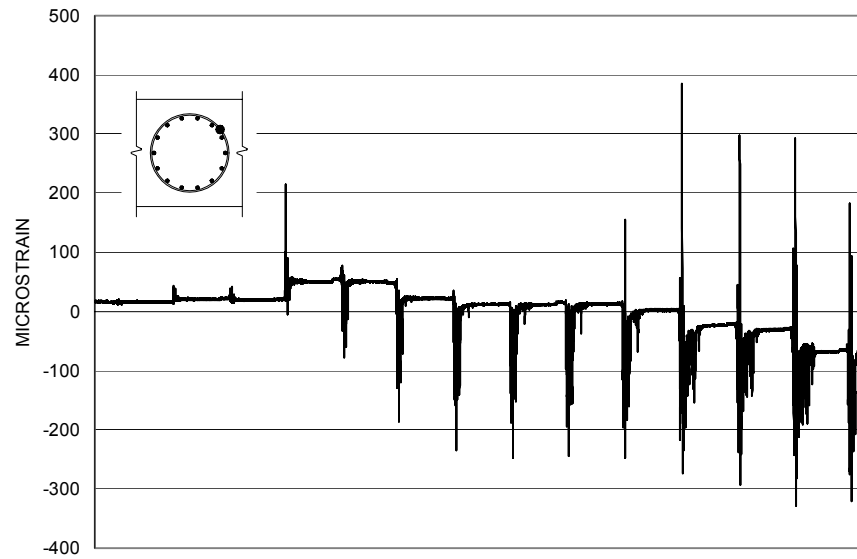
Figure A-98 Measured Strain in SG43 for SFCD3
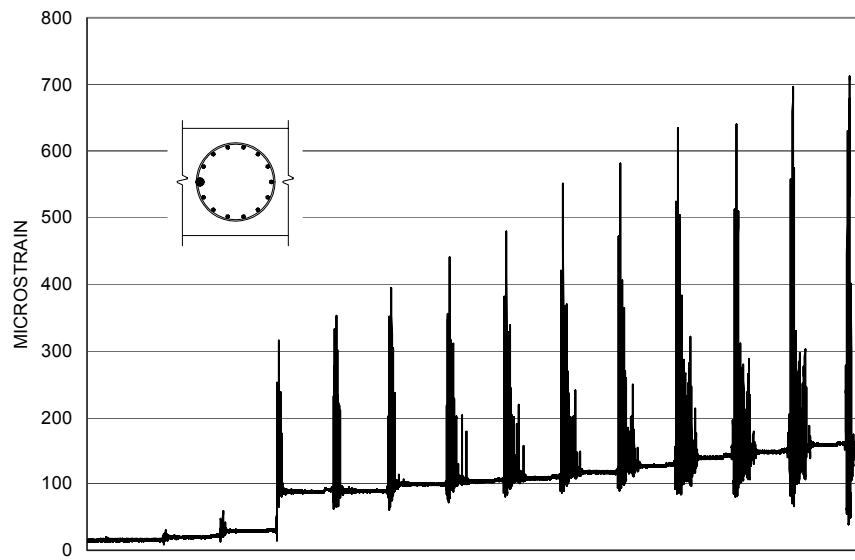
Figure A-99 Measured Strain in SG44 for SFCD3
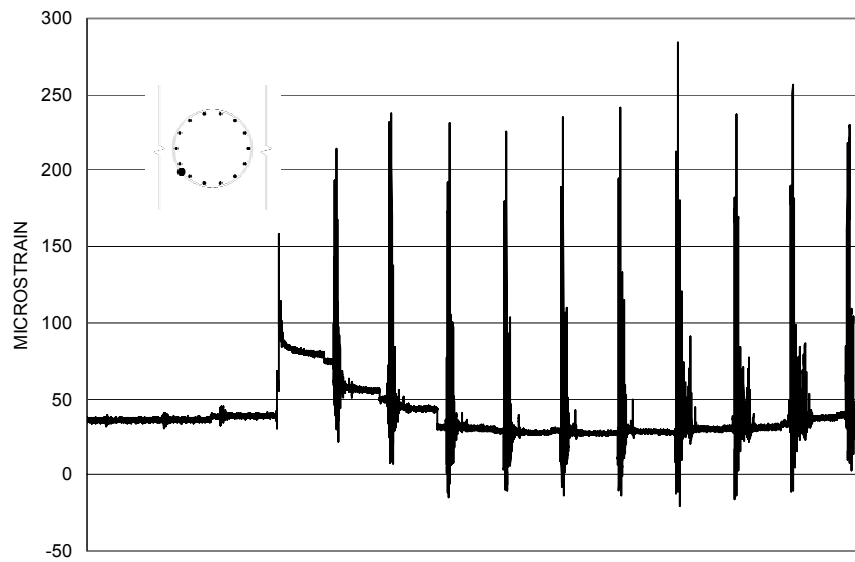
Figure A-100 Measured Strain in SG45 for SFCD3
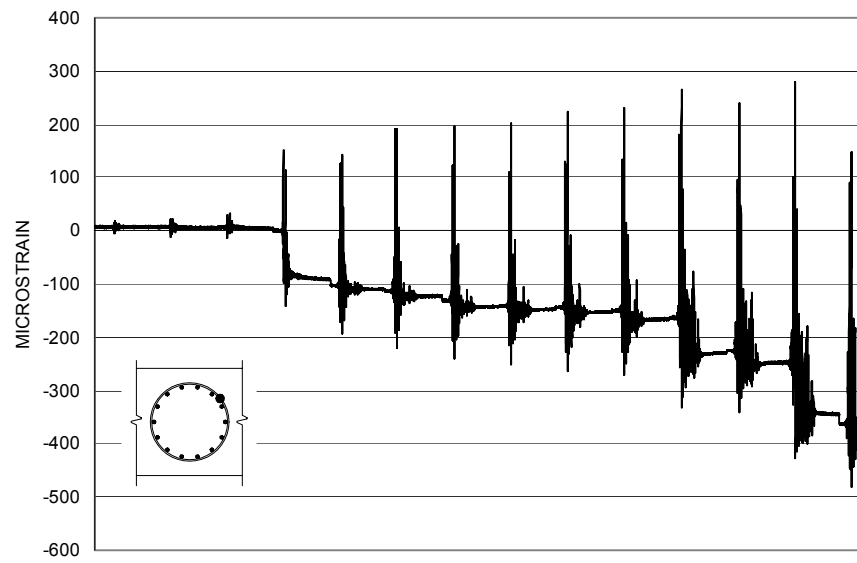
Figure A-101 Measured Strain in SG47 for SFCD3
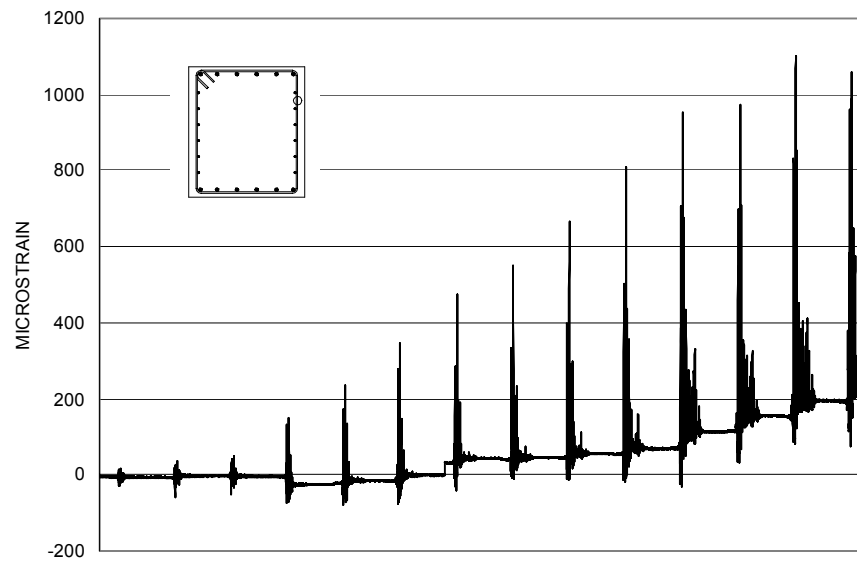
Figure A-102 Measured Strain in SG48 for SFCD3
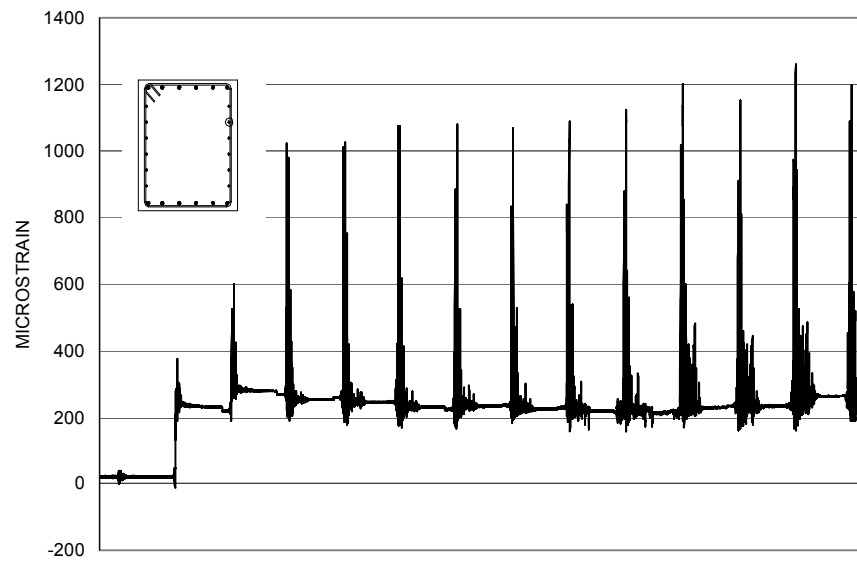
Figure A-103 Measured Strain in SG49 for SFCD3
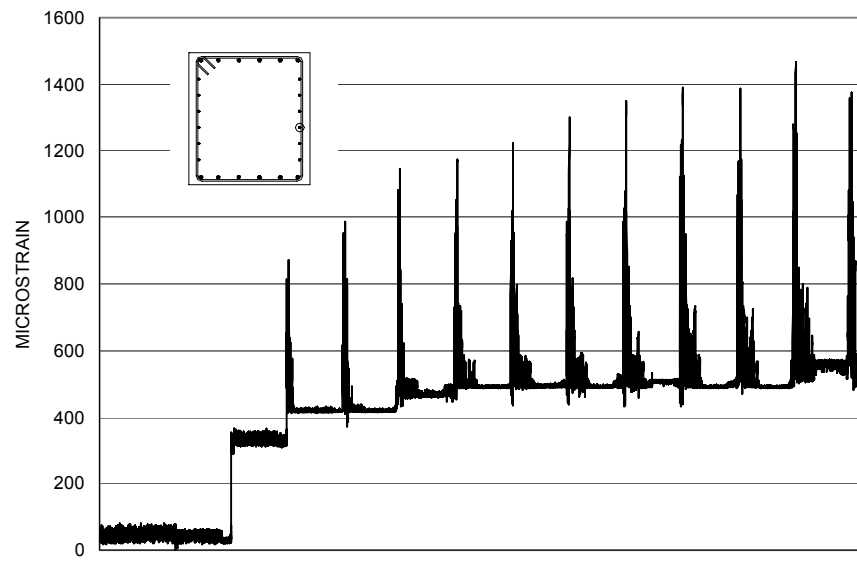
Figure A-104 Measured Strain in SG50 for SFCD3
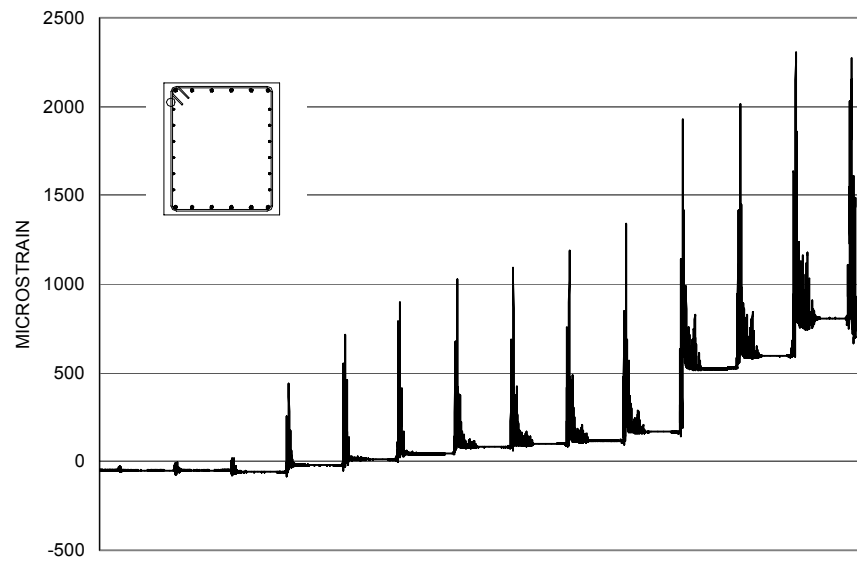
Figure A-105 Measured Strain in SG52 for SFCD3
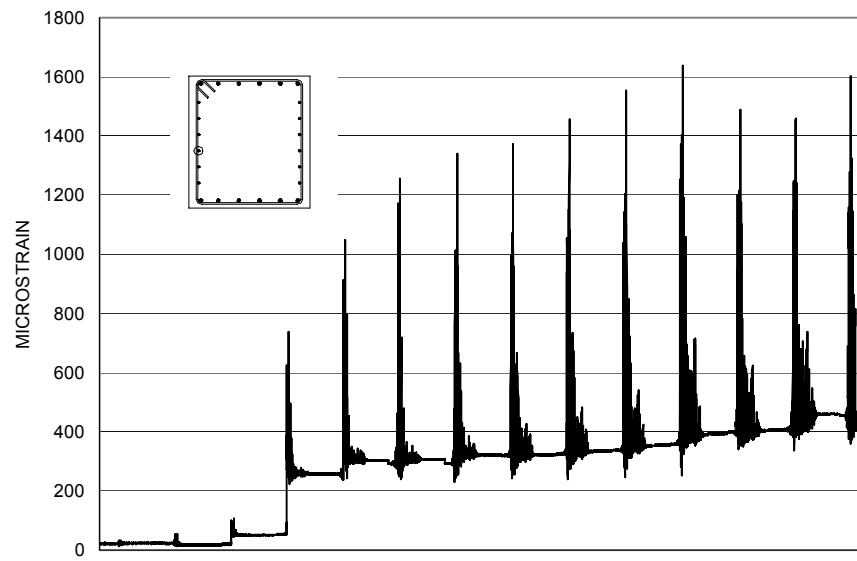
Figure A-106 Measured Strain in SG53 for SFCD3

246
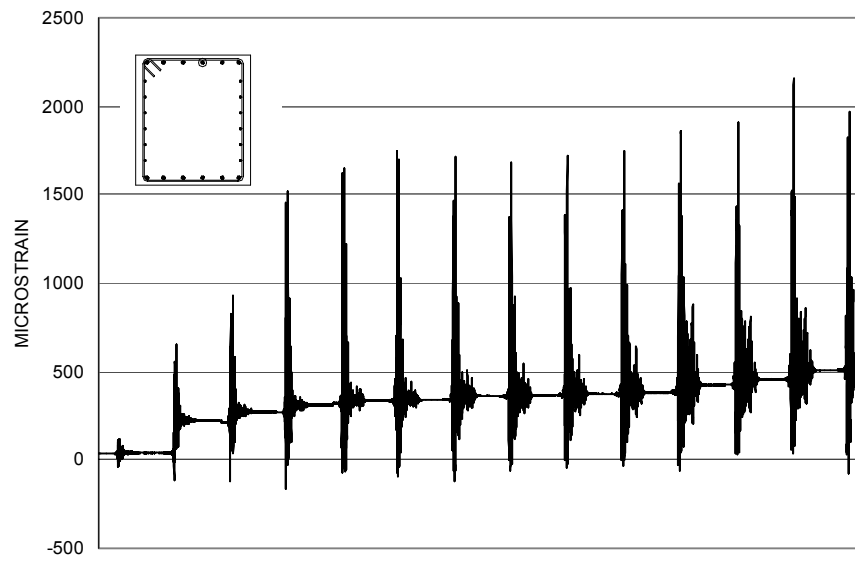
Figure A-107 Measured Strain in SG54 for SFCD3
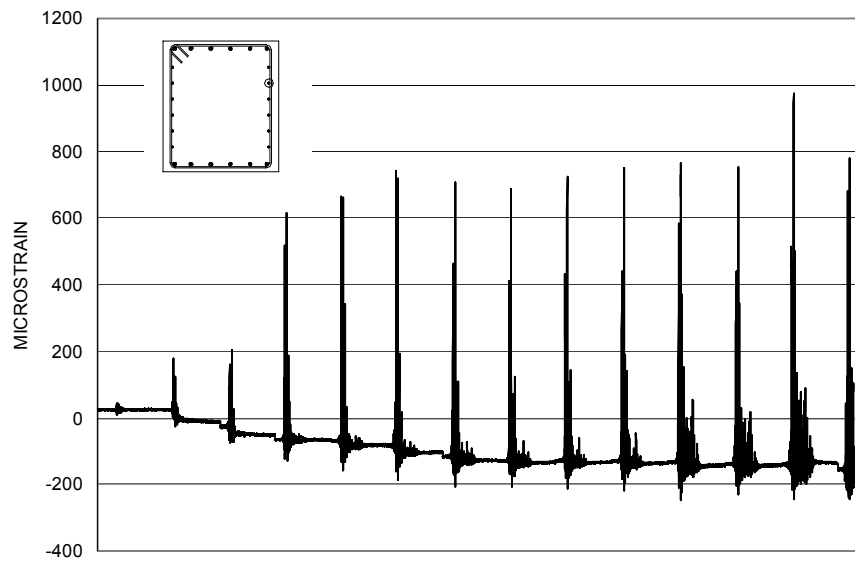
Figure A-108 Measured Strain in SG55 for SFCD3
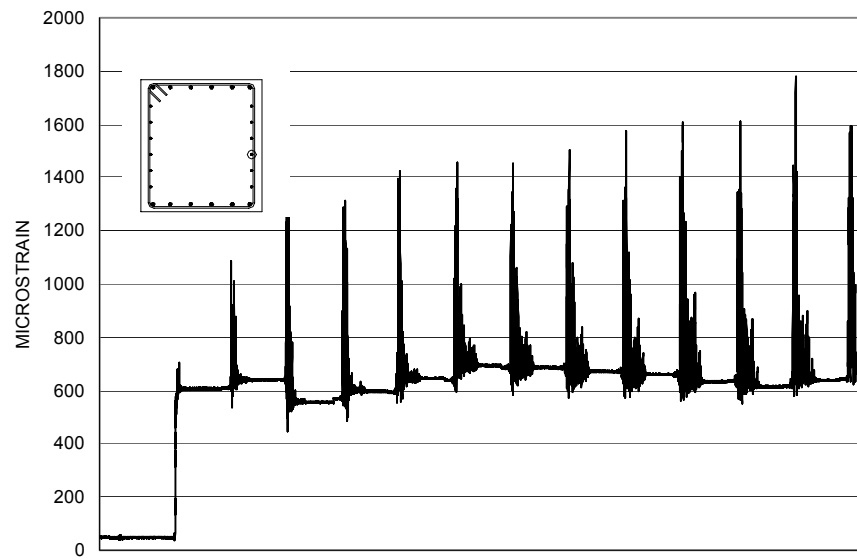
Figure A-109 Measured Strain in SG56 for SFCD3
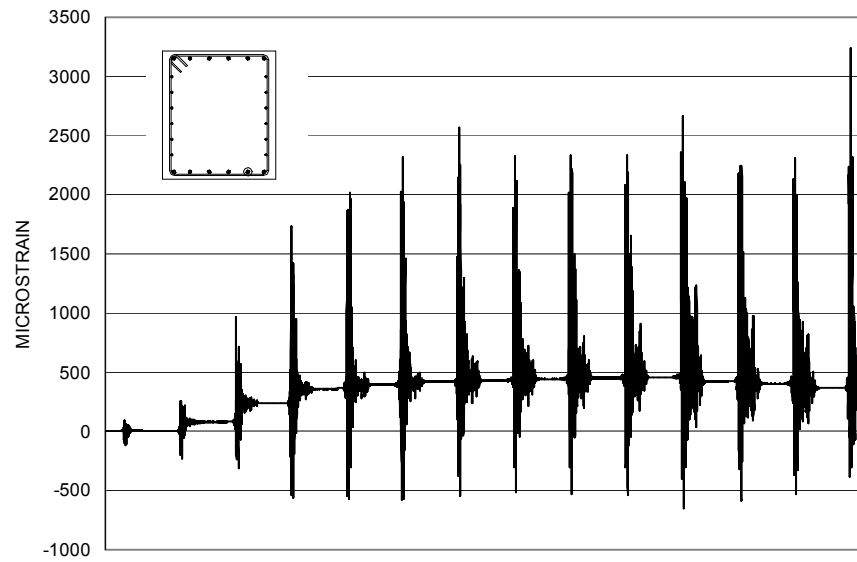
Figure A-110 Measured Strain in SG58 for SFCD3
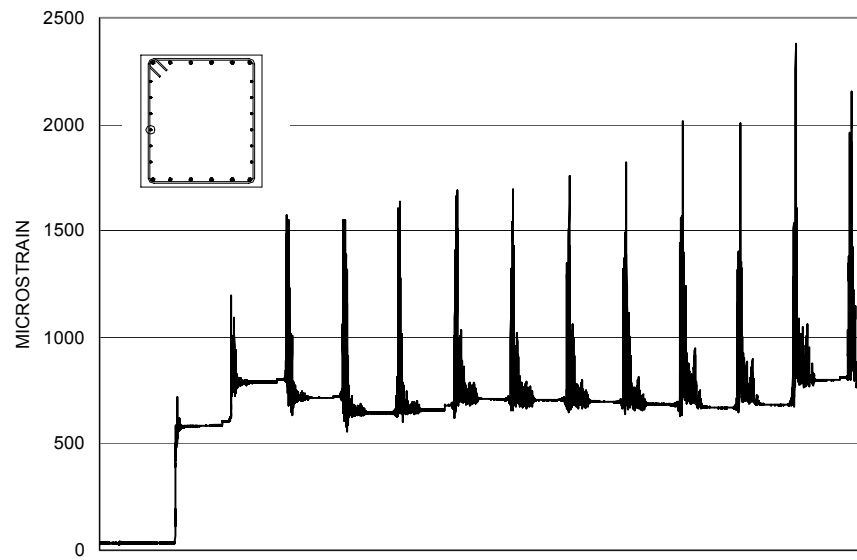
Figure A-111 Measured Strain in SG59 for SFCD3
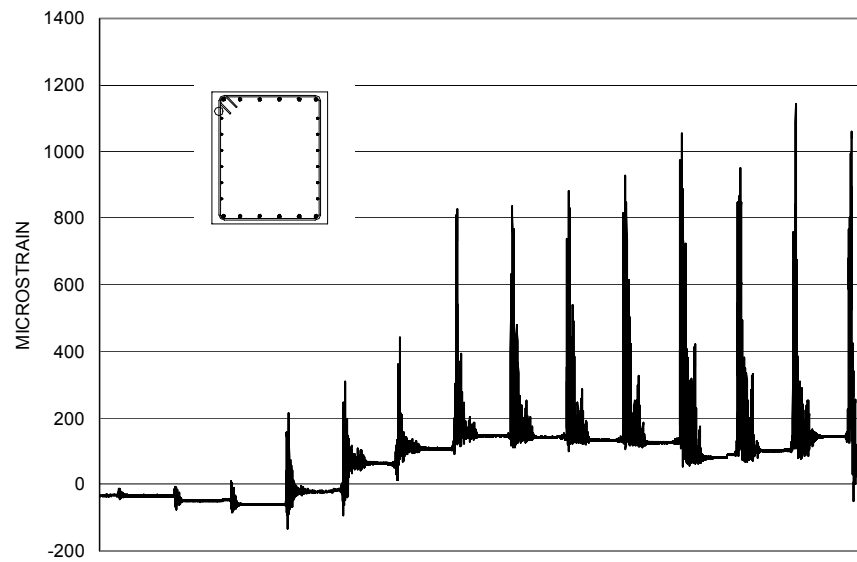
Figure A-112 Measured Strain in SG60 for SFCD3
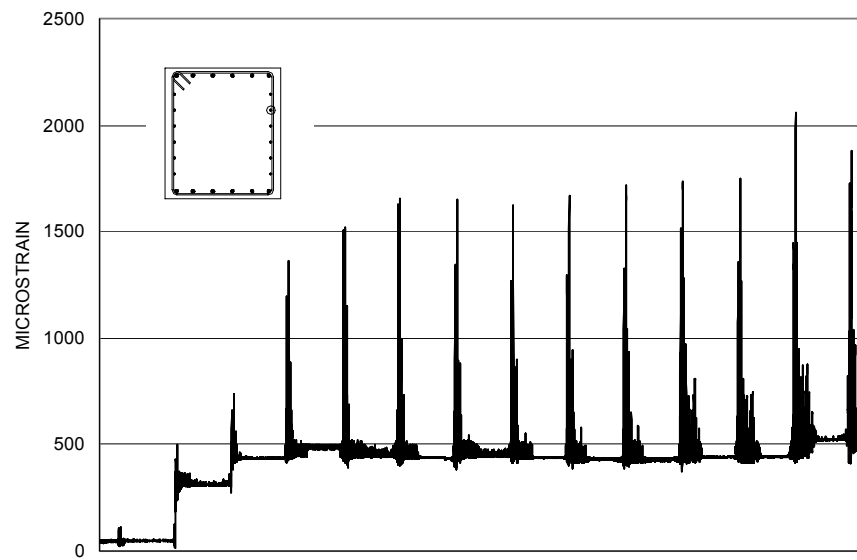
Figure A-113 Measured Strain in SG62 for SFCD3
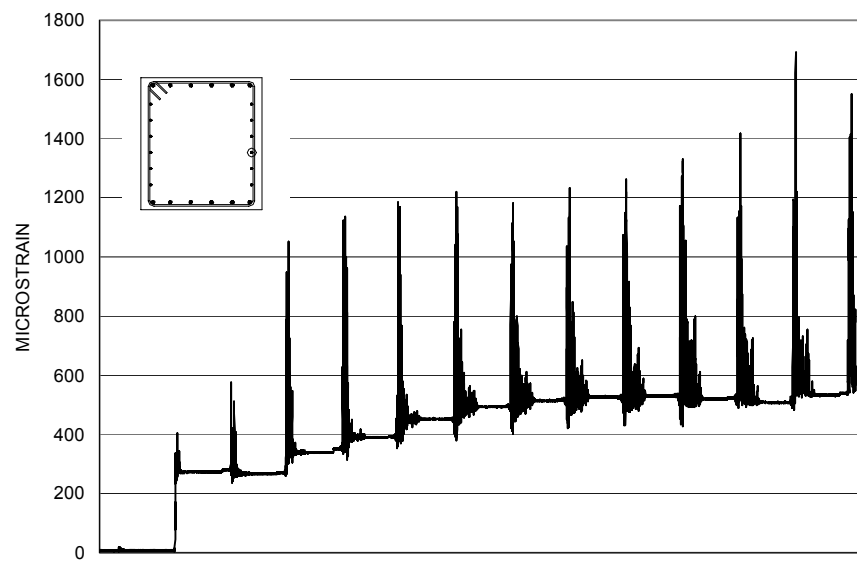
Figure A-114 Measured Strain in SG63 for SFCD3
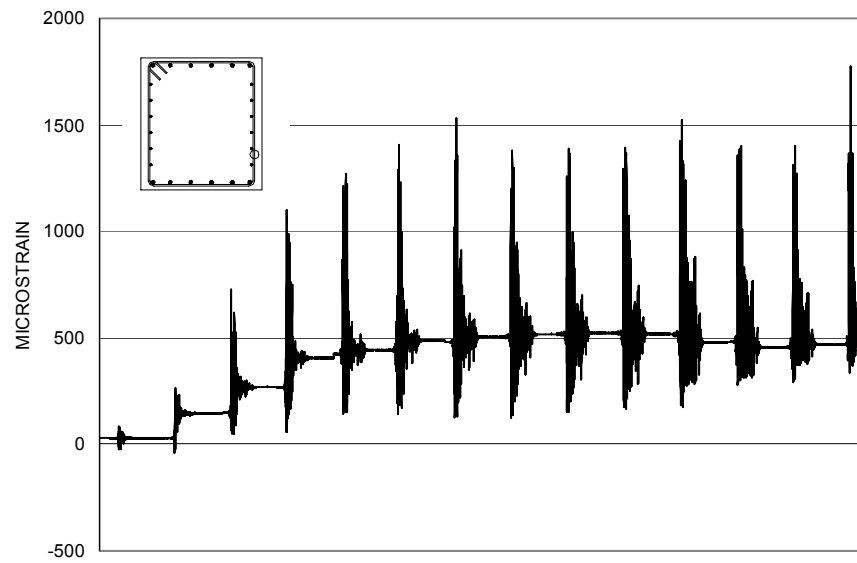
Figure A-115 Measured Strain in SG64 for SFCD3
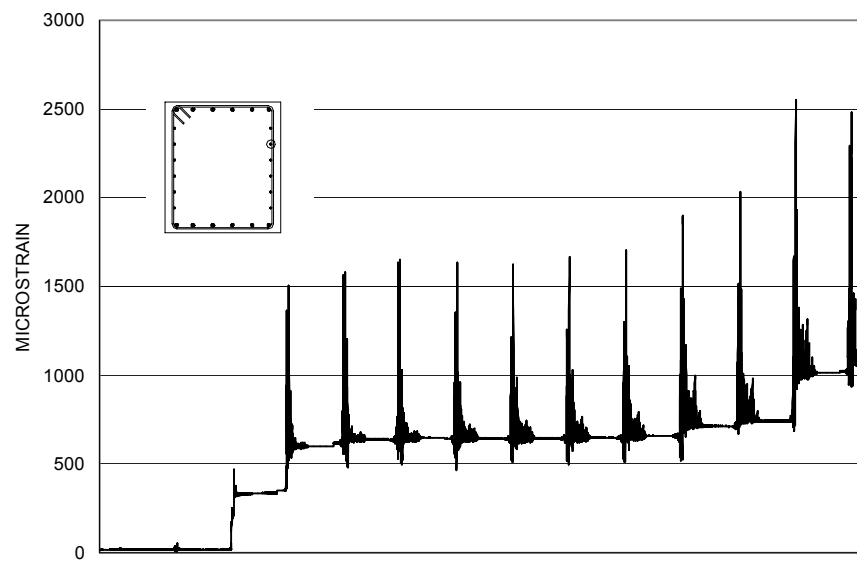
Figure A-116 Measured Strain in SG67 for SFCD3
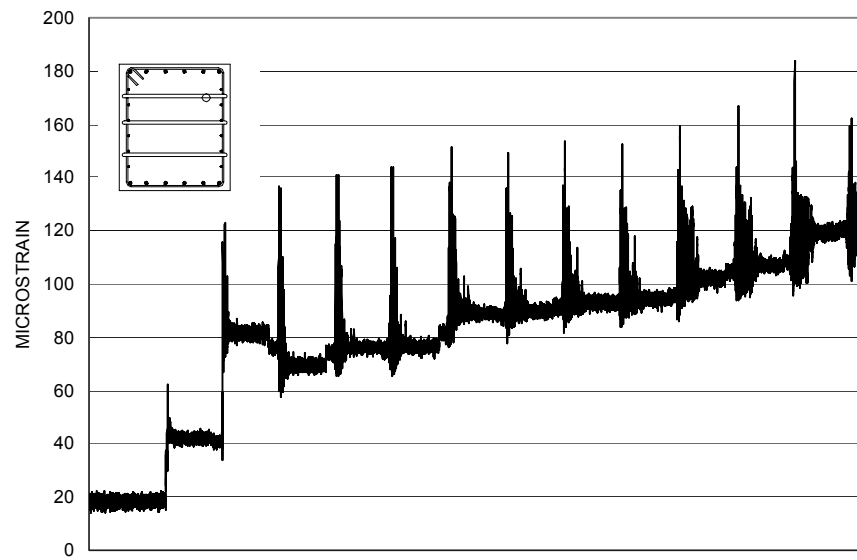
Figure A-117 Measured Strain in SG68 for SFCD3
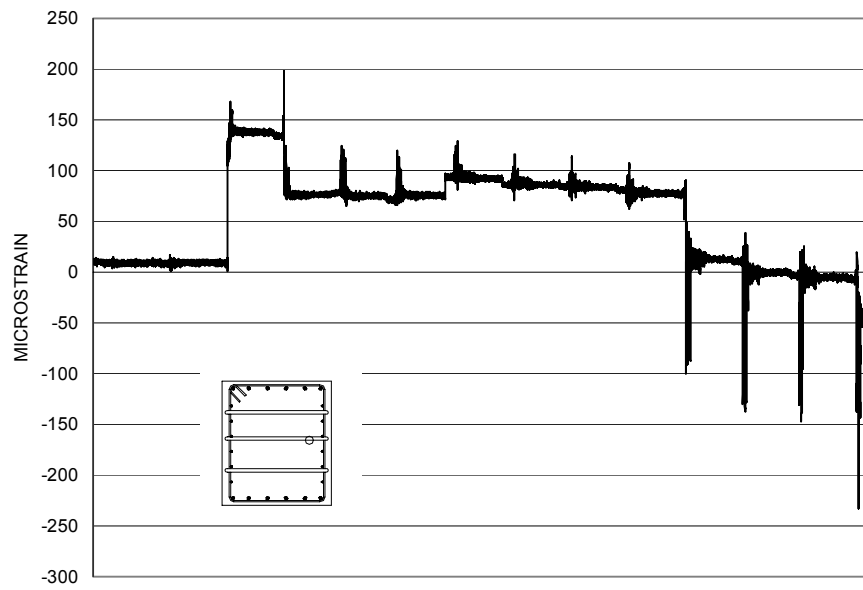
Figure A-118 Measured Strain in SG69 for SFCD3
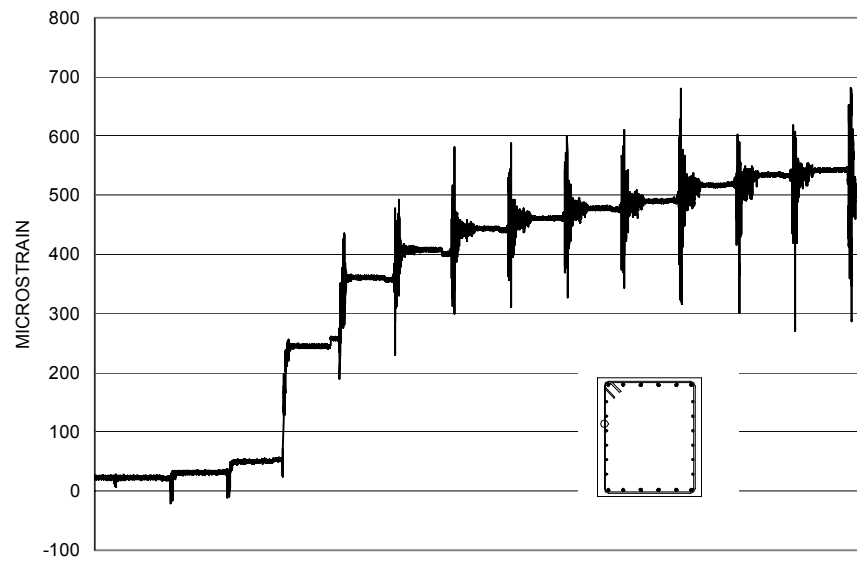
Figure A-119 Measured Strain in SG71 for SFCD3
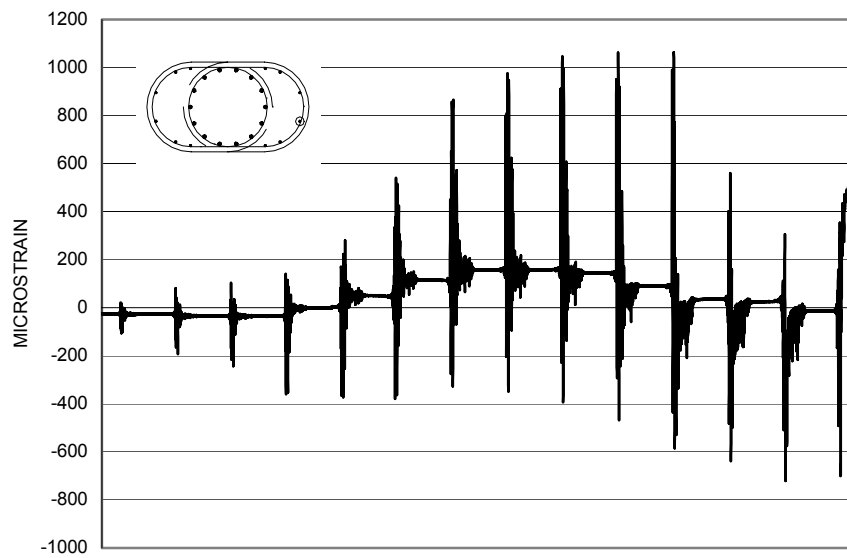
Figure A-120 Measured Strain in SG80 for SFCD3
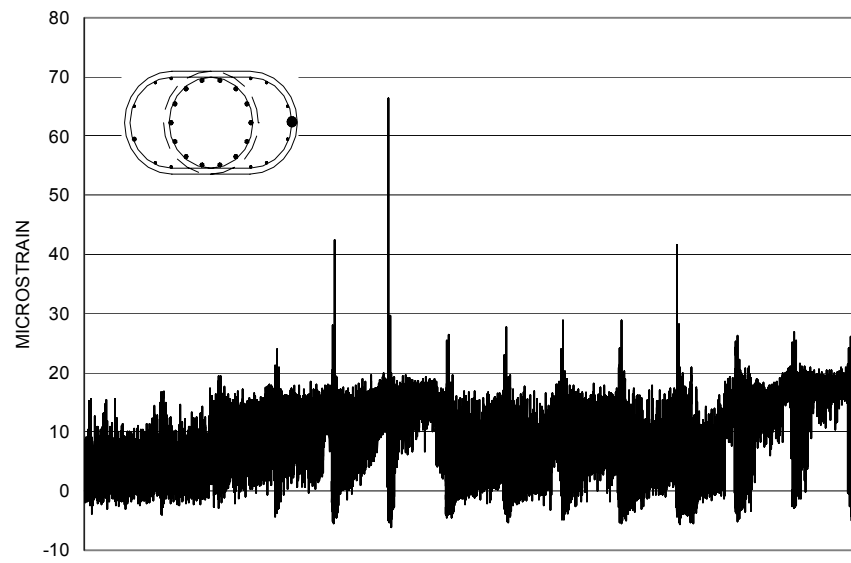
Figure A-121 Measured Strain in SG81 for SFCD3
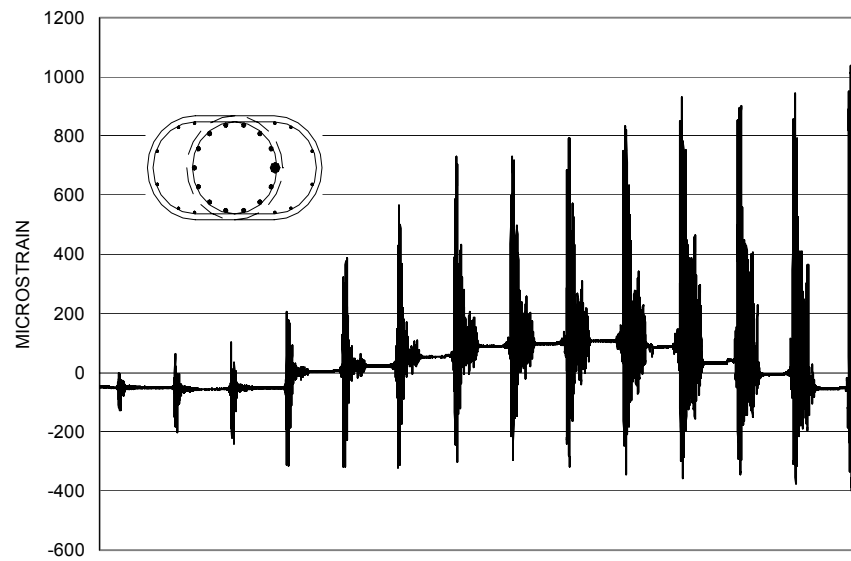
Figure A-122 Measured Strain in SG82 for SFCD3
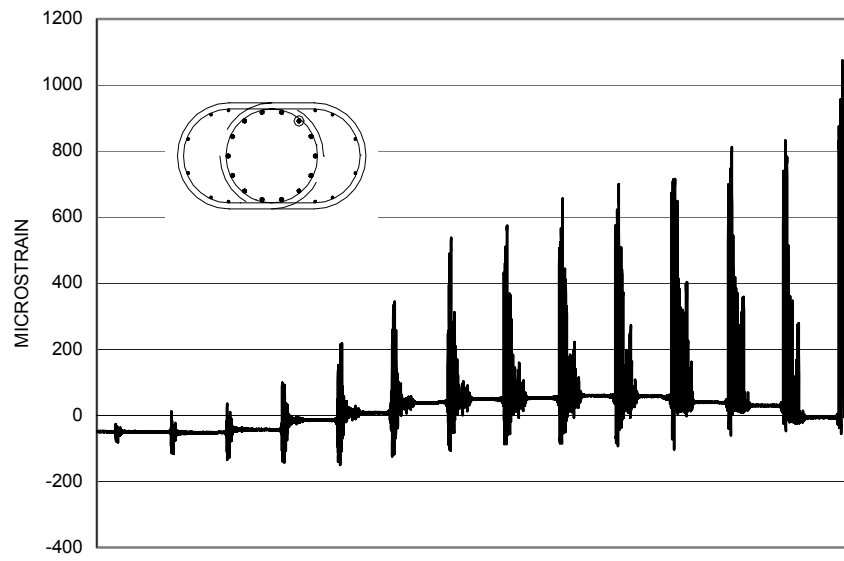
Figure A-123 Measured Strain in SG83 for SFCD3
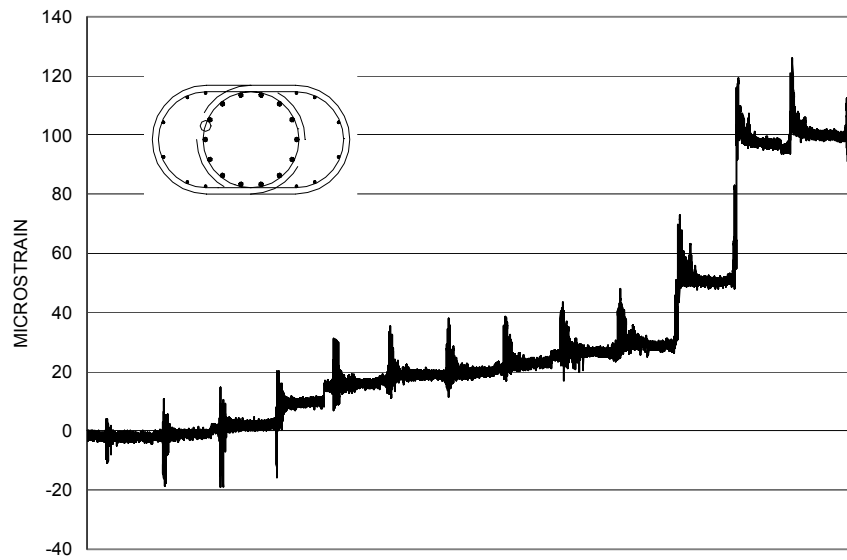
Figure A-124 Measured Strain in SG84 for SFCD3
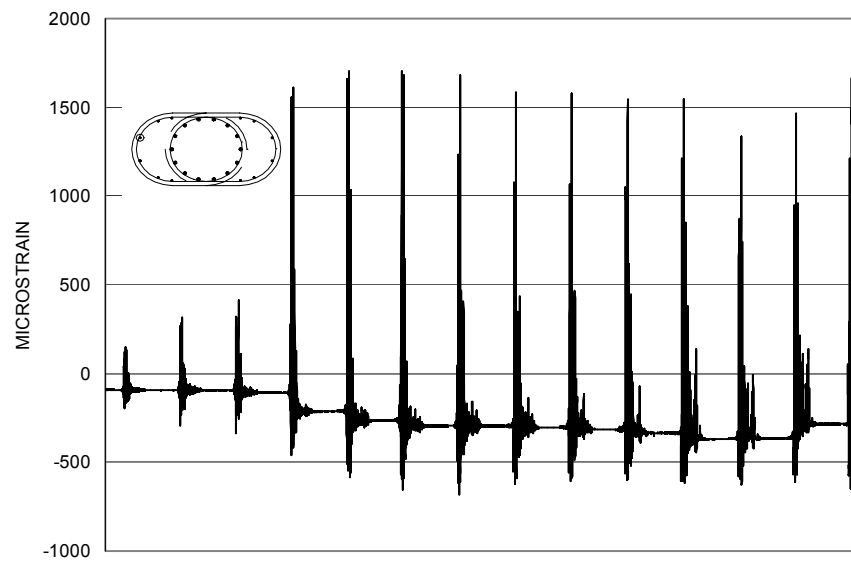
Figure A-125 Measured Strain in SG85 for SFCD3
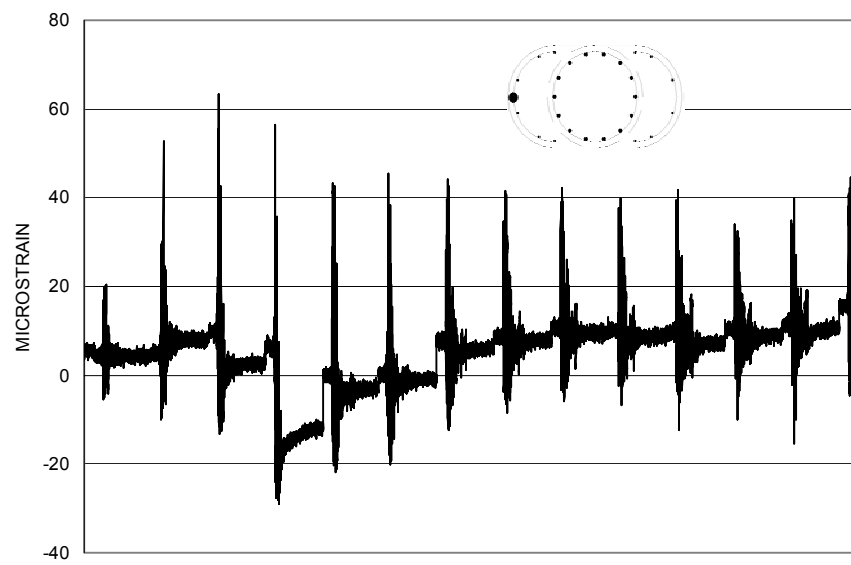
Figure A-126 Measured Strain in SG86 for SFCD3
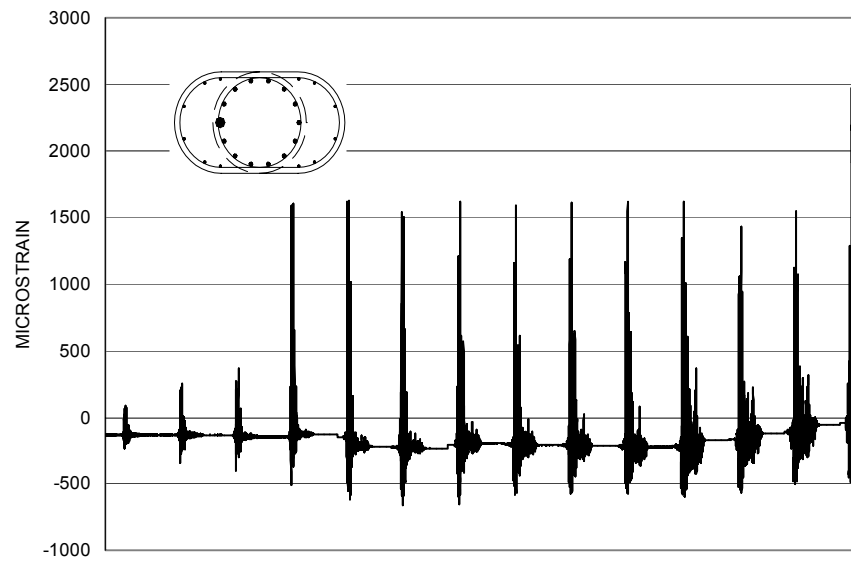
Figure A-127 Measured Strain in SG87 for SFCD3
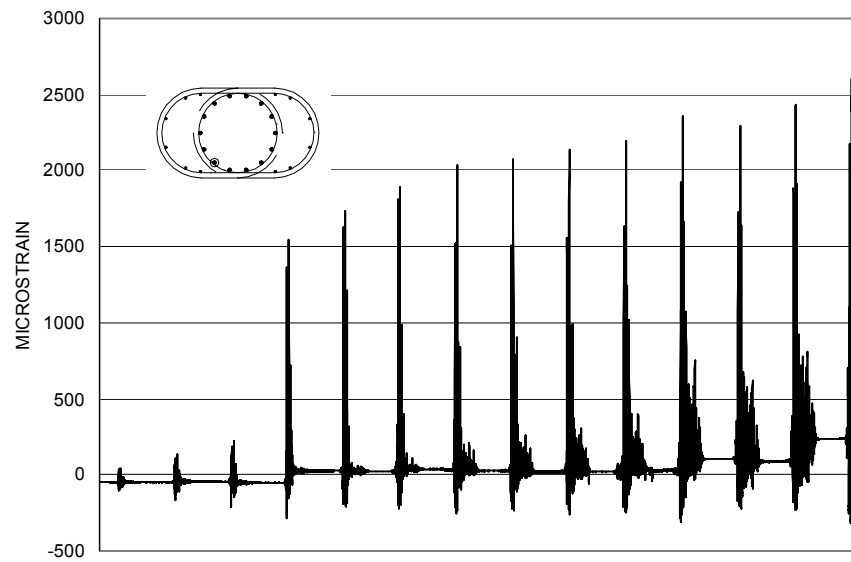
Figure A-128 Measured Strain in SG88 for SFCD3
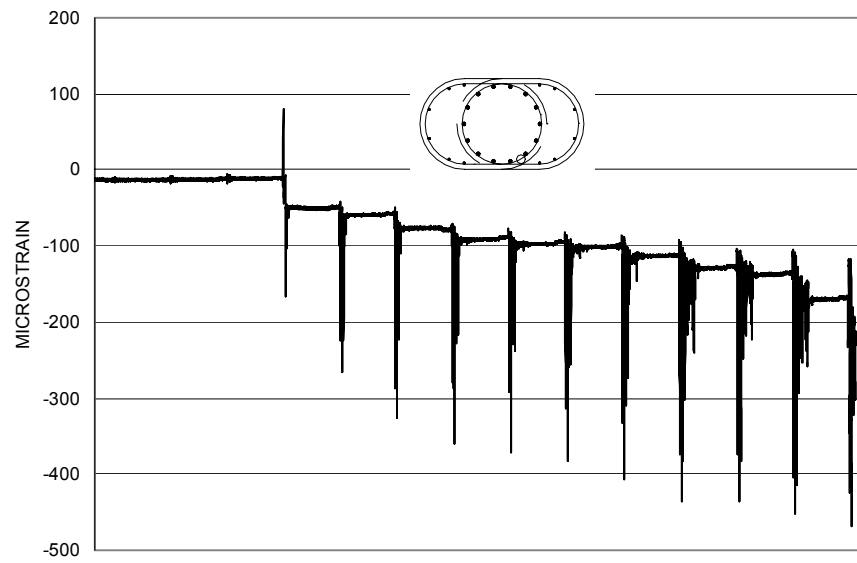
Figure A-129 Measured Strain in SG89 for SFCD3
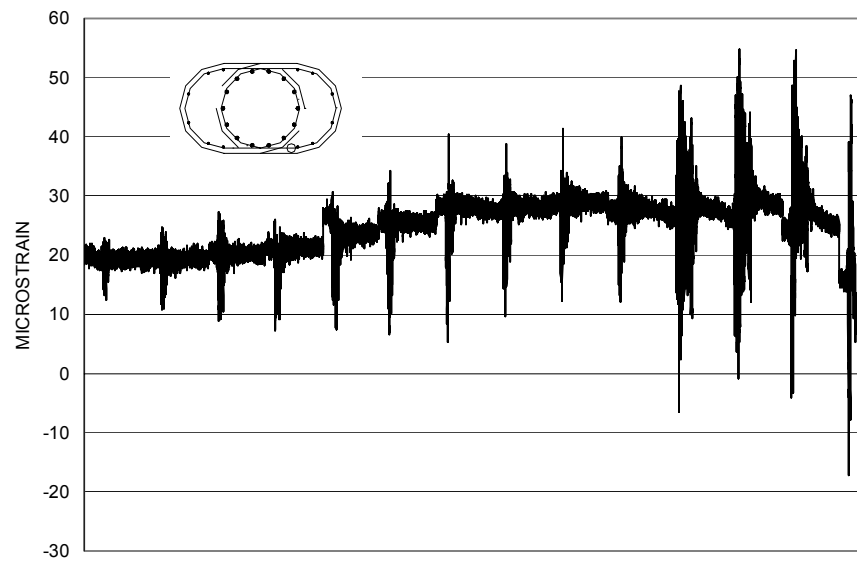
Figure A-130 Measured Strain in SG90 for SFCD3
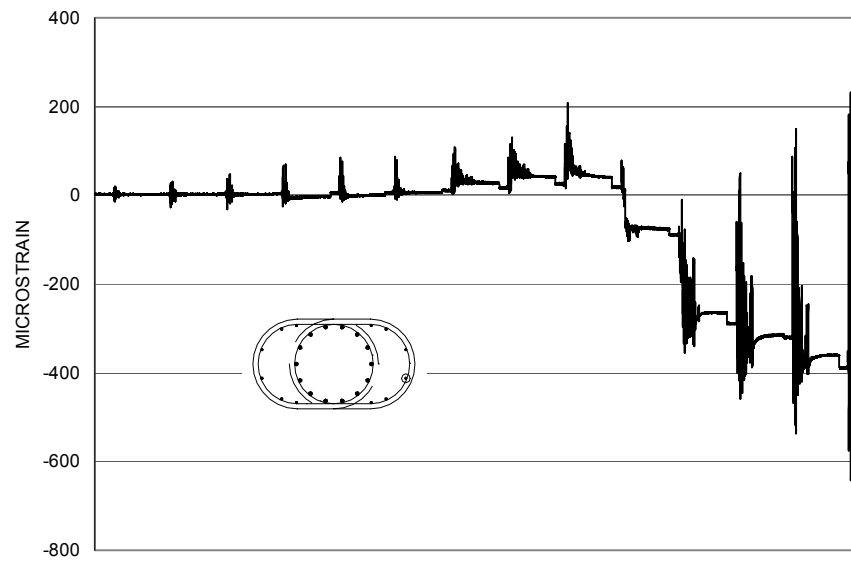
Figure A-131 Measured Strain in SG91 for SFCD3
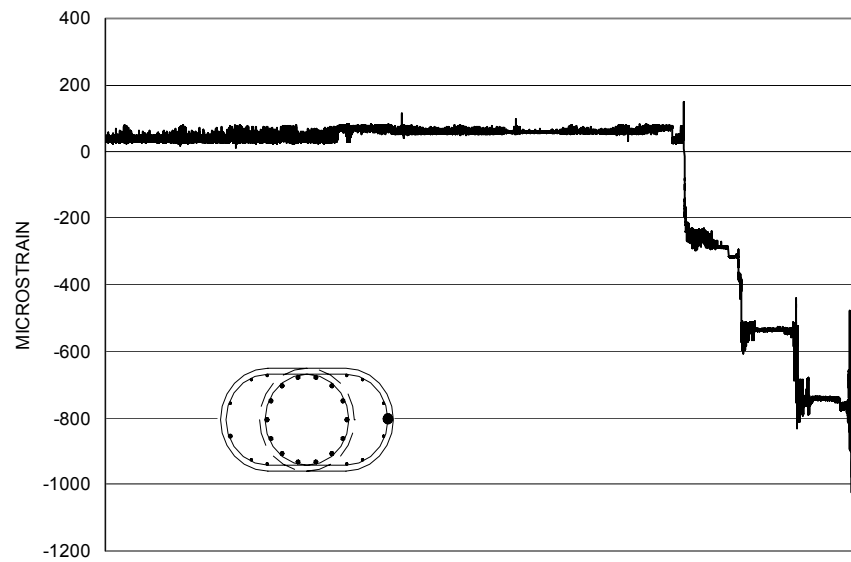
Figure A-132 Measured Strain in SG92 for SFCD3
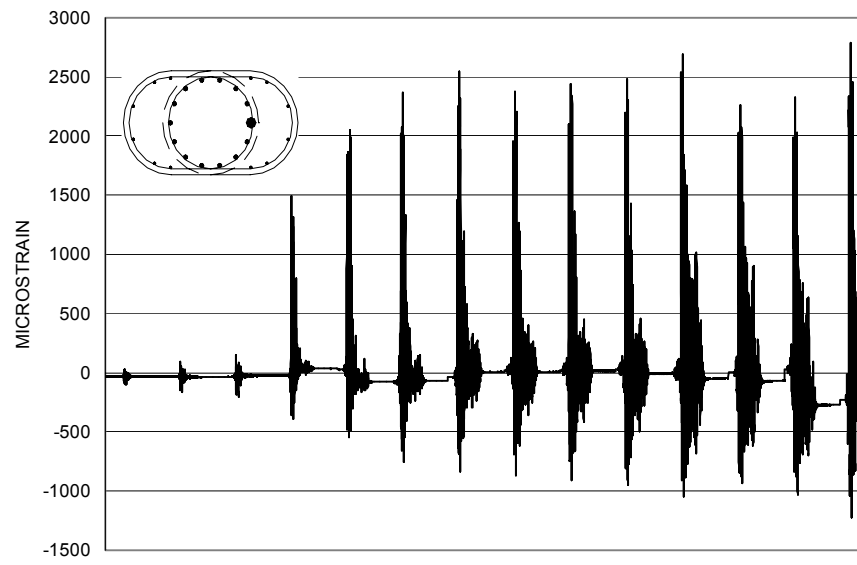
Figure A-133 Measured Strain in SG93 for SFCD3
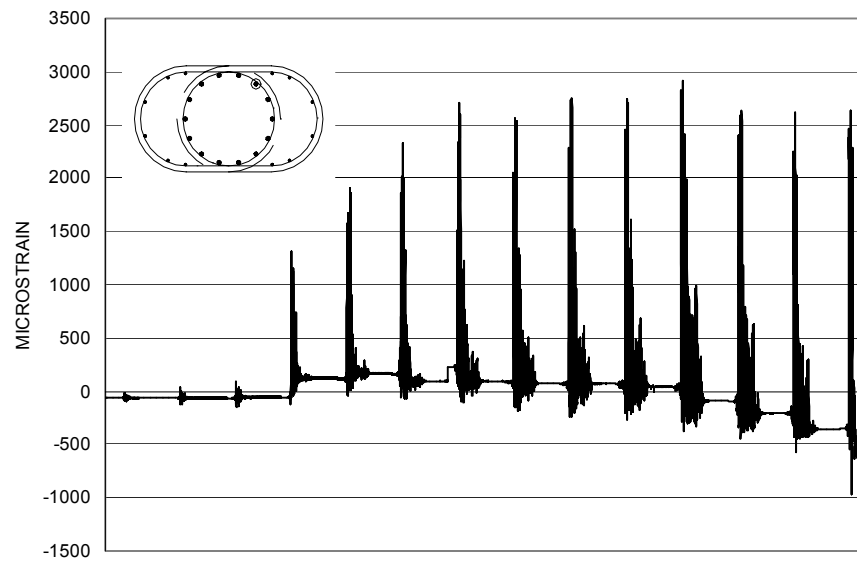
Figure A-134 Measured Strain in SG94 for SFCD3
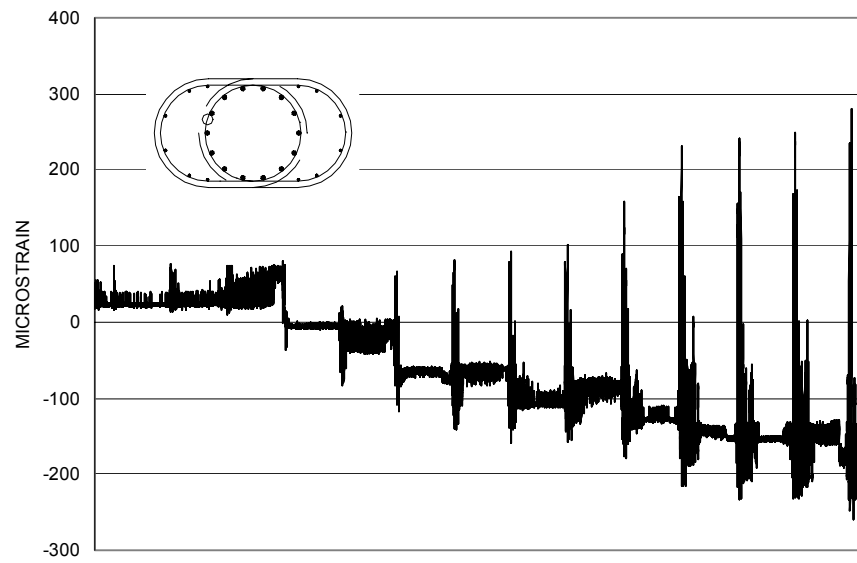
Figure A-135 Measured Strain in SG95 for SFCD3
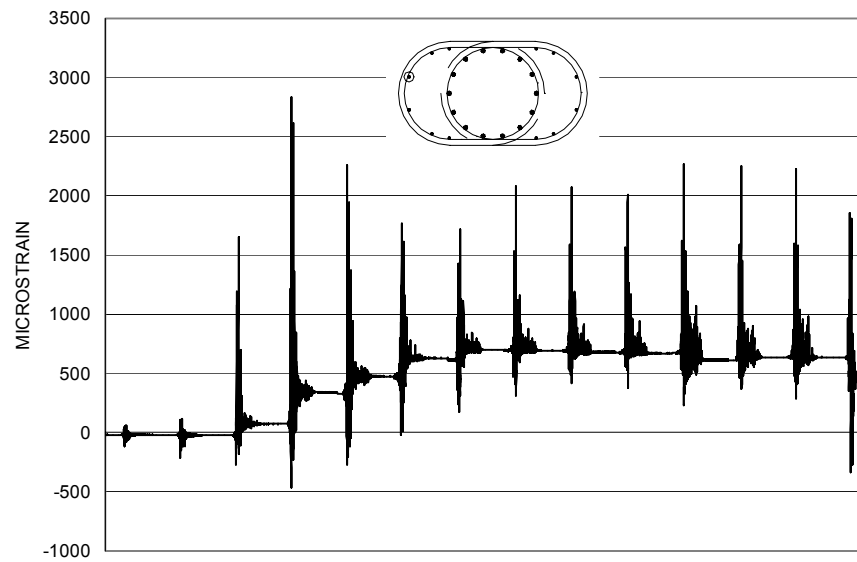
Figure A-136 Measured Strain in SG96 for SFCD3
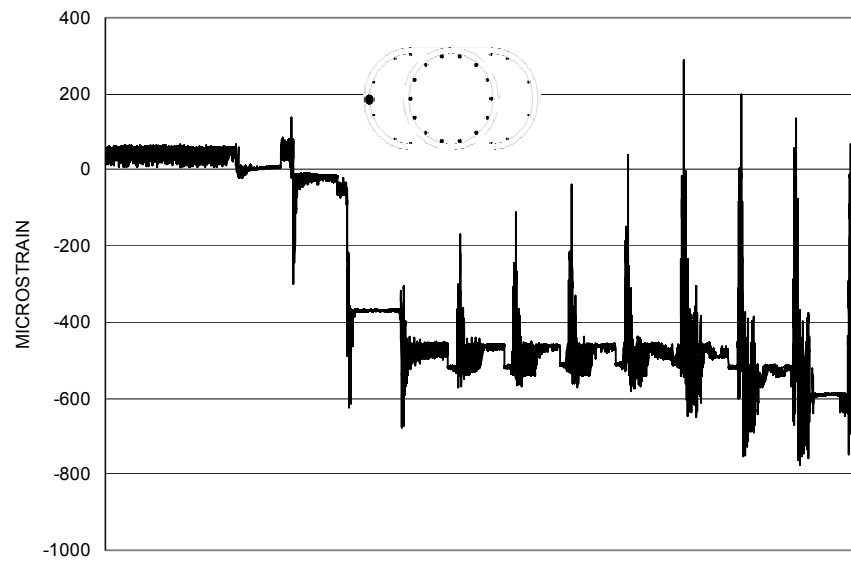
Figure A-137 Measured Strain in SG97 for SFCD3
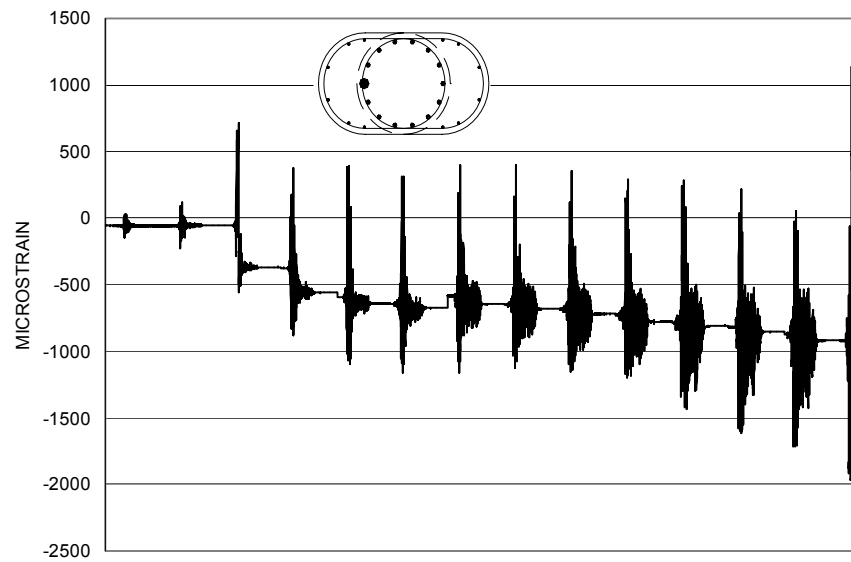
Figure A-138 Measured Strain in SG98 for SFCD3
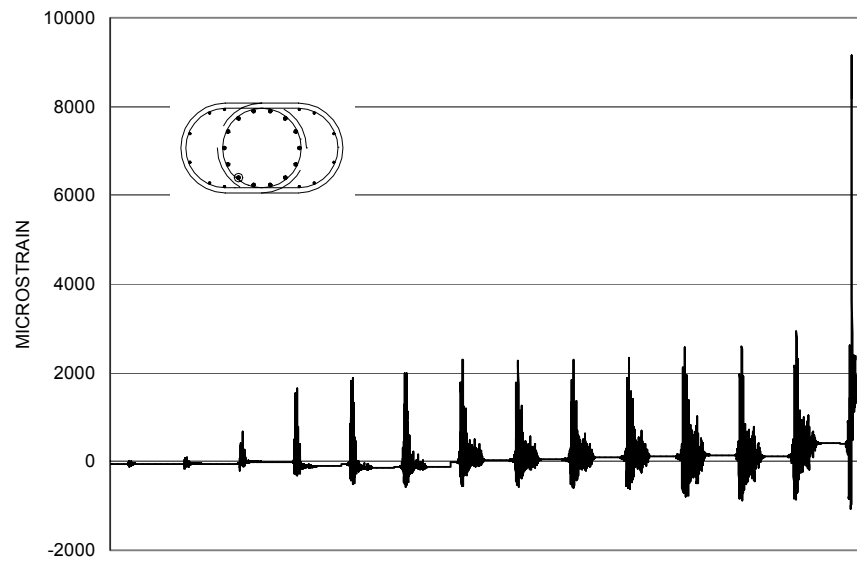
Figure A-139 Measured Strain in SG99 for SFCD3
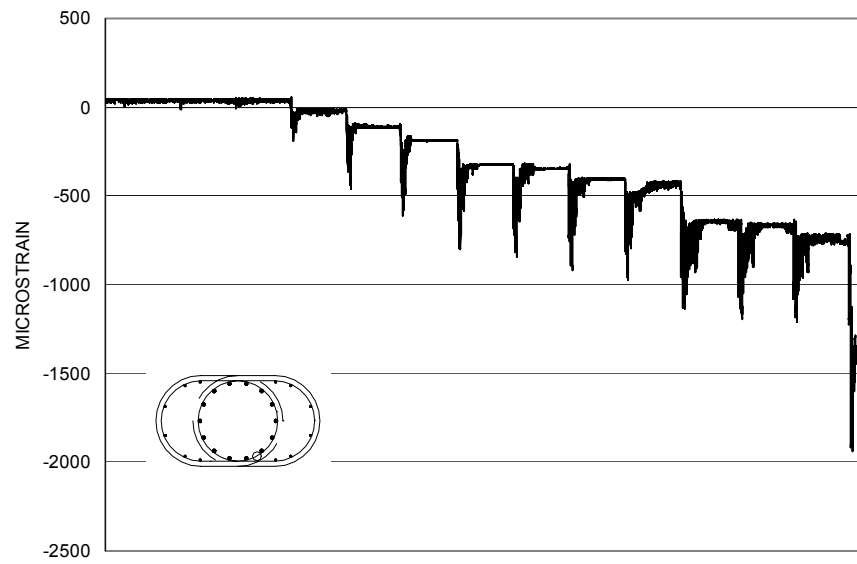
Figure A-140 Measured Strain in SG100 for SFCD3

263
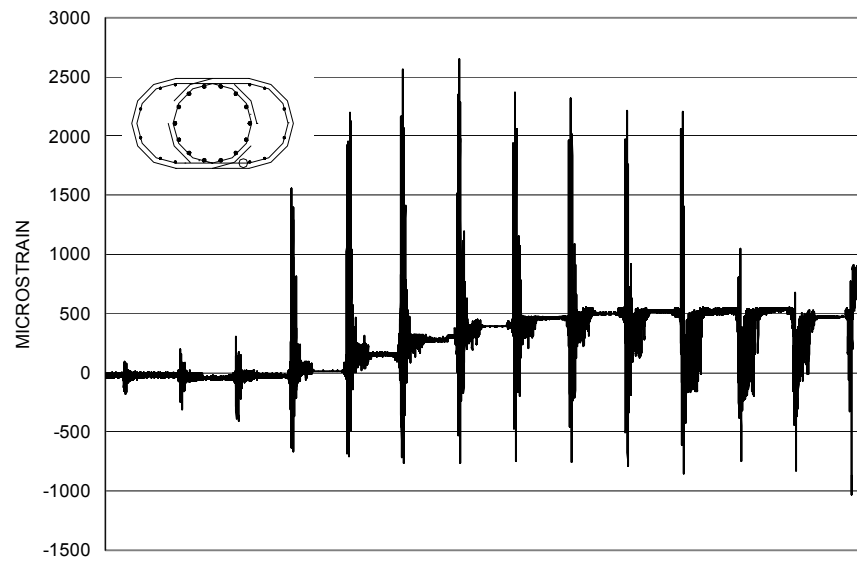
Figure A-141 Measured Strain in SG101 for SFCD3
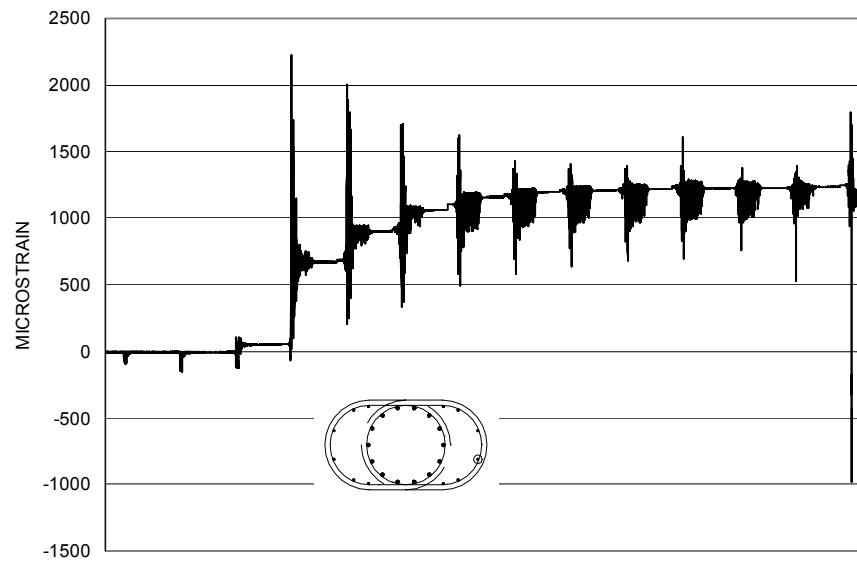
Figure A-142 Measured Strain in SG102 for SFCD3
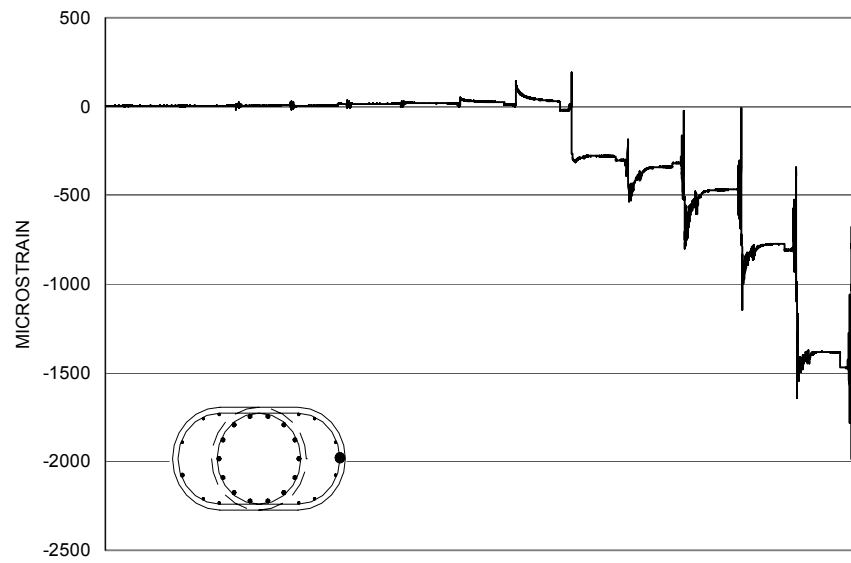
Figure A-143 Measured Strain in SG103 for SFCD3
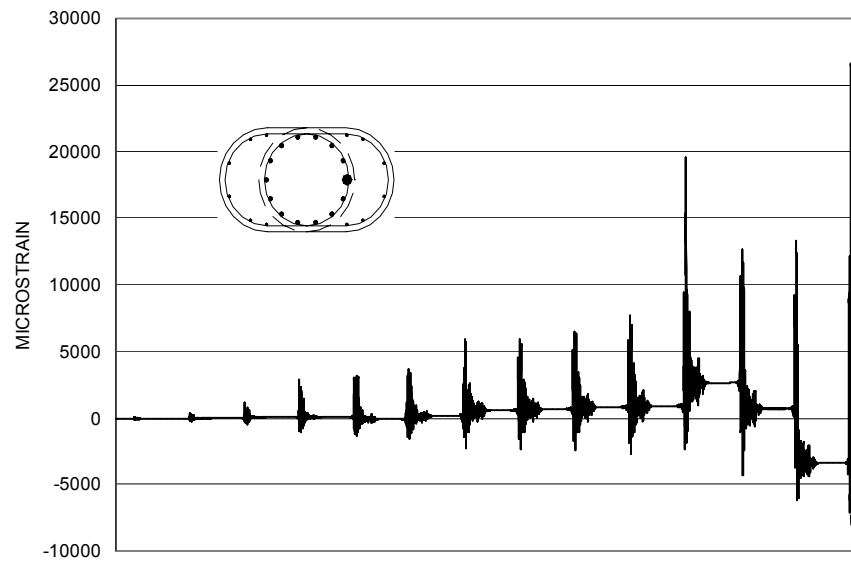
Figure A-144 Measured Strain in SG104 for SFCD3
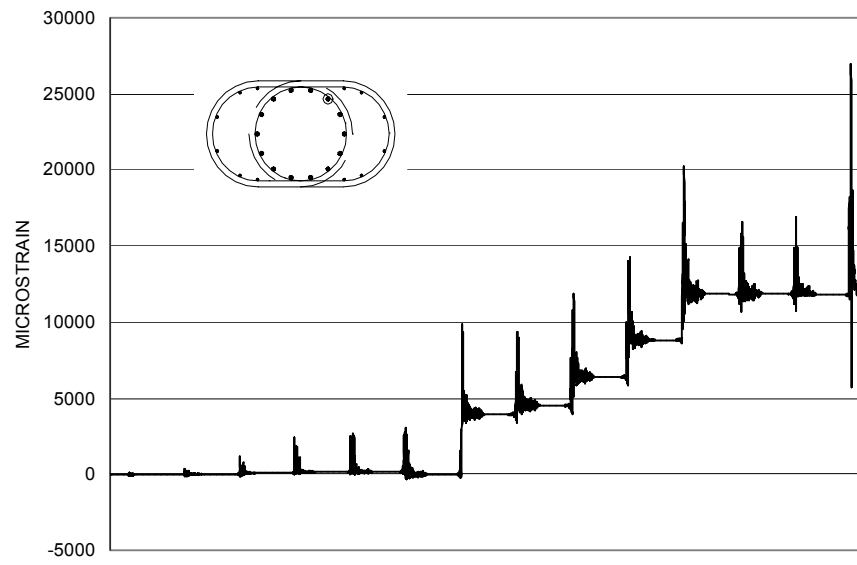
Figure A-145 Measured Strain in SG105 for SFCD3
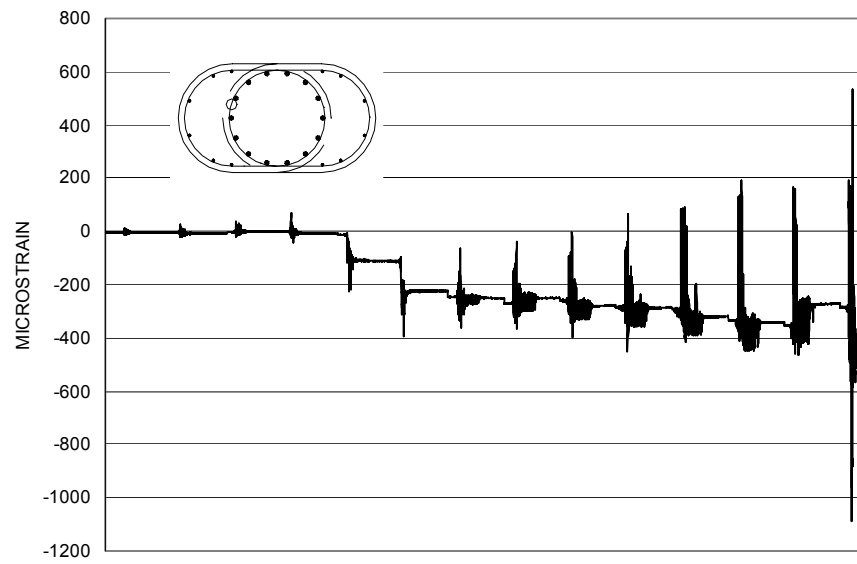
Figure A-146 Measured Strain in SG106 for SFCD3
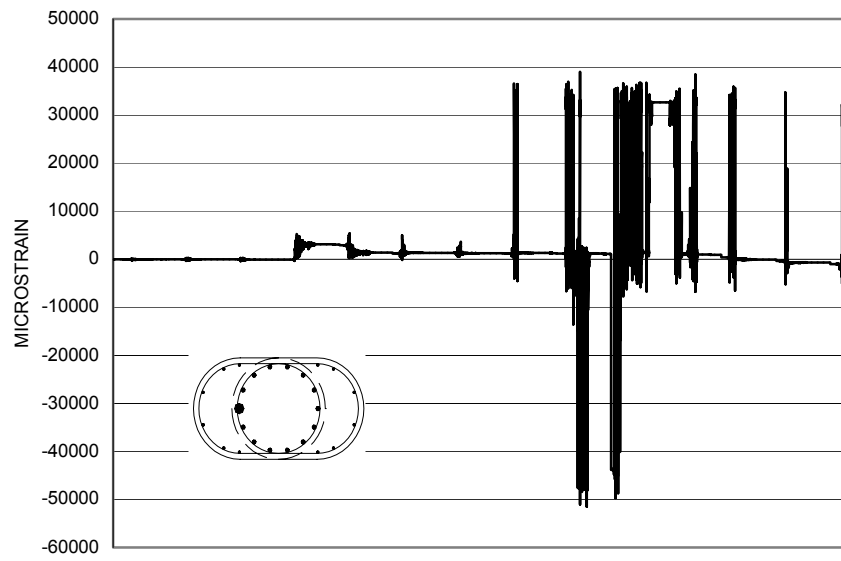
Figure A-147 Measured Strain in SG109 for SFCD3
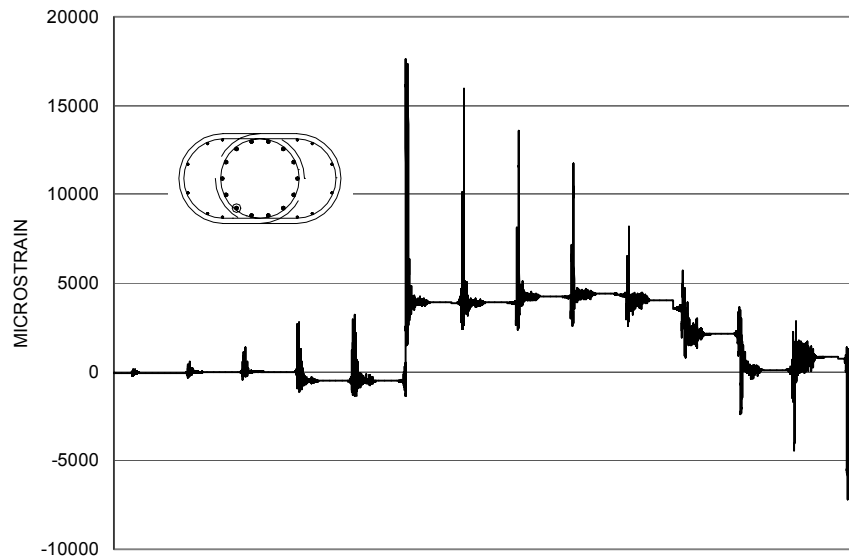
Figure A-148 Measured Strain in SG110 for SFCD3
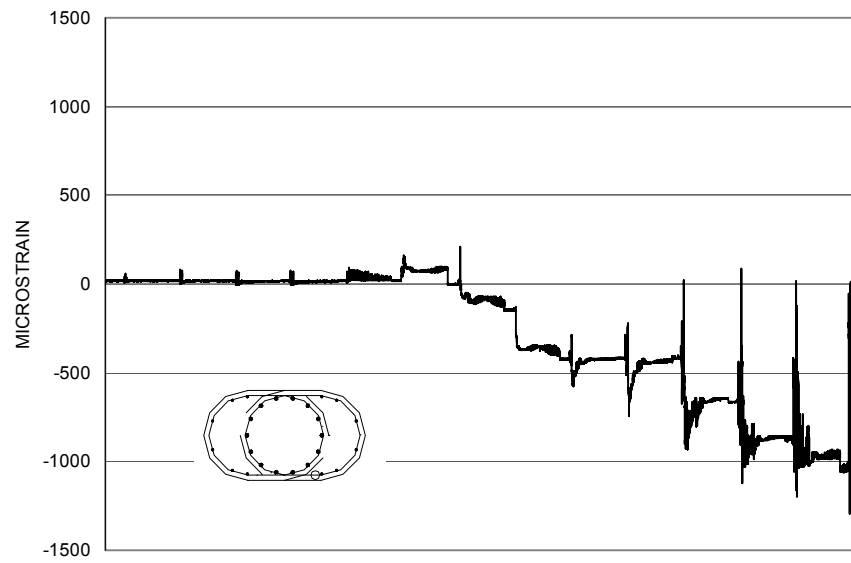
Figure A-149 Measured Strain in SG112 for SFCD3
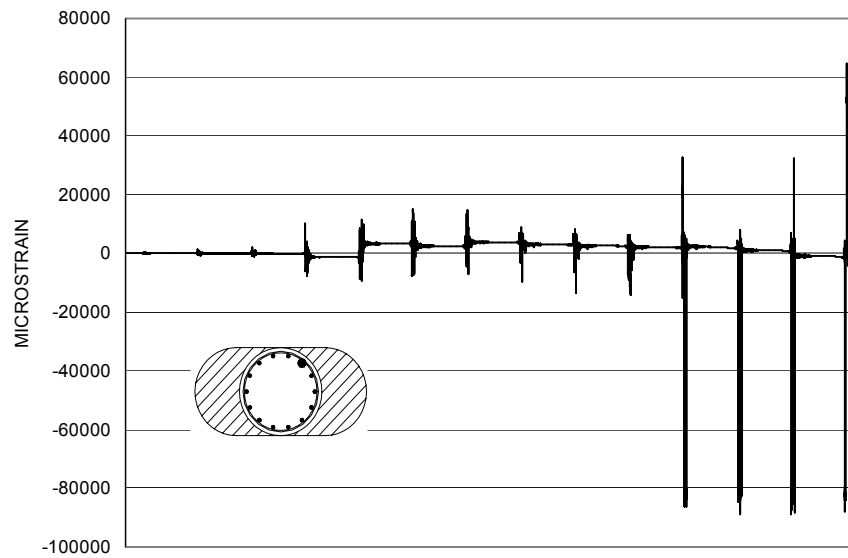
Figure A-150 Measured Strain in SG114 for SFCD3
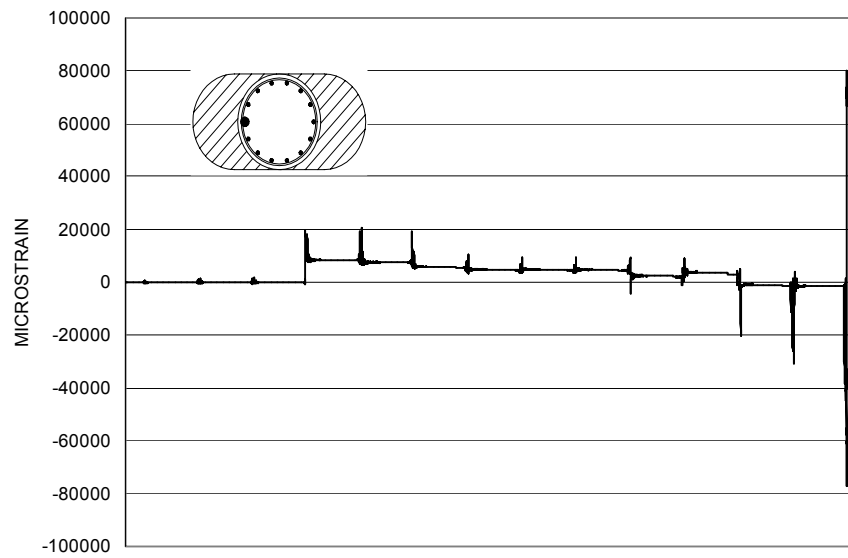
Figure A-151 Measured Strain in SG115 for SFCD3
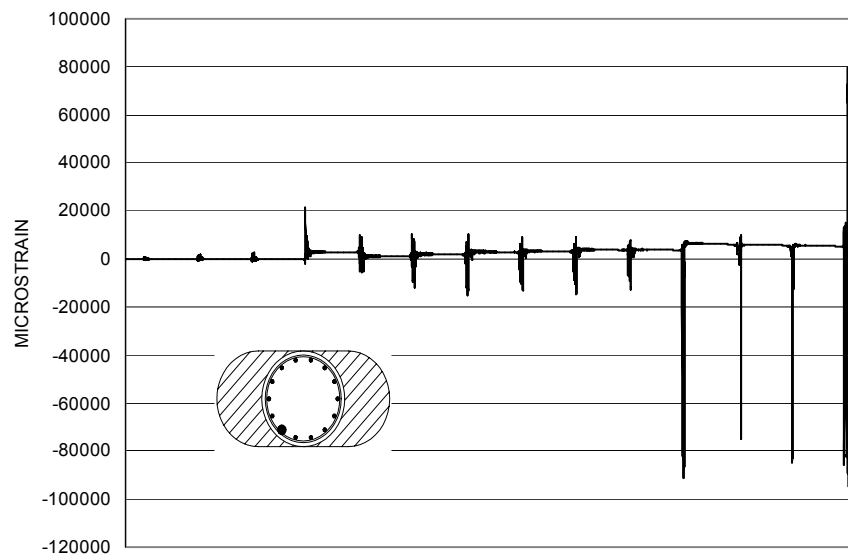
Figure A-152 Measured Strain in SG116 for SFCD3
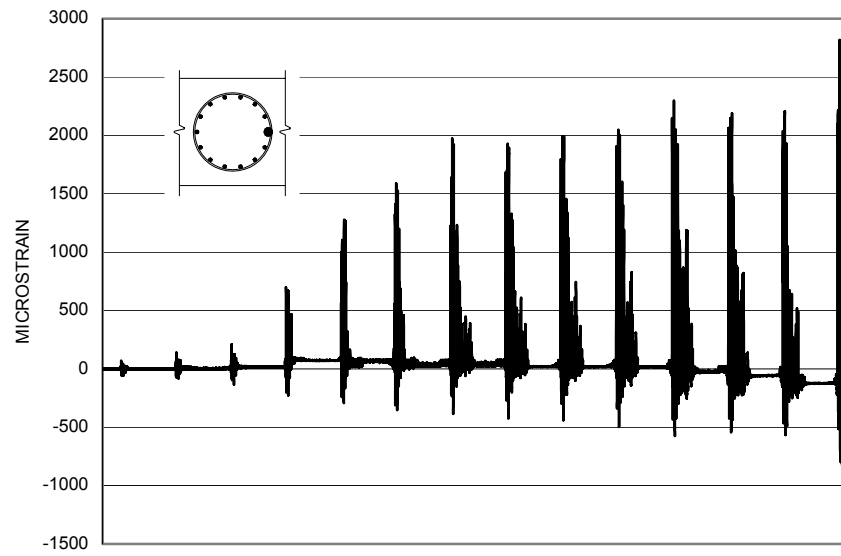
Figure A-153 Measured Strain in SG117 for SFCD3
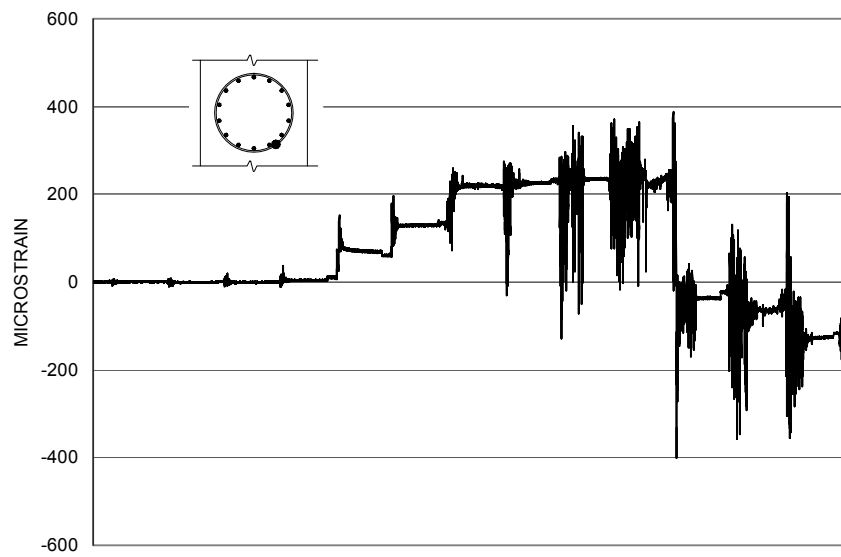
Figure A-154 Measured Strain in SG120 for SFCD3
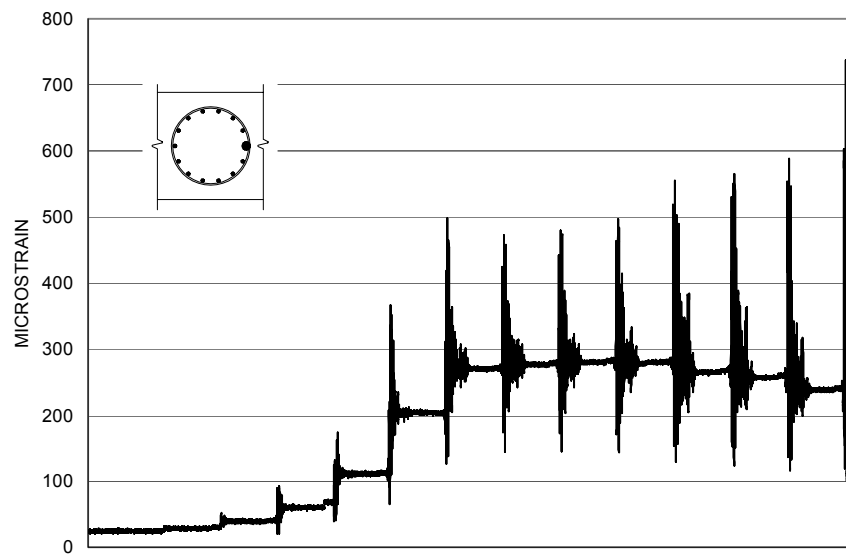
Figure A-155 Measured Strain in SG121 for SFCD3
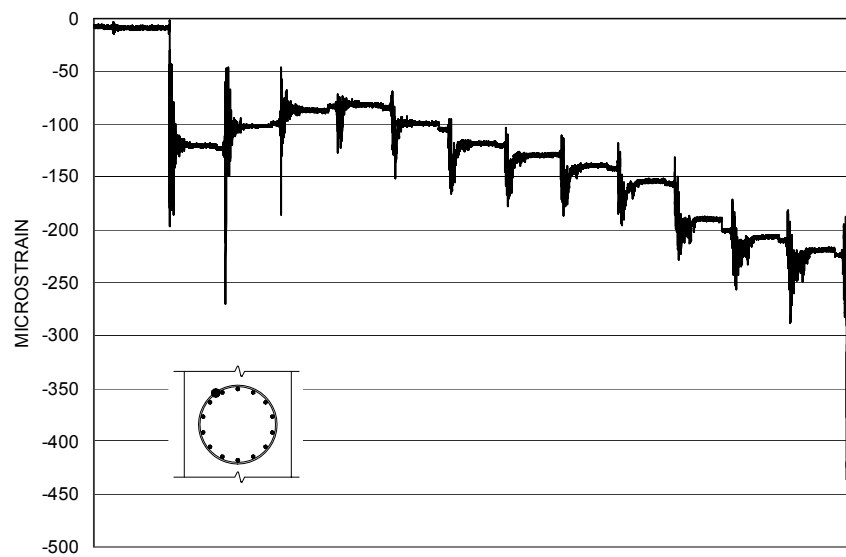
Figure A-156 Measured Strain in SG122 for SFCD3
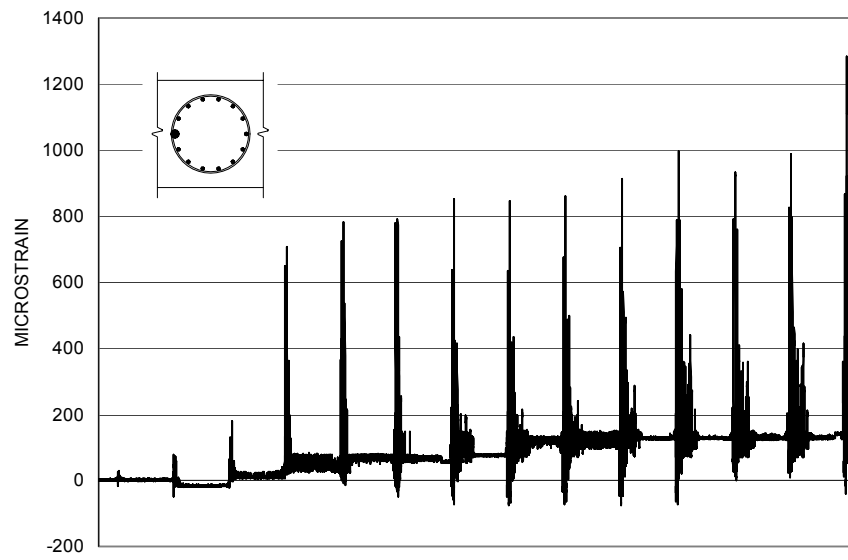
Figure A-157 Measured Strain in SG123 for SFCD3
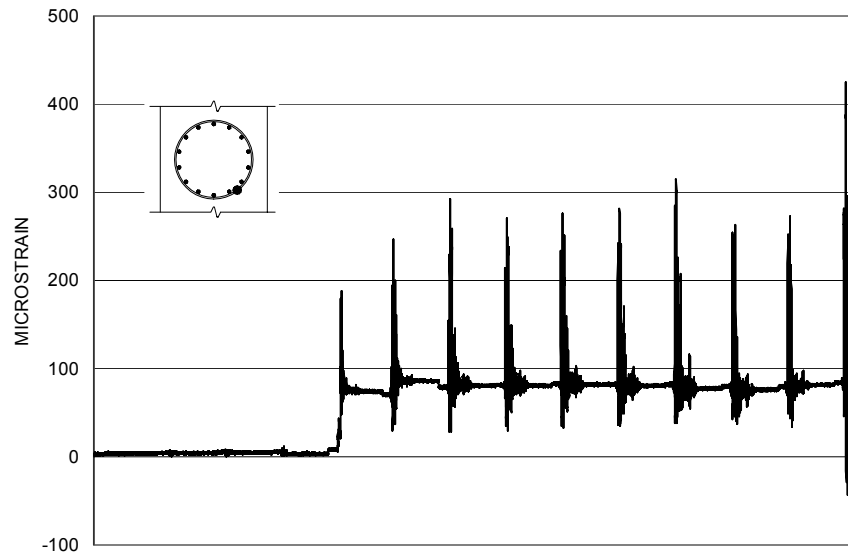
Figure A-158 Measured Strain in SG124 for SFCD3

272
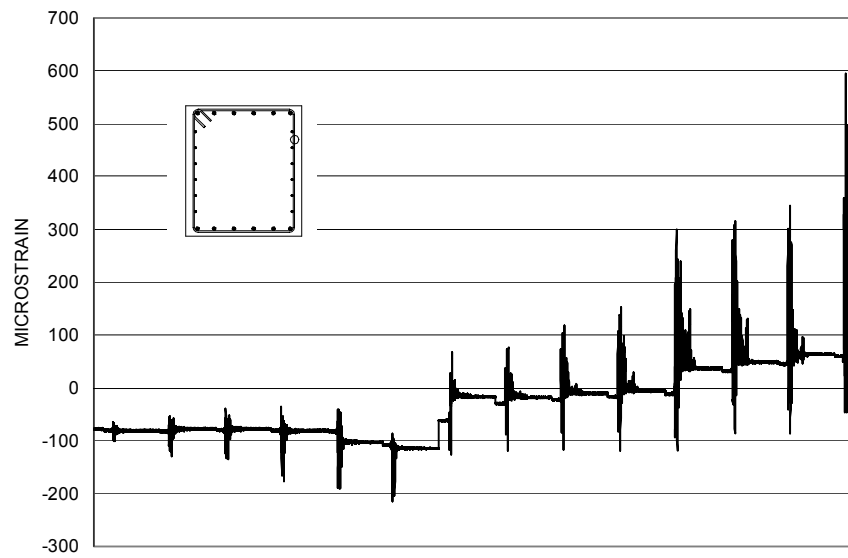
Figure A-159 Measured Strain in SG125 for SFCD3
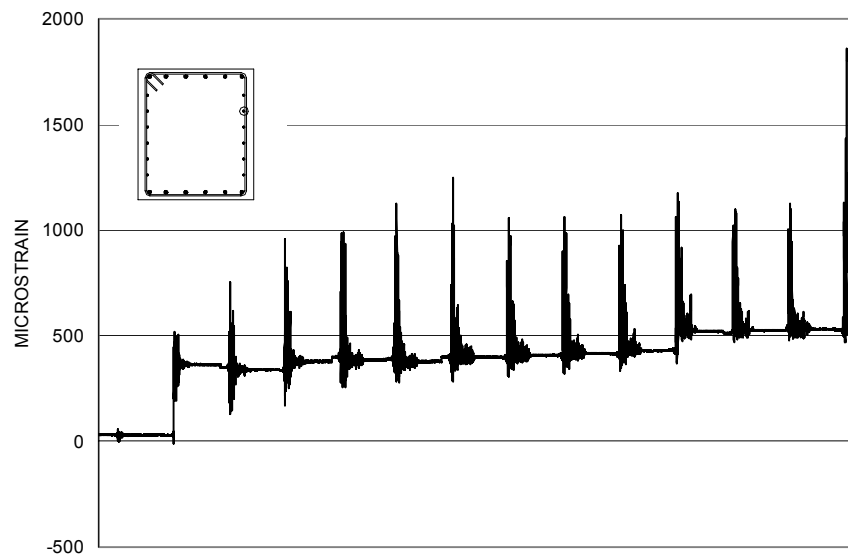
Figure A-160 Measured Strain in SG126 for SFCD3
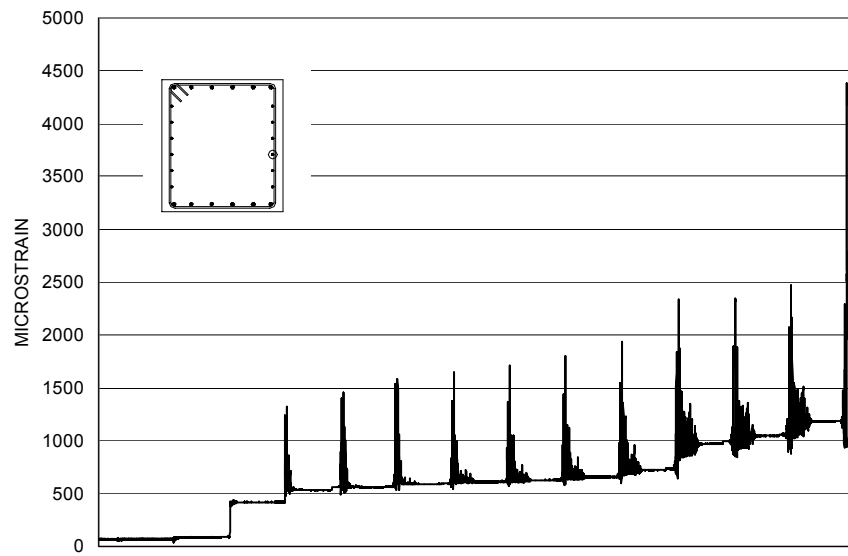
Figure A-161 Measured Strain in SG127 for SFCD3
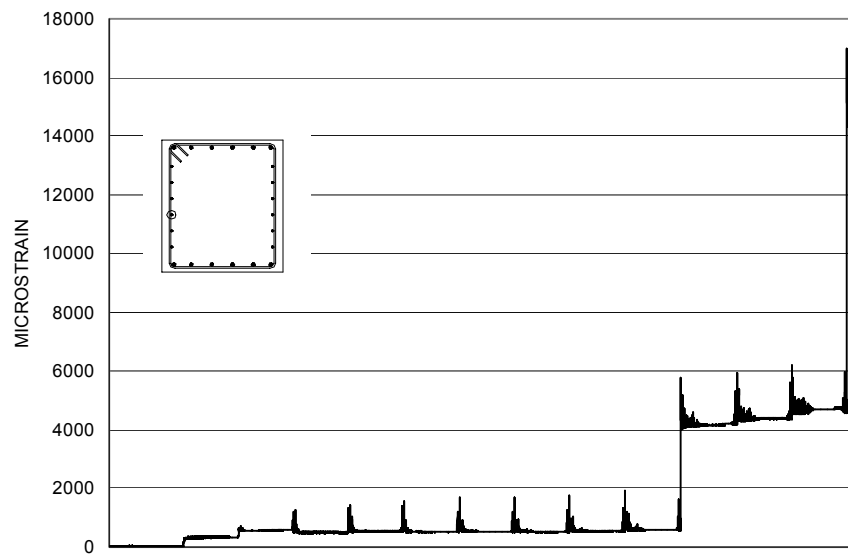
Figure A-162 Measured Strain in SG129 for SFCD3
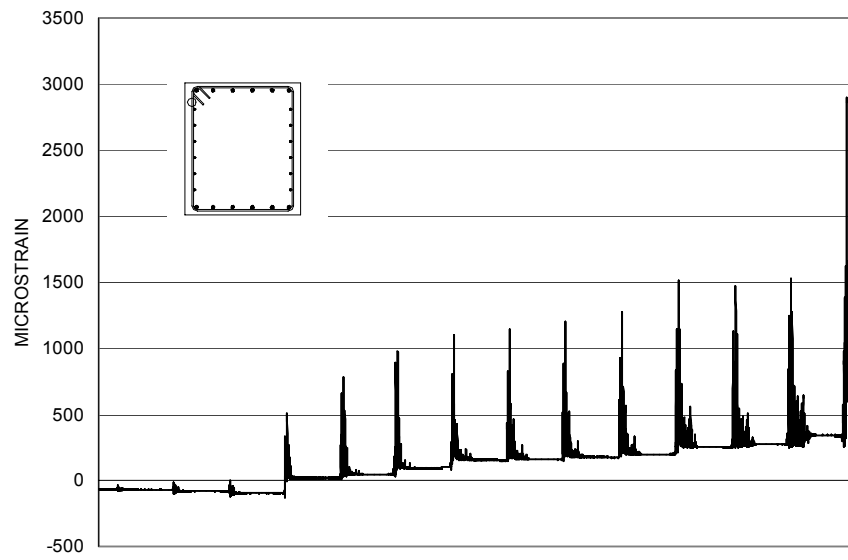
Figure A-163 Measured Strain in SG130 for SFCD3
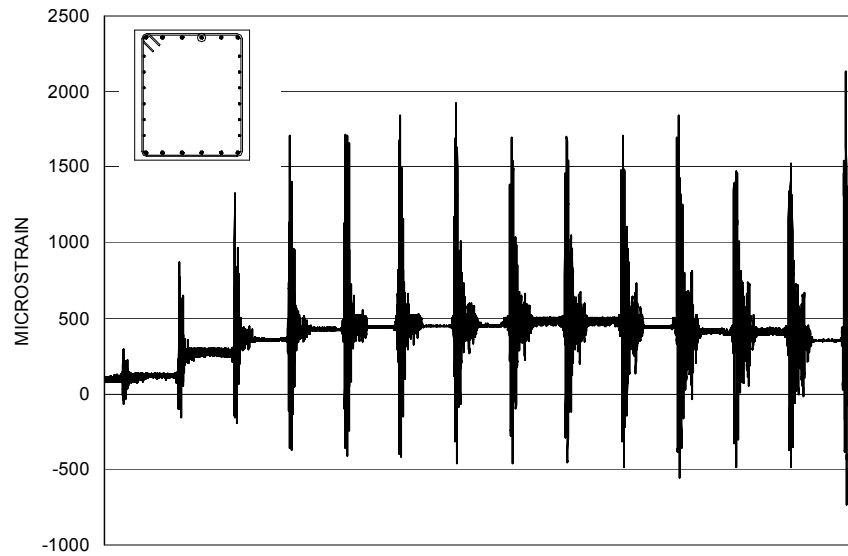
Figure A-164 Measured Strain in SG131 for SFCD3

275
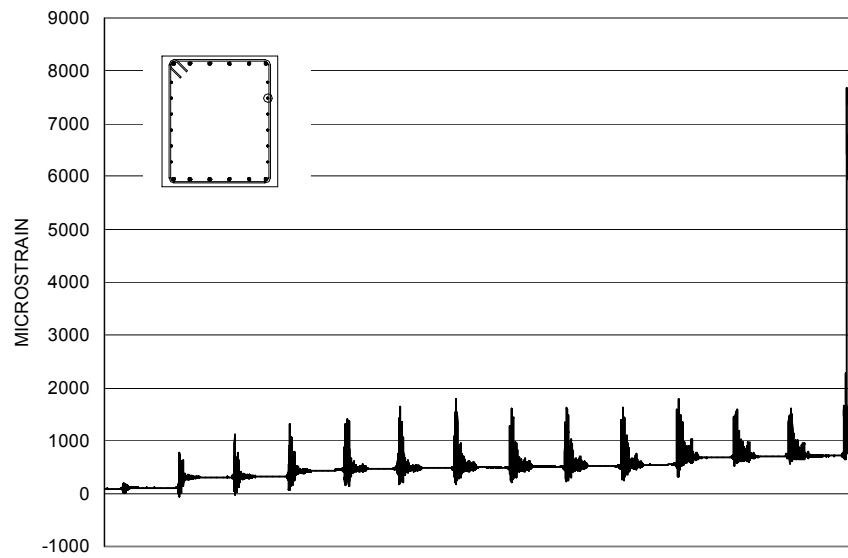
Figure A-165 Measured Strain in SG132 for SFCD3
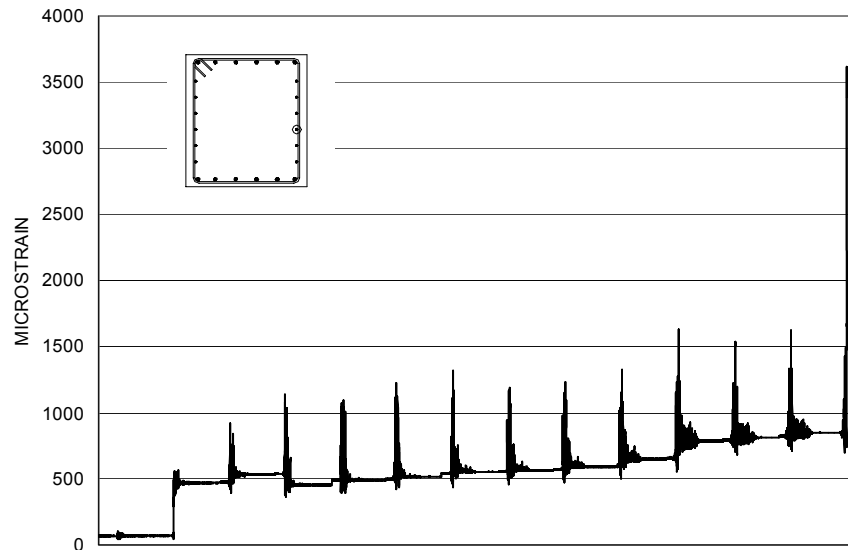
Figure A-166 Measured Strain in SG133 for SFCD3
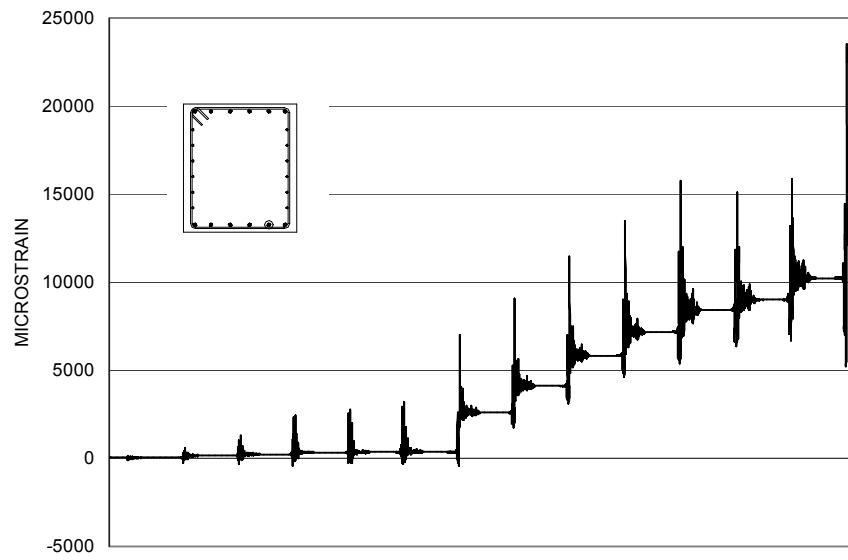
Figure A-167 Measured Strain in SG135 for SFCD3
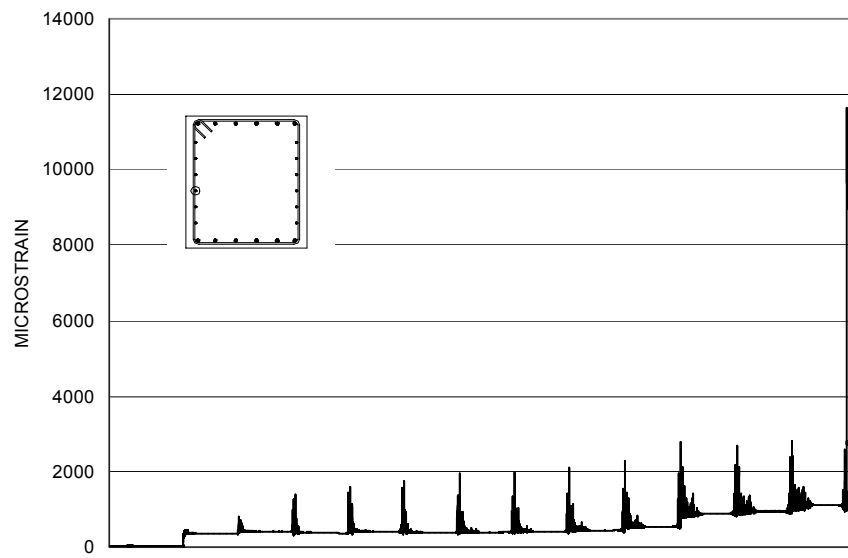
Figure A-168 Measured Strain in SG136 for SFCD3
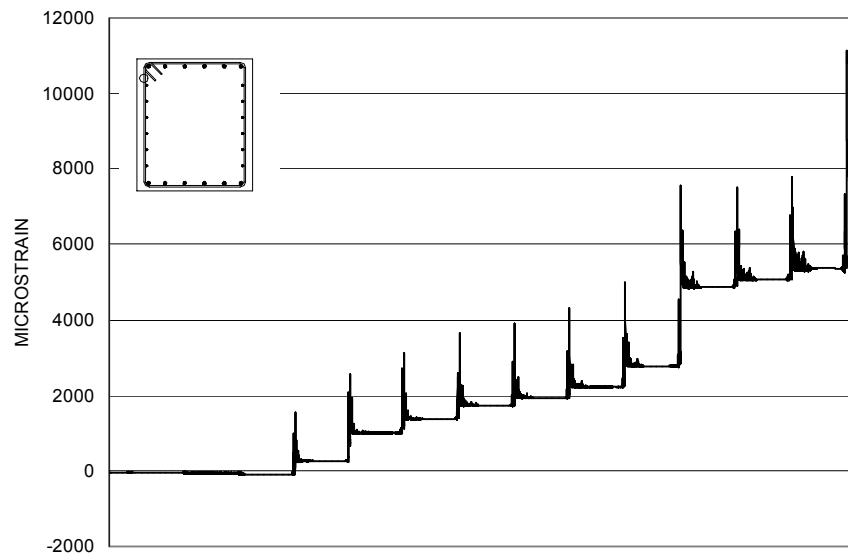
Figure A-169 Measured Strain in SG137 for SFCD3
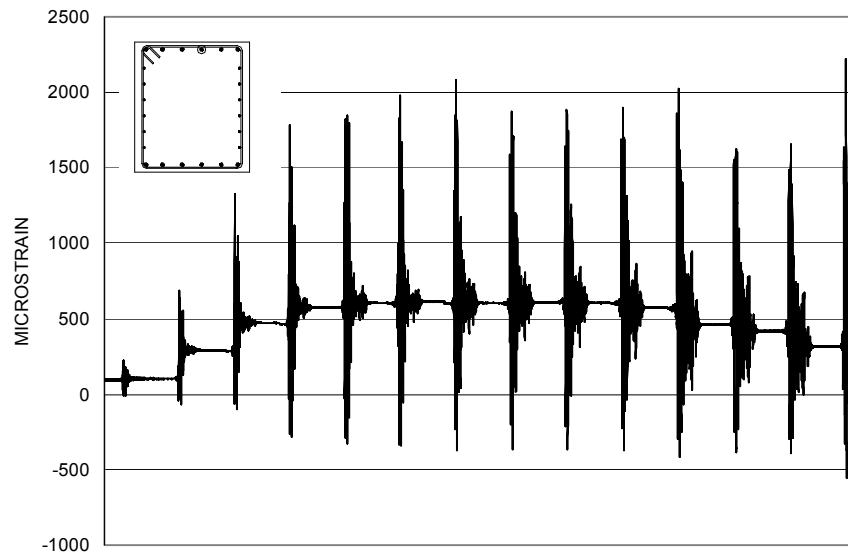
Figure A-170 Measured Strain in SG138 for SFCD3
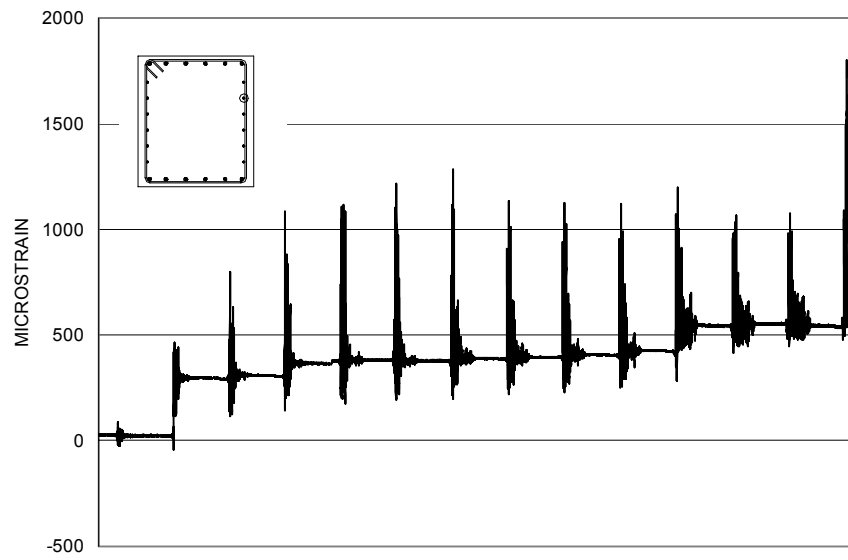
Figure A-171 Measured Strain in SG139 for SFCD3
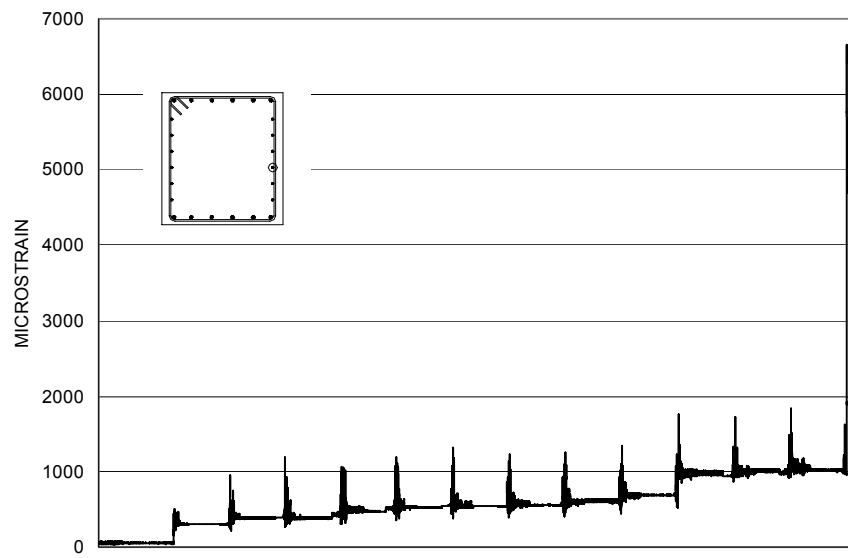
Figure A-172 Measured Strain in SG140 for SFCD3
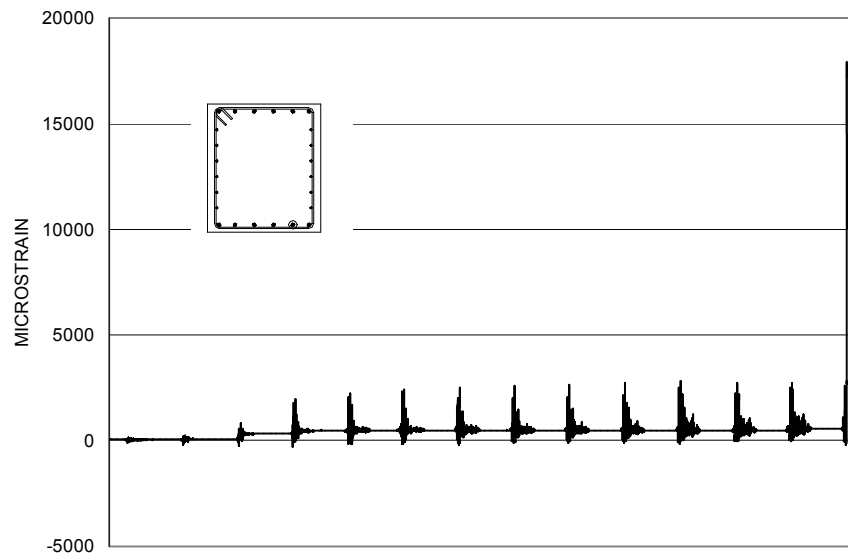
Figure A-173 Measured Strain in SG142 for SFCD3
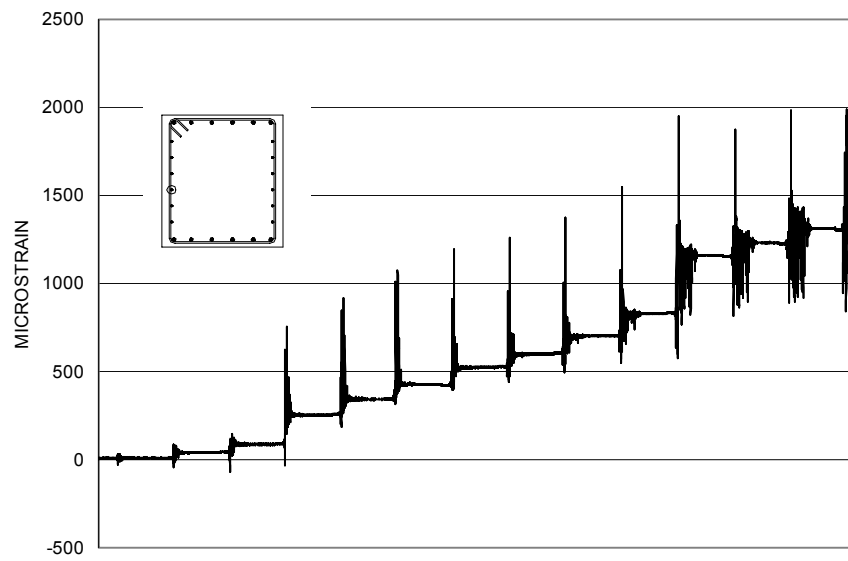
Figure A-174 Measured Strain in SG143 for SFCD3
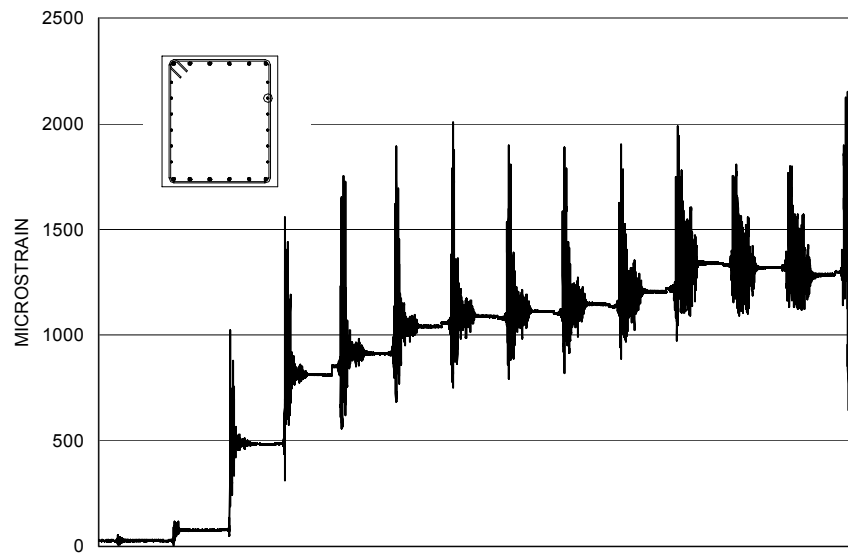
Figure A-175 Measured Strain in SG144 for SFCD3
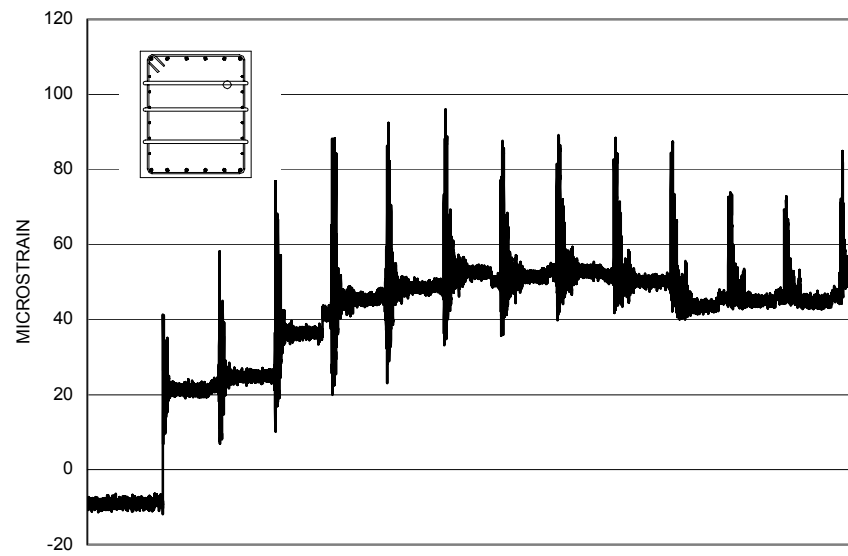
Figure A-176 Measured Strain in SG145 for SFCD3
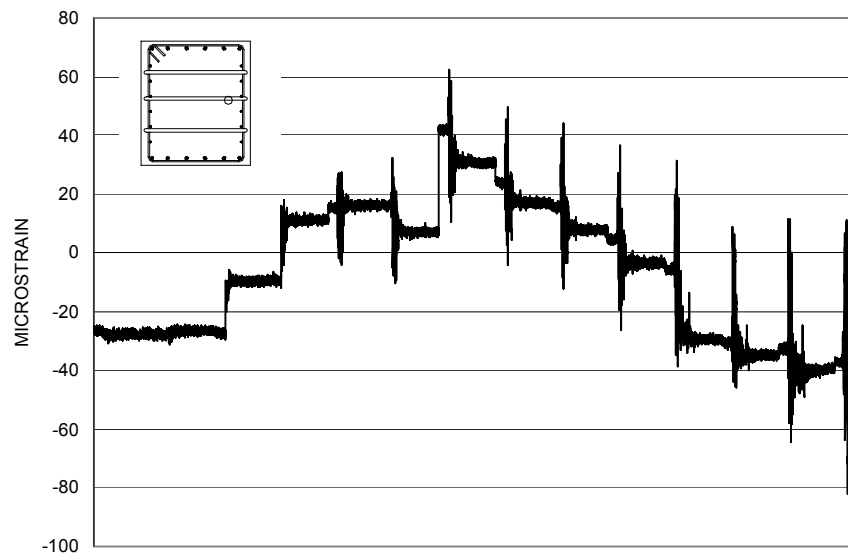
Figure A-177 Measured Strain in SG146 for SFCD3
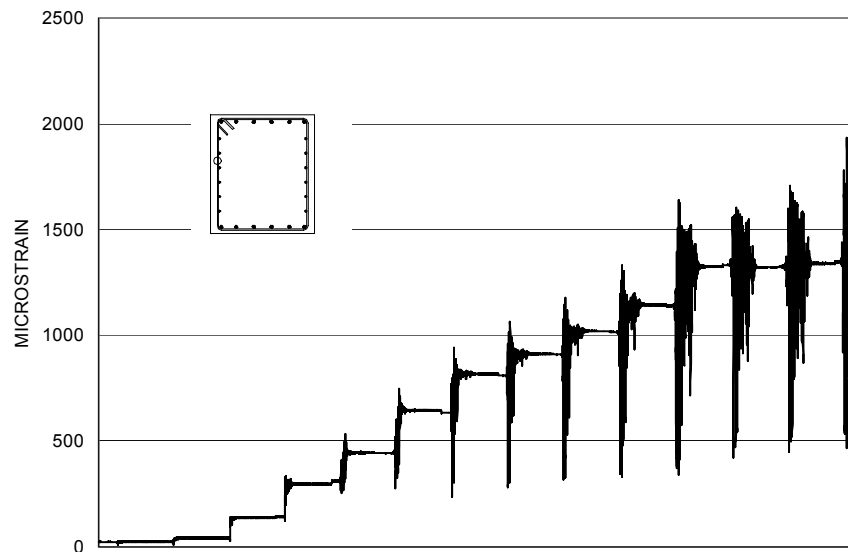
Figure A-178 Measured Strain in SG148 for SFCD3
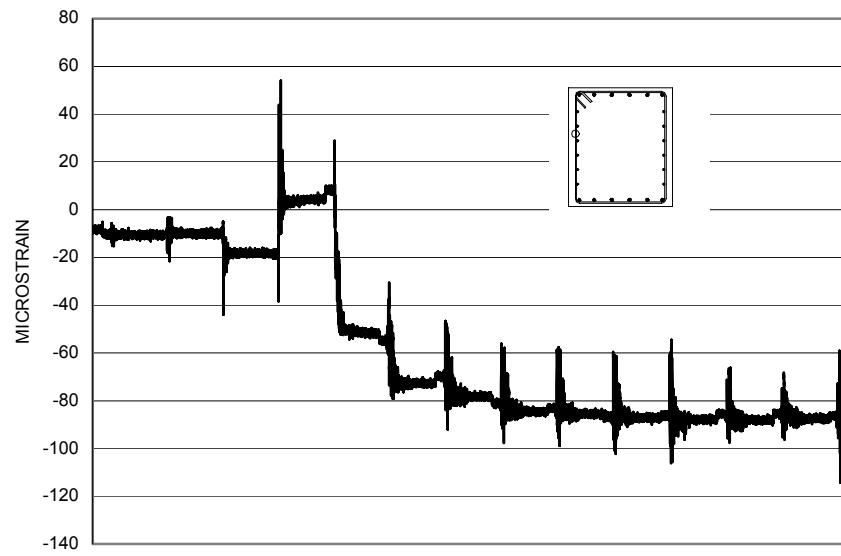
Figure A-179 Measured Strain in SG149 for SFCD3
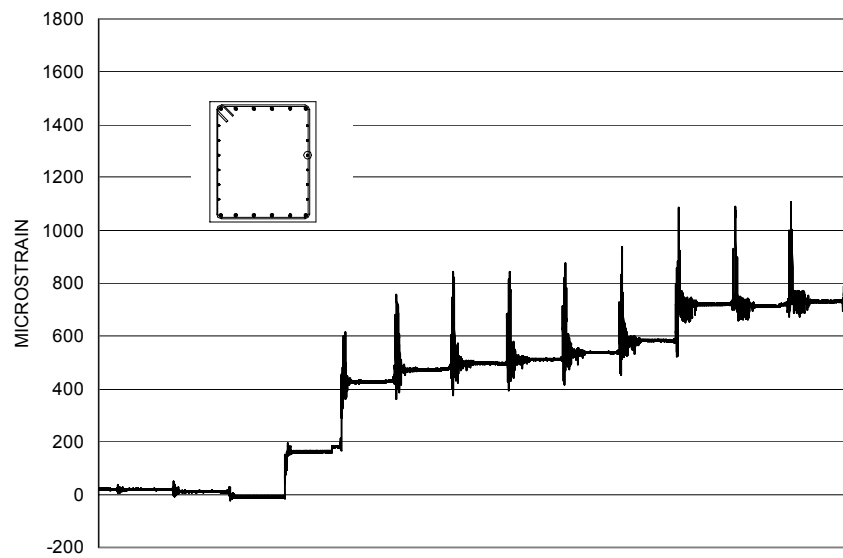
Figure A-180 Measured Strain in SG150 for SFCD3
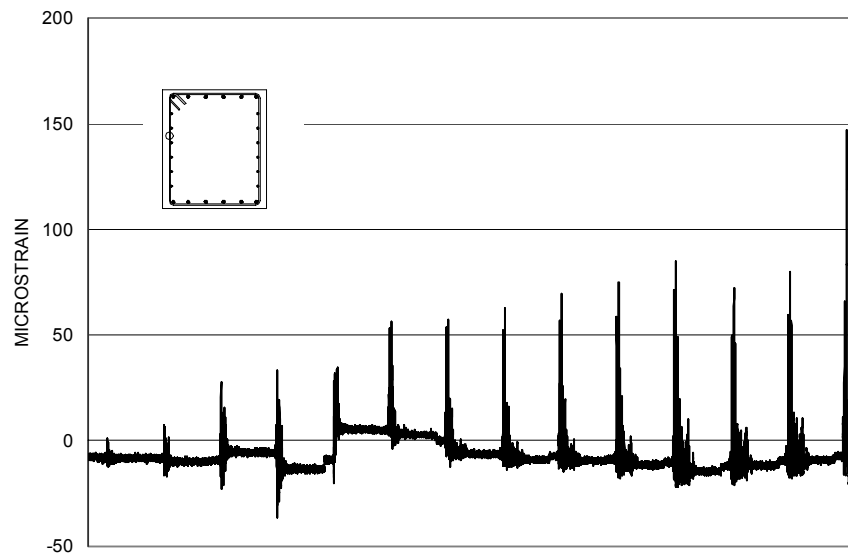
Figure A-181 Measured Strain in SG151 for SFCD3
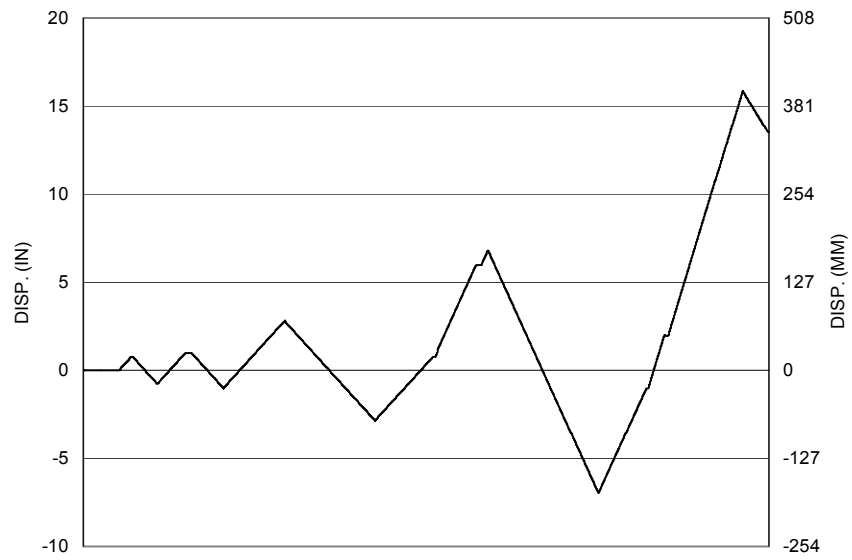
Figure A-182 Measured Displacement in Actuator for LFCD1S
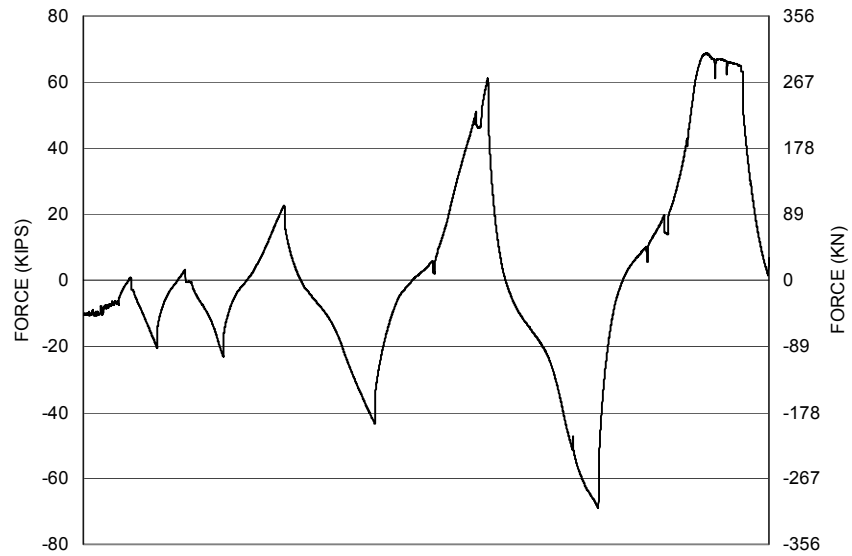
Figure A-183 Measured Force in Actuator for LFCD1S
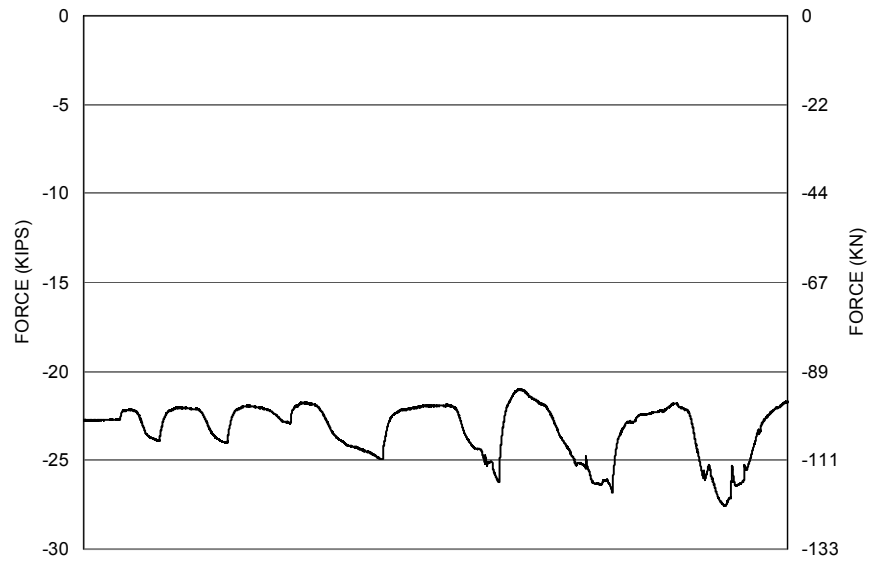
Figure A-184 Measured Force in North Axial Ram for LFCD1S
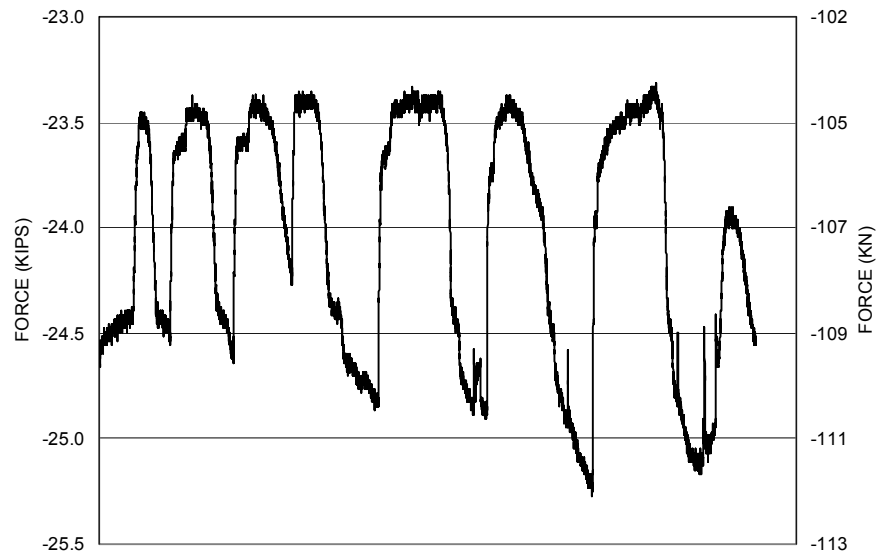
Figure A-185 Measured Force in South Axial Ram for LFCD1S
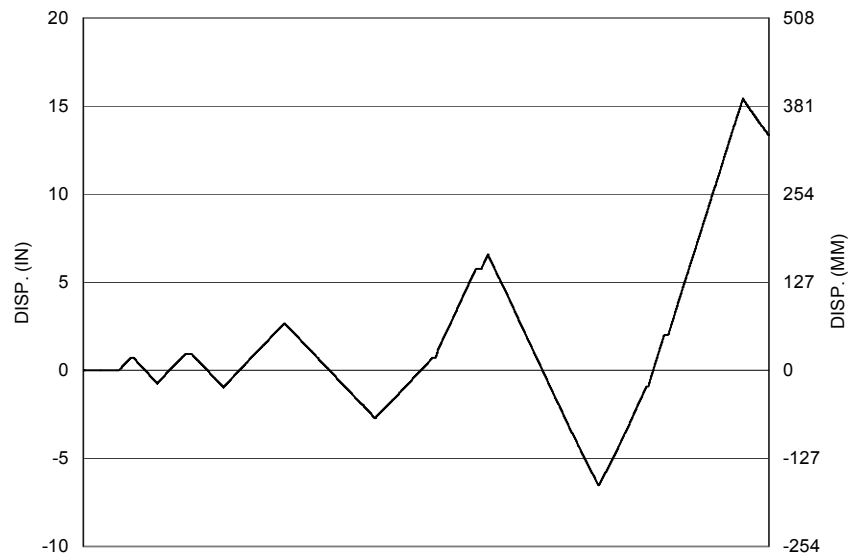
Figure A-186 Measured Displacement of the Beam for LFCD1S
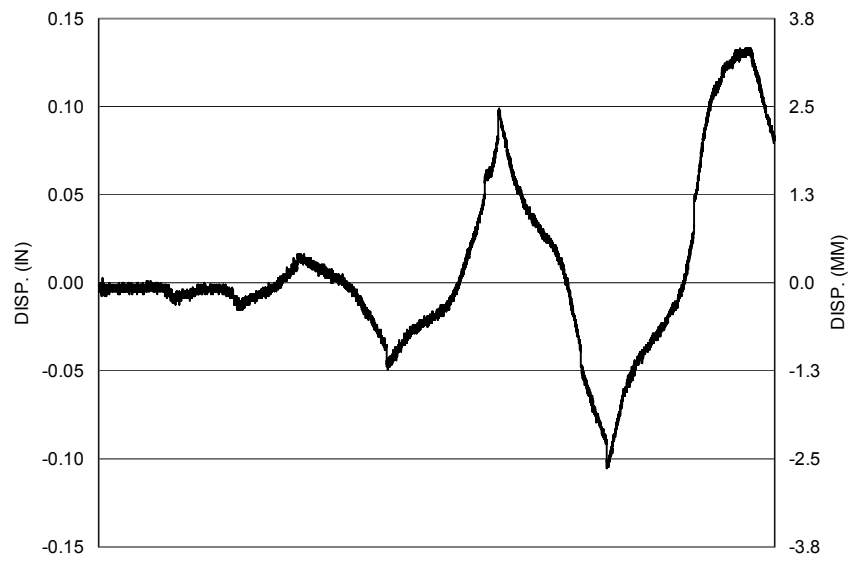
Figure A-187 Measured Displacement of the Footing for LFCD1S

287
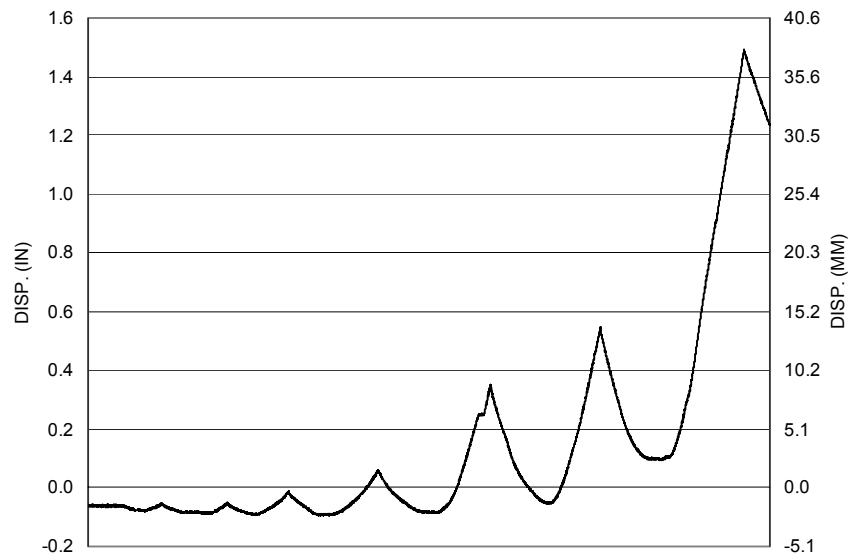
Figure A-188 Measured Vertical Displacement of the Beam at Center for LFCD1S
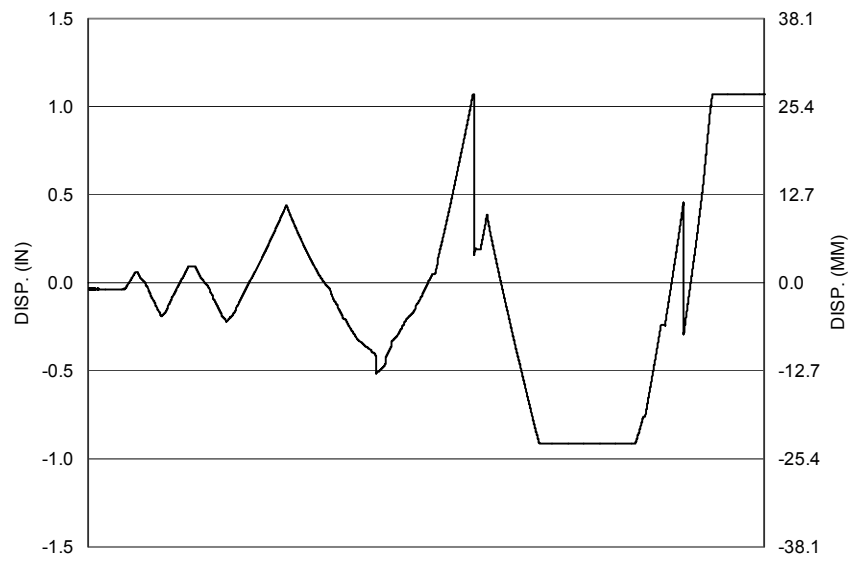
Figure A-189 Measured Displacement of NV1 for LFCD1S
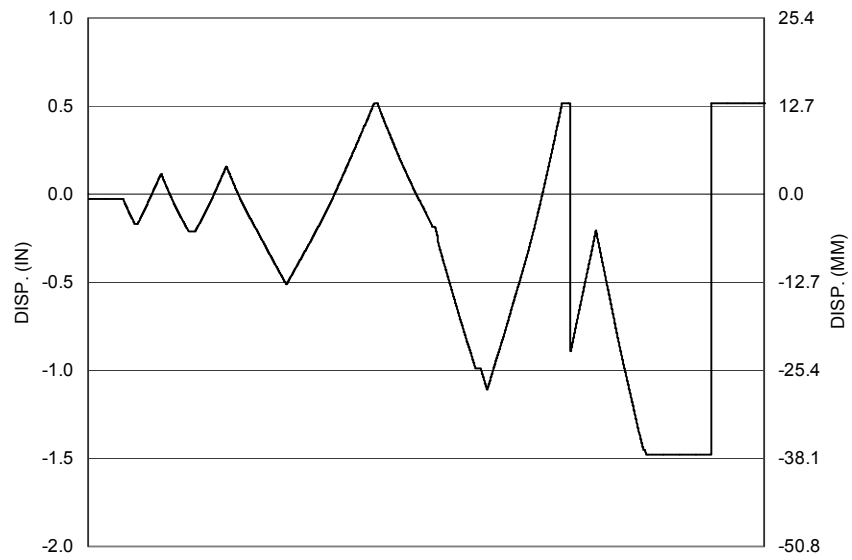
Figure A-190 Measured Displacement of NV2 for LFCD1S
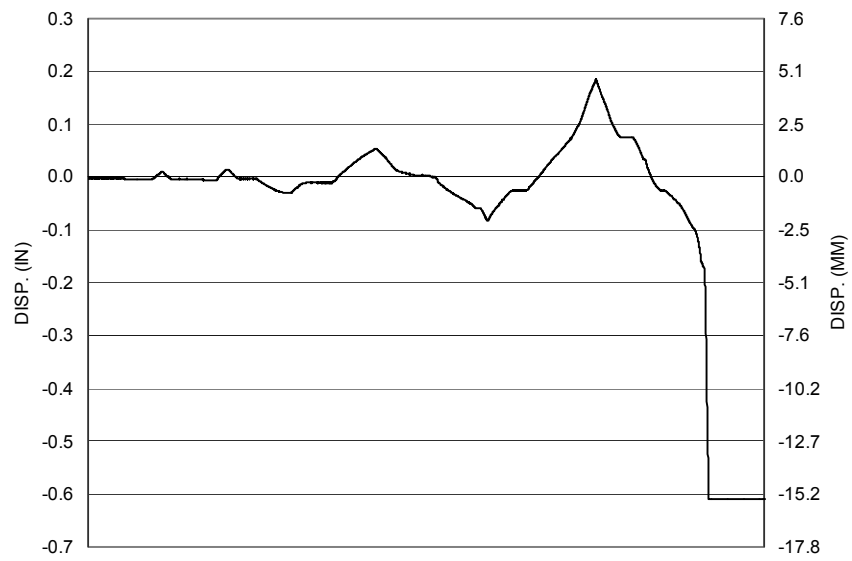
Figure A-191 Measured Displacement of NV3 for LFCD1S
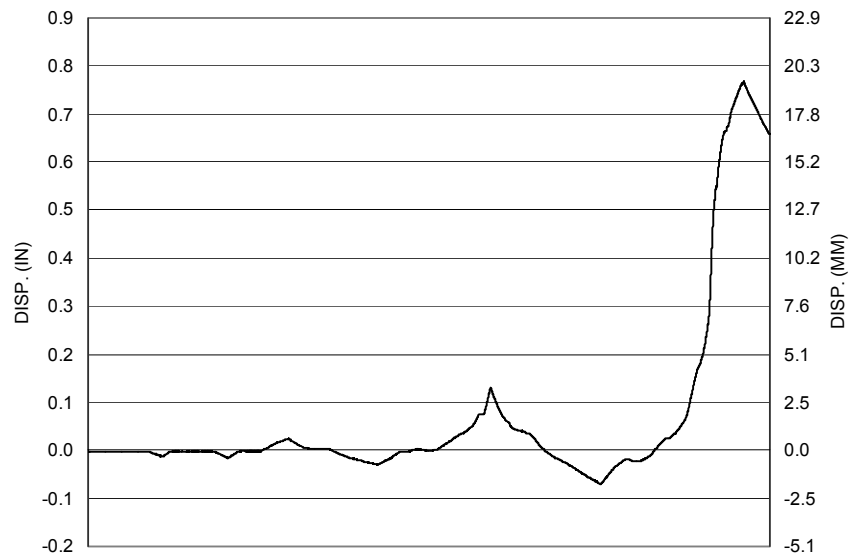
Figure A-192 Measured Displacement of NV4 for LFCD1S
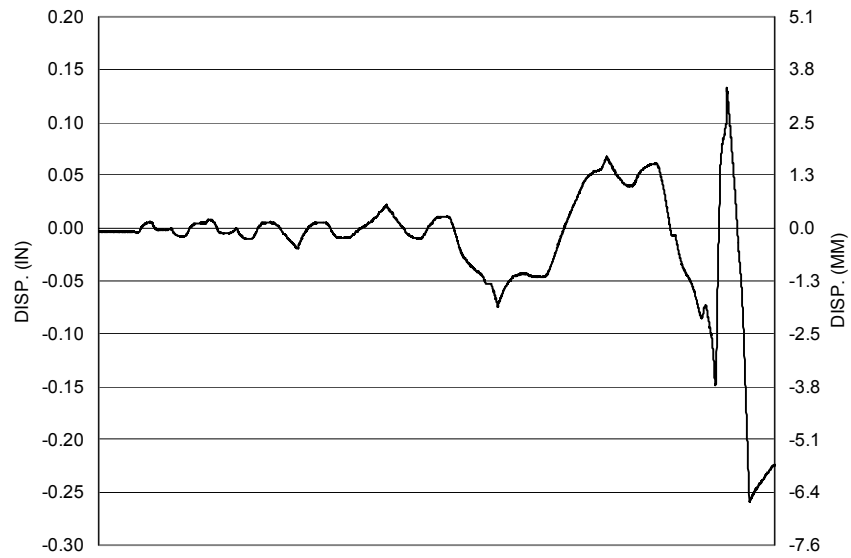
Figure A-193 Measured Displacement of NV5 for LFCD1S
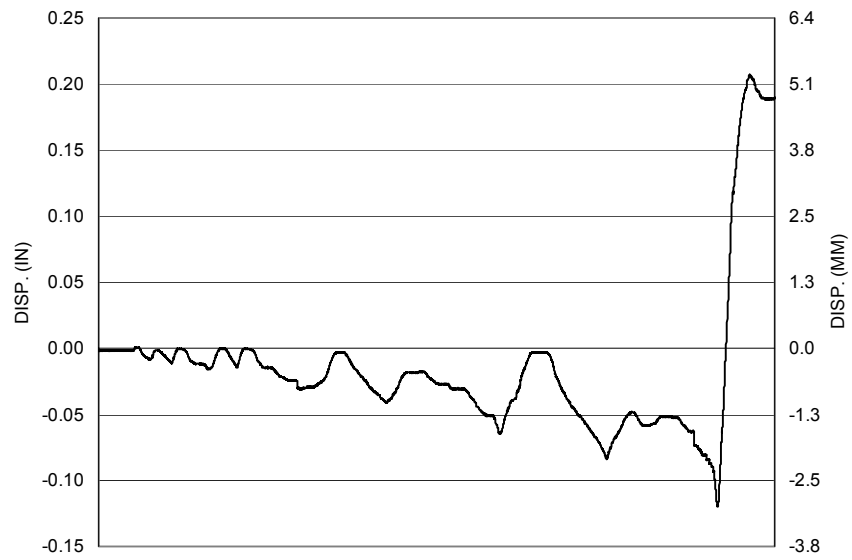
Figure A-194 Measured Displacement of NV6 for LFCD1S
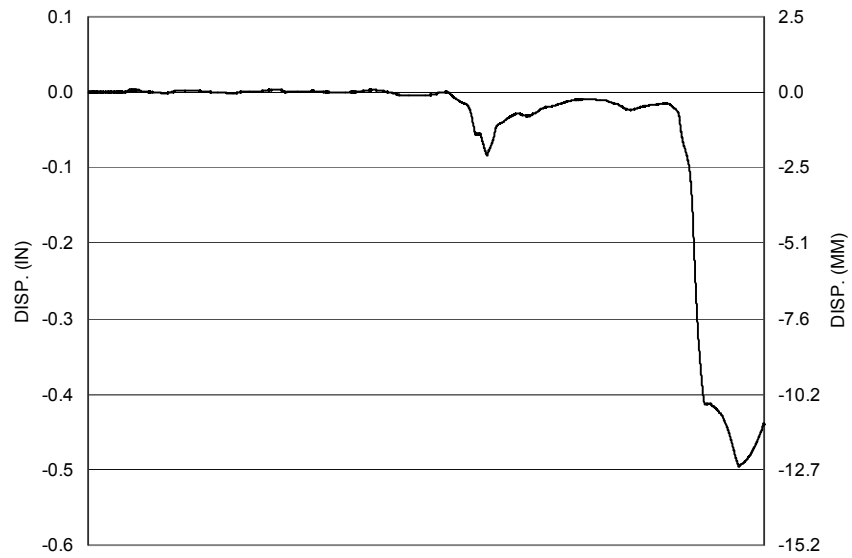
Figure A-195 Measured Displacement of NV7 for LFCD1S
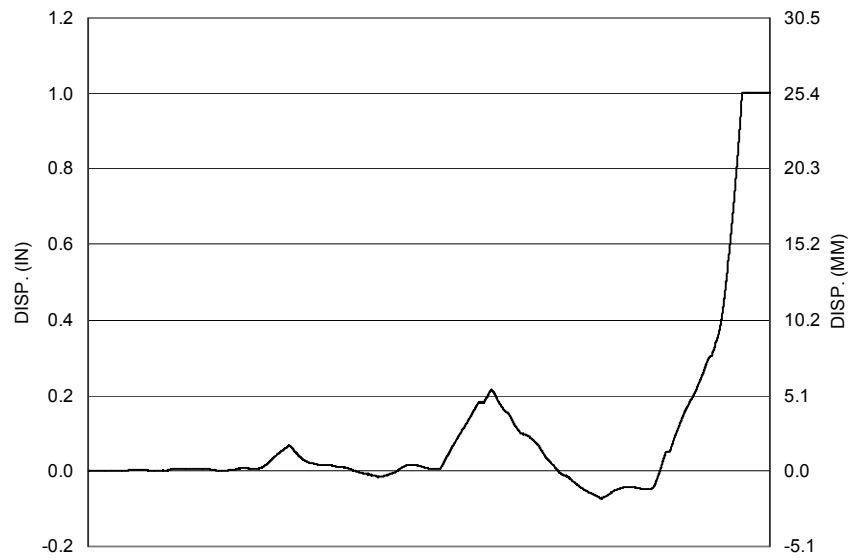
Figure A-196 Measured Displacement of NV8 for LFCD1S

Figure A-197 Measured Displacement of NV9 for LFCD1S
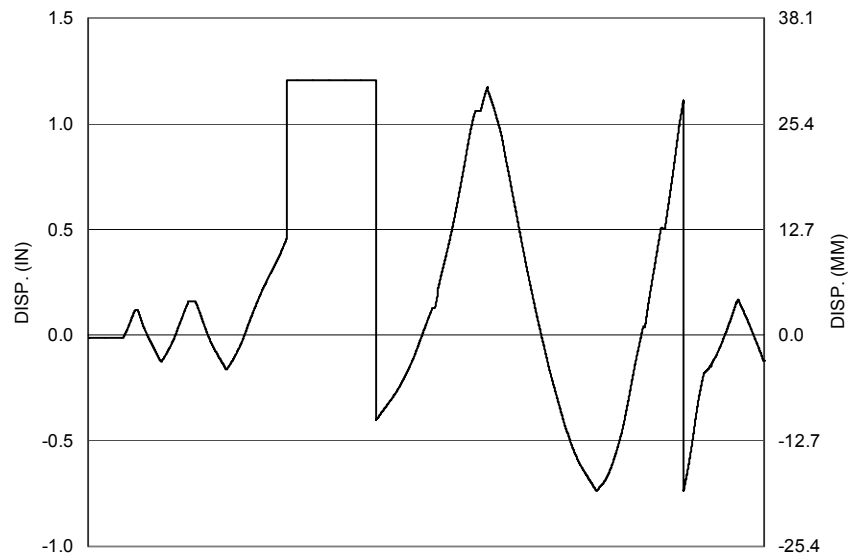
Figure A-198 Measured Displacement of NV10 for LFCD1S
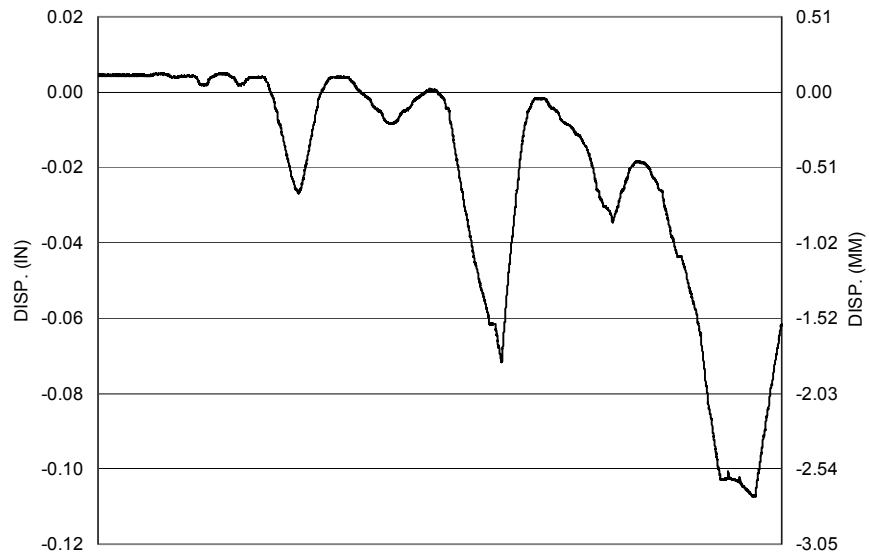
Figure A-199 Measured Displacement of NV11 for LFCD1S
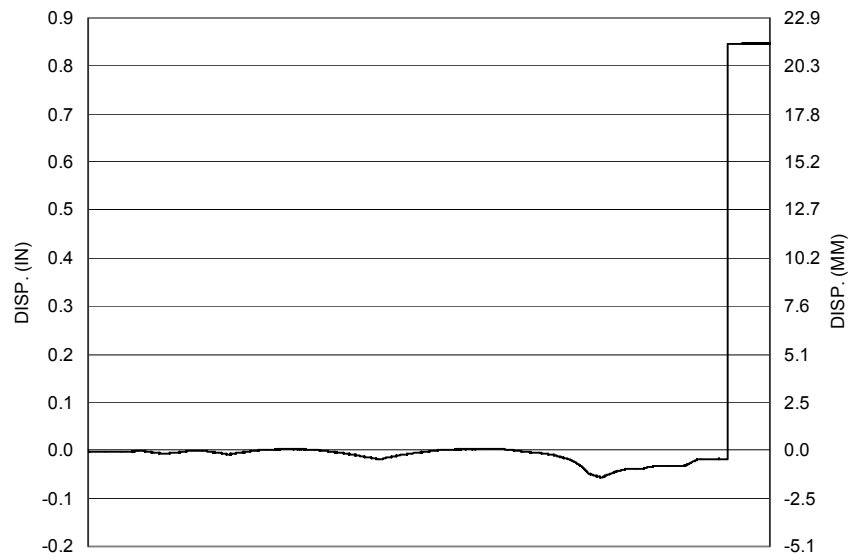
Figure A-200 Measured Displacement of NV12 for LFCD1S
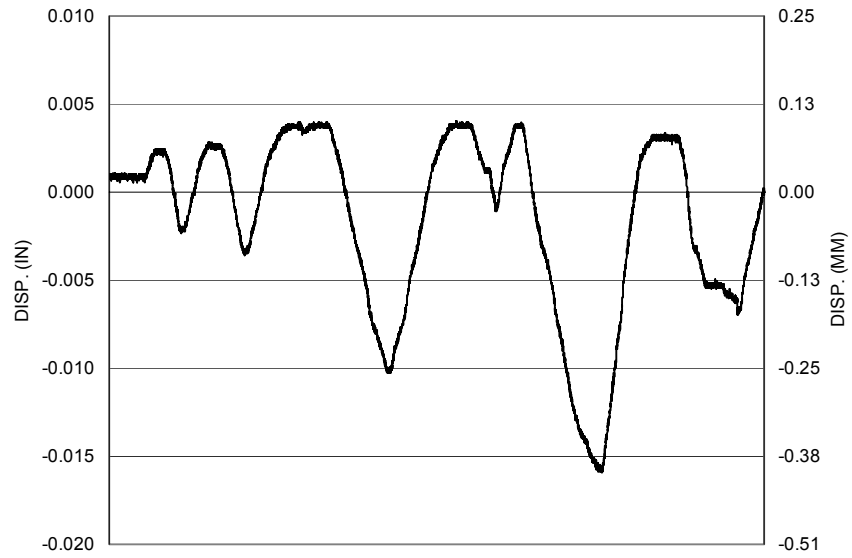
Figure A-201 Measured Displacement of NV13 for LFCD1S
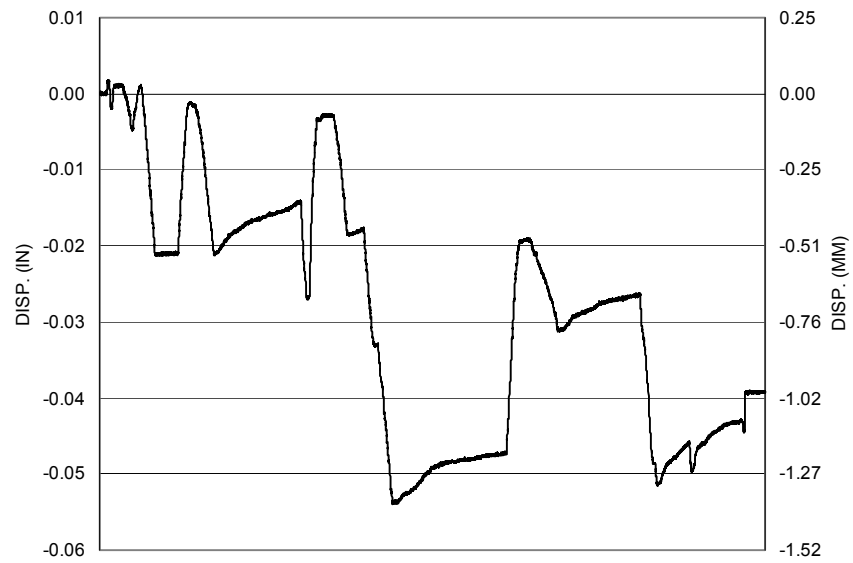
Figure A-202 Measured Displacement of NV14 for LFCD1S
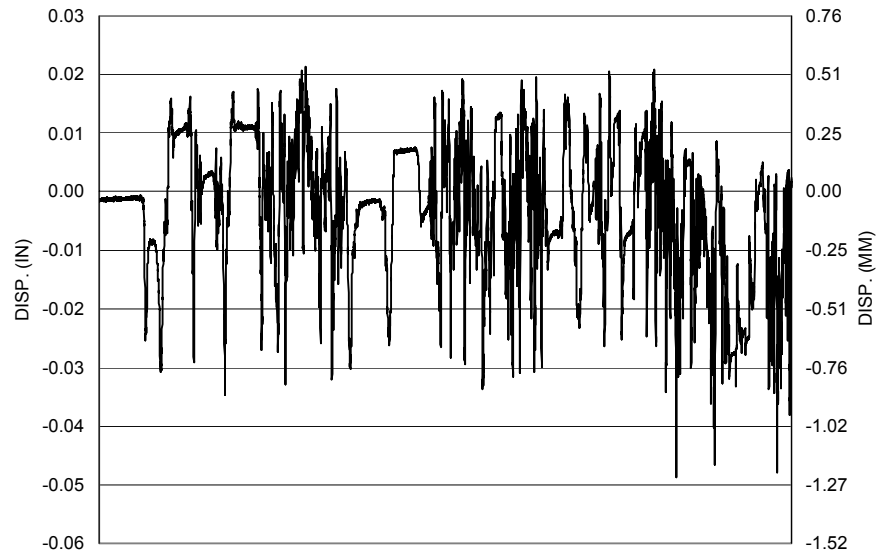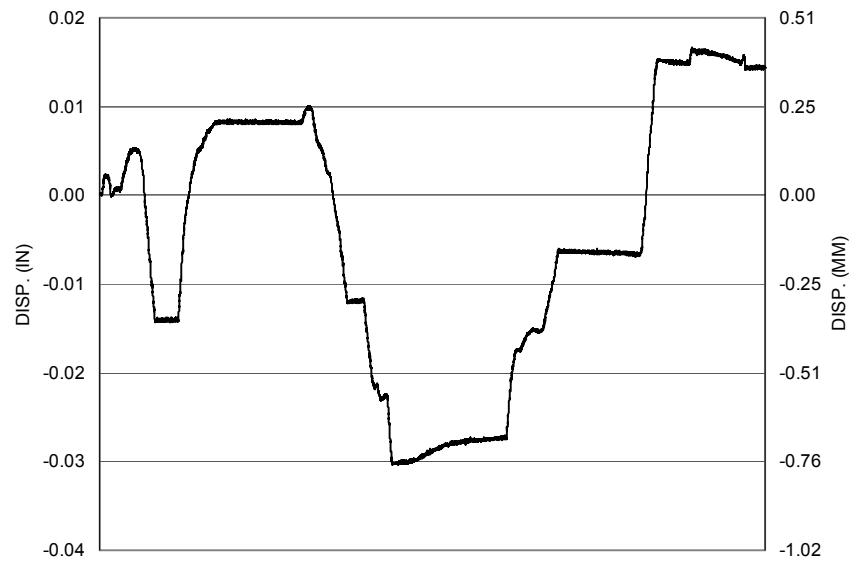

Figure A-203 Measured Displacement of NV15 for LFCD1S
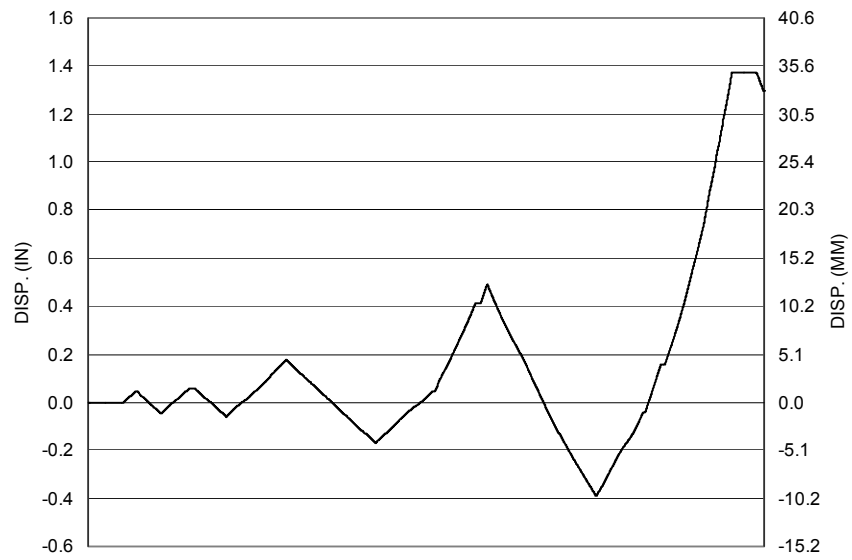
Figure A-204 Measured Displacement of NV16 for LFCD1S
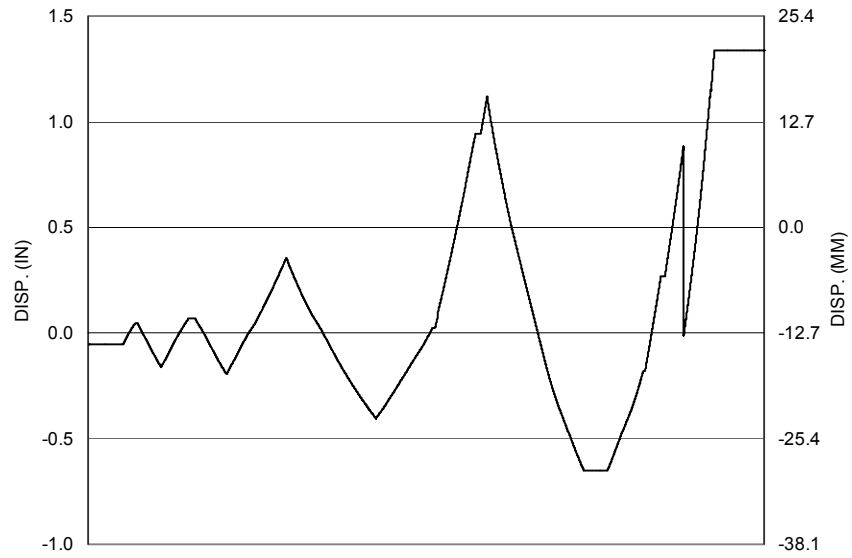
Figure A-205 Measured Displacement of NV17 for LFCD1S

Figure A-206 Measured Displacement of NV18 for LFCD1S

Figure A-207 Measured Displacement of NV19 for LFCD1S
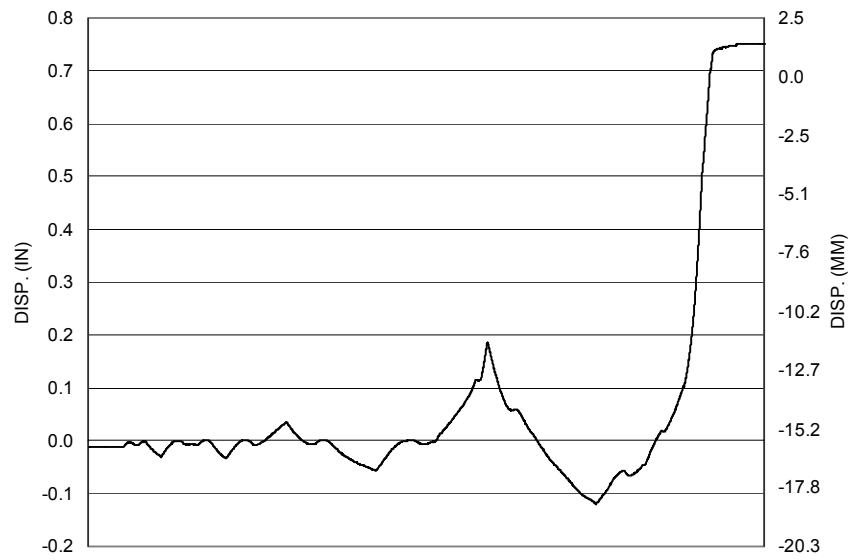
Figure A-208 Measured Displacement of NV20 for LFCD1S
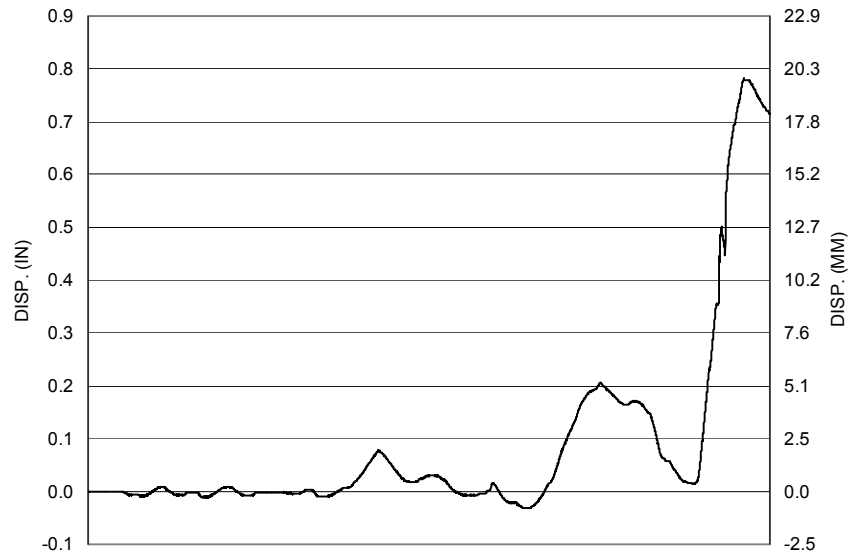
Figure A-209 Measured Displacement of NV21 for LFCD1S
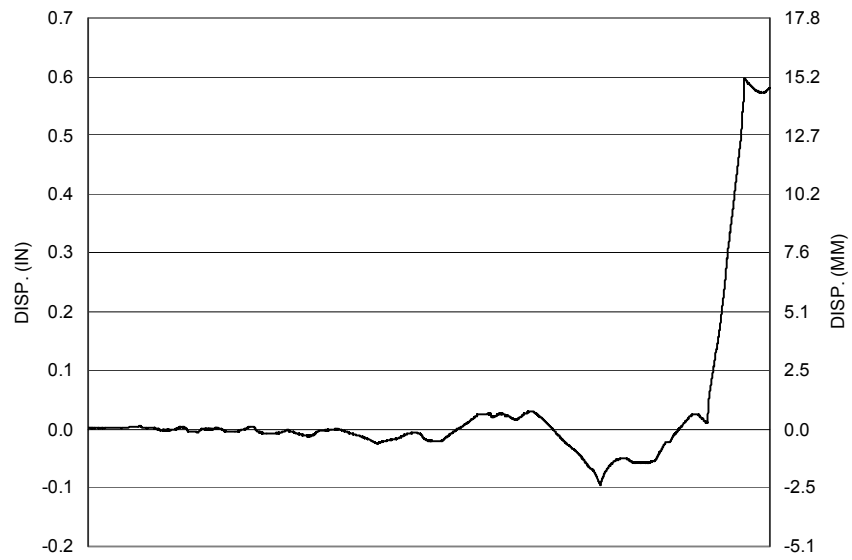
Figure A-210 Measured Displacement of NV22 for LFCD1S
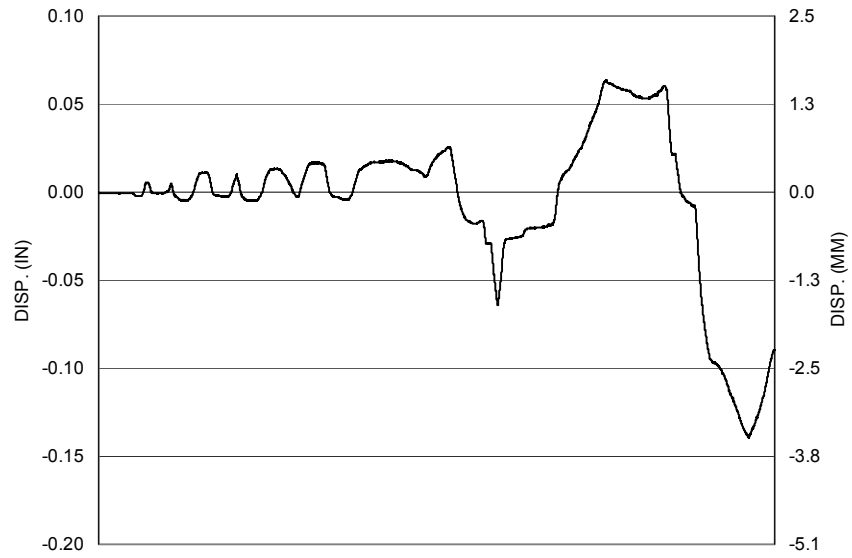
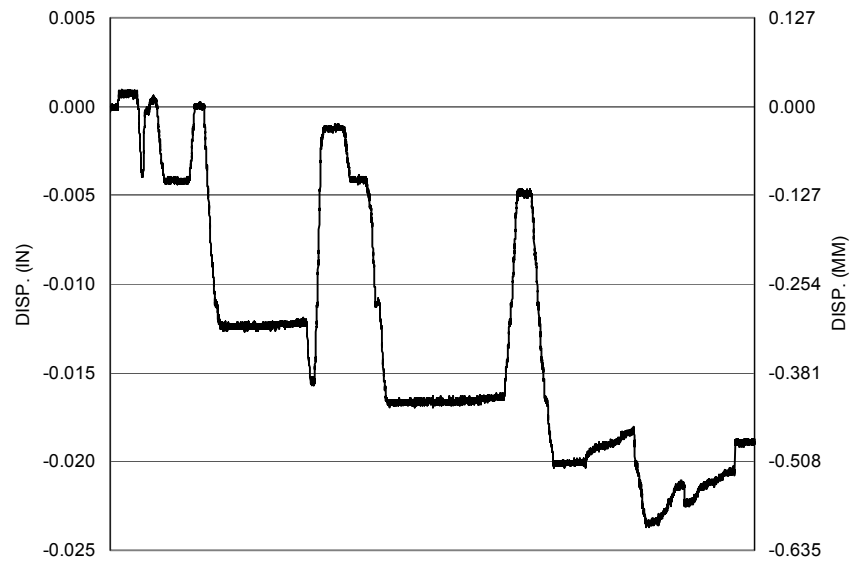**Figure A-211 Measured Displacement of NV23 for LFCD1S**
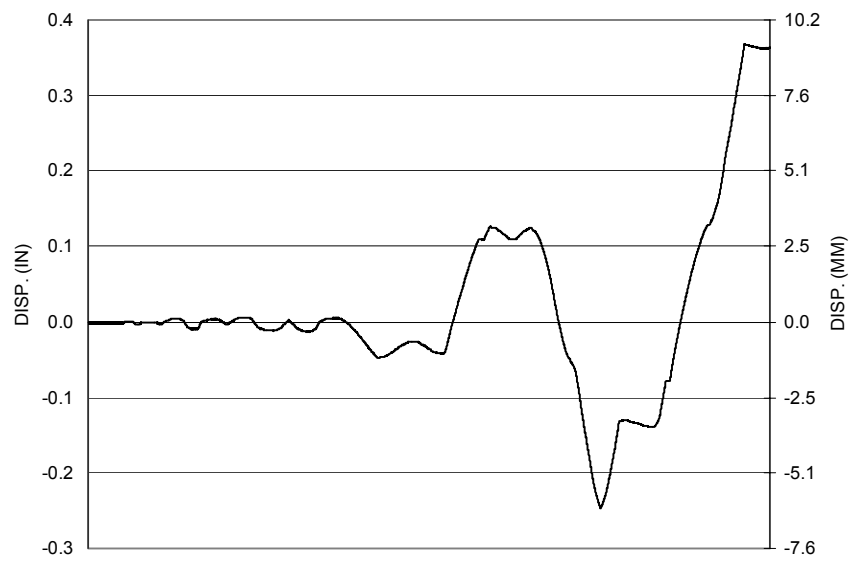
Figure A-212 Measured Displacement of NV24 for LFCD1S
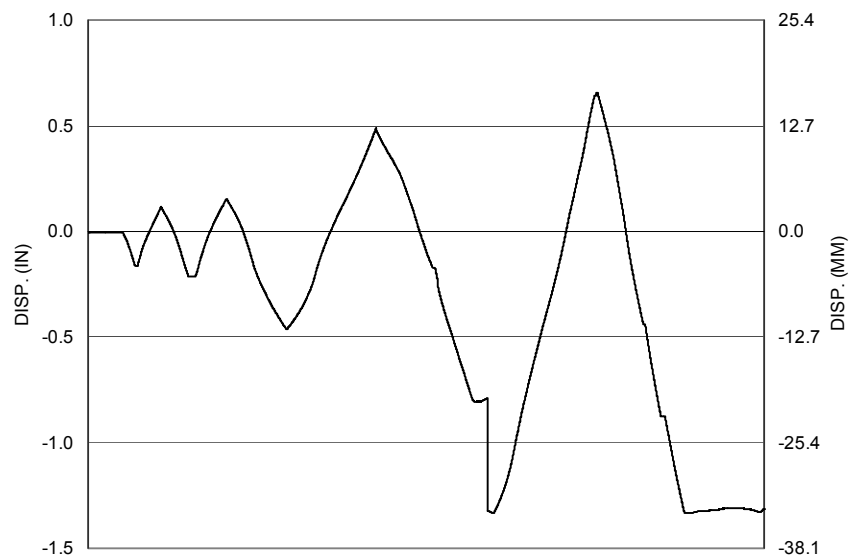
Figure A-213 Measured Displacement of NV25 for LFCD1S
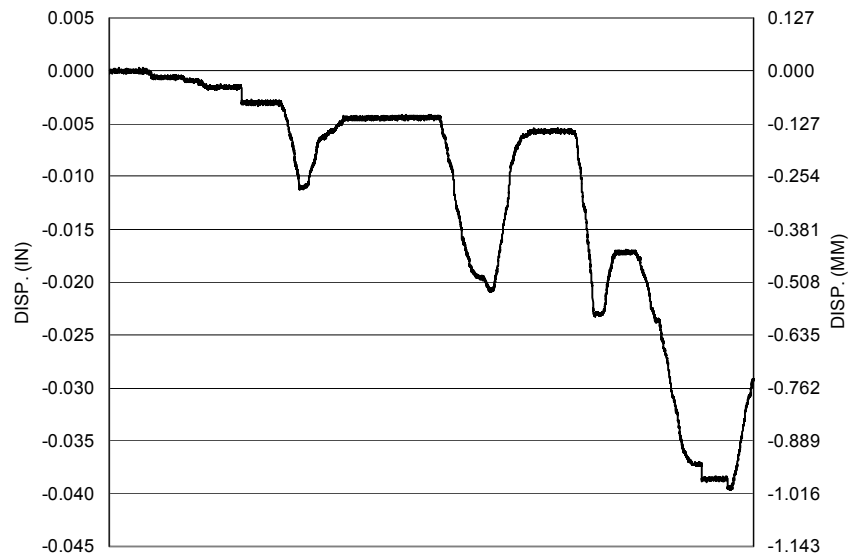
Figure A-214 Measured Displacement of NV26 for LFCD1S
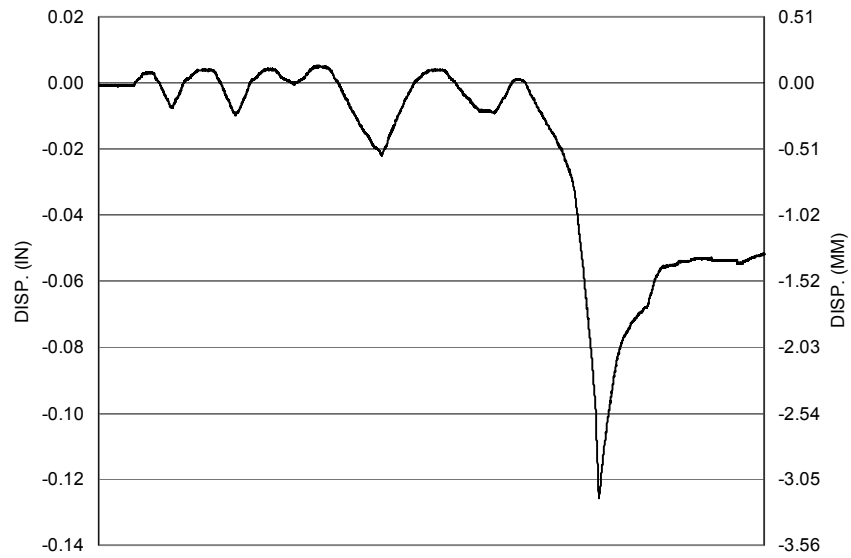
Figure A-215 Measured Displacement of NV27 for LFCD1S
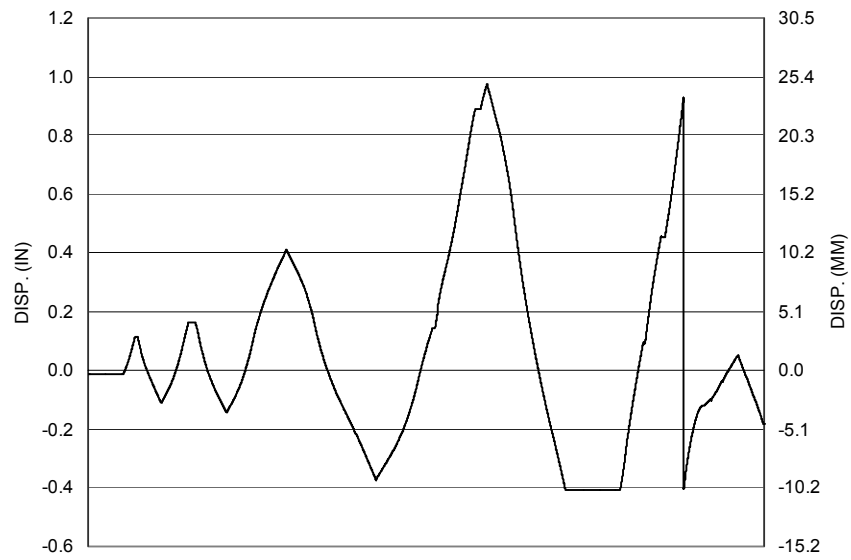
Figure A-216 Measured Displacement of NV28 for LFCD1S
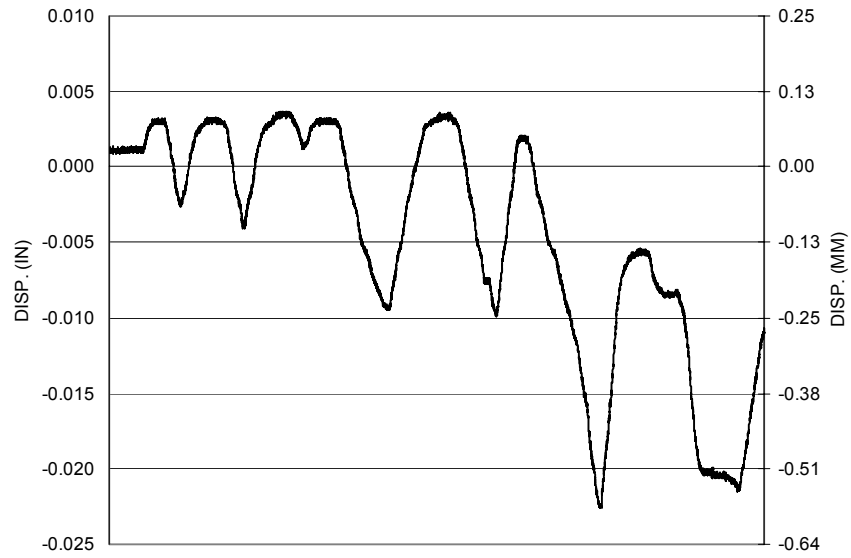
Figure A-217 Measured Displacement of NV29 for LFCD1S
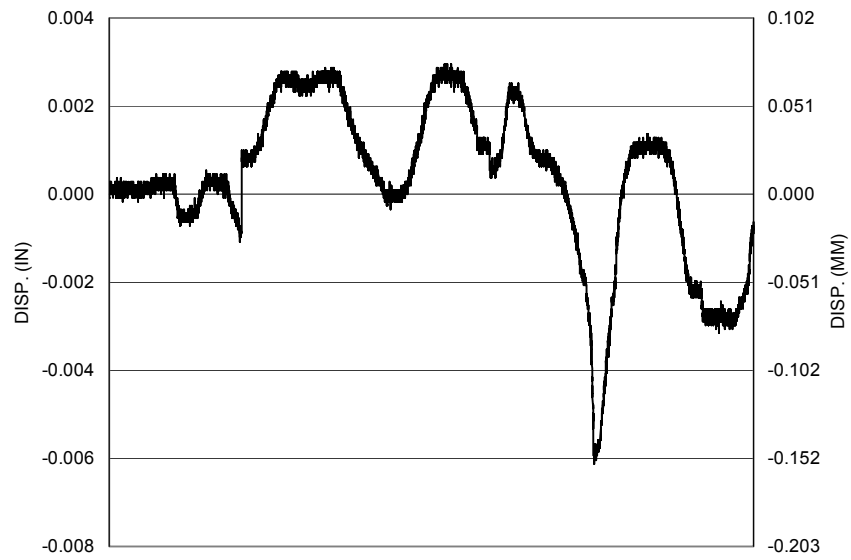
Figure A-218 Measured Displacement of NV30 for LFCD1S
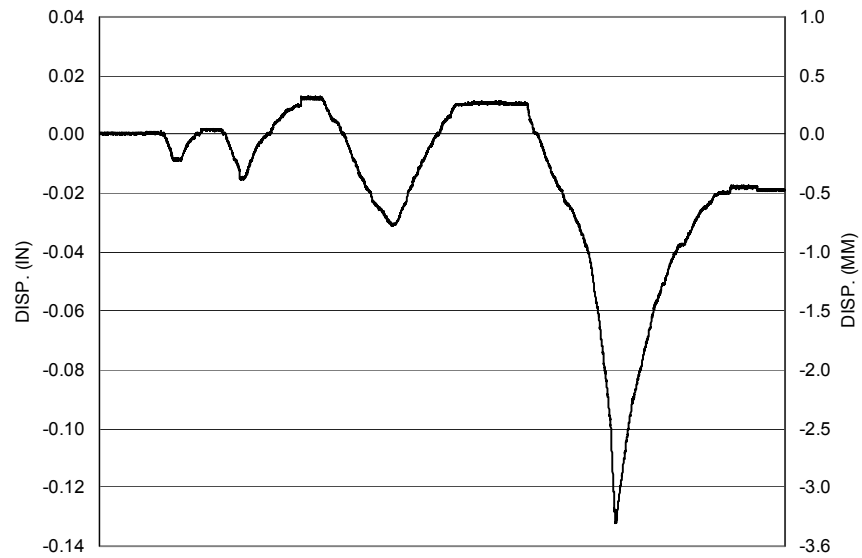
Figure A-219 Measured Displacement of NV31 for LFCD1S
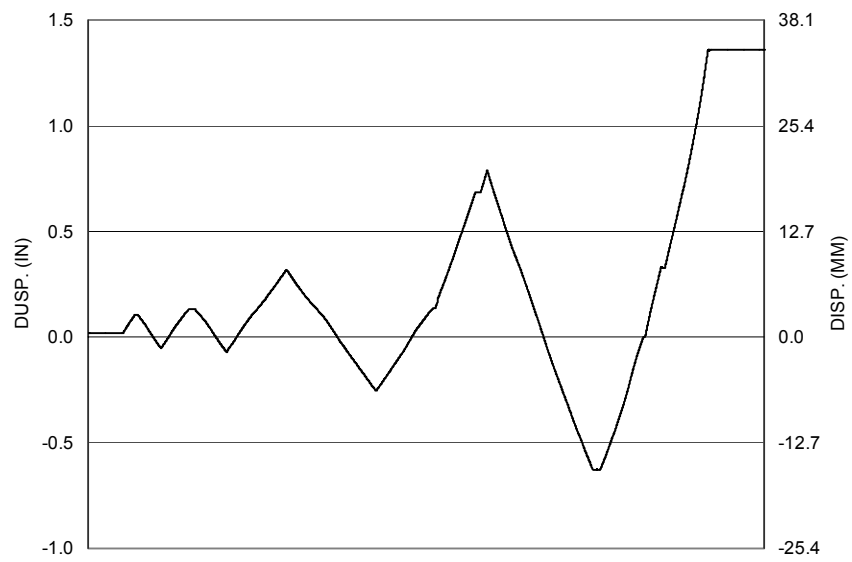
Figure A-220 Measured Displacement of NV32 for LFCD1S
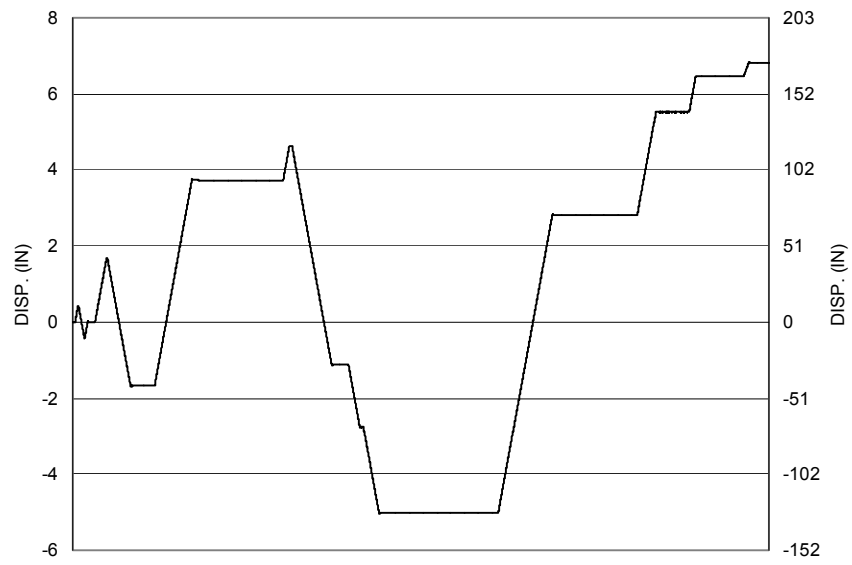
Figure A-221 Measured Displacement of Actuator for SFCD2S
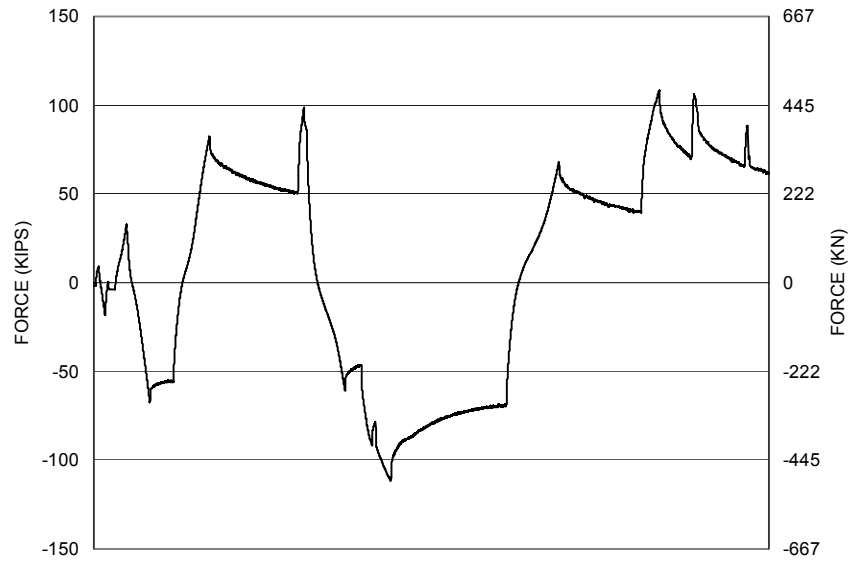
Figure A-222 Measured Force in Actuator for SFCD2S

305
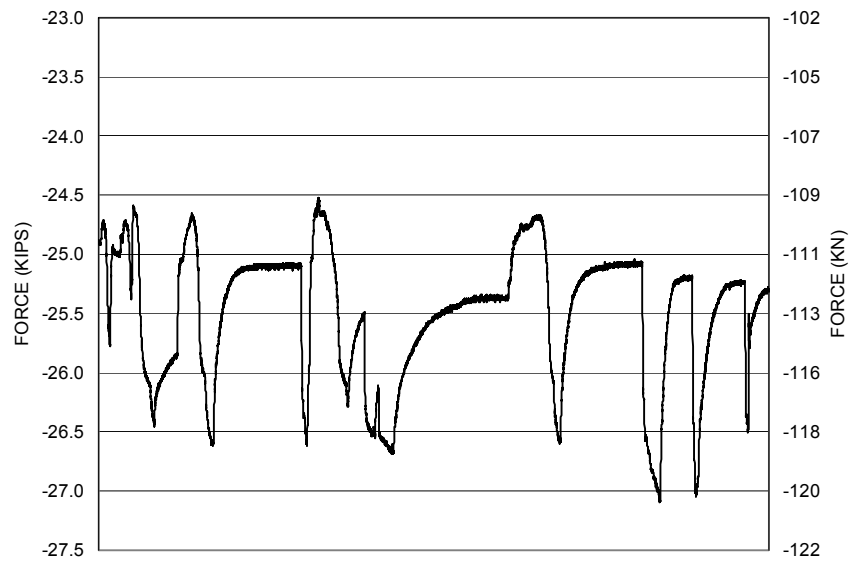
Figure A-223 Measured Force in South Axial Ram for SFCD2S
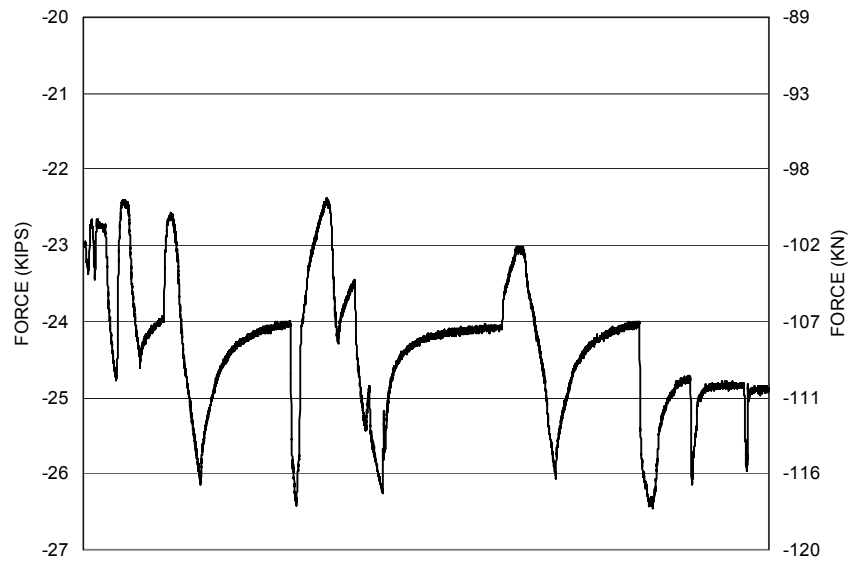
Figure A-224 Measured Force in North Axial Ram for SFCD2S

306
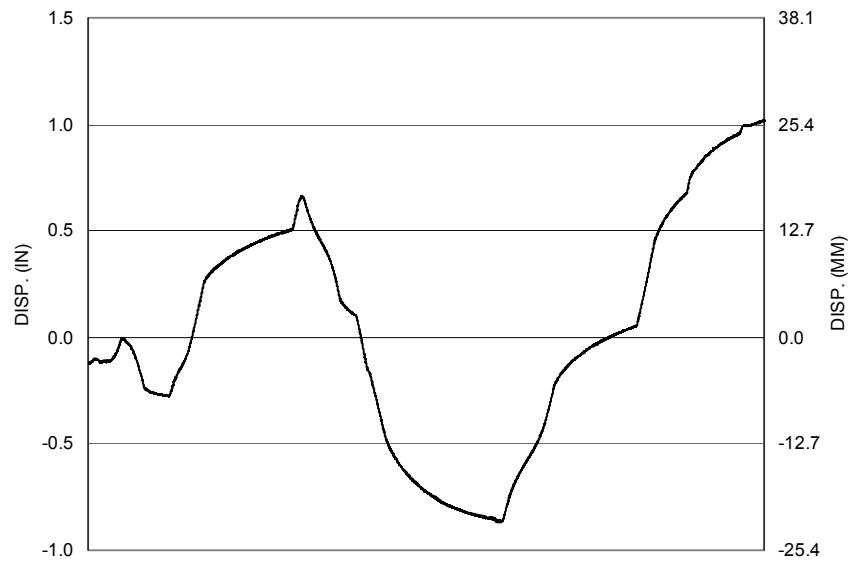
Figure A-225 Measured Displacement of Footing for SFCD2S
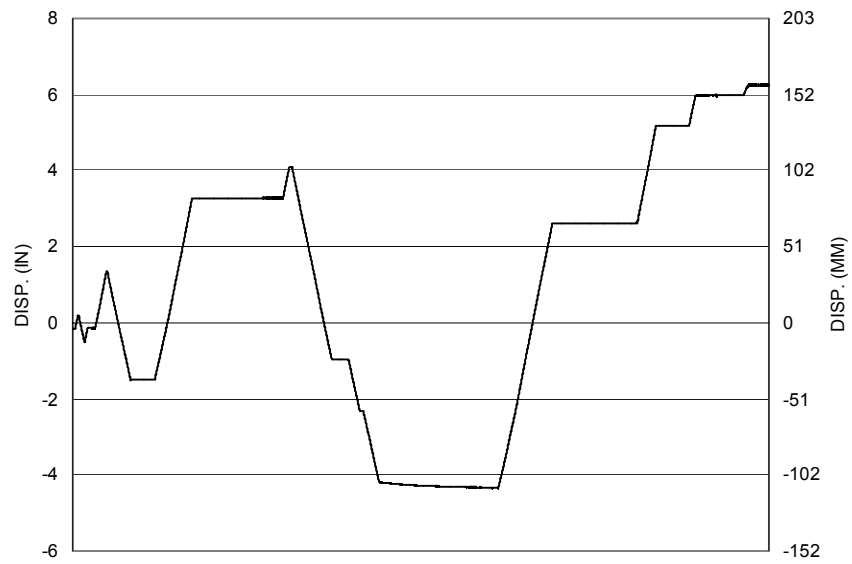
Figure A-226 Measured Displacement of Bent Top for SFCD2S
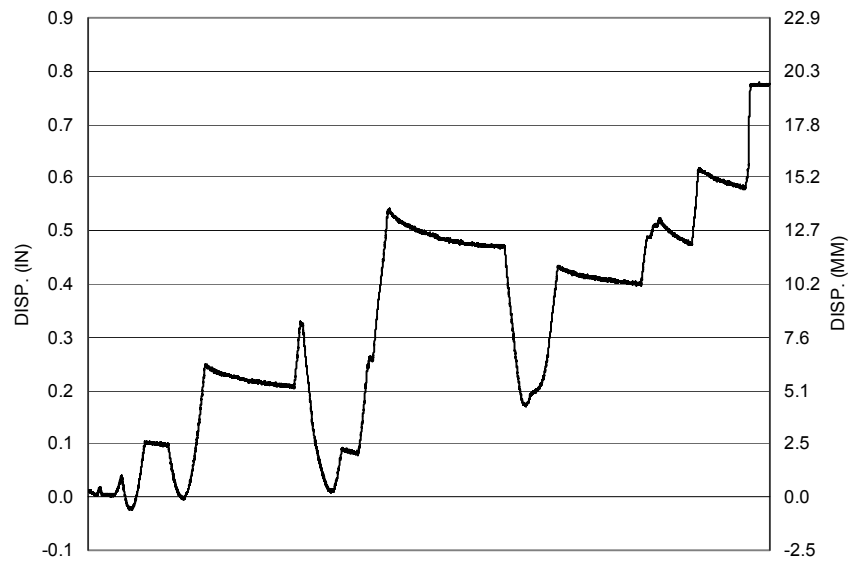
Figure A-227 Measured Vertical Displacement of Beam center for SFCD2S
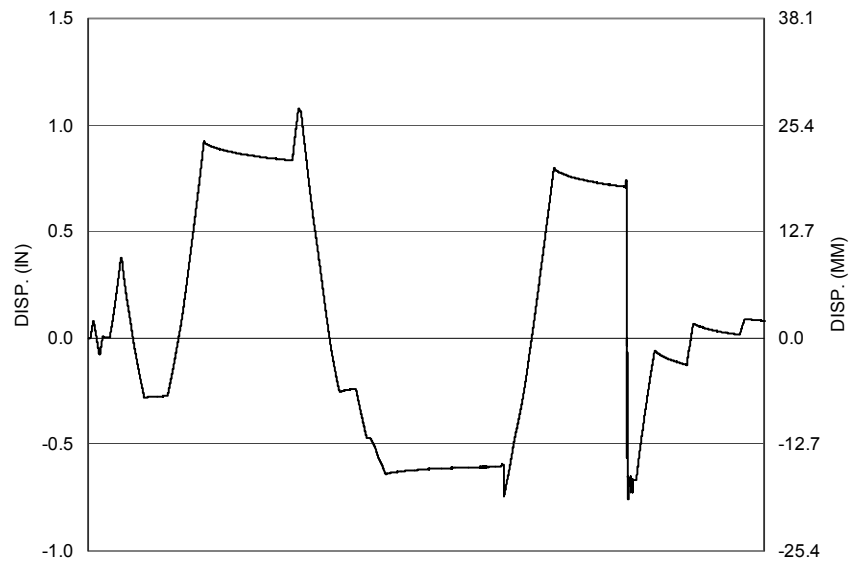
Figure A-228 Measured Displacement in NV1 for SFCD2S
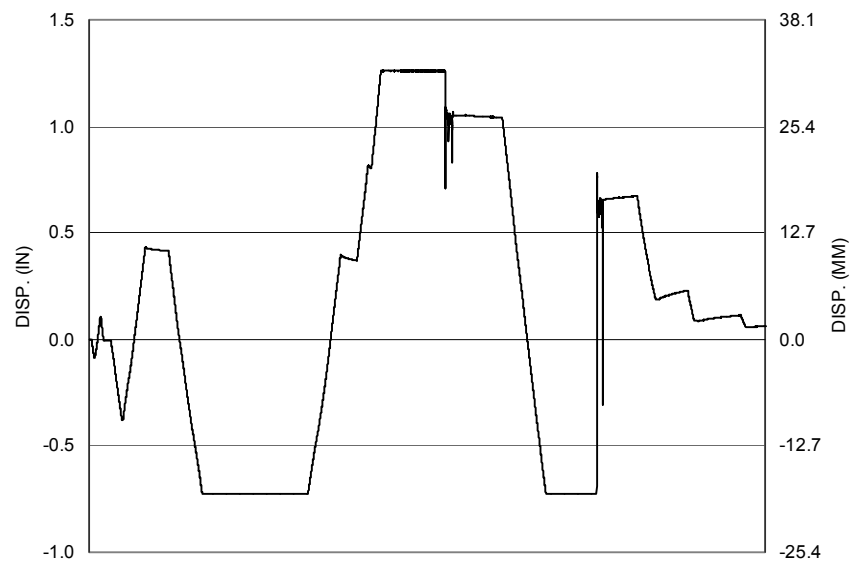
Figure A-229 Measured Displacement in NV2 for SFCD2S
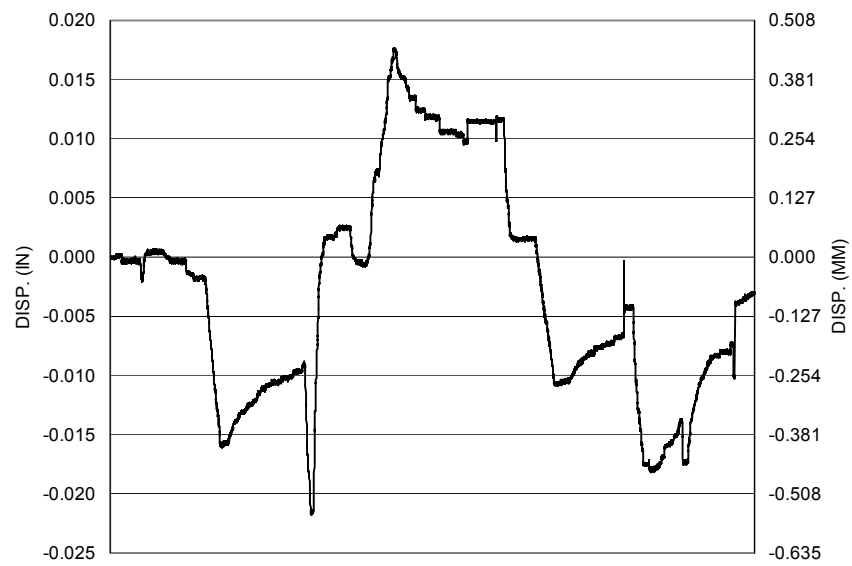
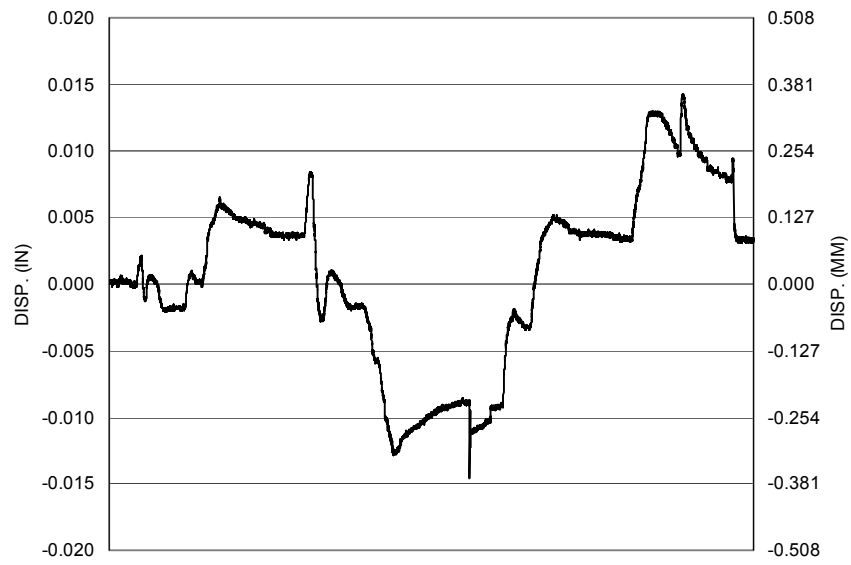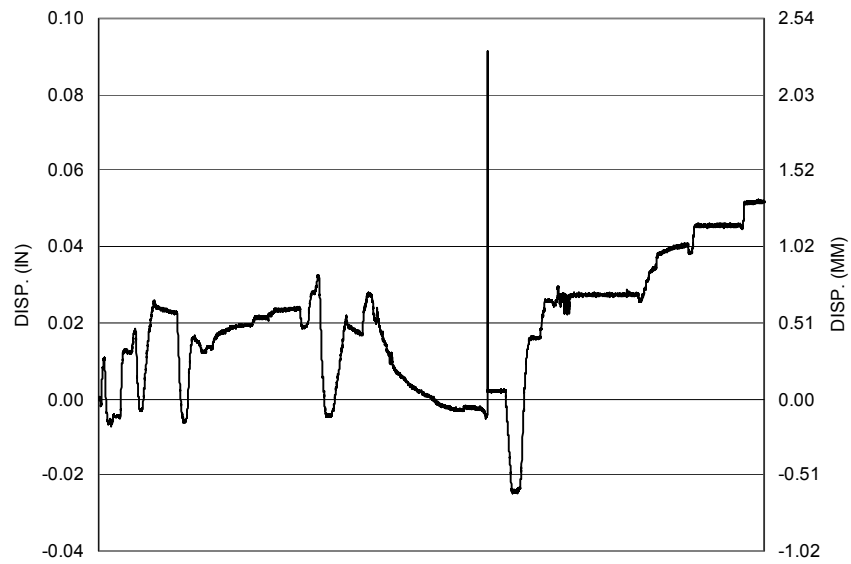
Figure A-230 Measured Displacement in NV3 for SFCD2S
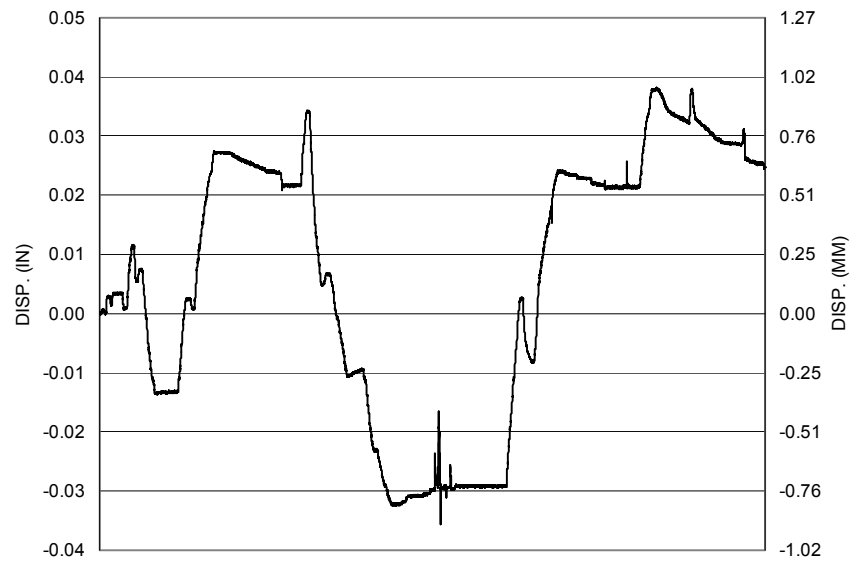
Figure A-231 Measured Displacement in NV4 for SFCD2S
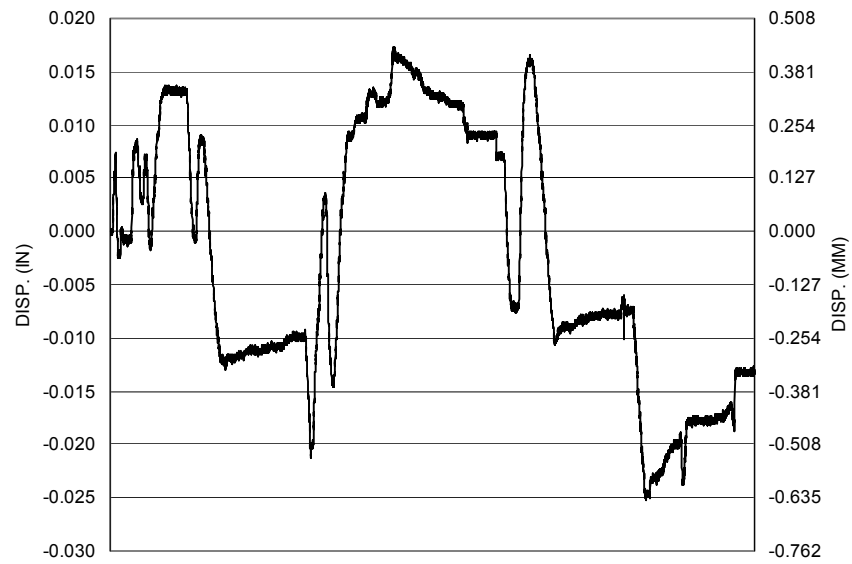
Figure A-232 Measured Displacement in NV5 for SFCD2S
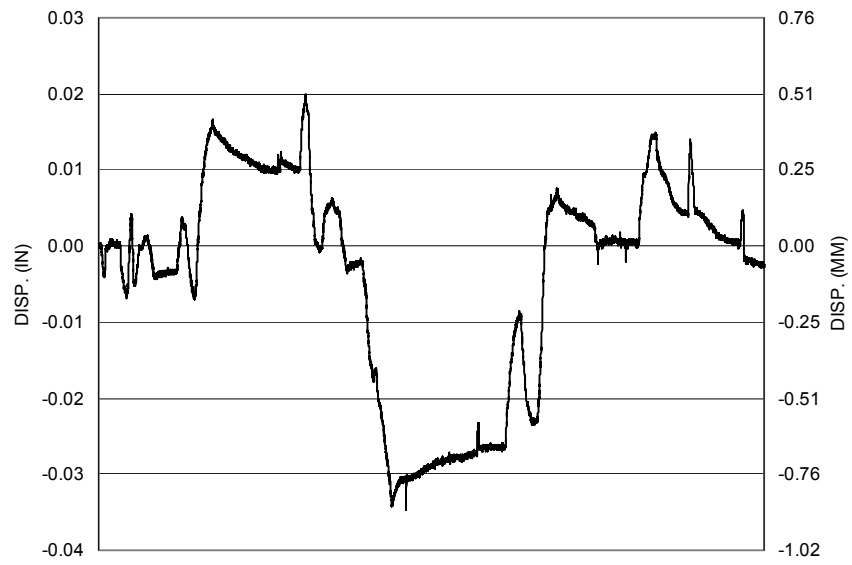
Figure A-233 Measured Displacement in NV6 for SFCD2S
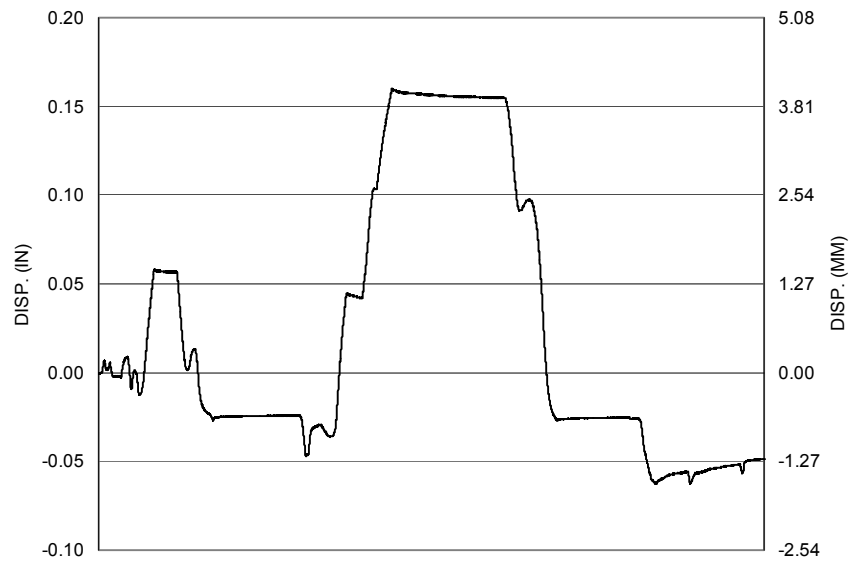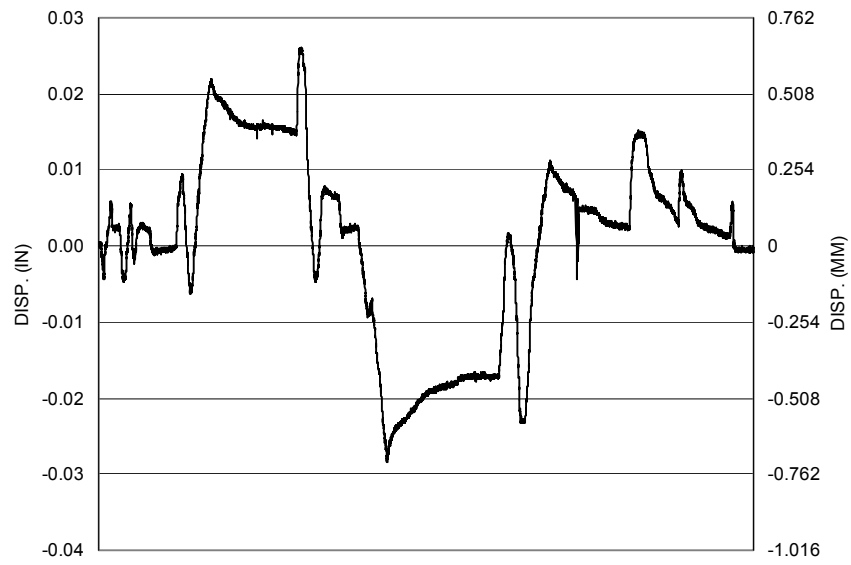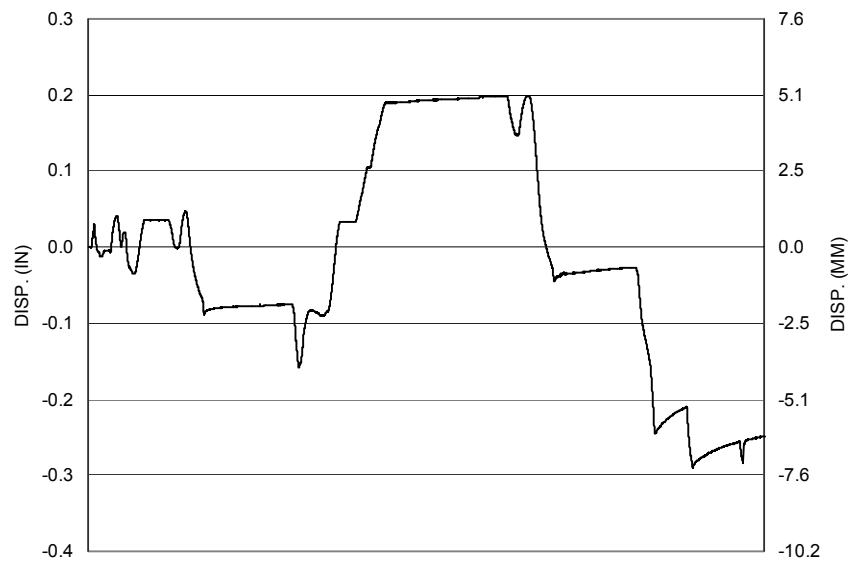

Figure A-234 Measured Displacement in NV7 for SFCD2S

311
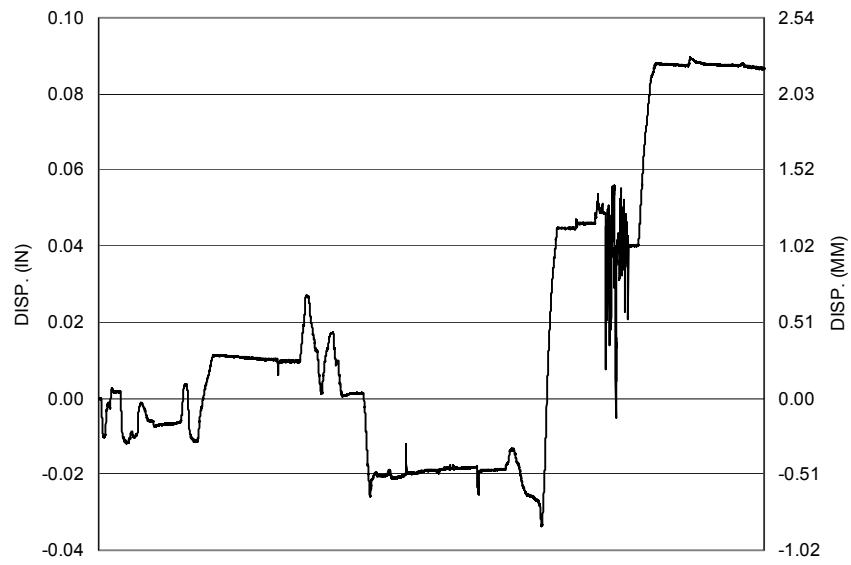
Figure A-235 Measured Displacement in NV8 for SFCD2S
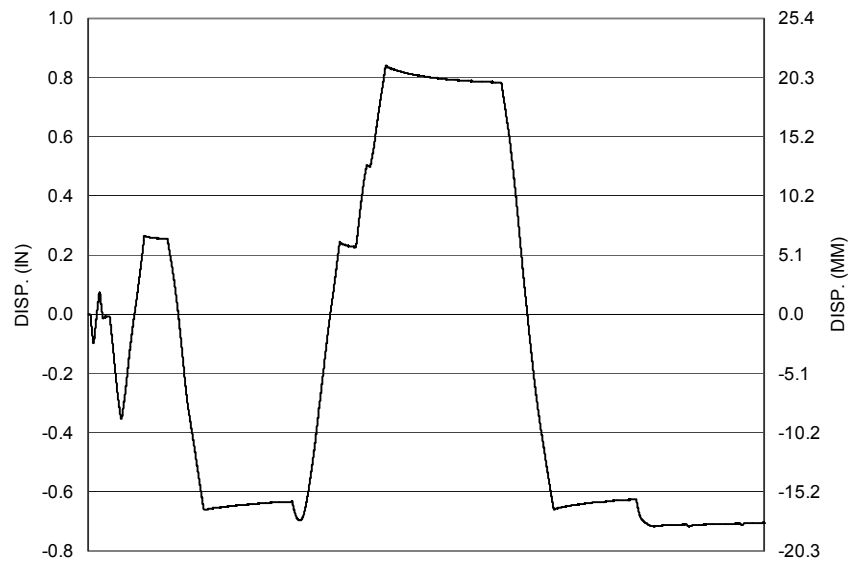
Figure A-236 Measured Displacement in NV9 for SFCD2S
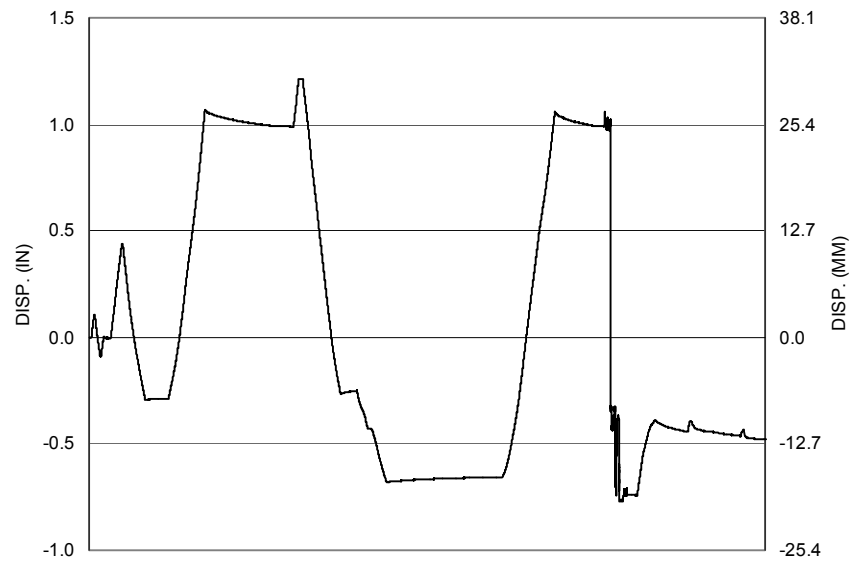
Figure A-237 Measured Displacement in NV10 for SFCD2S

Figure A-238 Measured Displacement in NV11 for SFCD2S

Figure A-239 Measured Displacement in NV12 for SFCD2S
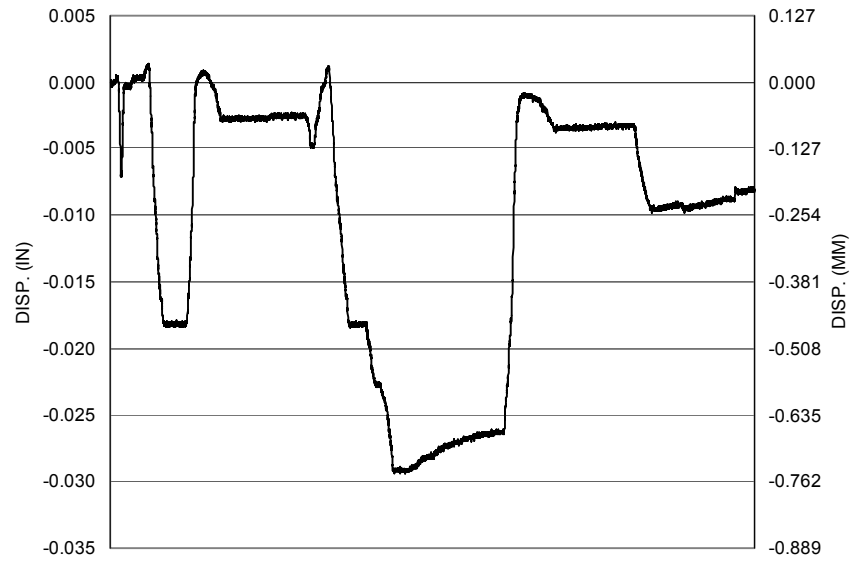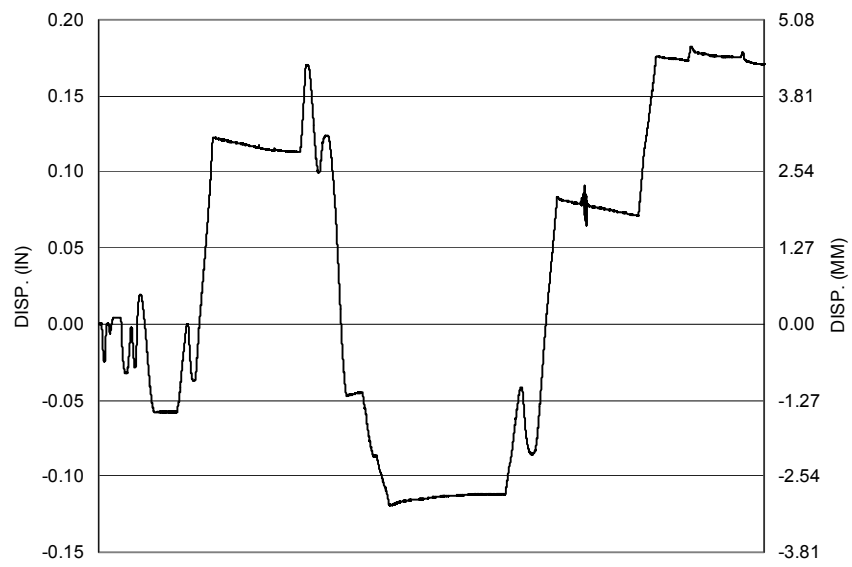

Figure A-240 Measured Displacement in NV13 for SFCD2S

314

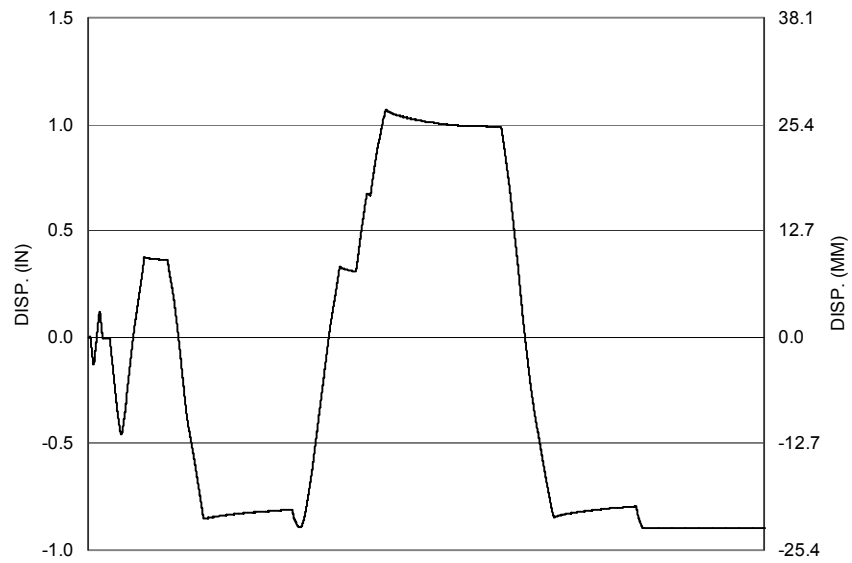**Figure A-241 Measured Displacement in NV14 for SFCD2S**
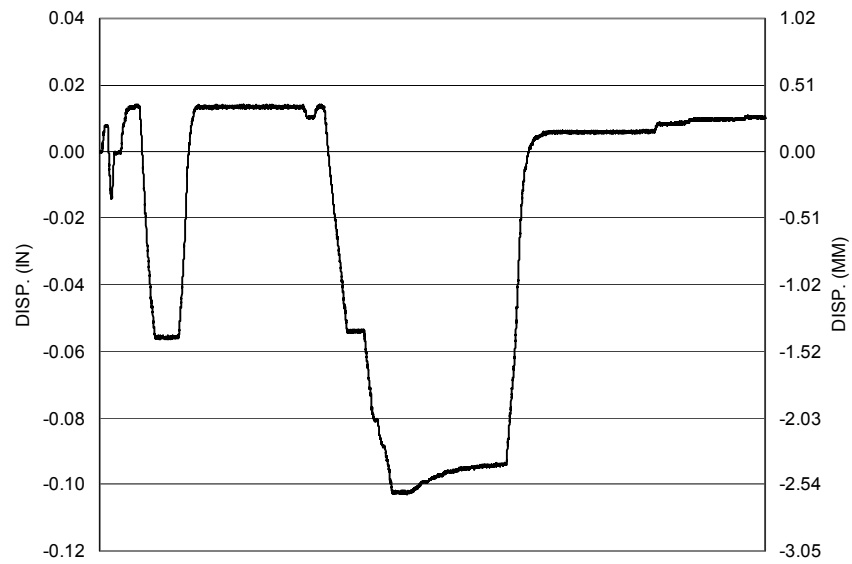
Figure A-242 Measured Displacement in NV15 for SFCD2S
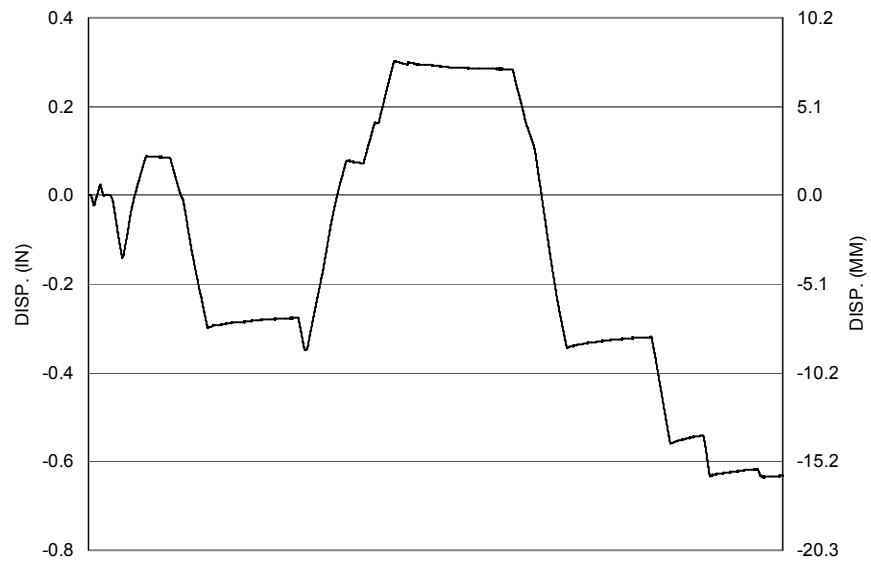
Figure A-243 Measured Displacement in NV16 for SFCD2S
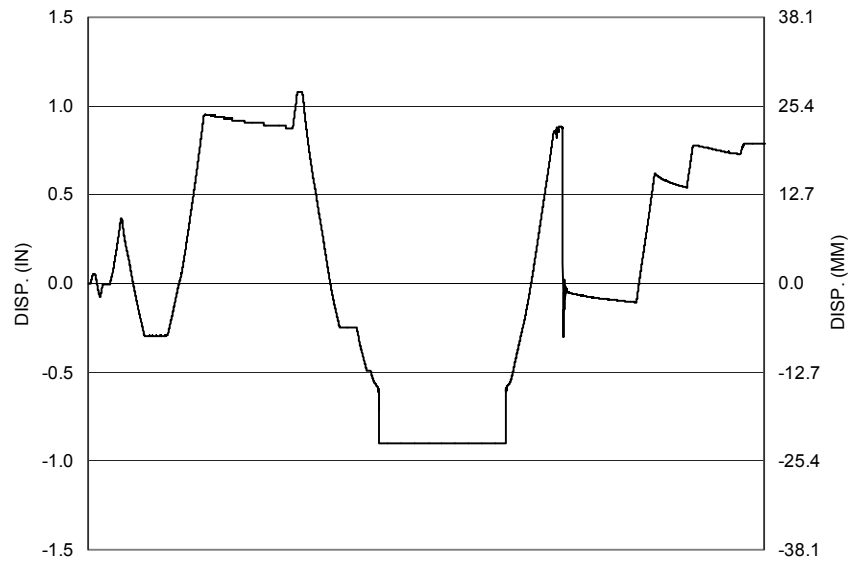
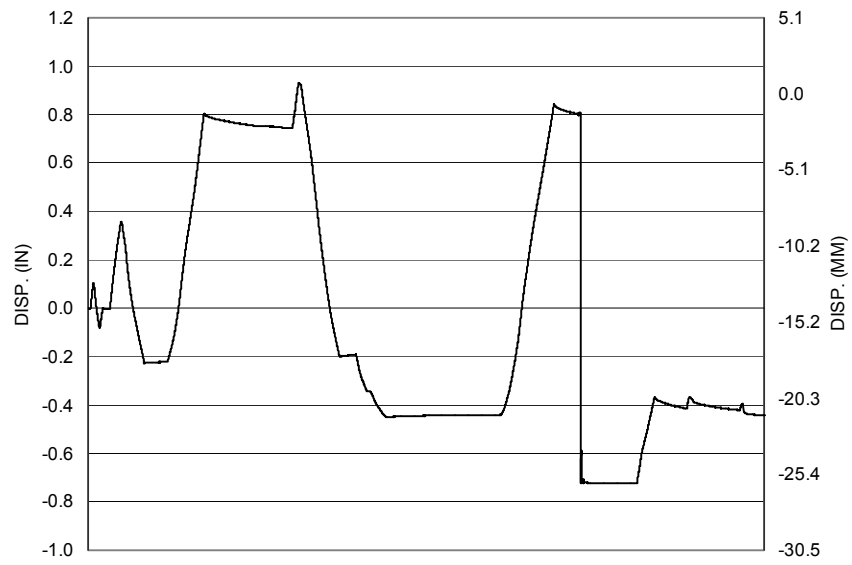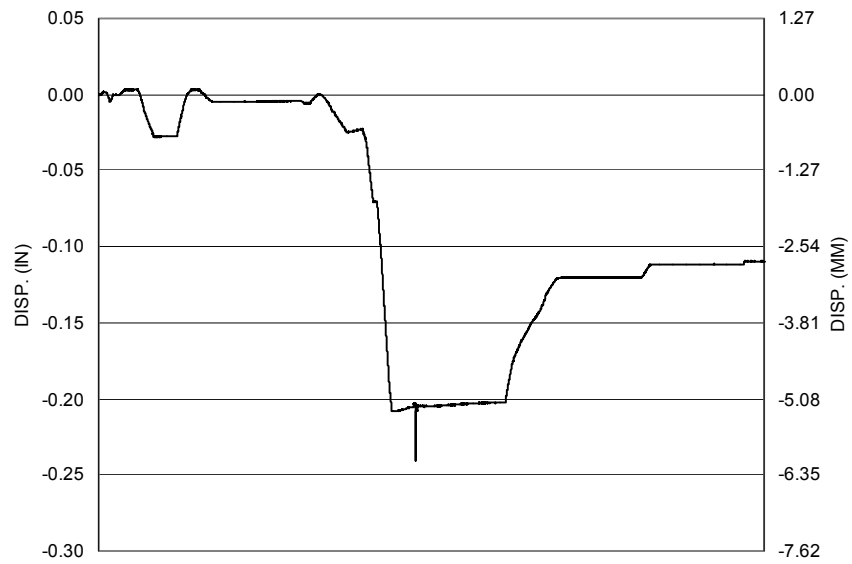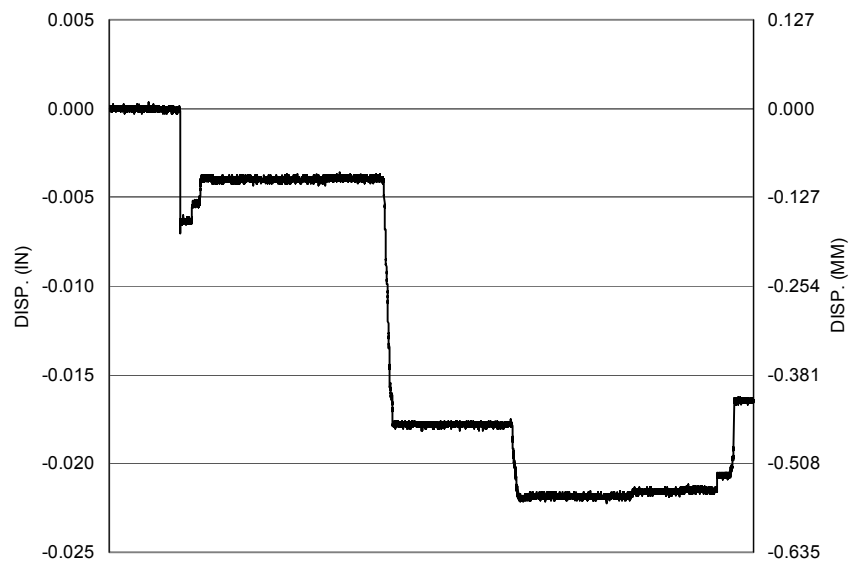**Figure A-244 Measured Displacement in NV17 for SFCD2S**

316
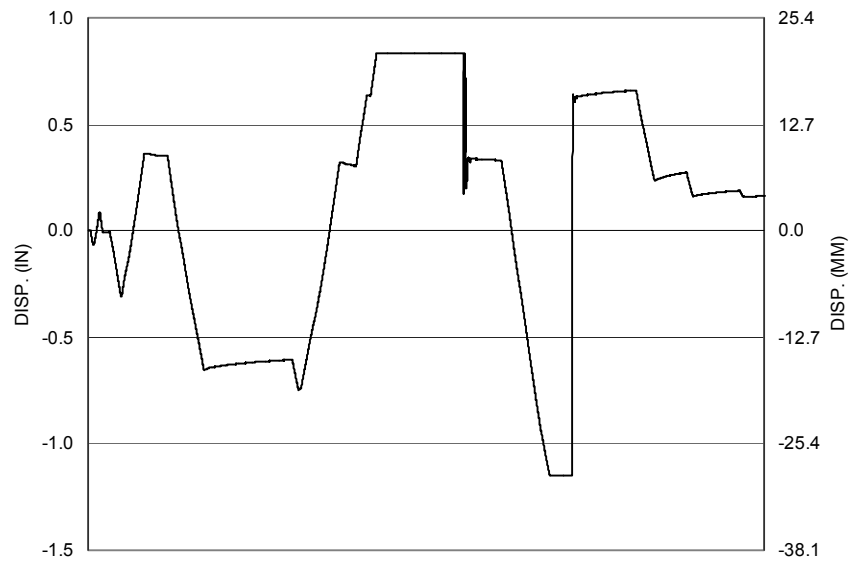
Figure A-245 Measured Displacement in NV18 for SFCD2S
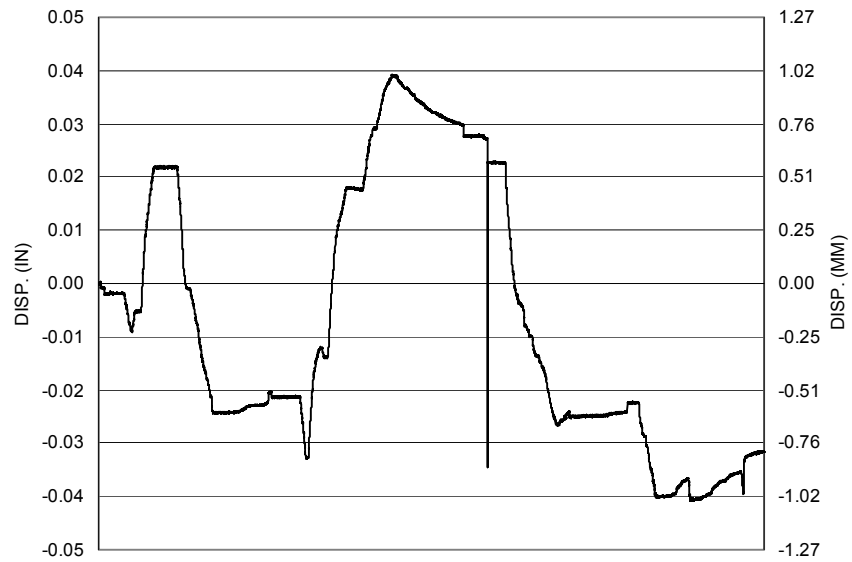
Figure A-246 Measured Displacement in NV19 for SFCD2S

Figure A-247 Measured Displacement in NV20 for SFCD2S

Figure A-248 Measured Displacement in NV21 for SFCD2S
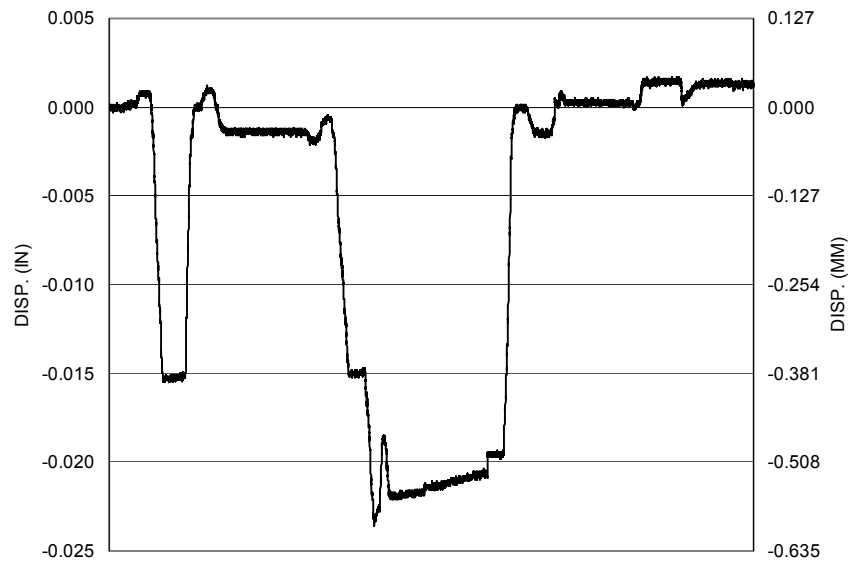
318

Figure A-249 Measured Displacement in NV22 for SFCD2S

Figure A-250 Measured Displacement in NV23 for SFCD2S

Figure A-251 Measured Displacement in NV24 for SFCD2S

Figure A-252 Measured Displacement in NV25 for SFCD2S

Figure A-253 Measured Displacement in NV26 for SFCD2S

Figure A-254 Measured Displacement in NV27 for SFCD2S

Figure A-255 Measured Displacement in NV28 for SFCD2S

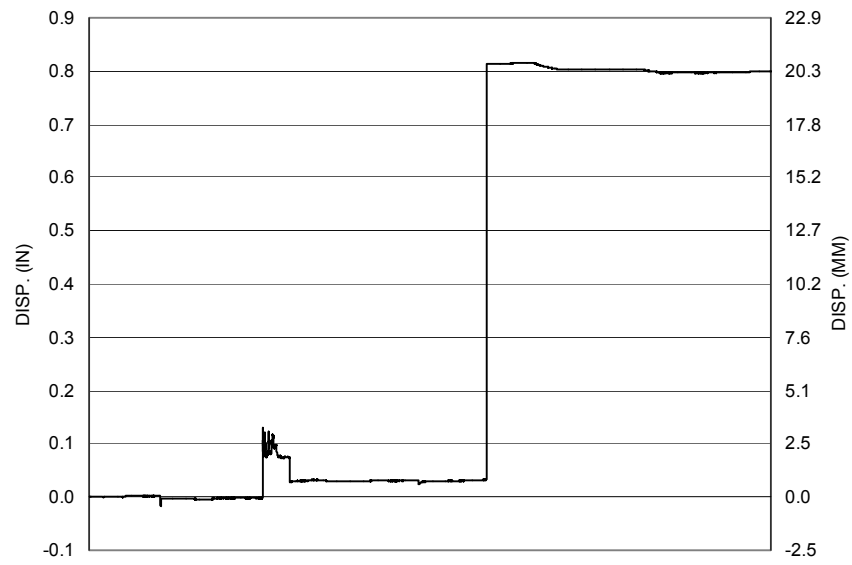**Figure A-256 Measured Displacement in NV29 for SFCD2S**

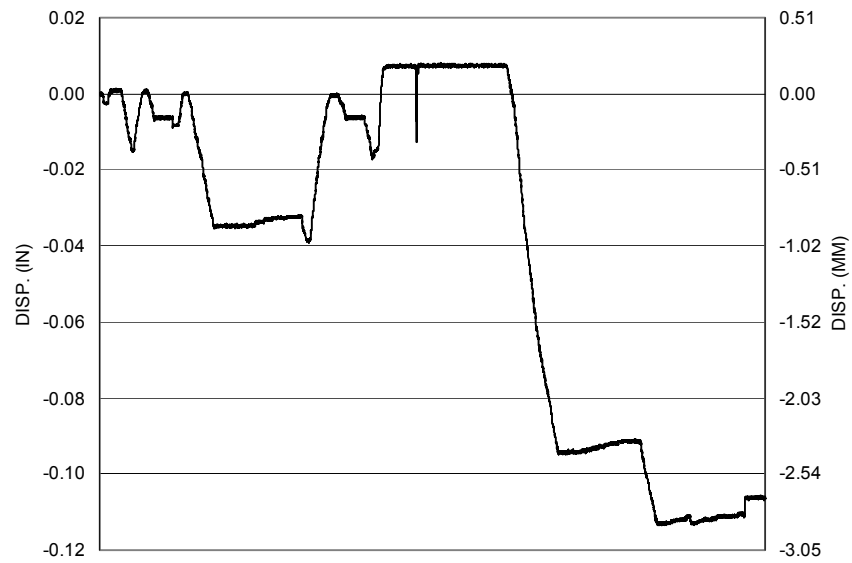**Figure A-257 Measured Displacement in NV30 for SFCD2S**
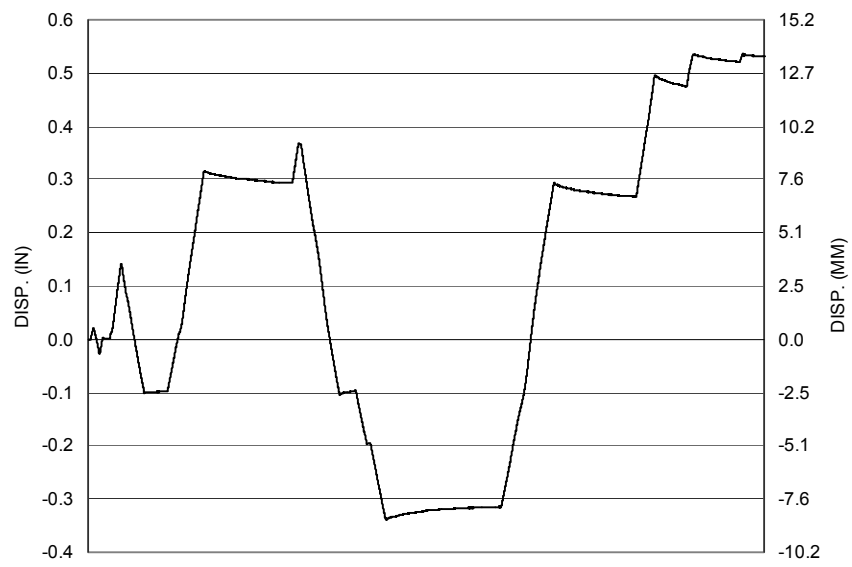

Figure A-258 Measured Displacement in NV31 for SFCD2S

Figure A-259 Measured Displacement in NV32 for SFCD2S